

Water Science and Technology Library

Ramakar Jha · V. P. Singh ·  
Vivekanand Singh · L. B. Roy ·  
Roshni Thendiyath *Editors*

# Hydrological Modeling

Hydraulics, Water Resources and Coastal  
Engineering

 Springer

# Water Science and Technology Library

Volume 109

## **Editor-in-Chief**

V. P. Singh, Department of Biological and Agricultural Engineering & Zachry  
Department of Civil and Environmental Engineering, Texas A&M University,  
College Station, TX, USA

## **Editorial Board**

R. Berndtsson, Lund University, Lund, Sweden

L. N. Rodrigues, Brasília, Brazil

Arup Kumar Sarma, Department of Civil Engineering, Indian Institute of  
Technology Guwahati, Guwahati, Assam, India

M. M. Sherif, Civil and Environmental Engineering Department, UAE University,  
Al-Ain, United Arab Emirates

B. Sivakumar, School of Civil and Environmental Engineering, The University of  
New South Wales, Sydney, NSW, Australia

Q. Zhang, Faculty of Geographical Science, Beijing Normal University, Beijing,  
China

The aim of the *Water Science and Technology Library* is to provide a forum for dissemination of the state-of-the-art of topics of current interest in the area of water science and technology. This is accomplished through publication of reference books and monographs, authored or edited. Occasionally also proceedings volumes are accepted for publication in the series. *Water Science and Technology Library* encompasses a wide range of topics dealing with science as well as socio-economic aspects of water, environment, and ecology. Both the water quantity and quality issues are relevant and are embraced by *Water Science and Technology Library*. The emphasis may be on either the scientific content, or techniques of solution, or both. There is increasing emphasis these days on processes and *Water Science and Technology Library* is committed to promoting this emphasis by publishing books emphasizing scientific discussions of physical, chemical, and/or biological aspects of water resources. Likewise, current or emerging solution techniques receive high priority. Interdisciplinary coverage is encouraged. Case studies contributing to our knowledge of water science and technology are also embraced by the series. Innovative ideas and novel techniques are of particular interest.

Comments or suggestions for future volumes are welcomed.

Vijay P. Singh, Department of Biological and Agricultural Engineering & Zachry Department of Civil and Environment Engineering, Texas A & M University, USA  
Email: [vsingh@tamu.edu](mailto:vsingh@tamu.edu)

All contributions to an edited volume should undergo standard peer review to ensure high scientific quality, while monographs should also be reviewed by at least two experts in the field.

Manuscripts that have undergone successful review should then be prepared according to the Publisher's guidelines manuscripts: <https://www.springer.com/gp/authors-editors/book-authors-editors/book-manuscript-guidelines>

More information about this series at <https://link.springer.com/bookseries/6689>

Ramakar Jha · V. P. Singh · Vivekanand Singh ·  
L. B. Roy · Roshni Thendiyath  
Editors

# Hydrological Modeling

Hydraulics, Water Resources and Coastal  
Engineering

 Springer



*Editors*

Ramakar Jha  
Department of Civil Engineering  
National Institute of Technology  
Patna, India

Vivekanand Singh  
Department of Civil Engineering  
National Institute of Technology Patna  
Patna, India

Roshni Thendiyath  
Department of Civil Engineering  
National Institute of Technology Patna  
Patna, India

V. P. Singh  
Department of Biological and Agricultural  
Engineering  
Texas A&M University  
College Station, TX, USA

L. B. Roy  
Department of Civil Engineering  
National Institute of Technology Patna  
Patna, India

ISSN 0921-092X

ISSN 1872-4663 (electronic)

Water Science and Technology Library

ISBN 978-3-030-81357-4

ISBN 978-3-030-81358-1 (eBook)

<https://doi.org/10.1007/978-3-030-81358-1>

© The Editor(s) (if applicable) and The Author(s), under exclusive license to Springer Nature Switzerland AG 2022

This work is subject to copyright. All rights are solely and exclusively licensed by the Publisher, whether the whole or part of the material is concerned, specifically the rights of translation, reprinting, reuse of illustrations, recitation, broadcasting, reproduction on microfilms or in any other physical way, and transmission or information storage and retrieval, electronic adaptation, computer software, or by similar or dissimilar methodology now known or hereafter developed.

The use of general descriptive names, registered names, trademarks, service marks, etc. in this publication does not imply, even in the absence of a specific statement, that such names are exempt from the relevant protective laws and regulations and therefore free for general use.

The publisher, the authors and the editors are safe to assume that the advice and information in this book are believed to be true and accurate at the date of publication. Neither the publisher nor the authors or the editors give a warranty, expressed or implied, with respect to the material contained herein or for any errors or omissions that may have been made. The publisher remains neutral with regard to jurisdictional claims in published maps and institutional affiliations.

This Springer imprint is published by the registered company Springer Nature Switzerland AG  
The registered company address is: Gewerbestrasse 11, 6330 Cham, Switzerland

# Contents

<b>1</b>	<b>Performance Improvement of Usbr VI Stilling Basin Model for Pipe Outlet</b> .....	<b>1</b>
	H. L. Tiwari, Arun Goel, A. K. Sharma, and Ankit Balvanshi	
<b>2</b>	<b>Bio-Inspired Genetic Algorithm for Optimal Design of Water Distribution Networks</b> .....	<b>9</b>
	Seelam Naga Poojitha and Vinayakam Jothiprakash	
<b>3</b>	<b>Assessments of Meteorological Drought Indices Using SPI and RDI in Mehsana Region, Gujarat, India</b> .....	<b>21</b>
	Pranav B. Mistry and T. M. V. Suryanarayana	
<b>4</b>	<b>Top Surface Soil Moisture Retrieval Using C-Band Synthetic Aperture Radar Over Kudremukh Grasslands</b> .....	<b>31</b>
	Punithraj Gururaj, Pruthviraj Umesh, P. E. Kukku Sara, and Amba Shetty	
<b>5</b>	<b>Meteorological Drought Assessment in the Bharathapuzha River Basin</b> .....	<b>43</b>
	M. A. Jincy Rose and N. R. Chithra	
<b>6</b>	<b>Experimental and Numerical Analysis of Mean Pressure Coefficient on C-Shaped Building with and Without Round Corner</b> .....	<b>55</b>
	Monalisa Mallick, Awadhesh Kumar, and Kanhu Charan Patra	
<b>7</b>	<b>A Framework for the Selection of Threshold in Partial Duration Series Modeling</b> .....	<b>69</b>
	Nibedita Guru and Ramakar Jha	
<b>8</b>	<b>Integrated RUSLE and GIS Approach for Estimating Soil Erosion of Watershed in Karjat</b> .....	<b>85</b>
	Raju Narwade and Shrikant Charhate	

<b>9</b>	<b>Swat Application for Water Balance Assessment of Koyna River Basin, Maharashtra, India</b> .....	<b>97</b>
	Amarsinh B. Landage and Ashok K. Keshari	
<b>10</b>	<b>Identification of Suitable Sites for Water Storage Structure in Andhiyarkore Watershed of Chhattisgarh State India</b> .....	<b>109</b>
	Parul Vinze and Ishtiyag Ahmad	
<b>11</b>	<b>Drought Analysis Using Standardized Precipitation Index and Supplemental Irrigation Planning in Banka, Bihar</b> .....	<b>125</b>
	Abhishek Kumar Choudhary and Vivekanand Singh	
<b>12</b>	<b>Multisite Calibration of the Ghataprabha Sub-Basin Using Soil and Water Assessment Tool</b> .....	<b>139</b>
	A. N. B. Gowda, Nagraj S. Patil, and Nataraja M	
<b>13</b>	<b>Agricultural Drought Assessment Using GIS: A Case Study</b> .....	<b>165</b>
	C. Prakasam and R. Saravanan	
<b>14</b>	<b>Design of Branched Pipe Networks Using Reliability and Total Annual Cost</b> .....	<b>183</b>
	Deepak Singh, Arkaja, Munendra Kumar, and Saurabh Sah	
<b>15</b>	<b>An Experimental Study on the Effect of Soil Characteristics and Infiltration Rate on Hortons Decay Constant</b> .....	<b>195</b>
	Anupal Baruah and Rishov Barua	
<b>16</b>	<b>Genetic Algorithm for Minimization of Variance of Pipe Flow-Series for Looped Water Distribution Networks</b> .....	<b>205</b>
	Shweta Rathi and Rajesh Gupta	
<b>17</b>	<b>Applications of Building Information Modelling for Water Infrastructure Development</b> .....	<b>221</b>
	M. P. Rahla Rabia and D. Sathish Kumar	
<b>18</b>	<b>Snow Cover Change in Kullu District Using Remote Sensing and Geographic Information System</b> .....	<b>231</b>
	Ashish Singh and R. K. Shukla	
<b>19</b>	<b>Forecasting Standardized Precipitation Index Using Wavelet-Coupled MARS and SVM Model in Punpun River Sub-Basin (Bihar), India</b> .....	<b>241</b>
	Lalit Kumar and Ramakar Jha	
<b>20</b>	<b>Error Due to DEM Sources in Catchment Area and River Network Using D8 Algorithm</b> .....	<b>259</b>
	Harikrishna Sukumaran and Sanat Nalini Sahoo	
<b>21</b>	<b>Dam Break Flow Simulation Model for Preparing Emergency Action Plans for Bargi Dam Failure</b> .....	<b>271</b>
	S. Verma, Sachin, and K. C. Patra	

<b>22</b>	<b>Discrepancy in Infiltration Equation Parameters While Using Ponded and Tension Boundary Pressure Head Conditions</b> .....	287
	Aparimita Priyadarshini Naik and Sreeja Pekkat	
<b>23</b>	<b>Using CartoDEM Data for Dam Break Flood Hazard Mapping in a Hilly Terrain</b> .....	299
	Pankaj Mani, Rakesh Kumar, and J. P. Patra	
<b>24</b>	<b>Hydrologic and Hydraulic Modelling of a Bridge</b> .....	317
	Jagadish Prasad Patra, Rakesh Kumar, and Pankaj Mani	
<b>25</b>	<b>New Approach to Evolve Soil Water Retention Curve in Lower Kosi Basin, India</b> .....	327
	Ray Singh Meena Meena and Ramakar Jha	
<b>26</b>	<b>Variability of Rainfall, Temperature, and Potential Evapotranspiration at Annual Time Scale Over Tapi to Tadri River Basin, India</b> .....	349
	Prem Mahyavanshi, V. D. Loliyana, and Priyank J. Sharma	
<b>27</b>	<b>Design of Water Distribution Network for Educational Institute for Revised Demand</b> .....	365
	Nishant Sourabh, Mustafa Batliwala, and P. V. Timbadiya	
<b>28</b>	<b>Application of Numerical Modelling for Geomorphological Evolution and River Bank Shifting Part of Damodar River</b> .....	375
	C. Prakasam and R. Aravinth	
<b>29</b>	<b>Study on Impact of Urbanization by SWAT Model in Iril River, Northeast India</b> .....	385
	Pradyumna Kumar Behera and Thiyam Tampasana Devi	
<b>30</b>	<b>Comparison of Soil Infiltration Models Under Varying Land Cover Conditions in a Micro Watershed of Western Himalayan Region</b> .....	395
	Tabasum Rasool, Sajad Ahmad, Abdul Qayoom Dar, and Mushtaq A.Wani	
<b>31</b>	<b>Rainfall–Runoff Studies of Brahmani River Basin Using ANN</b> .....	411
	Swagatika Biswal, Bandita Naik, and K. K. Khatua	
<b>32</b>	<b>Estimation and Management of Irrigation Water Using WEAP Model in Tandula Reservoir Command Area</b> .....	423
	Yashvant Kumar Tikariha and Ishtiyah Ahmad	
<b>33</b>	<b>Integrated Hydrological and Hydraulic Model for Prediction of Inflows into Hathnur Reservoir</b> .....	437
	Vishal Kachhwaha and P. L. Patel	

<b>34</b>	<b>Hydrologic Modeling with SWAT in an Eastern Indian River Basin Using Different Gridded Data Sets</b> .....	<b>447</b>
	Soorya Sudesan, Renji Remesan, and Dhruvajyoti Sen	
<b>35</b>	<b>Analysis of Seepage from Parallel Triangular Furrows by Inverse Hodograph and Conformal Mapping Technique</b> .....	<b>459</b>
	Kshyana Prava Samal and G. C. Mishra	
<b>37</b>	<b>Sustainable Rainwater Harvesting System and Storm Water Management: A Case Study in Raipur Airport</b> .....	<b>479</b>
	Digeshwar Prasad Sahu and Mani Kant Verma	
<b>38</b>	<b>Hydrological Modeling of Dam Inflow Data Under Restricted Upstream Abstraction Data</b> .....	<b>491</b>
	Mridusmita Debnath and Ashok Mishra	
<b>39</b>	<b>Assessment of Agricultural Drought Vulnerability Using Remote Sensing and GIS: A Case Study of Lower Cauvery Basin, Tamil Nadu, India</b> .....	<b>505</b>
	Ramanarayan Sankriti, Saravanan Subbarayan, Manjunath Aluru, Leelambar Singh, Jacinth Jennifer J, and Devanantham Abijith	
<b>40</b>	<b>Assessment of Impact of Spatial Distribution of Rainfall on Streamflow Modelling Using Arcswat in the Noyyal River Catchment Tamil Nadu, India</b> .....	<b>517</b>
	Leelambar Singh, Saravanan Subbarayan, J. Jacinth Jennifer, D. Abhijith, and Ramanarayan Sankriti	

## About the Editors

**Ramakar Jha** is Chair Professor in the Department of Civil Engineering and has 30 years of experience in the field of hydrology and water resources engineering. He is presently working as Chair Professor in the Department of Civil Engineering, National Institute of Technology (NIT) Patna, India, which is a premier institute in India under the Ministry of Human Resource Development, Government of India. He served at various levels from Scientist-B to Scientist-E1 at National Institute of Hydrology (NIH), Roorkee, India, and as Professor in the Department of Civil Engineering, NIT Rourkela. He has worked and working as Country Coordinator of UNESCO-GWADI and Principal Investigator for many international (EU-FP7, DAAD, ADB, AUS-Aid) and national research and consultancy projects (ISRO, DST, MoWR, MHRD). Moreover, he served as Chair for many administrative positions and received a couple of international and national awards for research papers. Presently, he is working as Dr. Rajendra Prasad Chair for Water Resources under the Ministry of Water Resources, Government of India, in the Department of Civil Engineering, NIT Patna, Bihar.

**V. P. Singh** Texas A&M Professor of Indian origin is receiving a prestigious award for his world-renowned work on water. He is receiving the 2013 Lifetime Achievement Award from the American Society of Civil Engineers-Environmental and Water Resources Institute, otherwise known as the ASCE-EWRI. The award is in recognition of his work in the field of hydrology, which is the study of water in all aspects, such as quality, distribution, preservation, and transportation. Some of the work he has done has even created an entire new branch of hydrology—called entropic hydrology—that is connected to the study of entropy, which means essentially the study of order and disorder as it relates to the physical universe. His work is considered fundamental for flood planning and water modeling around the world. Since earning his doctorate degree, he has held teaching positions in some of the most well-known universities in the USA. He was Associate Research Professor of civil engineering at George Washington University from 1977 to 1978, Associate Professor of civil engineering at Mississippi University from 1978 to 1981, and Adjunct Professor as well as Coordinator of the Environmental and Water Resources Systems Engineering Program at Louisiana State University from 1999 to 2006 and 2001 to 2006,

respectively. He joined Texas A&M University in 2006, where he currently wears a number of different hats. He is Professor of biological and agricultural engineering, Professor of civil and environment engineering, and Caroline and William N. Lehrer Distinguished Chair in Water Engineering (Hydrology). He has authored or edited around 10 published works in the fields of engineering and hydrology.

**Vivekanand Singh** is Professor in the Department of Civil Engineering and has 28 years of experience in the field of river hydraulics, groundwater, and water resources engineering. He has published research papers in international journals including ASCE Journal. He has done national projects and consultancy during his work at NIT Patna. Prior to this, he was Scientist at National Institute of Hydrology, Roorkee. He organized several summer courses, conferences, and workshops. He has been working as Editor in some Indian journal.

**L. B. Roy** is Professor in the Department of Civil Engineering and has 33 years of experience in the field of water resources engineering as well as geotechnical engineering. He has been serving the Water Resources Engineering Department for long time and carried out various field-based research activities for different river systems of the region with special emphasis to floods. He has been involved in many research projects and published several research papers in peer-reviewed journals. He has been working for Intellectual Property Rights (IPR) and received awards for various activities.

**Roshni Thendiyath** is Assistant Professor in the Department of Civil Engineering and has 9 years of experience in the field of water resources engineering. She earned her Ph.D. in civil engineering at the University of Pisa, Italy. After obtaining Ph.D., she had joined National Institute of Technology Calicut, India, as Adhoc Faculty and later joined National Institute of Technology Patna as Assistant Professor. She has supervised two Ph.D. and more than 30 master's theses. Furthermore, she has been awarded DST-SERB project for the topic Two-Phase Flows and Water Quality in Rivers, funded by the Department of Science and Technology, MHRD, India. Results obtained from her research have been published nearly 30 papers in international journals and more than 15 papers in international conferences and three chapters. She is active in a variety of professional bodies, and she has organized numerous workshops and conferences in her academic career.

# Chapter 1

## Performance Improvement of Usbr VI Stilling Basin Model for Pipe Outlet



H. L. Tiwari, Arun Goel, A. K. Sharma, and Ankit Balvanshi

**Abstract** Flow from the pipe outlets under a high head of water emerges in the form of a straight, concentrated shooting jet. Hydraulic structures called stilling basins have to be provided for reducing the energy of high-velocity flow to prevent erosion of the natural bed downstream and banks of river or canal so that the flow beyond the basin does not endanger the stability of bed and banks of the downstream channel. The experimental investigation leading to the development of a new stilling basin model design for a non-circular pipe outlet using a triangular splitter block along with USBR VI impact wall and sloping end sill is reported in this paper. On the basis of the present study, the new stilling basin design has been compared with USBR VI stilling basin. The main aim of this research paper is to present an experimental study for the purpose of improving the performance of the USBR VI stilling basin for a non-circular pipe outlet by developing new physical models in the laboratory. The new models were tested in a rectangular-shaped pipe outlet of size 10.8 cm × 6.3 cm, for the Froude numbers, namely  $Fr = 1.85, 2.85$  and  $3.85$  in comparison to USBR VI stilling basin model recommended for the pipe outlets. The new models have been developed by putting the triangular splitter block while keeping the other configuration of stilling basin geometry the same as suggested by the USBR VI stilling basin. The scour pattern was measured for each test run. The performance of the basin was compared by performance index (PI). After twelve test runs, it is found that, for a given Froude number range, by inserting the triangular splitter block with the same impact wall along with the end sill, the performance of stilling basin is improved, and also the length of the newly developed basin is reduced to 29% as compared to USBR VI stilling basin for given flow conditions.

---

H. L. Tiwari (✉) · A. K. Sharma · A. Balvanshi  
Department of Civil Engineering, Maulana Azad National Institute of Technology, Bhopal, India

A. Goel  
Department of Civil Engineering, NIT Kurukshetra, Kurukshetra, India



## 1.1 Introduction

Stilling basins are commonly used for the purpose of dissipating the excess kinetic energy of flowing water downstream of hydraulic structures like overflow spillways, sluices, pipe outlets, etc. in order to reduce the scouring of the riverbed and failure of the structure (Alikhani et al. 2010). Various types of recommended stilling basins used for pipe outlets are USBR VI stilling basin (Bradley and Peterka 1957), Manifold stilling basin (Fiala and Maurice 1961), Contra Costa energy dissipater (Flammer et al. 1970), USU energy dissipater (Garde et al. 1986), (Noshi 1999), Counter current energy dissipater (Goel 2008), Garde energy dissipater (Garde et al. 1986), Vema and Goel energy dissipater (Tiwari and Goel 2014), Tiwari (2013a, b) Tiwari and Goel (2016), Tiwari (2013a, b), Tiwari and Gahlot (2012) and Tiwari et al. (2011a, b), Verma and Goel (2000, 2003), etc. For any stilling basin, appurtenances play an important role in the reduction of the kinetic energy of flowing water. Any stilling basin for a pipe outlet consists of appurtenances like splitter block, impact wall, intermediate sill and an end sill. The use of an impact wall with an end sill is a common practice to reduce the jump length and confine it on the stilling basin (Vollmer and Khader 1971). The location of an impact wall is quite important for improving the dissipation of energy. In the USBR stilling basin type VI model, a hanging baffle wall along with sloping end sill is used as proposed by Bradley and Peterka (1957), Garde et al. (1986), and Tiwari et al. (2013, 2014) and they have also recommended the impact wall along with end sill. The present research paper investigates the basin performance to develop a new efficient and economical model for pipe outlet in comparison to USBR VI stilling basin model by inserting the splitter block along with sloping end sill and impact wall. Performance of stilling basin models is compared with performance index (PI). A higher value of PI indicates better performance of the model.

## 1.2 Experimental Arrangement and Procedure

The experiments were conducted in a recirculating laboratory flume of 0.95 m wide, 1 m deep and 25 m long. The width of the flume was reduced to 58.8 cm by constructing a brick wall along the length for keeping the ratio of the width of the basin to the equivalent diameter of rectangular outlet equal to 6.3 as per the design of Garde et al. (1986). A rectangular pipe of 10.8 cm  $\times$  6.3 cm was used to represent the outlet flow. The exit of the pipe was kept above stilling basin by one equivalent diameter ( $1d = 9.3$  cm). To observe the scour after the end sill of stilling basin, an erodible bed was made of coarse sand passing through IS sieve opening 2.36 mm and retained on IS sieve opening 1.18 mm. The maximum depth of scour ( $d_m$ ) and its distance from end sill ( $d_s$ ) were measured for each test after one hour run time. The depth of flow over the erodible bed was maintained equal to the normal depth of flow. The stilling basin USBR type VI model, proposed by Bradley and Peterka (1957), was fabricated with an impact wall of size 20.46 cm  $\times$  58.8 cm with a hood

of size 9.3cm x 58.8 cm, and sloping end sill of height 9.3 cm and base width 9.3 cm was fabricated. The discharge was measured by a calibrated venturi meter installed in the feeding pipe. With the operation of tail gate, the desired steady flow condition with normal depth was maintained (Fig. 1.1).

After one hour of the test run, the motor was switched off. The value of maximum depth of scour ( $d_m$ ) and its location from the end sill ( $d_s$ ) were noted. USBR VI model was tested with impact wall and end sill and then again models were tested by changing the location of impact wall at basin length of  $7d$ . All tested models with appurtenances are shown in Figs. 1.2, 1.3 and 1.4. All the testing were performed

**Fig. 1.1** Triangular shape splitter block

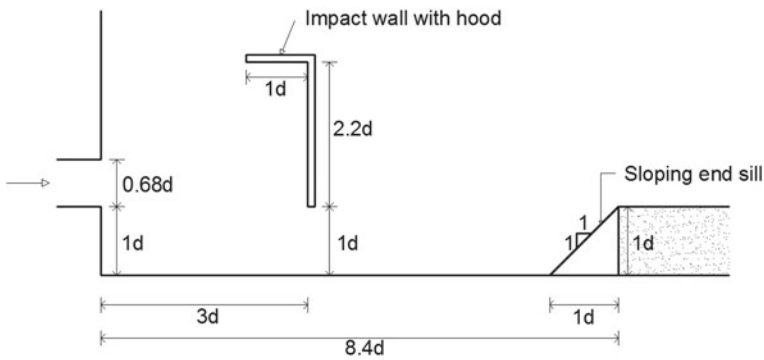
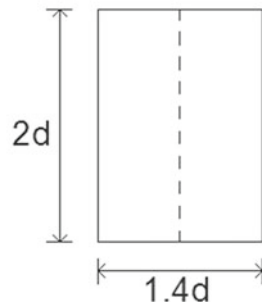
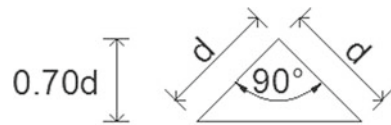


**Fig. 1.2** USBR VI model with impact wall and end sill (model MSM-6)

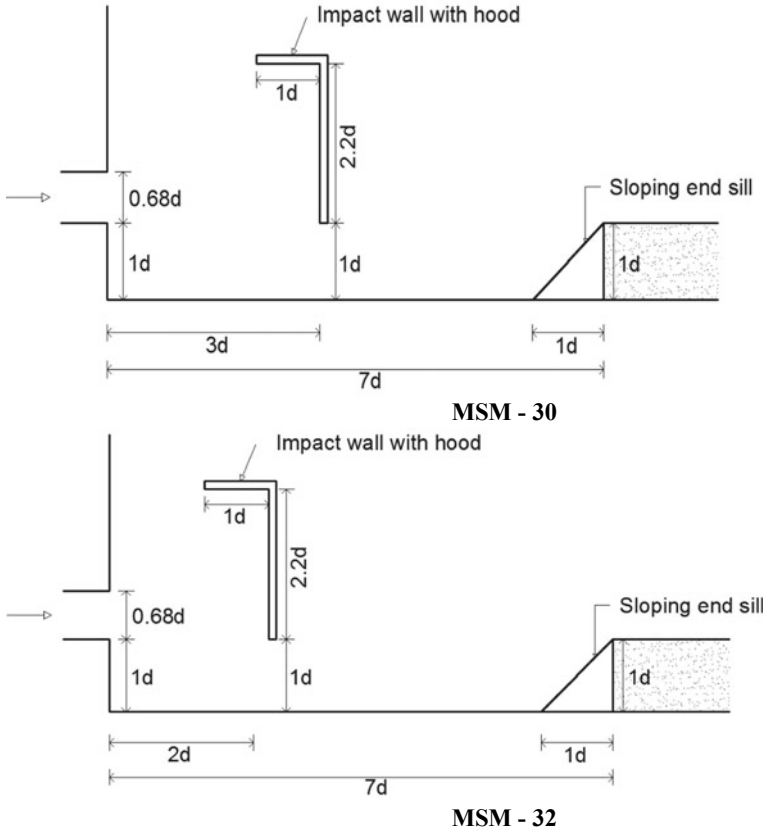


**Fig. 1.3** MSM-30 and MSM-32 at  $7d$  length of the basin with impact wall at  $3d$  and  $2d$

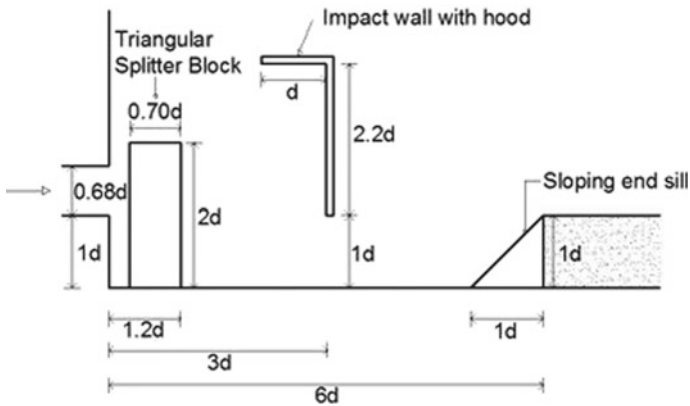


**Fig. 1.4** Model MSM-119 having triangular shape splitter block along with impact wall at  $3d$  and end sill

**Table 1.1** Scheme of experimentation

S. No	Model name	USBR VI impact wall with hood			End sill			Splitter block
		Size	Bottom gap with basin floor	Location from outlet exit	Height	Width	Location from outlet exit	
1	MSM-6	1d × 2.2d	1d	3d	1d	1d	8.4d	–
2	MSM-30	1d × 2.2d	1d	3d	1d	1d	7d	–
3	MSM-32	1d × 2.2d	1d	2d	1d	1d	7d	–
4	MSM-119	1d × 2.2d	1d	3d	1d	1d	6d	Triangular shape

for the constant running time of one hour and with the same erodible material for the Froude number = 3.85, and thus, totally 12 test runs were performed to evaluate the performance of stilling basin models for varying lengths of the basin from 8.4d to 6d as shown in Table 1.1.

### 1.2.1 Criteria for the Performance of Evaluation for a Stilling Basin

A stilling basin model that produces a smaller depth of scour at a longer distance is considered to have a better performance as compared to another stilling basin which results in a larger depth of scour at a shorter distance when tested under similar flow conditions (Verma and Goel 2000). The performance of stilling basin models was tested for the different Froude number (Fr) which is a function of channel velocity (v), the maximum depth of scour (d<sub>m</sub>) and its location from the end sill (d<sub>s</sub>). A new non-dimensional number, called as the performance index (PI) reported by Tiwari et al. (2010), has been used for comparison of the performance of stilling basin models. This is given as follows:

$$PI = \frac{Vxd_s}{2d_m \sqrt{g \frac{\rho_s - \rho_w}{\rho_w} d_{50}}} \tag{1.1}$$

where V—the mean velocity of the channel, d<sub>s</sub>—the distance of maximum depth of scour from end sill, d<sub>m</sub>—depth of maximum scour, g—gravitation acceleration, ρ<sub>s</sub>—density of sand, ρ<sub>w</sub>—density of water and d<sub>50</sub>—the particle size such that 50% of the sand particle is finer than this size. A higher value of performance index indicates a better performance of the stilling basin model. The value of the performance index for various runs on each model for different Froude numbers is given in Table 1.2.

**Table 1.2** Performance index for models tested at basin length 8.4d, 7d and 6d

S. No	Model name	$Fr = 1.85$			$Fr = 2.85$			$Fr = 3.85$		
		$d_m$	$d_s$	$PI$	$d_m$	$d_s$	$PI$	$d_m$	$d_s$	$PI$
1	MSM-6	3.2	10.5	2.67	4.4	12.5	2.63	4.6	15.5	3.42
2	MSM-30	3.4	9.5	2.27	6.4	14.8	2.14	6.8	20.4	3.05
3	MSM-32	2.9	8.4	2.36	3.7	11.6	2.91	5.6	16.4	2.98
4	MSM-119	3.3	12.1	2.98	4.2	17.7	3.91	4.8	17.9	3.79

### 1.3 Results and Discussions

As per USBR VI impact basin, impact wall of size  $1d \times 2.2d$  is placed at a distance of  $3d$  from the exit of the pipe outlet. End sill of one  $d$  height with a rectangular section having thickness  $0.2d$  was placed at a distance of  $8.4d$  from the exit of pipe outlet. MSM-6 was tested, which is actually a base model called as USBR VI impact basin model developed by Bradley and Paterka (1957).  $PI$  values are computed and mentioned in Table 1.2. These values are 2.67, 2.63 and 3.42 for  $Fr = 1.85, 2.85$  and  $3.85$ , respectively.

To evolve efficient and economical hydraulic energy dissipating models, the length of the basin was reduced to  $7d$ . First of all, the basin was evaluated by conducting the test runs for three Froude numbers in similar flow conditions with earlier tested impact wall located at  $3d$  along with sloping end sill fixed at  $7d$  and model was named as MSM-30. Performance indices were calculated as shown in Table 1.2. USBR VI impact wall was also evaluated at  $2d$  locations. The tested model was named as MSM-32 and  $PI$  values are computed as shown in Table 1.2.

To further economize the basin, triangular shape splitter blocks of size as shown in Fig. 1.1 were tested along with impact wall and end sill at basin length  $6d$  and the model was renamed as MSM-119. With the analysis of data shown in Table 1.2, it is concluded that model MSM-119 performs better among all models tested with values of  $PI$  as 2.98, 3.91 and 3.79 for Froude numbers 1.85, 2.85 and 3.85, respectively. Sets of these values are highest for all models tested. In this series of studies, it is also found that the location of appurtenance affects the basin performance as results of the model.

#### 1.3.1 Comparison of USBR VI with Newly Developed Model

On analyzing the USBR VI stilling basin model (MSM-6) proposed by Bradley and Peterka (1957) and newly developed stilling basin model (MSM-119) for non-circular pipe outlet, it is found that the value of performance index is MSM-101 ( $PI = 2.98, 3.91$  and  $3.79$  for Froude numbers 1.85, 2.85 and 3.85, respectively) which is higher side as compared to the value of performance index for USBR VI model ( $PI = 2.67, 2.63$  and  $3.42$  for  $Fr = 1.85, 2.85$  and  $3.85$ , respectively). Thus, there

**Table 1.3** Comparison of newly developed model

Name of model	<i>PI</i> for <i>Fr</i> = 1.85	<i>PI</i> for <i>Fr</i> = 2.85	<i>PI</i> for <i>Fr</i> = 3.85	Remark
MSM-6	2.67	2.63	3.42	USBR VI model Basin length = 8.4d
MSM-119	2.98	3.91	3.79	Newly developed model, basin length = 6d
Improvement of performance for all froude numbers				
Improvement in the performance of the designed model over USBR VI model	11.62%	48.67%	10.82%	Improved performance for all Froude numbers with 29% reduction in length as compared to MSM-6 model

is an improvement of performance in the range of 11–48.6% for the tested Froude number and also the length of the basin for the new design model is reduced from 8.4d to 6d. Reduction of the basin length from 8.4d to 6d (29%) makes the new stilling basin model (MSM-101) more economical as compared to USBR VI model (MSM-6). Comparative analysis is also shown in Table 1.3.

### 1.4 Conclusions

An experimental work was carried out in the laboratory by fabricating physical models, to make the USBR VI model more economical and efficient for non-circular pipe outlet stilling basins by using end sill and impact wall and triangular splitter block. The investigation was carried out at changing basin lengths (8.4d, 7d and 6d) for rectangular-shaped pipe outlets with 12 test runs for Froude numbers 3.85, 2.85 and 1.85. After experimental investigations, it is found that by simply inserting the triangular splitter block as shown in Fig. 1.1, the efficiency of the USBR VI model improved significantly, and at the same time, stilling basin model length reduced from 8.4d to 6d. The reduction of the length is more than 29%, which may lead to make the new stilling basin model more economical. During the study, it was found that the location of the impact wall affects the flow conditions and ultimately scour pattern downstream of the stilling basin. Further, it is suggested that the location of the splitter block should be varied, and accordingly, stilling basin model should be evaluated.

## References

- Alikhani A, Behrozi-Rad R, Fathi Moghadam M (2010) Hydraulic jump in stilling basin with vertical end sill. *Int J Phys Sci* 5(1):025–029
- Bradley JN, Peterka AJ (1957) Hydraulic design of stilling basins. *J Hydraul Eng* 83(5):1401–1406
- Fiala JR, Maurice LA (1961) Manifold stilling basins. *J Hydraul Div* 87(4):55–81
- Flammer GH, Skogerboe GV, Wei CY, Rasheed H (1970) Closed conduit to open channel stilling basin. *J Irrig Drain Div* 96(7124):1–11
- Garde RJ, Saraf PD, Dahigaonkar DJ (1986) Evolution of design of energy dissipator for pipe outlets. *J. Irrig Power* 41(3):145–154
- Goel A (2008) Design of stilling basin for circular pipe outlet. *Can J Civ Eng* 35(12):1365–1374
- Noshi HM (1999) Energy dissipation near the bed downstream end sill. *IHAR Proc*
- Tiwari HL, Gahlot VK (2012) Experiments on new stilling basin for pipe outlets. *STM, AISECT University* 2(2):17–20
- Tiwari HL (2013a) Analysis of baffle wall gap in the design of stilling basin models. *Int J Civil Eng Technol* 4(4):66–71
- Tiwari HL (2013b) Design of stilling basin with impact wall and end sill. *Int Res J Resent Sci* 2(3):59–63
- Tiwari HL, Gahlot VK, Seema T (2013) Reduction of scour depth downstream of stilling basin. *Int Res J Eng Sci* 2(7):20–25
- Tiwari HL, Goel A (2014) Effect of end sill in the performance of stilling basin *AJCEA* 2(2):60–63
- Tiwari HL, Goel A (2016) Effect of impact wall on energy dissipation in stilling basin. *KSCE J Civ Eng* 20(1):463–468
- Tiwari HL, Goel A, Gahlot VK (2010) Stilling basin below outlets works. *Int J Engg Sci Technol* 2(11):6380–6385
- Tiwari HL, Goel A, Gahlot VK (2011a) experimental study of sill controlled stilling basins for pipe outlet. *Int J Civil Eng Res* 2(2):107–117
- Tiwari HL, Goel A, Gahlot VK (2011b) Experimental study of effect of end sill on stilling basin performance. *Int J Eng Sci Technol* 3(4):3134–3140
- Tiwari HL, Gahlot VK, Sharma A (2014) Effect of Intermediate sill on the performance of stilling basins models, *Int J Sc Engg Tech* 3(4):414–417
- Verma DVS, Goel A (2000) Stilling basins for outlets using wedge shaped splitter blocks. *ASCE J Irrig Drain Eng* 126(3):179–184
- Verma DVS, Goel A (2003) Development of efficient stilling basins for pipe outlets. *ASCE J Irrig Drain Eng* 129(3):194–200
- Vollmer E, Khader MHA (1971) Counter current energy dissipator for conduit outlets. *Int J Water Power* 23(7):260–263

# Chapter 2

## Bio-Inspired Genetic Algorithm for Optimal Design of Water Distribution Networks



Seelam Naga Poojitha and Vinayakam Jothiprakash

**Abstract** The paper delineates the procedure for the optimal design of water distribution networks (WDNs) using population-based bio-inspired evolutionary optimization technique, Genetic algorithm (GA) coupled with simulation technique, Environment protection agency network (EPANET). GA is an efficient search-based optimization technique that simulates the natural selection process and evolves the best solution brought through the inheritance of genetic operator's crossover and mutation. EPANET is the simulation tool that emulates the hydraulic behavior and water quality state of the WDN. In the present study, the WDN design is progressed with the major objective of achieving a hydraulically efficient economical network. To demonstrate the design procedure, three benchmark problems, Two-loop network (TLN), Hanoi network (HN), and BakRyan network (BRN) are considered. The first two benchmark problems are designed as the new WDNs, and the third one is the rehabilitation network that is re-designed to bring to the hydraulically feasible state. On the application of the developed optimization model, the results obtained in terms of optimal cost are compared with the results reported in the literature with different optimization techniques. The minimum functional evaluations and the percentage of solution space explored are also compiled. For TLN, the optimal cost obtained (\$4,19,000) is found to be the global optimum solution (confirmed through analytical methods in past studies). For HN, a near-optimum solution of \$ 61,25,000 is obtained, and for BRN, an optimal solution of \$903,620 is obtained (which is consistent with the studies reported in the literature) at fewer functional evaluations. From the results, it is evident that GA is an efficient optimization technique in searching and converging to the optimum solution with a lower number of function evaluations. And from the detailed application of GA and the results reported, it can be concluded that GA is one of the best optimization techniques for handling complex optimization problems like WDNs.

---

S. N. Poojitha (✉) · V. Jothiprakash  
Department of Civil Engineering, Indian Institute of Technology Bombay, Powai, Mumbai,  
Maharashtra 400076, India



## 2.1 Introduction

WDN is the vital part of the water supply system (WSS) that transports treated water from the supply source at the treatment plant to communities. It is a complex interconnected network made of different components like pipes, nodes (junctions), tanks, valves, pumps, etc. The design of WDN is costly as it alone accounts for about 50 to 70% of the total cost invested for the design of WSS (Zhao 2003), and further, it is a complex problem that involves many interrelated design variables. The major task in the design of WDN is to fix the diameter of pipes optimally from the commercially available set of diameters for a given layout, length of the pipes, demand and minimum head requirement at demand nodes. The design procedure involves both optimization and simulation of the network. Optimization is necessary for choosing an optimal set of diameters efficiently to cater economy, i.e., every penny expended for its design is used efficiently. And, simulation is necessary to check for the adequacy of the network for its effective functioning. In the present study, EPANET software that works on gradient analysis is used. EPANET performs an extended period simulation of hydraulic and water quality behavior of the pipe networks under pressure (Rossman 2000). For optimization, the population-based optimization technique, GA, is used. Unlike the standard deterministic optimization techniques used in past literature (Duan et al. 1990; Alperovits and Shamir 1977), GA does not require simplification of the original problem, and it can deal with both continuous and discontinuous functions leading to its applicability to diverse problems and works with a population of possible solutions instead of a single-point solution for which it is most likely to end up at near global or global optimum solution. Another exceptional advantage of GA is its universality which means it can be applied quite straightforward to any type of network.

## 2.2 Methods

GA is a search-based optimization technique that works on the basis of natural selection. The convergence efficiency of GA depends on its operators like reproduction, crossover, and mutation. The first step in GA is to fix the number of population ( $N_{pop}$ ), the number of generations ( $N_{gen}$ ), crossover probability ( $P_c$ ), and mutation probability ( $P_m$ ) that are problem-specific. In the present study, the tournament method of selection is considered as the reproduction scheme. Through this scheme, considering four chromosomes that are selected randomly from the population set, the best chromosome based on the fitness function value is selected. This procedure of reproducing the best population members is repeated to make up the population size. Following the reproduction scheme, the crossover operator is applied to generate new population members by crossing over the features of the parent chromosomes. Then to maintain diversity among the population members, they are mutated. Thus, in GA, initially, the best populations are reproduced from the existing ones, using which the

offsprings are generated through a crossover operator and are then mutated using a mutation scheme to induce diversity in the population set. The search for the best possible solution is repeated using this entire GA mechanism until the termination criteria, i.e., the maximum generation size.

### 2.3 Methodology

Optimization of WDN involves searching for a minimum cost solution from the solution space that satisfies hydraulic conditions like conservation of energy, conservation of mass, the constraints on the selection of design components, and functional constraints. The hydraulic constraints of the design problem are handled by the EPANET software and are mathematically expressed as follows:

- (1) The continuity principle states that the mass of fluid flowing per unit time through a node is equal to the mass of fluid leaving that node

$$\sum Q_{inf} - \sum Q_{out} = Q_{ext} \quad (2.1)$$

where  $Q_{inf}$  = Inflow toward a node,  $Q_{out}$  = Outflow from a node, and  $Q_{ext}$  = External flow from a node.

- (2) Conservation of energy states that until no external energy is added to the system, total energy in the system is conserved at any point in time. For a looped system, the total head loss is expressed as follows:

$$\sum_{j \in l} \Delta H_j = 0 \quad (2.2)$$

where  $l$  = total number of loops and  $\Delta H_j$  = head loss in closed-loop 'j'.

In the present study, the pipe diameters of the WDN are considered as the design variable. And the constraint on component selection is directly handled by the optimization technique by selecting the diameters for the pipes from the commercially available options. The functional constraint, i.e., satisfying the minimum pressure head required at the demand nodes is taken care of by the static penalty function. Overall, the optimization function is the minimization of the design cost of the WDN and is mathematically represented as follows:

$$\text{Min } f(d_1, d_2, \dots, d_k) = \sum_{i=1}^k C(d_i, L_i) \quad (2.3)$$

$$\text{S. t. } H_n \geq H_{\min}.$$

where  $k$  = total number of pipes,  $n$  = number of nodes, and  $C$  = cost of the pipe per its unit length.

Overall, the optimization technique, GA, presents the possible alternate solution. And the hydraulic condition of the network for every alternate diameter set proposed by GA is simulated using EPANET software. For the simulated hydraulic condition, any violation in the pressure head at the demand nodes is penalized using the penalty function. This entire procedure of search, hydraulic simulation, and penalization of the infeasible solution is progressed until when the generation size reaches its maximum number. The step-by-step procedure of the algorithm developed, i.e., GA coupled with EPANET for optimally designing the WDN is delineated in the flow chart as presented in Fig. 2.1.

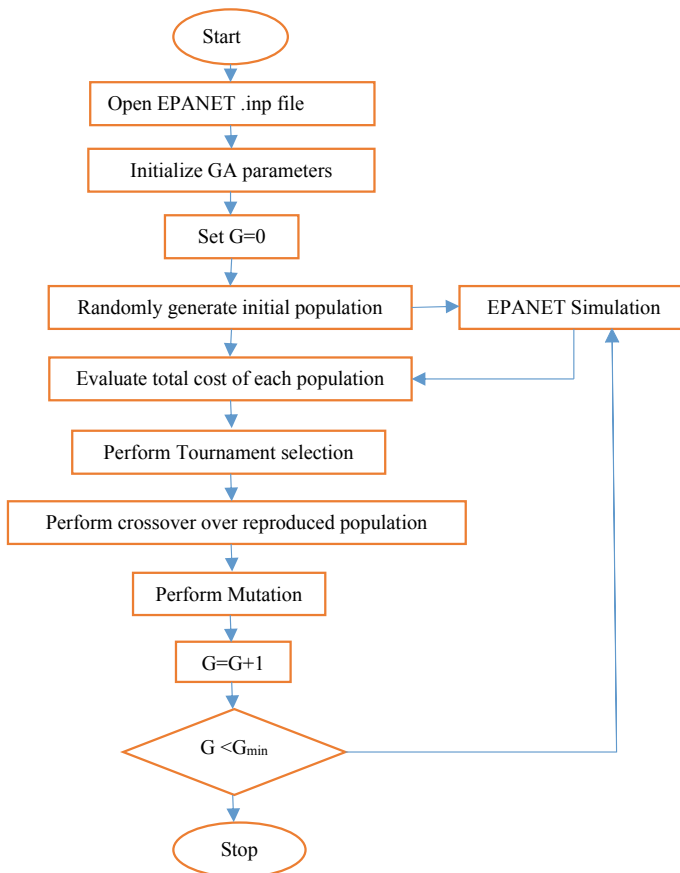


**Fig. 2.1** Model framework for design of WDN

### 2.4 Benchmark Problems Considered in the Study

Two-loop network (TLN), Hanoi network (HN), BakRyan network (BRN) are the most widely used benchmark problems in the domain of WDN optimal design.

TLN is the simple network of all benchmark problems consisting of eight pipes each of length 1000 m, six demand nodes, and one fixed head node (reservoir) as shown in Fig. 2.2. This hypothetical network was first used by Alperovits and Shamir (1977) and later by many researchers. The details of TLN are given in Table 2.1.

The HN is the new WDN planned for Hanoi city. As shown in Fig. 2.3, the HN is made up of thirty-four links, thirty-two nodes, and a reservoir with a fixed head of 100 m. HN was studied first by Fujiwara and Khang (1990) and later by many researchers. The details of HN are given in Table 2.2.

BRN is a gravity system consisting of fifty-eight pipes, thirty-five demand nodes, and a reservoir with a fixed head of 58 m as shown in Fig. 2.4. The minimum pressure head requirement at each demand node is 15 m. BRN is a rehabilitation network system under which the best possible options should be considered to improve the hydraulic efficiency of the existing system. It was first studied by Lee and Lee (2001) and later by Geem (2006). The nodal demands and commercially available details of BRN are given in Table 2.3. For all the benchmark problems considered in the study, the head loss is computed using Hazen-Williams’ empirical formula.

$$\Delta H = 10.6744C_{HW}^{-1.852}d^{-4.871}LQ^{1.852} \tag{2.4}$$

where  $\Delta H$  = Head loss in the pipe,  $C_{HW}$  = Hazen-Williams’ roughness coefficient,  $d$  = Diameter of pipe,  $L$  = Length of pipe, and  $Q$  = Discharge in the pipe.

**Fig. 2.2** Two-loop network (Savic and Walters 1997)

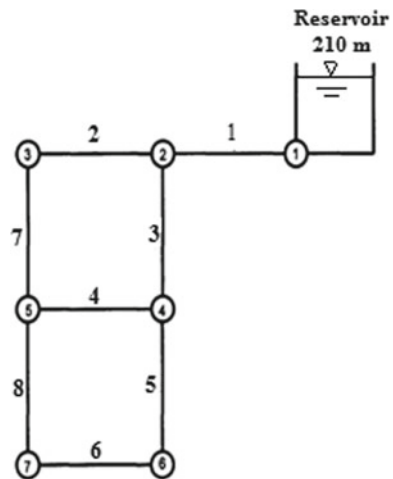


**Table 2.1** Details of the commercially available pipe diameters and nodal data for TLN (Alperovits and Shamir 1977)

Commercially available pipe diameter (in)	Commercially available pipe diameter (mm)	Cost of pipe (\$/m)	Node number	Elevation (m)	Minimum pressure required at demand nodes (m)	Demand (m <sup>3</sup> /h)
1	2	25.4	1	210	0	-1120
2	5	50.8	2	150	30	100
3	8	76.2	3	160	30	100
4	11	101.6	4	155	30	120
5	16	152.4	5	150	30	270
6	23	203.2	6	165	30	330
7	32	254	7	160	30	200
8	50	304.8				
9	60	355.6				
10	90	406.4				
11	130	457.2				
12	170	508				
13	300	558.8				
14	550	609.6				

Except for BRN, for all the remaining networks in the study, the Hazen-Williams roughness coefficient is considered as 130. For BRN, a value of 100 is considered in reference to the previous studies.

## 2.5 Results and Discussion

The control parameters of GA are calibrated through sensitivity analysis and their optimal values calibrated are compiled in Table 2.4.

The optimization model in combination of GA and simulation tool, EPANET is validated by applying it to three benchmark problems, TLN, HN, and BRN. Results of each benchmark problem in the present study in comparison with other studies are tabulated in Table 2.5. The generation number at which optimum solution has arrived and details of the average number of generations required to reach the optimum solution in 50 trials and percentage of solution space explored are tabulated in Table 2.6.

From the results, it is found that the developed model is able to converge to a global optimum solution of \$4,19,000 for TLN, a near-optimum solution of \$61,25,000 for HN, and an optimum solution of \$9,03,620 for BRN. And for all the three networks, the optimal solution found is consistent with the previous studies.

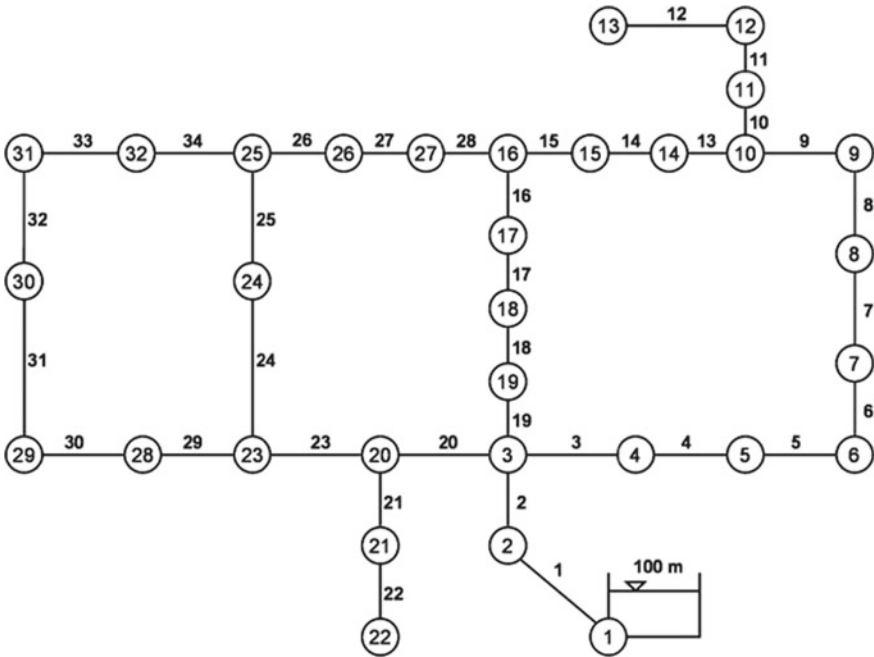


Fig. 2.3 Hanoi network (Savic and Walters 1997)

## 2.6 Conclusions

A comprehensive model for optimization of WDN with an evolutionary optimization technique, genetic algorithm coupled with EPANET, is developed. It is validated on three widely used benchmark problems TLN, HN, and BRN. The results obtained in terms of optimal cost are compared with previous studies. From the results, it is found that the developed model is efficient in obtaining near-optimal solutions with ease of computations. Its universality quality makes it easy for its explicit application to any type of WDN.

**Table 2.2** Details of the commercially available pipe diameters and nodal data for HN (Fujiwara and Khang 1990)

Commercially available pipe diameter (in)	Commercially available pipe diameter (mm)	Cost of pipe (\$/m)	Nodes	Demand (m <sup>3</sup> /h)	Pipe no	Length of pipe (m)
12	304.8	45.730	1	-19,940	1	100
16	406.4	70.400	2	890	2	1350
20	508.0	98.380	3	850	3	900
24	609.6	129.333	4	130	4	1150
30	762.0	180.800	5	725	5	1450
40	1016.0	278.300	6	1005	6	450
			7	1350	7	850
			8	550	8	850
			9	525	9	800
			10	525	10	950
			11	500	11	1200
			12	560	12	3500
			13	940	13	800
			14	615	14	500
			15	280	15	550
			16	310	16	2730
			17	865	17	1750
			18	1345	18	800
			19	60	19	400
			20	1275	20	2200
			21	930	21	1500
			22	485	22	500
			23	1045	23	2650
			24	820	24	1230
			25	170	25	1300
			26	900	26	850
			27	370	27	300
			28	290	28	750
			29	360	29	1500
			30	360	30	2000
			31	105	31	1600
			32	805	32	150
					33	860
					34	950

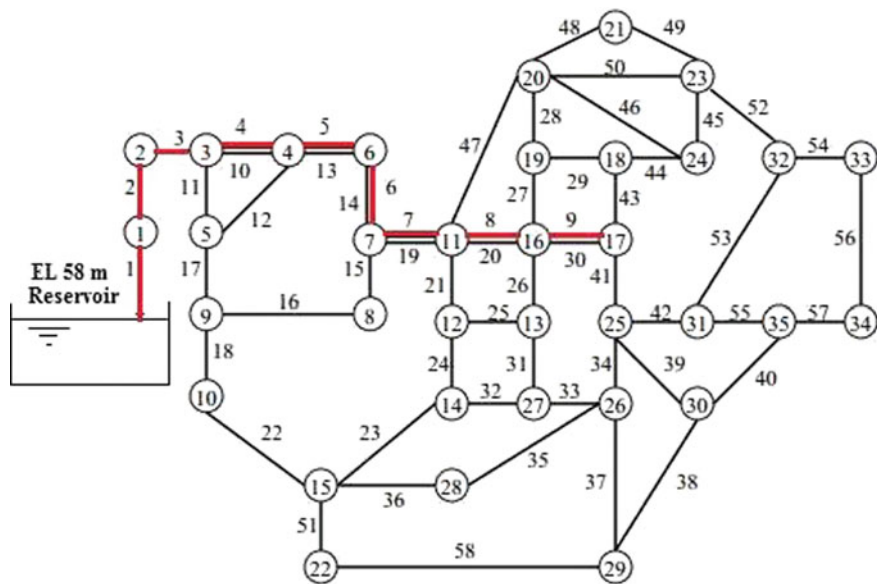


Fig. 2.4 BakRyan network Geem (2006)



**Table 2.3** Details of the commercially available diameters and nodal data for BRN (Geem 2006)

Commercially available pipe diameter (mm)	Cost of pipe (\$/m)	Node no	Demand (m <sup>3</sup> /d)	Elevation (m)
300	118	1	0	24.9
350	129	2	4231	29.9
400	145	3	3257	31.4
450	160	4	4528	40.8
500	181	5	1784	24.3
600	214	6	20,023	28
700	242	7	5673	22.4
800	285	8	2516	31.4
900	325	9	860	21.9
1000	370	10	334	17.6
1100	434	11	1512	17.8
		12	901	22.9
		13	853	14.1
		14	966	17.4
		15	2270	19.4
		16	1255	17.1
		17	1526	19.9
		18	1497	20.6
		19	716	36.4
		20	6900	23.5
		21	10,000	26.3
		22	636	34.3
		23	809	20.8
		24	2069	26.3
		25	1761	15.4
		26	2279	11.4
		27	1795	11.4
		28	1968	11.1
		29	2986	10.5
		30	2078	11.6
		31	1587	25.2
		32	4085	12.9
		33	4701	12.9
		34	0	18.2
		35	667	

**Table 2.4** Sensitivity analysis results

Benchmark problem	$P_c$	$P_m$	$N_{pop}$	Max $N_{gen}$
TLN	0.8	0.02	100	400
HN	0.9	0.025	100	1500
BRN	0.9	0.035	100	1000

**Table 2.5** Results of TLN, HN, and BRN in comparison with previous studies

	TLN	
<b>Studies</b>	<b>Optimal Cost obtained (\$)</b>	<b>Type of solution (in terms of length of each pipe either it is split pipe or full pipe)</b>
Alperovits and Shamir (1977)	4,97,525	Split pipe solution
Goulter et al. (1986)	4,35,015	Split pipe solution
Kessler and Shamir (1989)	4,17,500*	Split pipe solution
Eiger et al. (1994)	4,02,353*	Split pipe solution
Savic and Walters (1997)	4,19,000	Full length solution
Cunha and Sousa (1999), Suribabu (2010), and Samani and Mottaghi (2006)	4,19,000	Full length solution
<b>Present study</b>	<b>4,19,000</b>	<b>Full length solution</b>
	<b>HN (10<sup>6</sup>)</b>	
Fujiwara and Khang (1990)	5.354*	Full length solution
Fukiwara and Khang (1990)	5.562*	Split pipe solution
Eiger et al. (1994)	6.027*	Split pipe solution
Savic and Walters (1997)	6.073*, 6.195	Full length solution
Suribabu (2010)	6.081	Full length solution
Zheng et al. (2011)	6.081	Full length solution
Cunha and Sousa (1999)	6.056*	Full length solution
<b>Present study</b>	<b>6.125</b>	<b>Full length solution</b>
<b>BRN</b>		
Original network	9,54,920	Full length solution
Lee and Lee (2001)	9,03,620	Full length solution
Geem (2006)	9,03,620	Full length solution
Present study	9,03,620	Full length solution

**Table 2.6** Statistics of benchmark problems considered

Benchmark problem	Generation number at which optimal solution is located	Average generation size of successful trials	Available solution space	Minimum number of functional evaluations	Percentage of solution space explored to locate the optimum solution
TLN	43	66	14 <sup>8</sup>	4300	2.914E-06
HN	1294	1156	6 <sup>34</sup>	129,400	4.516E-22
BRN	34	189	11 <sup>9</sup>	3400	1.442E-06

## References

- Alperovits E, Shamir U (1977) Design of optimal water distribution systems. *Water Resour Res* 13(6):885–889
- Cunha MDC, Sousa J (1999) Water distribution network design optimization: simulated annealing approach. *J Water Resour Plan Manag* 125(4):215–221
- Duan N, Mays LW, Lansey KE (1990) Optimal reliability-based design of pumping and distribution systems. *J Hydraul Eng* 116(2):249–268
- Eiger G, Shamir U, Ben-Tal A (1994). Optimal design of water distribution networks. *Water Resour Res* 30(9):2637–2646
- Fujiwara O, Khang DB (1990) A two phase decomposition method for optimal design of looped water distribution networks. *Water Resour Res* 26(4):539–549
- Geem ZW (2006) Optimal cost design of water distribution networks using harmony search. *Eng Optim* 38(3):259–277
- Goulter IC, Lussier BM, Morgan DR (1986) Implications of head loss path choice in the optimization of water distribution networks. *Water Resour Res* 22(5):819–822
- Kessler A, Shamir U (1989) Analysis of the linear programming gradient method for optimal design of water supply networks. *Water Resour Res* 25(7):1469–1480
- Lee SC, Lee SI (2001) Genetic algorithms for optimal augmentation of water distribution Networks. *J Korean Water Resour Assoc* 34(5):567–575
- Rossman LA (2000) *Epanet 2 users manual*. U.S. Environmental Protection Agency, Washington, D. C., EPA/600/R-00/057, 2000
- Samani HM, Mottaghi A (2006) Optimization of water distribution networks using integer linear programming. *J Hydraul Eng* 132(5):501–509
- Savic DA, Walters GA (1997) genetic algorithms for least-cost design of water distribution networks. *J Water Resour Plan Manag* 123(2):67–77
- Suribabu CR (2010) Differential evolution algorithm for optimal design of water distribution networks. *J Hydroinformatics* 12(1):66
- Zheng F, Simpson AR, Zecchin AC (2011) A combined NLP-differential evolution algorithm approach for the optimization of looped water distribution systems. *Water Resour Res* 47(8):W08531
- Zhao HB (2003) *Water supply network theory and analysis*. China Building Industry Press, Peking

# Chapter 3

## Assessments of Meteorological Drought Indices Using SPI and RDI in Mehsana Region, Gujarat, India



Pranav B. Mistry and T. M. V. Suryanarayana

**Abstract** Drought is one of the natural disasters that in comparison with the other disasters is of tremendous importance due to intensity, duration, areal extent, economic damages and long-term effects. The present work focuses on comparisons of meteorological drought indices, i.e., Standardized Precipitation Index (SPI) and Reconnaissance Drought Index (RDI) for Mehsana district for 1901 to 2002 years. The results of this study show that the RDI is more sensitive than the SPI to climatic conditions and so we can't neglect the role of potential evapotranspiration in drought assessments. From the results and analysis, it is concluded that extreme dry years are 1904, 1911, 1923 and 1987 wherein severe dry years are 1915, 1918, 1948, 1968, 1972, 1974 and 2002. The results also showed that both indices behave in the same manner in various time scales (3, 6, 9 and 12 months), but RDI due to the use of potential evapotranspiration in similar climatic conditions is more sensitive than the SPI. So, it is recommended that the RDI index should be used as the proper drought index in drought monitoring systems for water resources planning and management. The percentage of drought-affected areas was 20% (Moderate dry 9%, Severe dry 7% and Extreme Dry 4%) and Normal conditions 66% which indicates that the Mehsana region is under dry conditions for most of the years in twentieth century.

### 3.1 Introduction

Drought is not only a physical occurrence that can be defined by weather conditions. A drought is defined as an extended period of unusually dry weather that causes water shortages and crop damage. Over the past century, an increase of the Earth's average surface temperature is of about  $+0.76^{\circ}\text{C}$  as per the Intergovernmental Panel on Climate Change, 2007 (IPCC 2007). The IPCC, in its 2007 report, predicts that temperature will rise by  $2.7\text{--}4.3^{\circ}\text{C}$  over India by the 2080s. The panel also predicted an increase in rainfall over India to be 6–8% and the sea level would rise by 88 cm by

---

P. B. Mistry · T. M. V. Suryanarayana (✉)

Water Resources Engineering and Management Institute, Faculty of Technology and Engineering, The Maharaja Sayajirao University of Baroda, Vadodara 391410, India  
e-mail: [drsurya-wremi@msubaroda.ac.in](mailto:drsurya-wremi@msubaroda.ac.in)

2100. The Irrigation Commission of India defines drought as a situation occurring in any area where the annual rainfall is less than 75% of normal rainfall. In general, there are three types of droughts based on relevance, duration and time of occurrence. The droughts are broadly divided into three classes as (a) Meteorological drought, (b) Hydrological drought and (c) Agricultural drought.

Drought indices are important elements of drought monitoring and assessment since they simplify complex interrelationships between many climate and climate-related parameters. Indices make it easier to communicate information about climate anomalies to diverse user audiences and allow scientists to assess quantitatively climate anomalies in terms of their intensity, duration, frequency and spatial extent (Wilhite and Glantz 1985).

The Standardized Precipitation Index (SPI) (McKee et al. 1993) addresses the variety of time scales on which precipitation deficits/surpluses can affect different aspects of the hydrologic cycle. While SPI index has less complexity and easily can be applied for each location, but its main disadvantage is using one parameter (rain) for describing water shortage (Tigkas et al. 2015). Drought cannot define in a region only with a shortage of rainfall but also evaporation should be considered. Therefore, in this study, a new drought index, Reconnaissance Drought Index (RDI), is used. Because in this index, precipitation and potential evapotranspiration are used for the calculation of different severities of drought, so this index has a more accurate scientific basis than other indices which use only rainfall as the input data (Tigkas et al. 2013).

## 3.2 Review of Literature

Reconnaissance Drought Index (RDI) (Tigkas et al. 2013) (initial or normalized expressions) is a single climatic index for the detection of possible climatic changes. Using data for various reference periods (12, 6 and 3 months). Similarly, (Thomas et al. 2015) considered RDI by considering the Penman-Monteith method used to estimate PET to analyze the climate change impacts on the drought scenario in the Bundelkhand region. Also, spatio-temporal variation of drought has been investigated and it was found that every drought event has its own characteristics in terms of its areal extent, its progression, withdrawal and severity. (Mistry and Suryanarayana 2019) Studied SPI in Banaskantha and shown that 6, 15 and 15% of extreme dry years, severe dry years and moderate dry years occur among drought years considered, which means 36% years are categorized into moderate to extreme drought years out of the total drought years.

### 3.3 Study Area and Data Collection

Mehsana district is located between 23°58' latitude and 72°36' longitude and elevation is 83 meters height that is equal to 272 ft. The district map of Mehsana is shown in Fig. 3.1. Mehsana is about 75 km from Ahmedabad. The major crops of Mehsana are Potato, Cotton, Tobacco, Oilseeds, Castor Seeds, Cumin, Psyllium and Anise. The average rainfall in the Mehsana district is 697 mm. The maximum temperature of the place is 43° and the minimum temperature is 12°. The Rriver flowing through the Mehsana district is Rupen (156 km) and Sabarmati (371 km).

### 3.4 Material and Methods

#### 3.4.1 Standardized Precipitation Index

The standardized Precipitation Index (SPI) is one of the indices that were presented for drought monitoring. It is calculated in short-term (3, 6 and 9 months) and long-term (12, 24 and 48 months) periods. In any time scale, the SPI mean may reach zero in a location and its variance becomes equal to 1. Using the SPI, a quantitative definition of drought can be established for each time scale. A drought event for time scale *i* is defined here as a period in which the SPI is continuously negative and the SPI reaches a value of -1.0 or less. The drought begins when the SPI first falls below zero and ends with a positive value. The classification of drought conditions based on SPI is calculated using Eq. 3.1 and classification is given below in Table 3.1.

$$SPI = \frac{x_i - X}{\sigma} \tag{3.1}$$

where *X*: the mean annual rainfall, *X<sub>i</sub>*: the annual rainfall at any year and *σ*: the standard variation.

**Table 3.1** Classification of SPI

SPI values	Drought condition
2.0 +	Extremely wet
1.5–1.99	Very wet
1.0–1.49	Moderate wet
-0.99 to + 0.99	Near normal
-1.0 to -1.49	Moderate dry
-1.5 to -1.99	Severe dry
-2.0 to less	Extreme dry

### 3.4.2 Reconnaissance Drought Index

The index, which is referred to as the Reconnaissance Drought Index, RDI, may be calculated by the following equations. The first expression, the initial value ( $\alpha_0$ ), is presented in an aggregated form using a monthly time step and may be calculated for each month of the hydrological year or a complete year. The  $\alpha_0$  is usually calculated for the year  $i$  in an annual basis as follows:

$$\alpha_0^{(i)} = \frac{\sum_{j=1}^{12} P_{ij}}{\sum_{j=1}^{12} PET_{ij}}; i = 1 \text{ to } N \text{ and } j = 1 \text{ to } 12$$

in which  $P_{ij}$  and  $PET_{ij}$  are the precipitation and potential evapotranspiration of the month  $j$  of the year  $i$ .

A second expression, the Normalized RDI, (RDI<sub>n</sub>) is computed using the following equation for each year, in which it is evident that the parameter  $\bar{a}_0$  is the arithmetic mean of  $a_0$  values calculated for the  $N$  years of data.

$$RDI_n^{(i)} = \frac{a_0^{(i)}}{\bar{a}_0} - 1$$

The third expression, the Standardized RDI (RDI<sub>st</sub>), is computed following a similar procedure to the one that is used for the calculation of the SPI. The expression for the Standardized RDI is as follows:

$$RDI_{st}^{(i)} = \frac{y^{(i)} - \bar{y}}{\hat{a}_y}$$

in which  $y^{(i)}$  is the  $n$   $a_0(i)$ , is its arithmetic mean and  $\hat{a}_y$  is its standard deviation. Table 3.2 shows the RDI values range and corresponding drought classification.

**Table 3.2** Classification of RDI

RDI values	Drought classification
2.00 or more	Extremely wet
1.5–1.99	Severely wet
1.00–1.49	Moderately wet
0–0.99	Normal conditions-wet
0 to –0.99	Normal conditions-dry
–1 to –1.49	Moderate drought
–1.5 to –1.99	Severe drought
–2 or less	Extreme drought

### 3.5 Results and Analysis

For the present study of meteorological drought analysis, yearly rainfall data of the Mehsana district is collected and shown in Fig. 3.2. The study of *SPI* and *RDI* indices gives the drought severity at various time durations of 3, 6, 9 and 12 months in the Mehsana district. The *SPI* and *RDI* were calculated according to the Hydrological year, i.e., 3 months (Oct–Dec), 6 months (Oct–Mar), 9 months (Oct–Jun) and 12 months (Oct–Sept). The results obtained for the number of drought years and wet years are as shown in Table 3.3.



**Fig. 3.1.** District map of Mehsana

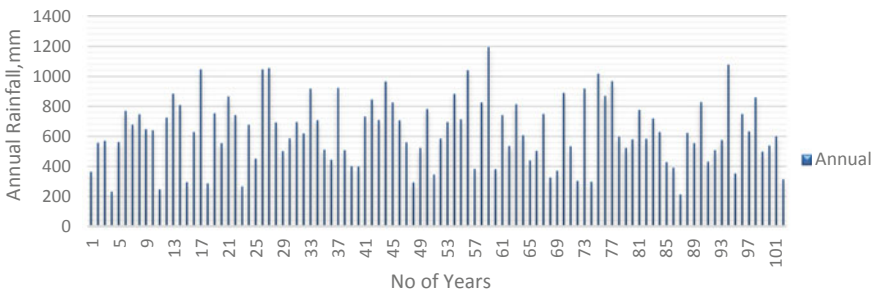


**Fig. 3.2** Annual rainfall variation



**Table 3.3** No. of drought years using *SPI* and *RDI*

	<i>SPI</i> 3	<i>RDI</i> 3	<i>SPI</i> 6	<i>RDI</i> 6	<i>SPI</i> 9	<i>RDI</i> 9	<i>SPI</i> 12	<i>RDI</i> 12
Extreme wet	1	0	1	0	0	0	1	0
Very wet	7	0	8	0	3	0	6	4
Moderate wet	11	18	6	12	14	14	11	12
Near normal	61	63	70	76	70	73	64	66
Moderate dry	10	6	10	5	7	6	9	9
Severe dry	12	15	3	3	5	5	8	7
Extreme dry	0	0	4	6	3	4	3	4

The results show that most of the years were below normal conditions, i.e., affected by drought. Also, it has been seen that in the Mehsana region. From the results and analysis, more accurate predictions are achieved using longer duration viz., 12 months so that extreme wet and very wet occurs for 1 and 6 times, respectively, using *SPI* 12 and 0 and 4 times using *RDI* 12 which is very less period.

The extreme wet conditions occur only 1 time by *SPI* 12 method whereas none of the year under extreme wet using *RDI* 12 method. Similarly, very wet conditions occur 6 times by *SPI* 12 method and 4 times by *RDI* 12 method. These show that the Mehsana region is under drought-prone zone in twentieth century of 1901–2002.

For calculation of *SPI*, only precipitation is considered whereas in *RDI*, both precipitation and *PET* are considered. Here, *RDI* is more sensitive than the *SPI* to climatic conditions and so we can't neglect the role of *ET0* in drought calculations. Obviously, this may be due to the fact that the *SPI* is less data demanding. In the extremely dry class, due to the lower amount of rainfall, evapotranspiration increases so that it causes decreasing in *RDI* values. The results also showed that both indices behave in the same manner. Based on the findings of this research, it is recommended that the *RDI* index should be used as the proper drought index in drought monitoring systems for water resources planning and management in Mehsana.

### 3.6 Comparisons of *SPI* and *RDI*

Figs. 3.3, 3.4, 3.5 and 3.6 show comparison graphs of *SPI* and *RDI* for 3, 6, 9 and 12 months in the study area.

Fig. 3.7 shows the number of years affected by drought conditions (moderate, severe and extreme) by means of *SPI* and *RDI* for various time scales (Table 3.4).

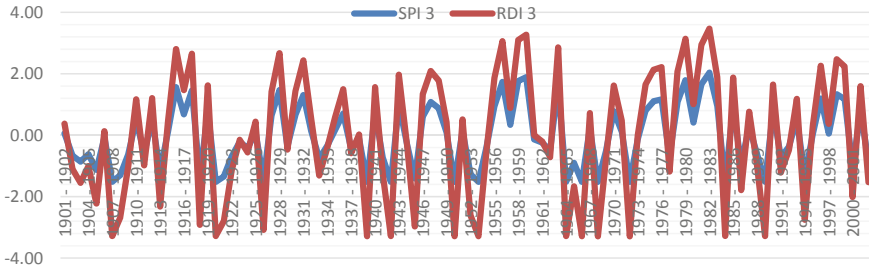


Fig. 3.3 Comparisons of *SPI* and *RDI* (3 months)

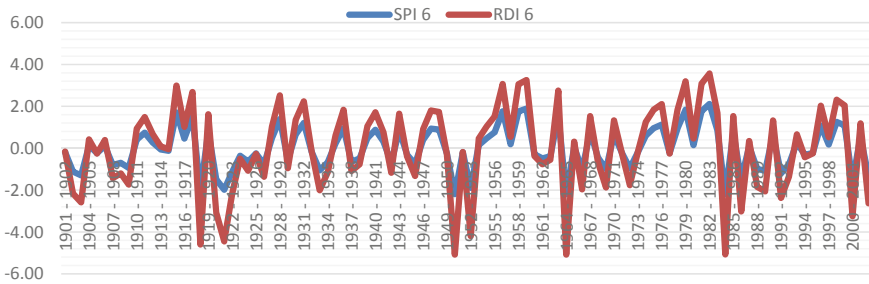


Fig. 3.4 Comparisons of *SPI* and *RDI* (6 months)

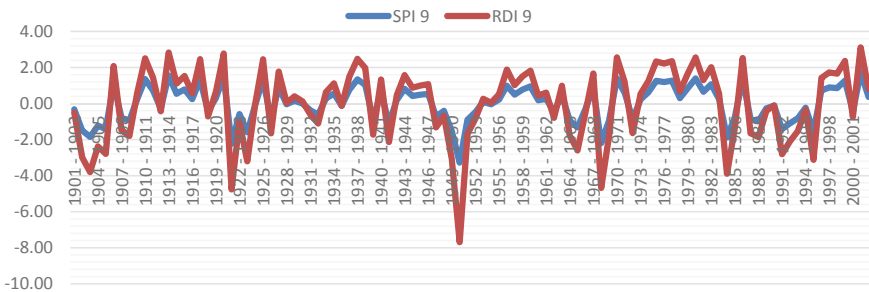
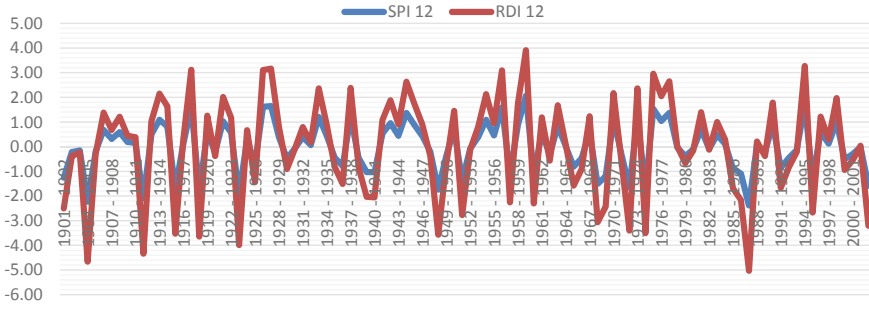


Fig. 3.5 Comparisons of *SPI* and *RDI* (9 months)

### 3.7 Conclusions

An assessment of meteorological droughts in the Mehsana area of Gujarat was conducted based on monthly precipitation and potential evapotranspiration data in the period from 1901 to 2002. Indices applied in this study include standardized precipitation index and reconnaissance drought index at time scales of 12 months. The results showed that *SPI* and *RDI* demonstrate the extreme and severe drought pattern successfully for the present region. The results show that using the *SPI* method, 1904,



**Fig. 3.6** Comparisons of *SPI* and *RDI* (12 months)

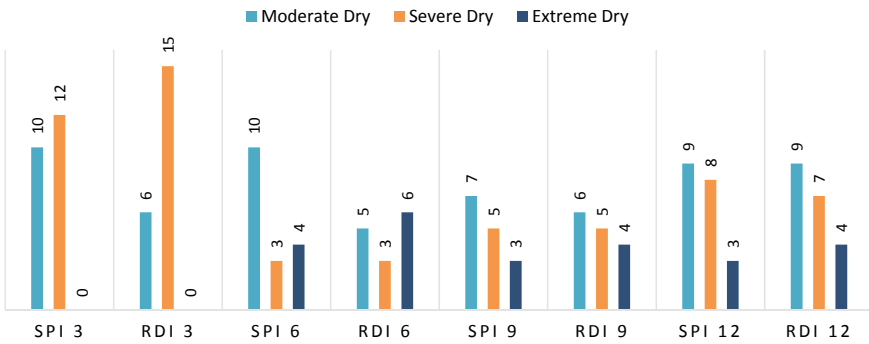


**Fig. 3.7** Comparisons of various time scales of *SPI* and *RDI*

**Table 3.4** Drought years using *SPI* 12 and *RDI* 12

	<i>SPI</i> 12	<i>RDI</i> 12
<i>Extreme dry</i>	1904, 1911, 1987	1904, 1911, 1923, 1987
<i>Severe dry</i>	1915, 1918, 1923, 1948, 1968, 1972, 1974, 2002	1915, 1918, 1948, 1968, 1972, 1974, 2002
<i>Moderate dry</i>	1901, 1939, 1940, 1951, 1957, 1960, 1969, 1986, 1995	1901, 1939, 1940, 1951, 1957, 1960, 1969, 1986, 1995

1911 and 1987 comes under extreme dry conditions and using the *RDI* method, 1904, 1911, 1923 and 1987 under extreme dry conditions so it shows the same results apart from the 1923 year. Where the 1923 year comes under severe dry conditions in *SPI*. Also, severe dry conditions years are 1915, 1918, 1948, 1968, 1972, 1974 and 2002. Also, from the analysis, it is concluded that the most accurate results were derived using *RDI* 12 in comparisons with other time scales and *SPI* method as well as actual situations in the Mehsana region. The method can provide valuable information for water resources planners and policymakers in developing appropriate management to cope with drought consequences. The percentage of drought-affected areas was

20% (Moderate dry 9%, Severe dry 7% and Extreme Dry 4%) and Normal conditions 66% which indicates that the Mehsana region is under dry conditions for most of the years in the twentieth century.

## References

- IPCC (2007) Climate change 2007: the physical science basis. contribution of working group i to the fourth assessment report of the intergovernmental panel on climate change [Solomon S, Qin D, Manning M, Chen Z, Marquis M, Averyt KB, Tignor M, Miller HL (eds)]. Cambridge University Press, Cambridge, United Kingdom and New York, NY, USA
- McKee TB, Nolan J, Kleist J (1993) The relationship of drought frequency and duration to time scales. In: Anaheim CA (ed) Preprints, 8th conference on applied climatology. American Meteorological Society, pp 179–184
- Mistry PB, Suryanarayana TMV (2019) Categorization of drought during twentieth century using precipitation in Banaskantha district, Gujarat, India. *Innovations in infrastructure. Adv Intell Syst Comput* 757:267–274
- Tigkas D, Vangelis H, Tsakiris G (2013) The RDI as a composite climatic index. *Eur Water* 41:17–22
- Tigkas D, Vangelis H, Tsakiris G (2015) DrinC: a software for drought analysis based on drought indices. *Earth Sci Inf* 8(3):697–709
- Thomas T, Jaiswal RK, Galkate RV, Nayak TR (2015) Reconnaissance drought index based evaluation of meteorological drought characteristics in Bundelkhand. *Int Conf Emerg Trend Eng Sci Technol Proced Technol* 24:23–30
- Wilhite DA, Glantz MH (1985) Understanding the drought phenomenon: the role of definitions. *Water Int* 10:111–120

# Chapter 4

## Top Surface Soil Moisture Retrieval Using C-Band Synthetic Aperture Radar Over Kudremukh Grasslands



Punithraj Gururaj, Pruthviraj Umesh, P. E. Kukku Sara, and Amba Shetty

**Abstract** Surface soil moisture is a key input factor not only for forest fire prediction models but also for hydrological models. It is the one that bifurcates between surface and subsurface runoff. Radar remote sensing has the ability to redeem topsoil moisture over large areas. In this study, Surface Soil Moisture (SSM) was estimated using a linear relationship between backscattered coefficients and volumetric soil moisture content over grasslands located in the tropical forested area. The field data for the study was measured over 42 test sites synchronized with satellite pass. Sentinel-1 Interferometric wide swath dual-polarized (VH and VV) data with 5.405 GHz frequency and central incidence angle of 23 having a repeat period of 12 days is used in this study. The SAR backscattered energy depends mainly on soil roughness and soil moisture. To simplify the analysis, surface roughness was eliminated using the change detection approach. On analysis, it was seen that vegetation does not show any interference with backscattered energy ( $R^2 = 0.0538$  and  $0.0346$  for VH and VV polarization, respectively). Volumetric soil moisture and backscattered energy showed a positive correlation with  $R^2 = 0.58$  and  $0.4$  for VH and VV polarization, respectively. The  $R^2$  performance of difference between Cross- and Co-polarizations backscattered energy is  $0.58$ . By taking account of all these backscattered coefficients, a Semi-empirical model was developed to retrieve SSM over the study area. This model achieved adjusted  $R^2 = 0.522$  with  $RMSE = 2.407$  at 95% confidence interval.

### 4.1 Introduction

Surface soil moisture holds a less amount of water in the hydrological cycle but it is very prominent in bifurcating surface and sub-surface runoff. Hydrological factor like soil moisture in mountainous terrain regulates the obtainability of water, variation of vegetation distribution and effects of erosion in the river process and contributes to global and regional climate variability (Bales et al. 2006). A better understanding

---

P. Gururaj (✉) · P. Umesh · P. E. K. Sara · A. Shetty  
Department of Applied Mechanics & Hydraulics, National Institute of Technology Karnataka,  
Mangalore, India

of soil moisture will enable us to understand the regional hydrological cycle and enable comprehensive management of natural resources (Nolin 2012; Bertoldi et al. 2014). The forest grasslands are the one which plays a prominent role in holding greater soil moisture and acts as recharge structures so studies about this will improve understanding of mountain hydrology.

Field measurement of soil moisture is more precise and laborious. Developments in the field of satellite remote sensing have given multiple techniques to estimate soil moisture over larger areas (Engman 1992). Various remote sensing platforms supporting soil moisture retrieval are ground-based, airborne-based or space-based. Space-borne satellites are given the best provision to cover larger areas with a short period of repetition. The high penetration power of Synthetic Aperture Radar (SAR) which is an active microwave sensor has given prominent results in redeeming soil moisture from a space platform. The launch of freely available Sentinel-1a and 1b has increased the researches in the field of SAR technology. From previous studies, it has been identified that backscattered energy ( $\sigma^\circ$ ) is directly linked to volumetric soil moisture in barren and grasslands (Oh et al. 1992; Dubois et al. 1995; Engman et al. 1992; Kornelsen and Coulibaly 2013; Das and Paul 2015; Rawat et al. 2018).

The key focus of this study is to develop a practicable model to redeem surface soil moisture using C-band SAR data of Sentinel-1a over mountainous terrain. The backscattered energy ( $\sigma^\circ$ ) is an outcome of soil moisture and surface roughness in the case of barren/grasslands whereas surface roughness is eliminated using dry season image (Zribi et al. 2007). Presently, the model was developed based on polarization, soil texture and dielectric behaviour of soil. This paper consists of three sections. The first section explains about the study area, data collection, experimental measurements and image analysis. The second section describes about the factors affecting soil moisture retrieval. The third section clarifies the study with developed model and validation.

## 4.2 Study Area and Data Products

### 4.2.1 Location

The Mountainous Terrain considered for this study is Kudremukh National Park (KNP) which is a part of the central Western Ghats which is also called as mining town. KNP is extends from Latitude 13°01'00" to 13°29'17" N and Longitude 75°00'55" to 75°25'00" E. The total area of KNP is 600.32 km<sup>2</sup>. The location is such that measurement of any hydro-metrological is difficult. If it is available, it is very sparse and limited. The average annual rainfall of the KNP is 7100 mm with 125 rainy days in a year. Tunga, Bhadra and Netravathi are the Majors Rivers of South India origins from KNP (Revised Kudremukh Management Plan Guide 2013). The soil of KNP varies from brownish loamy soil at the top and brownish clayey loamy soil at foothills. The location map of the study area is presented in Fig. 4.1.

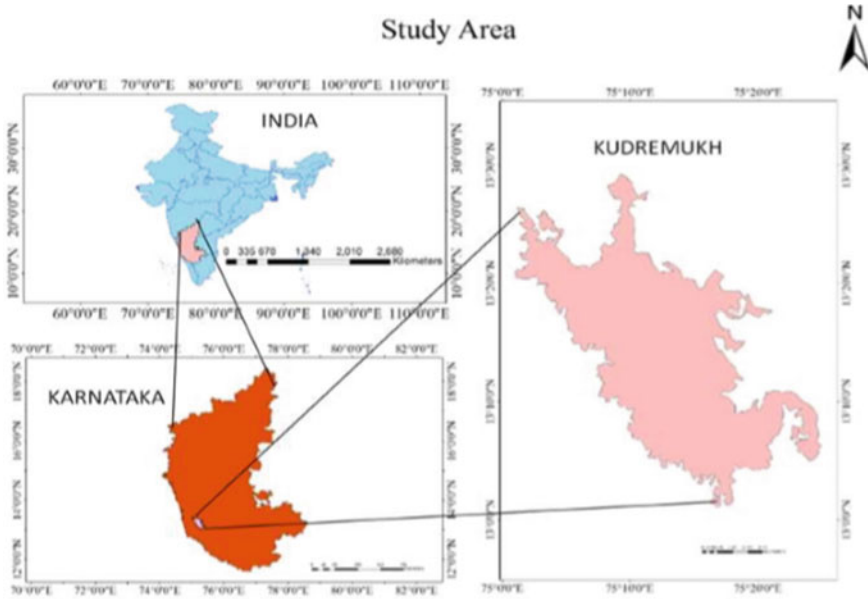


Fig. 4.1 Study area

Table 4.1 Specifications of satellite data used

Satellite	Date	Bands	Path	Row	Resolution	Polarization
Landsat-8	8/02/2017	1-5	145	51	30 * 30	-
Sentinel-1a	21/04/2017	C-band	63	549	15 * 20	VV & VH
	27/02/2018					

## 4.2.2 Remote Sensing Data and Pre-processing

### 4.2.2.1 Optical Data

The cloud-free Landsat-8 data of KNP is procured from USGS earth explorer. The various spectral bands are assigned with appropriate names and for the bands 5, 4 and 3, a layer stack is carried out. The pre-processing Landsat-8 images are carried using appropriate tools of ERDAS Imagine 9.3 software. The Landsat-8 data specifications are shown in Table 4.1.

### 4.2.2.2 Microwave Data

Sentinel-1a, C-band SAR microwave dual-polarized data is downloaded from the Alaska land facility service. The SNAP software is used to pre-process the images

of Sentinel-1a. Image calibration is carried out using Sentinel-1 toolbox kit. SAR images are subjected to some sort of noise which is called as speckle which decreases the image clarity and this should be removed using speckle filters. The lee sigma filter with size  $7 * 7$  is used to filter Sentinel-1a image using Sentinel Application Platform (SNAP). It is found that speckles also carry some information so complete removal of speckles will end up in loss of information. Geocoding is carried out and terrain correction is applied using SRTM DEM data using SNAP software. The Sentinel-1a data specifications are given in Table 4.1.

### 4.2.3 Experimental Measurements

For this study, Sentinel-1a image acquired on 27/02/2018 is used, with corresponding ground surveys performed on the same day and time (6:28 a.m. 2 h). From IMD rainfall data, it was made sure that there was no rainfall prior to 5 days and also during data collection. Ground Control Points (GCP) for every 42 positions were collected using a Trimble handheld GPS instrument. The two types of soil samples over 42 locations were collected from KNP and the experiments were carried out from the laboratory to estimate Gravimetric soil moisture, Bulk Density and Soil Texture. Soil moisture samples are collected in air-tight containers and initial weight was measured in the field. The other set samples are collected using a core cutter which is further used in the lab to calculate bulk density and soil texture (Hydrometer method). The soil moisture, bulk density and soil texture were calculated according to IS 2720-4, 1965. Some important equations used are shown in Eqs. (4.1, 4.2 and 4.3). Out of 42 samples, 31 samples were used to develop the model and 11 were used for validation.

$$\text{Gravimetric soil moisture (GSM)} = \frac{\text{Wet weight} - \text{dry weight}}{\text{dry weight}} * 100 \quad (4.1)$$

$$\text{Bulk Density of Soil} = \frac{\text{Dry soil weight}}{\text{volume of soil}} \quad (4.2)$$

$$\text{Volumetric Soil Moisture Content} = \text{GSM} * \text{Bulk density of Soil} \quad (4.3)$$

## 4.3 Methodology

Landsat-8 image of the study area was pre-processed and Land Use/Land Cover (LULC) Classification was carried using Maximum Likelihood Classifier. The image was classified into four categories namely Forest, Grasslands, Barren lands and water bodies. The grasslands and barren lands account for a total area of 20 and 9% of the



study area. From the classified image, barren and grasslands were extracted. The sampling locations for the field campaign are selected based on the accessibility and land cover. The selected sampling locations are made sure to fall on grass/barren lands by overlaying them on the LULC map and over which soil moisture is retrieved. The LULC map and sampling locations overlaid on the grasslands of KNP were shown in Figs. 4.2 and 4.3, respectively. Two SAR images of Sentinel-1a were procured for this study. One SAR image is used to develop a soil moisture model and other SAR images are selected during the dry season to eliminate the effect of surface

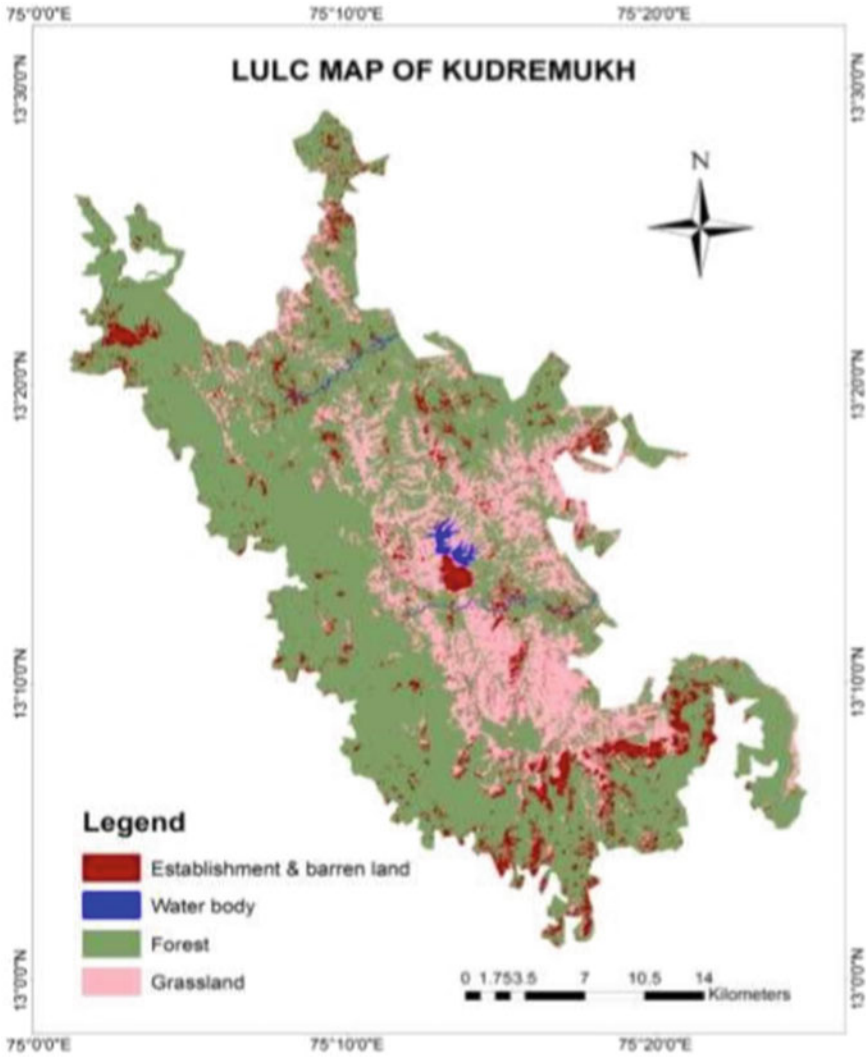


Fig. 4.2 LULC map of Kudremukh National Park

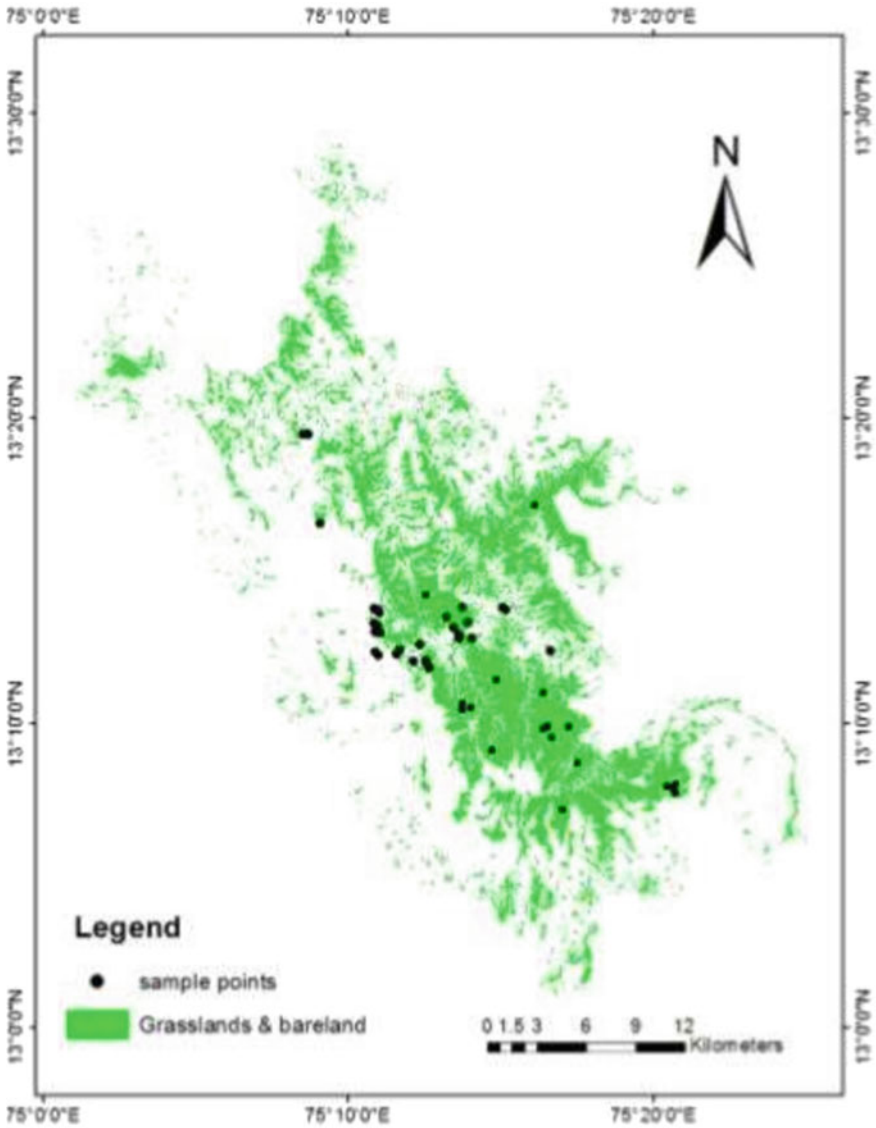


Fig. 4.3 Sampling locations of Kudremukh National Park

roughness parameter on backscattered energy (Zribi and Dechambre 2002; Zribi et al. 2007). The SAR image is converted into backscattered energy ( $\sigma^0$ ) using Eq. (4.4). NDVI map for KNP is also generated to check the influence of vegetation on the backscattered energy of the SAR image. The statistical relationship is established between and soil moisture and semi-empirical model is developed. The schematic flowchart of the overall methodology is shown in Fig. 4.4.

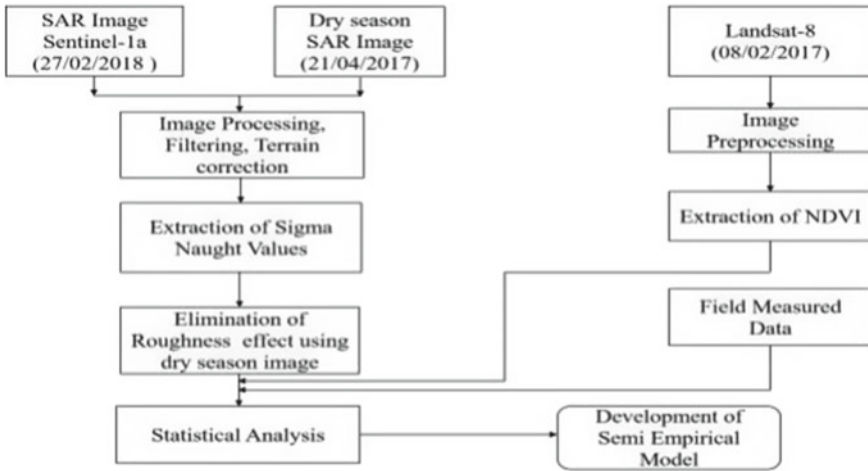


Fig. 4.4 Flowchart of methodology

## 4.4 Results and Discussion

### 4.4.1 Backscattered Coefficient ( $\Sigma^\circ$ ) and NDVI

NDVI map was developed using Landsat-8 image. The NDVI values of KNP over sampling locations were extracted using R software. The NDVI values vary between 0.33 and 0.017. The variation of NDVI with respect to different sampling locations is shown in Fig. 4.5. From Fig. 4.5, it is observed that the NDVI value is not more than 0.35 so there is no need for vegetation correction (Dobson et al. 1986). The relation between NDVI and Backscattered energy is presented in Fig. 4.6. The  $R^2$  of

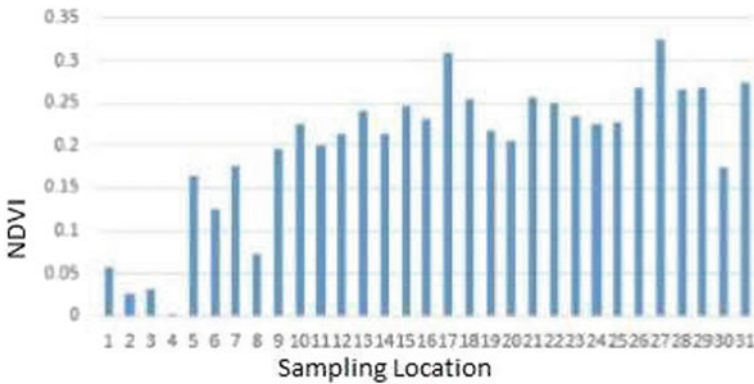


Fig. 4.5 NDVI value distribution across the sampling points

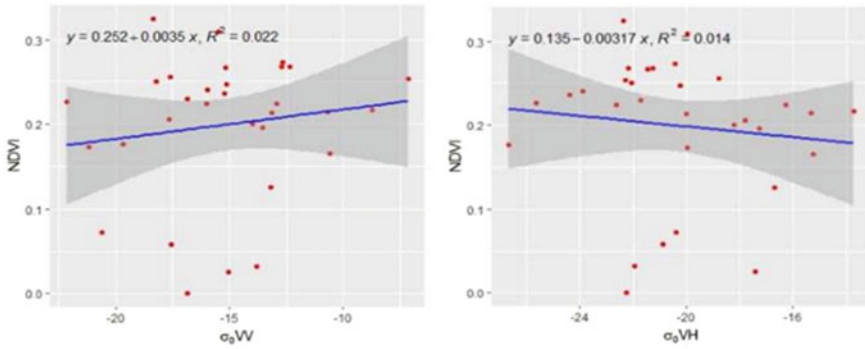


Fig. 4.6 Relation between NDVI and backscattered energy

NDVI between and is 0.022 and 0.0014, respectively. So correction for vegetation influence in  $\sigma^\circ$  energy is not required.

#### 4.4.2 Backscattered Coefficient ( $\Sigma^\circ$ ) and Volumetric Soil Moisture Content

Volumetric soil moisture was calculated using laboratory experiments. The mean for each of the sites is  $8.525 \text{ m}^3/\text{m}^3$  and ranges from 24.06 to  $2.28 \text{ m}^3/\text{m}^3$ . Derived  $\sigma^\circ_{VH}$  ranges from  $-22.152$  to  $-7.135$  decibels (dB) with a median value of  $-15.16$  dB and  $\sigma^\circ_{VV}$  ranges from  $-26.683$  to  $-13.712$  dB with a median value of  $-20.425$  dB. The relationship between  $\sigma^\circ$  and measured volumetric soil moisture is exemplified in Fig. 4.7 for the day 27/02/2018. From Fig. 4.7, the association with a correlation coefficient  $R^2$  of about 0.38 for VH polarization and 0.59 for VV polarization is identified. The results show that the VV polarization soil backscattering coefficient

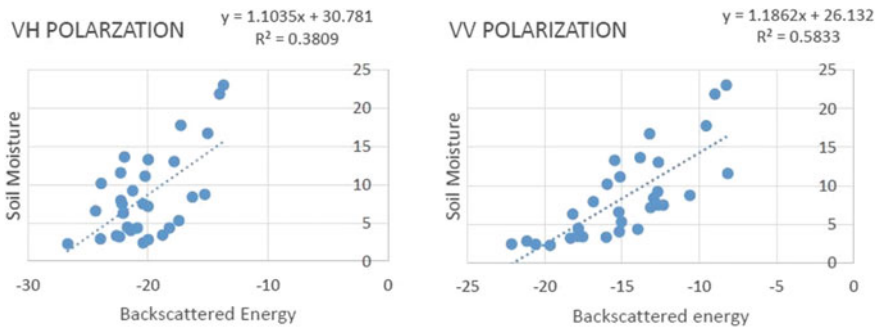


Fig. 4.7 Relationship between  $\sigma^\circ$  energy and ground truth soil moisture for VH and VV polarization

has the highest correlation with the measured soil moisture. This is because cross-polarization has a poorer penetration capability than co-polarization and is more susceptible to vegetation blocking.

### 4.4.3 Soil Moisture Model

The parameters which impact the sensitivity of  $\sigma^\circ$  values of SAR image to redeem soil moisture ( $M_v$ ) were accounted to develop a soil moisture model. Theoretically, soil moisture estimation using SAR data must account for soil moisture, soil roughness and vegetation parameter. Effect of soil roughness is nullified by using the change detection approach (Dry Season image). It was also found that vegetation did not affect the  $\sigma^\circ$  of VV and VH polarization. Multi-Linear Regression (MLR) analysis is carried out to develop a modeling which  $M_v$  acts as a free variable and  $\sigma_{vv}^\circ$  and  $\sigma_{vh}^\circ$  act as dependent variables. The developed model (Eq. 4.4) with MLR approach gave  $R^2 = 0.52$  and RMSE of 2.407 at a confidence interval of 95%. By using the developed surface, the soil moisture map that is developed for date 27/02/2018 is shown in Fig. 4.8.

$$M_v = 11.963 + 0.481 * \sigma_{vv}^\circ + 0.935\sigma_{vh}^\circ \quad (4.4)$$

Out of 42 sampling points, 31 were used for unbiased calibration of the model which includes all ranges of values, and the rest 11 were used for the validation. The obtained semi-empirical model is validated using 11 sampling locations. Figure 4.9 shows that the relation between modelled and measured soil moisture is significant and positive. The  $R^2$  performance between soil moisture observed and soil moisture modelled is found to be 0.56.

## 4.5 Conclusions

The developed model is mainly based on backscattered energy which makes the model look quite simple and practical to extract soil moisture over Grasslands using  $\sigma^\circ$  energy. The main benefit of this model is that it needs only time field data. The surface soil moisture variation was examined at 10 m resolution using field measurements and derived soil moisture from Sentinel-1a. From the study, it is noted that  $\sigma^\circ$  has an optimistic relationship with volumetric moisture content for VH and VV polarization with  $R^2 = 0.38$  and  $R^2 = 0.58$ , respectively. This developed model has adjusted  $R^2 = 0.522$  and RMSE = 2.407 at confidence interval of 95%. The developed model was validated with ground truth soil moisture values. It was found that measured vs observed soil moisture is having  $R^2 = 0.56$ . In this case, the ease of use of field data has greater importance on the operational results. In the absence of any measured data on soil moisture in such terrain, this study will be useful for

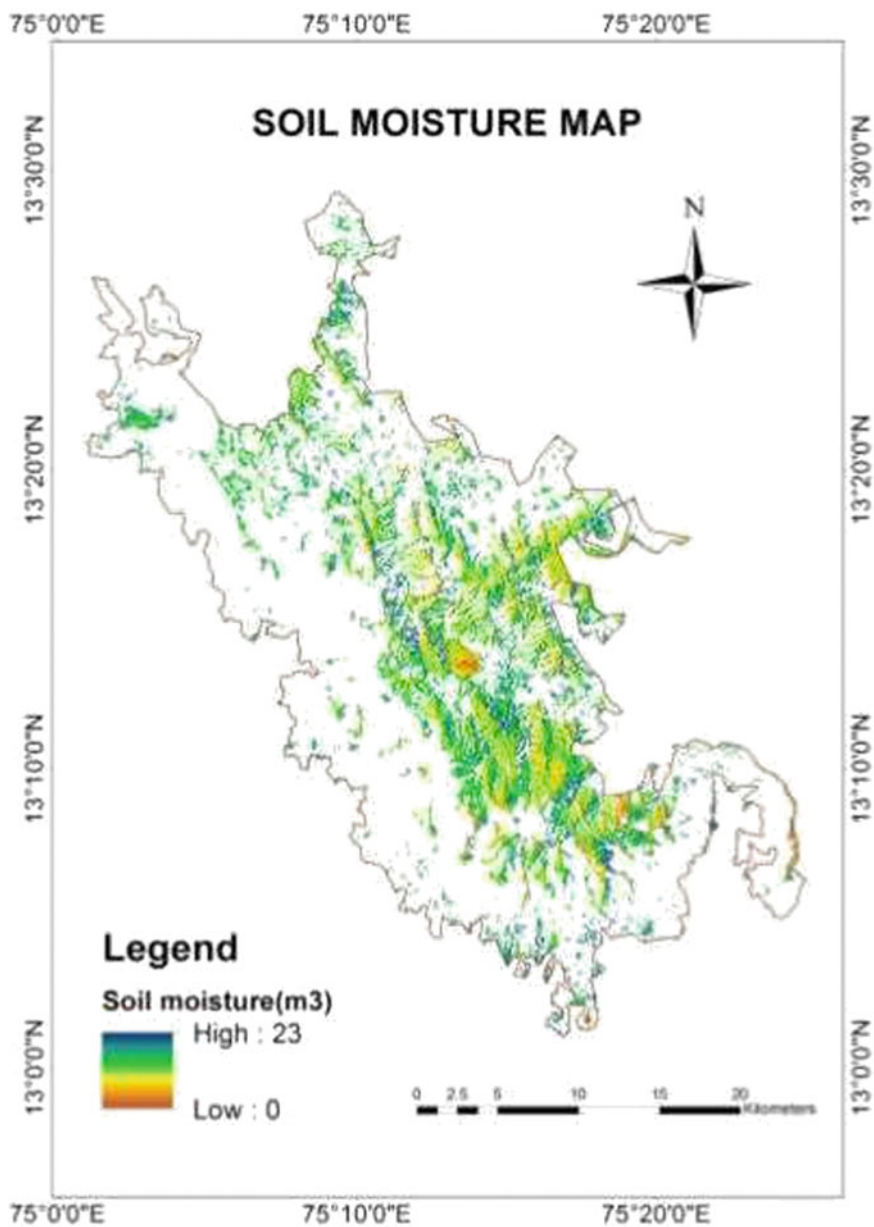
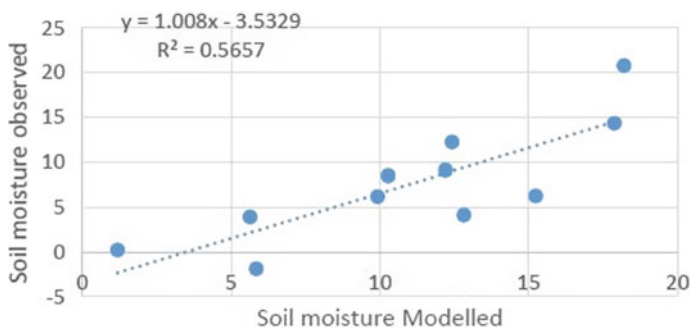


Fig. 4.8 Estimated soil moisture map of KNP on 27 Feb 2018



**Fig. 4.9** Correlation between modelled and observed soil moisture

future investigations on estimating stream flow and any hydrological parameters. The model can be improvised by inputting soil texture in terms of dielectric constant as future work.

## References

- Bales RC, Molotch NP, Painter TH, Dettinger MD, Rice R, Dozier J (2006) Mountain hydrology of the western United States. *Water Resour Res* 42:W08432. <https://doi.org/10.1029/2005WR004387>
- Bertoldi G, Chiesa SD, Notarnicola C, Pasolli L, Niedrist G, Tappeiner U (2014) Estimation of soil moisture patterns in mountain grasslands by means of SAR RADARSAT2 images and hydrological modelling. *J Hydrol* 516:245–257. <https://doi.org/10.1016/j.jhydrol.2014.02.018>
- Das K, Paul PK (2015) Soil moisture retrieval model by using RISAT-1, C band data in tropical dry and sub-humid zone of Bankura district of India. *Egypt J Remote Sens Space Sci* 18:297–310
- Dobson MC, Ulaby FT (1986) Active microwave soil moisture research. *IEEE Trans Geosci Remote Sens* GE-24:23–36
- Dubois PC, van Zyl J, Engman T (1995) Measuring soil moisture with imaging radars. *IEEE Trans Geosci Remote Sens* 33:915–926. <https://doi.org/10.1109/36.406677>
- Engman ET (1992) Soil moisture needs in earth sciences. In: Proceedings of IEEE international geoscience and remote sensing symposium (IGARSS), pp 27–47
- Kornelsen KC, Coulibaly P (2013) Advances in soil moisture retrieval from synthetic aperture radar and hydrological applications. *J Hydrol* 476:460–489
- Nolin AW (2012) Perspectives on climate change, mountain hydrology, and water resources in the Oregon Cascades, USA. *Mt Res Dev* 32(S1):S35–S46
- Oh Y, Sarabandi K, Ulaby FT (1992) An empirical model and an inversion technique for radar scattering from bare soil surfaces. *IEEE Trans Geosci Remote Sens* 30:370–381
- Rawat KS, Sehgal VK, Pradhan, Ray SS (2018) Semi-empirical model for retrieval of soil moisture using RISAT-1 C-Band SAR data over a sub-tropical semi-arid area of Rewari district, Haryana (India). *J Earth Syst Sci* 127:18. <https://doi.org/10.1007/s12040-018-0919>.
- Revised management plan for Kudremukh national park 2003–13 Report, Karnataka forest department, Karnataka
- Zribi M, Dechambre M (2002) A new empirical model to inverse soil moisture and roughness using two radar configurations. In: IEEE International geoscience and remote sensing symposium, vol 4, Toronto, Ontario, Canada, pp 2223–2225

Zribi M, Saux-Picart S, André C, Descroix L, Otlé C, Kallel A (2007) Soil moisture mapping based on ASAR/ENVISAT radar data over a Sahelian region. *Int J Remote Sens* 28(16):3547–3565. <https://doi.org/10.1080/01431160601009680>



# Chapter 5

## Meteorological Drought Assessment in the Bharathapuzha River Basin



M. A. Jincy Rose and N. R. Chithra

**Abstract** Drought is a creeping yet devastating phenomenon that affects nearly half of the population on the earth. Bharathapuzha river, the largest and second-longest of the rivers in Kerala, which was once a perennial river is now on the verge of its death. The river basin faces acute water shortage especially in the summer months of the year. The paper examines and explains the meteorological drought occurrence in the river basin with the help of a highly recommended indicator for drought, the SPI, and a simple and well-renowned rainfall trend detection technique, the non-parametric Mann–Kendall test, and Sen’s slope method for its magnitude. This study also forecasts the temporal drought behaviour in the catchment for RCP 4.5 and RCP 8.5 future climate change scenarios using the simulated precipitation data of CORDEX. Gridded daily precipitation data of IMD (Indian meteorological department) of 0.5-degree resolution was used to study the drought pattern of the river basin in the period of 1971–2005. This historical record analysis was performed to understand the variations in drought events during each of the timescales such as 1 month, 3 months, 6 months, 9 months and 12 months denoted as SPI-1, SPI-3, SPI-6, SPI-9 and SPI-12, respectively. The results indicate the presence of meteorological drought in the historic period as well as in the future scenarios. The Mann–Kendall trend test was done for rainfall over a period of 35 years and could find that the Mann–Kendall statistic  $S$  gives a decreasing trend with time. Sen’s slope gives a decrease in the magnitude of 14.3 mm/year. Thus, the results of the Mann–Kendall trend tests also support the statement of drought in the catchment. The analysis of RCP scenarios also indicates the presence of drought in the river basin with moderate to extreme drought where the frequency of the drought condition increases in the river basin up to 2039 and beyond which it reduces.

---

M. A. J. Rose (✉) · N. R. Chithra  
Department of Civil Engineering, National Institute of Technology, Calicut, Kozhikode 673601,  
India  
e-mail: [jincyrose\\_p170004ce@nitc.ac.in](mailto:jincyrose_p170004ce@nitc.ac.in)

## 5.1 Introduction

Drought is a grievous natural phenomenon that is least understood and complex in nature that affects more lives than any other natural hazard. This obviously has paved the way for more researches to define drought (Sheffield and Wood 2012; Mishra and Singh 2010; Tallaksen and Van Lanen 2004; Wilhite 2000; Wilhite and Glantz 1985). Most of the studies are extended in concern with the global scenarios where a regional approach is least prioritized and almost neglected. On a regional scale, drought is reflected in terms of reduction in rainfall, low flow in streams and rivers, declining groundwater levels, wilting of crops and collapsed economy leading to a disturbed societal status. Thus, drought is broadly classified into four, upon the variables involved in the analysis namely meteorological, hydrological, agricultural and socio-economic droughts (Tallaksen and Van Lanen 2004). Among these, hydrological drought analysis can be said to be a little complicated as it involves both climate as well as catchment characteristics. According to Palmer (1965) and Beran and Rodier (1985), drought is stated to be a meteorological phenomenon. The study in the river basin, thus, leads to an investigation of the meteorological drought analysis with the perspective that it being the most fundamental requirement of any drought study. As it is a creeping phenomenon, timely analysis, planning and management would help reduce the severity of the condition to an extent.

Indian Meteorological Department (IMD) classifies drought upon the rainfall deviations which accounts for the total of the season's actual rainfall with respect to the mean of long-term rainfall. As per the IMD, a drought event is said to occur when the total rainfall of a place for a particular season is 75% less compared to the mean of its long-term rainfall. A severe drought is declared if there is a 25% decrease in a season's rainfall compared to its long-term mean (<http://imd.gov.in/section/nhac/wxfaq.pdf>). Though the drought declaring deviation criteria varies spatially, many of the studies follow the deviation of rainfall as the drought intensity indicator due to its easiness. Since this indicator is strongly dependent on its mean, and as the mean rainfall values differ spatially, the distribution of deviation in rainfall cannot be applied uniformly. The Standardized Precipitation Index (SPI), thus, overcomes this situation where a probability distribution function is fitted to the actual rainfall to get a standardized departure. The supremacy of using SPI is that only rainfall data is needed for its computation and can also be compared across regions of different climatic zones.

In the past couple of decades, it is observed to have great anomalies in the general rainfall of the Bharathapuzha region. The river basin is also reported to have a serious water shortfall leading to drought conditions in recent years (Raj and Azeez 2010). Recently, a few studies in the Bharathapuzha river basin have been reported in context with the trend analysis (Raj and Azeez 2012; Jagadeesh and Anupama 2014; Varughese et al. 2017), temperature rise (Raj and Azeez 2010), decision-making process for managing environmental flows (Padikkal and Rema 2013), morphometric analysis using geographical information system environment (Magesh et al. 2013; Raj and Azeez 2012) and land use land cover changes (Raj

and Azeez 2010). As no study on the investigation of drought has been reported in the Bharathapuzha river basin, this paper investigates the occurrence of the meteorological drought assessment of the river basin with the Standardized Precipitation Index (SPI) recommended by the World Meteorological Organization (WMO) due to its spatial consistency. A simple rainfall trend analysis over the catchment uses the non-parametric Mann–Kendall test for trend detection and Sen’s slope method for its magnitude. The study also forecasts the temporal drought behaviour using simulated precipitation data of CORDEX (Coordinated downscaling regional experiment), for RCP 4.5 and RCP 8.5, the two different future climate scenarios.

## 5.2 Study Area and Data

### 5.2.1 Study Area

Bharathapuzha is the largest and second-longest of the 44 rivers in Kerala located at  $10^{\circ}25'N$  to  $11^{\circ}15'N$  and  $75^{\circ}50'E$  to  $76^{\circ}55'E$ . It is one among the four medium-sized rivers in Kerala which is 209 km long with a watershed of 6,186 km<sup>2</sup> in which 4400 km<sup>2</sup>, the majority area, falls within the state Kerala and the rest of the portion in Tamil Nadu. It was once a perennial river that originates in the Anamalai hills of Tamil Nadu and debouches into the Arabian Sea at Ponnani in Kerala. The basin receives about an average annual rainfall of 2060 mm. Seven reservoirs were constructed in this river by Kerala Government and four reservoirs by Tamil Nadu Government. Bharathapuzha river basin is having a unique physiographic feature. This region is divided into three prominent physiographic zones; high land with an altitude greater than 76 m, midland with an altitude ranging between 7.6 and 76 m and lowland where the altitude is less than 7.6 m. The river serves as a lifeline to three administrative districts in Kerala and two in Tamil Nadu and also supports the agricultural production system of the Kerala state, especially “the rice bowl of Kerala” in Palakkad. Thus, the river has a pivotal role in the societal, economic and agricultural aspects of the state. The location map of the study area is shown in Fig. 5.1.

### 5.2.2 Data Collection and Pre-processing

$0.5 \times 0.5$ -degree gridded daily precipitation data from the Indian meteorological department for the period of 1971–2005 (35 years) is used for the study. To forecast the SPI index, the freely downloadable ([http://cccr.tropmet.res.in/home/ftp\\_data.jsp](http://cccr.tropmet.res.in/home/ftp_data.jsp)) simulated precipitation data of CORDEX (Coordinated downscaling regional experiment), for two different future climate scenarios (RCP 4.5 and RCP 8.5) for a period of 2006–2099 (94 years), was used. The RCM used is the Conformal-Cubic

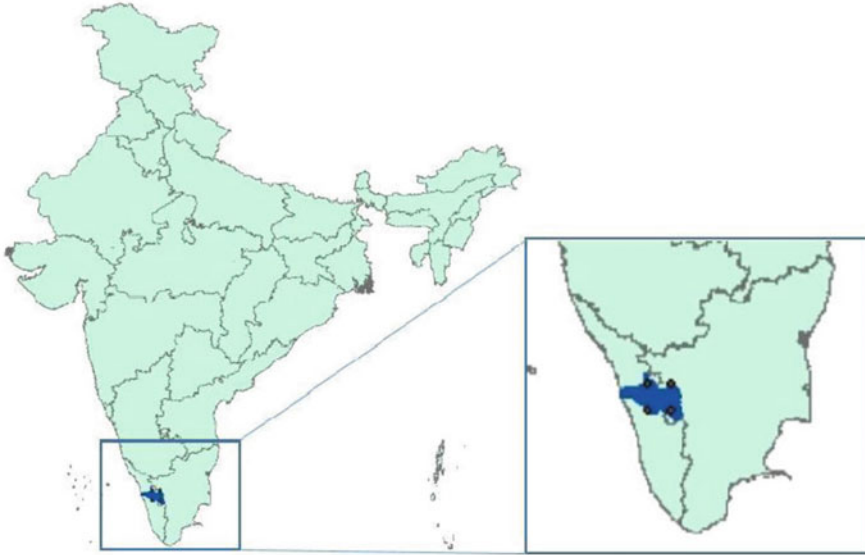


**Fig. 5.1** The study area location

Atmospheric Model (CCAM; McGregor and Dix 2001) by Commonwealth Scientific and Industrial Research Organization (CSIRO), and the driving GCMs used are ACCESS1.0 and CCSM4. A Linear Scaling (LS) bias correction was also applied for the data before the drought index calculation.

### 5.3 Methodology

Out of the several indices available, Standardized Precipitation Index (SPI) is the most recommended by the World Meteorological Organization (WMO) and widely accepted and used index, it requires only monthly or daily precipitation data, it can be compared across regions making it consistent in different climates, SPI determines the oddity of a current drought by the standardization of the index, it can be obtained for various time scales ranging from 1 to 48 months in general and hence was used to assess the meteorological drought of the area. The following is the outline of the works done for the drought assessment. (1) Delineation of the river basin in ArcGIS using ASTER Dem, which helps find the location of the grids chosen. (2) Extraction of the rainfall data from IMD (Indian Meteorological Department) for 35 years (1971–2005). (3) Trend detection using the Mann–Kendall test and its magnitude using Sen’s slope method. (4) SPI index calculation for time scales SPI-1, SPI-3, SPI-6, SPI-9 and SPI-12 with the aid of SPI\_SL\_6.exe calculator of the National Drought Mitigation Centre (NDMC), University of Nebraska. (5) Forecasted the

temporal drought behaviour using the simulated precipitation data from CORDEX for RCP 4.5 and RCP 8.5, the future climate scenarios chosen.

### 5.3.1 Delineation of the River Basin

Watershed delineation is done to demarcate the boundary of the area that contributes to the outlet of a river. The river basin was delineated with the help of ASTER (Advanced Spaceborne Thermal Emission and Reflection Radiometer) DEM (Digital Elevation Model) obtained from USGS Earth Explorer (<http://earthexplorer.usgs.gov>) that was freely downloadable. The ASTER DEM helps analyse the changes in the global environment such as warming, mineral research, desertification, acid rain and destruction of the ozone layer. The DEM also aids the geological research and natural resource exploitation and performs mission operations which reflect user requests regarding the data acquisition of the ASTER sensor. The ArcGIS 10.2.1 is aided with the delineation of the river basin. Four grid points of  $0.5 \times 0.5$ -degree resolution are selected on the catchment. The latitude and longitude of each grid chosen are  $(10.5^\circ, 76.5^\circ)$ ;  $(11^\circ, 76.5^\circ)$ ;  $(10.5^\circ, 77^\circ)$  and  $(11^\circ, 77^\circ)$ . The location of the grids on the map is given in Fig. 5.2.

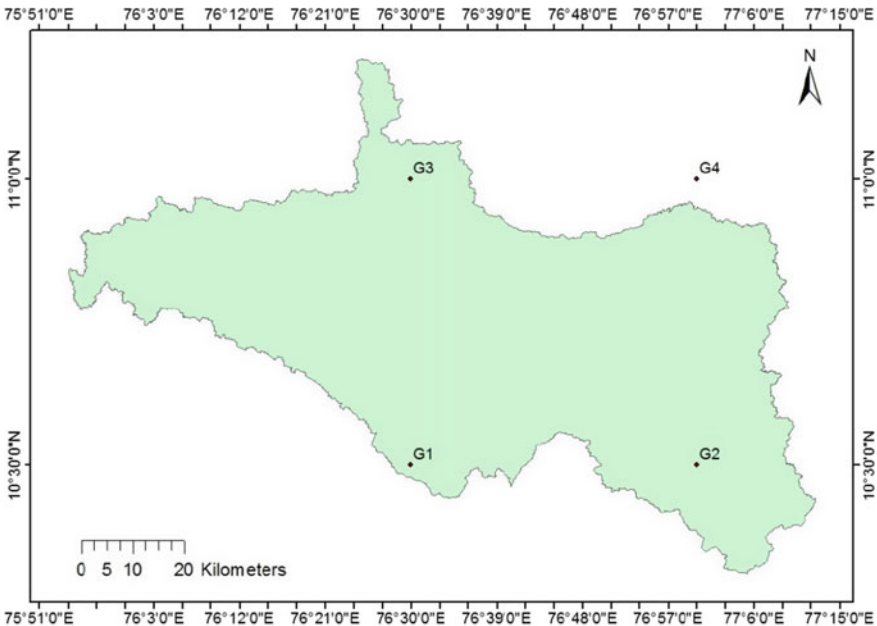


Fig. 5.2 Location of selected grid points

### 5.3.2 Trend Analysis

The rank-based Mann–Kendall test is a non-parametric test recently well used by the research community in order to detect trends in rainfall data (Mann 1945; Kendall 1975; de la Casa and Nasello 2010; Krishnakumar et al. 2009). The test statistic  $S$  is defined as follows:

$$S = \sum_{l=1}^{n-1} \sum_{j=i+1}^n \text{sgn}(x_j - x_i) \quad (5.1)$$

The data set length is indicated using  $n$ , and  $x_j$  denotes values of the sequential data.

$$\text{sgn}(y) = \begin{cases} 1 \dots \text{if}(y > 0) \\ 0 \dots \text{if}(y = 0) \\ -1 \dots \text{if}(y < 0) \end{cases} \quad (5.2)$$

When  $n \geq 8$ , the studies say that the test statistic  $S$  is approximately normally distributed with the mean  $E(S) = 0$  and variance as follows:

$$V(S) = \frac{n(n-1)(2n+5) - \sum_{i=1}^m t_i(t_i-1)(2t_i+5)}{18} \quad (5.3)$$

Here,  $m$  represents the number of tied groups and  $t_i$  is the size of the  $i$ th tied group. The standardized test statistic  $Z$  is computed by

$$\text{ZMK} = \begin{cases} \frac{S-1}{\sqrt{\text{var}(S)}} & \text{when } s > 0 \\ 0 & \text{when } s = 0 \\ \frac{S+1}{\sqrt{\text{var}(S)}} & \text{when } s < 0 \end{cases} \quad (5.4)$$

### 5.3.3 Standardized Precipitation Index for Drought Analysis

In the recent years, the Standardized Precipitation Index (SPI) has gained more prominence as an effective drought indicator highly recommended by the World Meteorological Organization (WMO) that can be compared spatially and temporally. This is because that the actual time series data of rainfall is first fitted to a probability distribution function to get a standardized departure that makes it spatially compatible. SPI calculation necessitates a long-term precipitation data that usually follows a gamma probability distribution function which is then converted into a normal distribution with its mean zero and standard deviations one. Edwards and McKee (1997) explained that the standard deviations with greater than median precipitation

imply a positive SPI value and less than median precipitation implies a negative SPI value. SPI can be computed for different time steps (1 month, 3 months, 6 months, 9 months, 12 months, 24 months, 48 months, etc.). These time steps denote the effect of deficit in precipitation upon various components in water resources namely soil moisture, streamflow, groundwater, etc. The severity of the drought event is decided upon the negative deviations. A severe drought event is said to occur with a higher magnitude. Thus, as the magnitude of negative deviation increases, the severity of drought is also said to increase. The onset of a drought event is indicated with the SPI value  $-1$  and the condition persists until the SPI values become positive again. Therefore, the severity of drought condition is explained within an SPI range where the condition is said to be moderately dry if the SPI value ranges between  $-1$  and  $-1.49$ , the condition is severely dry if the SPI falls between  $-1.5$  and  $-1.99$  and an SPI value less than  $-2.0$  being an extremely dry condition (McKee et al. 1993).

## 5.4 Results and Discussions

### 5.4.1 Trend Analysis

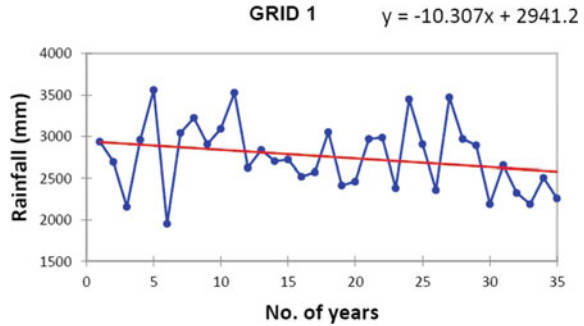
Trend analysis was done for the gridded rainfall data of IMD. The non-parametric Mann- Kendall test was done for the trend detection and Sen’s slope method for its magnitude. The Mann–Kendall test statistic  $S$  measures the trend in the data. The positive test statistic values indicate an increasing trend and negative values indicate a decrease in value over time. The magnitude of  $S$  will be commensurate with the strength of the trend (i.e., larger magnitudes indicate a stronger trend). Table 5.1 provides the information on the existence of a trend in the data. As the  $S$  value obtained for all the grids namely G1, G2, G3 and G4 are negative values, it can be stated that all the grids of the study area show a negative trend. A time series plot of grid 1 is shown in Fig. 5.3.

The defined threshold in the study is 5% with the null hypothesis that states there is no trend. As the trend is judged based on these thresholds, a trend was detected only for grids 1 and 4 at a 5% significance level. As there would be a trend in the data behind the selected threshold, the  $p$ -value calculated that is given in Table 5.1 explains

**Table 5.1** Results of the Mann–Kendall trend test and Sen’s slope estimator

Grid	Location		Mann–Kendall statistic ( $S$ )	$p$ -value (Two-tailed)	Sen’s slope value (mm/year)
	Latitude	Longitude			
G1	10.5	76.5	$-143.000$	0.044	$-14.905$
G2	10.5	77	$-107.000$	0.132	$-15.445$
G3	11	76.5	$-139.000$	0.280	$-16.45$
G4	11	77	$-77.000$	0.049	$-10.152$

Fig. 5.3 MK test for grid 1



the significance level that corresponds to the trend of the respective grids. Thus, grids 2 and 3 show a significant result at a threshold of 14, 29 and 6%, respectively. On an average, there is a decline in 14.3 mm of rainfall per year according to Sen's slope estimator.

The grids G1 and G4 have a lower  $p$ -value which can reject the null hypothesis even for a larger  $\alpha$ -value. They would be statistically significant at both 95% as well as 90% level of confidence. Thereby, we can conclude both the grids are not only statistically significant but also practically significant. Though grids G2 and G3 are not statically significant and differ by a greater margin when compared to  $\alpha$ -value of 0.05 and 0.1, still the magnitude of the trend which is quantified by Sen's slope is not too high when compared to statistically significant grid G1 ( $-14.905$ ), whereas G2 and G3 have values  $-15.445$  and  $-16.45$ , respectively.

#### 5.4.2 Standardized Precipitation Index (SPI)

The various time steps considered in the analysis are 1 month, 3 months, 6 months, 9 months and 12 months. The SPI values at a time step of 1 month are an indication of the soil moisture for a shorter time span as well as the crop stress. The seasonal precipitation estimates are obtained with the SPI of 3 months that includes short-to medium-term moisture conditions. A visible trend in precipitation from seasonal to medium term could be obtained on a time scale of 6 months. The long-term precipitation patterns as well an indication of inter-seasonal precipitation patterns are well rendered at a duration of the medium time scale of the 9-month SPI. A significant impact of dryness over the agricultural as well as the other sectors are alarmed at an SPI value less than  $-1.5$  at these time scales. The groundwater levels, stream flows and reservoir levels are usually explained by a time scale of 12 months SPI because in the case of longer time scales, the SPI values drift towards the value zero if there is no remarkable wetness or dryness experienced in the area unlike the shorter time scales (Pramudya and Onishi 2018).

Figure 5.4 gives the number of drought months that had affected grid 1 of the study area as per the IMD historic data (1971–2005) and the projected future climate



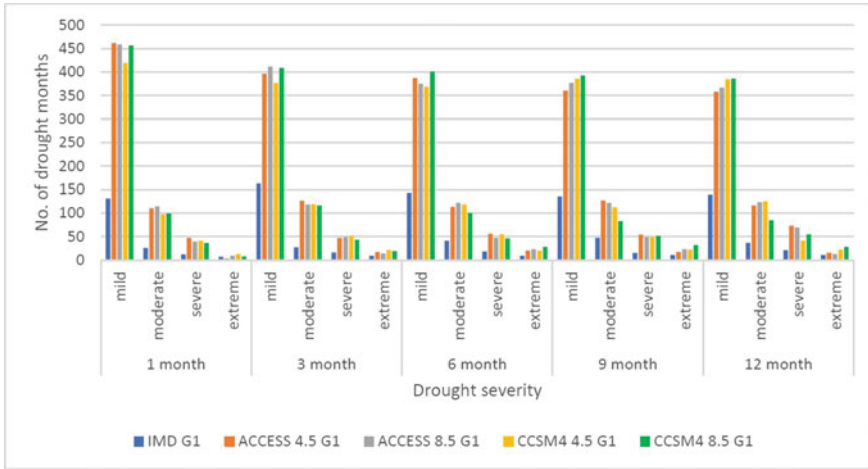


**Fig. 5.4** Number of drought months for grid 1

scenarios for a time period of (2006–2099) using GCM ACCESS 1.0 and CCSM4 for RCP 4.5 and RCP 8.5. The bar chart also compares the severity condition namely mild drought where the SPI value is within ( $0 > SPI > -0.99$ ), moderate dry ( $-1 > SPI > -1.49$ ), severely dry ( $-1.5 > SPI > -1.99$ ) and extremely dry ( $SPI < -2.0$ ) (McKee et al. 1993). The results show that the drought conditions would persist in the future with an increase in the number of drought months under mild and moderate drought events whereas a decrease in the severe and extreme drought months could be observed with time.

Figure 5.5 depicts the SPI drought index for the 12-month time scale of grid 1 for both the observed IMD gridded rainfall data set as well as the projected future climate scenarios. The GCMs chosen along with the two RCP scenarios are represented graphically. From the analysis, it is found that there was a decreasing trend in the SPI values indicating the drought condition of the basin whereas a wet period in the long run increases or that there is a positive trend. It can also be inferred that the frequency of drought with a higher severity would occur in the basin up to 2039 and beyond which the severity reduces. Though severe drought conditions are experienced in near future as per the analysis, a reduction in the severe and extreme drought events could be observed with time. The standard deviation among the two GCMs adopted was also found to be minimal and, thus, it justifies the data sets chosen.

## 5.5 Summary and Conclusions

The study was done on a once perennial tropical medium river basin of Kerala, the Bharathapuzha river basin, which in the recent decades becomes barely a trickle immediately after the monsoon. The objective of the study was to account for the

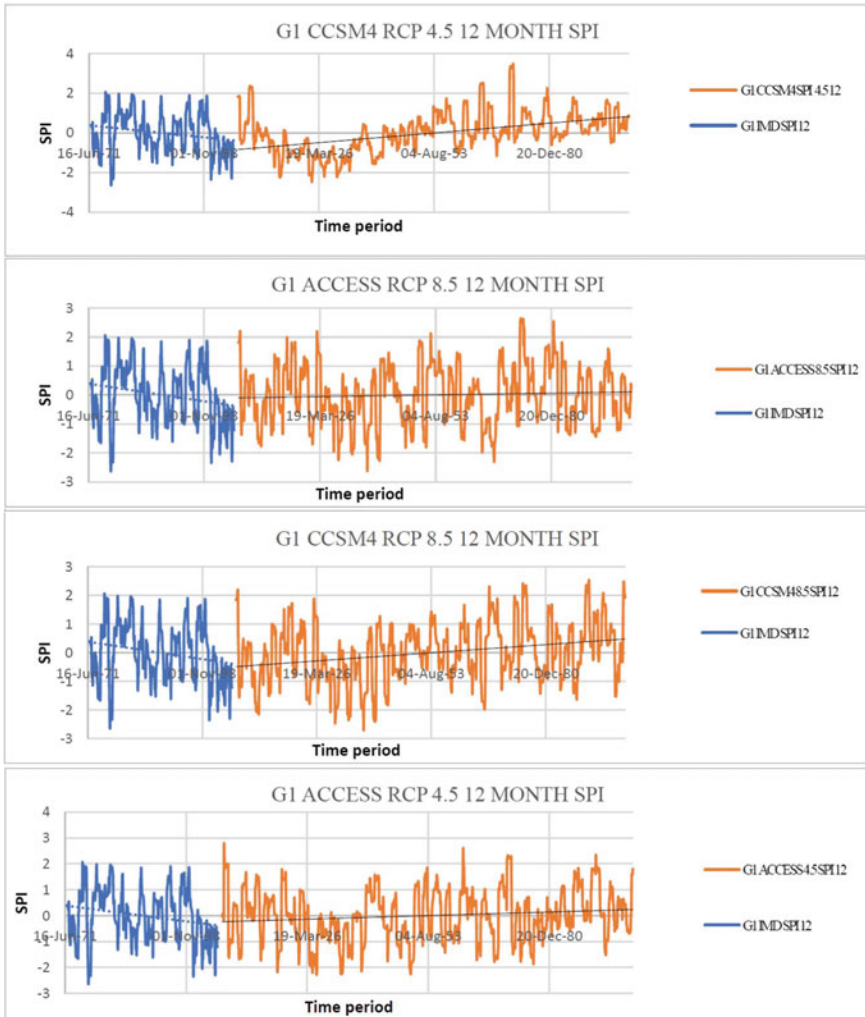


Fig. 5.5 AA12-month SPI for grid 1

presence of meteorological drought existence in the basin. An investigation on the observed IMD gridded rainfall data for 35 years reveals the drought existence that ranges from mild to extreme drought events for all the time scales (1, 3, 6, 9 and 12 months) where the decreasing trend of precipitation in the Mann-Kendall trend test along with Sen’s slope estimator also supports the drought condition experienced in the basin. The SPI values of the projected future climate scenario also explain that the river basin would experience a higher number of meteorological drought events in the future but with a reduction in the level of its severity. It was also noted that the severity of the drought condition as well the frequency of the drought events will be

more pronounced up to 2039 and beyond which a greater number of wetness periods are obtained.

## References

- Beran MA, Rodier JA (1985) Hydrological aspects of drought: a contribution to the International Hydrological Programme, vol 39. Unesco
- de la Casa A, Nasello O (2010) Breakpoints in annual rainfall trends in Córdoba, Argentina. *Atmos Res* 95(4):419–427
- Edwards DC, McKee TB (1997) Characteristics of 20th century drought in the United States at multiple time scales. *Climatology Rep.* 97–2, Department of Atmospheric Science, Colorado State University, Fort Collins, Colorado
- Jagadeesh P, Anupama C (2014) Statistical and trend analyses of rainfall: a case study of Bharathapuzha River basin, Kerala, India. *ISH J Hydraul Eng* 20(2):119–132
- Kendall MG (1975) Rank correlation methods, 4th edn. Charles Griffin, London
- Krishnakumar KN, Rao GP, Gopakumar CS (2009) Rainfall trends in twentieth century over Kerala, India. *Atmos Environ* 43(11):1940–1944
- Magesh NS, Jitheshlal KV, Chandrasekar N, Jini KV (2013) Geographical information system-based morphometric analysis of Bharathapuzha river basin, Kerala, India. *App Water Sci* 3(2):467–477
- Mann HB (1945) Nonparametric tests against trend. *Econom J Econom Soc* 245–259
- Mcgregor JL, Dix MR (2001) The CSIRO conformal-cubic atmospheric GCM. In: IUTAM symposium on advances in mathematical modelling of atmosphere and ocean dynamics. Springer, Dordrecht, pp 197–202
- McKee TB, Doesken NJ, Kleist J (1993) The relationship of drought frequency and duration to time scales. In: Proceedings of the 8th conference on applied climatology, vol 17, no 22. American Meteorological Society, Boston, MA, pp 179–183
- Mishra and Singh (2010) A review of drought concepts. *J Hydrol* 391(12):202216
- Padikkal S, Rema KP (2013) Informed decision making process for managing environmental flows in small river basins. *J Inst Eng (India): Series A* 94(1):43–52
- Palmer WC (1965) Meteorological drought. Weather Bureau Research Paper No. 45, US Department of Commerce, Washington, DC, 58 pp
- Pramudya Y, Onishi T (2018) Assessment of the standardized precipitation index (SPI) in Tegal City, Central Java, Indonesia. In: IOP conference series: earth and environmental science, vol 129, no 1. IOP Publishing, p 012019
- Raj PN, Azeez PA (2010) Land use and land cover changes in a tropical river basin: a case from Bharathapuzha River basin, southern India. *J Geogr Inf Syst* 2(04):185
- Raj PN, Azeez PA (2012) Trend analysis of rainfall in Bharathapuzha River basin, Kerala, India. *Int J Climatol* 32(4):533–539
- Sheffield J, Wood EF (2012) Drought: past problems and future scenarios. Routledge
- Tallaksen LM, Van Lanen HA (2004) Hydrological drought: processes and estimation methods for streamflow and groundwater, vol 48. Elsevier
- Varughese A, Hajilal MS, George B A (2017) Analysis of historical climate change trends in Bharathapuzha River Basin, Kerala, India. *Nat Environ Pollut Technol* 16(1)
- Wilhite (2000) Drought: a global assessment, vols I & II, Routledge hazards and disasters series, Routledge, London
- Wilhite DA, Glantz MH (1985) Understanding: the drought phenomenon: the role of definitions. *Water Int* 10(3):111–120

# Chapter 6

## Experimental and Numerical Analysis of Mean Pressure Coefficient on C-Shaped Building with and Without Round Corner



Monalisa Mallick, Awadhesh Kumar, and Kanhu Charan Patra

**Abstract** The distribution of wind-induced pressure coefficient on the surfaces of the C-shaped building with the varying angles of incidence and with and without round corner has been studied. For this, experiments have been carried out on a typical C-shaped building plan in a sub-sonic open circuit wind tunnel. Two different configurations of C-shaped models i.e., with outer curved and without outer curved C-shaped models were tested. The experimental findings were showed over an extended range of angles of incidence (0–180°) at an interval of 30°. Using Digital Sensor Array (DSA), the pressure coefficient data were recorded at the pressure tapping provided in a grid pattern throughout the surfaces. This procedure was repeated with all the surfaces undertaken, angle of incidence and building plan configuration. The surfaces data of pressure coefficient enabled the determination of mean pressure coefficient at the selected tapping locations. The surface pressure was found to vary significantly with the location on a particular surface and surfaces as well as with the angle of incidence. Pressure coefficient was influenced by building configuration, the extent of curved corners, wind angle of incidence, wind flow behaviour and surroundings on buildings. It has been observed that the curvature is effective in reducing pressure coefficient corresponding to no curvature. The experimental results thus obtained were supported by Numerical analysis. To achieve this, numerical investigation was carried out by using ANSYS FLUENT software. The analysis was carried out using Computational Fluid Dynamic (CFD) with k-e viscosity model and the results obtained were compared with the corresponding experimental data. Experimental and numerical study is carried out for comparison purposes and results have good agreement.

---

M. Mallick (✉) · A. Kumar · K. C. Patra

Dept. of Civil Engineering, National Institute of Technology, Rourkela, Odisha, India

A. Kumar

e-mail: [akumar@nitrkl.ac.in](mailto:akumar@nitrkl.ac.in)

K. C. Patra

e-mail: [kcpatra@nitrkl.ac.in](mailto:kcpatra@nitrkl.ac.in)

## 6.1 Introduction

With increased usage of a range of new innovative building design materials requires an accurate assessment of the wind action and its interaction with structures. The total force exerted upon the structures by wind is known as wind pressure. The horizontal load is used to account for the wind effects. Worldwide, majority of residential and commercial buildings are categorized as either low or high rise buildings. Moreover, buildings are prone to excessive damages with wind disasters. Therefore, the first important step in the wind-induced pressure analysis is to calculate accurate pressure on the walls of the structures. In general, different structures viz. buildings, dam, bridge, spillway and others are affected by wind-induced pressure. With the rapid developmental activities, the more and more structures are being constructed and therefore, there is increased in damage rate. Wind pressures on buildings are influenced by the building geometry, the extent of curved corners, angle of incidence of wind, surroundings and wind flow characteristics.

There are many situations where the available database, codes/standards, and analytical methods can't be used to estimate the wind pressure coefficients, wind loads on the claddings and supporting system of buildings. The aerodynamic shape of the building is uncommon/complex. However, in such situations, accurate estimation of wind pressure coefficients on the building claddings are obtained through the model test in wind tunnel Suresh Kumar et al. (2006). Further, the pressure coefficients/loads from standards are meant to be upper bounded scenario under limitations. Wind pressure information (i) does not account the aerodynamic effect of the actual shape of the structure since they are based on box-like buildings and (ii) do not allow for any detail directional effects and assume that the design wind speed always occurs from the aerodynamically severe wind direction. On the other hand, wind tunnel model studies are often used to assist in the prediction of design wind pressures for the cladding of buildings (i) do physically simulate and predicts the aerodynamic effect of the actual shape of the structure by modeling building in detail (ii) consider the directionality of the wind climate for the area where the study building is located, and (iii) overall provide indispensable wind effect data for the design of the cladding and structural framework.

Wind load is one of the significant forces of nature that must be considered in the design of buildings. The buildings and other civil engineering structures are three-dimensional bodies with a large variety of shapes and have complex wind flow patterns and therefore varied pressure distributions. Details of wind pressures on buildings are obtained by wind tunnel experimentation on small-scale models. The different shapes of the building are generally proposed by architects and designed by the structural engineers considering the complex wind effects. Uncertainty regarding calculation of wind load is quite high due to the vast ranges of possible interactions between structure and wind.

Lin et al. (2005), Macdonald et al. (1975), and Meroney (1988) studied on square, rectangular and cylindrical structures in a considerable investigation. Cook (1990) reported on wind pressures on irregular shapes buildings. Stathopoulos and Zhou

(1993), Zhou and Stathopoulos (1997) studied the wind loads on the stepped-roof building of L-shape plan view as well as an L-shaped cross-section through a numerical approach. They found a good agreement in the case of numerically and experimentally obtained results at normal wind incidence. Ahmad and Kumar (2001) examined interference with a similar building as well as three similar buildings placed on the upstream side at fifteen different locations. A hip roof building model (geometric scale 1:50) of plan with  $30^\circ$  roof slope was selected as the test building. Ho et al. (1990) studied a new approach is proposed to study the interference of local obstructions on low building wind loads from a statistical point of view through wind tunnel experiments. Lou et al. (2005) also carried out wind tunnel tests on a double-skin facade building to study the wind pressure distribution on each surface of the double-skin facades. Lu et al. (2007) carried out numerical simulation to investigate the wind pressure distributions on the surface of spherical tall buildings with and without curved annexes. Chakraborty et al. (2013) studied the pressure distribution on different faces of a+ plan shape tall building. The analysis was carried out using ANSYS FLUENT with k- $\epsilon$  viscosity model and the results obtained were compared with the results of wind tunnel test. Gomes et al. (2005) investigated the wind pressure distributions experimentally and numerically on the inner faces of L-shape and U-shape models. They found a good agreement for normal wind incidence, whereas differences have obtained for other angles of incidence. Chaudhary and Garg (2006) investigated the pressure and forced coefficients of typical shape building made from four rectangular shaped blocks arranged in a cruciform (cross) shape and it was concluded that building under consideration was subjected to significantly high-pressure coefficients as compared to the rectangular/square shape buildings. Wang et al. (2013) the characteristics of wind pressure on the scaffolding were studied for different building opening ratios, scaffolding geometries and wind directions. They compared experimental data with relevant current design recommendations. Amin and Ahuja (2008, 2011) presented their works on L- and T-shapes buildings with different configurations and estimated the average, minimum, maximum and root mean square values of pressure coefficients. Kim and Kanda (2013) studied on fluctuating values of wind pressures, flow separation and formation of vortex on tall buildings as well as conical shaped building. Chakraborty et al. (2014) carried out a comparative study between experimental and numerical method to predict wind effect on '+' plan shaped tall building. Bhattacharyya et al. (2014) measured the pressure distribution of E-shaped tall buildings by varying angle of incidences from  $0-180^\circ$ . Bhattacharyya and Dalui (2018) investigated mean wind pressures on E plan shaped tall building and compared both experimental and numerical results by CFD. For better comparison of the results, pressure contours on all the faces are also predicted by both methods. Yi and Li (2015) conducted experiment in a tall building at Hong Kong as well as wind tunnel model test to explain force and pressure coefficients and high frequency balance. The wind tunnel test result was seen to be fairly equivalent with full model test. Li and Li (2016) was also conducted wind tunnel test on L plan shaped tall building to quantify dynamic load across the wind. They proposed an empirical formulation by considering the side ratio and territory of the building to express wind load.

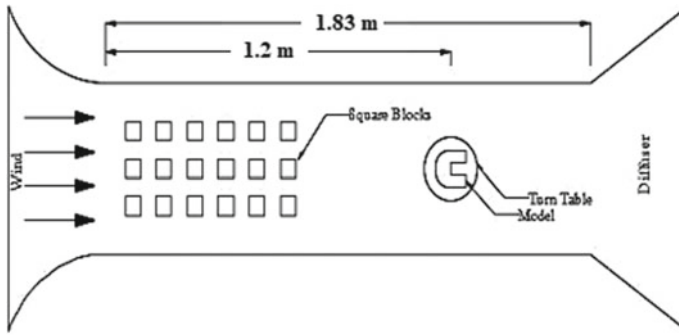


**Fig. 6.1** The schematic diagram of wind tunnel

No work on C-type building configuration with outer curved corner is reported by any investigator. In the present research work, detailed studies have been carried out by conducting extensive wind tunnel experimentations on various faces of a C-type building models of with and without outer corner curved surface.

## 6.2 Experimentation

### 6.2.1 Feature of Experimental Setup

Experiments were carried out in an open circuit sub-sonic wind tunnel in the Aerodynamics laboratory of the Department of Aerospace Engineering, Indian Institute of Technology Kharagpur, India. The wind speed was kept constant at 12.9 m/s. The wind tunnel with a bottom surface made up of plywood a test section of 1.83 m long and cross-sectional dimensions of 0.61 m  $\times$  0.61 m. Models were placed within boundary layer zone subsequently in the test section centrally at a distance of 1.2 m from the beginning of test section. To ascertain models within boundary layer zone, wooden cubic blocks of 25 mm size and clear spacing of 50 mm in all directions were fixed on 4 mm thick plywood sheet as shown in Fig. 6.1. The velocity profile inside the wind tunnel has a power-law index ( $n$ ) of 0.143. The velocity profile within wind tunnel test section and the turbulence intensity are shown in Fig. 6.2a, b respectively.

### 6.2.2 Details of Models

The models used for the experiments were made of transparent Perspex sheet of 3 mm thickness. To study the effect of corner curvature on pressure distribution, the overall size 120 mm  $\times$  120 mm  $\times$  80 mm of the models were kept constant. Details

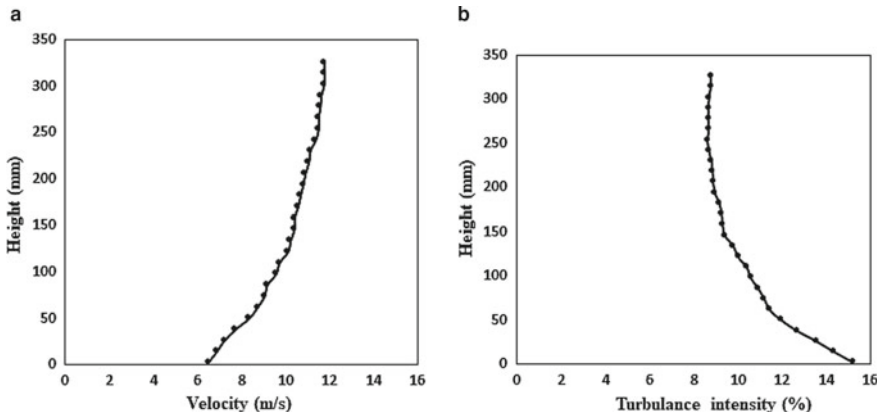


**Fig. 6.2** A Velocity profile at test section **b** turbulence intensity at test section

of the two C-shaped models, marked as C-1 and C-2 of with corner curvatures and without curvature is shown in Figs. 6.3a and 6.4 and in given Table 6.1.

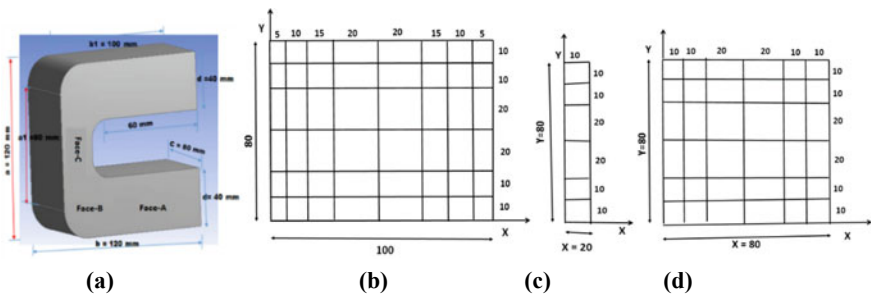


**Fig. 6.3** A C-shaped model (C-1), Pressure tapping locations at **b** Face A (side surface), **c** Face-B (curve surface), **d** Front Face-C (dimensions are in mm)

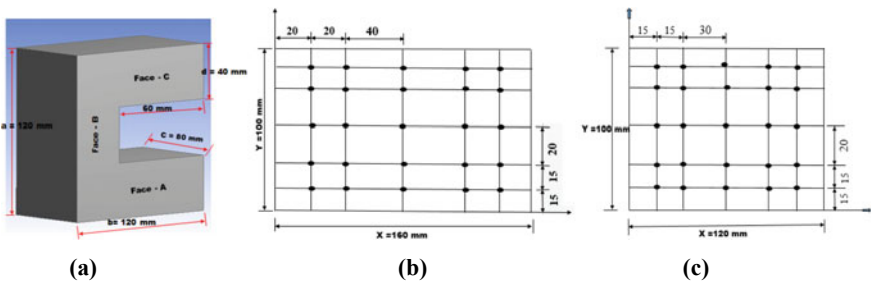


**Fig. 6.4** A C-shaped model (C-2), Pressure tapping locations at **b** Face A (side surface), **c** Face-B (Front surface) (dimensions are in mm)



**Table 6.1** Details of models

Model shape (1)	Model width (mm) (2)	Model length (mm) (3)	Model height (mm) (4)	Plan area (mm) (5)	Radius of curvature (mm) (6)
C-1	120	120	80	14,400	20
C-2	120	120	80	14,400	0

The models were fitted with 90 to 120 numbers of pressure tapping points. The pressure tapings of 5 rows were at different heights of 10, 20, 40, 60 and 70 mm from the bottom of the model to obtain a good distribution of pressures on all the faces of models. Figure 6.3b, c, d show pressure tapping locations at faces of C-1 model. Figure 6.4b, c show the pressure tapping locations at faces of C-2 model. The pressure tapping points were kept at less spacing near the wall boundaries to capture the high-pressure variation occurring at the point of flow separation and at larger spacing in the middle of the surfaces.

Free stream velocity during the experiment was measured with the help of Pitot tube. For making the pressure tapping points, plastic pipe of 2 mm internal diameter was inserted into the hole drilled on the model surface such that its one end flushed to the outer side of the model surface and the other end connected to the tube of 3 mm internal diameter and 500 mm length.

The free ends of tubes were connected to Digital Sensor Array (DSA) to record the fluctuating wind pressure at the corresponding tapping points. All data were measured by a DSA scan valve corporation, model DSA 3217/16 pox, USA. This DSA device was set to give average pressure of 5 s duration. At the same time, for greater accuracy, pressure measurement at each tapping point was repeated for three times and the mean of three pressure data was obtained.

The mean pressure coefficient ( $C_p$ ) for each tapping point was calculated by the equation mentioned as:

$$C_p = \frac{P - P_\infty}{P_0 - P_\infty} \quad (6.1)$$

where,  $p$  = mean pressure data obtained experimentally,  $P_\infty$  = static pressure in the reference tube and  $P_0$  = total pressure in the settling chamber.

The model was fixed with the turn table which is situated at the middle of the test section of the wind tunnel. With the help of turn table, the model was rotated up to 180° anticlockwise for measuring surface pressure at an interval of 30° angle. The front face of the model (face-C) was placed perpendicular to the wind flow direction. Mean Pressure coefficient on all the faces of C-shaped models were evaluated from the fluctuating wind pressure records at all pressure tapping points. This same procedure was repeated for all the models and surfaces under taken and the data was recorded for the analysis. The scope of the experiment is shown in Table 6.2.

**Table 6.2** Scope of the experiment

Models	C-1, C-2
Surfaces	Face A, Face B, Face C
Angle of incidence	0°, 30°, 60°, 90°, 120°, 150°, 180°
Radius of curvature	20 mm

### 6.3 Numerical Modelling

Numerical simulations have been carried out in this study through ANSYS Fluent using Computational Fluid Dynamic (CFD) technique, based on the control volume method. The RNG **k-ε** model is used to simulate the turbulence effects. The RNG model is developed using Re-Normalization Group (RNG) methods to solve the Navier–Stokes equations, to account for the effects of smaller scales of motion. The RNG approach, which is a mathematical technique that can be used to derive a turbulence model similar to the **k-ε** model.

#### 6.3.1 Numerical Analysis

For numerical analysis the models of C shaped building of different aspect ratios has been created in ansys and then analysed by using **k-ε** model of turbulence. Ansys (Fluent) uses finite element method to solve the governing equations, i.e. the region of interest is divided into the finite number of cells (the mesh or grid).

Data Considered in Numerical Analysis:

- Types of Fluid: Air
- Density of Air: 1.225 kg/m<sup>3</sup>
- Viscosity of Air:  $1.789 \times 10^{-5}$  kg s/m
- Turbulence Model: **k-ε** model
- Solver: pressure Based

#### 6.3.2 Domain and Meshing

The domain size as shown in Fig. 6.5a, b is considered as mentioned in Franke et al. (2004). The upstream side is considered as 5H from the face of the building, downstream side is taken as 15H from the face of the building, two side clearance of the domain is taken as 5H from the face of the building and top clearance is also taken as 5H from the top surface of the building. Such large size of domain helps in vortex generation at the leeward side of the building and backflow of wind can also be prevented.

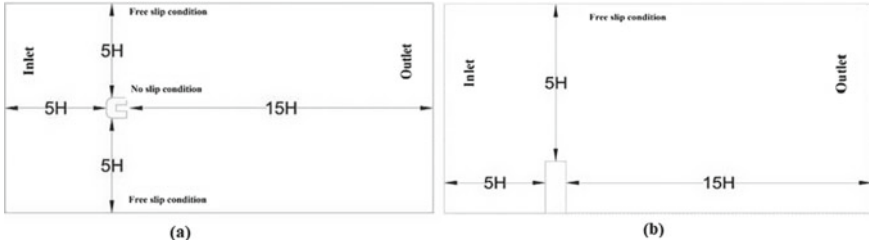
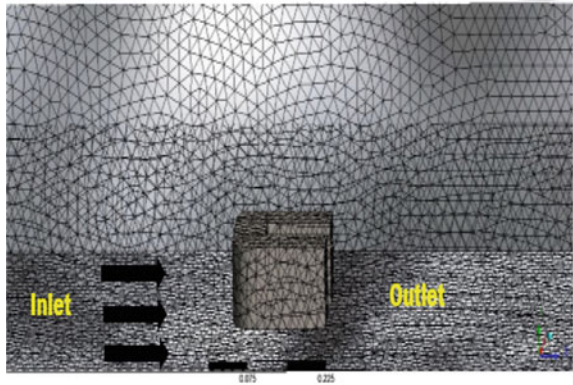


**Fig. 6.5** **a** Domain for the Plan and **b** Domain for the Plan elevation

**Fig. 6.6** Meshing of C-shape Model



Finite volume discretization approach is used to discretize the whole domain so that, separation of wind flow, up wash and downwash mechanisms can be happened similar to the experimental study. The discretization (Meshing) of C-shaped model is shown in Fig. 6.6.

### 6.3.3 Boundary Condition

For completing numerical modelling and simulation there are several boundaries conditions which are considered. The flow parameter at inlet, outlet wall and surface are needed to be considered. At inlet the velocity of flow is 12.9 m/s and the same velocity is provided for experimental procedure so that the result could be compared. The flow velocity at inlet is along positive X direction.

### 6.4 Results and Discussion

Mean pressure coefficient on different faces of C-shape building models were evaluated from fluctuating wind pressure records at all pressure point over an extended range of wind incidence angles from 0–180° at an interval of 30°. The pressure contours on the surfaces of C-shaped models placed at wind angle of incidence of 0, 90 and 180° are plotted and shown in Figs. 6.7, 6.7 and 6.8.

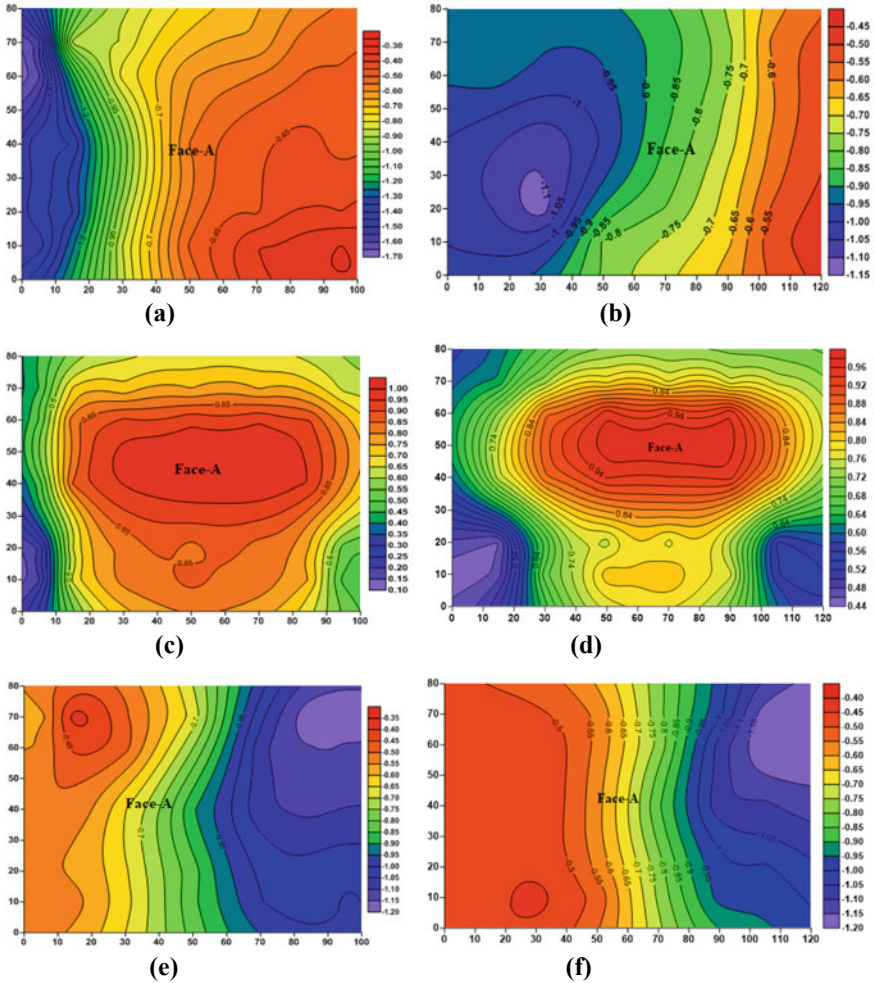


**Fig. 6.7** Comparison of mean surface pressure coefficient distribution on Face-A of model for angle of incidence **a** 0° for C-1, **b** 0° for C-2, **c** 90° for C-1, **d** 90° for C-2, **e** 180° for C-1, and **f** 180° for C-2

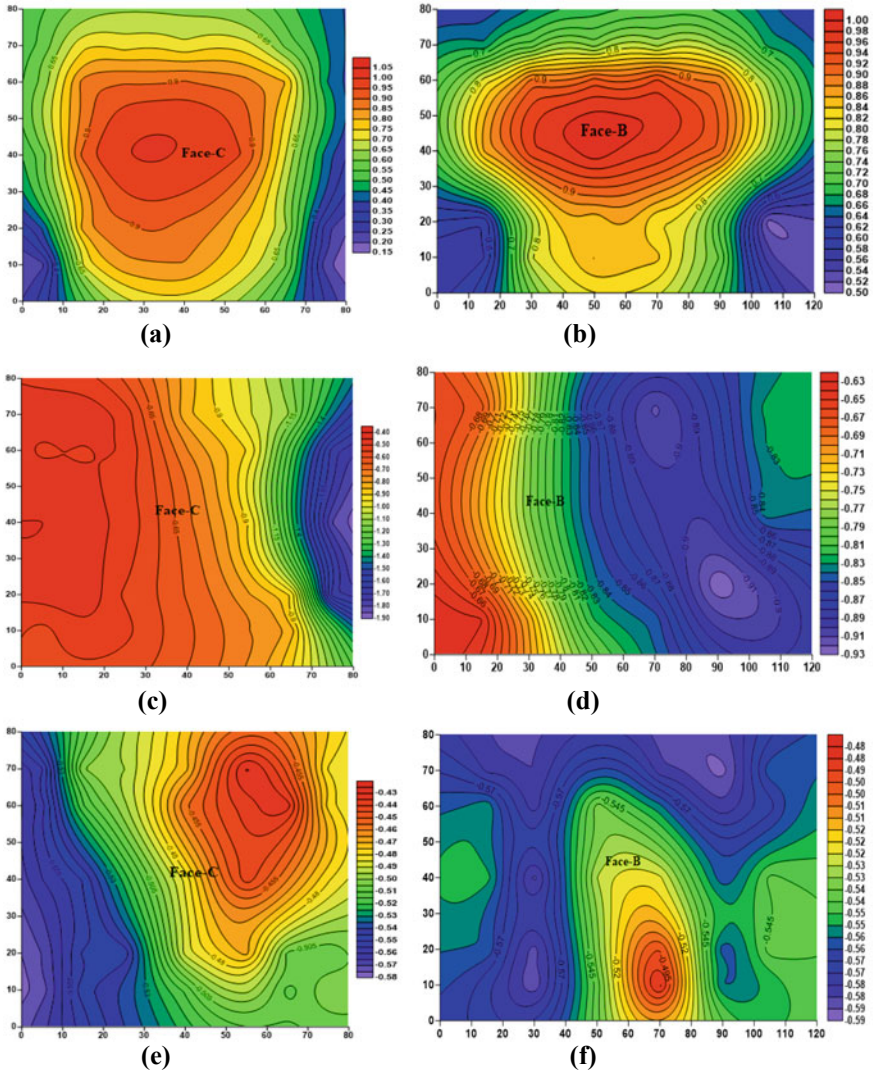


**Fig. 6.8** Comparison of mean surface pressure coefficient distribution on Face-C of model for angle of incidence **a** 0° for C-1, **b** 0° for C-2, **c** 90° for C-1, **d** 90° for C-2, **e** 180° for C-1, and **f** 180° for C-2

### 6.4.1 Experimental Results

For 0° angle of incidence, the placement of different faces has been defined in Fig. 6.3a as face-A is parallel to the wind direction (right face) with curved surface-B on the upstream (left) side, curved face-B between front face-C on the left and side face-A on the right. Face-C is normal to the direction of flow (front face).



Figure 6.7 show the variation of ( $C_p$ ) on face-A with various angle of incidences of both C-1 and C-2 building models. In case of C-1 model, at  $0^\circ$  angle of incidence, the entire surface is subjected to negative pressure with the maximum pressure coefficient is on the extreme left (upstream) side near the top of the face-A, and the minimum pressure coefficient towards the downstream side. But in C-2 model, the maximum negative pressure coefficient is less as compare to C-1 model due to no curvature effect and the flow detached suddenly.

At  $90^\circ$  angle of incidence, the surface becomes normal to the direction of flow and pressure distribution is almost symmetrical as in Fig. 6.7c, d. In this case Face-A is shifted to frontal face and C-2 model in Fig. 6.7d, the minimum positive pressure coefficient occurs in both lower side due to edge effect. For  $180^\circ$  angle of incidence,  $C_p$  is maximum on the right end side of the face which decreases further towards left side as in Fig. 6.7e. Again, from Fig. 6.7e, it can be seen that the maximum negative pressure coefficient is on the top right side whereas the minimum negative pressure coefficient is on the left top side of the surface. The shifting of locations of maximum and minimum positive and negative pressure coefficient with angle of incidence can be attributed to the shifting of the position of flow separation. But in Fig. 6.7f, minimum negative pressure coefficient occurs bottom left side of the face due to edge effect.

At  $0^\circ$  incidence angle (Fig. 6.8a), front Face-C is subjected to positive pressure throughout the surface. It increases from all edges to the center of the face. The central zone of the face is having maximum pressure coefficient. Due to curvature effect, the mean pressure coefficient is the minimum at top surface on both sides of the face and on the bottom side of the face, pressure coefficient is less as affected by the presence of bottom surface of the wind tunnel. But in Fig. 6.8b, the minimum pressure coefficient occurs at both bottom side of the face and the maximum positive pressure occurs at middle central part of the face. From  $90^\circ$  to  $180^\circ$  angle of incidence, the entire surface is under negative pressure with increased maximum negative value of pressure coefficient at  $90^\circ$  angle of incidence. The minimum negative pressure coefficient arises left side of the face and maximum negative pressure occurs right central part of the face in Fig. 6.8c. But in Fig. 6.8d, minimum pressure coefficient occurs left side and maximum  $C_p$  is at right central part of the face due to no curvature effect, the flow separation arises. For  $180^\circ$  angle of incidence, the minimum negative  $C_p$  is at top right side of the face in Fig. 6.8e but in Fig. 6.8f the minimum negative  $C_p$  occurs at right bottom side of the face.

### 6.4.2 Numerical Analysis

The flow around the C-1 shaped model for wind angles of  $0^\circ$  to  $180^\circ$  are shown in Figs. 6.9a–d and 6.10a–d. The features of flow observed are discussed below:

Figures 6.9a and 6.10a show the flow pattern around the C-1 model at C and  $180^\circ$  angle of incidence respectively. When model is placed at  $0^\circ$  angle of incidence, Face-A is side face and the negative pressure coefficient occurs. At  $0^\circ$  angle of incidence,

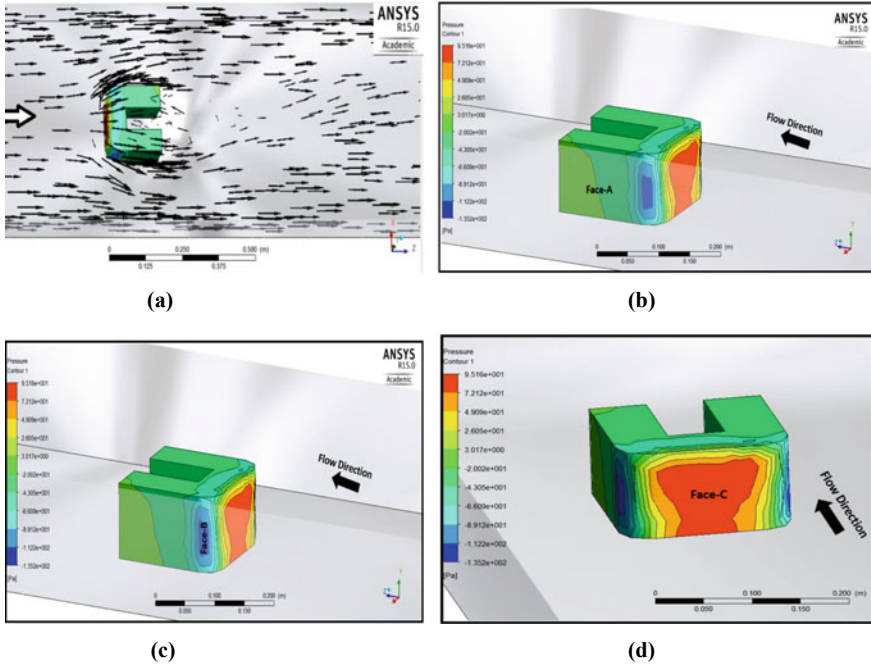


**Fig. 6.9** **a** Flow pattern around model C-1, **b** Model placed at 0°angle of incidence of Face-A, **c** Model placed at 0°angle of incidence of Face-B, and **d** Model placed at 0°angle of incidence of Face-

Face-C is situated in frontal face, the pressure on windward side is positive with maximum pressure occurring near the middle. Due to curvature effect minimum pressures is at left and right edge of front face of model. But in leeward side negative pressure occur. Figure 6.10b, c, d With the change of wind angle from 0–180° angle of incidence, the front Face-C is shifted wind ward to leeward side, the pressure distribution on leeward side is positive with maximum pressure occurring middle part of the faces and in wind ward side negative pressure occur.

### 6.5 Conclusions

The current study shows that pressure induced on model building is significantly affected by the model geometry, configuration, radius of curvature and angle of incidence. Pressure variation on the building is directly influenced by wind flow pattern The significant outcomes of the present study are summarized below.

- At zero angle of incidence of wind direction, the entire surface of Face-C of model C-1 is under positive pressure with maximum at the centre and then decreases

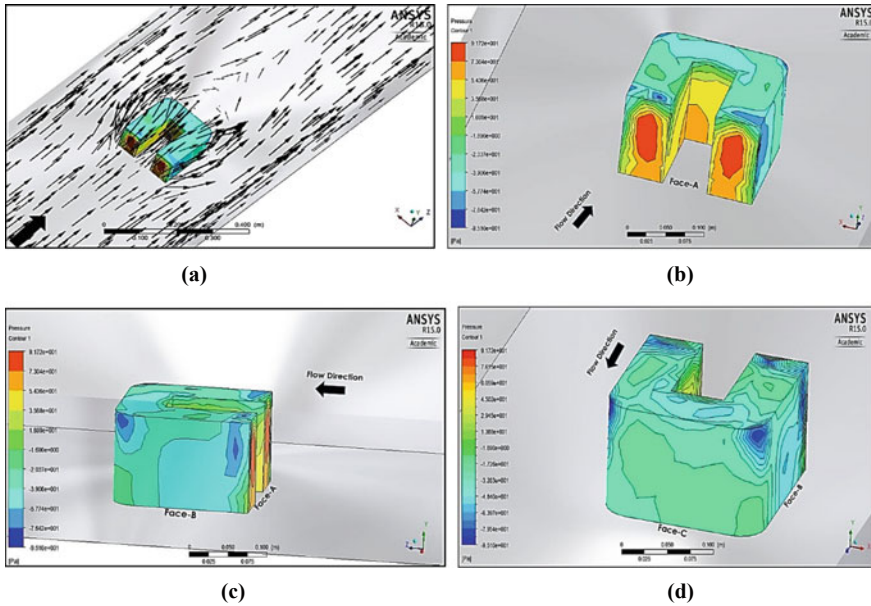


**Fig. 6.10** **a** Flow pattern around model C-1, **b** Model placed at  $180^\circ$  angle of incidence of Face-A, **c** Model placed at  $180^\circ$  angle of incidence of Face-B, and **d** Model placed at  $180^\circ$  angle of incidence of Face-C

towards the edges. The curvature has nominal effect on pressure coefficient on frontal Face-C.

- Face-A is subjected to negative pressure throughout with maximum towards extreme downstream side that decreases to a minimum towards upstream side. The suction on sides and leeward faces are significantly affected by the plan-shape of the models and wind orientation.
- The radius of curvature is affecting in reducing positive as well as negative pressure coefficient significantly on the surfaces of Face-A.
- Mean pressure coefficients are main objective of this study. Maximum positive mean pressure coefficients occur at front face of C.
- The study has been conducted with a C shaped model experimentally as well as numerically using wind tunnel test and CFD technique respectively.
- Vortex generation and different types of mechanism such as separation of flow, upwash and downwash are happened due to dynamic behavior of wind flow.



## References

- Ahmad S, Kumar K (2001) Interference effects on wind loads on low-rise hip roof buildings. *Eng Struct* 23(12):1577–1589
- Amin JA, Ahuja AK (2008) Experimental study of wind pressures on irregular plan shape buildings. In: BBAA VI international colloquium on: bluff bodies aerodynamics and applications. Milano, Italy
- Amin JA, Ahuja AK (2011) Experimental study of wind-induced pressures on buildings of various geometries. *Int J Eng Sci Technol* 3(5)
- Bhattacharya B, Dalui SK (2018) Investigation of mean wind pressures on ‘E’ plan shaped tall building. *Int J Wind Struct* 26(2):99–114
- Bhattacharya B, Dalui SK, Ahuja AK (2014) Wind induced pressure on E plan shaped tall buildings. *Jordon J Civil Engg* 8(2):120–134
- Chakraborty S, Dalui SK, Ahuja AK (2013) Experimental and numerical study of surface pressure on + plan shape tall building
- Chakraborty S, Dalui SK, Ahuja AK (2014) Wind load on irregular plan shaped tall building—a case study. *Wind Struct* 19(1):59–73
- Chaudhary KK, Garg RK (2006) Wind Induced flow field study for designing cruciform shaped buildings. 3rd National conference on wind engineering, Jadavpur University
- Cook NJ (1990) The designer’s guide to wind loading of building structures, building research establishment report, Part 2: static structures. Butterworths, London
- Franke J, Hirsch C, Jensen AG, Krus HW, Schatzmann M, Westbury PS, Miles SD, Wisse JA, Wright NG (2004) Recommendations on the use of CFD in wind engineering. In: Cost action C, vol. 14. pp C.1.1–C1.11
- Gomes M Gr, Rodrigues AM, Mendes P (2005) Experimental and numerical study of wind pressures on irregular-plan shapes. *J Wind Eng Ind Aerodynamics* 93(10):741–756
- Ho TCE, Surry D, Davenport AG (1990) The variability of low building wind loads due to surrounding obstructions. *J Wind Eng Ind Aerodyn* 36:161–170
- Kim YC, Kanda J (2013) Wind pressures on tapered and set-back tall buildings. *J Fluids Struct* 39:306–321
- Li Y, Li QS (2016) Across-wind dynamic loads on L-shaped tall buildings. *Wind Struct An Int J* 23(5):385–40
- Lin N et al (2005) Characteristics of wind forces acting on tall buildings. *J Wind Eng Ind Aerodyn* 93(3):217–242
- Lou W et al (2005) Wind tunnel test study on wind load characteristics for double-skin facade building with rectangular shape. *Jianzhu Jiegou Xuebao (J Build Struct)* 26(1):65–70
- Lu S-L et al (2007) Numerical study on the effects of curved annex on the wind loads on a spherical tall building. *Eng Mech* 2:021
- Macdonald AJ (1975) Wind loading on buildings. Applied Science Publishers Ltd., London, 72
- Meroney RN (1988) Wind-tunnel modeling of the flow about bluff bodies. *J Wind Eng Ind Aerodyn* 29(1–3):203–223
- Stathopoulos T, Zhou YS (1993) Numerical simulation of wind-induced pressures on buildings of various geometries. *Computational wind engineering 1*. Elsevier, pp 419–430
- Sureshkumar K, Irwin PA, Davies A (2006) Design of tall building for wind: wind tunnel vs. codes/standards. 3rd National conference on wind engineering. Calcutta, India, pp 318–325
- Wang F, Tamura Y, Yoshida A (2013) Wind loads on clad scaffolding with different geometries and building opening ratios. *J Wind Eng Ind Aerodyn* 120:37–50
- Yi J, Li QS (2015) Wind tunnel and full-scale study of wind effects on a super-tall building. *J Fluids Struct* 58:236–253
- Zhou Y, Stathopoulos T (1997) A new technique for the numerical simulation of wind flow around buildings. *J Wind Eng Ind Aerodyn* 72:137–147

# Chapter 7

## A Framework for the Selection of Threshold in Partial Duration Series Modeling



Nibedita Guru and Ramakar Jha

**Abstract** In flood frequency analysis, the modeling based on the Annual Maximum Flood (AMF) series remains the most popular approach; hence, an alternative approach based on the “Partial Duration Series (PDS) or Peaks Over Threshold (POT)” is considered, which captures more information about extreme events by fixing threshold values than the Annual Maximum Series (AMS) model. However, the use of the PDS approach in the hydrological application remains under-employed due to their complexities associated with the choice of an appropriate threshold and the selection of criteria for retaining flood peaks events. Additionally, an assumption is that the magnitude of the extreme events of a PDS is best described by a Generalized Pareto (GP) distribution. To date, the question arises on threshold value selection that best describes the PDS modeling. The objective of the present paper is to shed a framework on the above question regarding the guidelines on the appropriate selection of threshold value using different concepts and verify the independence and stationarity criteria of the extreme events for the modeling of the PDS in the Mahanadi River system, India, which uses daily discharge data from 22 stations with record length varying between 10 and 41 years.

### 7.1 Introduction

In India, floods are very common phenomena causing severe damage to human life, livestock, agriculture, and property. Hence, detailed knowledge of the probabilistic behavior of such floods is necessary. Frequency analysis can be used to obtain such knowledge and develop a link between peak values and recurrence interval (Meng et al. 2007). In flood frequency analysis, a series is a convenient sequence of data, such as hourly, daily, seasonal, or annual observations of a hydrological variable.

---

N. Guru (✉)

Department of Water Resources, National Remote Sensing Centre, ISRO, Hyderabad, India

Forest Ecology and Climate Change Division, Forest Research Institute, Dehradun, India

R. Jha

Department of Civil Engineering, National Institute of Technology, Patna, Patna, India

Flood frequency analysis can be carried out using the Annual Maximum Flood (AMF) approach or the Partial Duration Series (PDS) approach, also called Peak-Over-Threshold approach (POT). An AMF sample is constructed by extracting the maximum value of each year from a daily flow series. The PDS approach to hydrologic frequency analysis consists in retaining all peak values that “exceed” a certain base level  $t$  usually called “threshold”, thus, more than one extreme event in any year would be selected as peaks (Norbiato et al. 2007). PDS modeling has a lot of advantages including (i) it consists of more peak events by selecting the appropriate threshold having more information regarding the flood phenomena, and (ii) it analyzed both time of arrival and the magnitude of peaks. Above these advantages, the PDS approach remains underused and unpopular due to the nonexistence of a general framework regarding different approaches including the threshold selection criteria and model hypotheses about the independence, stationarity, and distribution of flood peaks. In counterpart, the AMF approach, select only the maximum values for each year that are independent. The literature regarding the PDS model also remains less and incoherent in relation to the various complexities. Rasmussen et al. (1994) highlighted that increase the popularity of the PDS model among experts, by inspecting different comprehensive guidelines of its use. Many researchers proposed methodologies based on the average number of peaks per year for threshold selection for different specific climatic and geographic regions (Taesombut and Yevjevich 1978; Konecny and Nachtnebel 1985). Besides, other researchers recommended based on return period to choose the threshold level.

The American Society of Civil Engineers (1949) used PDS and recommended the value of  $\lambda$  which does not consider more than 3–4 peak flood values in any one year above a threshold discharge. The US Geological Survey recommended that  $\lambda$  should be equal to three times the number of years ( $3N$ ) of available datasets. Cunnane (1973) suggested that for estimation of parameters, PDS having  $\lambda$  greater than 1.6 per year are more efficient than AMS, and the magnitude of peaks is modelled by an exponential distribution also, and  $\lambda$  equal to 2 is sufficient for flood quantile estimation. UK Flood Studies Report recommended that  $\lambda$  should range between 3 and 5 (Natural Environment Research Council 1975). The best results were obtained by (McDermott and Pilgrim 1982) for  $\lambda$  value equal to 1. The researchers (Tavares and da Silva 1983; Jayasuriya and Mein 1985) establish that a  $\lambda$  value of 2 or greater is suitable for the compound model following a Poisson distribution of occurrences and an exponential distribution of magnitudes. Hosking and Wallis (1987) studied that the PDS model could improve its performance when  $\lambda$  is equal to 5 in the case of geo-morpho-climatic modeling and  $\lambda$  is equal to 10 in the case of wind velocity modeling.

Rosbjerg and Madsen (1992) recommended a standardized method based on a predefined frequency factor  $k$  and mean and standard deviation of the original series:  $t = \bar{x} + k\sigma$ , and they set a value of  $k$  around 3. (Madsen et al. 1997) compared the performance of both the AMS and PDS approach and concluded that for estimation of quantile, PDS approach provides the efficient results for practical purposes. Martins and Stedinger (2001) found that the accuracy of flood quantiles resulting from a GEV-Poisson PDS model is somewhat indifferent for  $\lambda \geq 1$ . The  $\lambda$  value

ranging between 3 and 15 for homogeneous Italian regions was estimated by Claps and Laio (2003). Rosbjerg and Madsen (2004) conducted a frequency analysis based on rainfall data using a Bayesian framework in Denmark by suggesting a  $\lambda$  value between 2 and 3. Begueria (2005) examined the ordinary moments method for quantile estimation and concluded that there is no unique threshold value regarding the GP distribution parameters which has an effect on quantile estimation. Zvi (2009) proposed an Intensity–Duration–Frequency (IDF) curves on Partial Duration Series (PDS) at four stations of the Israel Meteorological Service and concluded that the proposed method is a superior one. Shinyie and Ismail (2012) estimated the parameters of Generalized Pareto distribution using five different methods based on the hourly rainfall data of five stations and analyzed the performance of various return periods using the Partial Duration Series (PDS) in Peninsular Malaysia. Also, the weighted average model is suggested, to estimate the T-year return level. Pham et al. (2014) examined the statistical properties of the PDS/GP with a change in average peaks per year ( $\lambda$ ) and illustrated that the GP distribution best describes PDS4 and PDS5 at almost all sites of the North Island region in New Zealand.

Even though the popularity of the PDS model for quantifying extreme events is to be increased among experts, it is often associated with various difficulties. Furthermore, there is no general recommendation existing for choosing an appropriate threshold affecting the modeling of the PDS together with the choice of appropriate distribution which plays an important role in satisfying the assumptions of the PDS model and to confirm consistent quantile evaluations. Henceforth, the following observations were made from the previous studies: (a) very little work has been done in the past to evolve any flood frequency distribution for predicting peak discharge floods of longer duration using PDS beyond a threshold, and (b) actual observations (peak discharge along with Highest Flood Level using Rating Curve at each location in the field) are not considered in most of the cases while selecting the most appropriate threshold values ( $t$ ) or average peak per year ( $\lambda$ ) values.

Keeping this in view, the objective of the present research includes the operational guidelines for selection of threshold value based on different concepts then test the performance of GP/PDS modeling based on the suitability of the GP distribution parameters coupled with the appropriate threshold value selected from different concepts and ensure the reliable estimation of quantile values of 22 locations of the Mahanadi River system, India (Fig. 7.1), as a very little work has been done by considering PDS model in the Mahanadi River basin. The developed approach is required to be used in the real field condition to protect and control floods of high return periods above HFL and avoid flood inundation causing severe damage to the countryside.

In the present study, extensive field data such as cross-section, water level including highest flood level, and discharge data of 22 sampling locations were collected for a period of 1971–2012 from various central and state government agencies.

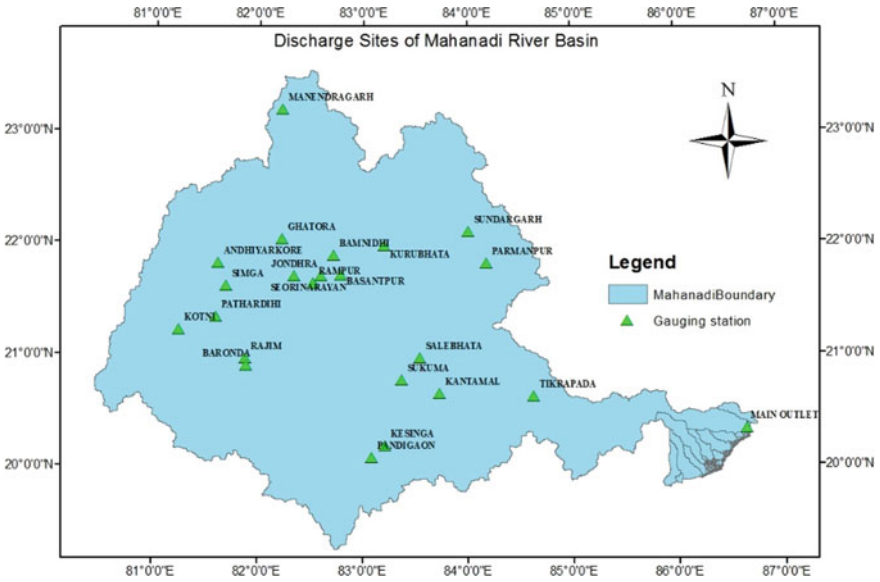


Fig. 7.1 Location of discharge sites of the Mahanadi River

## 7.2 Methodology

### 7.2.1 Overview of Partial Duration Series

The partial duration series is extracted from the daily time series data by using  $\lambda = p/n$ , where  $\lambda$  represents the average number of peaks each year,  $p$  is the total number of peaks, and  $n$  is the number of years. The resulting PDS is assumed to be independent and follow the Poisson distribution (Cunnane 1973). Generally, the average number of peaks per year ( $\lambda$ ) is increased, with a decrease of the threshold value ( $t$ ). Thus, an appropriate threshold value should be selected for the flood frequency analysis. If we set a higher threshold value, then only the actual peaks are selected and which are independent by following the Poisson distribution but can lead to a significant loss of information of high magnitude peaks that causes flood with increasing the uncertainty. In contrast, more peaks are selected with serial dependence of both time interval and magnitudes when a small threshold value is chosen by violating the assumption of independence but provide reliable distribution parameter estimation.

### 7.2.2 *Framework to Select the Threshold Values Using Different Concepts*

In this section, a framework is provided for the selection of threshold using different concepts described as below:

- (i) Considering an average number of flood peaks per year ( $\lambda = 1, 1.5, 2,$  and so on). There are possibilities of having two or more number of peak floods from one year and no flows from the other years as they are lying below the threshold value.
- (ii) Considering mean exceedance above threshold ( $\overline{M}_t - t$ ) is a linear function of the threshold value  $t$ , where  $\overline{M}_t$  is the average value of exceedances, and these criteria are equivalent for choosing the threshold to maximize the stability of the POT distribution parameter estimates.
- (iii) Considering observed Highest Flood Level (HFL) at each sampling location and the corresponding discharge values using Rating Curve. The values of discharge ahead of HFL cause a real flood situation in the field and cause flood inundation at various locations in the Mahanadi River basin. In fact, in most of the previous studies, the actual observations (peak discharge along with Highest Flood Level) in the field are not considered while selecting the threshold values and average peak per year ( $\lambda$ ) values.

However, threshold selection is strongly related to the hypothesis of independence, stationarity, and the combined GP-Poisson assumption. Hence, after the selection of threshold from different concepts, the above tests must be analyzed. Though the GP distribution is considered as the best distribution for the PDS series, challenging of their suitability is required, hence, we used two measures such as utilizes the L-moment ratio diagram and analyzes the stability of the GP parameters with a change in the threshold as it reduces the uncertainty of quantile estimation. The details of all the above analyses are described below.

### 7.2.3 *Randomness Test of PDS*

Independence criteria are essential to any statistical frequency analysis. According to the Water Resources Council (WRC 1976), successive flood events are divided by at least as many days as five plus the natural logarithm of square miles of the basin area. Also, the intermediate flows between two consecutive peaks must drop below 75% of the lowest of these two flood events. The autocorrelation test is another convenient test to check the independence criteria in the PDS (Miquel 1984) which comprises the number of peaks selected irrespective of their occurrence (Gordon et al. 2004). The randomness test (autocorrelation test) is done to find independent flood peaks from all the datasets above given threshold values at each station. When these datasets are independent, the autocorrelation function for all lags other than

zero is observed to be zero. The correlation coefficient ( $r_k$ ) is calculated using the following equation:

$$r_k = \frac{\sum_{i=1}^{N-k} (x_i - \bar{x})(x_{i+k} - \bar{x})}{\sum_{i=1}^N (x_i - \bar{x})^2} \quad (7.1)$$

where  $\bar{x} = \sum_{i=1}^N x_i$  is the overall mean.

Once the data are found to be random in nature, they may be used for frequency analysis.

## 7.2.4 Stationarity Test of PDS

Stationarity is another requirement to detect the presence of trends by means of the Mann–Kendall test following the statistic of  $Z = |S|/\sigma^{0.5}$ . It tests a null hypothesis  $H_0$  (no trend exists in the data) against an alternative hypothesis  $H_A$  (existence of increasing or decreasing trend).

## 7.2.5 Outline of GP-Poisson Distribution Model

### 7.2.5.1 Poisson Distribution Model

The occurrence of events exceeding the given threshold ( $t$ ) is best described by the Poisson distribution which follows a random process. The probability density function for the Poisson distribution is given by

$$f(m, \lambda_k) = \frac{e^{-\lambda_k} (\lambda_k)^m}{m!} \quad (7.2)$$

where  $m$  is the occurrences of numbers of peaks within the time interval  $(0, k)$ , and  $\lambda$  is the mean arrival rate which can be calculated from the sample. The Poisson assumption implies that the occurrences of the events are independent in nature.

The Dispersion measure is commonly used for testing the suitability of the fitted Poisson distribution. To obtain the optimum value of  $\lambda$  and to check the suitability of the fitted Poisson distribution, the Fisher Dispersion Index (DI) test was done using the following equation (Cunnane 1979; Lang et al. 1999):

$$DI = \frac{\sum_{i=1}^n (x_i - \bar{x})^2}{\bar{x}} \quad (7.3)$$

where  $\bar{x}$  stands for the sample mean.

The Dispersion Index technique is approximately distributed as a Chi-square ( $\chi^2$ ) statistic with  $(n - 1)$  degrees of freedom for larger values of  $n$  and the corresponding DI value is equal to 1.

### 7.2.5.2 GP Distribution Model

The PDS comprises all mutually independent peaks which follow the GP distribution. The GP distribution is defined by a location ( $\mu$ ), scale ( $\sigma$ ), and shape ( $\xi$ ). The Generalized Pareto (GP) distribution describes the highest values from continuous hydrological time series and has been carefully chosen by many authors for the Poisson distribution modeling (Van Montfort and Witter 1986; Hosking and Wallis 1987; Wang 1996; Madsen et al. 1997; Martins and Stedinger 2001). The cumulative distribution function of the GP distribution is given by

$$P(X \leq x | \mu, \sigma, \xi) = 1 - \left( 1 - \xi \cdot \frac{(x - \mu)}{\sigma} \right)^{\frac{1}{\xi}}, \xi \neq 0$$

$$P(X \leq x | \mu, \sigma, \xi) = 1 - \exp\left(-\frac{x - \mu}{\sigma}\right), \xi = 0 \quad (7.4)$$

For the shape parameter  $\xi = 0$ , the GP distribution transforms into a simple exponential distribution.

Even though the GP distribution is considered as the best distribution for the PDS series, challenging their suitability is required. Hence, we used two measures such as utilizes the L-moment ratio diagram and analyzes the stability of the GP parameters as described below.

The L-moment ratio diagram is drawn for each distribution, which shows the theoretical relationship between L-skewness ( $\tau_3 = \frac{\beta_3}{\beta_2}$ ) and L-kurtosis ( $\tau_4 = \frac{\beta_4}{\beta_2}$ ). The curve representing the L-moment ratios of the GP distribution is given as follows: (Hosking 1990).

$$\tau_4 = \frac{\tau_3(1 + 5 \cdot \tau_3)}{5 + \tau_3} \quad (7.5)$$

To satisfy the assumption, we fit another four additional probability distributions such as Generalized Logistic (GL), the Generalized Extreme Value (GEV), the Log-Normal (LN3), and the Pearson Type III (PEIII).

Since in PDS modeling the threshold value is known, there is no need to calculate the location parameter. After that, a quantile (QQ) plot showed the relation between the observed return levels against the estimated return levels associated with the  $i$ th Gringorten plotting position,  $F_i = \frac{i-0.44}{n+0.12}$ , where  $n$  is the number of data, and  $i$  is the rank of the data.



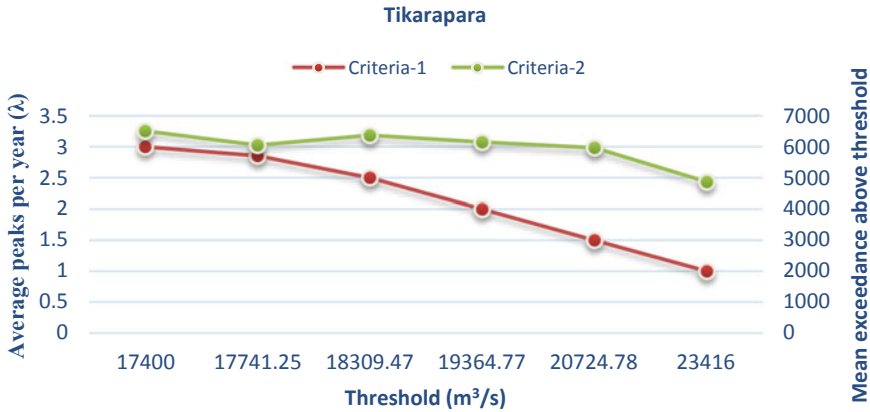


Fig. 7.2 Threshold values obtained using different concepts

### 7.3 Results and Discussion

#### 7.3.1 Threshold Values Using Different Concepts

Considering (i) average number of flood peaks per year ( $\lambda = 1, 1.5, 2,$  and so on), (ii) mean exceedance above the threshold, and (iii) observed Highest Flood Level (HFL) at each sampling location, corresponding discharge values using Rating Curve were obtained in each case. Results of the above concept based on threshold values are presented in Fig. 7.2 of one representative sampling location of the Mahanadi River basin to get an overview of datasets considered for the analysis over a threshold from the series. A threshold value of 18309.47 m³/s at Tikarapara station, leading to an average peak of 2.5 per year which is obtained from HFL, is selected based on concepts (i and iii). Also, concept (ii), i.e. the mean exceedance above the threshold is a stable function of the above threshold.

After the selection of threshold values, the different analysis which includes the hypothesis of independence, stationarity, and the combined GP-Poisson assumption is tested.

#### 7.3.2 Randomness Test of PDS

Following the concept discussed in Sect. 7.2.3, a minimum interval of 7–8 days between events for all the 22 discharge sites is used to help ensure that data used in the further analysis are independent. The randomness test is also done for all the sites to find independent flood peaks from all the datasets above given threshold values. For that, the Autocorrelation Function (ACF) of the original discharge data

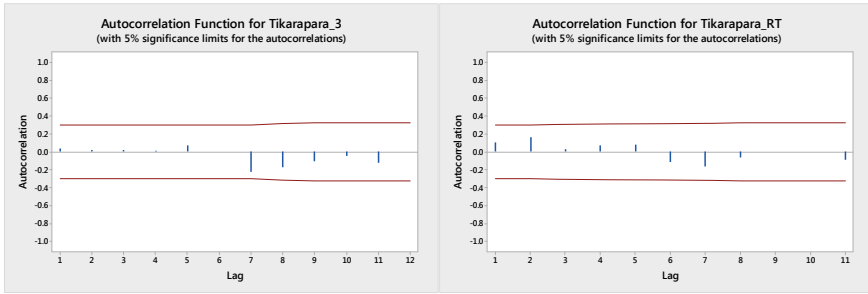


**Fig. 7.3** Autocorrelation function of the discharge data of Tikarapara and Rajim

and extracted PDS data is tested. The ACF plot indicates that the partial duration series of flood data are independent and can be used for further analysis. Figure 7.3 illustrates the ACF plots for Tikarapara, for  $\lambda = 3$ , and HFL obtained from the rating curve.

### 7.3.3 Stationarity Test of PDS

From the Mann–Kendall trend test, probabilities are computed from absolute Z Statistics with a confidence level  $\alpha = 0.05$  and found no trend in the PDS at almost all stations. But SStations Paramanpur and Simga showed a decreasing trend for  $\lambda = 1$  and Manendragarh showed decreasing trend for almost all threshold values.

### 7.3.4 Verification of the Poisson Distribution with Change in Threshold

The arrival of independent PDS peaks follows the Poisson distribution. To verify the above assumption, we calculated the Dispersion Index (DI) and tested the probability ( $p$ ) of the hypothesis for all 22 stations. Figure 7.4 shows a box plot of the DI values obtained at all stations with change in the threshold values, which specifies that the DI values increase with an increase in the values of the threshold with varying in between 1 and satisfied the probability ( $p$ ) hypothesis that the data follows a Poisson process, is accepted within the limits of  $0.05 < p < 0.95$ .

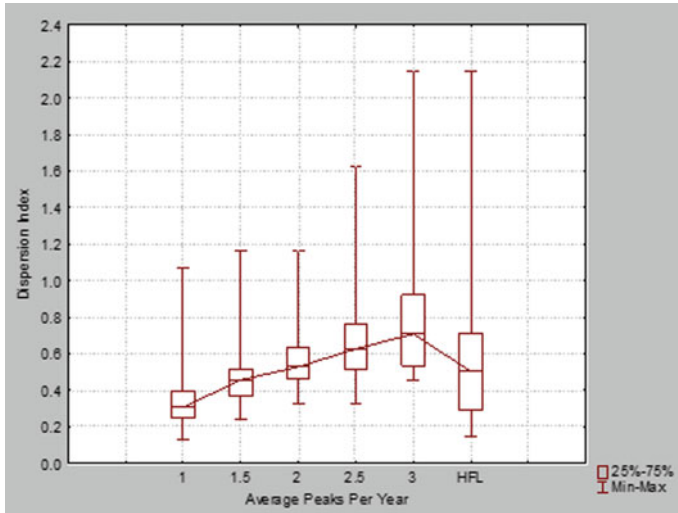


Fig. 7.4 The Poisson distribution of peak occurrences

### 7.3.5 GP Distribution Model

According to the assumption, the GP distribution is considered as the best distribution for the PDS series. To verify the above assumption, a challenge toward their suitability is required, and hence, we used two measures such as utilizes the L-moment ratio diagram and analyzes the stability of the GP parameters. The L-moment ratio diagram shows the grouping of the models’ datasets around the theoretical relationships between L-Cs and L-Ck of different probability distributions. The suitability of the GP distribution along with other four frequency distributions (Generalized Extreme Value (GEV), Generalized Pareto (GP), Pearson Type 3, Generalized logistic (GL), and Log-normal) describing different threshold values using various approaches were evaluated and are shown in Fig. 7.5. It is observed that in the case of  $\lambda$  equal to 1 (higher threshold value), the sample L-Cs and L-Ck values distribute over a widespread area signifying that a variety of distributions can be fitted for frequency analysis. When the  $\lambda$  values increases, the sample L-Cs and L-Ck values tend to group around the theoretical L-Cs and L-Ck curve of the GP distribution in almost all stations and found to be well represented in the cases for equal and more than  $\lambda = 2$  and HFL. However, stability occurs as we increase the  $\lambda$  value beyond 2. Interestingly, the flood inundation and damage take place for the  $\lambda$  value ranging between 2 and 3. Also, the HFL of almost all stations varies within this range. The higher  $\lambda$  value does not create any flood in the basin presently, even though it gives better agreement with GP distribution in the L-Moment diagram between L-Cs and L-Ck.

From Fig. 7.5, it has been observed that the GP distribution provides the best results in comparison to other frequency analyses in all the cases. Now, it was essential to

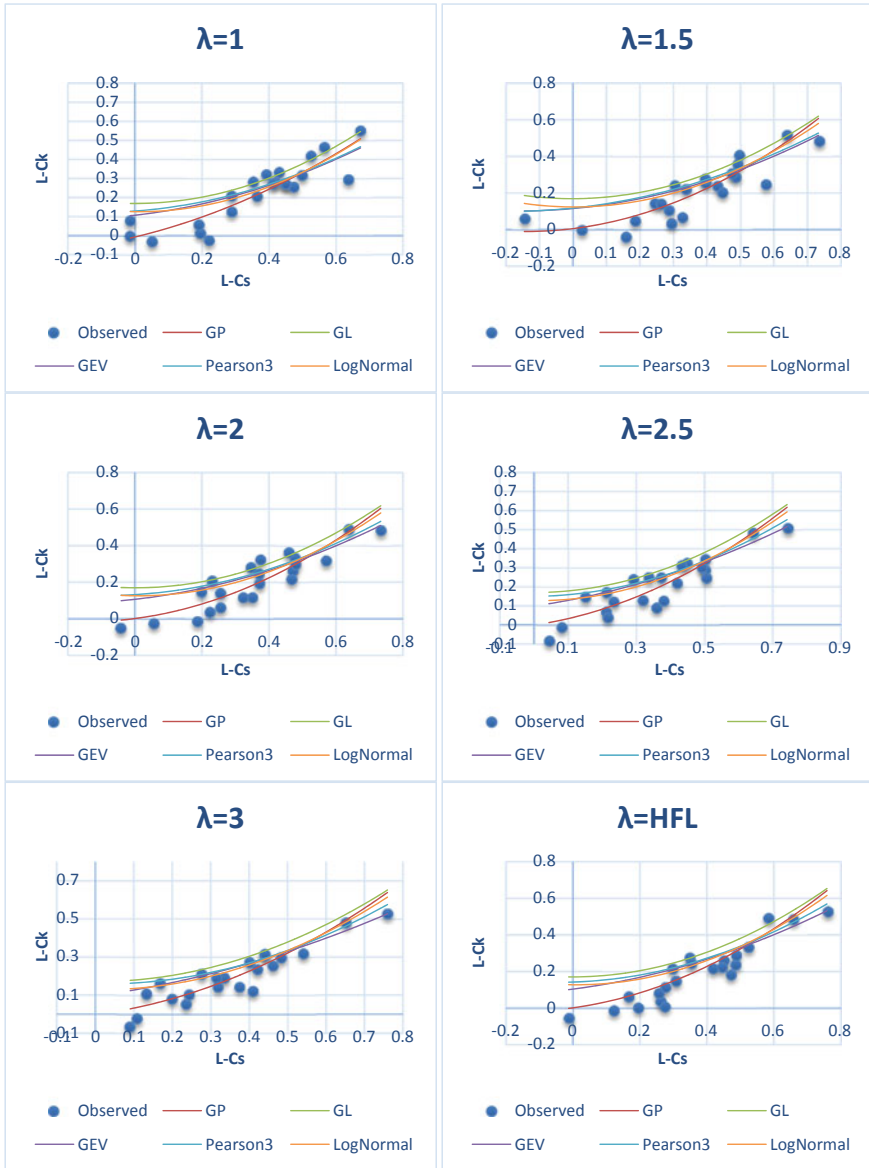
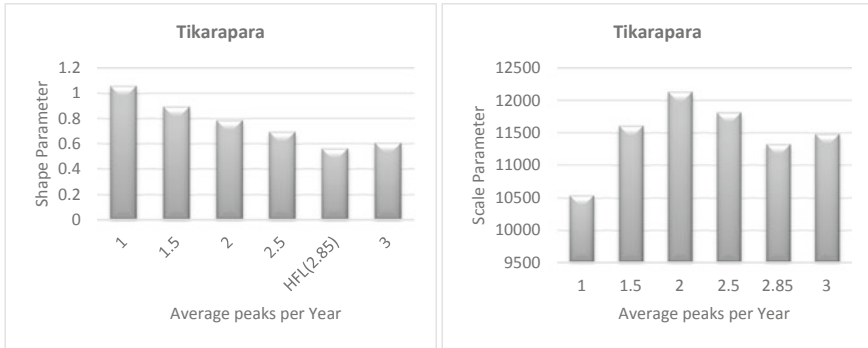


Fig. 7.5 L-moment diagram for the suitability of PDS



**Fig. 7.6** Shape and scale parameters for the PDS peak floods

evaluate the change in the GP distribution parameters, namely scale ( $\sigma$ ) and shape ( $\xi$ ) for different threshold ( $t$ ) or average peaks per year ( $\lambda$ ) values to obtain the optimum threshold value having constancy in model parameters. It has been observed that there is a gradual decrease in the value of scale ( $\sigma$ ) and shape ( $\xi$ ) parameters at all stations when the threshold values decrease and PDS peak flood data increases. As a result, the parameters of the GP distribution performed excellently to identify the optimal number of exceedance based on the threshold value. Figure 7.6 illustrates that the steadiness of the parameters with the increase in  $\lambda$  values for TIKARAPARA. From the figure, it is noted that the shape ( $\xi$ ) and scale ( $\sigma$ ) parameters begin to stabilize at threshold (17741.25 m<sup>3</sup>/s) obtained from HFL and corresponding discharge using Rating Curve at  $\lambda = 2.85$ . It has been observed that in all the 22 sampling locations, the beginning of stabilization of shape parameters takes place for  $\lambda$  values ranging between 2 and 3.

The stability of the GP parameter values has reduced the uncertainty of the quantile estimation by the selection of an appropriate threshold value. QQ plots for quantile estimates obtained using GP distribution were obtained for all the 22 sampling locations at the different threshold. Figure 7.7 illustrates the plots for the TIKARAPARA sampling location. Interestingly, from the figure, we can see at lower  $\lambda$  values (higher threshold), the higher quantiles are under-fitted and at higher  $\lambda$  values (lower threshold), the models tend to over-fit the higher quantiles. The quantiles obtained from higher return periods are much influenced by the shape ( $\xi$ ) and scale ( $\sigma$ ) parameters of the GP distribution model but for smaller return periods, it gives good results with the change in the threshold values.

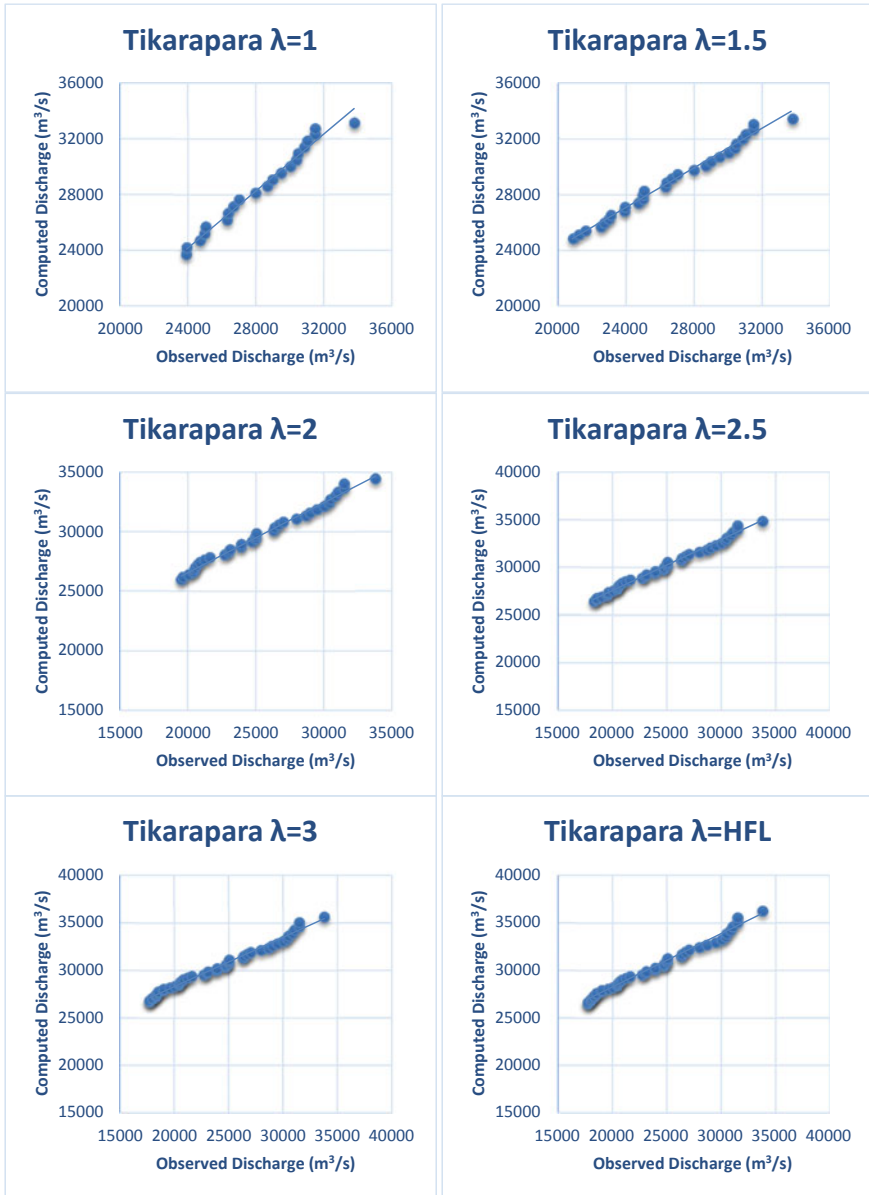


Fig. 7.7 QQ plots at Tikarapara station for a range of thresholds

## 7.4 Conclusions

An improvement of a set of measures for modeling the PDS approach is quite a challenging task, but it is necessary to raise the appreciation among the experts and researchers. One precise effort of the PDS approach is the choice of threshold level ( $t$ ) or average peaks per year ( $\lambda$ ). There is no exact value to be chosen instead to choose a range because of the different physiographic characteristics of the whole basin. A framework is provided on the basis of various concepts described in this research. In the present work, an attempt regarding the operational guidelines for selection of threshold values and their importance in the modeling of the Partial Duration Series (PDS) for 22 stations located in the Mahanadi River basin, India, was analyzed for a period of 1972–2012 years of daily discharge data and found that the threshold level having average peaks per year ( $\lambda$ ) value ranges inbetween 2 and 3 based on all concepts (i, ii, and iii) is suitable to best describe the PDS modeling. One of the major concerns regarding the PDS modeling is the randomness and nonstationarity presented with a certain threshold level. The time interval between peak arrival, autocorrelation, and the Mann–Kendall tests was effectively used to identify the presence of dependence and trends in PDS at all stations. From the results, it is concluded that the PDS is random and stationary at most stations. Another element, of the PDS approach, deals with the arrival process following the Poisson distribution which must be confirmed using the dispersion index test. The results show that the tests provided satisfying results concerning the Poisson assumption. The suitability of the GP distribution was also inspected using the L-moment ratio diagram and stability of GP parameters coupled with quantile estimation. For small  $\lambda$  values (higher threshold), different distributions were found to be fitted best but when the  $\lambda$  is equal to or greater than two, the GP distribution is provided well at each station. The stability of the GP parameters with different thresholds coupled with the quantile estimation was also inspected. The results concluded that the parameter values become stabilized with an increase of the threshold. Therefore, in the application of PDS in the Mahanadi River basin, the threshold value at different stations where the  $\lambda$  values ranging in between 2 and 3 which also includes the HFL at most stations is preferable. From QQ plots, we can see at lower  $\lambda$  values (higher threshold), the higher quantiles are under-fitted and at higher  $\lambda$  values (lower threshold), the models tend to over-fit the higher quantiles. The quantiles obtained from higher return periods are much influenced by the shape ( $\xi$ ) and scale ( $\sigma$ ) parameters of GP distribution model but for smaller return periods, it gives good results with the change in the threshold values. Though, the selection of appropriate threshold value for the modeling of the GP/PDS was studied at 22 single stations across the study area by assuming the whole basin is to be statistically homogenous. This assumption signifies a drawback of this research, and to prove the assumption, we need to develop a regional GP/PDS model.

**Acknowledgements** This research was supported by the National Institute of Technology, Rourkela, Odisha.

## References

- American Society of Civil Engineers (1949) Hydrology handbook
- Begueria S (2005) Uncertainties in partial duration series modelling of extremes related to the choice of threshold value. *J Hydrol* 303:215–230
- Claps P, Laio F (2003) Can continuous streamflow data support flood frequency analysis? An alternative to the partial duration series approach. *Water Resour Res* 39(8):1216. <https://doi.org/10.1029/2002WR001868>
- Cunnane C (1973) A particular comparison of annual maximum and partial duration series methods of flood frequency prediction. *J Hydrol* 18:257–271
- Cunnane C (1979) A note on the Poisson assumption in partial duration series models. *Water Resour Res* 15(2):489–494
- Deidda R (2010) A multiple threshold method for fitting the generalized Pareto distribution and a simple representation of the rainfall process. *Hydrol Earth Syst Sci Discuss* 7:4957–4994
- Gordon ND, McMahon TA, Finlayson BL, Gippel CJ, Nathan RJ (2004) Stream hydrology: an introduction for ecologists. Wiley, Chichester, West Sussex
- Hosking JRM (1990) L-moments analysis and estimation of distribution using linear combination of order statistics. *J Hydrol* 136:1–31
- Hosking JRM, Wallis JR (1987) Parameter and quantile estimation for the generalized Pareto distribution. *Technometrics* 29(3):339–349
- Jayasuriya MDA, Mein RG (1985) Frequency analysis using the partial series. In: 1985 Proceedings of Hydrology and Water Resources Symposium. Institution of Engineers, Australia, National Conference Publ No 85/2, pp 81–85
- Konecny F, Nachtnebel HP (1985) Extreme value processes and the evaluation of risk in flood analysis. *Appl Math Modelling* 9:11–15
- Lang M, Ouarda TBMJ, Bobée B (1999) Towards operational guidelines for over-threshold modelling. *J Hydrol* 225:103–117
- Madsen H, Rasmussen PF, Rosbjerg D (1997) Comparison of annual maximum series and partial duration series methods for modeling extreme hydrologic events. 1. At-site modelling. *Water Resour Res* 33(4):747–757
- Martins ES, Stedinger JR (2001) Historical information in a GMLE-GEV framework with partial duration and annual maximum series. *Water Resour Res* 37(10):2551–2557
- McDermott GE, Pilgrim DH (1982) Design flood estimation for small catchments in New South Wales. Australian Water Resources Council technical paper no. 73, Dept of National Development and Energy, 233
- Meng F, Li J, Gao L (2007) ERM-POT model for quantifying operational risk for Chinese commercial banks. In: Shi Y (ed) Lecture notes in computer science. Springer, Berlin, Heidelberg
- Miquel J (1984) Guide Pratique d'Estimation des Probabilités de Crues. Editions Eyrolles, Paris, 160 pp
- Natural Environment Research Council (1975) Flood studies report 1. Hydrological Studies. London
- Norbiato D, Borga M, Sangati M, Zanon F (2007) Regional frequency analysis of extreme precipitation in the eastern Italian Alps and the August 29, 2003—flash flood. *J Hydrol* 345:149–166
- Pham HX, Asaad YS, Bruce M (2014) Statistical properties of partial duration series: case study of North Island, New Zealand. *J Hydrol Eng* 807–815
- Rasmussen PF (1994) A regional index flood procedure based on partial duration series. INRS-Eau Internal Report, NSERC Strategic Grant No STR0118482, 17 pp
- Rosbjerg D, Madsen H (1992) On the choice of threshold level in partial duration series. In: Østrem G (ed) Nordic hydrological conference, Alta. NHP Rep 30, Oslo, pp 604–615
- Rosbjerg D, Madsen H (2004) Advanced approaches in PDS/POT modeling of extreme hydrological events. In: Hydrological sciences practice, 21st century, Proceeding, British hydrological society international conference, Imperial College, London



- Shinyie WL, Ismail N (2012) Analysis of t-year return level for partial duration rainfall series. *Sains Malays* 41(11):1389–1401
- Taesombut V, Yevjevich V (1978) Use of partial duration series for estimating the distribution of maximum annual flood peak. Hydrology paper no. 97, Colorado State University. FortCollins, CO, 71
- Tavares LV, Da Silva JE (1983) Partial duration series method revisited. *J Hydrol* 64:1–14
- Van Montfort MAV, Witter JV (1986) The generalized Pareto distribution applied to rainfall depths. *Hydrol Sci J* 31:151–162
- Wang QJ (1996) Direct sample estimators of L-moments. *Water Resour Res* 32(12):3617–3619
- Water Resources Council (WRC) (1976) Guidelines for determining flood flow frequency. Bulletin 17 of the Hydrology Subcommittee, Water Resources Council, Washington, DC
- Zvi AB (2009) Rainfall intensity–duration–frequency relationships derived from large partial duration series. *J Hydrol* 367(1–2):104–114

# Chapter 8

## Integrated RUSLE and GIS Approach for Estimating Soil Erosion of Watershed in Karjat



Raju Narwade and Shrikant Charhate

**Abstract** India being mainly an agricultural country, its economic, domestic consumption, industrial as well as financial sector depends on agriculture, which is adversely affected by soil erosion. Soil erosion within watersheds causes an increase in reservoir sedimentation, reducing their storage capacity and life span as well. Knowing the severity of erosion in an area contributes to effective soil conservation practices. Therefore, this study employs remote sensing, GIS and software to compute average annual soil loss in IWMP-45 Bhokarpada, Dist Raigad of Maharashtra by using the RUSLE equation. QGIS enables the extraction of spatial maps including DEM, rainfall erosivity, land slope, land use and land cover, data and values of the five RUSLE factors. Data for the study area has been obtained from Bhuvan, IMD (Indian Meteorological Department) and ISRO (Indian Space Research Organization). The results of this study area showed that the soil erosion was 163 ton/year in the study area which is severe and will require protection and conservation plans immediately. The soil erosion quantity mainly varies because of topography and land use-land cover. The study shows that under high and very high erosion region is about 21%.

### 8.1 Introduction

Soil erosion is a common phenomenon and land degradation problem which renders the land barren. It refers to the wearing away of a field's topsoil by the natural, physical forces, causing its detachment and transportation from one place to another. Natural forces like rain water flowing along the slopes of the land and wind erodes the nutrient-rich topsoil layer exposing the rocky layer underneath. Such barren

---

R. Narwade (✉)

Department of Civil Engineering, Pillai HOC College of Engineering and Technology, Rasayani  
Dist, Raigad, Maharashtra, India  
e-mail: [marwade@mes.ac.in](mailto:marwade@mes.ac.in)

S. Charhate

Amity School of Engineering and Technology, Bhatan, Post – Somathne, Panvel, Mumbai  
410206, Maharashtra, India

land does not support the growth of vegetation and hence can also not be used for agricultural purposes. To combat this problem as well as other natural resources degradation, the Government of India took up an initiative—the Integrated Watershed Management Program (IWMP), under the Department of Land Resources, Ministry of Rural Development. In the present study, satellite images, Digital Elevation Model (DEM) and rainfall data over the watershed were used to estimate soil loss in the Karjat region of Raigad District of Maharashtra by integrating the RUSLE model with GIS.

### ***8.1.1 Factors Affecting Soil Erosion***

The topography of the area includes features like land surface type and contour which affect the rate of erosion strongly. The intensity of rainfall is the highest controlling factor of soil erosion, since water washes or detaches soil much faster than other forces; therefore, it plays a big role. When rain occurs in form of a slow shower, it gets enough time to seep into the soil instead of splattering it hard, and the velocity of remaining rain water is less, which causes little or no erosion. Vegetation and land cover like forests and grasslands decelerates soil erosion effectively to a considerable extent. The roots of plants, trees, grasses, shrubs, etc. hold soil firmly in place. Properties of soil particles like texture, particle size distribution and the presence of type of minerals, salts and organic matter influence soil erosion along with other factors. Greater grain size and higher seepage of water into empty pores of soil (permeability) are causing absorption of water into it, rather than washing away, thus retarding erosion.

### ***8.1.2 Integrated Watershed Management Program***

To combat soil erosion as well as other natural resources degradation, the Government of India took up an initiative, the Integrated Watershed Management Program (IWMP), under the Department of Land Resources, Ministry of Rural Development. Some of its objectives include implementing technologies and techniques to prevent soil erosion by regenerating vegetation cover, reducing loss of the top layer of soil especially due to runoff and conserving natural resources like forests and rain water. Figure 8.1 shows the structure of a watershed.

#### **Study area**

The study area consists of a watershed coming under the IWMP-45 which is located in Karjat of Raigad district of the western part of Maharashtra state on the river named Bhatsol. The study area has fewer habitats which mainly consist of buildings or commercial areas, while a large part of it is barren, or else used for farming, and have forest covers. This particular area was selected for study purposes because of



Fig. 8.1 Structure of typical watershed (Source wiki spaces)

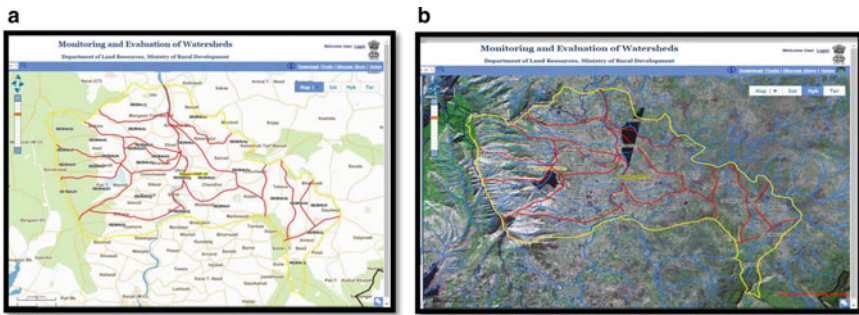


Fig. 8.2 a, b Terrain map of IWMP-45 watershed (Source Bhuvan Geoportal)

its moderate to heavy rainfall characteristics. Karjat has a tropical climate. There is significant rainfall in the monsoon months of the year. The average annual temperature is 26.9 °C. The average annual rainfall is 3933 mm and significant rainfall is in July with an average of 1591 mm and the driest month is January, with 0 mm (<http://en.climate-data.org/continent/asia>). Figure 8.2a, b shows the terrain map of IWMP-45 Watershed.

## 8.2 Methodology

Soil erosion in any area mainly depends upon its soil, topographic conditions and vegetation. There is variation in characteristics within the different subareas of the watershed. Satellite images, DEM and rainfall data over the watershed are used to predict soil loss in the watershed by integrating the RUSLE model with GIS. RUSLE

model was applied in the study area which requires a LULC map that can be extracted from remote sensing images, soil types and properties. The parameters of this model can be simply integrated with GIS for improved analysis. This is an advantage of a selection of the RUSLE method.

### 8.2.1 RUSLE Soil Erosion Model

The Revised Universal Soil Loss Equation (RUSLE) was used to estimate average annual soil loss (Renard et al. 1997). RUSLE is an empirical model, which relates soil loss and/or sedimentary yields to management and environmental factors directly through statistical relationships. The Universal Soil Loss Equation (USLE), U.S. Department of Agriculture (USDA) Natural Resources Conservation Service had developed this revised form. The RUSLE model is consisting of six factors. (1) Rainfall erosivity factor (*R*), (2) Soil Erodibility Factor (*K*), (3) Topographic Factors (*L* and *S*), (4) Crop Management Factor (*C*) and (5) Support Practice Factor (*P*). The main objective of the study was to integrate the RUSLE model with remote sensing and GIS techniques to estimate the erosion in IWMP-45, in the Karjat taluka of the Raigad district of Maharashtra, India and belongs to the Bhatsol River. In the present study, satellite images, Digital Elevation Model (DEM) is shown in Fig. 8.3 which is also used to estimate soil loss in the watershed by integrating the RUSLE model with GIS. The data availability from various sources is summarized in Table 8.1 and rainfall data of the watershed summarized in Table 8.2.

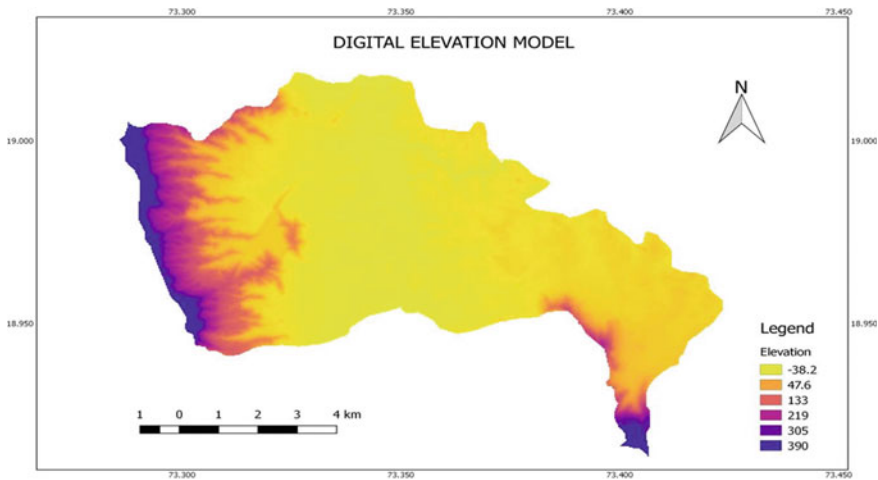


Fig. 8.3 Digital elevation model

**Table 8.1** Data availability from various sources

Sr. No.	Data	Source	Description
1	Digital elevation	<a href="http://www.bhuvan.nrsc.gov.in">www.bhuvan.nrsc.gov.in</a>	Satellite image
2	Satellite image	<a href="http://www.bhuvan.nrsc.gov.in">www.bhuvan.nrsc.gov.in</a>	Satellite image from LISS- 3
3	Soil data	Digital soil map of world	Food and agriculture organization
4	Rainfall data	IMD	Rainfall data for last 10 years

The RUSLE equation is given  $A = R \times K \times LS \times C \times P$  (Wischmeier and Smith 1978) (Where  $A$  is the average annual soil loss and  $R, K, LS, C$  and  $P$  are RUSLE parameters)

**Table 8.2** Average monthly rainfall data of Karjat. (Source <https://climate-data.org>)

Month	Jan	Feb	Mar	April	May	June	July	Aug	Sept	Oct	Nov	Dec
Temp	23.4	24.2	26.9	29.2	30.6	29.4	27.4	27.1	27.1	27.8	26	24.1
Rainfall (mm)	0	0	0	3	23	601	1591	1080	496	125	12	2

### 8.2.2 Computation of RUSLE Factors

#### (1) Rainfall Erosivity Factor ( $R$ )

Rainfall data for the last 10 years from the Karjat rain gauge station under the Indian Metrological Department was used to calculate  $R$ -factor for the watershed. Monthly rainfall data summarized in Table 8.3 was used to compute  $R$ -factor annually.

$$R = \sum_{i=1}^{12} 1.735 \times 10(1.5 \log 10(2P)) - 0.08188 \text{ (Wischmeier and Smith 1978)}$$

where  $R$  = Rainfall erosivity factor in  $\text{MJ mm ha}^{-1} \text{ h}^{-1} \text{ year}^{-1}$ .

The rainfall erosivity factor map is shown in Fig. 8.4. The value of the range of estimated  $R$ -factor varies from 920.7984 to 1888.589  $\text{MJ mm ha}^{-1} \text{ h}^{-1} \text{ year}^{-1}$ .

**Table 8.3** Rainfall stations and average rainfall in months

ID	Station	Latitude	Longitude	$R$
1	Karjat	18.9144	73.32645	920.7984
2	Kadav	18.9586	73.38138	1109.732
3	Neral	19.0267	73.31409	1888.589
4	Kashele	19.0086	73.42395	981.653

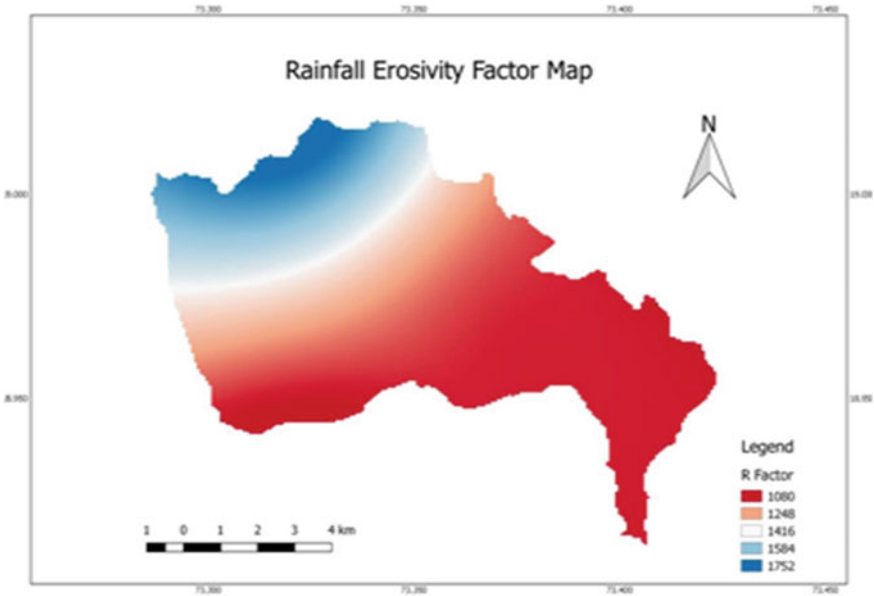


Fig. 8.4 Rainfall erosivity factor (*R*) map

**Soil Erodibility Factor (*K*)**

The soil map for the region is used to determine the soil erodibility factor. The soil map of the Karjat watershed shown in Fig. 8.5 was generated from the Digital Soil Map of the World (Food and Agriculture Organization (FAO) of the UN)

$$K = [2.1 \times 10^{-4}(12 - OM)M^{1.14} + 3.25(S - 2) + 2.5(P - 3)]/100$$

*K* = Soil Erodibility in tons/ac/unit rainfall index

*OM* = Per cent organic matter

*M* = (% MS + % VFS) (100 - % CL)

*MS* = percent silt

*S* = Structure Index

*P* = Permeability Index

The values of the *K*-factor were found to be varied in between 0.159 to 0.178.

**Topographic Factor (*LS*)**

Slope length factor (*L*) and slope steepness factor (*S*) are combined to get the topographic factor (*LS*). The influence of the topography of the region on erosion is given by the *LS*-factor. The *L*-factor shows the effect of slope length on erosion, while *S*-factor shows the effect of slope gradient on the same. It is the most important factor

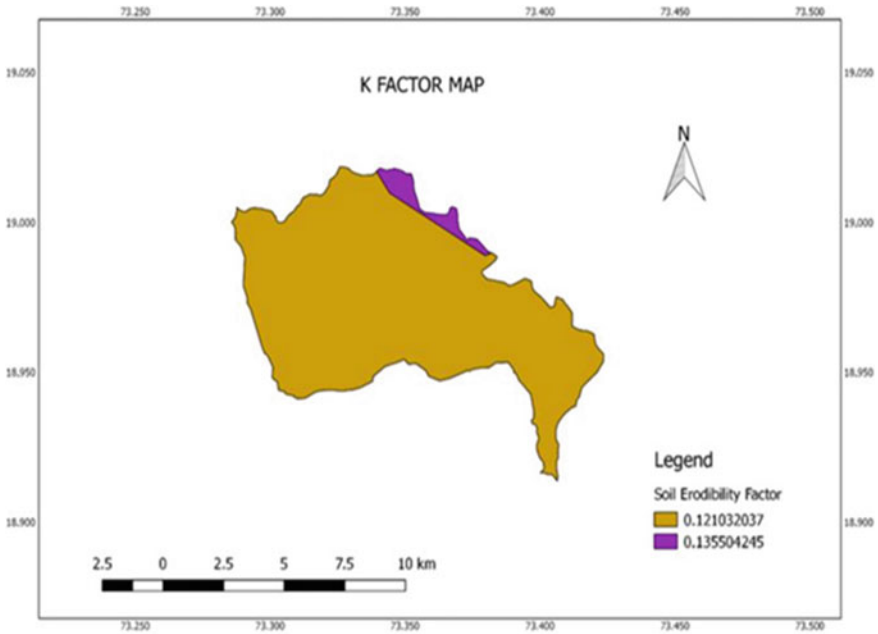


**Fig. 8.5** *K*-factor map

of the RUSLE model. The *LS*-factor map shall be determined from LISS 3 satellite image. Figure 8.6 shows the slope length and steepness (*LS*) for RUSLE.

### Support Practice Factor (*P*)

Erosion support practice factor (*P*-factor) is the ratio of loss of soil with a specific support practice to the corresponding loss with up and downslope cultivation (Wischmeier and Smith 1978). The lower value of the *P*-factor values for the study area summarized in Table 8.4. *P*-factor reduces soil erosion (Angima et al. 2003). LULC map which is used to determine the *P*-factor is shown in Fig. 8.7 and the support practice factor map is shown in Fig. 8.8.

### Cover management factor (*C*)

The cover and management factor (*C*) is the ratio of loss of soil from land cropped under specified conditions to the corresponding loss from clean-tilled, continuous fallow land (Wischmeier and Smith 1978). The *C*-factor is prepared from the LU/LC map shown in Fig. 8.9. The study area shall be classified into different land use classes. The values of the *C*-factor for each class shall be assigned from Table 8.5 (Kim et al. 2005).



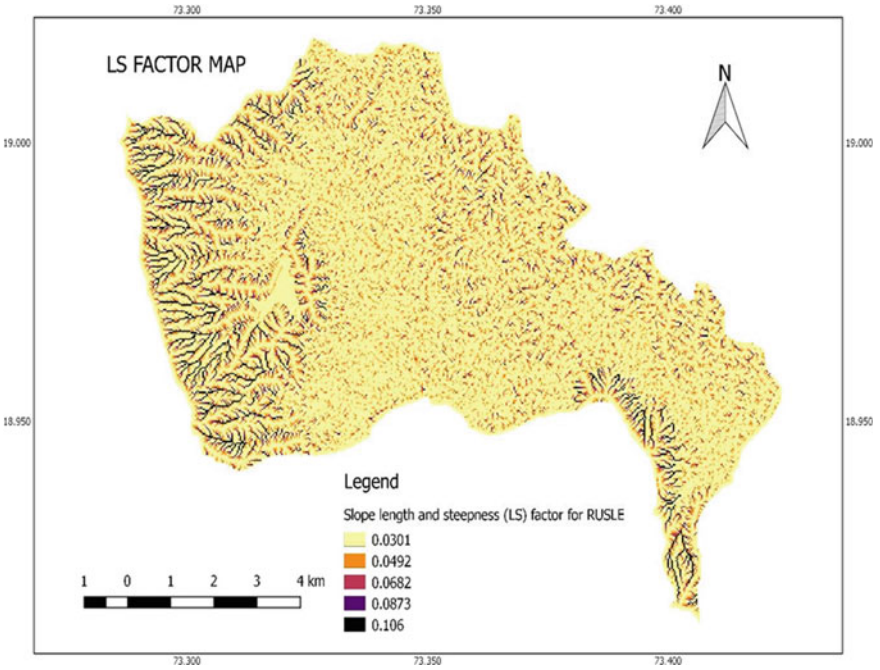


Fig. 8.6 Slope length and steepness for RUSLE

Table 8.4 P-factor values for study area

Land cover classes	Agricultural land	Agricultural land	Agricultural land	Agricultural land	Agricultural land
P-factor	0.4	0.1	1	0.1	0.5

### Generation of soil erosion map

Soil Erosion map has been generated after calculating the RUSLE factors. Figure 8.10 represents the final soil erosion map. The map shows the soil erosion is 163 ton/year in IWMP-45 Bhokarpada. The highly eroded soil is shown in Fig. 8.10 in red colour. The rate of soil erosion varies mainly on topography and land LULC shown in the map with different colours as lowest eroded region in bright colour and highly eroded area in dark red colour.

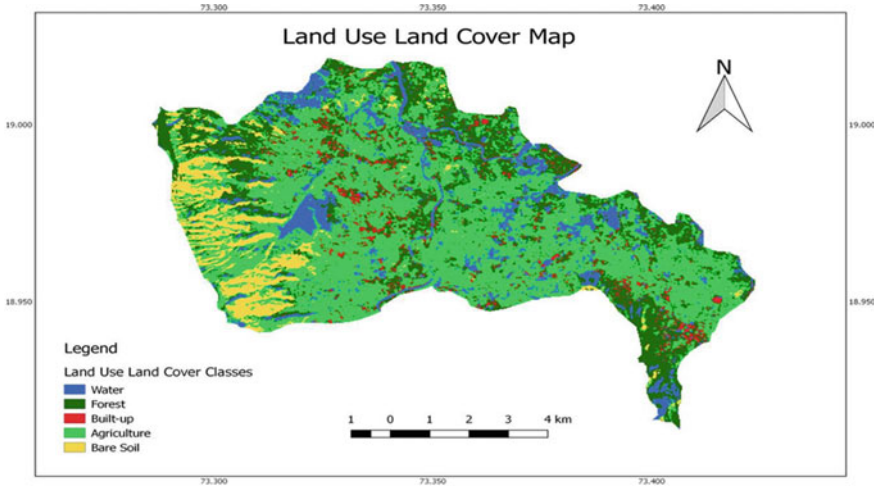


Fig. 8.7 Land use-land cover map

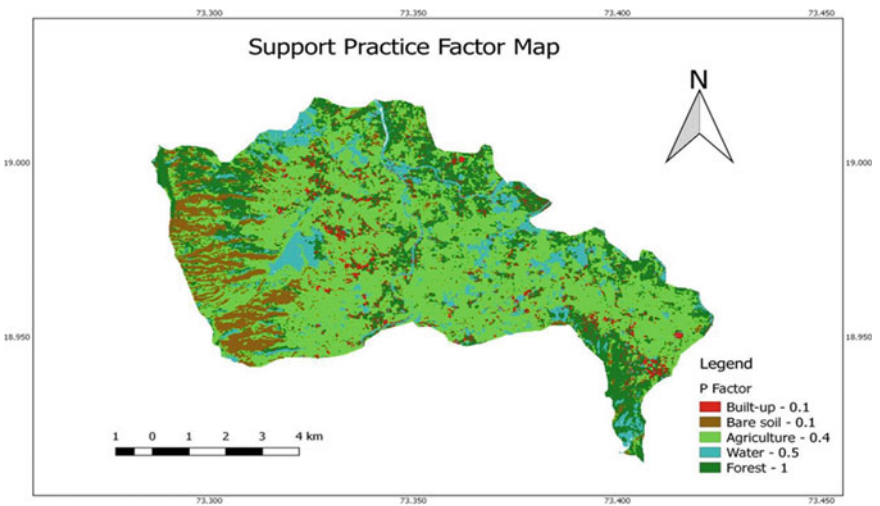
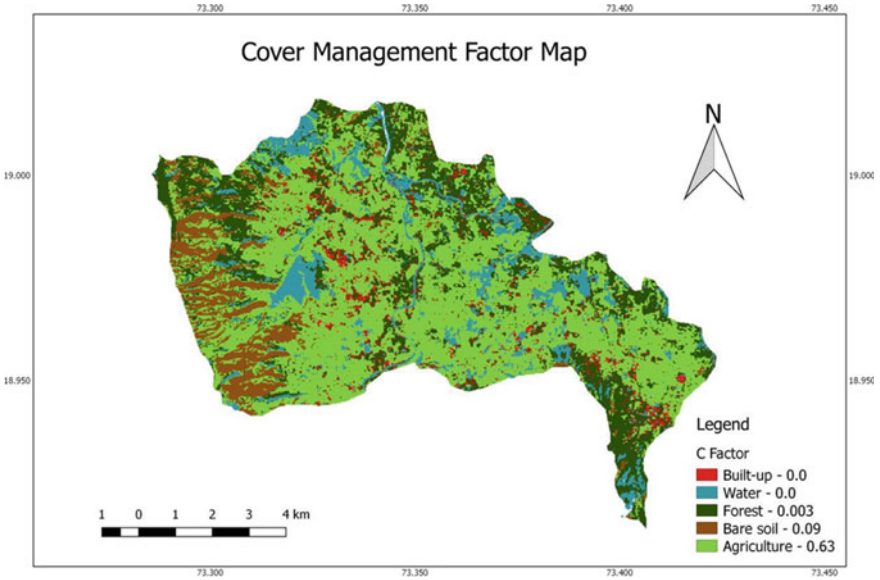


Fig. 8.8 Support practice factor map

### 8.3 Result and Analysis

Soil erodibility maps were generated by assigning *K*-factor values to respective soil types. The support practice factor (*P*) map which was generated from the LU/LC map showed a low value for the said region. Crop management factor (*C*) was prepared using the LULC Cover map. The average soil loss estimated in the IWMP-45 watershed was about 163 ton/year.



**Fig. 8.9** Cover management factor map

**Table 8.5** C-factor values for study area

Land use class	C-factor
Agriculture	0.63
Urban	0
Forest	0.03
Water	0
Bare ground	0.09
Other	0

### 8.4 Conclusion

There is high rainfall near the Karjat region in Neral. The rate of soil erosion in this catchment area is most important and it is very sensitive to rainfall. The rate of soil erosion depends on the average annual rainfall. Remote sensing and GIS play an important role in the estimation of soil erosion using the RUSLE model when integrated with GIS. The study shows that region under high and very high erosion is about 21%.

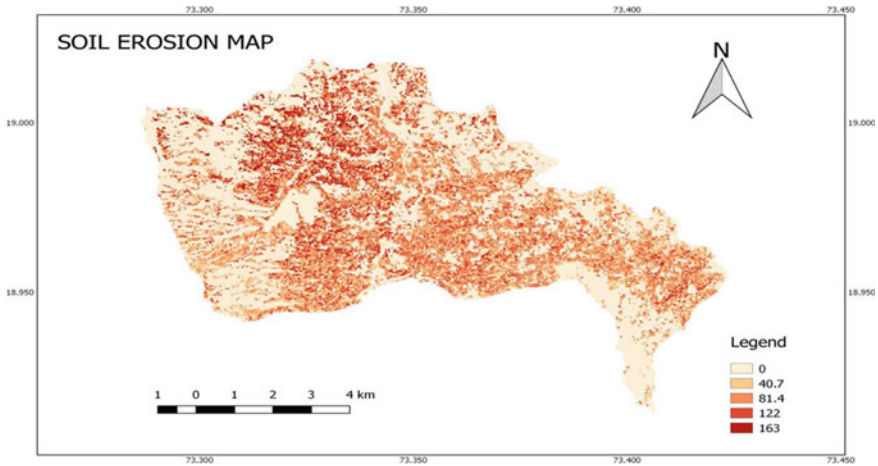


**Fig. 8.10** Soil erosion map

## References

- Angima SD, Stott DE, O'Neill MK, Ong CK, Weesies GA (2003) Soil erosion predicting using RUSLE for central Kenyan highland condition. *Agric Ecosyst Environ* 97(1-3):295-308
- Arekh S, Niazi Y, Kalteh AM (2010) Soil erosion and sediment yield modeling using RS and GIS techniques: a case study Iran. *Arab J Geosci* 5(2):285-296
- Fu BJ, Zhao WW, Chen LD, Zhang QJ, Lu YH, Gulinck H, Poesen J (2005) Assessment of soil erosion at large watershed scale using RUSLE & GIS: a case study in the Loess plateau, China. *Land Degrad Dev* 16(1):73-85
- Hesadi, Jalili KH, Hadidi M (2009) Applying RS and GIS for soil erosion and sediment estimation by MPSIAC model: a case study of Kenesht watershed in Kermanshah, Iran. *Geospatial World*
- Kim JB, Saunders P, Finn JT (2005) Rapid assessment of soil erosion using USLE & GIS Rio Lempa Basin, Central America using the universal soil loss equation and geographic information system. *Environ Manag* 36(6):872-885
- Renard KG, Foster GR, Weesies GA (1997) Predicting soil erosion by water: a guide to conservation planning with the Revised Universal Soil Loss Equatio (RUSLE). USDA agricultural handbook No. 703, 404 pp
- Wischmeier, Smith (1978) Predicting rainfall erosion losses: a guide of conservation planning. Agriculture handbook 537, United States, Department of Agriculture

## Website References

- [http://bhuvan.nrsc.gov.in/bhuvan\\_links.php](http://bhuvan.nrsc.gov.in/bhuvan_links.php)
- <http://www.imd.gov.in>
- <http://www.fao.org/home/en/>
- <http://www.iirs.gov.in>
- <http://www.en.climate.org>

# Chapter 9

## Swat Application for Water Balance Assessment of Koyna River Basin, Maharashtra, India



Amarsinh B. Landage and Ashok K. Keshari

**Abstract** Water resources management is very important for the sustainable growth of developing society as it is becoming a crucial resource in the present day. The knowledge of water balance and water yield of a river basin is an indispensable prerequisite in water resources management and sustainable development at basin level scale. The components of water balance are influenced by climate and physical characteristics of the catchment such as morphology, land use, and soil. Therefore, understanding the relationship between these physical parameters and hydrological components is necessary to assess the hydrologic response to climate and land cover variability in determining the water availability. Only after understanding the spatial and temporal variation and the interaction of these hydrologic components, one can scientifically formulate strategies for water conservation. Numerous integrated watershed models are available, but a choice of watershed development model depends upon the hydrologic components to be incorporated in the water balance. In this study, the Soil and Water Assessment Tool (SWAT), an integrated physically based distributed watershed model which uses a water balance equation for simulation of hydrology, has been used to analyze and quantify the water balance in the Koyna river basin, Maharashtra. The model uses DEM, land use, soil, and climate data. The watershed models partition rainfall into various hydrologic processes such as surface runoff, evapotranspiration, percolation, lateral flow, and base flow. with the constraint to account for all water entering, leaving, and being stored in a catchment. The model has been calibrated and validated for discharge at the outlet of the river basin. The calibration and validation efficiency has been tested by the coefficient of regression. Overall, SWAT demonstrated good performance in capturing the patterns and trends of the observed flow series. The model was found to produce a reliable estimate of aggregated monthly runoff which was demonstrated by Nash Sutcliff; efficiency and coefficient of regression superior to 0.85 for both calibration and validation periods indicate a predictive ability of the model and suggest its appropriateness for

---

A. B. Landage (✉) · A. K. Keshari  
Department of Civil Engineering, Indian Institute of Technology Delhi, New Delhi 110016, India  
e-mail: [cez168334@iitd.ac.in](mailto:cez168334@iitd.ac.in)

A. K. Keshari  
e-mail: [akeshari@iitd.ac.in](mailto:akeshari@iitd.ac.in)

estimation of water balance components and water yield in the study basin. Time series curves observed and simulated also showed very high similarity. Water balance components simulated by SWAT provided a baseline understanding of the hydrologic processes to deal with water management issues in the basin. The study suggests that the SWAT model could be a promising tool to predict water balance and water yield to support policies and decision-making for sustainable water management at the basin level.

## 9.1 Introduction

Water resources have become a critical element for socioeconomic development, especially in the arid and semi-arid regions. Water is an extremely essential element to sustain life and the increasing population is raising the demand for water. Availability of water is largely dependent on the rainfall distribution over an area, which again gets distributed into various components of interflow, surface runoff, evapotranspiration, etc. (Kundu et al. 2017; Wang et al. 2003). Water resources management is very important for the sustainable growth of developing society as it is becoming a crucial resource in the present day (Liu et al. 2008). Water resources management and hydrologic modeling studies are intrinsically related to the spatial processes of the hydrologic cycle. Developments in computer technology have revolutionized the study of hydrologic systems. Many computer models have been developed for hydrologic modeling and water resources management applications (Grassman et al. 2007). The knowledge of water balance and water yield of a river basin is an indispensable prerequisite in water resources management and sustainable development at basin level scale (Famiglietti and Rodell 2013).

The components of water balance are influenced by climate and physical characteristics of the catchment such as morphology, land use, and soil. Therefore, understanding the relationship between these physical parameters and hydrological components is necessary to assess the hydrologic response to climate and land cover variability in determining the water availability (White et al. 2011; Muttiah and Wurbs 2002; Arnold et al. 1998). Only after understanding the spatial and temporal variation and the interaction of these hydrologic components, one can scientifically formulate strategies for water conservation. Numerous integrated watershed models are available, but a choice of watershed development model depends upon the hydrologic components to be incorporated in the water balance. In this study, the Soil and Water Assessment Tool (SWAT), an integrated physically based distributed watershed model which uses a water balance equation for simulation of hydrology has been used to analyze and quantify the water balance in the Koyana river basin, Maharashtra.

## 9.2 Study Area

The Koyna River basin is a head-water basin on the east side of the main ridge of the Western Ghats, locally called the Sahyadri hill ranges, in the district of Satara, Maharashtra state, India (Fig. 9.1).

The gross storage capacity Koyna dam is of  $2797.15 \times 106 \text{ m}^3$ . The Koyna project is a multi-purpose project, but primarily designed as a hydro-electric project that supplies hydro-electric power to Maharashtra state, India with an installed capacity of 1920 MW. Koyna dam watershed has an elongated leaf shape, about 64 km in length and about 13 km in width with an area of  $891.78 \text{ km}^2$ . The water spread area at full reservoir level is  $115.36 \text{ km}^2$  which is about 13% of the total catchment area. Nearly 99% of the annual rainfall in this basin occurs during the south-west monsoon (June–October) and varies from 3000–5500 mm annually over the valley. The water released from the dam has been mainly utilized for agriculture and drinking purposes and simultaneously hydropower is generated during release (Naik et al. 2001).

Therefore, understanding the water balance is very important for studies on the operational management of reservoirs and river basins. Moreover, water balance studies provide an evaluation of an unknown water balance component from the difference between the known components (Dor et al. 2011).

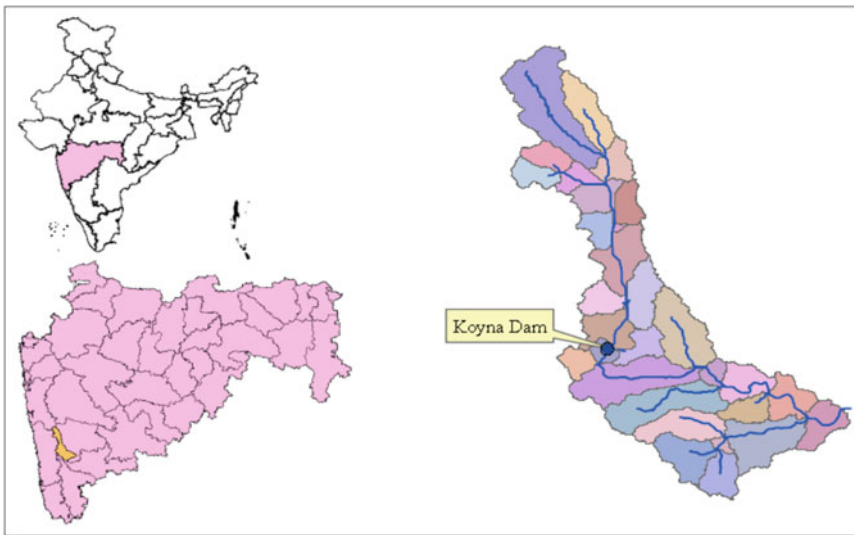


**Fig. 9.1** Location of Koyna River Basin



### 9.3 Data

SWAT input data included elevation, soil, LULC, temperature, precipitation, and streamflow. These data were constructed using the Arc SWAT graphical user interface that runs in ArcGIS. Elevation data were obtained from the Digital Elevation Model (DEM) created using Advanced Spaceborne Thermal Emission and Reflection Radiometer (ASTER) data of Earth Observing System of United States. The LULC map that was used in the study was developed based on LANDSAT satellite images. The daily temperature and precipitation data were acquired from Indian Meteorological Department. The soil-related data were obtained from the FAO map and the daily streamflow data was collected at one gauge and discharge station from Central Water Commission. The gridded meteorological data used for hydro-meteorological parameters estimation was obtained from Global Weather Generated data (Figs. 9.2, 9.3, 9.4 and 9.5).

### 9.4 Methodology

The Soil and Water Assessment Tool (SWAT) was developed by Arnold et al. (1998) for the Agricultural Research Service (ARS), United States Department of Agriculture (USDA). SWAT model which is a physically based model was developed for application to large and complex watersheds over long periods of time. SWAT is a physically based model and hence it requires extensive physical parameters to represent the real hydrological processes in the catchment scale. From topography data, the watershed is divided into a number of sub-catchments. The use of sub-catchments in a simulation is particularly beneficial when different areas of the catchment are dominated by land uses or soils dissimilar enough in properties to impact hydrology. Every sub-catchment is then subdivided into Hydrologic Response Units (HRUs). Every HRU is a unique combination of land use, soil, and management practices in a sub-catchment. Input information for each sub-catchment is grouped into the following categories: climate; hydrologic response units or HRUs; groundwater; and the main channel or reach, draining the sub-catchment. The final result of the entire basin is then obtained at the main outlet.

### 9.5 Results and Discussion

In the practical application of hydrologic models, modelers often select a single model among the several choices that are assumed to best represent the hydrologic system (Zhang et al. 2009). Therefore, before calibrating the water balance and streamflow, we need to have a profound understanding of the actual watershed characteristics and



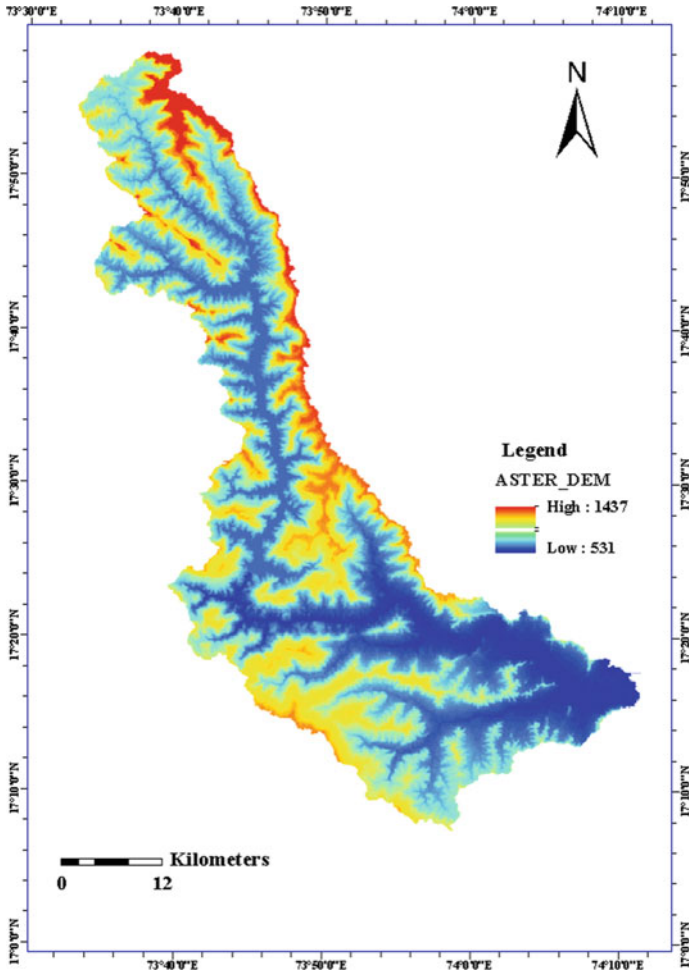


Fig. 9.2 Koyna Basin DEM

the information provided in previous SWAT literature (Neitsch et al. 2005) (Figs. 9.6 and 9.7).

In this study, the periods from 2001 to 2003, 2004 to 2010, and 2011 to 2013 were taken as warm-up period, calibration period, and validation period, respectively. The calibration carried out with the flow data from 2004 to 2010 shows the  $R^2$  value of 0.84 and the validation shows  $R^2$  value of 0.82 between the observed and the simulated flow. Validation is carried out with the flow data from 2011 to 2013. The accuracy assessment of the model has been carried out with the coefficient of determination ( $R^2$ ) (Legates and McCabe 1999). According to Figs. 9.6 and 9.7, the curves of the observed and simulated monthly values of Warunji gauge and discharge matched well, and the evaluation coefficients of the simulated monthly discharge were very

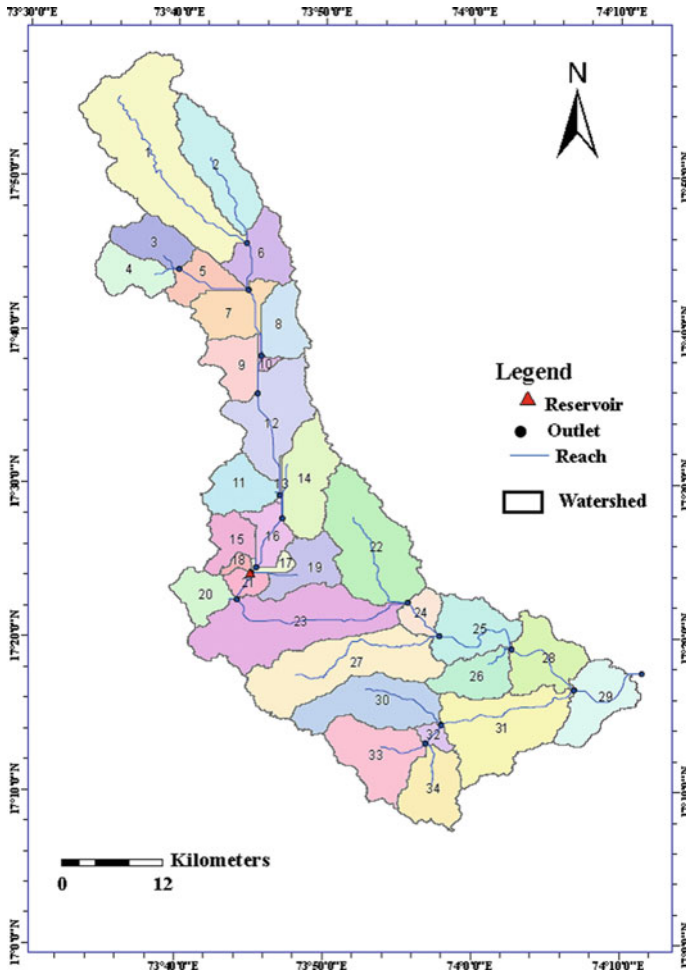


Fig. 9.3 Koyna River Sub-basins

good and listed in Table 9.1. In the validation process, the model was operated with input parameters set during the calibration process without any change and the results were compared to the remaining observational data to evaluate the model prediction. The monthly simulated and observed discharge of the Koyna River basin fitted well, which also could be indicated by the evaluation coefficients (Tables 9.1 and 9.2).

The input and output of water of the whole basin were quantified and the average monthly discharge was determined. On the monthly scale, considering the rainy and dry season, the related parameters were adjusted such as Cn2, Sol\_Awc, Sol\_K, and Alpha\_Bf to calibrate the proportion of surface runoff, lateral flow, and baseflow to total discharge. Because precipitation controls the water balance, it is critical that the

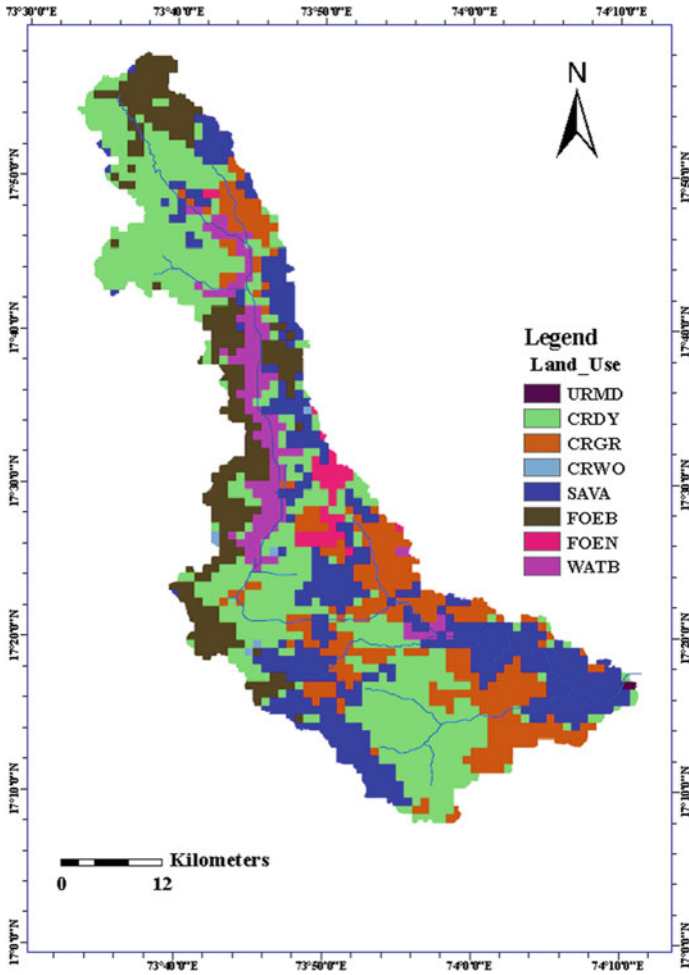


Fig. 9.4 LULC map

amount and distribution of precipitation in space and time are accurately simulated (Arnold et al. 1998).

The water balance was estimated based on the principle of conservation of mass (i.e., the water entering an area must leave the area or be stored within the area) and the annual partitioning of precipitation into ET and runoff, which is controlled by the temporal distribution of water supply (precipitation) and demand (ET) and is balanced by water storage in the soil.

Thus, the water balance can be expressed as follows:

$$R = P - ET + TWS$$

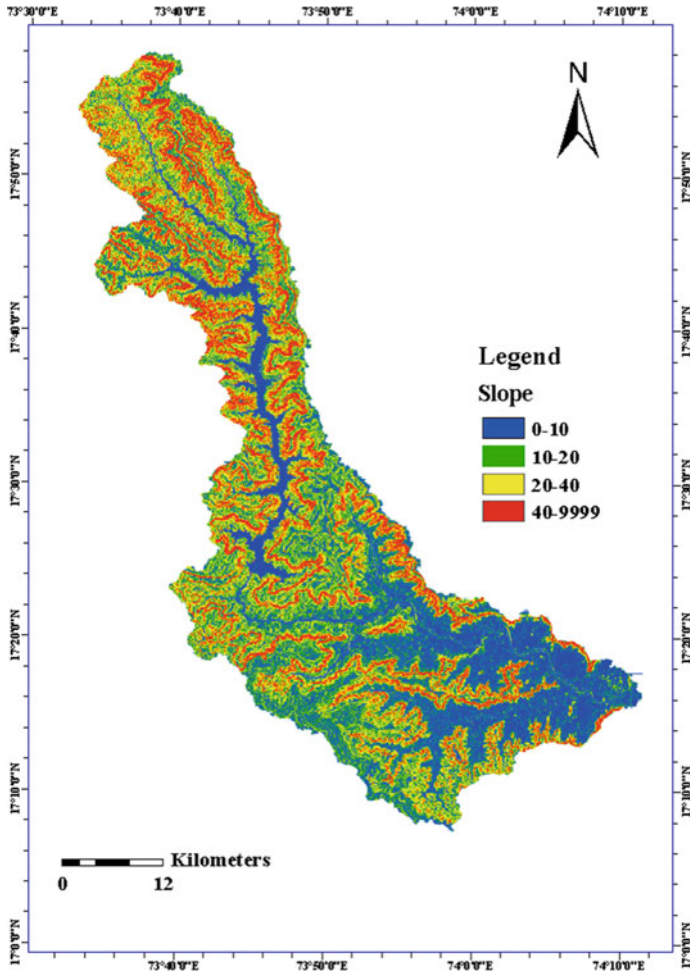


Fig. 9.5 Slope map

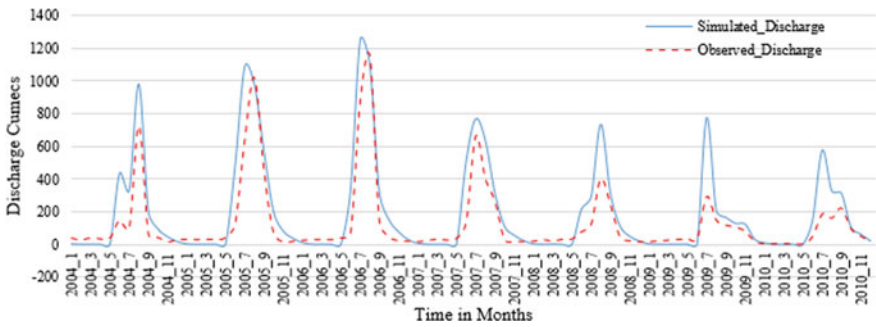
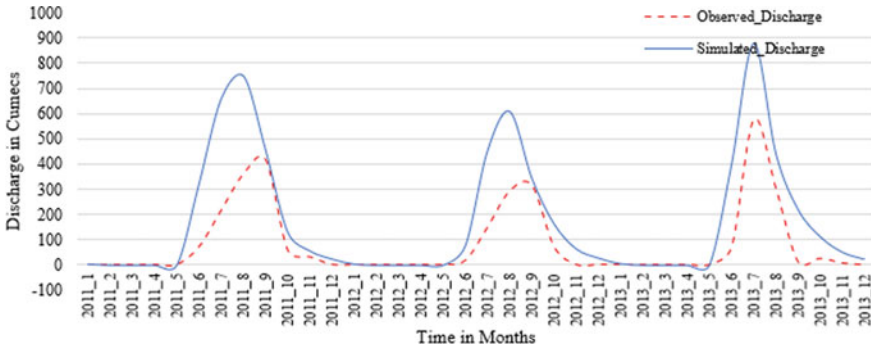


Fig. 9.6 Calibration for Discharge



**Fig. 9.7** Validation for Discharge

**Table 9.1** Objective measures achieved by SWAT at Warunji

Parameters	Calibration	Validation
Coefficient of determination ( $R^2$ )	0.84	0.82

**Table 9.2** Average monthly values of water balance components

Months	Rain (mm)	SURF Q (mm)	LAT Q (mm)	Water Yield (mm)	ET (mm)	PET (mm)
1	1.84	0.05	0.22	11.01	9.95	132.33
2	0.76	0.08	0.09	2.55	6.78	142.27
3	2.85	0.30	0.13	2.05	44.30	185.90
4	16.67	0.60	0.62	2.38	24.74	187.08
5	23.90	1.10	1.29	3.27	20.26	201.97
6	540.86	287.19	18.51	307.84	54.77	103.37
7	1,170.99	852.78	39.88	940.71	37.06	43.36
8	838.66	563.45	42.02	740.44	37.82	48.25
9	308.60	151.30	24.21	334.95	54.61	100.70
10	116.87	45.67	10.31	181.51	47.14	127.96
11	30.98	6.84	2.62	81.40	29.18	130.74
12	6.45	1.40	0.82	37.47	16.35	129.36

where R is river runoff, P is precipitation, ET is evapotranspiration, and TWS is total water storage (vegetation, surface detention, soil, and groundwater).

The estimated values from the models of all of the components should be reasonably accurate to determine the water availability in the different components of the hydrological cycle. In reality, there are always discrepancies between the observed values and model predictions due to measurement errors, inadequate data capture networks, and the difficulty of representing real-life complex spatial heterogeneity in

the model. Observed precipitation data that had been adequately checked for continuity and consistency were used in the simulations. River runoff was estimated using the model and compared to observed runoff. The groundwater and surface water withdrawals for consumptive and non-consumptive uses are not considered in this study. Based on the measured precipitation data and observed PET, the percentage runoff generation (runoff fraction) and conversion of PET to ET were estimated.

## 9.6 Summary and Conclusions

Based on the available geospatial and hydro-meteorological data, a SWAT model was developed for the Koyna River basin. The performance indicators  $R^2$  values in the model showed good performance for runoff simulation. There was close agreement between the monthly observed and calibrated runoff at the river basin scale, and the models accurately captured the flow patterns for most seasons. The calibration and validation procedures estimated water balance components and monthly streamflow that generally showed “satisfactory” model performance, though the model underestimated some peak flow events, including the low flows of a certain period. At the same time, the model simulated some peak flows that happened during intensive rainfall while the corresponding observed flows showed low values.

The calibration efficiency has been tested by the coefficient of regression. Overall, SWAT demonstrated good performance in capturing the patterns and trends of the observed flow series. The model was found to produce a reliable estimate of aggregated monthly runoff which was demonstrated by the coefficient of regression superior to 0.80 for both calibration and validation periods which indicate a predictive ability of the model and suggest its appropriateness for estimation of water balance components and water yield in the study basin. Time series curves observed and simulated also showed very high similarity. Water balance components simulated by SWAT provided a baseline understanding of the hydrologic processes to deal with water management issues in the basin. The study suggests that the SWAT model could be a promising tool to predict water balance and water yield to support policies and decision-making for sustainable water management at the basin level. Therefore, understanding the water balance will be useful for studies on the operational management of reservoirs and river basins.

## References

- Arnold JG., Srinivasan R, Muttiah RS, Williams JR (1998) Large area hydrologic modelling and assessment part 1: model development. *J Am Water Resour As* 34 (1):73–89
- Dor N, Syafalni S, Abustan I, Rahman M, Nazri M, Mostafa R, Mejus L (2011) Verification of surface-groundwater connectivity in an irrigation canal using geophysical, water balance and stable isotope approaches. *Water Resour Manag* 25:2837–2853
- Famiglietti JS, Rodell M (2013) Water in the balance. *Science* 340(6138):1300–1301

- Gassman PW, Reyes MR, Green CH, Arnold JG (2007) The soil and water assessment tool: historical development, applications, and future research directions. *Trans ASABE* 50:1211–1250
- Kundu S, Khare D, Mondal A (2017) Past, present and future land use changes and their impact on water balance. *J Environ Manag* 197:582–596
- Legates DR, McCabe GJ (1999) Evaluating the use of “goodness-of-fit” measures in hydrologic and hydroclimatic model validation. *Water Resour Res* 35:233–241
- Liu Y, Gupta H, Springer E, Wagener T (2008) Linking science with environmental decision making: experiences from an integrated modeling approach to supporting sustainable water resources management. *Environ Model Softw* 23(7):846–858
- Muttiah RS, Wurbs RA (2002) Scale-dependent soil and climate variability effects on watershed water balance of the SWAT model. *J Hydrol* 256(3–4):264–285
- Naik PK, Awasthi AK, Anand A, Mohan PC (2001) Hydrogeologic framework of the Deccan terrain of the Koyna River basin, India. *Hydrogeol J* 9(3):243–264
- Neitsch S, Arnold J, Kiniry J, King K, Williams J (2005) Soil and water assessment tool (SWAT) Theoretical documentation. Blackland Research Center, Texas Agricultural Experiment Station, Temple, Texas, (BRC Report 02–05)
- Wang Z, Liu C, Huang Y (2003) The theory of SWAT model and its application in Heihe basin. *Prog Geograph* 22:79–86
- White ED, Easton ZM, Fuka DR, Collick AS, Adgo E, McCartney M, Awulachew SB, Selassie YG, Steenhuis TS (2011) Development and application of a physically based landscape water balance in the SWAT model. *Hydrol Process* 25(6):915–925
- Zhang X, Srinivasan R, Bosch D (2009) Calibration and uncertainty analysis of the SWAT model using genetic algorithms and Bayesian model averaging. *J Hydrol* 374:307–317

# Chapter 10

## Identification of Suitable Sites for Water Storage Structure in Andhiyarkore Watershed of Chhattisgarh State India



Parul Vinze and Ishtiyaq Ahmad

**Abstract** Water storage structures play an important role in watershed management. Water storage structures are used to store surplus water that is flowing over the land. It is necessary to construct a water storage structure at a suitable location; therefore, identification of suitable sites becomes important. In the study, RS (Remote Sensing) and GIS (Geographical Information System) techniques are used to convert geospatial data into the required format. For the identification of suitable sites, the input parameters used for overlay analysis were Soil, LULC, stream order, slope, settlement, lineament, geology and runoff coefficient. All layers have been reclassified and ranking assigned to different classes according to the specification of the water storage structures. In weighted overlay analysis, all the reclassified layers are overlaid on the basis of their priorities and Analytic Hierarchy Process (AHP) has been used for determining the priority for each layer. As a result of weighted overlay analysis, total of 410 sites have been found suitable for different water storage structures; these sites include 209 check dams, 24 percolation ponds, 175 subsurface dykes and 2 farm ponds.

### 10.1 Introduction

Drought in an area shows the scarcity of water, this can be generated by any of the reasons, i.e. Lesswater supply, less rainfall and poor infiltration capacity of soil, etc. In recent years, majority of the districts in Chhattisgarh state have been declared as drought-prone areas. There are 21 districts among 27 districts of Chhattisgarh facing the drought problem. Kawardha district in Chhattisgarh is one of these districts. This problem can be mitigated by some conservation measures. Sometimes even though enough water is available, drought exists; this situation arises when surplus water flows over the land and the infiltration rate is very less. Therefore, some techniques should be adopted so that the water can infiltrate into the ground. Water storage is one of the beneficial ways to increase infiltration. Water availability for different purposes

---

P. Vinze · I. Ahmad (✉)

Department of Civil Engineering, National Institute of Technology Raipur, G.E. Road, Raipur, India



particularly for irrigation and domestic is of great concern in the near future. Hence, it becomes necessary to build a water storage structure to store water and utilize it in a proper manner. Storage structures require considerable investment and hence it is important to identify the suitable location of these structures before execution (Ahmad and Verma 2016). The aim of this study is to identify a suitable location for water storage structure under the guidelines of Integrated Mission for Sustainable Development (IMSD) using remote sensing and GIS techniques (Ahmad and Verma 2016; Kolekar et al. 2017).

## 10.2 Description of the Study Area

The study area is a part of Sheonath river watershed. Andhiyarkore is a G & D site of CWC situated in the Bemetara district, which has been considered as the outlet for this study. Andhiyarkore watershed is situated in Chhattisgarh between  $81^{\circ} 1' 39''$ – $81^{\circ} 36' 25.78''$  longitude and  $21^{\circ} 45' 32.17''$ – $22^{\circ} 30' 15.78''$  latitude. It covers 2245.36 km<sup>2</sup> area. The area comprises of two districts, namely: Kawardha and Bemetara (Ground water brochure of Durg district 2012–2013; Ground water brochure of Kawardha district 2012–2013). The area covers 7 blocks which are Pandariya, Bemetara, Kawardha, Saja, Nawagarh, Bodla and Sahaspur lohara. Four blocks covered by the study area are situated in Kawardha district (Ground water brochure of Kawardha district 2012–2013) and 3 blocks are situated in Bemetara district (Ground water brochure of Durg district 2012–2013). There are 14 rain gage sites that are located in and around the study area (Fig. 10.1).

## 10.3 Methodology

For the identification of suitable sites, different types of data are required, which includes:

1. Digital Elevation Model (DEM) from BHUVAN.
2. LULC from National Remote Sensing Agency, Hyderabad.
3. Soil data from NBSS and LUP, Nagpur.
4. Rainfall data from CG WRD Raipur and CWC.

The identification of suitable sites has been carried out with step by step procedure as shown in the flowchart. The preparation of different layers and weighted overlay analysis has been done with the help of ArcGIS to prepare a site suitability map. In the study, 8 parameters are considered for the identification of suitable sites, viz. Slope, lineament, geology, stream order, runoff coefficient, LULC, soil and settlement. These parameters have been selected on the basis of their influence on the selection of water storage sites (Fig. 10.2).

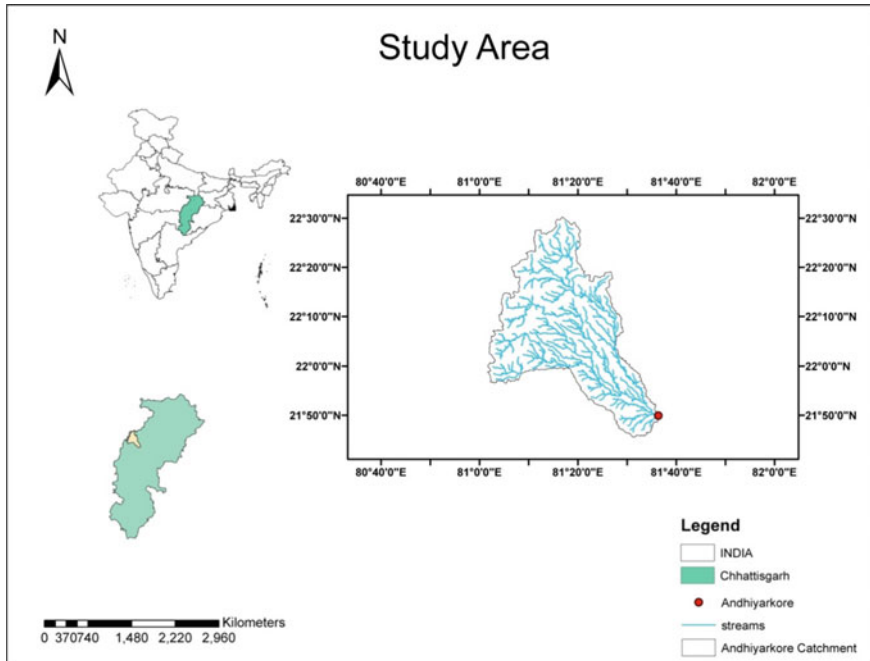


Fig. 10.1 Location map of study area

### 10.3.1 Slope

The slope has been determined with the help of the tool “Slope” (3D analyst) in ArcGIS. Digital elevation model of the study area has been used as the input for determining slope. The slope for the study area has been found out in the range of 0–196.177 (percentage rise) (Fig. 10.3).

### 10.3.2 Lineament

Lineament is a very important layer in the study. Lineament is digitized with the help of ArcGIS web map services and BHUVAN. Lineament running more than 1 km is considered as major lineament and less than 1 km is considered as minor lineament (Fig. 10.4).

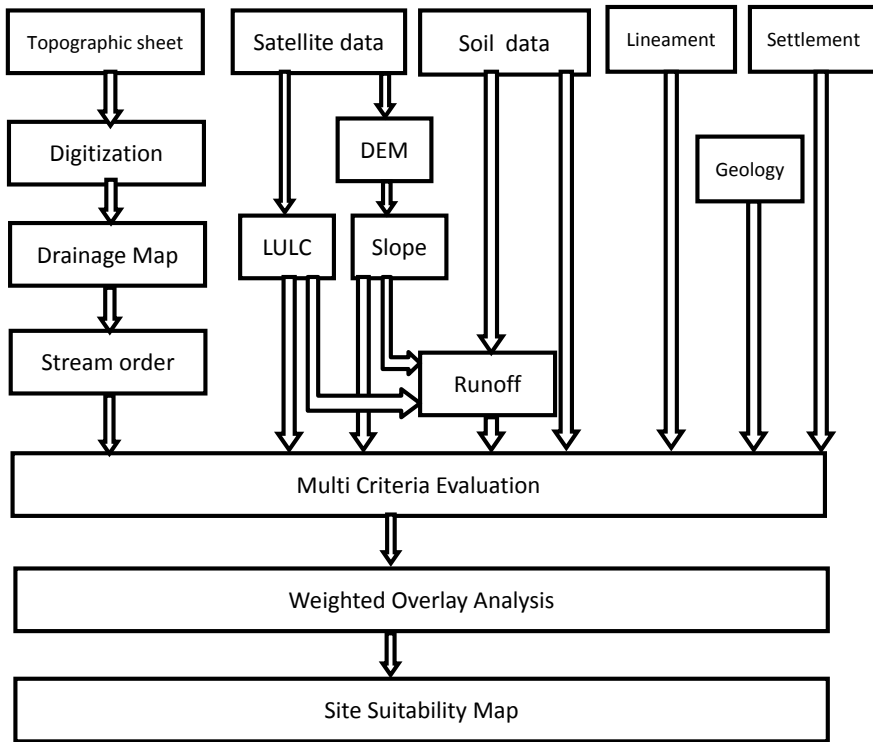


Fig. 10.2 Flowchart of methodology

### 10.3.3 Geology

Geological formation gives information about the properties of land. Permeability is one of the important properties which are used to decide suitability for water storage structure. In the study, the geology layer has been prepared with the help of information given in the Central Ground Water Board report 2012–2013 (Ground water brochure of Durg district 2012–2013; Ground water brochure of Kawardha district 2012–2013) (Fig. 10.5).

### 10.3.4 Stream Order

Stream order is a number assigned to a stream, which defines the size of the stream. The lowest stream order defines the smallest stream and the highest stream order defines the longest stream. Andhiyarkore watershed is having streams of order 1 to 6. The stream order layer has been prepared with the help of the stream order tool in ArcGIS (Fig. 10.6).

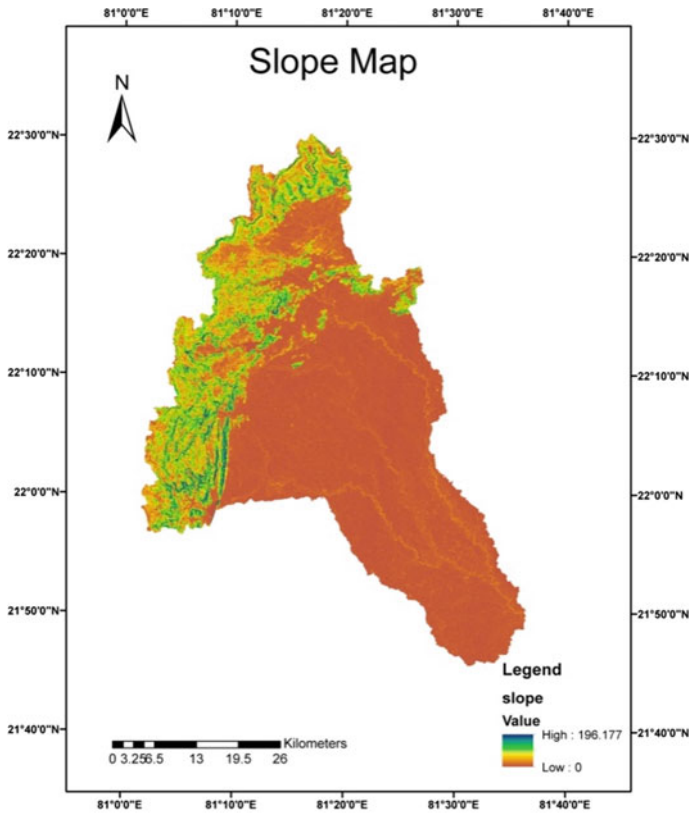


Fig. 10.3 Slope map of study area

### 10.3.5 Runoff Coefficient

Runoff coefficient is the ratio of runoff to the total rainfall. Runoff coefficient layer is prepared with help of GIS techniques. Runoff is calculated using SCS CN method. Runoff coefficient shows the runoff potential of the area. The study area is having a minimum runoff coefficient of 0.434 and a maximum of 1 (Fig. 10.7).

### 10.3.6 Land Use and Land Cover

Land use and land cover define the imperviousness of the ground surface. Imperviousness is a very important part of the runoff and infiltration process and both parameters decide the suitability of the water storage site. For the present study, land use and land cover data have been collected from National Remote Sensing Agency, Hyderabad (Fig. 10.8).

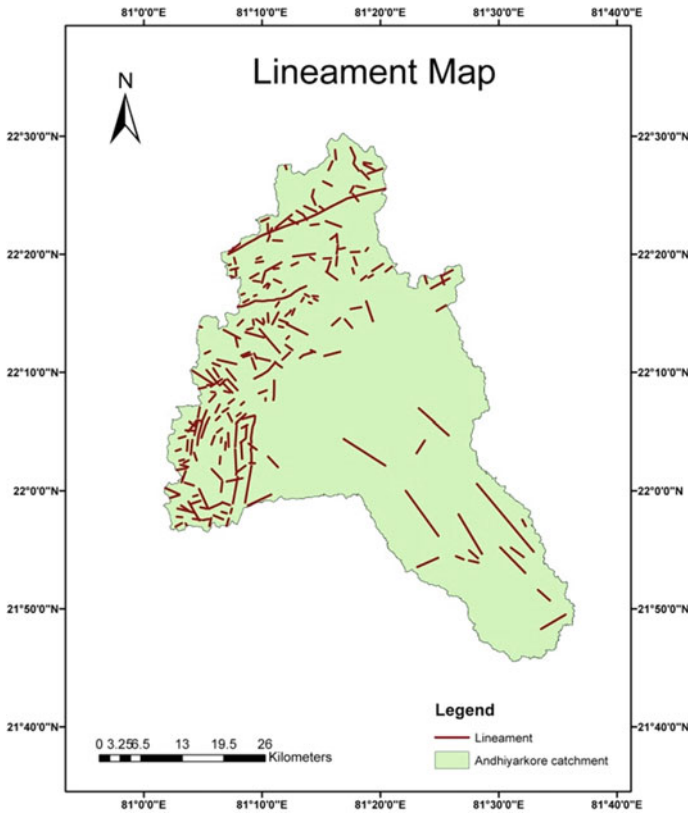


Fig. 10.4 Lineament map of study area

### 10.3.7 Soil

In the present study, the soil map for Andhiyarkore catchment has been prepared using hydrological soil group classification. This analysis uses only four types of HSG that are A, B, C and D within the soil map. This layer is very important as it is directly related to runoff and infiltration (Fig. 10.9).

### 10.3.8 Settlement

As per the census of 2011, there are 508 villages in the study area. These settlements were shown in terms of latitude and longitude. A buffer zone of 200 m was created around each settlement (Fig. 10.10).

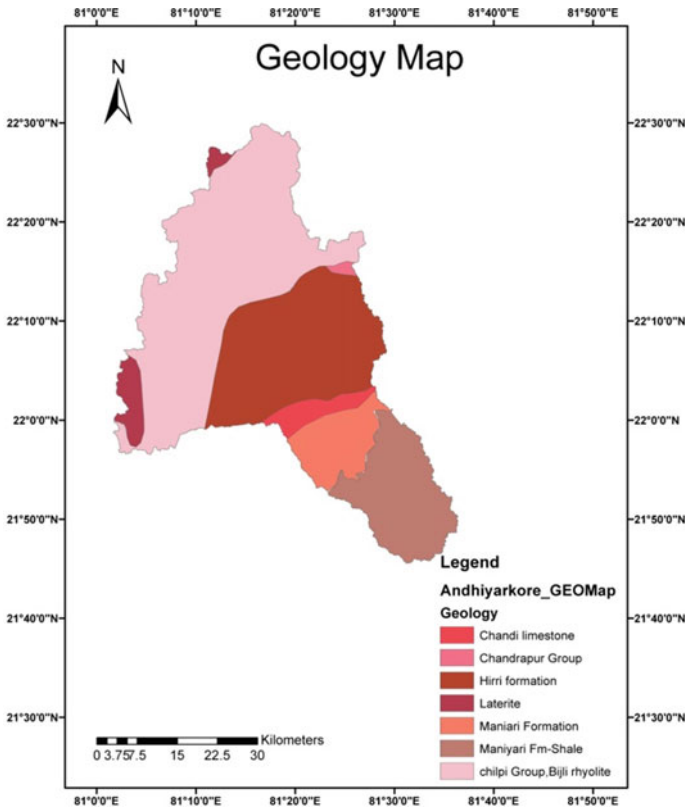


**Fig. 10.5** Geology map of study area

After preparing these 8 layers with help of ArcGIS tool, all layers were converted into raster. All raster layers were reclassified using reclassify tool as per the specification of different water storage structures (Prasad et al. 2014; Saxena et al. 2017).

All reclassified layers were assigned appropriate weights, which were calculated using Saaty’s Analytic hierarchy process (AHP) (Al-shabeeb 2016; Pramanik 2016). Weights signify the priorities of layers as per their significance in water storage. After assigning weights, all layers were integrated using weighted overlay analysis, a tool in ArcGIS. Overlay analysis gives site suitability zones in raster format which are further converted into points. The final output has been generated showing locations of different water storage structures.

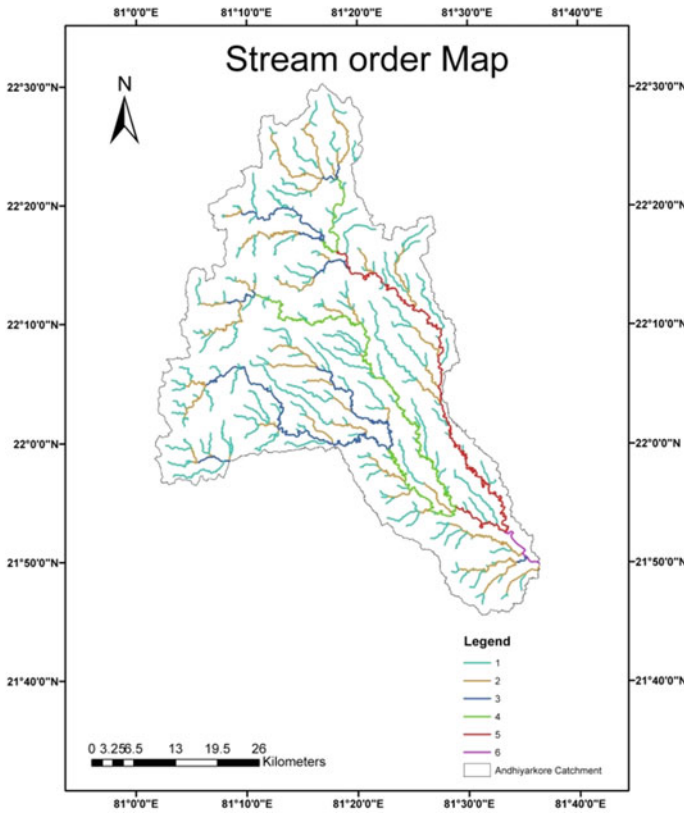


Fig. 10.6 Stream order map of study area

### 10.3.9 Suggested Suitable Sites

For identification of the suitable sites two criteria have been adopted, they are as follows:

1. 200 m buffer zone has been created around each settlement (village) and suitable sites located inside the buffer zone were eliminated.
2. Subsurface dykes located stream order <4 were eliminated (Ramakrishnan et al. 2009) (Table 10.1).

## 10.4 Results

After reclassification of thematic layers, all layers are overlaid with their AHP priorities using weighted overlay analysis. The total number of 535 suitable sites is found out after overlay analysis. After finding total suitable sites, conditions for suitable

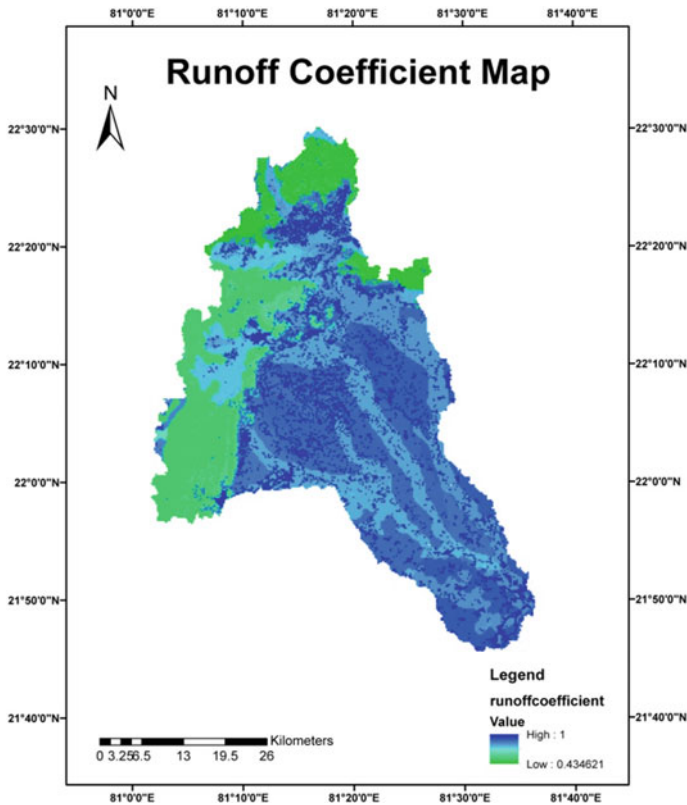


**Fig. 10.7** Runoff coefficient map of study area

sites have been applied. Sites that are not satisfying these conditions have been eliminated and we get 410 sites as the suggested suitable sites; these sites include 209 check dams, 24 percolation ponds, 175 subsurface dykes and 2 farm ponds (Fig. 10.11 and Table 10.2).

## 10.5 Conclusion

All suitable sites are helpful in reducing the drought problem in the Andhiyarkore catchment. In the study, different water storage structures have been suggested, these results can be easily utilized while planning a water management plan. By constructing the suggested suitable sites, the problem of drought can be mitigated. This study is useful in planning water conservation plans in Andhiyarkore watershed. Further, the result of this study demonstrated that the integrated remote sensing and



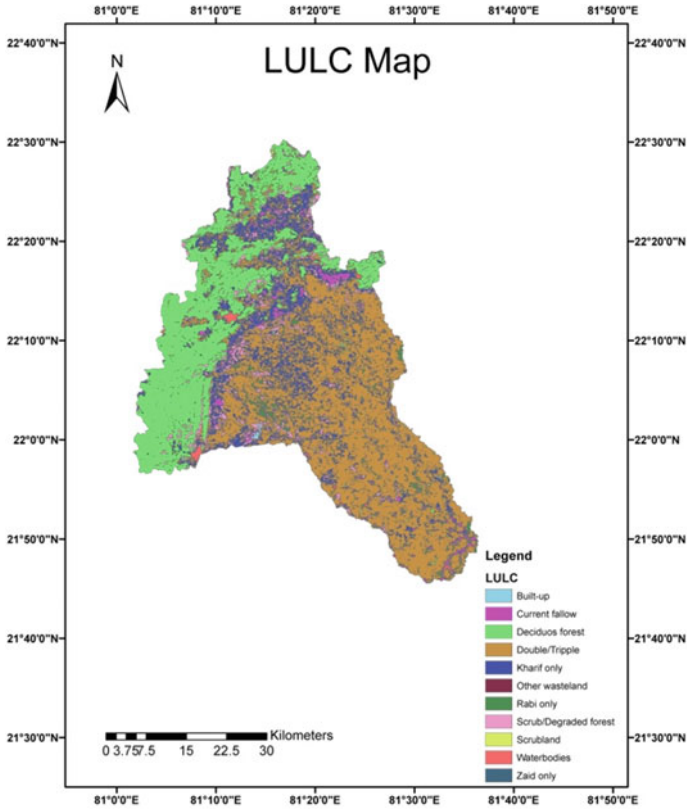


Fig. 10.8 LULC map of study area

GIS-based approach is a powerful tool for assessing site suitability mapping for water storage structure (Singh et al. 2009).

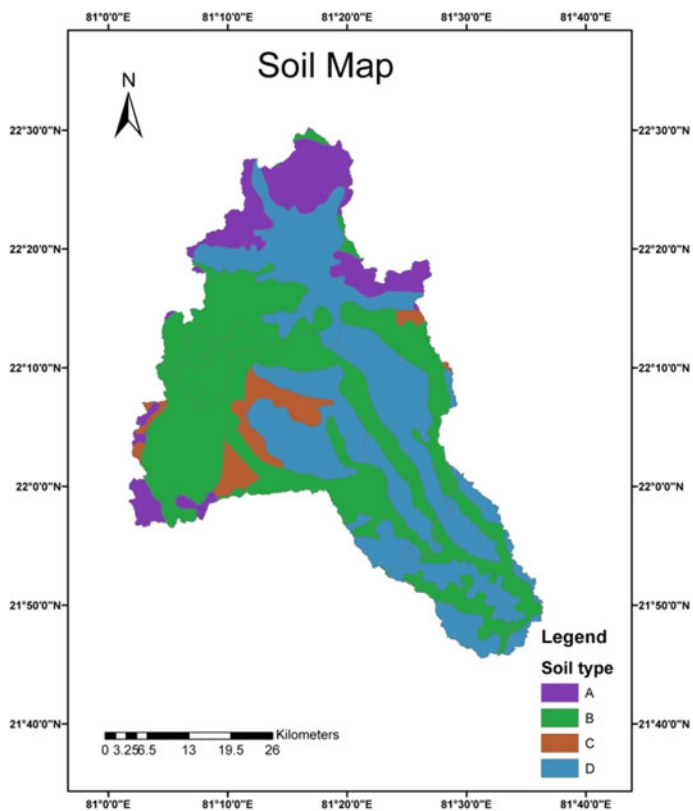


Fig. 10.9 Soil map of study area

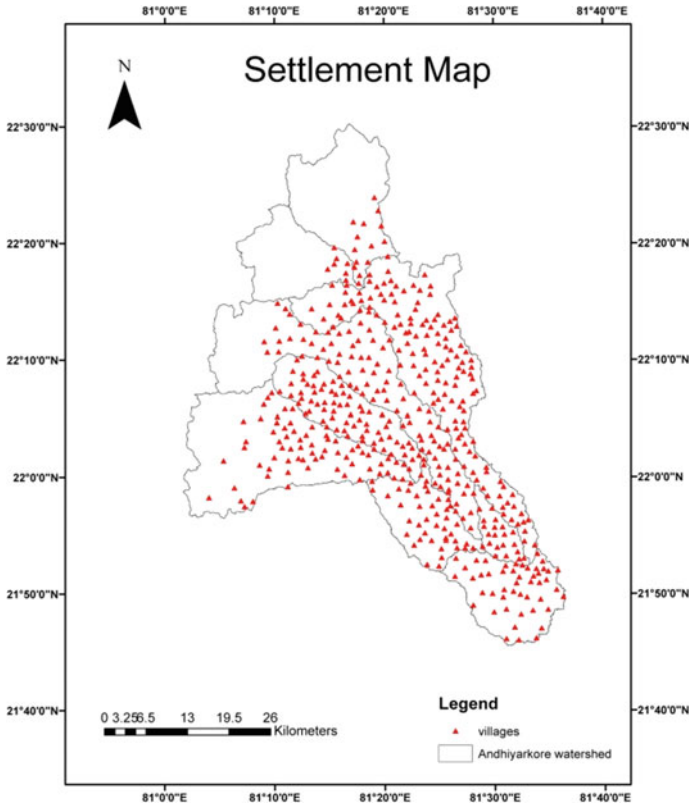


Fig. 10.10 Settlement map of study area

**Table 10.1** Weights and ranking assigned to different parameters and their classes, respectively (Ramakrishnan et al. 2009)

Parameters	Classes	Type of structure	Rating	AHP priority%
Geology	ManiyariFm-Shale, Maniari Formation, Chandrapur Group, Chilpi Group, Bijli rhyolite	Farm pond	1	4
	Chandi limestone, Hirri formation	Check dam	2	
	Laterite	Not applicable	5	
Runoff coefficient	0.434–1	Check dam	2	23
Stream order	1	Farm pond	1	19
	2	Percolation pond	4	
	3	Check dam	2	
	4–6	Subsurface dyke	3	
Slope	0–3	Subsurface dyke	3	27
	3–5	Farm pond	1	
	5–10	Percolation pond	4	
	10–15	Check dam	2	
	>15	Not applicable	5	
Lineament	100 m	Not applicable	5	3
Settlement	200 m	Not applicable	5	2
Soil	HSG A	Not applicable	5	13
	HSG B	Percolation pond	4	
	HSG C	Subsurface dyke	3	
	HSG D	Check dam	2	
LULC	Built-up, Deciduous forest and Agriculture land	Not applicable	5	9
	Scrub land	Percolation pond	4	
	Water bodies	Check dam	2	
	Other wastelands	Farm pond	1	

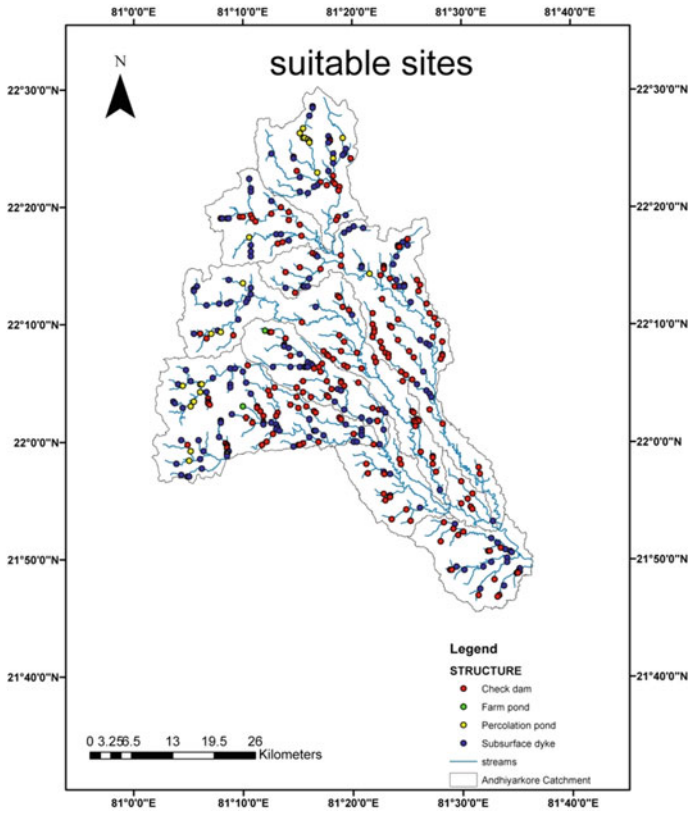


Fig. 10.11 Suitable sites

Table 10.2 Suggested suitable sites

Structure	Number
Check Dam	209
Percolation Pond	24
Subsurface Dyke	175
Farm pond	2

**Acknowledgements** The authors are grateful to acknowledge the support provided by Chhattisgarh Water Resource Department, Raipur, National Remote Sensing Centre (NRSC) Hyderabad and National Bureau of Soil Survey & Land Use Planning (NBSS&LUP) Nagpur.

## References

- Ahmad I, Verma MK (2016) Site suitability mapping for water storage structures using remote sensing & GIS for Sheonath Basin in Chhattisgarh State. *Int J Appl Eng Res* 11(6):4155–4160
- Al-shabeeb AR (2016) The Use of AHP within GIS in selecting potential sites for water harvesting sites in the Azraq Basin—Jordan. *J Geogr Inf Syst* 8(01):73
- Ground water brochure of Durg district, Chhattisgarh 2012–2013
- Ground water brochure of Kawardha district, Chhattisgarh 2012–2013
- Kolekar S, Chauhan S, Raavi H, Gupta D, Chauhan V (2017) Site selection of water conservation measures by using rs and gis: a review. *Adv Comput Sci Technol* 10(5):805–813
- Pramanik MK (2016) Site suitability analysis for agricultural land use of Darjeeling district using AHP and GIS techniques. *Model Earth Syst Environ* 2(2):56
- Prasad HC, Bhalla P, Palria S (2014) Site suitability analysis of water harvesting structures using remote sensing and GIS—A case study of pisanan watershed, Ajmer District, Rajasthan. *Int Arch Photogr, Remote Sens Spat Inf Sci* 40(8):1471
- Ramakrishnan D, Bandyopadhyay A, Kusuma KN (2009) SCS-CN and GIS-based approach for identifying potential water harvesting sites in the Kali Watershed, Mahi River Basin. India. *J Earth Syst Sci* 118(4):355–368
- Saxena A, Jat MK, Kumar S (2017) Optimum site selection of water harvesting structures using geospatial analysis and multi criteria evaluation techniques. *Hydro-2017 International*, L.D. College of Engineering Ahmedabad, India
- Singh JP, Singh D, Litoria PK (2009) Selection of suitable sites for water harvesting structures in Soankhad watershed, Punjab using remote sensing and geographical information system (RS&GIS) approach—a case study. *J Ind Soc Remote Sens* 37(1):21–35

# Chapter 11

## Drought Analysis Using Standardized Precipitation Index and Supplemental Irrigation Planning in Banka, Bihar



Abhishek Kumar Choudhary and Vivekanand Singh

**Abstract** In this paper, drought analysis has been carried out using the Standard Precipitation Index (SPI) method in the Banka district of Bihar. Further, supplemental irrigation planning has also been made for the dry spell period. Available daily and annual rainfall data from the year 2010 to 2015 and from 1972 to 2002, respectively, have been analyzed to identify the dry spell durations and critical dry spell (CDS) durations within the dry spells. Based on the CDS durations, supplemental irrigation requirement has been computed. It was found that the study area has been continuously affected by the drought of mild to moderate intensities. Three hydrological droughts were observed from 1992 to 2002. This study also reveals that all major crops are subjected to water shortage due to erratic rainfall distribution resulting in small dry spells even in monsoon. The study area has recorded a continuous departure of rainfall from the mean value. The crop water requirements of these crops vary from 113.7 to 274.8 mm during a particular month of their growth period. The provision of supplemental irrigation becomes necessary as the rainfall alone is insufficient for better crop production and thus supplemental irrigation requirements of these crops are even higher. The supplemental irrigation requirements for rice, wheat, sugarcane and maize have been computed as 154.5 mm, 298.2 mm, 854.7 mm and 557.4 mm, respectively.

### 11.1 Introduction

Drought is the extreme hydrological phenomenon representing a disaster due to the longer duration of water deficit. According to the India Meteorological Department (IMD), drought is a situation when annual rainfall is less than 75% of the normal rainfall. The National Commission on Agriculture (1976) categorized drought in India based on the concept of utilization as Meteorological Drought, Hydrological

---

A. K. Choudhary (✉)

Department of Civil Engineering, Bhagalpur College of Engineering, Bhagalpur 813210, India

V. Singh

Department of Civil Engineering, N I T Patna, Patna 800005, India

Drought, and Agricultural Drought. A dry spell is an interval between two consecutive wet spells of 7 days with a magnitude of at least 25 mm of rain (Atal and Zende 2015). At least 4 out of 7 days must have rainfall of more than 2.5 mm for a wet spell. The rainfall is consistently below a fixed threshold during the dry spell. This threshold value is obtained by dividing the average annual precipitation by the mean number of rainy days. Dry spells at critical crop growth stages affect the growth and the ultimate production of the crop. When the available soil moisture in the top 50 cm soil layer gets depleted by 50% during the duration between the end of a wet spell and start of another wet spell, it is termed as a critical dry spell.

Panigrahi and Panda (2003) studied the supplemental irrigation to rice crop in the monsoon season and pre-sowing irrigation to mustard crop in winter for a rain-fed farming. They found an increase of 39 and 15% in the crop yield of rice and mustard, respectively, with the optimum quantity of water supplied to the farm. The limited quantity of water application at critical growth stages is widely known as Supplemental Irrigation (SI). Thus, it is an effective response to mitigate the adverse impacts of soil moisture stress on rain-fed crop yields during dry spells. SI is required when rainfall fails to provide sufficient water for plant growth to increase and stabilize crop yields (Oweis 1997). Banka district of Bihar is a drought-affected area. A major part of the district suffers drought during a larger period of the year. The southern parts of the regions, i.e. Chandan, Katoria, Bounsi are highly affected by drought as these parts are on higher elevation and cropping is dependent on rainfall to a great extent. In order to mitigate this situation, it is necessary to provide additional water to the rain-fed crops by planning supplemental irrigation for the dry spell.

## 11.2 Study Area

The study area, Banka district of Bihar, lies between latitudes 24° 30' 00" N–25° 07' 00" N and longitude 86° 30' 00" E to 87° 12' 00" E. It is situated in the south-eastern region of the state of Bihar. Figure 11.1 shows the location map of the study area. Banka district has a major area, about 60% as a hilly region. The northern part of Banka has an alluvial plain, whereas the southern part has hilly tracks. There is an easy ascent in land beginning near or after Banka, Barahat, and therefore, hilly tracks commence in the south of Banka. The district has irregularly scattered and denuded moderate-height hills. The wide variety of soils of Banka are broadly categorized into two distinct groups—the alluvial soil and the hilly soil. The alluvial soils are characterized by fine texture with light to dark grey colour, whereas the hilly soils are characterized by their coarse-grained texture with acidic nature, low nitrogen content, medium to high potash content (CGWB 2007).

The main rivers, i.e. Chandan, Badua and Burigeria in the district don't have sufficient water in lean seasons. All these rivers originate in the southern hilly parts and flow down towards the northern and north-eastern parts and join River Ganga. The onset of monsoon is in June and rains continue till September. The average annual rainfall is 1168 mm. The land is most suitable for



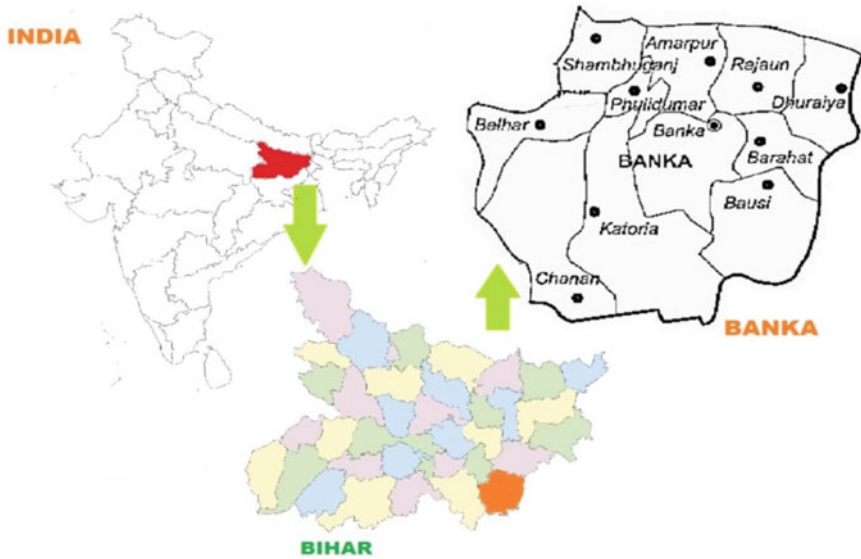


**Fig. 11.1** Location map of the study area

Paddy and hence 70% of the land is cultivated with Paddy crop (CGWB 2007). Agriculture in the southern part of the district is mainly dependent on rainfall. However, as the elevation decreases northwards various other sources of irrigation also have an important role. Among these sources, canals irrigate the maximum area, whereas dug wells are the least used irrigation source. Table 11.1 shows the extent of the area under different sources of irrigation. Out of the 3019.35 Km<sup>2</sup> total area, 460 Km<sup>2</sup>. area is covered with forests, a cultivable area of 1730 Km<sup>2</sup>. with a net sown area of 1460 Sq<sup>2</sup>. Banka, Bounsi and Katoria are the main forest ranges.

**Table 11.1** Sources of irrigation in Banka

Source	Irrigated area (Km <sup>2</sup> )
Dugwell	20
Tubewell/Borewell	270
Tank/ponds	190
Canals	330
Other sources	340
Gross irrigated area	1150

## 11.3 Methodology

### 11.3.1 Study of Drought and Identification of Dry Spell

The drought study requires various meteorological data such as precipitation, temperature, etc. which in turn are used to calculate various drought indices. However, this study is based on the Standard Precipitation Index (SPI) method which requires only precipitation data. This is because of the fact that SPI is a very versatile drought index as it can be calculated on any timescale, and therefore, is applicable for all three types of drought: Meteorological, Agricultural, and Hydrological (McKee et al. 1993).

#### 11.3.1.1 Standardized Precipitation Index (SPI)

The Standard Precipitation Index (SPI) was developed to quantify the precipitation deficit of multiple timescales (McKee 1993). SPI is represented for multiple timescales, i.e. 1-month SPI, 3-month SPI, 6-month SPI, 9-month SPI and 12-month SPI to 24-month SPI. 1- or 2-month SPI is the indicator for meteorological drought, anywhere between 1-month to 6-month SPI for agricultural drought and 6-month up to 24-month for hydrological drought. This is because meteorological and soil moisture conditions (agricultural) respond to precipitation anomalies on relatively short timescales, e.g. 1–6 months, whereas streamflow, groundwater and reservoir storage respond to longer-term precipitation anomalies of the order of 6 months to 24 months or longer. The importance of SPI can be understood by the fact that it is as effective in analyzing wet periods/cycles as it is in analyzing dry periods/cycles. A scale ranging from +2.00 or more to –2.00 or less has been defined by McKee et al. (1993) to classify the various wet and dry periods. Table 11.2 represents the SPI scale values for the classification of drought. The values above 0.00 on the SPI scale represent the wet conditions from normal to extreme while the values below 0.00 represent the dry conditions from normal to extreme.

**Table 11.2** SPI values for drought classification

SPI	Category
+2.00 or more	Extremely wet
+1.50 to +1.99	Very wet
+1.00 to +1.49	Moderately wet
–0.99 to +0.99	Near normal
–1.00 to –1.49	Moderately dry
–1.50 to –1.99	Very dry
–2.00 or less	Extremely dry

Standardized precipitation is the difference from the mean for a specified time period divided by the standard deviation, where the mean and standard deviation are determined from past records (McKee et al. 1993).

Mathematically it can be expressed as

$$\text{SPI} = \frac{X_{ij} - X_{im}}{\sigma} \quad (11.1)$$

where

$X_{ij}$  Precipitation at  $i$ th year and  $j$ th observation.

$X_{im}$  Long term mean of precipitation.

$\sigma$  Standard deviation.

The monthly rainfall data for a period from 1972 to 2002 is analyzed to obtain the SPI values for different timescales 3-, 6-, 9- and 12-months and seasonal values have been worked out. There it is evident that the occurrence of drought is subjected to the amount of rainfall in a particular duration. Figure 11.2 shows the mean monthly rainfall in the study area for the duration of 1972–2002. It can be seen from Fig. 11.2 that most of the rainfall occurs during mid-June to mid-October, which is the monsoon period for the study area. July receives the peak amount of rainfall, while December has the least.

Precipitation is not uniform throughout the entire area of Banka. Quite often, the study area receives a good quantity of rainfall. Despite of this, the sowing of Paddy crop in the southern parts is delayed.

Precipitation being the only data requirement makes the SPI advantageous for regions where data are limited. But this is also the disadvantage of this method because with this data only, precipitation deficit can be quantified and no information regarding important characteristics like soil–water balance, evapotranspiration can be obtained.

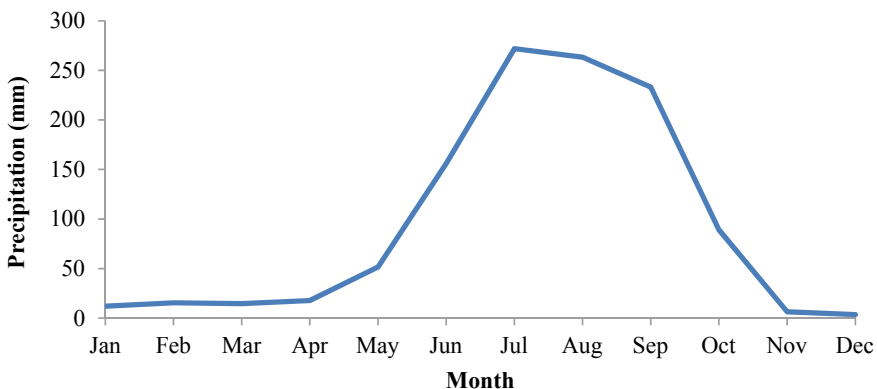


Fig. 11.2 Mean monthly precipitation

### 11.3.1.2 Dry Spell and Its Identification

A dry spell is a term related to agricultural drought. It is a period of a few days or weeks. Dry spells at the time of critical crop growth stages affect the growth and the ultimate production of the crop. This threshold value is obtained by dividing the average annual rainfall by the mean number of rainy days. In this study, 2.5 mm rainfall has been taken as the threshold value for identifying the wet spells and thereby the dry spells. The rainfall is consistently below a fixed threshold during the dry spell. This threshold value is obtained by dividing the average annual precipitation by the mean number of rainy days. Taking 2.5 mm as the threshold value and from the definition of the wet spell, “a period of 7 days with at least 25 mm rainfall”, the wet spells can be marked and dry spells can be easily identified. The period between two consecutive wet spells is known as a dry spell. Dry spells at critical crop growth stages affect the growth and the ultimate production of the crop. Critical dry spells can be identified as the lengths of the three longest dry spells in a year among the dry spells greater than seven days (Peiris et al. 2008).

Analysis of dry spell is one of the most important parameters for the planning of supplemental irrigation during prolonged dry days in monsoon.

## 11.3.2 Planning of Supplemental Irrigation for the Dry Spell

### 11.3.2.1 Calculation of Crop Water Requirements

In May 1990, Food and Agriculture Organization (FAO) in collaboration with the World Meteorological Organization (WMO) and the International Commission for Irrigation and Drainage organized a consultation of researchers and experts, to review the FAO methodologies on crop water requirements and to advice on the revision and update of procedures. The FAO Penman-Montieth method is the sole standard method recommended with a strong likelihood of correctly predicting  $ET_o$  in a wide range of locations and climates.

The Penman–Monteith method is used for the computation of the potential evapotranspiration,  $ET_o$  (FAO, 56)

$$ET_o = \frac{0.408\Delta(R_n - G) + \gamma \frac{900}{T+273} u_2 (e_s - e_a)}{\Delta + \gamma(1 + 0.34u_2)} \quad (11.2)$$

where  $ET_o$  = reference evapotranspiration [mm /day];  $R_n$  = net radiation at the crop surface [ $MJ m^{-2} /day$ ];  $G$  = soil heat flux density [ $MJ m^{-2} /day$ ];  $T$  = mean daily air temperature at 2 m height [ $^{\circ}C$ ];  $u_2$  = wind speed at 2 m height [m /s];  $e_s$  = saturation vapour pressure [kPa];  $e_a$  = actual vapour pressure [kPa];  $\Delta$  = slope vapour pressure curve [ $kPa /^{\circ}C$ ];  $\gamma$  = psychrometric constant [ $kPa /^{\circ}C$ ].

$$\text{Crop Evapotranspiration, } ET_c = K_c \times ET_o \quad (11.3)$$

where  $K_c$  = Crop Coefficient.

The selection of crop coefficient,  $K_c$ , is entirely based on crop, crop development stage and prevailing climatic conditions. The FAO Paper No. 56 Table 12 tabulates crop coefficient,  $K_c$ , values for different crops under a different set of climatic conditions.

The initial stage crop coefficient  $K_{c,ini}$  values are a function of the average interval between two wetting events, evapotranspiration and wetting event importance. Therefore,  $K_{c,ini}$  must be taken accordingly considering light or heavy wetting event. The mid-stage crop coefficient  $K_{c,mid}$  values depend upon climate and crop height. For different climate sets and crop heights, the wind speed is different. Therefore,  $K_{c,mid}$  values are adjusted to suit the soil of the area. The end stage crop coefficient  $K_{c,end}$  values depend upon water management practices. The frequent the irrigation, the higher is the value of  $K_{c,end}$  and vice versa.

### 11.3.2.2 Effective Rainfall

Dependable Rain (FAO formula)

$$P_{eff} = 0.6P - \frac{10}{3}; \quad \text{for } P_{month} \leq \frac{70}{3} \text{ mm} \quad (11.4)$$

$$P_{eff} = 0.8P - \frac{24}{3}; \quad \text{for } P_{month} > \frac{70}{3} \text{ mm} \quad (11.5)$$

### 11.3.2.3 Dry Crop

The standard plantation date and base period of a particular crop varies in different regions. FAO Paper No. 56 Table 11 gives the length of various crop stages. But in order to get a reasonable value suitable to a particular region, it is necessary to enquire the farmers. The crop goes through four stages during its entire growth period. These are,

**Initial Stage:** It is the stage when the seed germinates during its early growth stage covering 10% of the ground.

**Development Stage:** This stage starts when the initial stage ends and continues till the attainment of effective ground cover of about 70–80%.

**Mid-Season:** This stage starts from the attainment of effective full ground cover and continues till the time of the start of maturity indicated by discolouring or falling of leaves.

**Late Stage:** This stage starts from the end of mid-season until full maturity or harvest.

The rooting depth, critical depletion and yield response factors during the various stages are other necessary data that can be directly obtained from the FAO Paper No. 56 and then need to be adjusted to suit the area.

#### 11.3.2.4 Soil

Soil is an important factor in calculating crop water requirements. It includes various parameters like the type of soil, field capacity (FC), wilting point (WP), rate of infiltration, total available water (TAW).

Banka has clay loam texture soil. For clay loam soil, the FC ranges from 24 to 32%, WP has a range of 11–16% and available water per meter depth is about 0.17–0.29 m.

#### 11.3.2.5 Supplemental Irrigation Requirements

The crop failure is normally due to water stress in the soil during critical dry spells. This stress can be removed or mitigated by proper planning of supplemental irrigation. Careful consideration of the crop variety, its critical stages, dry spell analysis, etc. is necessary for optimum planning of supplemental irrigation. The benefit of supplemental irrigation can be achieved only when there is a high probability of a dry spell. For this purpose, it is, therefore, necessary to mark the critical dry spell first. Banka, a major part doesn't get optimum benefits of rainfall because of their high elevation resulting in a heavy runoff.

The supplemental irrigation requirement is calculated as the difference between the crop evaporation during the critical dry spell and the effective rain during the same critical dry spell.

$$\text{SIR} = \text{ET}_c - P_{\text{effective, CDS}} \quad (11.6)$$

## 11.4 Results and Discussion

### 11.4.1 Drought Study

A drought event starts when the SPI value reaches below zero and ends when SPI becomes positive again. The positive sum of the SPI for all the months within a drought event reports drought magnitude. The 3-month, 6-month, 9-month and 12-month timescales represent the SPI values for March, June, September and December, respectively. The SPI values have also been plotted in Figs. 11.3, 11.4, 11.5 and 11.6 for timescales 3-month, 6-month, 9-month and 12-month, respectively. From

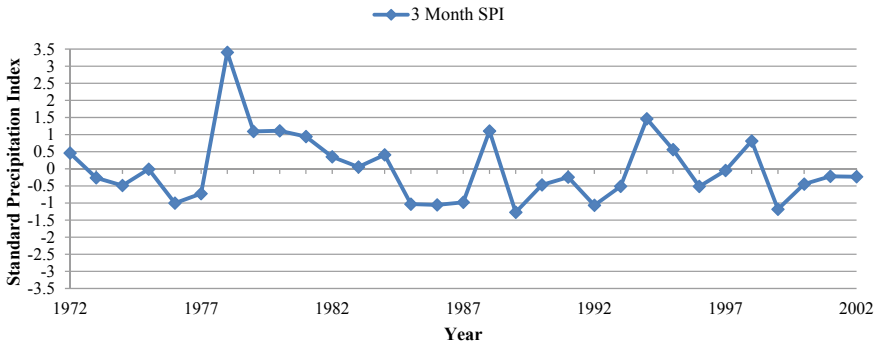


Fig. 11.3 Variation of SPI values on 3-month timescale

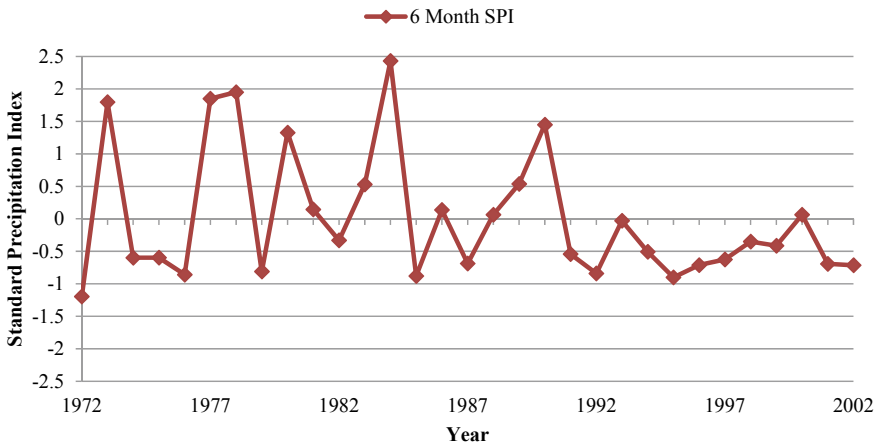


Fig. 11.4 Variation of SPI values on 6-month timescale

Fig. 11.3, it can be seen that from 1972 to 2002, there were 18 years when the SPI values were below 0.00 indicating the occurrence of meteorological drought. The SPI value reached its minimum in 1989. Figure 11.4 shows that from 1972 to 2002, there were 19 years when the SPI values were below 0.00 indicating the occurrence of agricultural drought. The SPI value reached its minimum in 1972. Figure 11.5 shows that from 1972 to 2002, there were 18 years when the SPI values were below 0.00 indicating the occurrence of a drought somewhere between agricultural and hydrological drought. The SPI value reached its minimum in 2001. Figure 11.6 shows that from 1972 to 2002, there were 21 years when the SPI values were below 0.00 indicating the occurrence of a drought somewhere near hydrological drought. The SPI value reached its minimum in 1992.

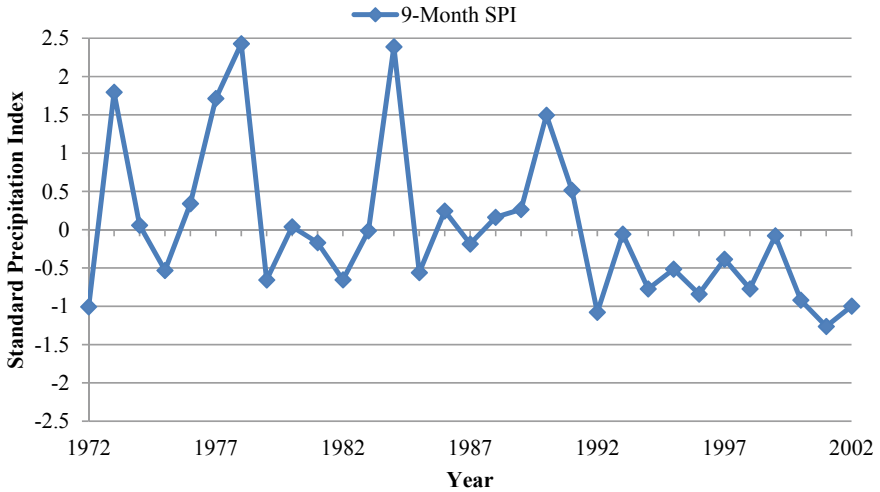


Fig. 11.5 Variation of SPI values on 9-month timescale

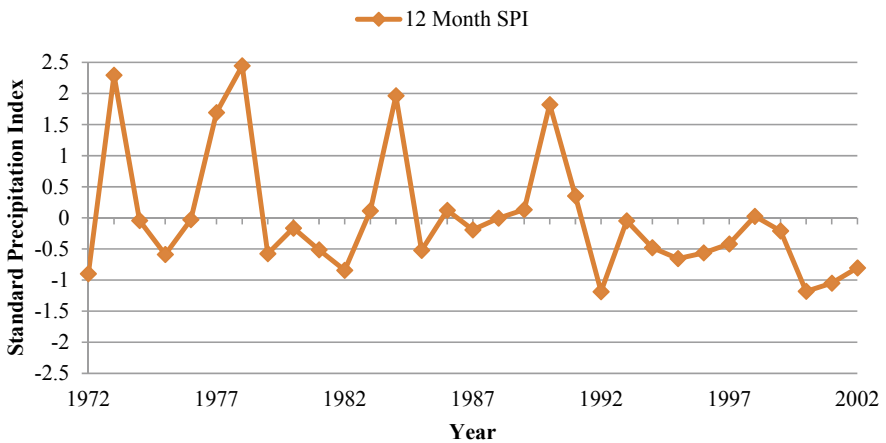


Fig. 11.6 Variation of SPI values on 12-month timescale

From SPI plots of 3-month, 6-month, 9-month and 12-month, it can be seen that mild drought is very common in the study area. The study area frequently faces agricultural drought of moderate intensity. 7 out of 31 years faced agricultural drought of moderate intensity. 3 out of 31 years faced hydrological drought of moderate intensity.



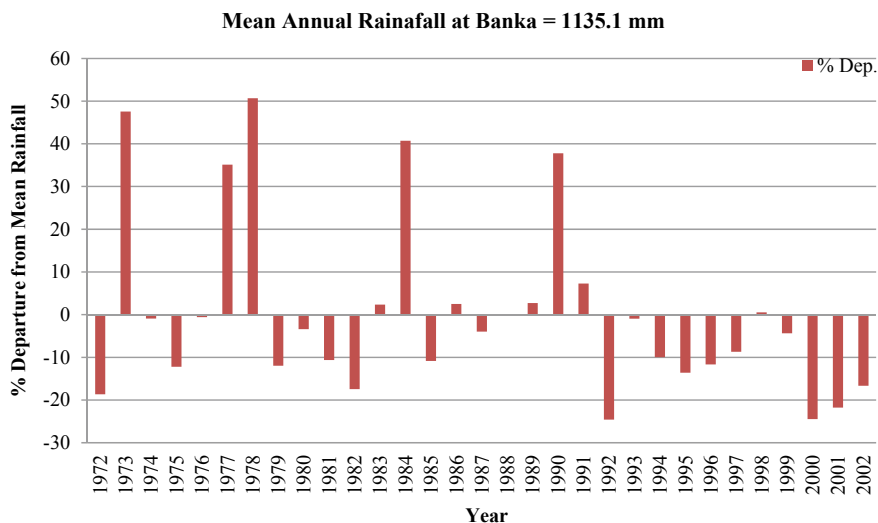


Fig. 11.7 Percentage annual rainfall departure from mean

### 11.4.2 Rainfall Departure

The rainfall departure shows the behaviour of rainfall and its relative impact on the agricultural drought condition of the study area. The rainfall records at Banka from 1972–2002 were analyzed and it was observed that, out of these 31 years, 21 years have a record of having precipitation less than the mean. From the year 1992, there is a continuous departure from the mean except 1998. The departure is varying from a minimum of 1% to a maximum of 25%. Figure 11.7 shows the percentage departure of annual rainfall from the mean annual rainfall for the period 1972–2002. Figure 11.7 shows that the highest departure in rainfall occurred in 1992.

If Figs. 11.3, 11.4, 11.6 and 11.7 is observed carefully, it is found that the departure in rainfall affects the occurrence of drought. The 9-month and 12-month SPI directly vary with the rainfall.

### 11.4.3 Critical Dry Spells

From the definition of a rainy day as given by the IMD, a threshold value of 2.5 mm has been considered to find out the dry spell durations. Among these, the critical dry spells are identified as the dry spells with the longest duration. The dry spell starting in the last decade of September which continues to nearly the mid of December is the longest critical dry spell of 67 days.

### 11.4.4 Computation of Supplemental Irrigation Requirement

The Supplemental Irrigation Requirement (SIR) for the four major crops paddy, wheat, sugarcane and maize are 154.5 mm, 298.2 mm, 854.7 mm, and 557.4 mm, respectively. The highest value of the supplemental irrigation requirement is for the sugarcane crop, whereas the lowest value is for the paddy (Table 11.3).

This requirement can be achieved by utilizing the available resources in an optimum way along with practicing rainwater harvesting. Further, it is necessary to train and facilitate the farmers of the southern part of Banka so that they can harvest the rainwater and utilize it to get optimum benefits. The north-east region of Banka district where sugarcane is grown has availability of water but lack of techniques makes it a costly affair. There are some small dams within the study area but they too

**Table 11.3** Supplemental irrigation requirement for various crops

CDS month	CDS period	No. of days in CDS	K <sub>c</sub>	ET <sub>c</sub> in CDS (mm)	Eff. Rain during CDS (mm)	SIR (mm)	Total (mm)
<i>Crop name—Rice</i>							
Jun	21/06	1	1.05	7.05	4.44	2.61	154.5
Sep	02/09–19/09	17	1.14	104.21	91.23	12.98	
Sep/Oct	25/09–31/10	36	1.10	191.16	52.25	138.91	
<i>Crop name—Wheat</i>							
Nov	15/11–30/11	15	0.30	13.80	0.00	13.80	298.2
Dec	01/12–31/12	31	0.68	77.19	0.00	77.19	
Jan/Feb	04/01–28/02	56	1.14	207.20	0.00	207.20	
<i>Crop name—Sugarcane</i>							
Feb/Mar	10/02–01/03	20	0.40	37.20	0.60	36.60	854.7
Mar	04/03–15/03	11	0.47	27.39	0.00	27.39	
Mar	17/03–30/03	14	0.64	52.36	0.00	52.36	
Apr	14/04–24/04	11	0.96	90.64	0.10	89.64	
Apr/May	27/04–10/05	14	1.19	126.70	5.50	121.20	
May/June	18/05–12/06	26	1.19	243.88	60.82	183.06	
Sept/Oct/ Nov/Dec	25/09–02/12	67	1.19	415.40	71.00	344.40	
<i>Crop name—Maize</i>							
Feb/Mar	10/02–01/03	20	0.70	55.60	1.43	54.17	557.4
Mar	04/03–15/03	11	0.86	50.05	0.00	50.05	
Mar	17/03–30/03	14	1.04	85.54	0.00	85.54	
Apr	14/04–24/04	11	1.21	98.12	0.10	98.02	
Apr/May	27/04–10/05	14	1.21	128.94	5.50	123.44	
May/June	18/05–12/06	26	0.98	241.54	95.35	146.19	

have water only during monsoon and in non-monsoon periods they supplement crop growth to a limited extent only. Also, being a remote area, Banka district remains out of focus and gets very little attention from the administration as well as the government.

## 11.5 Conclusion

Drought analysis has been carried out in the Banka district of Bihar using Standard Precipitation Index (SPI) method. The monthly rainfall data have been used for this purpose. Precipitation being the only parameter required and data constraints makes the SPI method the first choice over other drought indices and best-suited method for monitoring drought in the study area. The flexibility to calculate the SPI values on different timescales such as 1-, 2-, 3-, 6-, 9- and 12-month is the beauty of this method. The crop water requirements of the four major crops: rice, wheat, sugarcane and maize having percentage cropping area of 70%, 30%, 15% and 10%, respectively, in their respective cropping periods are estimated, which vary from 113.7 to 274.8 mm during a particular month of their growth period. From this study, it can be concluded that the study area is frequently subjected to a drought of mild to moderate intensity. Dry Spell duration ranges from a minimum of 8 days to a maximum of 67 days. There is a continuous departure of rainfall from the mean ranging from 3 to 26%. A maximum departure of 25% was observed since 1992. Rainfall deficit has affected the crop yield, and therefore, Supplemental Irrigation is a necessity to maintain the crop yield. Supplemental Irrigation requirement for rice, wheat, sugarcane and maize are 154.5 mm, 298.2 mm, 854.7 mm and 557.4 mm, respectively.

## References

- Afzal J, Noble DH, Weatherhead EK (1992) Optimization model for alternative use of different quality of irrigation waters. *J Irrig Drain Eng ASCE* 118(2). 1992:218–228
- Atal KR, Zende AM (2015) Wet and dry spell characteristics of semi-arid region, Western Maharashtra, India. In: 36th IAHR world congress, The Hague, The Netherlands, pp 1–6
- Central Ground Water Board (2007) Ground water information booklet, Banka District, Bihar State, July, 2007
- FAO Irrigation and Drainage Paper No. 56, Crop Evapotranspiration
- McKee TB, Doesken NJ, Kleist J (1993) The relationship of drought frequency and duration of time scales. In: VIIIth conference on applied climatology. American Meteorological Society, Anaheim CA, pp 179–186
- Murthy CS, Sessa Sai MVR Agricultural drought monitoring and assessment. Remote Sens Appl NRSC, ISRO, Chapter 13, 303–329
- Oweis T (1997) Supplemental irrigation: a highly efficient water-use practice. International Center for Agricultural Research in the Dry Areas, Aleppo, Syria

- Panigrahi B, Panda SN (2003) Optimal sizing of on-farm reservoirs for supplemental irrigation. *J Irrig Drain Eng* 129(2):117–128. ASCE
- Peiris T, Kularathne J (2008) Assessment of climate variability for coconut and other crops: a statistical approach. *J CORD* 24(1):35–53

# Chapter 12

## Multisite Calibration of the Ghataprabha Sub-Basin Using Soil and Water Assessment Tool



A. N. B. Gowda, Nagraj S. Patil, and Nataraja M

**Abstract** Understanding hydrological forms at the catchment scale using hydrological model parameters is fundamental for improving water resources. Hydrological models are used in catchments of spatially heterogeneous to calibrate by lump parameters. A multisite calibration method is adopted for the Ghataprabha sub-basin which is present in the Krishna basin. Multisite calibration methods are used to know better pursuance of the model. Multisite calibration is the process of calibrating one or more Discharge Gauge Stations within the catchment area. A Multisite calibration is carried out for the four discharge gauges of Ghataprabha sub-basin in the Krishna basin. The objective of the study is to predict the Surface Runoff and to know the effect of Multisite calibration in the Catchment. The Soil and Water Assessment Tool (SWAT) is used at four different discharge gauges, which improves the model performance and improve the accuracy of runoff prediction. Comparatively, the model is calibrated to a single gauge station at the outlet of the watershed, the flow predicted at the other monitoring points was inaccurate. So, it states the importance of multisite calibration for the development of the reliable watershed model in the Ghataprabha sub-basin. The results show the difference in hydrological behaviour at the upstream and downstream of the watershed for the different parameter values. The model is calibrated for the monthly time series. All the multisite calibration results were above the minimum value of 0.69 and 0.6 for Coefficient of Determination ( $R^2$ ) and Nash Sutcliffe Efficiency (NSE), respectively. Our outcomes state that the multisite calibration parameter values are more sensible than those acquired from single-site calibration. These results are more valuable because of the huge significance in the geographical features of the catchment, human activities and climate changes in the watershed. The multisite calibration method makes the division of large catchments into smaller catchments and the applying of parameters for the multisite calibration to the whole watershed gives better results. Hence, the multisite calibration for the large basin is reliable to get good results.

---

A. N. B. Gowda (✉)  
Clear water dynamics Pvt. Ltd, Bengaluru, Karnataka, India

A. N. B. Gowda · N. S. Patil · N. M  
Department of Water and Land Management, Centre for PG studies, VTU, Belagavi, Karnataka, India

## 12.1 Introduction

The Watershed model plays an important role to analyze the effect of land use and climate change on water resources. The characteristics of the land surface area are recognized by the understanding of hydrological, biological and other processes of the watersheds by the importance of spatial variability (Arnold et al. 1998, 2012). Spatial variability is important in hydrological modelling (Bai et al. 2017; Kangsabanik and Murmu 2017). The spatial information on the natural resources and the physical parameters are valuable and real time, these data are provided by Remote Sensing Satellites (Sohoulande Djebou 2018). For watershed modelling, GIS is an effective tool. The estimation of runoff uses remotely sensed data (Bharath et al. 2020a). This helps in the planning of water resources projects and is suitable for soil and water conservation measures. Hydrological modelling of the watershed is carried by the extraction of watershed parameters using RS and GIS (Kannan et al. 2007). The Soil and Water Assessment Tool is a widely used hydrological model. The calibration process is an important process in developing the watershed model. The different methods of calibration are Single-site Calibration (SSC), Sequential calibration (SC) and Multisite calibration (MSC). The multisite calibration determines the most accurate parameter for small watersheds. The model application has been demonstrated for the Ghataprabha sub-basin in the Krishna watershed. The soil and assessment tool model (SWAT) is applied for the study area. The model is run for land use/land cover, soil data, slope data and all the meteorological data. In this study area, the multisite calibration is carried out to estimate the surface runoff and to know the characteristics of the catchment. The Ghataprabha catchment consists of four discharge gauges, namely: Goturu, Daddi, Gokak and Bagalkot. A multisite calibration is carried out to all four discharge gauges. The aim of this study is to predict the surface runoff and to know the effect of multisite calibration in the watershed, which improves the model performance and increases the accuracy of runoff prediction (Kinthada 2014; Migliaccio and Chaubey 2007). Comparatively, the model is calibrated to a single gauge station at the outlet of the watershed, the flow predicted at the other monitoring points was inaccurate (Malagò et al. 2015; Niraula et al. 2012). So, it states the importance of multisite calibration for the development of the reliable watershed model in the Ghataprabha sub-basin. Along the stretch of Ghataprabha river, the reservoir is located, the two monitoring stations were present upstream of the reservoir and the other two are present downstream of the reservoir (Bharath et al. 2020b). While calibrating the upstream stations the values of other monitoring stations are increased comparatively at the downstream, due to changes in the hydrological conditions of upstream monitoring stations. These outcomes are more reliable due to the significant difference in the topographical features of the catchment, human activities and climate changes in the watershed. The multisite calibration method makes the division of large catchments into smaller catchments and the application of calibrated parameters of the multisite calibration to the whole watershed gives better results. Hence, the multisite calibration for the large

basin is reliable to get good results. The model performance is checked by Coefficient of determination ( $R^2$ ), Nash Sutcliffe efficiency (NSE), Percent Bias (PBIAS) and RMSE-Observations Standard Deviation Ratio (RSR). Satisfactory results are obtained for the model and the model performance is achieved by within the accurate results.

## 12.2 Study Area

Krishna river is India's second-largest river, which is the western ghats of Mahadev range near Mahabaleshwar, located at the height of 1337 m above the MSL. The stretch of the Krishna river is 1400 km and meets the Bay of Bengal in Andhra Pradesh. Tributaries of this river are Tungabhadra, Musi, Ghataprabha, Bhima, Malaprabha, Muneru and Palleru. Ghataprabha is the southern tributaries of the upper Krishna river. Catchment lies between latitudes of  $15^{\circ} 45' N$  to  $16^{\circ} 25' N$  and longitude of  $74^{\circ} 00'$  to  $75^{\circ} 55'$  (Fig. 12.1). Ghataprabha originates at an altitude of 884 m in the region of western ghats, Maharashtra, and flows 60 km east through districts of Sindhudurg and Kolhapur in Maharashtra, and enters Karnataka. In Karnataka, the Ghataprabha river flows 216 km through Belgaum and past Bagalkot, after 283 km, the river joins a right bank of the Krishna river at Kudalasangama at an elevation of 500 m at 16 km from Almatti.

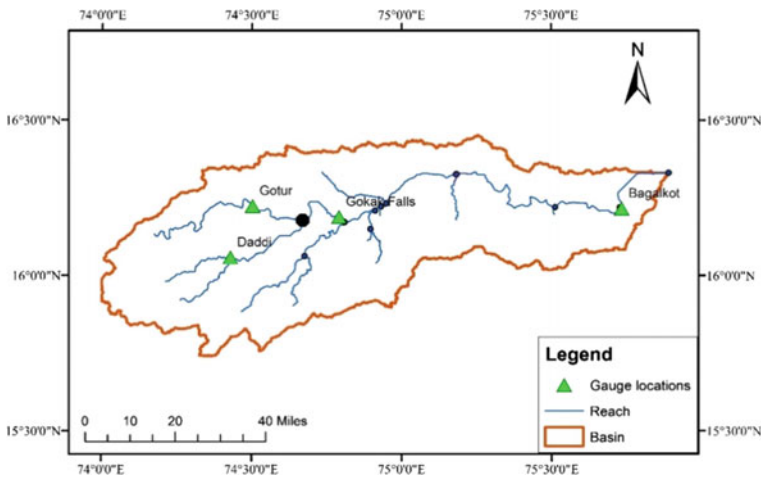


Fig. 12.1 Map of the Ghataprabha Sub-basin with Discharge Gauge Stations

## 12.3 Methodology

The SWAT model is a hydrological model applied to the river catchment to quantify the impact of land practice management on water resources, agricultural, sediment and chemical yield in a large complex catchment area with varying in the land use, soil and other management conditions over a long period of time. The main components of SWAT model include surface runoff, weather, return flow, evaporation, transmission losses, percolation, crop growth, reservoir storage, irrigation, reach routing, groundwater flow, pesticide and nutrient loading and water transfer. The input data required for the SWAT model are Digital Elevation Model (DEM), Land Use/Land Cover and Soil map are collected as suggested by (Kangsabanik and Murmu 2017; Sreedevi et al. 2013). The SWAT model involves the process of watershed delineation, land use/soil/slope reclassification, HRUs creation, weather data incorporation writing input files and model simulation. SWAT model requires some of the specific information of weather, topography, vegetation, soil properties and land management practices that occur in the watershed. Other additional database input files are soil database and weather generator database. These databases are the collection of weather and soil database parameters from the soil and weather stations. SWAT begins with the Watershed delineation, watershed delineated to the sub-basins, then sub-basin is divided to areas of homogeneous similarity between the land use, soil type and this is known as Hydrological Response Units (HRUs).

### 12.3.1 Description of SWAT Steps

#### 12.3.1.1 Watershed Delineation

Watershed Delineation is based on the Digital Elevation Models (DEMs). In Watershed delineation, generates the streamflow network and catchment is divided into sub-basin for the generation of outlets. The Digital Elevation Model (DEM) map of the Ghataprabha sub-basin is shown below (Fig. 12.2).

#### 12.3.1.2 HRU Analysis

The area of the Sub-basin is divided into Hydrological Response Units. HRU's are created with raster data. These HRUs process the sub-basin details of Land use/Land cover, Soil type and Land Slope. The geo-processed raster data of Land-use/Land-cover map, Soil map and land slopes are considered for the HRU analysis. The map details are created with a lookup table and these are reclassified and overlay analysis is carried out. The maps of land use/land cover (Fig. 12.3), soil type (Fig. 12.4) and land slope (Fig. 12.5) are shown below.



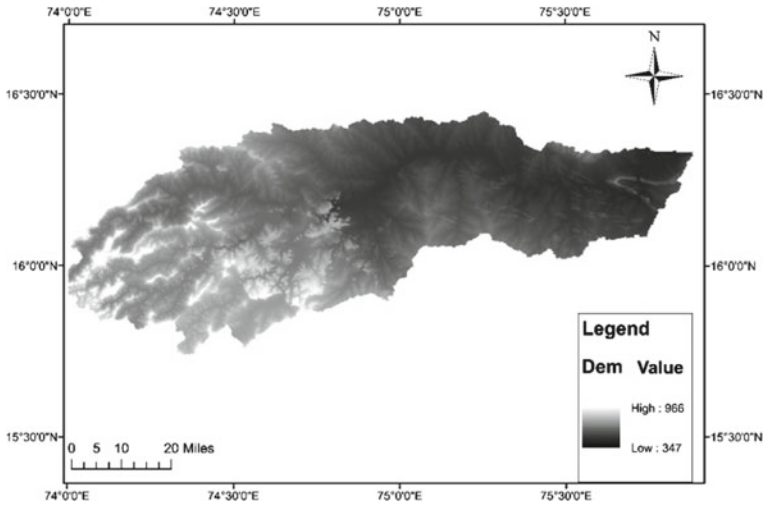


Fig. 12.2 DEM of Ghataprabha Sub-Basin

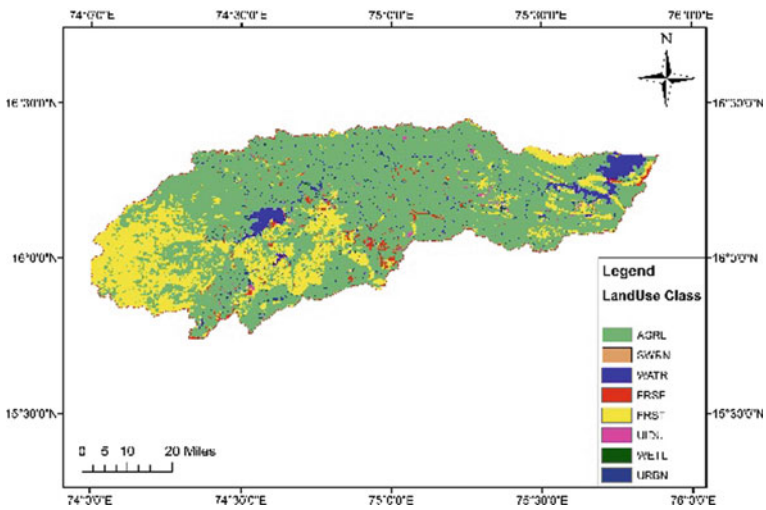


Fig. 12.3 Map of land use/land cover

The percentage of land use/land cover and description of the land-use classes is mentioned below (Table 12.1), The description of the soil classes is mentioned below (Table 12.2)

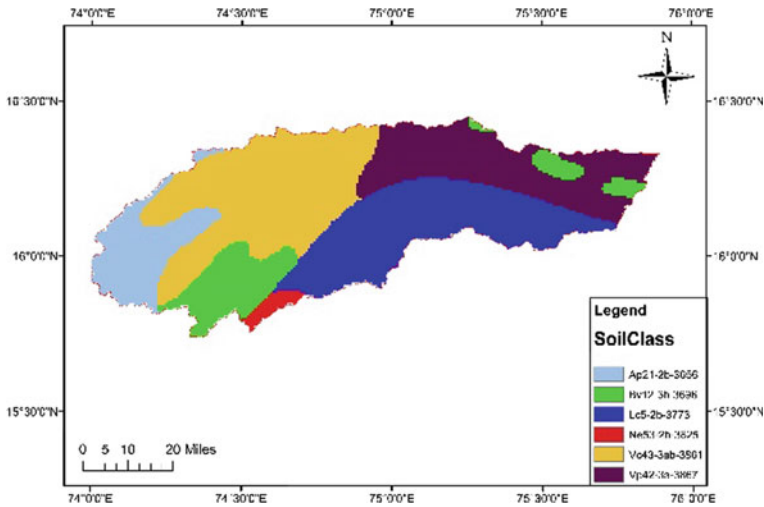


Fig. 12.4 Map of soil class

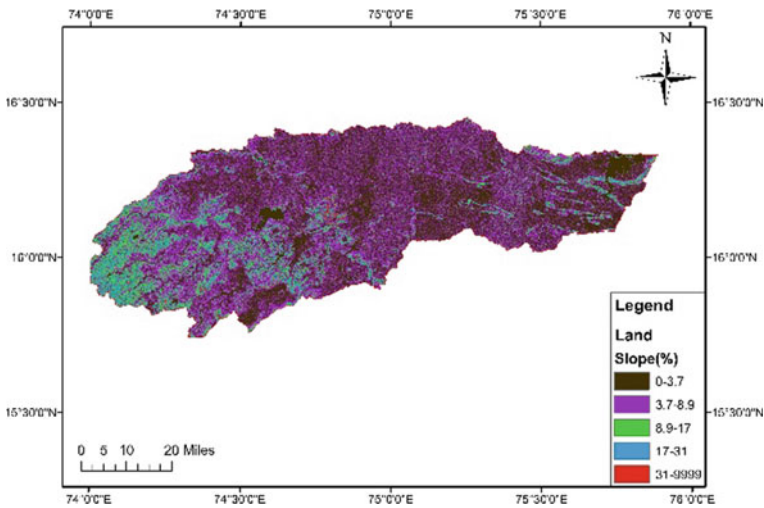


Fig. 12.5 Land slope

### 12.3.1.3 Weather Stations Data

The SWAT model requires the data of precipitation, maximum and minimum Temperature, relative humidity, wind speed and solar Radiation. These data are collected in the daily time series, the values for all these parameters are the records of observed data. From all the SWAT data input, the model is executed for the time series, i.e. daily, monthly and yearly for required years. From the output flow, the SWAT model

**Table 12.1** Description of land-use classes

Sl. no	LULC Code	% of Area	Land use description
1	AGRL	72.05	Agricultural Land-Generic
2	SWRN	0.096	South Western Range
3	WATR	3.36	Water bodies
4	FRSE	1.485	Evergreen Forest
5	FRST	21.559	Forest area
6	UIDU	0.336	Urban Industrial area
7	WETL	0.012	Wetlands
8	URBN	1.102	Urban area

**Table 12.2** Description of soil classes

Sl. no	Soil class	Soil name
1	Ap21-2b-3656	Sandy Clay Loam
2	Bv12-3b-3696	Clay Loam
3	Lc5-2b-3773	Loam
4	Ne53-2b-3825	Sandy Clay Loam
5	Vc43-3ab-3861	Clay
6	Vp42-3a-3867	Clay

gives us to estimate the surface runoff, sediment transport, nutrients and pesticides transport, reservoir operation and water management studies. From the flow out of the SWAT model calibration and validation of the model is carried out.

## 12.4 Calibration Process

Multisite calibration is the process of calibrating one or more discharge stations within the catchment area. The Multisite calibration is carried out in the Ghataprabha sub-basin, because of the hydrological parameters change between the upstream and downstream of the reservoir present in the catchment area. In the catchment, there are four discharge gauges available, they are: Goturu, Daddi, Gokak and Bagalkot. The reservoir is present in the catchment, i.e. HIDIKAL Dam, the two discharge gauges are present in the upstream of the reservoir and the other two are in the downstream of the reservoir. A separate calibration is carried out to all the four gauges. The calibration and validation are carried out to the entire catchment area. The description of the four discharge gauges is tabulated below (Table 12.3).

**Table 12.3** Description of discharge gauge stations

Station no	Station	Sub-basin no	Area (ha)
1	Goturu	16	88,121.8044
2	Daddi	19	49.7963
3	Gokak	12	17,379.8262
4	Bagalkot	7	53,838.9838

### 12.4.1 Station 1: GOTURU

The value of  $R^2 = 0.57$ ,  $NSE = 0.44$ ,  $PBIAS = +73.81$  and  $RSR = 0.74$  before the calibration. In this basin, the parameters fitted for calibration and these sensitive parameters values were changed for the calibration process. The sensitive parameters and their calibrated values were noted below (Table 12.4).

In this calibration, the most sensitive parameters are  $CH_{N_2}$ ,  $REVAP_{MN}$ ,  $SOL_K$ . The  $CH_{N_2}$  is Manning's coefficient for the main channels. The threshold depth in the shallow aquifer for the re-evaporation ( $REVAP_{MN}$ ) is 900 mm, which the land is capable of releasing less water for the evaporation in the Shallow Aquifer. The Saturated Hydraulic Conductivity of this catchment is very high due to the sandy\_clay\_loam soil, so the soil hydraulic conductivity is 1000 mm/hr.

The comparison graph of observed and simulated flow and  $R^2$  value of Goturu station is given below for the before and after calibration process. The calibration is carried for 11 years (1983–1993). And validated for 8 years (1998–2005) (Figs. 12.6, 12.7, 12.8, 12.9, 12.10 and 12.11).

**Table 12.4** Parameters used for calibration of Goturu Station

Parameters	Range	Initial value	Final value
$CN_2$	35–98	87	90
$CH_{N_2}$	0.01–0.3	0.014	0.3
$CH_{K_2}$	0–500	0	50
$ALPHA_{BF}$	0–1	0.048	0.2
$GW_{DELAY}$	0–500	31	50
$RCHRG_{DP}$	0–1	0.05	0.2
$GWQMIN$	0–5000	1000	1500
$GW_{REVAP}$	0.02–0.2	0.02	0.2
$REVAP_{MN}$	0–1000	750	900
$SOL_{AWC}$	0–1	0.104	0.2
$SOL_K$	0–2000	8.36	1000
$SOL_Z$	0–3500	300	500

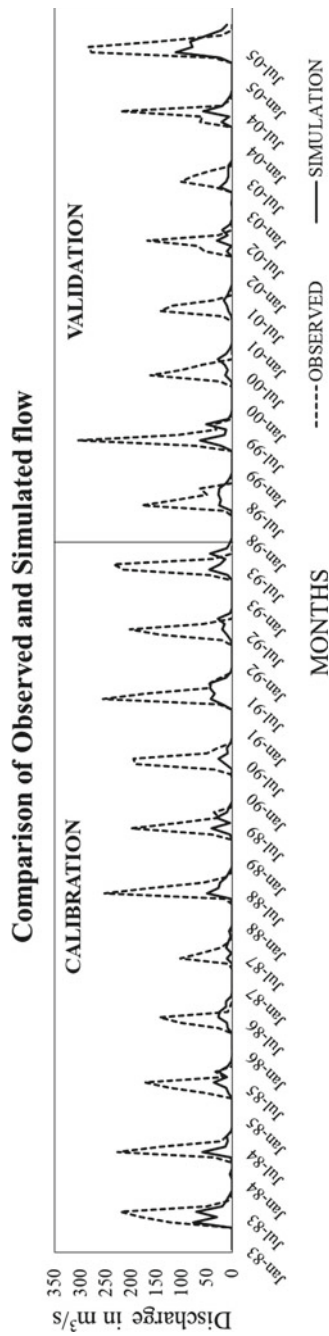
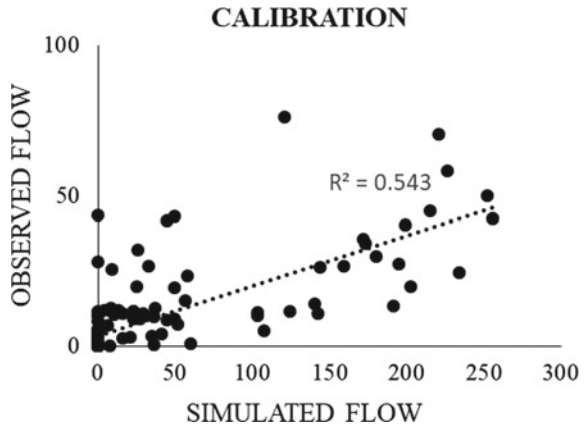
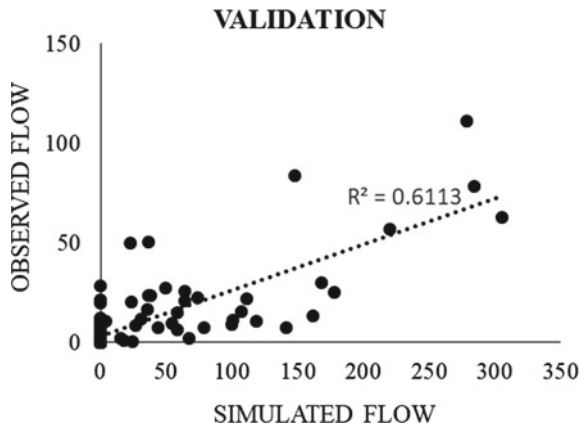


Fig. 12.6 Comparison of observed and simulated values before adjustment of parameters for Goturu Station

**Fig. 12.7** Scattered plot of coefficient of determination ( $R^2$ ) for calibration of Goturu Station before parameters adjustment



**Fig. 12.8** Scattered plot of coefficient of determination ( $R^2$ ) for validation of Goturu Station before parameters adjustment



### 12.4.2 Station 2: DADDI

When the calibration of the Goturu station is carried, some of the sensitive parameters are changed in the Daddi station even though the separate calibration is carried for each station. In the Daddi station, the model is sensitive to the  $CH\_N_2$ ,  $CH\_K_2$ ,  $SOL\_K$ . The calibrated values of sensitive parameters for the Daddi station are listed below (Table 12.5).

The comparison graph of observed and simulated streamflow and  $R^2$  value of Goturu station is given below for the before and after calibration process. The calibration is carried for 11 years (1983–1993). And validated for 7 years (1995–2001) (Figs. 12.12, 12.13, 12.14, 12.15, 12.16, and 12.17).

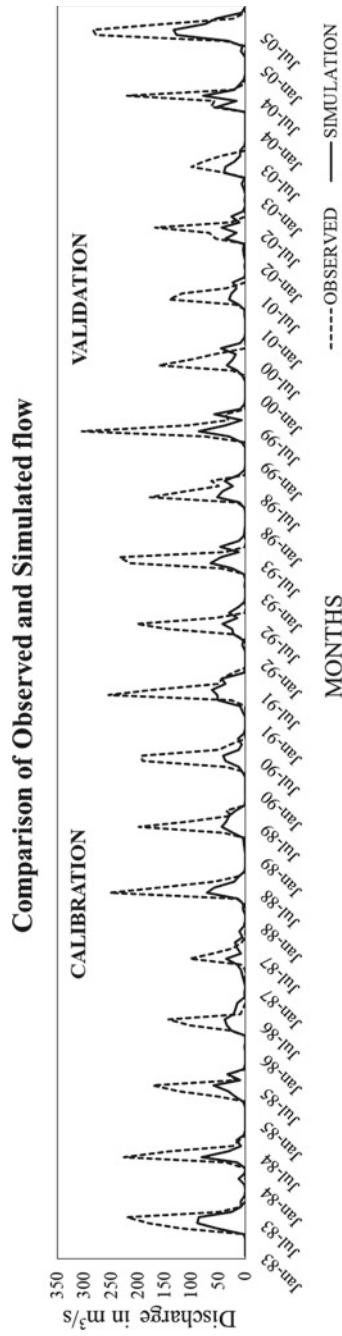
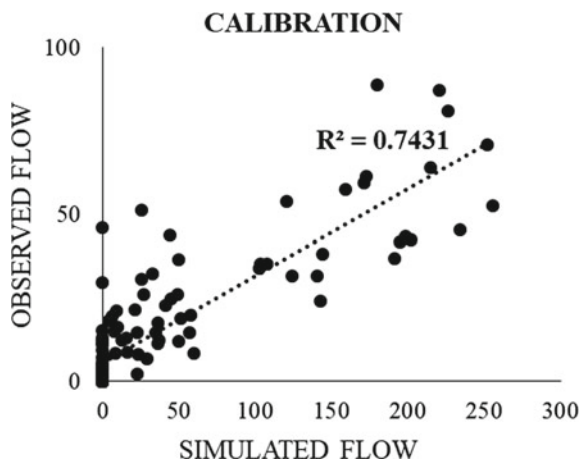
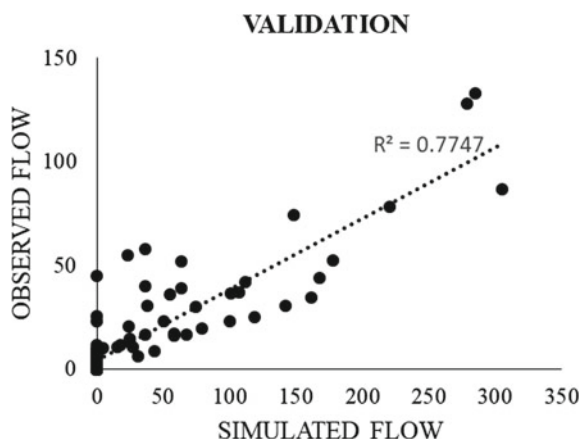


Fig. 12.9 Comparison of observed and simulated values after adjustment of parameters for Goturu Station

**Fig. 12.10** Scattered plot of coefficient of determination ( $R^2$ ) for calibration of Goturu Station after parameters adjustment



**Fig. 12.11** Scattered plot of coefficient of determination ( $R^2$ ) for validation of Goturu Station after parameters adjustment



**Table 12.5** Parameters used for calibration of Daddi Station

Parameters	Range	Initial value	Final value
CH_N <sub>2</sub>	0.01–0.3	0.014	0.1
CH_K <sub>2</sub>	0–500	0	200
SOL_K	0–2000	1.72	100

### 12.4.3 Station 3: GOKAK

In Gokak station, the catchment is in the hard rock region, hence the CN<sub>2</sub> value is gone below and the infiltration is moderate. In some of the regions, the soil which is sandy loam and possesses the CH\_N<sub>2</sub>, CH\_K<sub>2</sub> and SURLAG are much sensitive. Some of the region is forest and the canopy storage CANMX is 50 for the calibrated



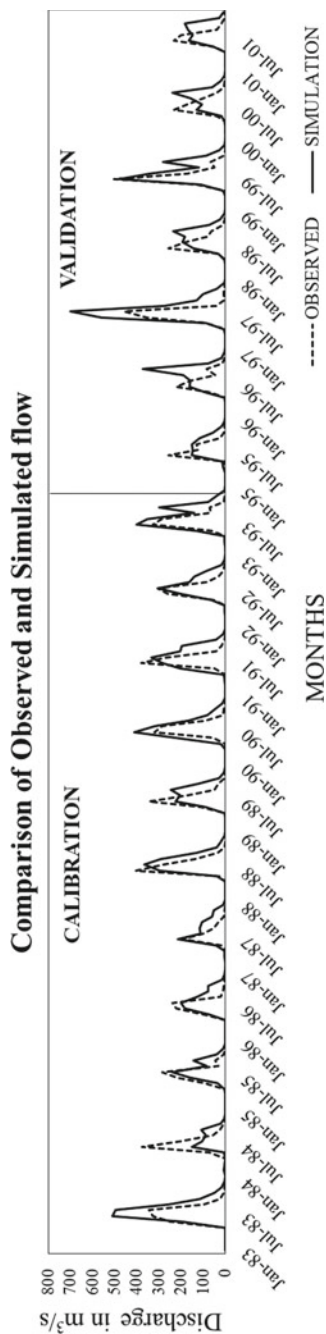
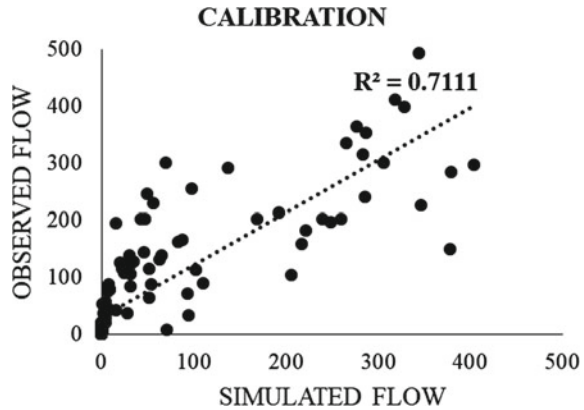
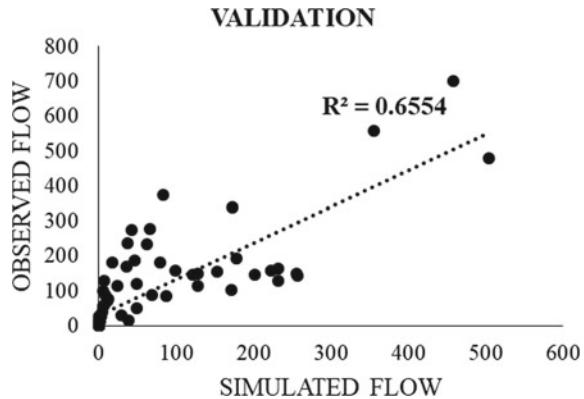


Fig. 12.12 Comparison of observed and simulated values before adjustment of parameters for Daddi Station

**Fig. 12.13** Scattered plot of coefficient of determination ( $R^2$ ) for calibration of Daddi Station before parameters adjustment



**Fig. 12.14** Scattered plot of coefficient of determination ( $R^2$ ) for validation of Daddi Station before parameters adjustment



value. The sensitive parameter which shows the changes in the calibration is shown below (Table 12.6).

The comparison graph of observed and simulated streamflow and  $R^2$  value of Goturu station is given below for the before and after calibration process. The calibration is carried for 10 years (1984–1993) and validated for 7 years (1998–2004) (Figs. 12.18, 12.19, 12.20, 12.21, 12.22 and 12.23).

#### 12.4.4 Station 4: BAGALKOT

This station is calibrated at the last, and due to the calibration of the other three stations, some of the parameters are slightly changed in the Bagalkot stations. The calibration is continued and some of the sensitive parameters were mentioned below in the Table 12.7 this region is sandy loam. The infiltration that occurs will be

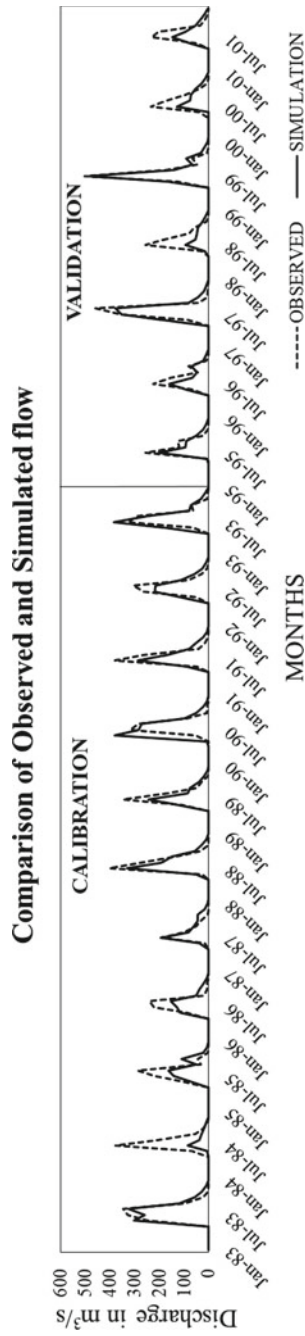
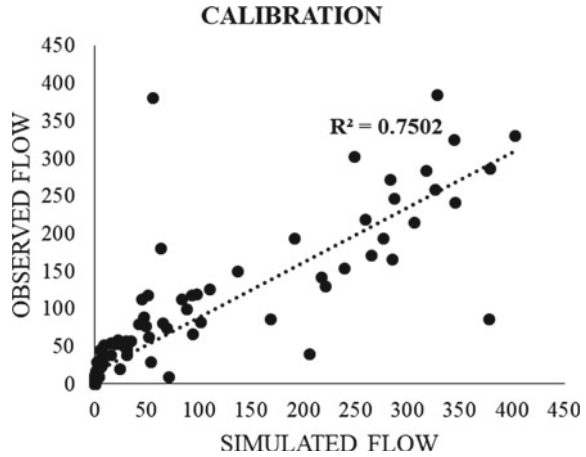
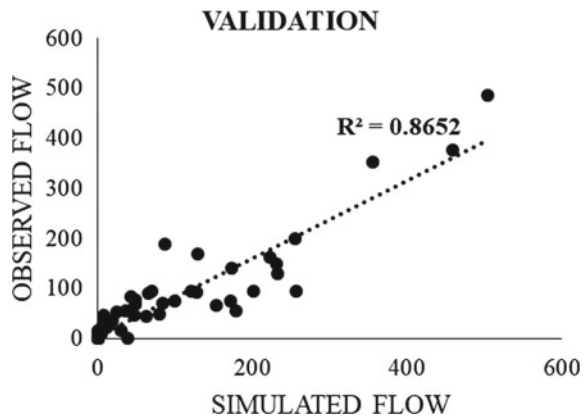


Fig. 12.15 Comparison of observed and simulated values after adjustment of parameters for Daddi Station

**Fig. 12.16** Scattered plot of coefficient of determination ( $R^2$ ) for calibration of Daddi Station after parameters adjustment



**Fig. 12.17** Scattered plot of coefficient of determination ( $R^2$ ) for validation of Daddi Station after parameters adjustment



**Table 12.6** Parameters used for calibration of Gokak Station

Parameters	Range	Initial value	Final value
CN <sub>2</sub>	35–98	87	75
CH_N <sub>2</sub>	0.01–0.3	0.014	0.3
CH_K <sub>2</sub>	0–500	0	400
SOL_K	0–2000	1.72	10
CANMX	0–100	0	50
SURLAG	0–24	2	4

moderate, the deep aquifer percolation (RCHRG\_DP) for this region is 0.2 and the base flow recession (ALPHA\_BF) is 0.2. The results of this station are satisfactory.

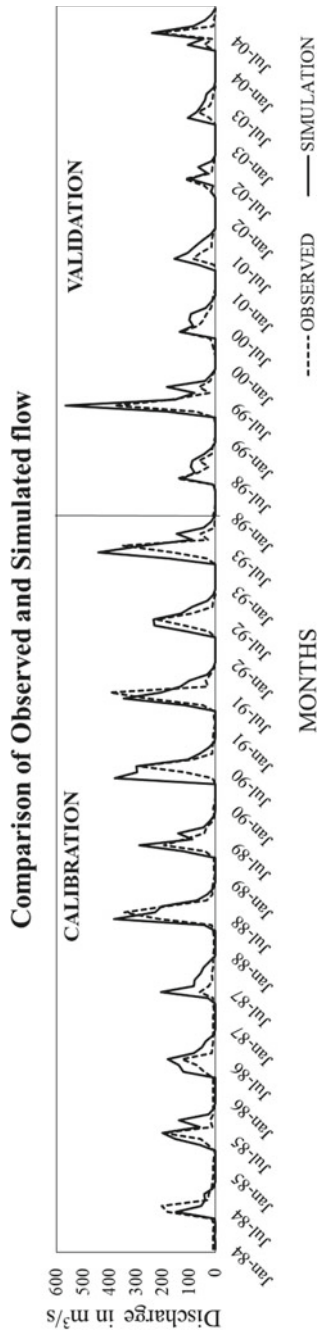
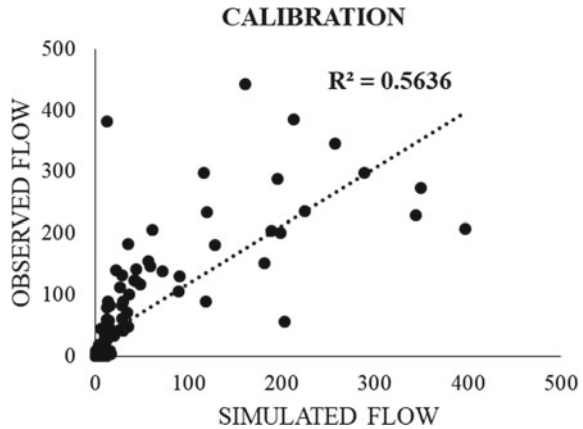
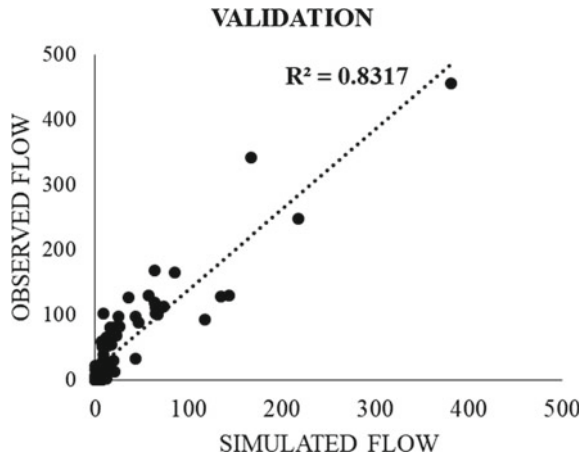


Fig. 12.18 Comparison of observed and simulated values before adjustment of parameters for Gokak Station

**Fig. 12.19** Scattered plot of coefficient of determination ( $R^2$ ) for calibration of Gokak Station before parameters adjustment



**Fig. 12.20** Scattered plot of coefficient of determination ( $R^2$ ) for validation of Gokak Station Before parameters adjustment



The comparison graph of observed and simulated streamflow and  $R^2$  value of Goturu station is given below for the before and after calibration process. The calibration is carried for 10 years (1984–1993) and validated for 6 years (1994–1999) (Figs. 12.24, 12.25, 12.26, 12.27, 12.28 and 12.29).

## 12.5 Results

The calibration and validation is carried for all the four discharge stations and the “Coefficient of determination ( $R^2$ ), Nash Sutcliff efficiency (NSE), Percent Bias (PBIAS) and RMSE-Observations Standard Deviation Ratio (RSR)” are carried for both Calibration and Validation. The values are listed below in Table 12.8 for all the discharge stations. The SWAT model is satisfactory for all values. The value of

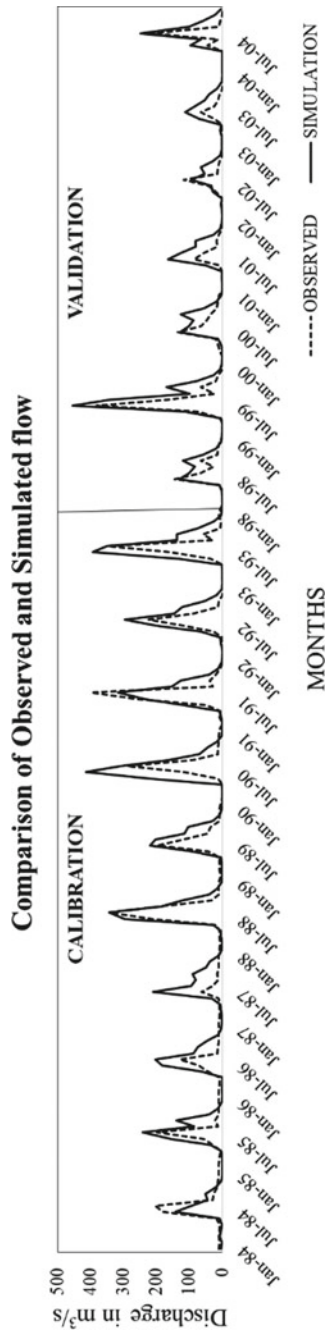


**Fig. 12.21** Comparison of observed and simulated values after adjustment of parameters for Gokak Station

**Fig. 12.22** Scattered plot of coefficient of determination ( $R^2$ ) for calibration of Gokak Station after parameters adjustment

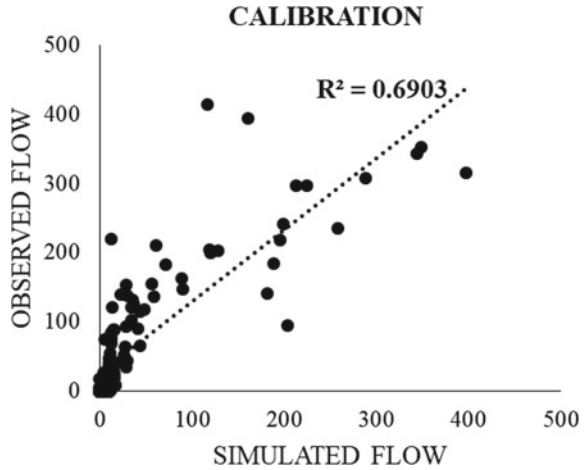


**Fig. 12.23** Scattered plot of coefficient of determination ( $R^2$ ) for validation of Gokak Station after parameters adjustment

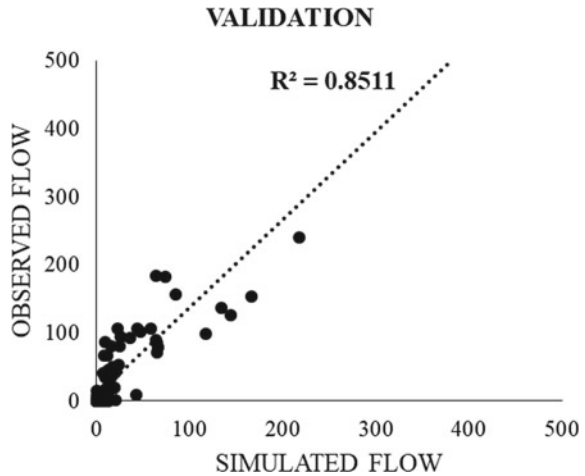


**Table 12.7** Parameters used for calibration of Bagalkot station

Parameters	Range	Initial value	Final value
ALPHA_BF	0-1	0.048	0.2
RCHRG_DP	0-1	0.05	0.2
GWQMIN	0-5000	1000	1500
REVP_MN	0-1000	750	900
SOL_K	0-2000	8.36	1000



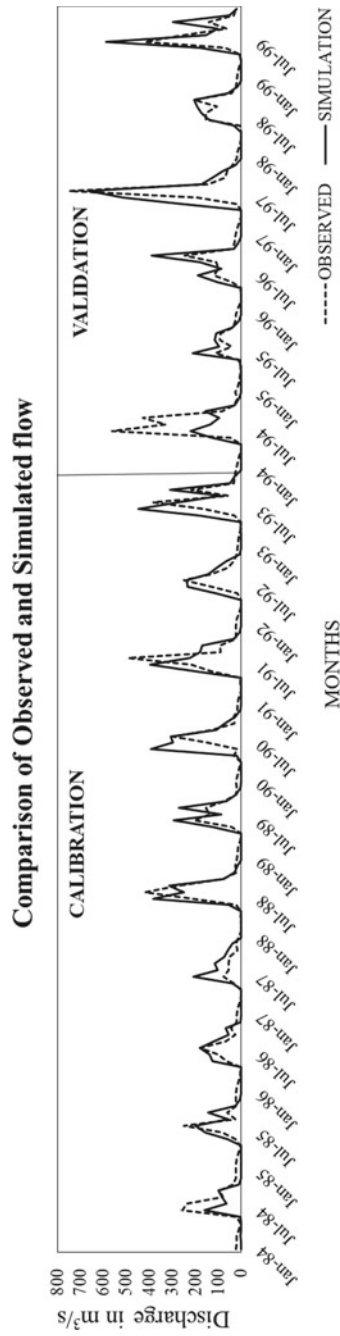
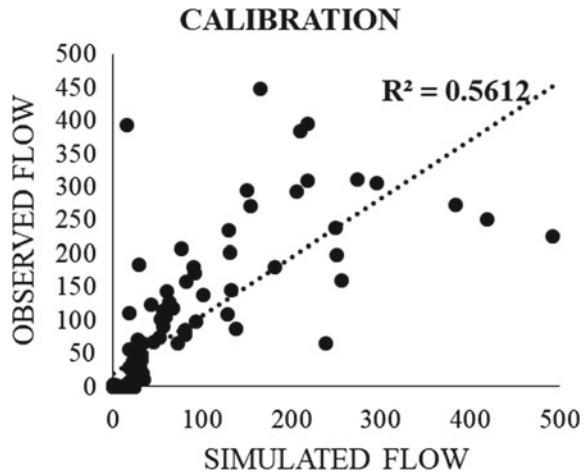
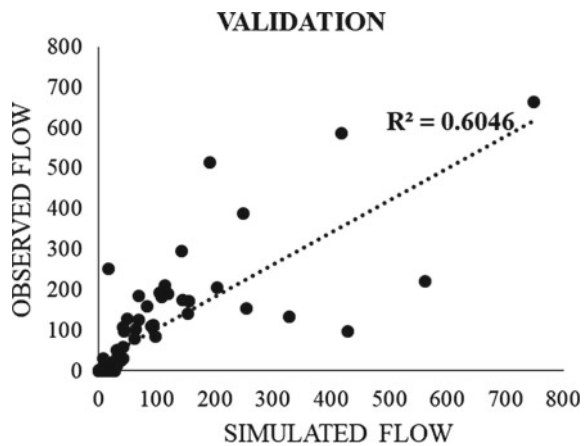


Fig. 12.24 Comparison of observed and simulated values before adjustment of parameters for Bagalkot Station

**Fig. 12.25** Scattered plot of coefficient of determination ( $R^2$ ) for calibration of Bagalkot Station before parameters adjustment



**Fig. 12.26** Scattered plot of coefficient of determination ( $R^2$ ) for validation of Bagalkot Station before parameters adjustment



PBIAS for the Goturu is not within the permissible limit ( $\pm 25\%$ ) due to the very low flow out from the SWAT model simulation. The rest of the results are satisfactory for the SWAT model simulation.

## 12.6 Conclusion

The study investigated that multisite calibration is more effective than the single-site calibration. In multisite calibration, the catchment is divided into smaller sub-basin, hence the accurate results can be achieved with the help of Soil and Water Assessment Tool (SWAT Model). This methodology identifies the standards for calibrating the model in this catchment and presenting the hydrologic results. The calibrating

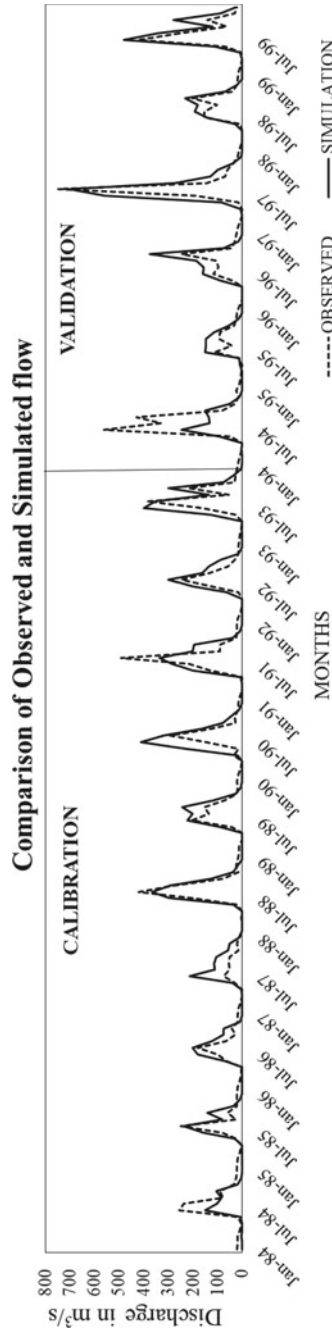
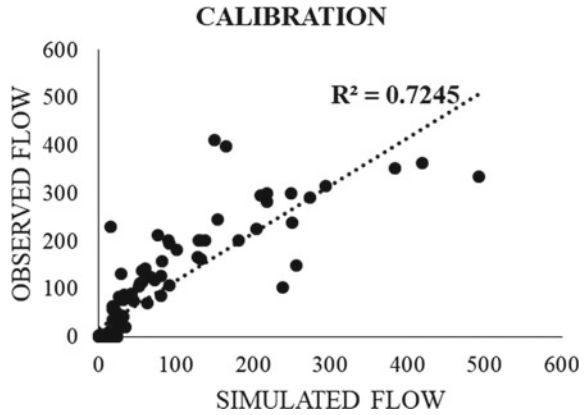
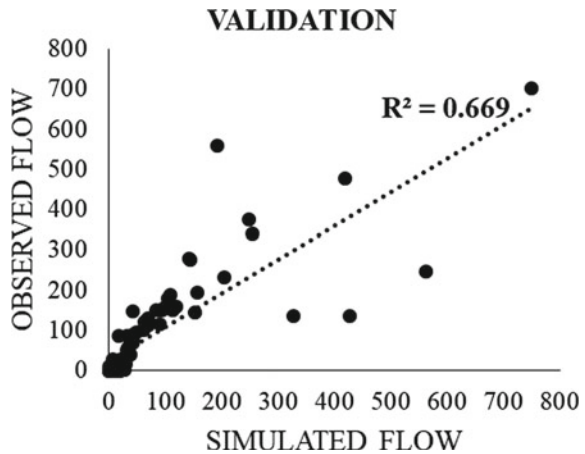


Fig. 12.27 Comparison of observed and simulated values after adjustment of parameters for Bagalkot Station

**Fig. 12.28** Scattered plot of coefficient of determination ( $R^2$ ) for calibration of Bagalkot Station after parameters adjustment



**Fig. 12.29** Scattered plot of coefficient of determination ( $R^2$ ) for validation of Bagalkot Station after parameters adjustment



**Table 12.8** Calibration and validation results for the multisite calibration

Discharge station	Calibration results				Validation results			
	$R^2$	NSE	PBIAS	RSR	$R^2$	NSE	PBIAS	RSR
Goturu	0.74	0.65	+59.08	0.59	0.77	0.71	+53.03	0.53
Daddi	0.75	0.99	+2.12	0.02	0.86	0.98	+11.85	0.12
Gokak	0.69	0.74	-18.23	0.33	0.85	0.69	-7.8	0.38
Bagalkot	0.7	0.58	-20.56	0.21	0.6	0.61	-9.8	0.1

parameters are easily identified for the specific basin in the multisite calibration. The flow prediction of the catchment is accurate due to the multisite calibration. The model developed was calibrated well at the discharge stations based on the

model evaluation parameters and it is validated for acceptance. The values of Coefficient of determination ( $R^2$ ), Nash Sutcliff efficiency (NSE), Percent bias (PBIAS) and RMSE-observations standard Deviation Ratio (RSR) are much improved in the multisite calibration. All the results are within the satisfactory limit. Results from this study state the importance of multisite calibration. The SWAT model was calibrated and validated well and the model is satisfactory for all the results, hence the multisite calibration is more effective than the single-site calibration.

## References

- Arnold JG, Srinivasan R, Muttiah RS, Williams JR (1998) Large area hydrologic modeling and assessment part I: model development. *J Am Water Resour Assoc* 34(1):73–89. <https://doi.org/10.1111/j.1752-1688.1998.tb05961.x>
- Arnold JG, Moriasi DN, Gassman PW, Abbaspour KC, White MJ, Srinivasan R, Santhi C, Harmel RD, Van Griensven A, Van Liew MW, Kannan N, Jha MK (2012) SWAT: model use, calibration, and validation. *Trans ASABE* 55(4):1491–1508
- Bai J, Shen Z, Yan T (2017) A comparison of single- and multi-site calibration and validation: a case study of SWAT in the Miyun Reservoir watershed, China. *Front Earth Sci* 11(3):592–600. <https://doi.org/10.1007/s11707-017-0656-x>
- Bharath A, Preethi S, Manjunatha M, Tangadagi RB (2020) Prediction of Temperature Data for Ghataprabha Sub 26:140–144
- Bharath A, Manjunatha M, Tangadagi RB, Preethi S (2020b) J Green Eng (JGE) Environ Assess Rainwater Harvesting GITAM Campus 10(4):1776–1785
- Kangsabanik S, Murmu S (2017) Rainfall-runoff modelling of Ajay river catchment using SWAT model. *IOP Conf Ser Earth Environ Sci* 67(1). <https://doi.org/10.1088/1755-1315/67/1/012033>
- Kannan N, White SM, Worrall F, Whelan MJ (2007) Sensitivity analysis and identification of the best evapotranspiration and runoff options for hydrological modelling in SWAT-2000. *J Hydrol* 332(3–4):456–466. <https://doi.org/10.1016/j.jhydrol.2006.08.001>
- Kinthada NR (2014) Land use/land cover and NDVI analysis for monitoring the health of micro-watersheds of Sarada River Basin, Visakhapatnam District, India. *J Geol Geosci* 03(02):146. <https://doi.org/10.4172/2329-6755.1000146>
- Malagò A, Pagliero L, Bouraoui F, Franchini M (2015) Comparaison de jeux de paramètres calés de modèles SWAT pour les péninsules ibérique et Scandinave. *Hydrol Sci J* 60(5):949–967. <https://doi.org/10.1080/02626667.2014.978332>
- Migliaccio KW, Chaubey I (2007). Comment on Cao W, Bowden BW, Davie T, Fenemor A. 2006. ‘Multi-variable and multi-site calibration and validation of SWAT in a large mountainous catchment with high spatial variability’. *Hydrological Processes* 20(5):1057–1073. *Hydrol Process* 21(23):3226–3228. <https://doi.org/10.1002/hyp.6491>
- Niraura R, Norman LM, Meixner T, Callegary JB (2012) Multi-gauge calibration for modeling the Semi-Arid Santa Cruz watershed in Arizona-Mexico border area using SWAT. *Air, Soil Water Res* 5:41–57. <https://doi.org/10.4137/ASWR.S9410>
- Sohoulande Djebou DC (2018) Assessment of sediment inflow to a reservoir using the SWAT model under undammed conditions: a case study for the Somerville reservoir, Texas, USA. *Int Soil Water Conserv Res* 6(3):222–229. <https://doi.org/10.1016/j.iswcr.2018.03.003>
- Sreedevi PD, Sreekanth PD, Khan HH, Ahmed S (2013) Drainage morphometry and its influence on hydrology in an semi arid region: using SRTM data and GIS. *Environ Earth Sci* 70(2):839–848. <https://doi.org/10.1007/s12665-012-2172-3>

# Chapter 13

## Agricultural Drought Assessment Using GIS: A Case Study



C. Prakasam and R. Saravanan

**Abstract** Agricultural drought is the shortage of water from either meteorological or hydrological sources, which in turn diminishes the irrigation water for crop production. In this period, the decline of soil moisture content and consequent crop failure occurs. The agricultural drought assessment, as well as management, can be done more accurately with the help of geospatial techniques. These techniques help in monitoring the trend in the occurrence of drought or the reasons for its temporal variations. The Pilavakkal irrigation system, Srivilliputhur taluk, Virudhunagar District, Tamil Nadu, consists of two reservoirs, namely, Periyar and Kovilar constructed across Periyar and Kovilar rivers situated by 5 km apart. The two rivers are the tributaries of the river Arjunanadhi, which is a tributary to the river Vaippar. The total area registered under the system as a whole is 2845 ha (7027 acres) of which 222.4 ha (549 acres) are double croplands. The crop lands are being fed by 40 tanks through these anicut. Even though the irrigation system has nominal sources of water, the area is prone to drought often because of various factors. It is being an agricultural area of prime importance to understand the Pilavakkal irrigation for its agricultural drought. The present research is an attempt to assess the agricultural vulnerability in the Pilavakkal region by means of agricultural drought indices such as Normalized Difference Vegetation Index (NDVI), Vegetation Condition Index (VCI), Land Surface Temperature (LST), Land Surface Water Index (LSWI) by using MODIS data for the drought year 2016 and using LANDSAT data for the same in the year 2017. The present research's aim is to provide an agricultural drought assessment spatially for the past two years and find the impact of drought in various locations for this drought year and non-drought year and also various mitigation measures such as sustainable use of water resources, crop pattern, suggestion of suitable crops, etc. are recommended which allows the authorities or farmer to cope up the drought in nearby future.

---

C. Prakasam (✉)

Department of Geography, School of Earth Sciences, Assam University, Diphu Campus, Karbi Anglong, Assam 782462, India

R. Saravanan

Department of Civil Engineering, Chitkara University, Himachal Pradesh 174103, India

## **13.1 Introduction**

Drought has no exact definition. Broadened hydro-meteorological factors, financial variables and distinctive water requests in various districts have fended off specialists from ordering/altering the exact meaning of drought. Although particular meaning of drought may change by segment and area, it is essentially an extended period of months or years, in which precipitation is not as much as the yearly normal, bringing about water shortage. It is a natural threat as the aftereffect of a risky occurrence because of delayed inadequacy in water accessibility. The basics for this occurrence to happen might be less rainfall, uneven precipitation supply, more noteworthy essentials of water than accessibility or the blends of all the other.

### ***13.1.1 Types of Drought***

The drought is extensively described in three categories. They are Meteorological drought, Hydrological drought and Agricultural drought. Any of these categories or combinations of these could generate a fourth category of drought called Socio-economic drought.

#### **13.1.1.1 Meteorological Drought**

The essential driver of a drought begins with the need for precipitation. The Meteorological droughts rely upon insufficiencies in precipitation, Dracup et al. (1980). At whatever point the genuine rainfall over an area is under 75% of the long haul climatological mean, the resulting drought is known as Meteorological drought.

#### **13.1.1.2 Hydrological Drought**

The occasion of Hydrological drought is perceptible from the available water in the surface water resources on account of diminished precipitation events or sum. Hisdal et al. (2001) researched that Hydrological droughts are often stood out from Meteorological droughts.

#### **13.1.1.3 Agricultural Drought**

The absence of water from either meteorological or hydrological sources diminishes the irrigation water for edit generation. Horticultural drought suggests a period with declining soil dampness content and resulting crop disappointment (Mishra and Singh 2010).

#### 13.1.1.4 Socio-Economic Drought

Socio-economic drought is the distress of water resources to meet water demand. In this way, associating droughts with supply and demand of water in an economically feasible way (AMS 2004). This investigation centers on agricultural drought. Evaluating the agricultural drought indices as drought indicator, could accept a basic part in farming drought impact assessment.

Agricultural drought has an important influence on the economy of agrarian nations like India, where more than 70% of livelihood depends upon farming. Around sixteen percentage of India's total area is drought inclined. Agricultural drought assessment is fundamental for taking appropriate remedial measures for improvement of drought situation. Remote sensing data and GIS application have been given an impression of being exceedingly useful for drought monitoring.

Rahman et al. (2020) estimated the crop-specific damage in Iowa, Nebraska and Texas, using a newly developed Disaster Vegetation Damage Index (DVDI). The damage has been assessed on a qualitative scale. The results of damage assessment are validated through the NDVI profile and yield loss in percentage. Areffian et al. (2020) MODIS data in a mountainous area could be a key tool in detecting the effects of intensive drought on natural vegetation cover. Alamdarloo et al. (2020). Climate does not have an important role in the drought hazard index, but it is the most crucial factor to classify drought vulnerability index. Njounwet et al. (2020) assessed the agricultural drought for Sudano-Sahelian region of Cameroon. The agricultural drought hazard was quantified based on its frequency and intensity. The Sahelian and Sudanian climatic conditions were found to be very high agricultural drought hazard zones, especially where the maize and peanut grain crops are concerned. Dey et al. (2020) used the RAI (rainfall anomaly index), VCI (vegetation condition index), Yield anomaly index (YAI) to quantify the agricultural drought in West Bengal. Using these indices, it was evident that during the study period of 1997–2017, the years 2000–2001 and 2010–2011 had experienced severe drought. Adedeji et al. (2020) developed drought monitoring remote-sensing techniques such as VCI and NDVI. This could play an invaluable role in food security and drought preparedness. Mohammed et al. (2020) linked the meteorological drought evolution and vegetation greening for Syria. The Meteorological drought was assessed using the standardized precipitation index (SPI) at a 12-month timescale. The time series of SPI were correlated with the normalized difference vegetation index (NDVI). The increase in the frequency and intensity of meteorological drought, combined with a series of unrest and political instability, have drastic impacts on the agricultural sector in Syria, with serious implications for crop yield.

The present research work assesses the agricultural drought using the GIS application in the study area. Traditional methods of drought assessment and monitoring rely upon rainfall data, which are limited in the region, often incorrect and specifically difficult to find in real time.



## 13.2 Study Area

The study area decided for research is the Pilavukkal scheme consisting of twin reservoirs; to be specific: Periyar and Kovilar. The total area registered under the system, in general, is 2845 ha (7027 sections of land) of which 222.4 ha (549 sections of land) are twofold croplands. They crop lands are being fed by all under the 40 tanks feed by through these anicut. Accordingly supplementation of supply to them is influenced. Periyar and Kovilar main trenches are operated at varying methods of supply based on the water system demand and the system water accessibility. The Arjunanadhi, a noteworthy tributary of Vaippar, begins from the surplus course of the above enormous tank and joins the Vaippar underneath the Nenmeni Anicut. The ayacut under the system is accounted for languishing over the need of a couple of wettings to procure a decent collect. No particular calendars are followed. Outlets are worked based on the water system demand. Distribution from the tanks to the command area is done by the agriculturists. Drawing water from the tanks is generally not separated based on crop stage and it is continuous, with the exception during rainy season. The outlets are not worked according to requirements. Being the run of the river type system, the upper lands utilize more water while the last part confronts inadequacy.

### 13.2.1 Command Area

Periyar and Kovilar reservoirs shared to supply the old command fed by 40 tanks of the system. There are various anicuts over the river at different areas which occupy water to various tanks through feeder channels. The water system conspire floods an indirect command area of 3792 ha through a system of tanks.

### 13.2.2 Agricultural Performance

Agriculturists are growing cotton beats, millets and so forth during summer (March–May) either rain fed or supplied by wells. No water is permitted from the reservoirs for these late spring crops and here and short term paddy exceeding an area of 683 ha if any raised by agriculturists. A careful analysis of the system demonstrates that there exist three unique areas, specifically, well-to-do, swing and the shortage with huge distinction in cropping intensity. The last part of the system (deficiency) is subjected to enduring water lack. Henceforth the tanks situated in this location need to permit impartial supply. There are two rain gauge stations in the Pilavakkal scheme, one at Periyar Dam and the other at Watrap. For any situation, according to the NWMP report, the rainfall is exceptionally unusual and is fewer than seventy-five percentage of the mean in twenty percentages of years. Thus, the area can be

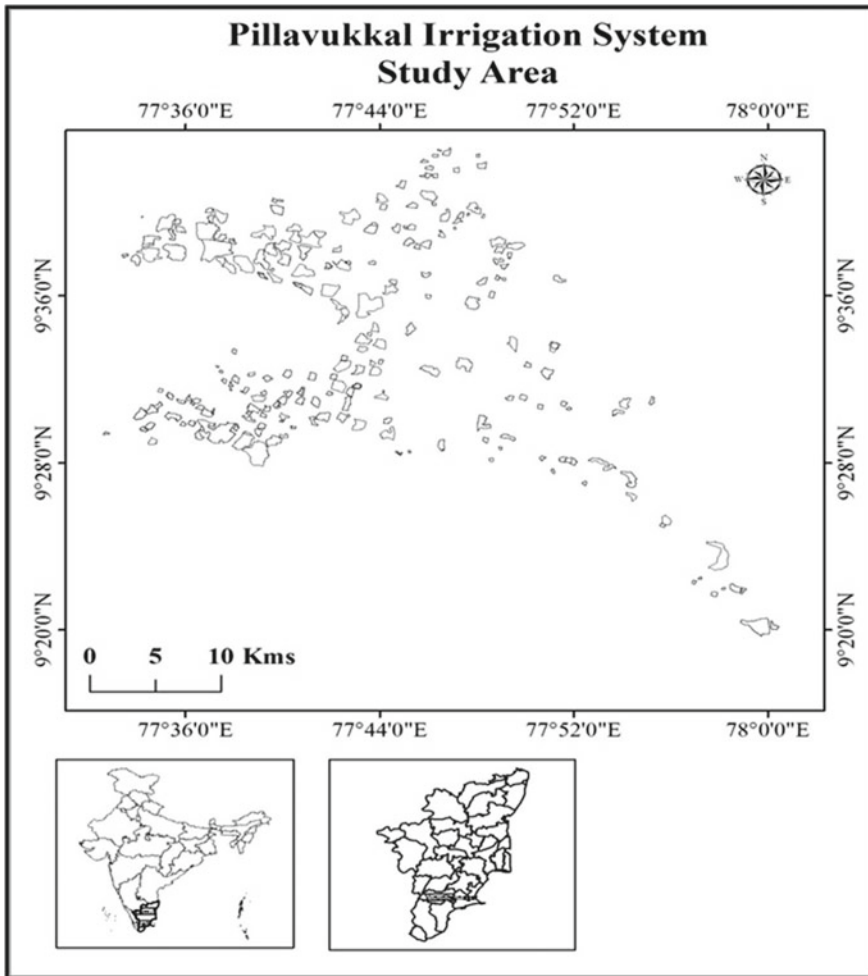


**Fig. 13.1** Study area

delegated drought inclined area according to the standards settled by the Indian Meteorological Department (Fig. 13.1).

### 13.2.3 Water Resources

#### 13.2.3.1 Surface Water

The average annual inflow of Kovilar and Periyar reservoirs based on the historic inflow records are 4.250 mm<sup>3</sup> and 19.88 mm<sup>3</sup> separately, giving a total annual inflow

of 24.13 mm<sup>3</sup>. A combined maximum annual inflow of 103.610 mm<sup>3</sup> during the year 1984–85 and a minimum annual inflow of 5.944 mm<sup>3</sup> were experienced during the year 1986–87. Out of 13 years from 1978 to 1990–91, the inflow is more than the mean inflow just for a long time. The most extreme inflow happened during November. Aside from the reservoir, the tanks additionally get runoff from their individual catchments and likewise, through feeder channels taking off from the rivers. These inflows have not been estimated until now and all things that have considered historic records of inflow into the tanks are not accessible. It is additionally exceptionally troublesome and time-consuming activity to measure and repair the inflow of all the forty tanks, profited by the system.

### **13.2.3.2 Groundwater**

Groundwater assumes a critical part in supplementing Pilavakkal command. A total number of 1233 wells are functioning in the command area of the system.

### **13.2.3.3 Climate, Topography and Soil**

The command area experiences a tropical atmosphere reliably. There is no meteorological station open within the Pilavakkal water system. For any situation, there is one station maintained by the groundwater wing of the state Public Works Division situated at Kavalur at a separation of 20 km from the Pilavakkal scheme. The most extraordinary mean temperature of 38.34 °C occurs during May and the minimum mean temperature of 20.04 °C occurs during January. In like manner, the maximum and minimum humidity is 67.01% during November and 41.5% during March, individually. The basins are subjected to a state of being tight and flanked by the slopes on the north and south close by its initial compass. The terrain on the north of the river is delicately sloping towards south-southeast to undertake the river. Correspondingly the terrain on the south of the river is sloping towards North-Northeast. As a rule, the dirt in the command area is dull red topsoil soil with pH (Hydrogen molecule fixation) ranging from 7.5 to 9.00. Concerning extravagance status, Nitrogen (N) content is low and Phosphate (P) and Potassium (K) content is medium. The dirt is appropriate for raising paddy, cotton, millets and sugarcane.

### **13.2.3.4 Areas and Cropping Pattern**

The old command of 3125.19 ha has been confined for paddy during the crop season; whereas a transient paddy has been allowed over an area of 667 ha in a manner of speaking. To the degree, the new command concerned over an area of 518 ha has been confined for long haul paddy. Supply and supplementation from the reservoirs are influenced only for the above areas. No scheduling for releasing water is done to old

(or) new command. According to the NWMP report, the water utilize effectiveness for the old command is worked out as 48.1% and for the new command is 77.6%.

### 13.3 Materials and Methods

Chopra (2006) had stressed upon the use of RS and GIS in the field of Drought Risk Evaluation. An effort has been made to derive drought risk areas facing agricultural, as well as meteorological drought, by use of temporal images from NOAA-AVHRR (8 km)-based Normalized Difference Vegetation Index (NDVI) (1981–2000) and meteorological-based Standardized Precipitation Index (SPI). It was evident from the study that central and northeastern parts of Gujarat are more prone to drought either agricultural or meteorological. Parida (2006, January) used the combination of both remotely sensed land surface reflectance and thermal properties from Terra MODIS to give importance to changes in both land surface temperature and NDVI over a region in the real world. The study found VTCI and WDI as an index, which has the capability of identifying the drought stress on a regional scale. The result observed that as duration of stress in 8 days' basis increasing the crop yield decreasing. Safari Shad et al. (2017) conducted the research using the extracted vegetation indices from Moderate Resolution Imaging Spectroradiometer (MODIS) sensor data during 2000–2008. In Esfahan province, monthly rainfall data from 25 stations were used to derive the Standardized Precipitation Index (SPI) at a 3-month scale, March to September. Based on the results of this study, it can be concluded that the NDVI and VCI indices concerning MODIS sensor can be a good alternative for estimating the drought with respect to meteorological indices and consequently can give a better idea on drought conditions in the study area. Siddiqui (2004) stated that the occurrence of drought makes the land incapable of cultivation throughout the year and this situation renders harsh and inhospitable environmental conditions for human beings, livestock population and biomass potential and plant species. Rathore (2004) said that there is an urgent need to make an effort to monitor and mitigate drought disasters with reference to the span of time.

#### 13.3.1 Drought Indices

##### 13.3.1.1 Normalized Difference Vegetation Index (NDVI)

NDVI is an index of vegetation health and density (Sruthi and Aslam 2015). The NDVI is the most generally calculated vegetation index. It contrasts in a range of -1 to +1. The NDVI is a calculation between the Infrared channel (0.78–0.90  $\mu\text{m}$ ) and Red channels of the visible region (0.63–0.69  $\mu\text{m}$ ).

$$\text{NDVI} = (\lambda_{\text{NIR}} - \lambda_{\text{red}}) / (\lambda_{\text{NIR}} + \lambda_{\text{red}})$$

where  $\lambda_{\text{NIR}}$  and  $\lambda_{\text{red}}$  are the reflectance in the NIR and red bands, respectively.

### 13.3.1.2 Land Surface Temperature (LST)

It is calculated like VCI, yet its formulation was adjusted to mirror vegetation's response to temperature (the higher the temperature the more outrageous the drought) (Sruthi and Aslam 2015)). LST depends on brilliance temperature and speaks to the deviation of the present month's (week's) esteem from the recorded most extreme.

$$\text{LSTIJ} = \frac{(\text{BT}_{\text{max}} - \text{BT}_j)}{(\text{BT}_{\text{max}} - \text{BT}_{\text{min}})} * 100$$

where BT is the brightness temperature. The maximum and minimum estimations of BT are calculated from the long haul record of remote-sensing pictures for each schedule month or week j.

### 13.3.1.3 Vegetation Condition Index (VCI) or Enhanced Vegetation Index

The Vegetation Condition Index (VCI) looks at the current NDVI to the scope of qualities seen in a similar period in earlier years (Dutta et al. 2015).

$$\text{VCIJ} = \frac{(\text{NDVI}_j - \text{NDVI}_{\text{min}})}{(\text{NDVI}_{\text{max}} - \text{NDVI}_{\text{min}})}$$

The VCI is communicated in percentage and gives a thought where the observed esteem is situated between the extreme qualities (minimum and maximum) in the earlier years. Lower and higher qualities indicate terrible and great vegetation state conditions, separately. Where, NDVImax and NDVImin are calculated from the long-term record (e.g. 18 years) for that month (or week) and j is the index of the current month (week).

### 13.3.1.4 LSWI: Land Surface Water Index

$$(\lambda_{\text{NIR}} - \lambda_{\text{SWRI}}) / (\lambda_{\text{NIR}} + \lambda_{\text{SWRI}})$$

where NIR and SWIR spectral bands in lieu of using the 1240 nm NIR band and the SWIR may be represented by the 1640 nm or 2130 nm spectral bands, Dutta et al. (2015). The LSWI is a proportion of fluid water particles in vegetation shelters that interact with the sunlight-based radiation, and consequently, LSWI is sensitive to the total measure of fluid water in the product (Table 13.1).

**Table 13.1** Drought indices

Drought index	Range	Normal condition	Severe drought
NDVI	-1 to +1	Based on the location	-1
LSWI	-1 to +1	0	-1
EVI	0 to 100%	50	0
LST	0 to 100%	50	0

**Indices:****13.3.2 Data Collection**

Principally keeping in mind the goal to understand the existing system, a field survey has been completed. The data gathered from the field survey helps in understanding the source and purpose behind drought inclined zone in the framework. Other than the data gathered from the data community for remote-sensing procedures, a questionnaire survey is conveyed to gather the data regarding the harvest compose, irrigation pattern, water utilize pattern and so on.

With a specific goal to evaluate the drought using remote sensing, the following data are utilized: crop compose per plot and corresponding area, rainfall data, soil outline, utilize delineate, infrared and thermal bands of MODIS L1B Image, irrigation framework compose, discharge data, trim compose, limit of the tanks. With the accessibility of data, the following methods are considered for the drought assessment of the framework.

**13.3.2.1 Remotely Sensed Data**

The MODIS data was downloaded from LP DAAC through EOS Data Gateway. A congregated diverse data was collected like climatic data and satellite data. We downloaded MODIS satellite photos and Landsat8 data of the month from September to December of post-rainstorm time of 2016 (Figs. 13.2, 13.3, 13.4, and 13.5) and 2017 (Fig. 13.6), respectively. The drought indices were calculated and listed below. The results also show that the NDVI derived from the MODIS data are more correlated with the field data of the vegetation cover than the Landsat-derived NDVI (Li et al. 2010). Since drought is inherently a complex phenomenon and its monitoring relies on the availability of good quality data, the performance of drought indices could be different from place to place, Jain et al. (2015).

NDVI analysis for the year 2017 was carried out using Landsat 8 data and the results are given below.

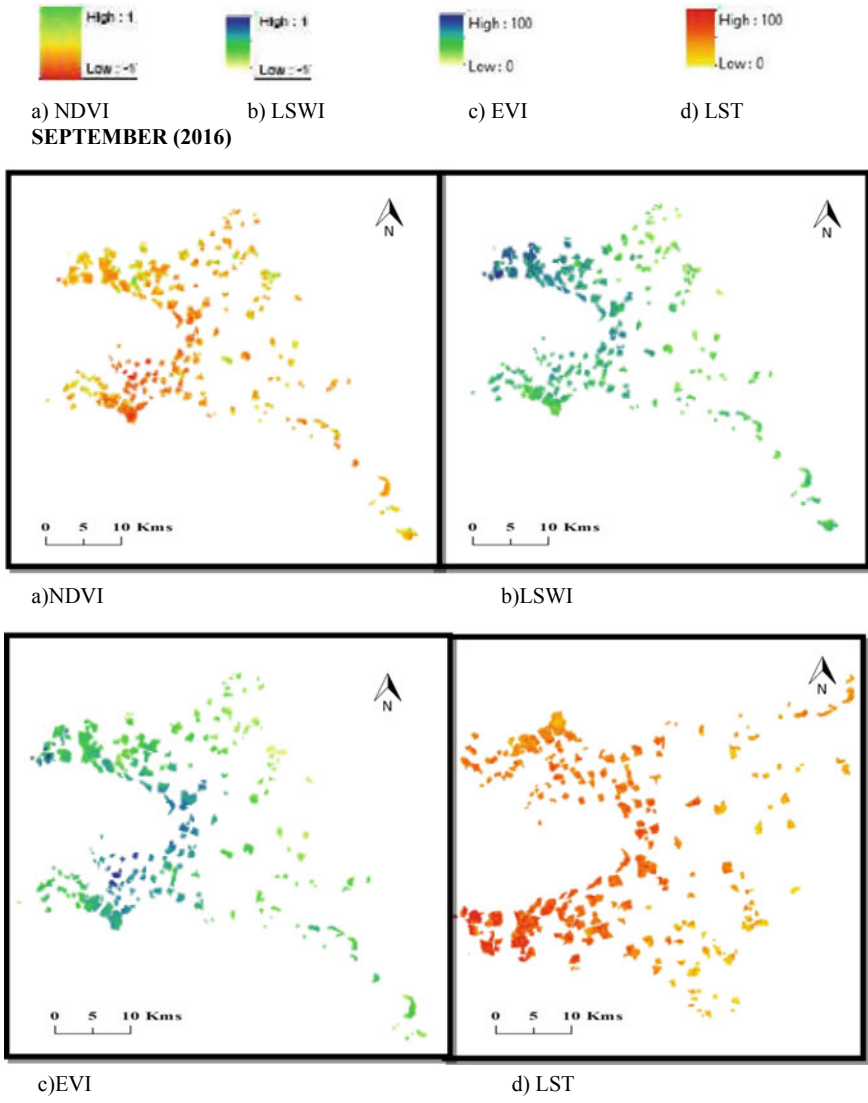


Fig. 13.2 Indices for September month

### 13.4 Results and Conclusion

Agricultural drought monitoring is one of the three main actions in agricultural drought risk management plans, which also include drought preparedness and drought response actions (Hazaymeh and Hassan 2016). The present examination

OCTOBER (2016)

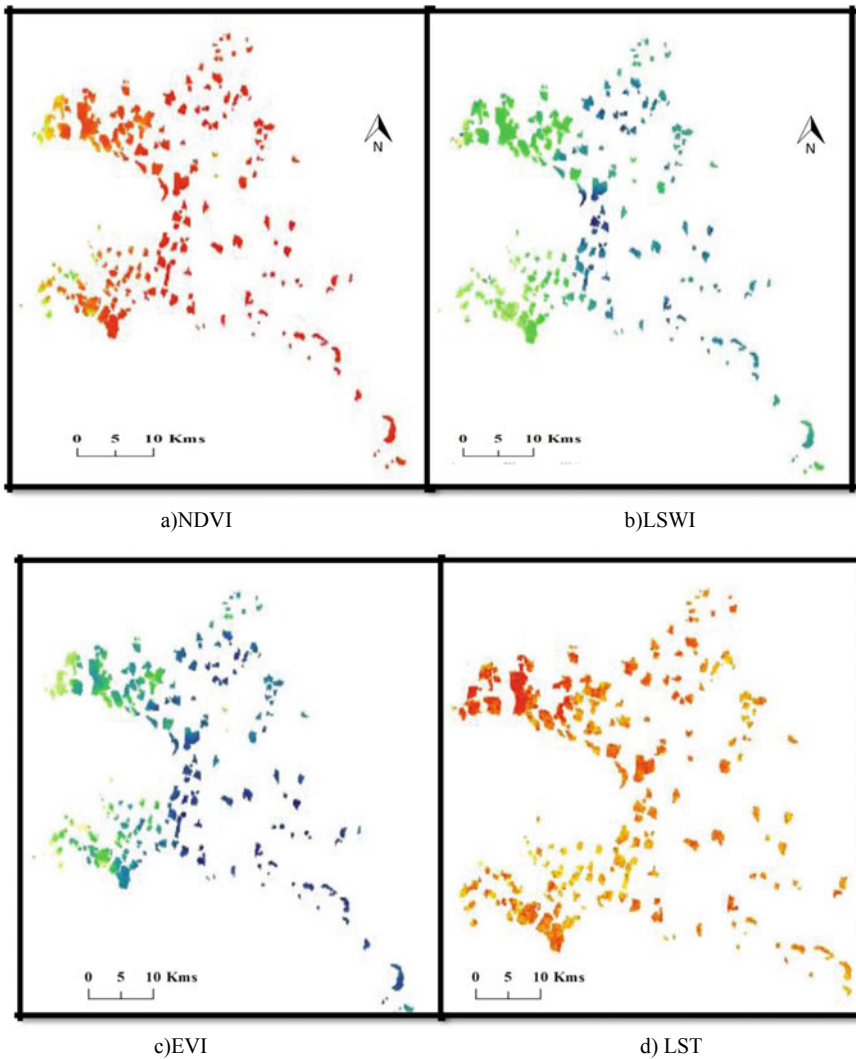


Fig. 13.3 Indices for October month

identifies the spatial-temporal degree of drought over Pillavukkal scheme using GIS-based drought assessment. MODIS-derived vegetation indices are helpful to monitor, find the spatial-temporal degree of agricultural drought. It additionally demonstrates and legitimizes the value of GIS approach for recognizing drought-associated apprehension for agriculture which depends upon rain. Not at all like the meteorological data accessible from insufficiently circulated weather stations, can GIS-based indices be effectively utilized for delineating the spatial-transient degree of farming drought.



NOVEMBER (2016)

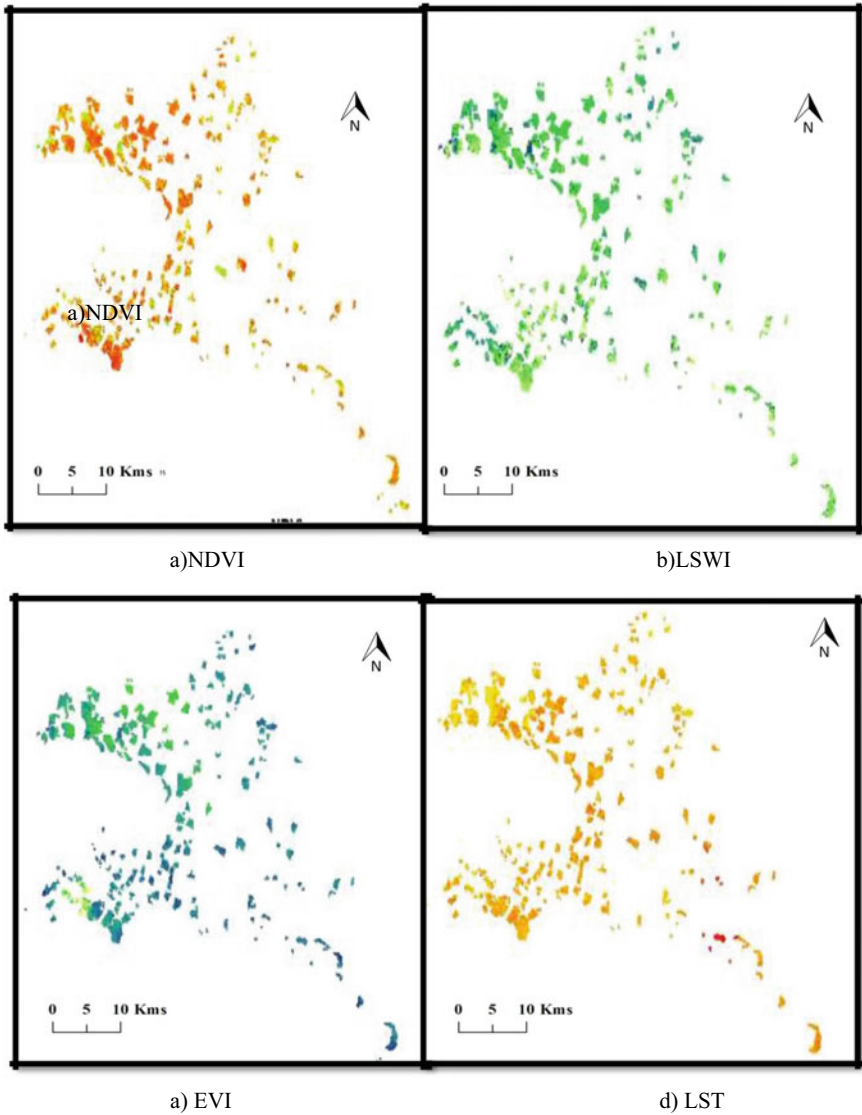
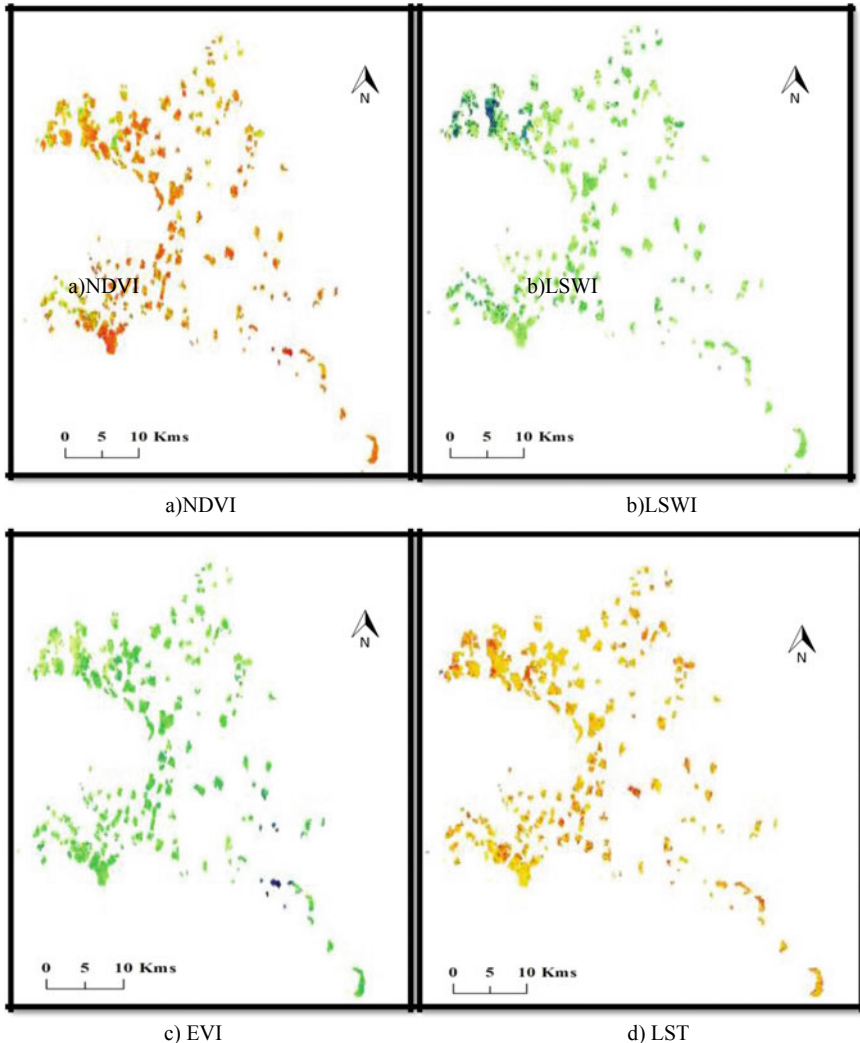


Fig. 13.4 Indices for November month

Northeast rainstorm season was chosen to deliver vegetation drought indices during 2016 and 2017. The advantage of NDVI is that it provides a measure of vegetation health or greenness conditions and is sensitive to darker and wet soil conditions; also demonstrates time lag in response to soil moisture which makes it disadvantageous.

## DECEMBER (2016)



**Fig. 13.5** Indices for December month

For the VCI, the advantage is that it provides vegetation greenness conditions, but it requires data over a longer time period (Hazaymeh and Hassan 2016).

It was observed that VCI fails to accurately map the actual extent of agricultural drought during the early sowing period. This limitation of VCI is mainly contributed to its dependence on vegetation index (NDVI) for drought mapping (Sivakumar et al. 2010, June). Normalized Difference Water Index (NDWI) uses both the bands in the near infrared region and is very sensitive to the liquid water content of vegetation canopy and so rainfall, Chakraborty et al. (2010).

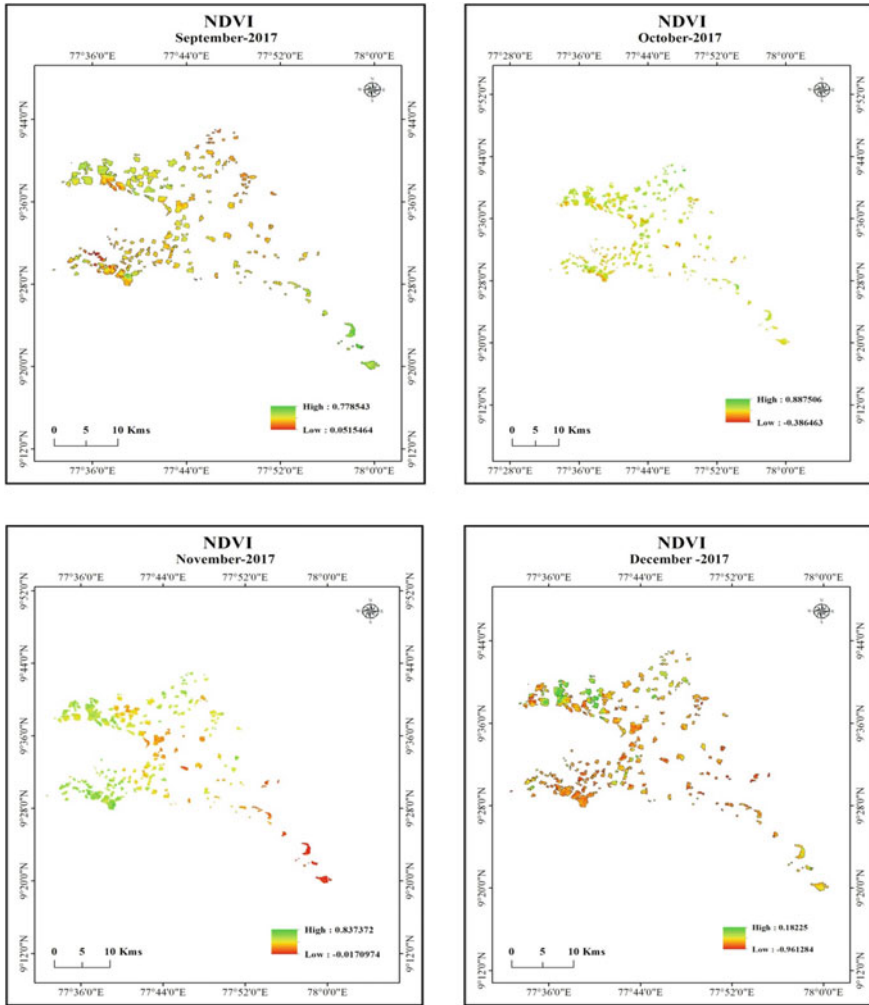


Fig. 13.6 NDVI indices (2017)

The estimations of NDVI were calculated for every pixel of the picture. The vegetative drought was watched and understood through NDVI, VCI and TCI indices. NDVI differs between  $-0.1$  and  $+0.1$ . Pixels with  $0.0-0.05$ ,  $0.05-0.1$ ,  $0.1-0.5$  and  $0.5-1.0$  qualities have been delegated as no vegetation, poor vegetation, moderate vegetation, and great vegetation, separately. According to Figures recorded minimal, extreme droughts happened in October and November. After the calculation of NDVI, VCI was processed using band math. In view of the drought levels, extraordinary, extreme, moderate, slight and ordinary droughts were obtained by the methods for thickness cut. VCI indicates that the greater part of the areas is in drought in October and November. TCI was calculated using the brightness temperature. TCI indicates

that the greater part of the areas is in drought from September to December. In the case of 2017, the NDVI analysis itself shows the Pillavukal scheme as vegetation healthy region with respect to many factors.

The analysis of agricultural drought for its indices during drought (2016) and normal year (2017) gives away an idea that the drought occurrence can be unexpected besides many factors. This study helped in understanding the drought spatially and temporally. In order to cope up with the drought, recommendations can be provided in terms of Early Warning System and farmer's preparedness. In light of this, all accessible mediums of communication and mindfulness ought to be utilized to pass on information about any type of catastrophe. Also, the farmers have to adapt new techniques, change crop type and pattern during the drought period as mitigation measures.

### ***13.4.1 Recommendation in Terms of Early Warning System***

Accordingly, information about anticipated weather or climate changes ought to be communicated to them on time in order to have the capacity to strategize in front of such impending disasters so as to diminish their level of defenselessness to such debacles. In light of this, all accessible mediums of communication and mindfulness ought to be utilized to pass on information about any type of catastrophe.

### ***13.4.2 Recommendation in Terms of Farmers' Preparedness***

Most farmers claimed that they were not set up for the dry season as a result of the absence of information about impending debacles, while others guaranteed that they didn't comprehend what to do to get ready regardless of whether they approached such information. This research made it realized that with farmers' financial status, level of education and absence of profitable information, it is unthinkable for them to oversee and adapt to dry spells without outside help or help from governments and offices at all levels. Making accessible helpful information around an impending dry season may not be sufficient; there is additionally the need to go above and beyond by providing information about how to adapt to such catastrophes.

**Acknowledgements** The author expresses his sincere thanks to Dr. M. Krishnaveni, Professor Center for Water Resources, Anna University, Tamil Nadu for guiding during the research work.

## References

- Adedeji O, Olusola A, James G, Shaba HA, Orimoloye IR, Singh SK, Adelabu S (2020) Early warning systems development for agricultural drought assessment in Nigeria. *Environ Monit Assess* 192(12):1–21
- Alamdarloo EH, Khosravi H, Nasabpour S, Gholami A (2020) Assessment of drought hazard, vulnerability and risk in Iran using GIS techniques. *J Arid Land* 1–17
- Areffian A, Eslamian S, Sadr MK, Khoshfetrat A (2020) Monitoring the effects of drought on vegetation cover and ground water using MODIS satellite images and ANN. *KSCE J Civil Eng* 1–11
- Chakraborty A, Sehgal VK (2010) Assessment of agricultural drought using MODIS derived normalized difference water index
- Chandrasekara K, Saia MS, Beheraa G (2011) Assessment of early season agricultural drought through land surface water index (LSWI) and soil water balance model. *ISPRS-Int Arch Photogramm Remote Sens Spatial Inform Sci* 3820:50–55
- Chopra P (2006) Drought risk assessment using remote sensing and GIS: a case study of Gujarat. ITC
- Dey M, Dutta D, Roy AD (2020) Spatiotemporal extent of agricultural drought over western part of West Bengal. In: *Habitat, ecology and ekistics*. Springer, Cham, pp 247–261
- Dracup JA, Lee KS, Paulson EG Jr (1980) On the definition of droughts. *Water Resour Res* 16(2):297–302
- Dutta D, Kundu A, Patel NR, Saha SK, Siddiqui AR (2015) Assessment of agricultural drought in Rajasthan (India) using remote sensing derived Vegetation Condition Index (VCI) and Standardized Precipitation Index (SPI). *Egypt J Remote Sens Space Sci* 18(1):53–63
- Hazaymeh K, Hassan QK (2016) Remote sensing of agricultural drought monitoring: a state of art review. *Aims Environ Sci* 3(4):604
- Hisdal H, Stahl K, Tallaksen LM, Demuth S (2001) Have streamflow droughts in Europe become more severe or frequent? *Int J Climatol* 21(3):317–333  
<https://edcimswww.cr.usgs.gov/pub/imswelcome/>
- Jain VK, Pandey RP, Jain MK, Byun HR (2015) Comparison of drought indices for appraisal of drought characteristics in the Ken River Basin. *Weather Climate Extremes* 8:1–11
- Li Z, Li X, Wei D, Xu X, Wang H (2010) An assessment of correlation on MODIS-NDVI and EVI with natural vegetation coverage in Northern Hebei Province, China. *Procedia Environ Sci* 2:964–969
- Mishra AK, Singh VP (2010) A review of drought concepts. *J Hydrol* 391(1–2):202–216
- Mohammed S, Alsafadi K, Al-Awadhi T, Sherief Y, Harsanyie E, El Kenawy AM (2020) Space and time variability of meteorological drought in Syria. *Acta Geophys* 68(6):1877–1898
- National Water Management Project (NWMP) report (1992)
- Njouenwet I, Vondou DA, Dassou EF, Ayugi BO, Nouayou R (2020) Assessment of agricultural drought during crop-growing season in the Sudano-Saharan region of Cameroon. *Nat Hazards* 1–17
- Parida BR (2006) Analysing the effect of severity and duration of agricultural drought on crop performance using terra-MODIS satellite data and meteorological data. ITC American Meteorological Society (AMS) 2004 Supplement to the Bulletin of the American Meteorological Society, vol 86, Number 4
- Rahman MS, Di L, Yu E, Lin L, Yu Z (2020) Remote sensing based rapid assessment of flood crop damage using novel disaster vegetation damage index (DVDI). *Int J Disaster Risk Sci* 1–21
- Rathore MS (2004) State level analysis of drought policies and impacts in Rajasthan, India (vol. 93). IWMI
- Safari Shad M, Ildoromi A, Akhzari D (2017) Drought monitoring using vegetation indices and MODIS data (case study: Isfahan Province, Iran). *J Rangeland Sci* 7(2):148–159
- Siddiqui AR (2004) Regional evaluation of desertification hazards in the aridlands of Western Rajasthan (an unpublished Ph.D. thesis). AMU, Aligarh, Uttar Pradesh, India, 221

- Sivakumar M, Stone R, Sentelhas PC, Svoboda M, Omondi P, Sarkar J, Wardlow B (2010) Agricultural drought indices: summary and recommendations. In: Agricultural drought indices proceedings of an expert meeting, pp 172–197
- Sruthi S, Aslam MM (2015) Agricultural drought analysis using the NDVI and land surface temperature data; a case study of Raichur district. *Aquatic Procedia* 4:1258–1264

# Chapter 14

## Design of Branched Pipe Networks Using Reliability and Total Annual Cost



Deepak Singh, Arkaja, Munendra Kumar, and Saurabh Sah

**Abstract** The branched and looped type networks are the two basic configurations of water distribution. The branched pipe networks are generally designed by traditional and optimization methods. In the traditional method, a pipeline is designed by balancing the available energy against the loss of energy due to friction, whereas in the optimization methods, the cost is minimized. For ensuring regular water supply, it is essential to consider the reliability of the water distribution network, which depends on the failure rate of pipes, quality and quantity of water available at the source, and pressure requirements at demand nodes. Therefore, the reliability of the system needs to be incorporated while minimizing the total cost of the distribution system. In this paper, an enumerative method using both the reliability and total annual cost is developed for designing the branched pipe networks. The method satisfies pressure and discharges requirements along with the recommended values of the minimum and maximum velocities in the pipes. In this method, different sets of pipe sizes are taken to calculate the reliability and cost of the network, and that set of the pipe network is selected, which has the highest ratio of reliability to cost. To calculate the ratio of reliability to cost, the capital cost or the total annual cost can be used. The total annual cost is the sum of the annual fixed and annual energy costs. The applicability of the developed method is illustrated with the help of a design example. It was found that the reliability of the branched network varied with the total annual cost, as well as the capital cost, of the network for different sets of pipe diameters in the network. Further, it was found that the reliability for the designed network using total annual cost was higher than using capital cost. Therefore, the total annual cost should be preferred over the capital cost in the design to establish the balance between reliability and economy. The presented method provides a straightforward approach for water supply engineers to determine economical as well as reliable branched pipe networks.

---

D. Singh (✉) · M. Kumar · S. Sah

Department of Civil Engineering, Delhi Technological University, New Delhi 110042, India

Arkaja

Department of Civil Engineering, IFTM University, Moradabad 244001, UP, India

## 14.1 Introduction

Water is the greatest resource of humanity. It not only helps in survival, but also helps in making life comfortable and luxurious. In this, water distribution system plays an important role in supplying water to consumers for different uses such as domestic, publically, commercial and industrial. Therefore, it is very important that the water distribution system performs well. A perfectly reliable or well performed water distribution system should supply desired quality of water in required quantities with desired residual heads to all consumers throughout the design period. The performance of the system is determined by estimating the reliability of the water distribution system. In general, reliability is the probability that the system will perform its function appropriately for a specified time period under a given service condition. Reliability of water distribution system depends on the availability of raw water at the source, transmission of raw water to treatment plants, treatment of raw water to the desired quality, and transmission, storage, and distribution of the treated water, without deteriorating its quality, to the tapping points of the consumers in the required quantities and at desirable residual heads throughout the design period. Traditionally, a pipeline is designed by balancing the energy head against the loss of energy head. In the optimization methods, the optimal solution was obtained by minimizing the cost of the network. In the recent past, efforts have been made by the researcher's to use heuristic methods like Genetic Algorithms (Simpson et al. 1994; Savic and Walters 1997), nonlinear programming (Shamir 1974; Lansey and Mays 1989; Verma et al. 1997), Simulated Annealing (Cunha and Sousa 1999), ant colony optimization (Maier et al. 2003). Further, in order to analyze the reliability of water distribution systems, different approaches are presently being employed by researchers and analysts (Rowell and Barnes 1982; Kettler and Goulter 1985). In the present study, the reliability-based design of the branched water distribution network using total annual cost satisfying the minimum and maximum velocity requirement is presented to determine the best set of optimal pipe sizes with desired reliability for different links of a pipe network.

## 14.2 Methodology

The reliability-based method for designing a branched pipe network involves the computation of the total annual cost of the network calculation of system reliability. These are described as:



### 14.2.1 Pipeline Cost

The cost of a pipeline varies with the diameter, and annualized fixed cost of the pipeline can be obtained as.

$$F_c = C_r \times I_c \quad (14.1)$$

where,  $I_c$  = Initial cost of the pipeline (Rs/m);  $C_r$  = Capital recovery factor which can be calculated as.

$$C_r = \frac{i(1+i)^n}{(1+i)^n - 1} \quad (14.2)$$

where,  $i$  = Decimal equivalent annual interest rate;  $n$  = Life of the pipe (year).

### 14.2.2 Energy Cost

The annual energy cost for overcoming frictional head loss can be calculated as.

$$E_c = \frac{73.5Q \times h_f \times t \times C_e}{75\eta} \quad (14.3)$$

where  $E_c$  = Annual energy cost (Rs);  $Q$  = Flow rate (liter/s);  $h_f$  = Frictional head loss of pipe (m);  $t$  = Annual use (hours);  $C_e$  = Cost of electricity (Rs/kW h);  $\eta$  = Efficiency of pump (%).

The value of head loss  $h_f$  can be calculated by different formulae such as Darcy-Weisbach, Hazen-Williams formula, Manning's formula, etc. According to Darcy-Weisbach formula, energy head loss is given as:

$$h_f = \frac{fLV^2}{2gD} \quad (14.4)$$

where,  $h_f$  = Frictional loss or frictional energy head loss (m);  $f$  = Darcy-Weisbach friction factor for pipe material (dimensionless);  $L$  = Length of pipe (m);  $D$  = Inside diameter of pipe (m);  $V$  = Mean velocity of flow through the pipe (m/s);  $g$  = Acceleration due to gravity ( $m^2/s$ ).

The friction factor can be calculated using Swamee and Jain (1976) formula

$$f = \frac{0.25}{\left[ \log_{10} \left( \frac{\epsilon}{3.7d} + \frac{5.74}{Re^{0.9}} \right) \right]^2} \quad (14.5)$$

where  $\varepsilon$  = Average height of roughness elements (m);  $R_y$  = Reynolds Number.

The value of  $R_y$  can be calculated as

$$R_y = \frac{4Q}{\pi \vartheta D} \quad (14.6)$$

In this study,  $\varepsilon$  is taken as 0.00025 m for cast iron Pipes. Where  $\vartheta$  is the kinematic viscosity ( $\text{m}^2/\text{s}$ ). In this study, the value of  $\vartheta$  is taken as  $10^{-6} \text{ m}^2/\text{s}$ .

### 14.2.3 Total Annual Cost

The total annual cost of a pipeline can be represented as the sum of the annual fixed cost and annual energy cost.

$$T_c = F_c + E_c \quad (14.7)$$

### 14.2.4 Reliability

In reliability of water distribution networks, the working and closure times for pipes, pumps, and valves can be obtained by considering availability and unavailability during the time interval of one year (365 days).

The working condition probability and the shutdown or closure probability of pipe, using the break rate  $N(y) \text{ km}^{-1} \text{ yr}^{-1}$  for a pipe length  $L$  km for year  $y$  can be obtained as

Failure rate  $F(t)$  of a pipe per year depends on the pipe break rate. It varies with pipe diameter and can be obtained as.

$$F(t) = N(y) \times L \quad (14.8)$$

Using the failure rate and MTTR, the closure and working times of a pipe, ratio of working time to total time, i.e., probability of system element per year are

$$\text{Closure time per year} = N(y)LT_r \quad (14.9)$$

and

$$\text{working time per year} = 365 - N(y)LT_r \quad (14.10)$$

$$\text{working condition probability per year } p_i = \frac{365 - N(y)LT_r}{365} \quad (14.11)$$

The system should be satisfactory to an acceptable level during the entire design period. The analysis period is considered one year (365 days), the last year of the design period. If the network has an acceptable reliability level this year, it is naturally acceptable for the earlier years.

#### 14.2.4.1 Node Reliability Parameter

Node reliability parameter or probability of node  $j$  can be defined as the product of working condition probability of pipes upstream of node  $j$ .

$$R_{nj} = \prod_{i=1}^{\text{nlink}} p_i \quad (14.12)$$

#### 14.2.4.2 Volume Reliability Parameter $R_v$

Volume reliability parameter  $R_v$  is the ratio of total available outflow volume to required outflow volume for the entire network for all states during the period of analysis. Thus.

$$R_v = \left( \frac{\sum_j V_j^{\text{avl}}}{\sum_j V_j^{\text{req}}} \right) = \left( \frac{\sum_j q_j^{\text{avl}} t_j}{\sum_j q_j^{\text{req}} t_j} \right) \quad (14.13)$$

In which  $V_j^{\text{avl}}$  is the available volume at demand node  $j$ ;  $V_j^{\text{req}}$  is the required flow at demand node  $j$ ;  $q_j^{\text{avl}}$  is the available discharge rate at demand node  $j$ ;  $q_j^{\text{req}}$  is the required discharge rate at demand node  $j$ ;  $t_j$  is the time duration for each demand node (same for all nodes);  $j$  is denoting the demand node.

#### 14.2.4.3 System Reliability Parameter

To describe the reliability of a water distribution network by a single parameter called system reliability parameter ( $R_s$ ) is proposed in analysis. Thus

$$R_s = R_v F_t F_n \quad (14.14)$$

where,  $F_t$  = time factor; and  $F_n$  = node factor.

The time factor is defined as.

$$F_t = \frac{\sum_J P_J}{J} \quad (14.15)$$

where  $J$  = total number of demand nodes.

The node factor is the geometric mean of the node reliability parameters and is defined as.

$$F_n = \left( \prod_{j=1}^J R_{nj} \right)^{1/J} \quad (14.16)$$

### 14.2.5 Reliability Cost Ratio

The cost of a network increases with an increase in the pipe size of a network. Hence, the reliability of the system also increases. However, with a decrease in pipe sizes, the corresponding cost and reliability also decrease. A satisfactory network can be selected by the ratio of reliability to cost. Therefore, to design, a network that set of pipe sizes is selected which has the largest value of reliability cost ratio.

## 14.3 Design Example and Discussion

A design example is presented to show the applicability of the developed reliability-based model. The following subsections describe the design example, its solution, and related discussion.

### 14.3.1 Example

A water distribution pipe network is to be designed for supplying water to a residential area from one source, as shown in Fig. 14.1. In designing a water distribution network, the following conditions and data were used.

- Design period = 30 years;
- Daily use hours = 10;
- Decimal equivalent annual interest rate = 10%;
- Efficiency of pump = 70%.
- Cost of electricity  $C_e$  = Rs. 2.5/kW h;
- Repair time = 2 days.

Potential pipe sizes for each pipe by considering the minimum and maximum velocity constraints are also given in Table 14.3. The potential diameters and their

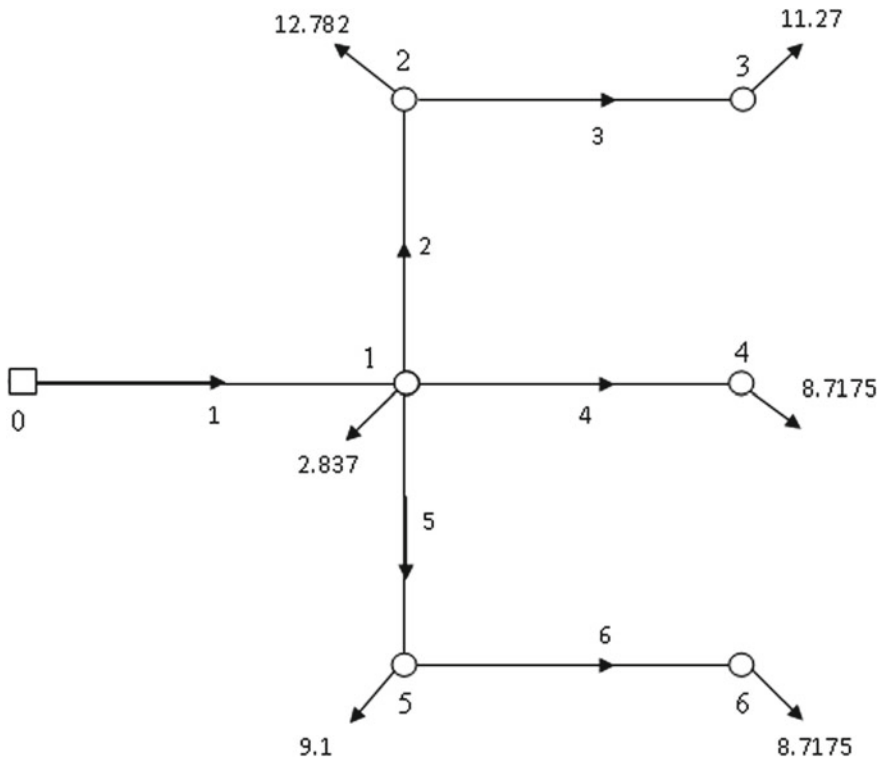


**Fig. 14.1** Branched network

unit costs of S and S centrifugally cast (spun) iron pipes (Class LA) used in the network are given in Table 14.1 as applicable in the rate analysis report of the Public Works Department for block 87 Rudrapur (Udhamsingh Nagar), Uttarakhand, India, for the year 2014–2015. Pipe break rates taken from Bhave (2003) for different pipe sizes are given in Table 14.2. Pipe lengths, diameters, and flow rates through each pipe are given in Table 14.3. The designer is interested in determining that combination of pipe sizes, which results in the maximum value of the ratio of reliability to the total annual cost for the distribution network.

### 14.3.2 Solution

The given data is used to calculate the total annual costs. Data from Table 14.1 is used to calculate the total annual cost in Rs/m by Eq. (7) for each pipe size. The pipe break rate from Table 14.2 is used to calculate the reliability parameters of the pipe network.

**Table 14.1** The unit cost of available CI pipe sizes

S. No.	Pipe diameter (mm)	Cost per unit length (Rs./m)
1	100	1075.60
2	125	1339.60
3	150	1598.10
4	200	2715.00
5	250	3543.40
6	300	4779.60
7	350	5728.90
8	400	7549.20
9	450	9141.00
10	500	10,616.70
11	600	14,845.70

**Table 14.2** Break rate data for different pipe sizes

S. No.	Pipe diameter (mm)	Break rate (breaks/km/yr)
1	100	1.36
2	150	1.04
3	200	0.71
4	250	0.39
5	300	0.07
6	350	0.05
7	400	0.05
8	450	0.04
9	500	0.04
10	600	0.04

Potential pipe sizes for each pipe by considering the minimum and maximum velocity constraints are also given in Table 14.3. The minimum permissible value is taken as 0.6 m/s and the maximum permissible value is taken as 2.5 m/s. Different possible sets of pipe networks were made by changing the diameters of different links taken from Table 14.3. Different possible sets of diameters are given in Table 14.4. The system reliability and Total annual coat was calculated for each set of pipe network.

**Table 14.3** Flow rates in different pipe links and available potential pipe sizes

Link No.	(U/S-D/S) Node	Length (m)	Flow rate (liter/s)	Pontential pipe size (mm)	Velocity (m/s)
1	0-1	1200	53.455	200	1.701
				250	1.088
				300	0.756
2	1-2	1100	24.0525	150	1.361
				200	0.765
3	2-3	1000	11.27	100	1.434
				150	0.637
4	1-4	1200	8.7175	100	1.109
5	1-5	1000	17.8475	100	2.272
				150	1.009
6	5-6	1100	8.7175	100	1.109

It was found from the solution that the ratio of reliability to total annual cost is maximum for Set XXII, which comprises pipe sizes 200, 150, 100, 100, 150, 100 mm for link 1, 2, 3, 4, 5, 6, respectively. Similarly, It was found from the solution that the ratio of reliability to capital cost is maximum for Set XXIV, which comprises pipe sizes 200, 150, 100, 100, 100, 100 mm for link 1, 2, 3, 4, 5, 6, respectively. The design results as the best set of pipe sizes for the network obtained by using two types of cost are given in Table 14.5.

From Table 14.5, it is clear that in order to arrive at a reliable network of pipes, total annual cost should be preferred in the reliability-based design for calculating the ratio of reliability to cost.

**Table 14.4** Possible sets of pipe sizes of a branched network

Set No.	Diameters (mm) for link number					
	1	2	3	4	5	6
I	300	200	150	100	150	100
II	300	200	100	100	150	100
III	300	200	150	100	100	100
IV	300	200	100	100	100	100
V	300	150	150	100	150	100
VI	300	150	100	100	150	100
VII	300	150	150	100	100	100
VIII	300	150	100	100	100	100
IX	250	200	150	100	150	100
X	250	200	100	100	150	100
XI	250	200	150	100	100	100
XII	250	200	100	100	100	100
XIII	250	150	150	100	150	100
XIV	250	150	100	100	150	100
XV	250	150	150	100	100	100
XVI	250	150	100	100	100	100
XVII	200	200	150	100	150	100
XVIII	200	200	100	100	150	100
XIX	200	200	150	100	100	100
XX	200	200	100	100	100	100
XXI	200	150	150	100	150	100
XXII	200	150	100	100	150	100
XXIII	200	150	150	100	100	100
XXIV	200	150	100	100	100	100

## 14.4 Conclusions

The developed reliability-based design methods for branched networks can be used to obtain the economic network for the desired level of reliability by considering the permissible values of minimum and maximum velocity. On comparing the ratio of reliability to cost, it was found that the use of total annual cost should be preferred over the capital cost in the design to establish the balance between reliability and economy.



**Table 14.5** Comparison of results for capital cost and total annual cost

Cost consideration	Set No	Diameter (mm)	Reliability	Cost	Reliability cost ratio
Capital cost	XXIV	200	0.959697483	9,640,990	$9.954 \times 10^{-08}$
		150			
		100			
		100			
		100			
		100			
Total annual cost	XXII	200	0.961391817	1,359,641.72	$7.070 \times 10^{-07}$
		150			
		100			
		100			
		150			
		100			

## References

Bhave (2003) Optimal design of water distribution networks. Narosa publishing house, New Delhi, India

Cunha MC, Sousa J (1999) Distribution network design optimization: simulated annealing approach. *J Resour Plan Manage* 125(4):215–221

Kettler AJ, Goulter IC (1985) An analysis of pipe breakage in urban water distribution networks. *Can J Civ Eng* 12(2):286–293

Lansey K, Mays L (1989) Optimization model for water distribution system design. *J Hydraul Eng. ASCE* 115(10):1401–1418

Maier HR (2003) Ant colony optimization for the design of distribution systems. *J Resour Plan Manage* 129(3):200–209

Rowell WF, Barnes WJ (1982) Optimal layout of water distribution systems. *J Hydraul Div. ASCE* 108(1):137–148

Savic DA, Walters GA (1997) Genetic algorithms for least-cost design of distribution networks. *J Resour Plan Manage* 123(2):67–77

Shamir U (1974) Optimal design and operation of water distribution systems. *Water Resour Res* 10(1):27–36

Simpson AR, Dandy GC, Murphy LJ (1994) Genetic algorithms compared to other techniques for pipe optimization. *J Resour Plan Manage* 120(4):423–443

Swamee DK, Jain AK (1976) Explicit equations for pipe flow problems. *J Hydraul Div* 102:657–664

Verma R, Biswal MP, Biswas A (1997) Fuzzy programming technique to solve multi-objective transportation problems with some non-linear membership functions. *J Fuzzy Sets Syst* 91(1):7–43

# Chapter 15

## An Experimental Study on the Effect of Soil Characteristics and Infiltration Rate on Hortons Decay Constant



Anupal Baruah and Rishov Barua

**Abstract** Infiltration is the process by which water on the ground surface seeps into the soil and the infiltration rate is the velocity at which water enters the soil. It continuously affects the magnitude and distribution of the overland flow and acts as an indicator of the soil's ability to allow movement of water into and through the soil profile. Field measurement of infiltration is often a monotonous task. The infiltration rates can be measured using field methods like single-ring infiltrometer and double-ring infiltrometer and can be measured by various empirical methods proposed by different researchers. In many hydrological aspects like runoff estimation, soil moisture budgeting, and irrigation, study of infiltration is very much important. Different soil characteristics such as plastic limit, liquid limit, and the liquidity index influence the infiltration capacity as well as infiltration rate. This study aims to investigate the variation of Horton's exponential decay constant with respect to the variation of soil characteristics collected from different locations in Guwahati City. In order to carry out the proposed work, three soil samples were collected from three different locations and the infiltration test has been carried out using single-ring infiltrometer ( $d = 15$  cm) to find out the infiltration rates. Results indicate that the decay constant varies considerably with the variation of the soil properties.

### 15.1 Introduction

Infiltration is the process by which water on the ground surface enters the soil surface. Precipitation falling on the soil wets down and starts penetrating into the soil. The water is driven into the porous soil by the force of gravity. First, the water wets soil grains and then the extra water moves down due to gravitational force. The rate at which a soil absorbs the water in a given time is called infiltration rate and it depends on soil characteristics such as hydraulic conductivity, soil structure, and vegetation cover. The study of infiltration comes in many hydrological problems like runoff estimation, soil moisture budgeting, and the planning of irrigation. Infiltration

---

A. Baruah (✉) · R. Barua  
IIT Guwahati, Guwahati, India

has an important place in the hydrological cycle. Johnson et al. (1979) studied that the infiltration rate has applications, such as liquid waste disposal, evaluation of potential septic tank disposal fields, leaching and drainage efficiencies, irrigation requirement. Champatiray (2014) found that four types of setup can be used in ring infiltrometer, i.e., open single or double-ring infiltrometer and sealed single or double-ring infiltrometer. Abbaspour (2007) performed a laboratory test to investigate the infiltration rate of soil samples for different particle sizes. Bapeer (2011) finds that the infiltration capacity results coincide with the acquired Liquid limit and Plastic limit, indicating that the grain size highly affects the infiltration capacity. Raghunath (2006) investigated the effect of land use in heavy clayey soil on soil infiltration rate by using double-ring infiltrometer. Based on the results, it appears that the initial infiltration rate depended mainly on the water content in heavy clayey soil and was additionally affected by the amount of cracks caused by the plant root and earth movement. Kumar (2014) found that soil conditions effects infiltration rate. From the graphs of infiltration rates against the time, it is found that initial infiltration rates were high and decreased with time up to constant.

The spatial variation of the soil properties and its effect on the infiltration characteristics has been investigated in this work. This study also investigates the influence of soil particle size on Horton's decay constant.

## 15.2 Methodology

In order to carry out the experimental work, three different locations have been selected in the Narengi area, Guwahati, Assam (Figs. 1 and 2). The soil samples have been collected from the respective study area and particle size distribution curves are prepared as shown in Figs. 3, 4 and 5. The infiltration rate is examined from the single-ring infiltrometer test. The ring is driven below the soil approximately 15–17 cm, and the water is poured into the ring gradually. The water depth is measured using a steel scale. Water is poured from the top using a graduated jar and the amount of water added with respect to time is noted. The infiltration rate is noted till it becomes constant (Tables 15.1 and 15.2).

## 15.3 Results and Discussion

To find out the decay constant from the infiltration rate, the following equation is used

$$i = i_c + (i_0 - i_c)e^{-k.t} \quad (15.1)$$

where

**Fig. 15.1** Infiltrometer installed at the Study Area-1



- $i$  infiltration rate at time  $t$ , mm/hr;  
 $i_0$  initial infiltration rate, mm/hr;  
 $i_c$  final infiltration rate, mm/hr;  
 $k$  rate constant in dimension of time,  $t$  ( $1/t$ ).

In this method, a simple regression procedure which was proposed by Mudia-reet al. (2011) was adapted to estimate the Horton's decay constant ' $k$ ' of the Horton infiltration model from the field measured values, it basically involves the determination of the value of ' $k$ ' as the slope of the line that best fit between  $\ln y$  and elapsed time ( $t$ ). From Eq. 15.1

$$\Rightarrow i - i_c = (i_0 - i_c) e^{-k.t} \quad (15.2)$$

$$\Rightarrow (i - i_c)/(i_0 - i_c) = e^{-k.t} \quad (15.3)$$

Taking Logarithm on both sides—

$$\Rightarrow \ln ((i - i_c)/(i_0 - i_c)) = -k.t \quad (15.4)$$

**Fig. 15.2** Infiltrometer installed at the Study Area-2



**Table 15.1** Values of 'k' for different soil samples

Soil sample	Soil sample A	Soil sample B	Soil sample C
Value of 'k'	2.32	4.19	4.25

$$\begin{aligned} \text{Let, } y &= (i - i_c)/(i_0 - i_c) \\ \Rightarrow \ln y &= -k.t \end{aligned} \tag{15.5}$$

After plotting, the average value of 'k' for each soil sample has been found by the above-mentioned procedure. Different soil characteristics, from the samples, are evaluated from the laboratory experiments. The variation of the particle sizes from the collected samples is presented in Fig. 3a–c.

From the particle size distribution curve for the three samples, it is observed that  $D_{50}$  for the first two samples, it is approximately equal to 1mm. However, for the third sample (Sample C), it is higher than 1mm indicating the presence of coarser particles in that region. Figure 4a–c indicates that the rate of infiltration rate decreases with the increase in time and finally reaches an equilibrium state. From these curves, it is noticed that the rate of variation of the infiltration characteristics is primarily dependant on the soil particle size as in the case of sample C the infiltration rate curve reaches the equilibrium state within a very short duration as compared to the other

**Table 15.2** Different soil characteristics for different soil samples

Location	Natural water content(%)	Liquid limit	Plastic limit	Plasticity index	Effective size			Co-efficient of uniformity	Co-efficient of curvature	K
					D10	D30	D60			
Assam Down Town University	5.68	27.73	22.41	5.32	0.36	0.54	0.94	2.61	0.86	2.3
Narengi	17.98	40.03	24.88	22.05	0.44	0.78	1.5	3.41	0.92	4.19
Amgoan	23.05	52.04	25.92	28.99	0.45	1.18	3.55	7.89	0.87	4.25

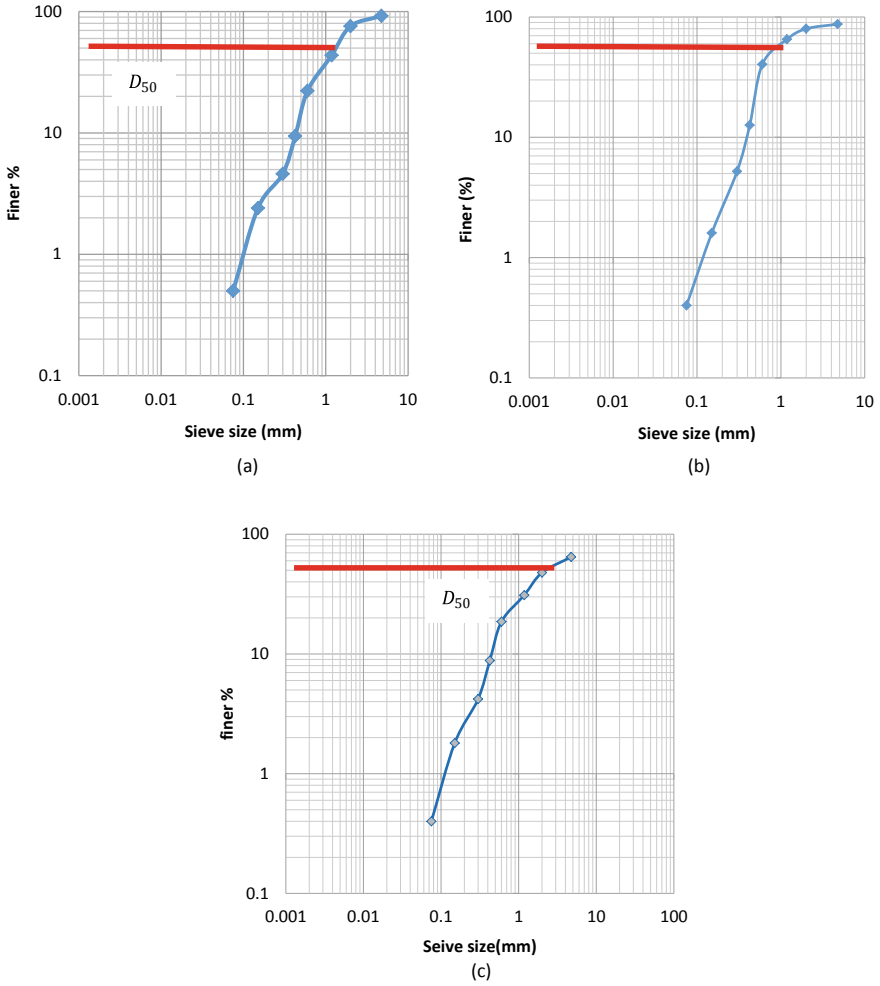
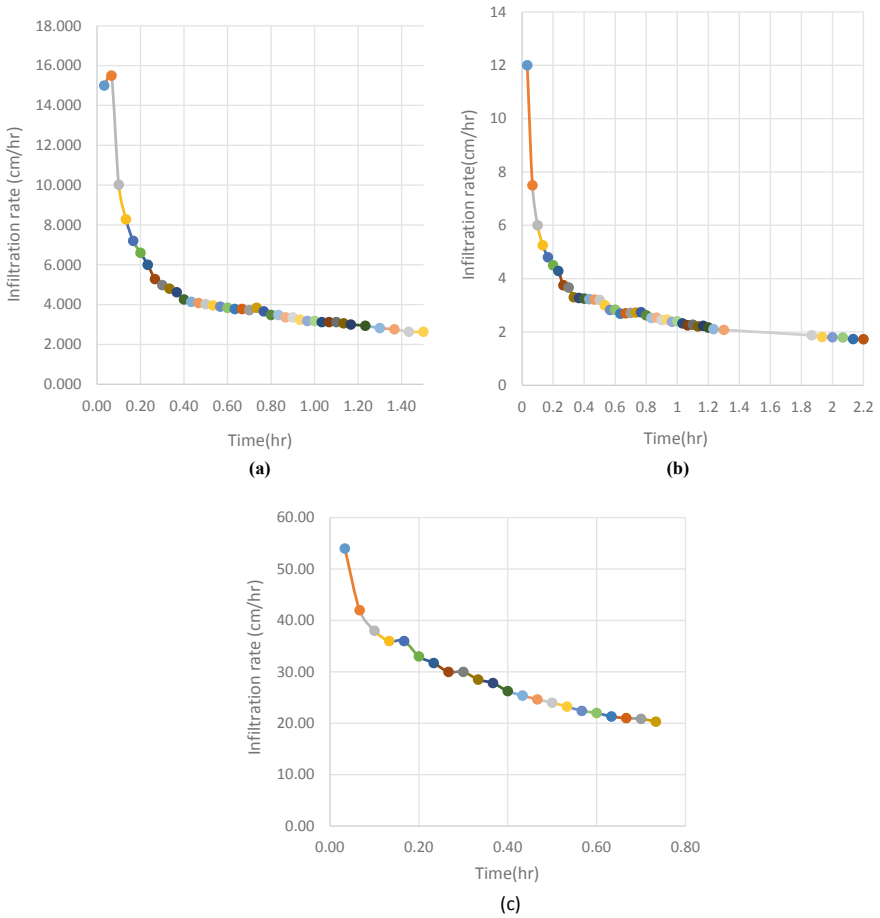


Fig. 15.3 Particle size distribution graph for a Soil Sample A b Soil Sample B c Soil Sample C

two samples. From the experimental plot (Fig. 5a–c), it is observed that Horton’s decay parameter varies with the soil properties.

### 15.4 Conclusion

In this work, an experimental study has been conducted to investigate the influence of soil parameters on the infiltration rate. Three different samples have been collected and particle size analysis was carried out. A single-ring infiltrometer is used to check



**Fig. 15.4** Infiltration rate vs cumulative time for soil **a** Sample A **b** Sample B **c**

the variation of infiltration rate with respect to time (hr). It is found that the soil particle size immensely affects the infiltration parameters. The study can be further extended by considering the rainfall data in the analysis.



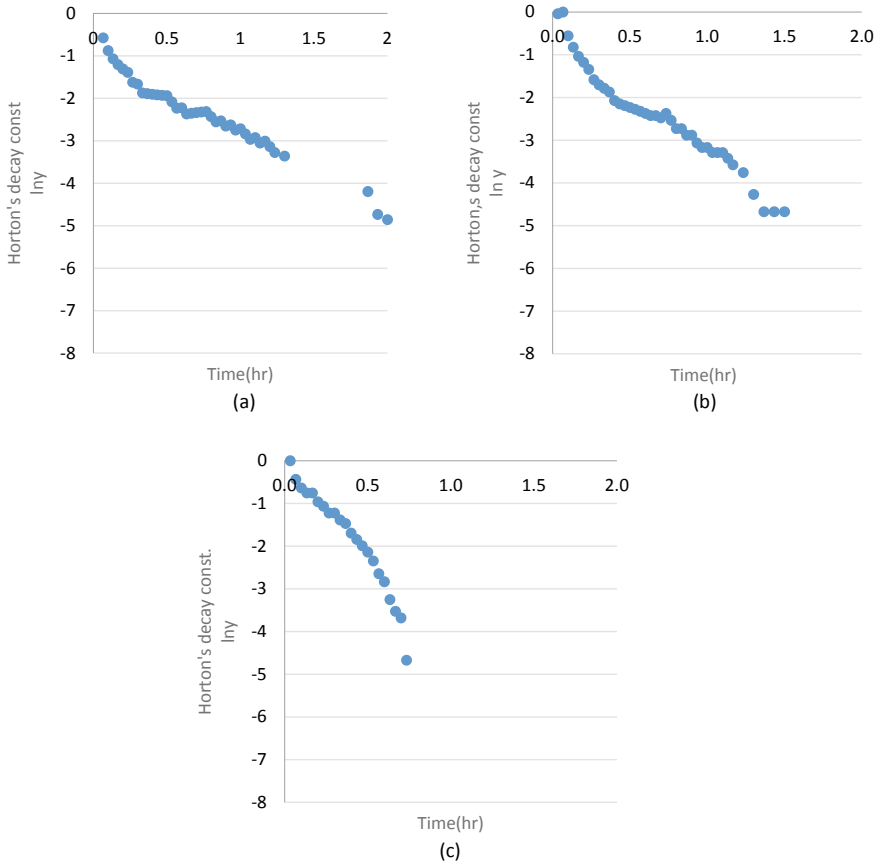


**Fig. 15.5** Horton's decay const versus time (hr) **a** Sample A **b** Sample B **c** Sample C

## References

- Abbaspour KC, Yang J, Maximov I, Siber R, Bogner K, Mieleitner J, Srinivasan R (2007) Modelling hydrology and water quality in the pre-alpine/alpine Thur watershed using SWAT. *J Hydrol* 333(2–4):413–430
- Bapeer GB (2011) The study of infiltration rate and atterberg limits of soils in Koi Sanjaq City, Erbil Governorate, Kurdistan Region, North Iraq. *Iraqi Bull Geol Min* 7(2):41–55
- Champatiray A (2014) Experimental study for determination of infiltration rate of soils in field using double ring infiltrometer (Doctoral dissertation)
- Johnson CB, Mannering JV, Moldenhauer WC (1979) Influence of surface roughness and clod size and stability on soil and water losses. *Soil Sci Soc Am J* 43(4):772–777
- Mudiare OJ, Abdulkadir A, Wuddivira MN, Abdu N (2011) Use of horton infiltration model in estimating infiltration characteristics of an alfisol in the Northern Guinea Savanna of Nigeria. *J Agric Sci Technol A* 1(2011):925–931
- Raghunath HM (2006) *Hydrology, principles, analysis and design*. New Age International Publishers

# Chapter 16

## Genetic Algorithm for Minimization of Variance of Pipe Flow-Series for Looped Water Distribution Networks



Shweta Rathi and Rajesh Gupta

**Abstract** Several measures for reliability assessment have been developed to incorporate in the design of looped water distribution networks (WDNs). The reliability measures that do not account network performance under failure conditions are easy to evaluate and also easy to incorporate in the design. However, they provide poor representation of system reliability. On the other hand, performance-based reliability measures require more computational efforts and direct incorporation in optimization algorithms is difficult. Therefore, several surrogate measures like resilience index, surplus head, surplus power, etc., have been suggested to reduce computational efforts and easy incorporation in design. Rathi et al. (<https://ojs.library.queensu.ca/index.php/wdsa-ccw/article/view/12036>, 2018) critically analyzed the analytical method and observed that it may fail to provide minimum variance. They concluded that only magnitude of flow should be considered in obtaining the variance. Further, for feasibility of design solution, loop flows must be acyclic. In this study, a new formulation and a novel methodology based on Genetic Algorithm is proposed to fix flows in various pipes for minimizing variance of pipe flow-series subject to the satisfaction of flow continuity at different nodes. Two benchmark problems are considered for illustration of proposed methodology. It is observed that the new methodology based on GA provided minimum variance pipe flows without any prior knowledge of flow direction. A linear programming (LP)-based design methodology available in literature for design of WDNs with fixed flows is used to compare the level-one redundant design solutions for FOWN in Washington DC based on flow-distribution by minimizing the variance using analytical method with that obtained by the proposed GA-based optimization method.

---

S. Rathi (✉) · R. Gupta

Department of Civil Engineering, Visvesvaraya National Institute of Technology, Nagpur 440010, India

## 16.1 Introduction

The performance of a looped water distribution network (WDN) is affected by various abnormal conditions such as those arising due to component failure or uncertainties in various input parameters. How well, a WDN can perform under various conditions can be indicated through its reliability. A simplest way to quantify reliability is through level of redundancy (Ormsbee and Kessler 1990; Agrawal et al. 2007; Gupta et al. 2015) defined as its capacity to sustain component failure condition without affecting performance in part or full. Thus, a level-one redundant system can sustain any single-pipe-failure. The level of redundancy provides discrete value of reliability as 0, 1, and 2 and so on, and fails to quantify in between. Several performance-based approaches that quantify the reliability using certain indices such as system reliability (Bao and Mays 1990) node, volume and network reliability factor (Gupta and Bhawe 1994), failure index (Tanyimboh et al. 2016), and so on, which quantify the reliability between 0 and 1 have been proposed. These indices depict network capacity to work under different conditions in a better way. However, their incorporation in design methodology requires lot of computation efforts. Recently, several surrogate measures of reliability, for example, network resilience (Todini 2000; Prasad and Park 2004; Liu et al. 2016; Creaco et al. 2016), surplus power (Vaabel et al. 2006), Tsallis entropy (Singh and Oh 2015), flow entropy (Tanyimboh and Templeman 1993) have been suggested to simplify reliability-based design process. In a similar attempt, Martinez (2007) suggested network design based on flow uniformity in each loop. Flow uniformity is considered to provide better network performance in the case a pipe is isolated for repairs. Gupta et al. (2014) compared cost of level-one redundant designs of few networks taken from the literature which were designed using flow-distribution models of Tanyimboh and Templeman (1993), Bhawe and Gupta (2004), Suribabu and Neelakantan (2005), and Chiong (1985). It was observed that flow-distribution selected by minimizing variance (Chiong 1985) provided the minimum cost for achieving level-one redundancy. Rathi et al. (2017) studied the influence of pipe flow distribution quantified through variance of flow-series on cost and reliability with two simple networks. Network reliability was observed to be more when the variance of flow-series was less and was maximum when variance of flow-series was minimum.

Martinez (2007) proposed an analytical method to obtain pipe flows that provide minimum variance of flow-series. A critical analysis of analytical method carried out by Gupta et al. (2018) and Rathi et al. (2018) showed that analytical method may fail in providing the minimum value of variance. Gupta et al. (2018) and Rathi et al. (2018) illustrated that there are an infinite set of possible flow distributions for any looped network that will satisfy the node continuity equations and hence there are an infinite set of possible variances. Only three flow distributions considered in Rathi et al. (2018) for illustration and results of analytical method are discussed. Further, limitations of analytical method and new formulation for minimizing the variance of flow-series in looped water distribution are also discussed. We critically analyzed the analytical method and observed that it may fail to provide minimum variance.

We concluded that only magnitude of flow should be considered in obtaining the minimum value of variance. Further, for feasibility of design solution, loop flows must be acyclic. In this paper, the new mathematical formulation of variance optimization problem is suggested with necessary conditions and a new methodology based on GA is used for obtaining optimal flow distribution (pipe flows) to minimize variance of flow-series without any knowledge of flow direction. Global minimum value of variance is obtained using GA. Two benchmark problems, namely, two-loop network from Kadu et al. (2008) and a network of the Federally Owned Water Main (FOWM) System of Washington D.C. from Ormsbee and Kessler (1990) are considered for illustration of proposed methodology. Further, methodology proposed by Gupta et al. (2015) is considered herein which was suggested for level-one redundant design using Linear Programming for flow-distribution obtained by minimizing variance using analytical method. Herein, optimized flow-distribution by minimizing variance using GA is used and better design is found for illustrative FOWN system.

## 16.2 New Formulation for Minimum Variance

Martinez (2007) formulated the problem of minimizing the variance of pipe flow-series as

$$\text{Min } V_Q = \frac{1}{N} \left( \sum_{x=1}^N (Q_x - \bar{Q}_x)^2 \right) \quad (16.1)$$

$$\text{Subjected to } \sum_{\substack{x \text{ connected} \\ \text{at node } j}} Q_x - q_j = 0, \text{ for all } j = 1, \dots, J \quad (16.2)$$

where  $N$  = number of pipes in the network;  $Q_x$  = flow in any pipe  $x$ ;  $\bar{Q}_x$  = mean of pipe flow-series; and  $q$  is the demand at node  $j$ . When flow directions in different pipes are not known, these are suitably assumed and the final solution is obtained which may consist of some negative values. The negative value implies flow in opposite to the assumed direction and hence objective function of Eq. (16.1) should consider only magnitude.

Using a single loop network, analytical method is suggested by Martinez (2007). He showed that for minimum variance “the algebraic summation of pipe flows in every loop to be zero while satisfying the continuity equations at all the nodes.” He further claimed that unique solution is obtained irrespective of the chosen flow direction. Gupta et al. (2018) and Rathi et al. (2018) analyzed that the loop-flow equations that require the summation of loop flows should be zero for each loop is not a sufficient condition for insuring a minimum variance of flows solution. The main drawback in the analytical method is that flow opposite to the direction obtained by analytical methods is considered negative in evaluating the variance.

In Rathi et al.'s (2018) study, it is seen that the optimization model solved using generic NLP provided minimum variance when correct flow direction was known. However, to know the flow directions in priori that would result in minimum variance will be difficult in a large network. The problem is considered for solving with GA. The pipe flows are taken as decision variable. As discussed earlier, both  $\overline{Q}_x$  and  $V_Q$  are obtained by considering only the magnitude of flow values in different pipes. Further, additional conditions which assure all pipe flows in any closed loop are not cyclic (all clockwise or all anti-clockwise) are imposed from hydraulic consideration.

Thus, the problem of minimizing the variance of pipe flow-series for solving using GA is modified as

$$\text{Min } V_Q = \frac{1}{N} \left( \sum_{x=1}^N (|Q_x| - \overline{Q}_x)^2 \right) \quad (16.3)$$

Further, flow-directions in different pipes of a loop should not be same, i.e., all clockwise or anti-clockwise, as this may not allow algebraic summation of head loss in a loop to be zero. Hence, acyclic condition for flows in each loop needs to be imposed along with continuity equations as in Eq. (16.2) as above. Note that when direction of flow in all pipes are correctly known, the solution will contain all positive values of  $Q$  and the solution will be same whether we solve problem defined by Eqs. (16.1) and (16.2), or by Eqs. (16.3) and (16.2). In a small network, the same can be achieved by trial and error method. However, a general method is required for solving large network problems. Genetic algorithm-based method is proposed herein.

Instead, the all flow values irrespective of direction should be considered as positive when determining the variance of flows. The only restriction that needs to be imposed is that the flow direction in all pipes of any loop should not be same, i.e., all clockwise, or all anti-clockwise. We illustrated that there are an infinite set of possible flow distributions for any looped network that will satisfy the node continuity equations and hence there are an infinite set of possible variances.

### 16.3 Genetic Algorithm

GA works on the Darwin principle of ‘‘Survival of fittest’’ (Goldberg 1989) and has been applied successfully to obtain several near optimal solution of combinatorial optimization problem. Although global optimal solution is not guaranteed, the chances of reaching to global optimal solution are more. The main advantage in GA is that the objective function and the constraints are considered separately. Population is generated and each member of population is checked for constrained conditions. Fitness of a member not satisfying the constraint is reduced by applying penalty in an attempt to allow it to evolve in next generation with lesser chance of selection. GA parameters are used to develop new population and the entire process of evaluation,

selection, and modification continues for several generations. At the end of which best solution is considered as optimal solution.

The GA is observed to be more suited for discrete optimization problems in which decision variable takes only discrete values. However, it can also be used for solving optimization problem in which decision variables are of continuous nature.

GA optimization proposed herein is based on the following.

### ***16.3.1 Decision Variables***

Instead of considering all pipe flows as decision variable, only one pipe flow from each loop is considered as basic unknowns. Knowing their values, flows in the remaining pipes of the network can be obtained by satisfying the continuity equation. This helps in reducing the number of unknowns as well as satisfies the constraints equations requiring flow-balancing at each node.

### ***16.3.2 Representation Scheme***

Herein, real coding scheme, real numbers are used for representation of coding length of string. The initial population is generated using random number generators for each member considering the range of minimum and maximum value of flow in the network.

### ***16.3.3 Feasibility Conditions and Penalty Function***

Each solution is checked for acyclic flow conditions. If all the flows in a particular loop are in clockwise or anti-clockwise directions, then penalty is adopted. Penalty function consisted of a multiplier ( $M$ ) by which the variance is increased.

### ***16.3.4 Fitness Function***

Fitness of each string is evaluated using reciprocal of variance values (Eq. 16.3) along with penalty multiplier. Larger the variance, smaller will be its fitness.

### 16.3.5 *Reproduction Operator*

A tournament selection scheme is used as reproduction operator (Goldberg and Deb 1991). In tournament selection, a pair of solutions is selected from the population and the best one is retained. By repeating the process for specified number of times, a mating pool of suitable size is formed which will contain multiple copies of good potential solutions and a few or no copy of less fit solutions.

### 16.3.6 *Crossover*

Crossover operator creates new off-springs after selection by partially exchanging information among parent-solution strings. Herein, two parent strings, say P1 and P2, are selected at random from the original population. A crossover position (site) is chosen at random between the first and last bit of the parents. Two off-springs O1 and O2 are created from P1 and P2, respectively, in which all the substrings before the crossover points remain same as in respective parent, and beyond the crossover site averaged values from P1 and P2 are used. The probability of crossover is taken as 95%.

### 16.3.7 *Elitism*

Elitism operator preserves the best and a few better solutions from a current population for the next population. Herein, two best solutions are preserved in each generation.

Several GA runs were carried out with a different population size and numbers of generation. Best solution from different GA run is reported.

A simple two-loop network from Kadu et al. (2008) as shown in Fig. 16.1 is considered to illustrate the methodology and compare the values of variance of flow-series by analytical and GA-based proposed optimization method. Node 1 is a source node with constant HGL of 100 m. The demand nodes are labeled 2–6, the minimum required HGLs in meters, and the nodal demands in m<sup>3</sup>/min are shown in Fig. 16.1. Links 1–7 and their lengths in meters given in parenthesis are shown along the links. The head loss is given by the Hazen–William formula, in which exponents of discharge  $Q$  and diameter  $D$  are taken as 1.85 and 4.87, respectively. For head loss and Length in meters,  $Q$  in m<sup>3</sup>/min, and  $D$  in mm; multiplying constant is  $2.234 \times 10^{12}$  in Hazen–William's Equation. The Hazen–Williams coefficient is 130 for all links.

The network involves seven unknowns. However, if pipe discharges in one pipe of each loop are known, others can be determined by applying continuity equations. Therefore, pipe flows  $Q_6$  and  $Q_7$  from loop 1 and loop 2 are considered unknown



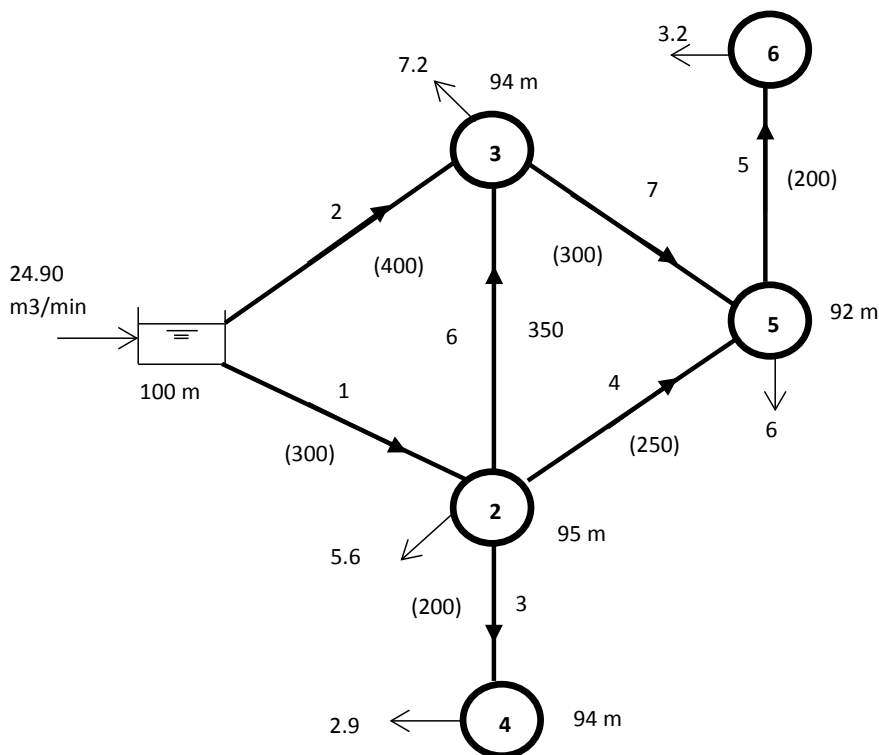


Fig. 16.1 Single source water distribution network (Kadu et al. 2008)

and others are calculated based on the flow values of these pipes. This helped in reducing the number of unknowns and handling the constraints defined by continuity equations, Eqs. 16.2. Other constraints requiring acyclic flow conditions in each loop are handled using penalty. Different GA parameters as in Table 16.1 are set for obtaining optimal flow distribution. Several GA runs were carried out. The optimal solutions obtained for five times are reported in Table 16.1.

The minimum value of variance is obtained as 16.9416, for example, network using GA. The pipe discharges in different pipes are using GA as:  $Q_1 = 11.0320 \text{ m}^3/\text{min}$ ,  $Q_2 = 13.868 \text{ m}^3/\text{min}$ ,  $Q_3 = 2.9 \text{ m}^3/\text{min}$ ,  $Q_4 = 5.8427 \text{ m}^3/\text{min}$ ,  $Q_5 = 3.2 \text{ m}^3/\text{min}$ ,  $Q_6 = -3.3107 \text{ m}^3/\text{min}$ ,  $Q_7 = 3.3573 \text{ m}^3/\text{min}$ . Negative sign indicates that a flow direction in pipe 6 is from 3 to 2 instead of 2 to 3. It is observed that flow direction in pipe 6 is opposite to that of assumed direction. Different GA parameters are set for obtaining optimal flow distribution and Several GA runs is carried out and optimal solutions are obtained with five times run using proposed GA based methodology and the parameters are reported in Table 16.1. Network is designed using LP techniques and its cost is evaluated as Rs. 52,08,195. Reliability using demand satisfaction ratio are obtained and calculated as 0.722

**Table 16.1** GA parameters used

GA parameters	Description
Selector	Tournament
Crossover type	As discussed in 3.6
Penalty multiplier	Fitness value is multiplied by 1000 times
Elitism	The best chromosome in each generation is included unchanged in the next generation
Crossover probability	0.95
Mutation probability	0.05
Number of generations	20
Population size	200
Running time	Maximum of 5 min for network 1 on PC Intel(R) Core(TM)2 Duo CPU E8500 @ 3.16 GHz, 4.00 GB memory

Using the analytical methodology suggested by Martinez (2007) of satisfying the loop-flow equations with node flow continuity equations, the following flow-distribution is obtained as  $Q_1 = 12.6125 \text{ m}^3/\text{min}$ ;  $Q_2 = 12.2875 \text{ m}^3/\text{min}$ ;  $Q_3 = 2.9 \text{ m}^3/\text{min}$ ;  $Q_4 = 4.4375 \text{ m}^3/\text{min}$ ;  $Q_5 = 3.2 \text{ m}^3/\text{min}$ ;  $Q_6 = 0.325 \text{ m}^3/\text{min}$ ; and  $Q_7 = 4.7625 \text{ m}^3/\text{min}$ . The obtained flow directions are as shown in Fig. 16.1. The variance is obtained as  $V_Q = 19.5108$ . Cost and Reliability (in terms of demand satisfaction ratio) values are also obtained using analytical method by Chiong's model. Obtained values of cost and reliability are 46,97,871 and 0.714 respectively. Thus, the lower variance resulted in higher network reliability.

## 16.4 Optimal Design for Level-One Redundancy

As discussed earlier, several methodologies have been suggested for design of level-one redundant systems (Ormsbee and Kessler 1990; Gupta and Bhave 1996; Agrawal et al. 2007; Dongare and Gupta 2014; Gupta et al. 2015). Gupta et al. (2015) used LP technique for flow-distribution obtained by analytical method of minimizing variance of flow-series. The two-phase method iterative starts by considering head loss constraints only for all-pipe-working conditions to get optimal design in first phase. This design is checked for one-pipe failure conditions in second phase and most critical failure condition is identified. Head loss constraints for the most critical failure condition are additionally included in the first phase and process of adding the constraints in LP formulation continues till satisfactory design for one-pipe failure condition is obtained.

The method of Gupta et al. is used herein in which initial flow distribution is obtained by minimizing the variance of flow-series using GA. However, while including the failure conditions, constraints are written with observed flows during failure condition with latest design. The Federally Owned Water Main (FOWM)

System of Washington D.C. (Ormsbee and Kessler 1990) is selected to illustrate an application of proposed methodology and comparison of results.

### 16.5 Illustrative Network

The FOWM System, as shown in Fig. 16.2, has one source and 16 demand nodes. Ormsbee and Kessler (1990) labeled Source Node as S (herein labeled 1) and demand nodes 1 through 16 (herein labeled 2 through 17). Links are labeled 1–22, the same as done by Ormsbee and Kessler. Interested readers may find the link and the node details from Ormsbee and Kessler (1990). Ormsbee and Kessler (1990) provided designs for three loading conditions: (1) Maximum day demand loading condition (MDD); (2) Peak-hour demand loading condition (PHD); and (3) Maximum day demand plus fire loading condition (MDDF). Herein, comparison is shown in detail with PHD condition.

This FOWM system is strengthened by the proposed GA-based model and method. Initially, Links 20–22 are added as done by Ormsbee and Kessler (1990) so as to achieve topologic redundancy of level-1. The minimum required HGL,  $H_j^{min}$ , is considered as the node elevation. The desirable HGL,  $H_j^{des}$ , at a node is taken as the node elevation plus the required pressure head of 28.16 m (40 psi) for the MDD and PHD conditions, and 14.08 m (20 psi) for the MDDF condition.

Assuming normal working condition, a flow-distribution corresponds to minimum variance is obtained in the network using Proposed GA-based model as given in Col. 2 of Table 16.2. Corresponding flow directions are shown in Fig. 16.2. The LP problem is then formulated using these flows and associated distribution. A pair of path head loss constraints is written for demand nodes 3, 4, 7, 10, 12, and 17. The two paths

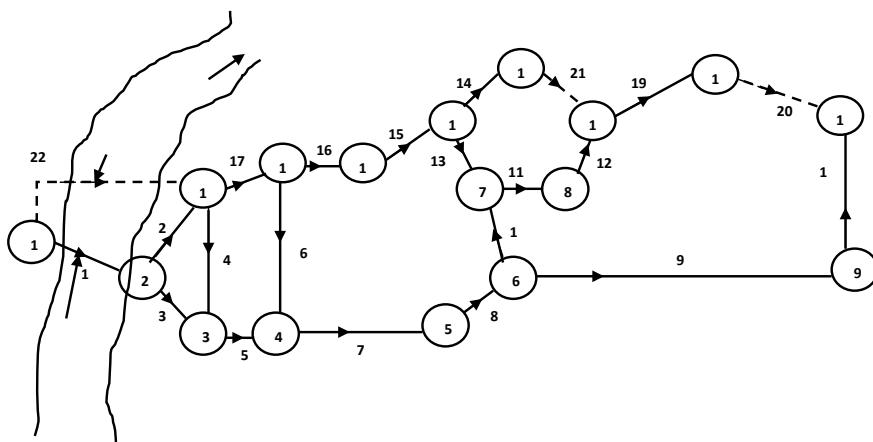


Fig. 16.2 FOWM system layout

**Table 16.2** Flow-distribution used in LP for PHD loading

Pipe	Pipe flows in m <sup>3</sup> /min using proposed model during absence of			
Number	No-pipe	Pipe-1	Pipe-16	Pipe-9
(1)	(2)	(3)	(4)	(5)
1	12.0439	–	16.3038	16.2347
2	6.0372	–3.6635	6.528	11.7671
3	6.0067	3.6635	9.7758	4.4676
4	5.7275	3.4297	8.8018	3.3650
5	9.5642	4.9230	16.4078	5.6625
6	0.8966	0.4758	1.9172	0.5762
7	9.5908	4.5278	17.454	5.3678
8	6.0708	1.0068	13.933	1.8467
9	3.4175	6.4497	6.6492	–
10	2.6534	5.4428	7.2838	1.8467
11	4.1584	1.1765	2.1933	6.0889
12	4.1584	1.1763	2.1923	6.0889
13	2.9251	8.0393	–3.6715	5.6622
14	3.0641	3.0128	1.7975	4.5501
15	7.4092	12.4722	–0.454	11.6323
16	7.8592	12.9262	–	12.0863
17	9.0558	13.7050	2.2202	12.9657
18	1.9975	5.0297	5.2292	–1.42
19	4.3825	1.3493	1.1498	7.7989
20	3.8725	0.8383	0.6388	7.2879
21	1.6441	1.5928	0.3775	7.2879
22	8.9361	20.9870	4.6832	3.1301

Note Negative flow values shows flow in opposite to direction shown in Fig. 16.2

from source node 1 to node 3 are 1–2–3 and 1–17–3. The two paths from source node to node 4 are 1–2–3–4 and 1–17–16–4 and so on. The cost of the network in iteration 1 is \$2,377,566. The network is found completely satisfactory under 0-pipe failure condition but found deficient under the individual failure of pipes 1, 9, 15, 16, and 17 with available flows of 13.0571, 20.226, 16.89, 16.5148, and 18.2128 m<sup>3</sup>/min, respectively, against the requirement of 20.98 m<sup>3</sup>/min. This showed that failure of pipe 1 is most critical. So, another flow-distribution is obtained using EPANET analysis by removing pipe 1 as shown in Col. 3 of Table 16.3. Now, the network is redesigned by adding the path constraints of this new flow-distribution along with those previously considered. The improved solution is given in Table 16.3 (Iteration 2). The cost of network becomes \$3,508,723 in the second iteration. The network is now found deficient under failure of pipes 9, 15, 16, 17, and 18, having the failure of

**Table 16.3** Design details for PHD loading using proposed methodology

Iteration	Flow-distribution for failure of	Design solution			Cost in \$	Deficient under failure of	Critical pipe				
		Pipe	Length (m)	Dia (mm)							
1	No-pipe	19	296.117	254.0	2,377,566	1, 9, 15, 16, 17	1				
		20	914.40	254.0							
		21	355.28	254.0							
		22	2571.97	355.6							
			1085.63	406.4							
2	No-pipe	19	111.721	254.0	3,508,723	9, 15, 16, 17, 18	16				
	Pipe-1	20	914.40	254.0							
		21	355.28	254.0							
		22	1414.41	457.2							
			2216.17	609.6							
3	No-pipe	7	904.561	304.8	4,331,155	1, 9, 17, 18	9				
	Pipe-1		448.749	355.6							
	Pipe-16	8	409.73	406.4							
		19	114.223	254							
		20	914.4	254.0							
		21	335.28	254.0							
		22	1597.77	457.2							
			2059.83	609.6							
	4	No-pipe	7	904.561				304.8	4,429,122	1, 17	1
		Pipe-1		448.749				355.6			
Pipe-16		8	409.73	406.4							
Pipe-9		19	341.38	254							
		20	608.88	254.0							
			305.52	304.8							
		21	355.28	254.0							
		22	1597.77	457.2							
			2059.83	609.6							
5		Pipe-1	5	147.147	304.8	4,459,430*	-	-			
	Pipe-16	7	1311.59	304.8							
	Pipe-9	8	409.73	406.4							
		19	341.38	254							
		20	611.91	254.0							
			302.49	304.8							
		21	355.28	254.0							
		22	1506.21	457.2							

(continued)

**Table 16.3** (continued)

Iteration	Flow-distribution for failure of	Design solution			Cost in \$	Deficient under failure of	Critical pipe
		Pipe	Length (m)	Dia (mm)			
			2151.39	609.6			

\* Solution obtained in fourth trial

pipe 16 as most critical. The same procedure is again followed by obtaining the flow-distribution for failure of pipe 16 (Col. 4, Table 16.3) and by imposing additional path constraints in the LP model for improving design (Table 16.3, Iteration 3). After the third iteration, the cost increased to \$4,331,155 and network is found deficient under failure of pipes 1, 9, 17, and 18. Now, failure of pipe 9 is most critical among all three. The network is redesigned by incorporating additional path constraints for flow-distribution obtained by EPANET analysis after removing pipe 9. The network cost now becomes \$4,429,122. Herein, NFA showed that the network is still deficient during failure of pipes 1 and 17. Thus, the flow-distribution obtained during failure of pipe 1 using NFA is more critical than that used during design. Therefore, the design is repeated with the flow distribution obtained in the analysis. The revised cost becomes \$4,459,430. The total cost of the network becomes \$4,459,430, and the network is found completely satisfactory during failure of any single pipe. Complete design is given in Table 16.3. Comparison of the design is given in Table 16.4.

## 16.6 Summary and Conclusions

A critical analysis was carried out by Rathi et al. (2018) for the analytical method of obtaining the flow-distribution for minimum variance of flow-series in a looped network. Analytical method was observed to fail in providing minimum variance of flow-series. A new modified formulation and a methodology based on Genetic algorithm are suggested in this study to obtain the correct solution to the problem of minimizing variance of flow-series. It is observed that the new methodology based on GA is very efficient to provide minimum variance pipe flows without any knowledge of flow direction. Application to a two-loop problem designed using LP for flow-distribution obtained by proposed methodology showed higher reliability values in terms of demand satisfaction ratio as compared to design obtained with flow-distribution from analytical method. Gupta et al. (2015) used a two-phase iterative method for level-one redundant optimal design based on flow-distribution obtained by analytical method. Herein, this methodology is used with flow-distribution obtained by proposed GA-based method. Level one redundant design solution for the illustrative FOWM System shows that design obtained herein has the minimum cost as compared to several other design solutions based on different methods.

**Table 16.4** Design solutions by proposed methodology and comparison with others

Link	Solution by Ormsbee and Kessler (1990)—Solu. A		Solution by Agrawal et al. (2007)—Solu. B		Solution by Dongre and Gupta (2014) methodology—Solu. C		Solution by Gupta et al. (2015) methodology—Solu. D		Solution by proposed methodology—Solu. E	
	Diameter (mm)	Length (m)	Diameter (mm)	Length (m)	Diameter (mm)	Length (m)	Diameter (mm)	Length (m)	Diameter (mm)	Length (m)
Case: peak-hour loading condition										
3	406.4	452.40	—	—	—	—	—	—	—	—
5	406.4	440.43	—	—	—	—	—	—	304.8	147.15
—	304.8	138.68	—	—	—	—	—	—	—	—
6	—	—	355.60	486.63	304.8	486.63	254.00	322.14	—	—
7	304.8	1341.12	254.00	1353.31	254.0	1353.31	304.80	1310.60	304.8	1311.60
8	457.2	490.73	355.60	490.73	355.6	490.73	406.40	490.73	406.4	490.73
19	304.8	341.38	254.00	341.38	254.0	341.38	254.00	341.38	254.00	341.38
20	355.6	914.40	304.80	914.40	304.8	914.40	304.80	695.36	304.80	302.49
—	—	—	—	—	—	—	254.00	219.04	254.00	611.91
21	406.4	335.28	254.00	335.28	254.0	335.28	254.00	355.28	254.00	355.28
22	609.6	2993.14	609.60	3657.60	609.6	3657.60	457.20	1038.14	457.20	1506.21
—	457.2	664.46	—	—	—	—	609.60	2619.46	609.60	2151.39

Note Network cost: Case 1: Solution A = \$5,339,886; Solution B = \$4,980,178; Solution C = \$4,939,405; Solution D = \$4,669,069; Solution E = \$4,459,430

## References

- Agrawal ML, Gupta R, Bhavne PR (2007) Reliability-based strengthening and expansion of water distribution networks. *J Water Resour Plan Manage* 133(6):531–541. [https://doi.org/10.1061/\(ASCE\)0733-9496\(2007\)133:6\(531\)](https://doi.org/10.1061/(ASCE)0733-9496(2007)133:6(531))
- Bao Y, Mays LW (1990) Model for water distribution system reliability. *J Hydraul Eng* 116:1119–1136
- Bhavne PR, Gupta R (2004) Optimal design of water distribution networks for fuzzy demands. *Civ Eng Environ Syst* 21(4):229–245. <https://doi.org/10.1080/10286600412331314564>
- Chiong C (1985) Optimization of closed loop network. PhD thesis CIH, CUJAE University, Havana, Cuba (in Spanish)
- Creaco E, Franchini M, Todini E (2016) The combined use of resilience and loop diameter uniformity as a good indirect measure of network reliability. *Urban Water J* 13(2):167–181. <https://doi.org/10.1080/1573062X.2014.949799>
- Dongre S, Gupta R (2014) GA for optimal upgrading of water distribution networks for level-1 redundancy. In: EWRI world environment and water resource congress 2014 organized by ASCE, Portland, June 1–5, 2014
- Goldberg DE, Deb K (1991) A comparative analysis of selection schemes used in genetic algorithms. *Proc of foundations of Genetic Algorithms 1 (FOGA-1)*:69–93
- Gupta R, Bhavne PR (1994) Reliability analysis of water distribution systems. *J Environ Eng* 120(2):447–460. [https://doi.org/10.1061/\(ASCE\)0733-9372\(1994\)120:2\(447\)](https://doi.org/10.1061/(ASCE)0733-9372(1994)120:2(447))
- Gupta R, Burle YL, Abdy Sayyed MAH, Rathi S (2014) Comparison of flow-distribution models for design of water distribution networks with redundancy. *Procedia Eng* 89:848–855. [18.2c4b3917.1532500561.df6812d](https://doi.org/10.1016/j.procs.2014.03.017)
- Gupta R, Kakwani N, Ormsbee L (2015) Optimal upgrading of water distribution network redundancy. *J Water Resour Plan Manage* 141(1). [https://doi.org/10.1061/\(ASCE\)WR.1943-5452.0000529](https://doi.org/10.1061/(ASCE)WR.1943-5452.0000529), [https://doi.org/10.1061/\(ASCE\)WR.1943-5452.0000434](https://doi.org/10.1061/(ASCE)WR.1943-5452.0000434)
- Gupta R, Palod N, Rathi S (2018) Defining the variance minimizing problem with respect to looped water distribution networks. In: HYDRO 2018, NIT Patna, Dec 18–21, 2018
- Kadu M, Gupta R, Bhavne PR (2008) Optimal design of water networks using a modified genetic algorithm with reduction in search space. *J Water Resour Plan Manage* 134(2):147–160
- Liu H et al (2016) Reliability surrogate measures for water distribution system design: comparative analysis. *J Water Resour Plan Manage* 143(2):04016072
- Martínez J (2007) Quantifying the economy of water supply looped networks. *J Hydraul Eng* 133(1(88)):88–97. [https://doi.org/10.1061/\(ASCE\)0733-9429\(2007\)133\(1\(88\)\):88-97](https://doi.org/10.1061/(ASCE)0733-9429(2007)133(1(88)):88-97)
- Ormsbee L, Kessler A (1990) Optimal upgrading of hydraulic network reliability. *J Water Resour Plan Manage ASCE* 116(6):784–802. [https://doi.org/10.1061/\(ASCE\)0733-9496\(1990\)116:6\(784\)](https://doi.org/10.1061/(ASCE)0733-9496(1990)116:6(784))
- Prasad TD, Park NS (2004) Multi-objective genetic algorithms for design of water distribution networks. *J Water Resour Plann Manage*. 130(2):73–82. [https://doi.org/10.1061/\(ASCE\)0733-9496\(2004\)130:1\(73\)](https://doi.org/10.1061/(ASCE)0733-9496(2004)130:1(73))
- Rathi S, Palod N, Gupta R, Ormsbee L (2017) Influence of pipe discharges on cost and reliability of looped water distribution networks. In: Urbanization challenges in emerging economies ASCE India conference, 12–14 December, New Delhi, India
- Rathi S, Gupta R, Ormsbee L (2018) Directional dependency of minimum variance of flow series in looped water distribution networks. In: 1st international WDSA/CCWI 2018, joint conference, Kingston, Ontario, Canada, July 23–25, 2018. <https://ojs.library.queensu.ca/index.php/wdsa-ccw/article/view/12036>
- Singh VP, Oh J (2015) A Tallis entropy-based redundancy measure for water distribution networks. *Physica A: Statistical Mechanics and its Applications*. 421:360–376. <https://doi.org/10.1016/j.physa.2014.11.044>



- Suribabu CR, Neelakantan TR (2005) Design of water distribution networks by a non-iterative two stage optimization. *ISH J Hydraul Eng* 112(2):18–39. <https://doi.org/10.1080/09715010.2005.10514779>
- Tanyimboh TT, Templeman AB (1993) Optimum design of flexible water distribution networks. *Civ Eng Syst* 10(3):246–258. <https://doi.org/10.1080/02630259308970126>
- Tanyimboh TT, Siew C, Saleh S, Czajkowska A (2016) Comparison of surrogate measures for the reliability and redundancy of water distribution systems. *Water Resour Manage* 30:3535–3552. <https://doi.org/10.1007/s11269-016-1369-8>
- Todini E (2000) Looped water distribution networks design using a resilience index based heuristic approach. *Urban Water* 2(2):115–122. 18.2c4b3917.1532502247.e54c1bd
- Vaabel J, Ainola L, Koppel T (2006) Hydraulic power analysis for determination of characteristics of a water distribution system. In: *Water distribution systems analysis symposium*

# Chapter 17

## Applications of Building Information Modelling for Water Infrastructure Development



M. P. Rahla Rabia and D. Sathish Kumar

**Abstract** Development of a generalized representation of a water network for a building at minimal cost, that follows water conservation practices is an explicit requirement for a sustainable infrastructure design. A fast, integrated, easily sharable, sophisticated and parametric integrated building modelling and analysis tool is required to attain this objective. Currently, 2D CAD-based manual modelling and analysis is carried out in different application platform to meet the local regulations. This technique may cause inherent errors due to its 2D representation of elements, resulting in monetary loss and wastage of time. Building Information Modelling (BIM) is a promising technology that minimizes such errors due to its enhanced dimensional capabilities. BIM provides a single realistic virtual representation of an infrastructure project, supported by an object-oriented relational database management system. BIM has broad applications in infrastructure development and management in the urban water sector. It includes water supply and drainage network planning, modelling, analysis and flood management. The capabilities of BIM can be enhanced further by integrating it with Geographic Information System (GIS) where the analysis and modelling can be extended to the regional level. However, awareness of technology among the stakeholders and standardization of the technique is essential for further progress.

### 17.1 Introduction

Plumbing system design and water conservation analysis is an inevitable part of almost all building construction and city planning. Building construction and city water planning are becoming complex due to growing demand and the technical advancements in the water supply and drainage elements. Inclusion of sustainable and climatic conditions for design calculation lead to tedious computations. A considerable volume of data is to be processed to achieve water conservation and energy efficiency for a building design by an expert team. Conventionally, plumbing designers

---

M. P. R. Rabia · D. S. Kumar (✉)

Department of Civil Engineering, National Institute of Technology, Calicut, India  
e-mail: [sathish@nitc.ac.in](mailto:sathish@nitc.ac.in)

conduct calculation by following the approved design codes, and the final results are presented in Two-Dimensional Computer-Aided Design (2D CAD) drawings. As the traditional design process is manual and lacks collaborative approach, it leads to insufficient documentation, visualization and coordination. Considerable rework, loss in productivity, time consumption for iterative studies, and estimation errors are the major drawbacks of the conventional system. The changes in a 2D CAD drawing of plumbing design must be manually updated in other interrelated drawings, schedule and schematics, which lead to possible compounding errors and time loss. A consolidated building model is absent in 2D CAD, leading to poor documentation and data collection difficulties for city-level water network planning and conservation. These drawbacks can be nullified to a great extent by the adoption of Information and Communication Technologies (ICT) such as Building Information Modelling (BIM) in Architecture, Engineering and Construction (AEC) industry (Sacks et al. 2011; Lee et al. 2006; Singh et al. 2011).

BIM is a digital *n*th dimensional representation for establishing and managing data for projects across its entire span from initial planning to demolition. It thus helps to provide more potential approaches to planning, designing, visualizing, coordinating, preserving and handling and sharing our construction necessities. Many researchers have pointed out that the efficacy of BIM can be realized by the substantial increase in the productivity, which is attained by abating several construction losses, cost and time interruptions (Sacks et al. 2011). Multi-disciplinary inquiries of construction information are easily achievable through BIM, as the model has an intelligible spatial, temporal and functional association between building artefacts. The appealing characteristic of BIM includes alleviating rework and calculation time, augmenting productivity, minimizing labour costs and improving the work product's constancy. The comparison between traditional and BIM-based water system modelling is illustrated in Fig. 17.1.

The importance and scope of BIM are increasing worldwide, and it has been embraced by many governments and industries for infrastructure management. They promote and enforce BIM modelling for their construction schemes bestowed to the respective building system modelling necessities. The topmost three important BIM-based activities involved in the water sector as specified by Smart Market BIM Research report by Dodge Data and Analytics are the creation of bid/construction drawings (72%), clash detection and avoidance (70%), quantities and cost estimation integration (40%). The same report states that around 88% of developers deployed BIM in the water sector for water and wastewater treatment systems and about 52% for hydro-electric systems (The Business Value of BIM for Water Projects 2018). Software packages for BIM applications are available from popular software vendors like Autodesk (Revit), ACCA software (Edificius), Trimble (Tekla), etc. Implementation of BIM 5D technology for hard fill dam construction was endeavoured in Valsamiotis Dam in Chania using Autodesk's Revit software (Nasika 2016). Using WaterGEMS, a reduction of 5 to 10% of the overall design time has been attained for the water distribution network's comprehensive design. The cost of fittings and pipeline has also reduced down by the same amount (BIM Benley's WaterGEMS 2018). Prominent manufacturers of sanitary fixtures provide BIM data with complete

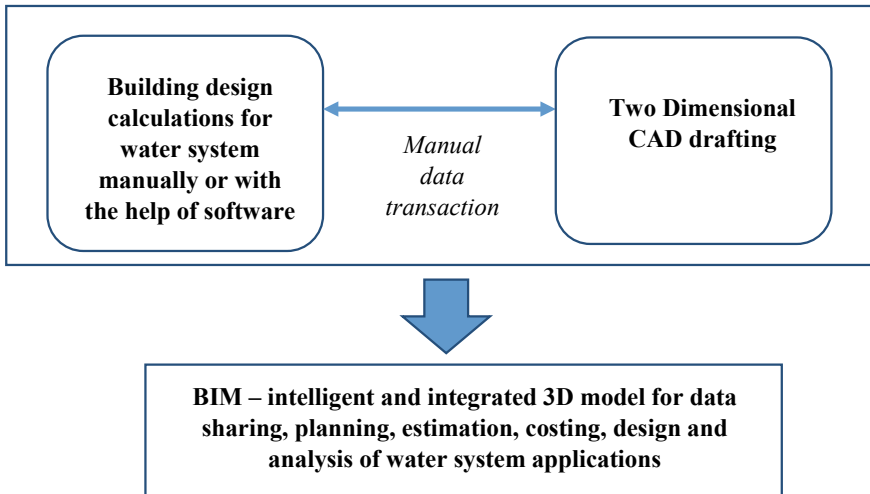


**Fig. 17.1** 2D CAD versus BIM for water network modelling

specifications for their products which aid the designers and contractors effectively (GROHE 2018). The major applications of BIM for water system analysis and design are presented in Table 17.1.

The following section presents the benefits of BIM-based water network system design and analysis. Section 17.3 presents BIM-based plumbing and water system integrated analysis. BIM and GIS combined water infrastructure planning is presented in Sect. 17.4. A case study is discussed in Sects. 17.5 and 17.6 deals with limitations of BIM. Conclusions are summarized in Sect. 17.7.

**Table 17.1** Major applications of BIM for water system analysis and design

Classification	Applications
Water system design	Modelling and design calculations of water distribution and drainage network, nth dimensional modelling and renderings, bill of quantities and schedules of equipment, costing, material specification and prefabrication data, water network schematic diagram, dam modelling
Water system analysis	Building water consumption, automated code checking, sustainability assessment such as LEED, coordination between systems, financial and conservation iterative studies, pipe pressure loss calculations, greywater reclamation, rainwater harvesting and artificial recharge quantification
GIS	Possibilities of BIM- and GIS-based water system infrastructure planning at a city level, flood analysis, flood damage assessments, city water information modelling and smart built environments

## 17.2 BIM Water Network System Design Potentials

BIM technology has profound application in the field of building water network system design. With the assistance of BIM applications, water network modelling is carried out with the spatio-temporal and functional characteristics between its elements. The 3D modelling of plumbing systems is carried out on the architectural model by following design codes. The basic elements of water networks are realistic and smart such that design calculations and modelling become easier. BIM plumbing components are required to be arithmetically interlinked by default. A single network model is capable of conducting necessary computations according to regulations and provide qualitative and quantitative assessments. As BIM modelling offers a 3D environment, coordination with other trades, isometric plumbing drawings and sectional views complying with the actual building dimensions are obtained in a split second. BIM objects can be set to detect the hosting errors and clearance requirements automatically. Therefore, errors can be minimized during the design process. By default, the BIM design model can provide quantities according to user specifications (Wei et al. 2017; BIM4Water 2017).

Before the actual construction begins, by analysing the virtual 3D digital model interface, checking between systems and coordination can be done, and the best alternative can be chosen. As the information system stores all the details of material with specifications, quantity computations can be automated using the BIM tools as per user directives. A schedule can be prepared as similar to the pivot table tool of MS Excel. One of the process benefit derived from BIM is prefabrication. Since the representation of the BIM-based model is realistic, prefabrication becomes easier (Korman and Lu 2011). As the prefabrication process involves representatives from different disciplines to detect and solve the issues, the model will aid better coordination.

Application Programming Interfacing (API), a software intermediary is provided by most BIM applications to satisfy user demands. Specific tools based on the user requirement can be developed by following the procedures laid out by the BIM software. Such tools are used to extract necessary information from the BIM model and display the results after processing it. Redundant tasks such as code checking and customized estimation and costing can be done quickly. Autodesk's Revit allows user to develop add-in tools as macros or external add-in tools by writing programs in .NET supported languages such as Visual Basic and C#. The modelling is to be standardized to avoid gross errors and to extract the information accurately. Martins and Monteiro (2013) developed a BIM-based automated tool for water supply systems. The tool allows automatic code checking that is associated with a database. It aids to manage activities efficiently, and thus reduces the cost of reconfiguration as well as labour.

### 17.3 BIM-Based Water System Analysis

BIM offers a coherent building model comprising all components of building realistic virtual models and the interrelationship between the components. Such a model is required to conduct integrated water analysis of the building. Analysis can be done faster without data loss, and automated tools increase efficiency compared to traditional methods. Assessments are possible by using pre-defined average values according to building types and regional standards or using user-estimated values. The primary water-based calculations done using BIM are pressure loss analysis, connectivity checking, rainwater and greywater potential assessments, iterative water consumption measurements, clash detection and all other types of possible user-defined API-based analysis (Azhar et al. 2011). The BIM modelling if accurate, then the analysis can probably be done in a fraction of time by BIM authored tools with a detailed report for further improvements. Developers can concentrate on sustainability and water conservation revisions in-depth as redundant iterative studies are done by BIM automatically. Matured BIM applications provide platforms for different water-based analysis such as Autodesk's Green Building Studio and "Water System Calculations" by Intelika Ltd. (BEST Directory 2018; Water System 2018). As BIM can provide geometrical information, it is possible to conduct micro flood analysis for a project site integrating other applications such as ArcGIS (Amirebrahimi et al. 2015).

### 17.4 BIM and GIS Combined Water Infrastructure Planning and Management

As BIM is a detailed and easily sharable digital data repository of a project, many methods exist to extract necessary information by using technologies such as data mining using API. Major applications of BIM- and GIS-based hydrological assessment and management are shown in Fig. 17.2. Required data can be exported to the GIS platform from related BIM file for regional level water planning, operation and maintenance, data standardization of water consumption and flood management. BIM- and GIS-based integrated planning have the capability for more realistic replication of the water distribution network. It leads to developing an optimal method for water handling at an early stage of the project itself. An independent optimization at the building level and further optimization at the city level are possible using BIM- and GIS-based modelling (Farooq et al. 2017). Better decision-making, change management and visualization are possible in BIM- and GIS-based planning approach. The same can be extended to city-level water planning.

Optimal planning of urban water distribution system considering the technical, economic, behavioural and environmental factors is a challenge for developers. A suitable method for effective integrated planning of urban water distribution networks is by optimizing hydrological requirements both inside and outside of a building in

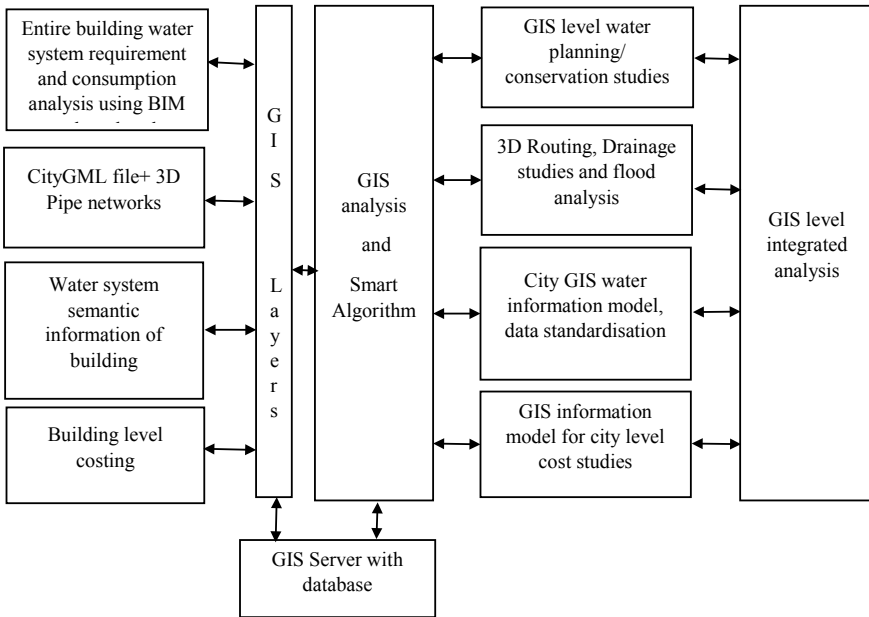


Fig. 17.2 BIM and GIS integrated water system modelling

the early stage of the project. Virtual modelling is necessary to conduct water system analysis for the entire building (semantic modelling concept). Semantic information system based bottom-up approach planning is a preferred method for handling the large volume of data from every water artefact in an urban system. The integration of BIM and GIS can accomplish the same. BIM and GIS integration aids for real-time operation and maintenance management in a water distribution network as material specification, location of the fault, historical data and cost requirements are readily obtainable from the combined model. The integration also shows its potential for flood management purposes. When independent use of BIM and GIS may not efficiently suffice for the flood management, their integration serves the purpose (Amirebrahimi et al. 2015). From BIM model building, 3D details and water system information can be exported to GIS for flood modelling, analysis, real-time management and damage assessments. BIM and GIS integrated flood modelling and management, considering a dam break scenario was proposed by Rabia and Kumar (2018).

By gathering building-level water consumption design calculations from the BIM model and comparing with the actual water consumption from the monthly bill after construction for different archetypes in GIS, it is possible to obtain the normalized water consumption at a regional level. As gathering information from BIM files are easy, cost incurred for standardization will be less, and it will act as base information for the policymakers.

## 17.5 Case Study

The case study for a plumbing network modelling and its GBS-based water system integrated analysis are presented in this section. A novel API has been developed for water outlet estimation. An Autodesk Revit-based plumbing design for an office with 178 users is considered, and a part of a building's plumbing network is shown in Fig. 17.3. Blue colour indicates cold water conduits and red indicates hot water conduits. Pressure loss analysis for the same network is carried out using the Revit in-built tool and is shown in Fig. 17.4. The same model is analysed using GBS to calculate water usage and costs. The results are shown in Fig. 17.5.

For getting user-defined plumbing information, an Autodesk Revit-based Add-In tool is developed. Using Microsoft Visual Studio C# language, the coding was carried out as per Autodesk Revit API guidelines for filtering plumbing fixtures and processing the information. It is used for calculating the number of outlets and water requirements. The user interface and the case study results are shown in Fig. 17.6.

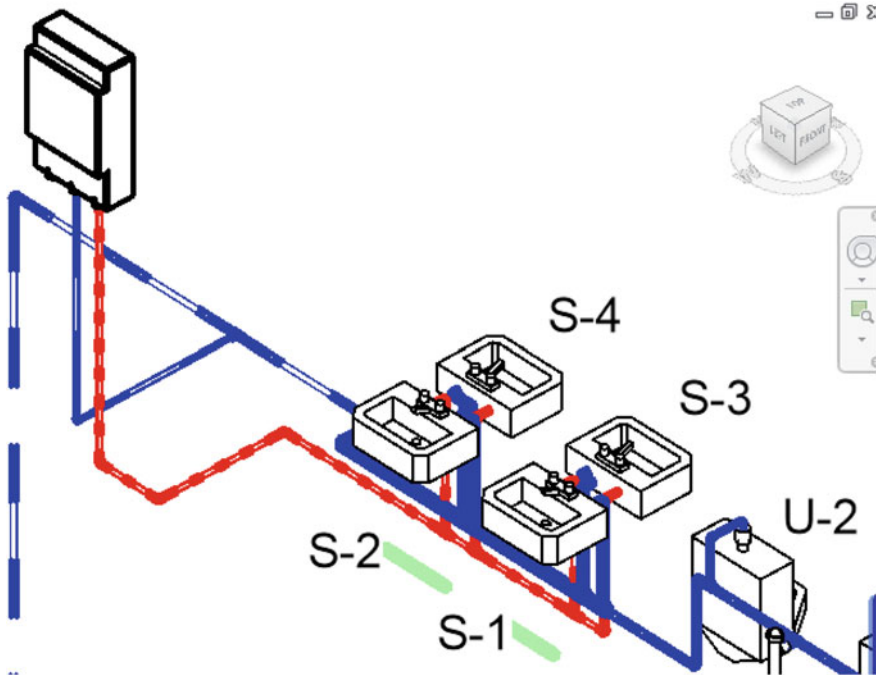


Fig. 17.3 A sample water distribution system in Autodesk Revit (adopted from Autodesk)



Domestic Cold Water 1										
<b>System Information</b>										
System Classification	Domestic Cold Water									
System Type	Domestic Cold Water 1									
System Name	Domestic Cold Water 1									
Abbreviation										
Fluid Type	Water									
Fluid Temperature	16 °C									
Fluid Dynamic Viscosity	0.00112 Pa-s									
Fluid Density	998.9114 kg/m³									
<b>Total Pressure Loss Calculations by Sections</b>										
Section	Element	Flow	Size	Velocity	Velocity Pressure	Length	K Coefficient	Friction	Total Pressure Loss	Section Pressure Loss
1	Pipe	1.7 L/s	25 mmø	4.3 m/s	-	70	-	4926.85 Pa/m	346.7 Pa	185301.0 Pa
	Fittings	1.7 L/s	-	4.3 m/s	9070.1 Pa	-	1.387559	-	12585.3 Pa	
	Plumbing Fixture	1.7 L/s	-	-	-	-	-	-	172369.0 Pa	
2	Pipe	2.2 L/s	25 mmø	5.5 m/s	-	1100	-	8279.00 Pa/m	9108.7 Pa	9108.7 Pa
	Fittings	2.2 L/s	-	5.5 m/s	15241.3 Pa	-	0	-	0.0 Pa	
								14300.70		

Fig. 17.4 Pressure loss calculation

LEED® Water Efficiency
Help

**Water Usage and Costs**

Total: **3,715,467 L / yr**    \$5,004 / yr

Indoor: 2,652,082 L / yr    \$4,270 / yr

Outdoor: 1,063,385 L / yr    \$734 / yr

Net Utility: **3,715,467 L / yr**    \$5,004 / yr

Source: AWWA Research Foundation 2000 Residential / Commercial and Institutional End Uses of Water.

**Water Usage Estimator**  
Change inputs and click "Estimate" to update Water Usage and Costs.

Estimate   Save   Reset

**Indoor Water Factors**

Number of People: 178  
(Typical people for this building type/size: 168)

Percent of Time Occupied (%): 26

**General Information**

Project Title: rme\_advanced\_sample\_project (2)

Run Title: rme\_advanced\_sample\_project Analysis

Building Type: Office

Floor Area: 4,454 m²

**Unit Water Prices**

Water: 0.69 \$ / m³    Sewer: 0.92 \$ / m³

**Outdoor Water Factors**

Irrigated Area\* (m²): 1000

Timed Sprinklers: Yes

Pool: No

Other Equipment/Fixtures: No

Usage: 25 L / day

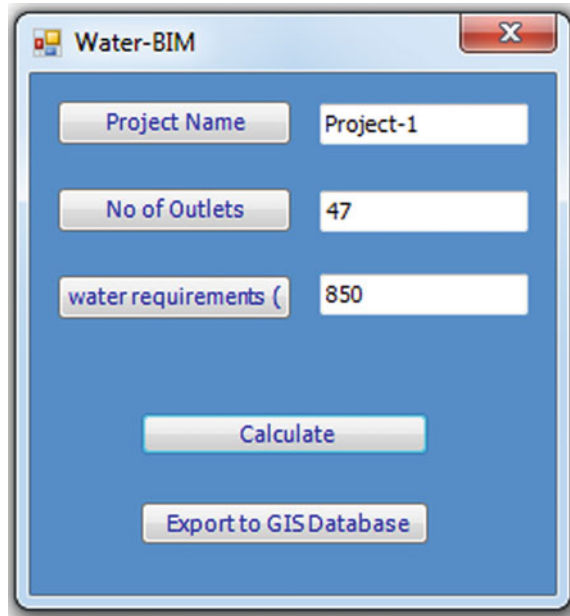
\*Irrigated area is a placeholder. Site data from Building Information Model is not incorporated.

Fig. 17.5 GBS-based water usage and cost estimation

## 17.6 Current Limitations in Implementing BIM-Based Techniques

BIM is perceived as a valuable technology and procedure to enhance productivity and surge the integration across various trades all through construction processes. The significant issues in BIM implementation are its directorial and user-centred problems. Adequate training is to be provided in order to realize the advantages of BIM-based techniques in order to reduce errors. Ceaseless support by the government and building code regulatory agencies are required for its effective execution and

**Fig. 17.6** The user interface windows form



Field Label	Value
Project Name	Project-1
No of Outlets	47
water requirements (	850

Buttons: Calculate, Export to GISDatabase

standardization. BIM initiation at different levels like State or National should be taken to get fruitful results. After adopting BIM, major hurdles are in the form of hardware upgrade costs and software costs. High Level of Detail (LoD) modelling may not be profitable for small-scale construction works such as residential buildings. BIM and GIS integrated approach may become complicated due to interoperability issues, data loss, expert and hardware requirements.

## 17.7 Conclusions

Potentials of a BIM-based system for integrated water systems modelling has been presented in this article. With the advent of BIM-based tools, water networks analysis has been simplified due to the single information repository model available for multi-disciplinary data transactions in a collaborative environment. The scope of emergent BIM technology is to be increased to maximize productivity, efficiency, value engineering and optimization. Commercial success can also be achieved through its lifecycle deployment and utilization of BIM data for regional level planning. The government should standardize the BIM application prospects in water infrastructure development and authenticated high-level research. The authorized agencies involved in policymaking should overcome the limitations as mentioned above to maximize its benefits.

## References

- Amirebrahimi S, Rajabifard A, Mendis P, Ngo T (2015) A framework for a microscale flood damage assessment and visualization for a building using BIM–GIS integration. *Int J Digit Earth* 9(4):363–386. <https://doi.org/10.1080/17538947.2015.1034201>
- Azhar S, Carlton W, Olsen D, Ahmad I (2011) Building information modeling for sustainable design and LEED® rating analysis. *Autom Constr* 20(2):217–224. <https://doi.org/10.1016/j.autcon.2010.09.019>
- BIM innovation in water network analysis with Benley's WaterGEMS (2018) [www.technicalreviewmiddleeast.com](http://www.technicalreviewmiddleeast.com); <https://www.technicalreviewmiddleeast.com/power-a-water/water-a-environment/bim-innovation-in-water-network-analysis-with-benley-s-watergems>. Accessed 23 Sep 2018
- BIM4Water (2017) BIM guidance for the water industry [Ebook]. <https://www.britishwater.co.uk/Media/Download.aspx?MediaId=1217>. Accessed 23 Sep 2018
- BEST Directory (2018) Autodesk green building studio. <https://www.buildingenergysoftwaretools.com/>; <http://www.buildingenergysoftwaretools.com/software/autodesk-green-building-studio>. Accessed 23 Sep 2018
- Farooq J, Sharma P, Kumar RS (2017) Applications of building information modeling in electrical systems design. *J Eng Sci Technol Rev* 10(6):119–128. <https://doi.org/10.25103/jestr.106.16>
- GROHE (2018) GROHE—BIM data—services for you. <https://pro.grohe.com>; <https://pro.grohe.com/ie/29013/services-for-you/bim-data/>. Accessed 23 Sep 2018
- Korman T, Lu N (2011) Innovation and improvements of mechanical, electrical, and plumbing systems for modular construction using building information modeling. *AEI* 2011. [https://doi.org/10.1061/41168\(399\)52](https://doi.org/10.1061/41168(399)52)
- Lee G, Sacks R, Eastman C (2006) Specifying parametric building object behavior (BOB) for a building information modeling system. *Autom Constr* 15(6):758–776. <https://doi.org/10.1016/j.autcon.2005.09.009>
- Martins J, Monteiro A (2013) LicA: a BIM based automated code-checking application for water distribution systems. *Autom Constr* 29:12–23. <https://doi.org/10.1016/j.autcon.2012.08.008>
- Nasika C (2016) Application of building information modeling (BIM) technologies on hardfill dam construction (Diploma). <http://www.ntua.gr/>
- Rabia R, Kumar S (2018) Integrated flood modelling and damage assessment using BIM and GIS, compendium of technical papers, vol 2. In: International dam safety conference 2018, Kerala - January 2018. [https://www.damsafety.in/ecm-includes/PDFs/Conference/IDSC2018/Compendium\\_Vol-2.pdf](https://www.damsafety.in/ecm-includes/PDFs/Conference/IDSC2018/Compendium_Vol-2.pdf)
- Sacks R, Eastman C, Lee G, Teicholz P (2011) *BIM handbook*, 2nd edn. Wiley
- Singh V, Gu N, Wang X (2011) A theoretical framework of a BIM-based multi-disciplinary collaboration platform. *Autom Constr* 20(2):134–144. <https://doi.org/10.1016/j.autcon.2010.09.011>
- The Business Value of BIM for Water Projects (2018) [www.Construction.Com](http://www.Construction.Com); <https://www.construction.com/toolkit/reports/business-value-bim-water-projects>
- Water System Calculations | Revit | Autodesk App Store (2018) <https://apps.autodesk.com>; <https://apps.autodesk.com/RVT/en/Detail/Index?id=2474350890404891568&applLang=en&os=Win64>. Accessed 23 Sep 2018
- Wei T, Chen G, Wang J (2017) Application of BIM technology in building water supply and drainage design. In: IOP conference series: earth and environmental science, vol 100, p 012117. <https://doi.org/10.1088/1755-1315/100/1/012117>

# Chapter 18

## Snow Cover Change in Kullu District Using Remote Sensing and Geographic Information System



Ashish Singh and R. K. Shukla

### 18.1 Introduction

There is a large hue and cry everywhere around the globe concerning warming and global climate change. Warming is the century scale rise of the worldwide temperature. According to IPCC's (Intergovernmental Panel on Climate Change) Fifth Assessment Report (AR5), the average temperature of earth's surface has increased to 0.85°C. Because of the rise in temperature of earth surface, snow cover is decreasing. According to recent study by the Himachal Pradesh State Council for Science, Technology and Environment's (HIMCOSTE) State Centre for Climate Change, "rapidly climate change is degrading the snow cover of Himalayan rivers originating in Himachal Pradesh". "There is an overall reduction in the area under seasonal snow cover during the winter of 2017–18 in comparison to the winter of 2010–16 period in Himachal Himalaya"—HIMCOSTE. Snow and glaciers are very important sources of freshwater because most of the earth's fresh water is stored in it in the form of snow. But due to climate change and global warming, most of the glaciers present on the earth's surface are reduced during the time span of last 100 years. Presently, 10% of the earth's landmass is covered with snow, out of which 13.9% is in Greenland, 0.51% is in North America, 0.77% is in the Himalayas, 84.16% is in the Antarctic, 0.37% is in Africa, 0.15% is in South America and 0.06% is in Europe. Snow cover is one of the most sensitive land cover over the earth's surface, that's why time-to-time monitoring, assessment as well as mapping of these is very important. The present study is an effort to find out the changes in snow cover in Kullu district (HIMACHAL PRADESH) using geoinformatic techniques.

Industrialization, increase in temperature and greenhouse effect are the main reasons for climate change. Industries emit greenhouse gases as well as harmful

---

A. Singh · R. K. Shukla (✉)

Department of Civil Engineering, Madan Mohan Malaviya University of Technology, Gorakhpur, Uttar Pradesh, India

e-mail: [drshukla\\_gkp@rediffmail.com](mailto:drshukla_gkp@rediffmail.com)

gasses that affect the natural balance of air which causes change in climate. Industrialization and population explosion causes loss of forest cover. For an ideal natural climate, there should be 33% forest cover, 33% animals and 33% human population. But by the end of twentieth century, forest cover has been reduced 15 to 16%.

Studying climate change helps to understand what causes the changes and prepares us for any natural hazard or extreme changes that can be predicted. It also helps to identify between manmade and natural causes of climate change and how that changes have an impact on human and the environment.

According to IPCC fifth assessment report (AR5), the global surface temperature increase, by the end of the twenty-first century is likely to exceed 1.5 °C relative to the 1850 to 1900 period for most scenarios, and is likely to exceed 2.0 °C for many scenarios. The average temperature in many regions has been increasing in recent decades. The global average temperature has increased by 0.2 to 0.6 degree Celsius during the last century.

## 18.2 Objectives of Study

In mountains, snow cover plays an important role in the land cover pattern. In the study of over 2,00,000 glaciers since the mid-nineteenth century, it was found that 2/3 of the current glacier melting due to human influence on the climate. This loss of mass from glaciers is caused primarily by warming over those glaciers and this warming is in turn being caused primarily by the CO<sub>2</sub> concentration in the atmosphere. “We can clearly detect an anthropogenic effect on glaciers and it’s been steadily rising over the last 100 years”, said ben Marzeion, a climate scientist at the University of Innsbruck in Austria (<https://www.independent.co.uk/climate-change/news/melting-glaciers-are-caused-by-manmade-global-warming-study-shows-9669572.html>). “In the 19th century and first half of the 20th century we observed that glacier mass loss attributable to human activity is hardly noticeable but since then it has steadily increased”, said ben Marzeion, the lead author of the study published in the journal Science. Due to change in climate, worst impact occurs in agriculture sectors because it is the most sensitive sector to climate change. The nature, growth rate and characteristics of vegetation are dependent on the climate of the region and these nature and characteristics of vegetation are also determined by the climate of the region. Increase in the mean seasonal temperature can affect the duration of many crops and hence it reduces final yield.

Therefore, the objective of the present study is to evaluate the changes in the area of snow cover during the periods 2016, 2017 and 2018. These changes can be helpful to demonstrate and correlate with the changes in annual temperatures.

## 18.3 Study Area

Kullu is a district of Himachal Pradesh, located on the bank of Beas River in Kullu valley. Kullu valley is also known as the “valley of the god” or “dev bhumi” because of the presence of a number of pilgrimage sites of the Hindus, Buddhists and Sikhs alike. It is situated between 31.9579° N and 77.1095° E with the elevation of 1279 m above sea level. Kullu has an area of 5503 sq. Km with the population of 3,79,865 (2001). The temperature observed in winter is in the range between -4 and 20° C with some snowfall. Evening and morning during winter season are very cold. Annual highest temperature in summer ranges from 24 to 34° C during May to August. July and August are the rainy seasons and have around 150 mm rainfall monthly (<https://en.wikipedia.org/wiki/kullu#climate>).

## 18.4 Observed Climatological Trend Over Study Area

### 18.4.1 Temperature

The state of Himachal shows a significant increasing trend of 0.06° C/yr. on annual mean maximum temperature and 0.02° C/yr. on annual mean temperature for the period of 1951–2010. The annual mean minimum temperatures have shown a decreasing (-0.01° C /yr.) trend over the state for the same time period (Dheeraj et al. 2016). The seasonal mean temperature trends for the 1951–2010 period shows a significant increasing trend for most seasons viz. winters (0.02° C/yr.), monsoons (0.03° C/yr.) and post-monsoon (0.02° C/yr.) but not significantly increasing for summers (0.01° C/yr.) (Dheeraj et al. 2016).

### 18.4.2 Rainfall

The trends over the district rainfall in the last 25 years have shown an increasing trend of 33.5, 54.3 and 51.5% for Kinnaur, Chamba and Lahaul and Spiti, respectively, whereas a decreasing trend of 8.7, 13.3 and 26.6% for Solang, Shimla and Sirmour, respectively (Hp-sapcc 2012, <http://www.hpccc.gov.in/>). Between 1951 and 2010, rainfall decreased by -3.26 mm/year and for the same time period seasonal rainfall for summer increased by 0.31 mm/year. Rainfall that occurred in winter, monsoon and post-monsoon season for 1951–2010 decreased by -0.18 mm/year (Hp-sapcc 2012, <http://www.hpccc.gov.in/>).

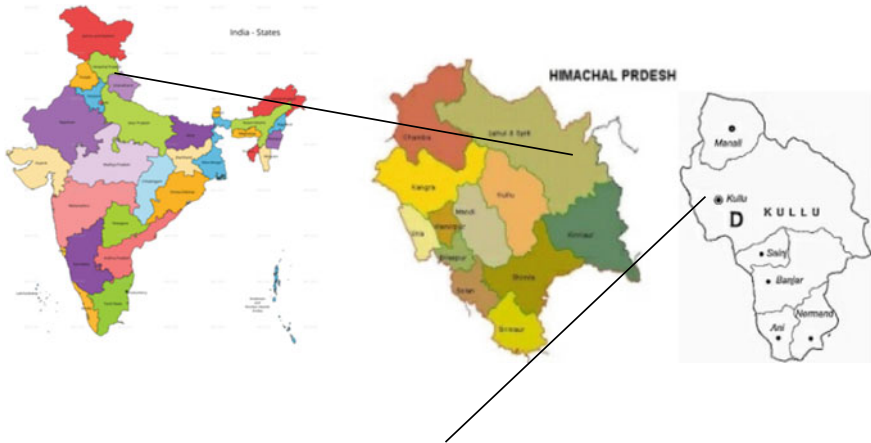


**Fig. 18.1** Location of the study area

### 18.4.3 *Snowfall and Coldwave*

Almost 22 coldwaves were found in the period of 1901–1999, out of which 18 incidents were seen in between 1978 and 1999. The analysis of different altitudes in Himachal shows the decrement of snowfall for recent 20 years of observation (Fig. 18.1).

## 18.5 Methodology

The present work is getting started by downloading the satellite image of Landsat for years 2016 and 2018. For all years, image of same month, that is, February is selected, because the month of February is quite cloudless and there is maximum snow cover in this month. Then these satellite images were resampled, resampling digitized the pixel values from the existing cell values in QGIS. QGIS is free and open source cross-platform desktop geographic information system. It finds applications that required viewing, editing and analysis of geographic data.

Snow is highly reflective in the visible part of the EM spectrum and highly absorptive in the near-infrared or shortwave infrared part of spectrum. Normalized Difference Snow Index (NDSI) is the normalized difference of two bands, one in the visible and one in the near-infrared or short-wave infrared part of spectrum (<https://ntrs.nasa.gov/archive/nasa/casi.ntrs.nasa.gov/20100031195.pdf>) Dorothy et al. 2010). Normalized Difference Snow Index (NDSI) technique is used to validate the snow cover. Normalized Difference Snow Index (NDSI) technique is used to valid the snow cover. NDSI is the difference of two bands, one in the visible and one in the near-infrared or short-wave infrared part of spectrum.

**Table 18.1** Band characteristics of Landsat

Bands	Wavelength (micrometres)	Resolution (metres)
Band 1—ultra blue (coastal/aerosol)	0.435–0.451	30
Band 2—blue	0.452–0.512	30
Band 3—green	0.533–0.590	30
Band 4—red	0.636–0.673	30
Band 5—near-infrared (nir)	0.851–0.879	30
Band 6—shortwave infrared (swir) 1	1.566–1.651	30
Band 7—shortwave infrared (swir) 2	2.107–2.294	30
Band 8—panchromatic	0.503–0.676	15
Band 9—cirrus	1.363–1.384	30
Band 10—thermal infrared (tirs) 1	10.60–11.19	100* (30)
Band 11—thermal infrared (tirs) 2	11.50–12.51	100* (30)

Source <https://landsat.usgs.gov/what-are-band-designations-landsat-satellites>

$$\text{NDSI} = (\text{green} - \text{swir}) / (\text{green} + \text{swir})$$

Band characteristics of Landsat 8 are given in Table 18.1. Now NDSI for Landsat 8 is given by

$$\text{NDSI} = (\text{band 3} - \text{band 6}) / (\text{band 3} + \text{band 6})$$

## 18.6 Results and Discussion

Figure 18.2 shows the snow cover and snow-free area in 2016. Around 32.27% (1776 km<sup>2</sup>) of study area is covered with snow in 2016. Snow-free area is about 67.73% (3727 km<sup>2</sup>).

Figure 18.3 shows the snow cover and snow-free area in 2017. Around 33.74% (1857 km<sup>2</sup>) of study area is covered with snow in 2017. Snow-free area is about 66.26% (3646 km<sup>2</sup>).



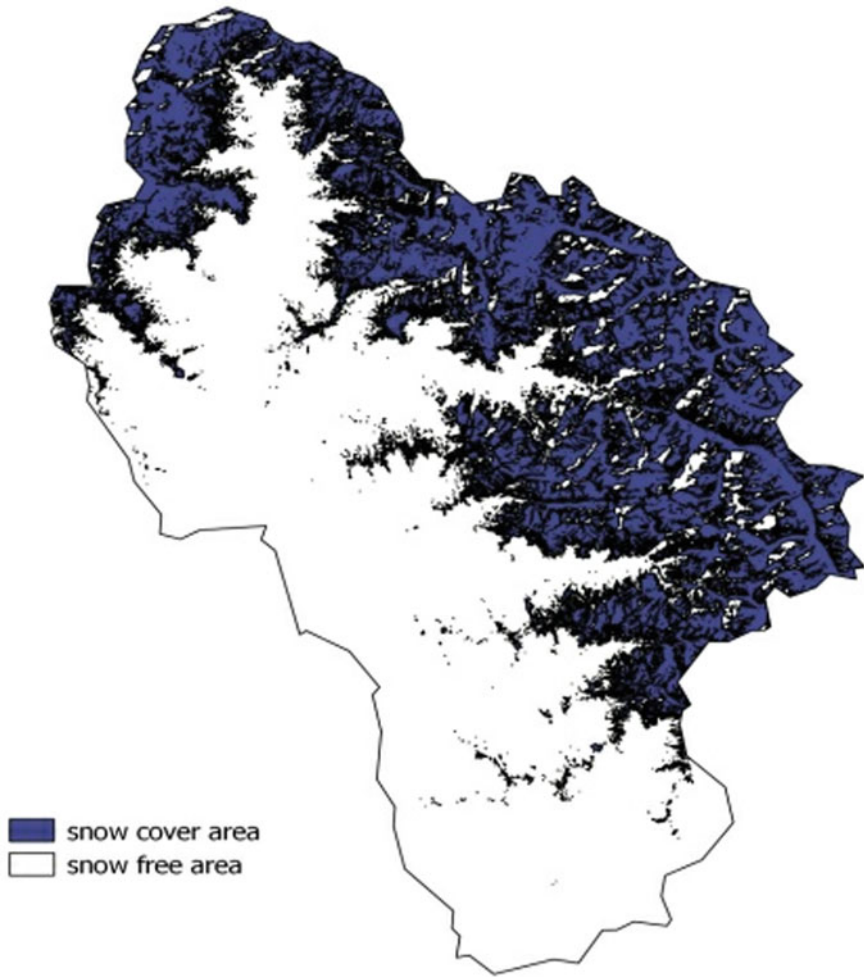


**Fig. 18.2** Snow cover in 2016

Figure 18.4 shows the snow cover and snow-free area in 2018. Around 10% (545 km<sup>2</sup>) of study area is covered with snow in 2018. Snow-free area is about 90% (4958 km<sup>2</sup>) (Table 18.2).

### 18.7 Conclusion

In the present study, it is found that the area under snow cover is declining in Kullu district. The point is validated by using geoinformatic techniques. Satellite images for the year 2016, 2017 and 2018 used for the generation of FCC (False Colour

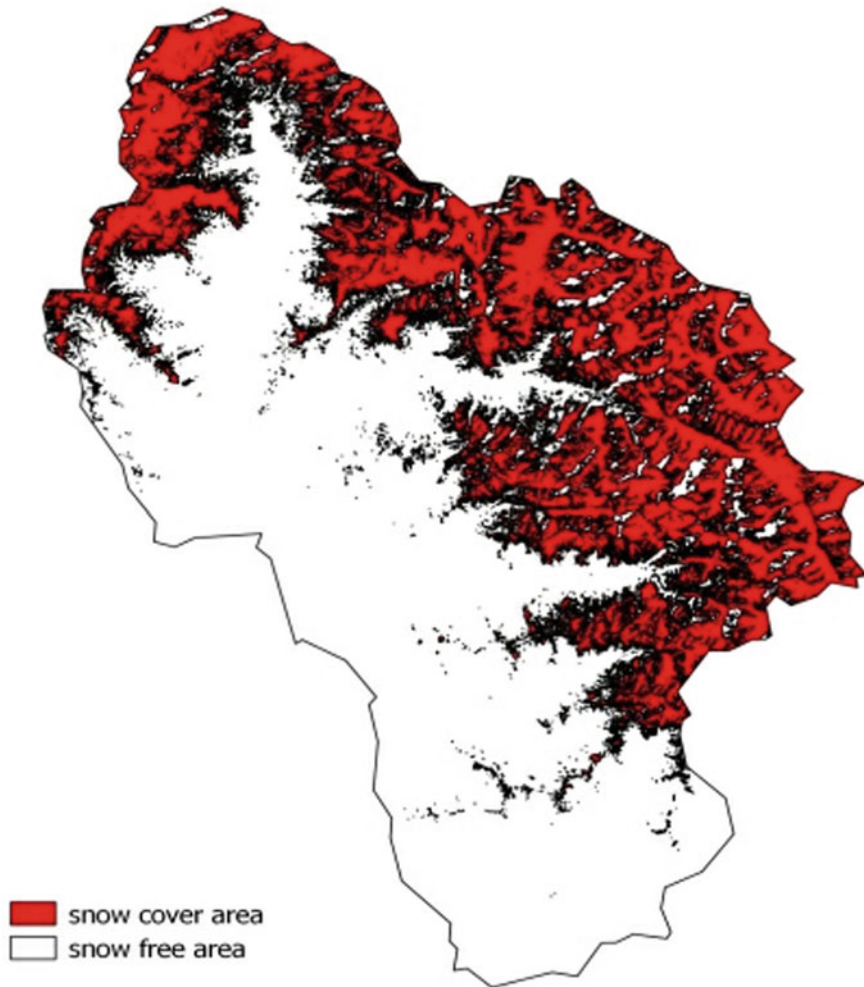


**Fig. 18.3** Snow cover in 2017

Combination) required bands were layer stacked. To specify the area covered by snow, the FCC images were classified using supervised classification technique and the maximum likelihood supervised classification algorithm was applied to classify the study area. For getting some more information about the snow cover, the NDSI technique is also used. NDSI is actually a ratio between visible band and SWIR band (Fig. 18.5).

Snow cover in 2016, 2017 and 2018 are 1776 km<sup>2</sup>, 1857 km<sup>2</sup> and 550 km<sup>2</sup>, respectively. Snow-free area of Kullu district for the year 2016, 2017 and 2018 are 3727 km<sup>2</sup>, 3646 km<sup>2</sup> and 4953 km<sup>2</sup>, respectively. Difference of snow cover area of Kullu in between 2017 and 2018 was around 1310 km<sup>2</sup>. Around 23–24% of snow

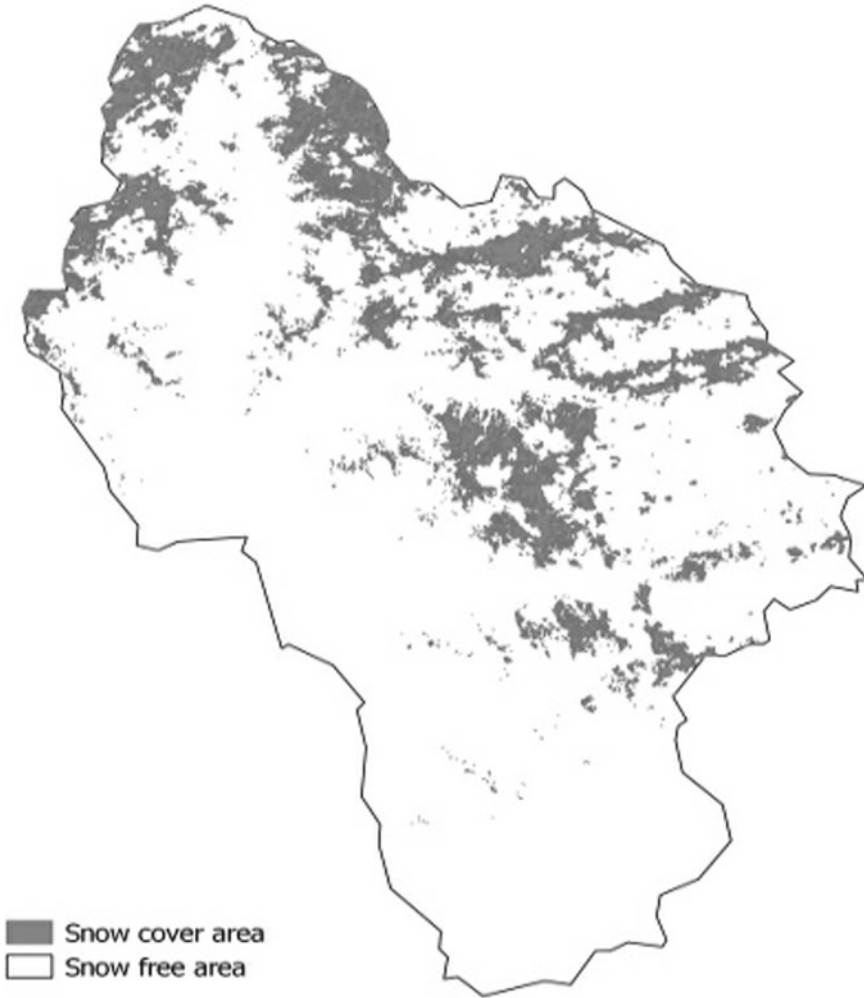


**Fig. 18.4** Snow cover in 2018

**Table 18.2** Snow cover area and percentage snow cover area for 2016, 2017 and 2018

S.no	Year	Snow cover area (km <sup>2</sup> )	Percentage of snow cover area
1	2016	1776	32.27%
2	2017	1857	33.74%
3	2018	545	10%

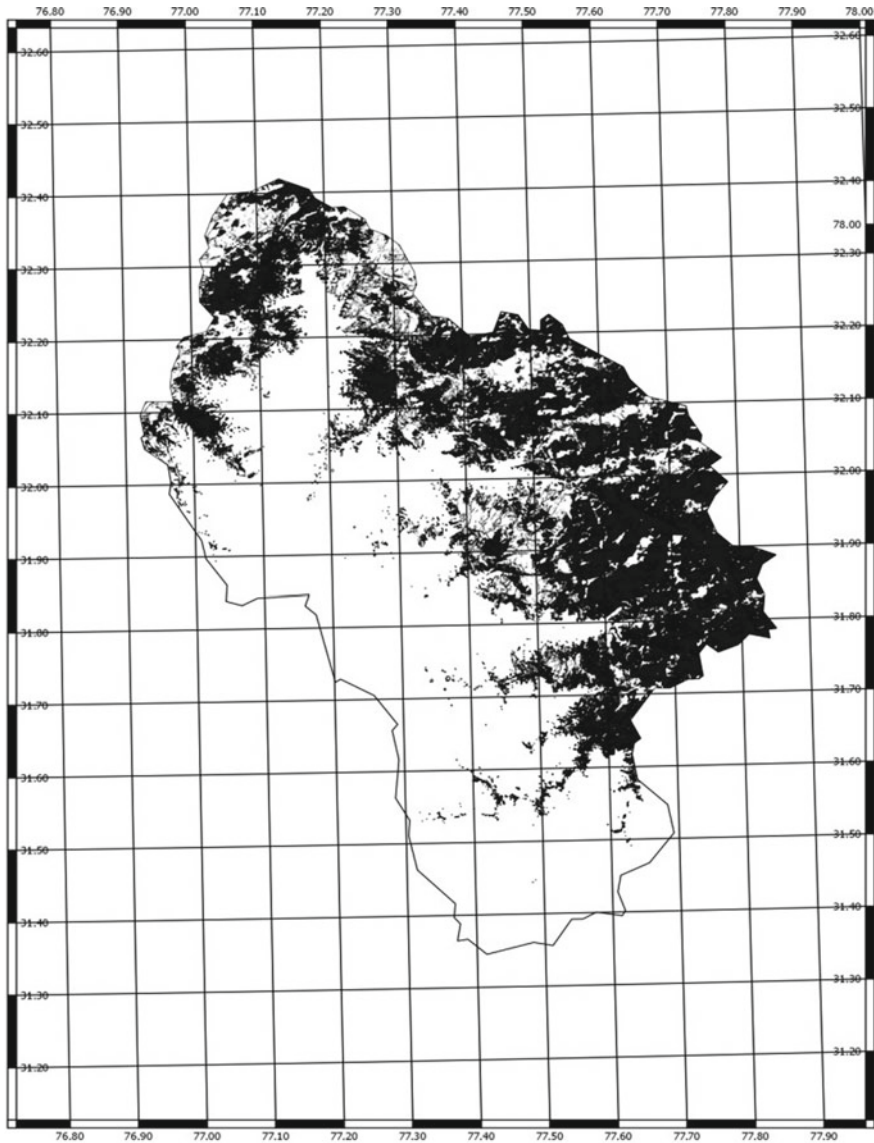


Fig. 18.5 Snow cover difference in between 2017 and 2018

cover was decreased in between 2017 and 2018. In some places like Solang valley, Deo Tibba, Norbu, Shitidhar, Ladakhi and some more places observed less or no snowfall in 2018 as compared to 2017.

## References

- Anupama M (2014) Climate change and its impact on agriculture. *Int J Sci Res Publ* 4(4)
- Assessment of seasonal snow cover variation during the year 2015–2016 in Himachal Pradesh using space data (2016) Report number scste/sccc/snow glacier
- Bengtsson L, Westerstrom G (1992) Urban snowmelt and runoff in northern Sweden. *Hydrol Sci J* 37(3):263–275
- Bratati D Snow cover change in Uttarakashi and its impact on local livelihood structure. *Remarking an analysis*, 2:110–114
- Burkhardt J, Kylling A, Schaaf CB, Wang Z, Bogren W, Stovvold R et al (2017) Unmanned aerial system nadir reflectance and modis nadir brdf-adjusted surface reflectances intercompared over Greenland. *The cryosphere* 11:1575–1589
- Connor S (2018) Melting glaciers are caused by man-made global warming. <https://www.independent.co.uk/environment/melting-glaciers-are-caused-by-man-made-global-warming-study-shows-9669572.html>. Last access 22 July 2018
- Data source—<https://earthexplorer.usgs.gov/>
- Dheeraj R, Anoop S, Deepak P (2016) Key issues in estimating energy and greenhouse gas savings of biofuels: challenges and perspectives. *Biofuel Res J* 10:380–393. [https://www.biofueljournal.com/article\\_15102\\_a46d968aa47a767c971b1ec496affcc.pdf](https://www.biofueljournal.com/article_15102_a46d968aa47a767c971b1ec496affcc.pdf)
- Dorothy K, Riggs, George A (2010) Normalized-difference snow index (ndsi). Publication date: May 06, 2010, Document ID:20100031195
- Hp-sapcc (2018) Himachal Pradesh state strategy and action plan on climate change (2012). Department of environment, science and technology, govt. of Himachal Pradesh. <http://www.moef.nic.in/sites/default/files/sapcc/himachal-pradesh.pdf>. last access 28 July 2018
- IPCC fifth assessment report (AR5). <https://www.ipcc.ch/report/ar5/syr/>
- Sunita N, Prodipto G, Joyti P, Preeti S (2009) Climate change perspectives from India. United nations development programme. [http://www.undp.org/content/dam/india/docs/undp\\_climate\\_change.pdf](http://www.undp.org/content/dam/india/docs/undp_climate_change.pdf). Last access 25 July 2018.

# Chapter 19

## Forecasting Standardized Precipitation Index Using Wavelet-Coupled MARS and SVM Model in Punpun River Sub-Basin (Bihar), India



Lalit Kumar and Ramakar Jha

**Abstract** The scarcity of precipitation and shortage of water supply through natural and artificial water sources leads to a very precarious and dangerous hazard known as drought. Standardized Precipitation Index (SPI), which is the widely used index, is used to define and monitor drought generally. Standardized Precipitation Index (SPI) is developed to measure severity of drought. The forecasting of drought is essential for drought-risk management. To warn drought condition, effective strategies are being developed and proposed; thus, different models are used for powerful mitigation, which give quantitative information to the future drought conditions. In this paper, we have used wavelet-coupled MARS (WMARS) and wavelet-coupled SVM (WSVM) models for SPI forecasting in the Punpun river basin of Bihar region using historical precipitation data for three districts. Finally, a comparative study is done between the traditional MARS, SVM, and wavelet-coupled model, i.e., WMARS and WSVM, with the help of different model statistical performance matrices such as Root Mean Square Error (*RMSE*), Mean Absolute Percentage Error (*MAPE*), and Coefficient of Determination ( $R^2$ ). On the statistical performance matrices, results of wavelet-coupled MARS (WMARS) model gives significantly best result and SVM model gives the least result. Based on the study, we can conclude that wavelet application to traditional model enhances statistical performance matrices and gives more accurate SPI forecast.

### 19.1 Introduction

The scarcity of precipitation and shortage of water supply through natural and artificial water sources leads to a very precarious and dangerous hazard known as drought. It is a protracted period of deficient precipitation. Drought is a most dangerous and influential natural hazard. It claims more deaths in the world compared to any other

---

L. Kumar · R. Jha (✉)

Department of Civil Engineering, National Institute of Technology Patna, Patna 800005, Bihar, India

e-mail: [rj@nitp.ac.in](mailto:rj@nitp.ac.in)

natural hazard. Its impact fluctuates from place to place. It occurs frequently in the arid and semi-arid region (Wilhite 2002). Drought is disastrous not only for people but also for any kind of living organisms. A shortage of rain leads to stunted or minimal crop growth and animals cannot get adequate drinking water and fodder. Therefore, people face acute shortage of food and water. The standardized departure of rainfall from rainfall probability distribution function is expressed as SPI and thus, SPI record has risen up significantly in the late year as potential of drought indicator allowing comparison between space and time (Kumar et al. 2009). The SPI (McKee et al. 1993) is taken worldwide as a drought-monitoring index. The SPI is calculated to improve the monitoring of drought (McKee et al. 1993). Forecasting of SPI is very important for drought-risk management. Powerful mitigation and moderation methodology is required for the cautious thoughts of models which give quantitative information to the future drought conditions (Şen 2015; Wilhite and Hayes 1998; Wilhite et al. 2000a). Observation of drought event is concluded by concentrating the difference in drought records in future with present and chronicled hydrological information (Deo and Şahin 2016; Wolters et al. 2015). Predictive models are assessed to check reliable condition to admonish drought occurrence (Mishra and Singh 2011). Forecasting of drought is dependent on SPI where drought indicator is a data-driven model, developed for anticipating in various geographic areas. An SPI-based philosophy for calculating drought transition possibility is done in Sicily, Italy (Cancelliere et al. 2007). Adaptive-network-based fuzzy inference system (ANFIS), Artificial neural network (ANN), Wavelet-ANFIS, and Wavelet-ANN were used for predicting SPI for Azerbaijan, Iran (Shirmohammadi et al. 2013). The models ANN, Support vector regression (SVR), and wavelet neural system are developed and compared for SPI estimation in Awash River, Ethiopia (Belayneh and Adamowski 2012). The SPI-based estimates were developed using ANN for San Francisco (Santos et al. 2009). ANFIS, M5 display tree (M5Tree), and an MLP were developed and used for calculation of SPI (Choubin et al. 2016). The MARS, LSSVM, and M-5 TREE model were developed and compared to forecast drought in New South Wales, Australia (Deo et al. 2017).

In this study, we have used MARS, SVM, wavelet-coupled MARS (WMARS), and wavelet-coupled SVM (WSVM) models for SPI forecasting in the Punpun river basin of Bihar region using historical precipitation data for three districts. Finally, a comparative study is done between the traditional MARS, SVM, and wavelet-coupled model, i.e., WMARS and WSVM with the help of different model performance matrices.

## 19.2 Theoretical Overview

In this study, we provide basic theory of wavelet, MARS, and SVM to develop the statistical model. Firstly, we have described MARS and SVM statistical model and lastly, concluded with wavelet theory used to develop the hybrid models (W-MARS and W-SVM).



### 19.2.1 Multivariate Adaptive Regressions Spline (MARS)

The term MARS was introduced by Friedman (1991), it was used to solve regression type problem. MARS tends to analyze the contribution of each input variable and build the model for forecasting based on input variables (Cheng and Cao 2014). MARS build the nonlinear and complex relationships between input and target variable (Deo et al. 2015) as given by:

$$y = c_0 + \sum_{m=1}^m c_m B_m(x) \tag{19.1}$$

where  $c_0 =$  constant,  $B_m(x) = m^{th}$  basis function,  $c_m =$  coefficient of  $m^{th}$  basis function, and  $m =$  no. of basis function.

MARS develop basis function based on two-sided truncated power function in Fig. 19.1 (Samui and Kim 2015). The truncated power function is expressed as:

$$b_q^-(x - t) = [-(x - t)]_+^q = \begin{cases} (t - x)^q, & x > t \\ 0, & \text{otherwise} \end{cases} \tag{19.2}$$

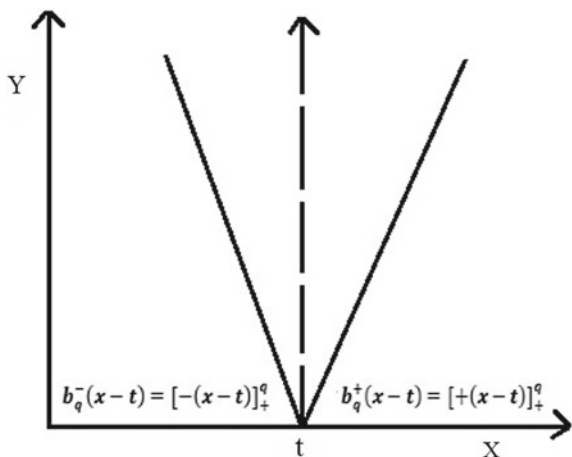
$$b_q^+(x - t) = [+(x - t)]_+^q = \begin{cases} (x - t)^q, & x > t \\ 0, & \text{otherwise} \end{cases} \tag{19.3}$$

where  $q =$  power,  $t =$  knot location,  $b_q^-(x - t)$ , and  $b_q^+(x - t) =$  spline functions.

MARS model is developed by the following two steps:

**Forward step:** first, basis functions are used for defining Eq. (19.1) and overfitting can happen in this progression because basis functions are too large in number.

**Fig. 19.1** Basic functions and knot location





**Backward step:** An additional basis function is expelled to avoid overfitting from Eq. (19.1).

Basis function expulsion is based on generalized cross-validation (GCV) value.

The determination of GCV value has been resolved from the accompanying equation:

$$GCV = \frac{\frac{1}{N} \sum_{i=1}^N [y_i - f(x_i)]^2}{\left[1 - \frac{C(B)}{N}\right]^2} \tag{19.4}$$

where  $N$  = number of data and  $C(B)$  = complexity penalty.

$$C(B) = (B + 1) + dB \tag{19.5}$$

where  $d$  = penalty for every included basis function (BF) of the model.

### 19.2.2 Support Vector Machine (SVM)

The Support vector machine (SVM) model is a regulated machine learning model, which solves classification as well as regression issues and applies an adaptable portrayal of boundary class. In regression analysis, the Nonlinear relationship takes place between dependent and independent variables.

$$y = f(x) + noise = [w \cdot \varphi(x) + b] + \varepsilon \tag{19.6}$$

$w$  = weight vector,  $\varphi(x)$  = nonlinear mapping function,  $b$  = bias, and  $\varepsilon$  = permissible error.

The primary problem is to locate the suitable function  $f$ . The function  $f$  is determined by training a dataset to optimize error function in SVM model. Error function is reduced in SVM model Eq. (19.7). On the basis of constraint in Eq. (19.8),

$$\frac{1}{2} \|w\|^2 + c \sum_{i=1}^N \xi_1 + \xi_1^* \tag{19.7}$$

$$\begin{cases} y_1 - b - [w \cdot \varphi(X_1)] \leq \varepsilon + \xi_1 \\ [w \cdot \varphi(X_1)] + b - y_1 \leq \varepsilon + \xi_1^* \\ \xi_1, \xi_1^* \geq 0 \end{cases} \tag{19.8}$$

where  $c$  = penalty parameter,  $y_1$  = forecasted output,  $\xi_1$  and  $\xi_1^*$  = slack variables.

### 19.2.3 Wavelet

Wavelet is a special mathematical function (waveform) which oscillates like a wave with an amplitude having roughly zero mean in given period. They break down the given set of data (signal) into different frequency range scale. Wavelet enables to view time-series data (signal) into multiple resolutions.

### 19.2.4 Discrete Wavelet Transforms (DWT)

DWT is a process of transforming the signal into different frequency range for statistical analysis. Temporal resolution is the important feature advantage of DWT over Fourier transform. It is localized to time and frequency both. The most commonly used discrete wavelet transforms was developed by Ingrid Daubechies (Daubechies 1988) (Fig. 19.2).

The number of decomposition level of time-series data is determined by Eq. 19.9 (Yang et al. 2016).

$$J = \log_2(N) \tag{19.9}$$

where  $J$  = maximum level of decomposition,  $N$  = no. of time-series data.

## 19.3 Study Area and Data Collection

The Punpun river of south Bihar is a tributary of river Ganga, originating from Chotanagpur (Jharkhand) at an elevation 300 m and travels nearly 200 km to meet the Ganga river near Fathua (Bihar). Aurangabad, Jehanabad, and Patna metrological data of Punpun river sub-basin (Bihar) is studied. Monthly precipitation and Average Temperature data for a 100-year period (1902–2002) is taken from the India water

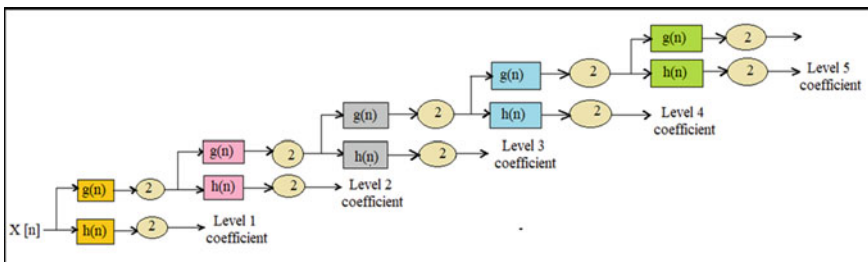
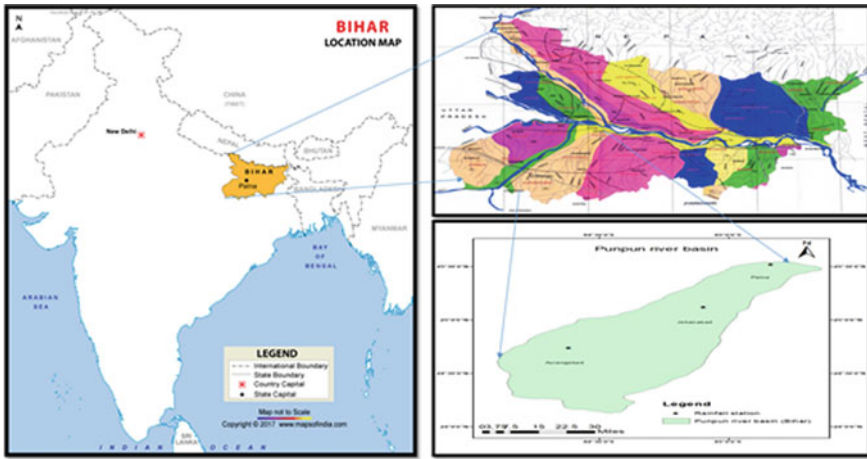


Fig. 19.2 Mallat's decomposition tree

**Table 19.1** Climatic characteristics of Punpun river sub-basin

Observation station	Latitude	Longitude	Elevation (above msl) (m)
Aurangabad	24°45'00.0000" N	84°22'12.0108" E	116
Jehanabad	25°12'50.1408" N	84°59'22.3980" E	71
Patna	25°36'45.6372" N	85°09'31.9500" E	58



**Fig. 19.3** Plots the study location

portal ([http://www.indiawaterportal.org/met\\_data/](http://www.indiawaterportal.org/met_data/)). Climatic characteristic of study area is listed in Table 19.1 and the study area is shown in Fig. 19.3.

### 19.4 Methodology

The monthly precipitation and average temperature data for three stations, i.e., Aurangabad, Jehanabad, and Patna (Bihar) of Punpun river basin is taken from Jan 1902–Dec 2002. The monthly precipitation and monthly average temperature data are used as an input variable and the SPI is taken as output variable to MARS and SVM regression model. The SPI is calculated in MATLAB 2017a software (Fig. 19.4).

Further, the monthly precipitation and monthly average temperature data are transformed using Daubechies (Db3) Discrete wavelet transformation (DWT). The data signal is transformed into five different levels of frequency range class for optimum result (Yang et al. 2016). This transformed data are used as input variable and SPI is taken as output variable for the MARS and SVM model. Wavelet is coupled with MARS and SVM for the formation of WMARS and WSVM. 75% of total data is taken for model training and remaining 25% data is used for testing purpose. The

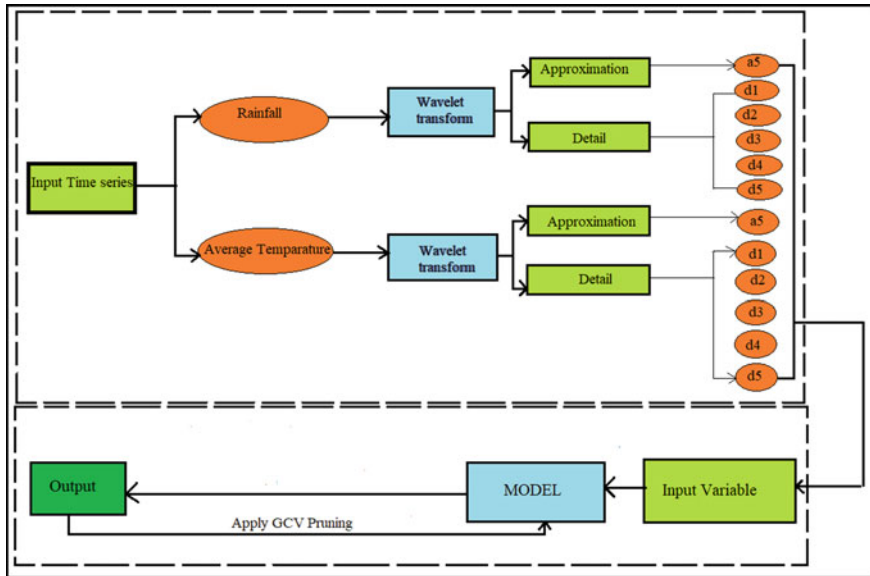


Fig. 19.4 The workflow of wavelet-coupled model

MARS, SVM, WMARS, and WSVM model is dependent on input–output features of data. Training data is helpful to build the model and testing data are taken to check the adequacy of model.

### 19.4.1 Calculation of Standardized Precipitation Index

Standardized Precipitation Index (SPI) was first introduced by (McKee et al. 1993), in which the gamma probability density function is fitted to monthly rainfall ( $P$ ) distribution. The gamma distribution function is given by  $g(P)$ :

$$g(p) = \frac{1}{\beta^\alpha \Gamma(\alpha)} P^{\alpha-1} e^{-x/\beta} \tag{19.10}$$

Parameters,  $\alpha$  and  $\beta$ , can be calculated from maximum likelihood solution:

$$\alpha = \frac{1}{4A} \left( 1 + \sqrt{\frac{1 + 4A}{3}} \right) \tag{19.11}$$

$$\beta = \frac{\alpha}{P} \tag{19.12}$$

where  $A = \ln(\bar{P}) - (\sum \ln(\bar{P}))/N$ , and  $N$  = no. of precipitation station.

The cumulative probability is given by:

$$G(P) = \int_0^P g(P)dP = \frac{1}{\beta^\alpha \Gamma(\alpha)} \int_0^P x^{\alpha-1} e^{-P/\beta} dP \tag{19.13}$$

Assuming,  $t = P/\beta$ , Eq. (19.14) becomes an incomplete gamma distribution function:

$$G(P) = \frac{1}{\Gamma(\alpha)} \int_0^P t^{\alpha-1} e^{-t} dt \tag{19.14}$$

As the gamma distribution function is undefined for  $P = 0$ ,

The cumulative probability is denoted by:

$$H(P) = q + (1 - q)G(P) \tag{19.15}$$

where  $q$  = probability of zero.  $H(P)$  = cumulative probability (converted into a standard random variable with zero mean and having a variance of one). The monthly SPI value is given by:

$$SPI = \begin{cases} +\left(t - \frac{c_0+c_1t+c_2t^2}{1+d_1t+d_2t^2+d_3t^3}\right), & 0.5 < H(P) \leq 1.0 \\ -\left(t - \frac{c_0+c_1t+c_2t^2}{1+d_1t+d_2t^2+d_3t^3}\right), & 0 < H(P) \leq 0.5 \end{cases} \tag{19.16}$$

where  $t$  is calculated from Eq. (19.17),

$$t = \begin{cases} \sqrt{\ln \frac{1}{[H(P)]^2}}, & 0 < H(P) \leq 0.5 \\ \sqrt{\ln \frac{1}{[1.0-H(P)]^2}}, & 0.5 < H(P) \leq 1.0 \end{cases} \tag{19.17}$$

where  $c_0 = 2.515517$ ,  $c_1 = 0.802853$ ,  $c_2 = 0.010328$ ,  $d_1 = 1.432788$ ,  $d_2 = 0.189269$ , and  $d_3 = 0.001308$  (McKee et al. 1993).

Classification of different ‘drought’ condition with their SPI ranges is given in Table 19.2.

**Table 19.2** .

Drought condition	SPI range
Extreme wet	>2.0
Severe wet	1.50–1.99
Moderate wet	1.00–1.49
Normal	0.99–0.99
Moderate dry	–1.00 to 1.49
Severe dry	–1.50 to –1.99
Extreme dry	<–2.0

### 19.4.2 Application of Discrete Wavelet Transformation (DWT)

In this paper, Daubechies (Db3) Discrete wavelet transformation (DWT) is used to transform the data signal up to five different levels of frequency range class for optimum result. The transformed signal data is used as an input variable to build a model. The DWT decomposition of signal is used for better model development and best forecasting result (Yang et al. 2016).

The wavelet transformation of hydro metrological data of Punpun river sub-basin (Bihar) is shown below in Fig. 19.5a–c.

### 19.4.3 Model Performance Evaluation Criteria

In machine learning, MARS, SVM, WMARS, and WSVM models are used to calculate different statistical metrics such as Coefficient of Determination ( $R^2$ ), Root Mean Square Error (RMSE), and mean absolute percentage error (MAPE).

$$RMSE = \sqrt{\frac{1}{N} \sum_{i=1}^N (SPI_{i,0} - SPI_{i,f})^2} \tag{19.18}$$

$$MAPE = \frac{100}{N} \sum_{i=1}^N \left| \frac{SPI_{i,0} - SPI_{i,f}}{SPI_{i,0}} \right| \tag{19.19}$$

$$R^2 = \left[ \frac{\sum_{i=1}^N (SPI_{i,0} - SPI_0)(SPI_{i,f} - SPI_f)}{\sqrt{\sum_{i=1}^N (SPI_{i,0} - SPI_0)^2 \sum_{i=1}^N (SPI_{i,f} - SPI_f)^2}} \right]^2, -1 \leq R^2 \leq 1 \tag{19.20}$$

where  $N$  = no. of test samples,  $SPI_0$  =  $i$ th observed SPI value, and  $SPI_f$  =  $i$ th forecasted SPIs value.

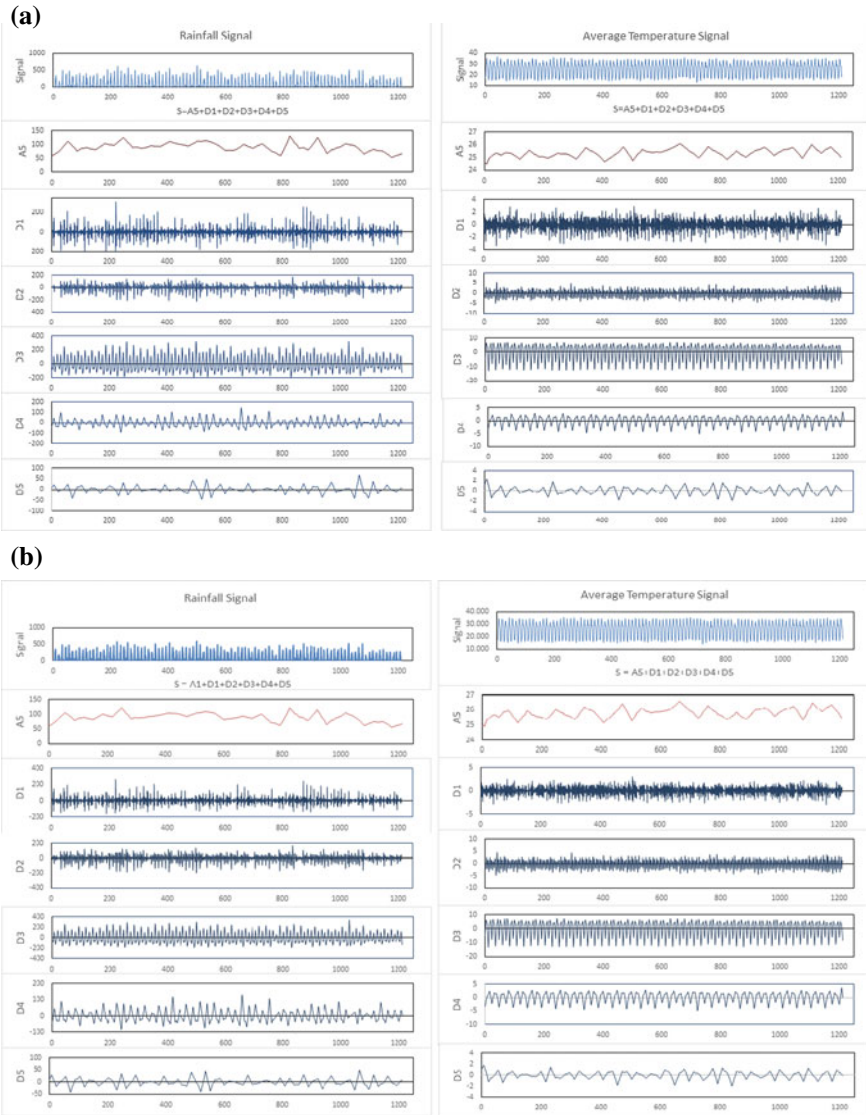


**Fig. 19.5** a Wavelet transformation of hydrometeorological data, Aurangabad. b Wavelet transformation of hydrometeorological data, Jehanabad. c Wavelet transformation of hydrometeorological data, Patna

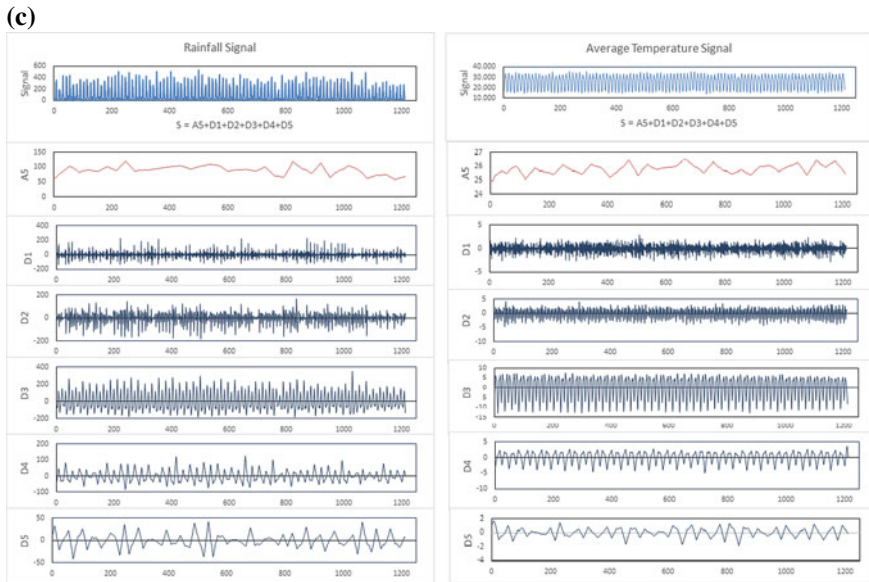


Fig. 19.5 (continued)

For evaluation of the different models, *RMSE* and *MAPE* calculation is done to measure the prediction ability of statistical models. *RMSE* reduces goodness-of-fit for higher value of SPI (Deo et al. 2017), whereas *MAPE* is a measure of prediction accuracy of a forecasting method in statistics.  $R^2$  value shows the performance of a model. It is bounded by  $[-1, 1]$ , if a value of  $R^2$  is nearest to 1 then the model is said to be a good model for prediction.

## 19.5 Result and Discussion

In this study, results obtained from forecasting monthly SPI in Punpun river sub-basin are used to validate their capability in drought modeling. MARS, SVM, WMARS, and WSVM are compared, based on statistical performance metrics (Eqs. 19.18–19.20). The WSVM model gives the best result while the SVM model gives the least result as shown in Tables 19.3, 19.4 and 19.5, which shows the statistical performance metrics of the non-wavelet model, i.e., MARS and SVM and wavelet-coupled model, i.e., WMARS and WSVM in terms of mean statistical performance metrics of Punpun river sub-basin (Bihar).

Based on statistical performance metrics in Table 19.3, in Aurangabad station, the wavelet-coupled model (WMARS and WSVM) outperforms the traditional model (MARS and WSVM). The WSVM has the maximum value of  $R^2 = 0.690$  in training and  $R^2 = 0.640$  in testing; hence, the value of  $R = 0.830$  in training and  $R = 0.800$ .



**Table 19.3** Statistical performance metrics of MARS, SVM, WMARS, and WSVM model

Station	Model	Training				Testing			
		R	R <sup>2</sup>	RMSE	MAPE	R	R <sup>2</sup>	RMSE	MAPE
Aurangabad	MARS	0.260	0.071	0.960	1.160	0.200	0.040	0.943	1.190
	WMARS	0.805	0.649	0.590	1.295	0.748	0.569	0.629	1.627
	SVM	0.220	0.050	0.960	1.054	0.200	0.040	0.980	1.049
	WSVM	<b>0.830</b>	0.690	0.550	1.674	<b>0.800</b>	0.640	0.600	1.820
Jehanabad	MARS	0.219	0.048	0.965	1.108	0.178	0.032	0.968	1.054
	WMARS	0.804	0.648	0.588	1.376	0.767	0.589	0.625	1.397
	SVM	0.200	0.040	0.960	1.070	0.244	0.060	0.970	1.122
	WSVM	<b>0.806</b>	0.650	0.580	1.745	<b>0.793</b>	0.610	0.630	1.847
Patna	MARS	0.258	0.067	0.953	1.120	0.173	0.030	0.975	1.221
	WMARS	0.772	0.597	0.357	1.636	0.764	0.584	0.631	1.418
	SVM	0.200	0.040	0.970	1.064	0.244	0.060	0.970	1.128
	WSVM	<b>0.824</b>	0.680	0.560	1.488	<b>0.787</b>	0.620	0.610	1.685

WSVM has lowest RMSE value of 0.550 and non-wavelet-coupled model has the highest RMSE value of 0.960. The MAPE value is lower in traditional model as compared to wavelet-coupled model for Aurangabad SPI determination. WSVM model is the best model in this study for forecasting drought at Aurangabad station. The WSVM models gives the significant and best result in Aurangabad as shown in Fig. 19.6a, b.

Statistical performance metrics of Jehanabad station is shown in Table 19.3. The wavelet-coupled model (WMARS and WSVM) outperforms the traditional model (MARS and WSVM). The WSVM has the maximum value of  $R^2 = 0.650$  in training and  $R^2 = 0.610$  in testing; hence, the value of  $R = 0.806$  in training and  $R = 0.793$ . WSVM has the lowest RMSE value of 0.580 and non-wavelet-coupled model has the highest RMSE value of 0.960. The WSVM models gives the significant and best result in Jehanabad as shown in Fig. 19.7a, b.

Statistical performance metrics of Patna station is shown in Table 19.3. The wavelet-coupled model WSVM outperforms all different models used in this study. The WSVM has the maximum value of  $R^2 = 0.680$  in training and  $R^2 = 0.620$  in testing; hence, the value of  $R = 0.824$  in training and  $R = 0.787$ . WSVM has lowest RMSE value of 0.580 and non-wavelet-coupled model has the highest

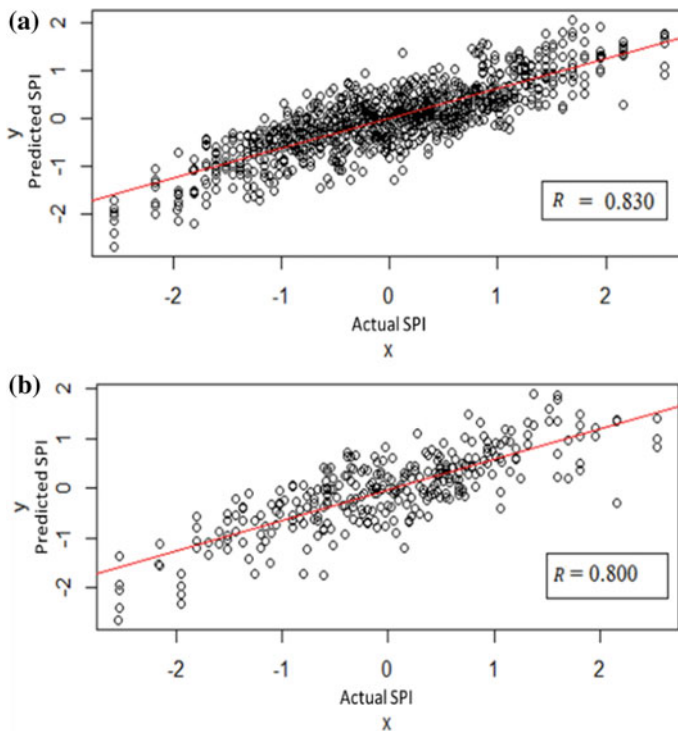


**Fig. 19.6** WSVM model performance for **a** training dataset and **b** testing dataset in Jehanabad

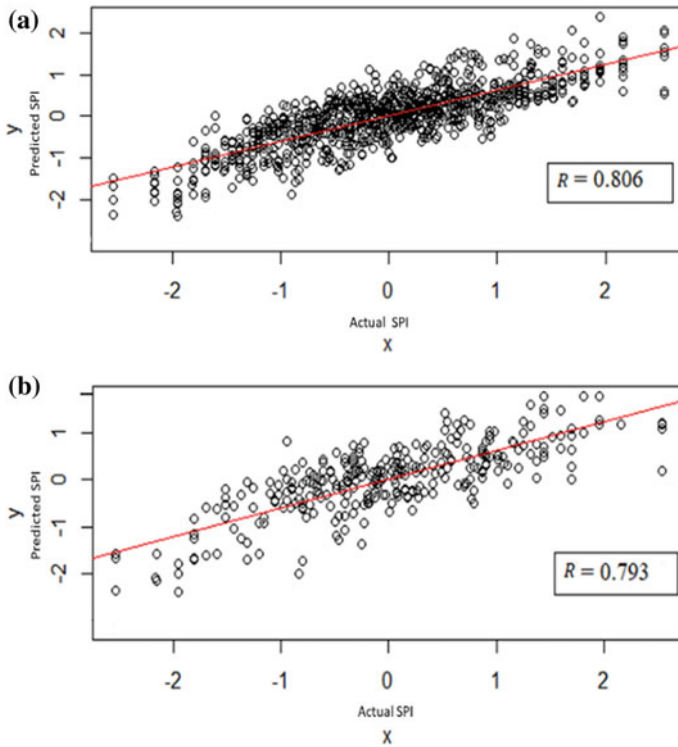


**Fig. 19.7** WSVM model performance for **a** training dataset and **b** testing dataset in Jehanabad

RMSE value. The WSVM model is a better model to forecast drought situation at Patna. The WSVM models gives the significant and best result in Patna as shown in Fig. 19.8a, b.

The statistical performance metrics of the non-wavelet model (traditional model) are generally similar in their approach and magnitude to those of other models. As verified from several statistical regression tools including regression coefficient of correlation ( $R$ ), the coefficient of determination ( $R^2$ ), Root mean square error ( $RMSE$ ), and Mean absolute percentage error ( $MAPE$ ), the margin of difference is relatively very small in SVM as compared to MARS. As we coupled wavelet with these models (WMARS and WSVM), then the margin of difference is relatively very large as compared to non-wavelet models (Fig. 19.8).

Among the following methods of non-coupled traditional models, i.e., SVM and MARS have the lowest  $R^2$  value. The wavelet-coupled model, i.e., WMARS and WSVM have the highest  $R^2$  value in the sub-basin. Among all these, model WSVM has the highest  $R^2 = 0.690$  at Aurangabad and SVM has the lowest  $R^2 = 0.650$  at Jehanabad in training, respectively. Wavelet-coupled model has the lowest RMSE value and non-wavelet-coupled model has the highest RMSE value, respectively,

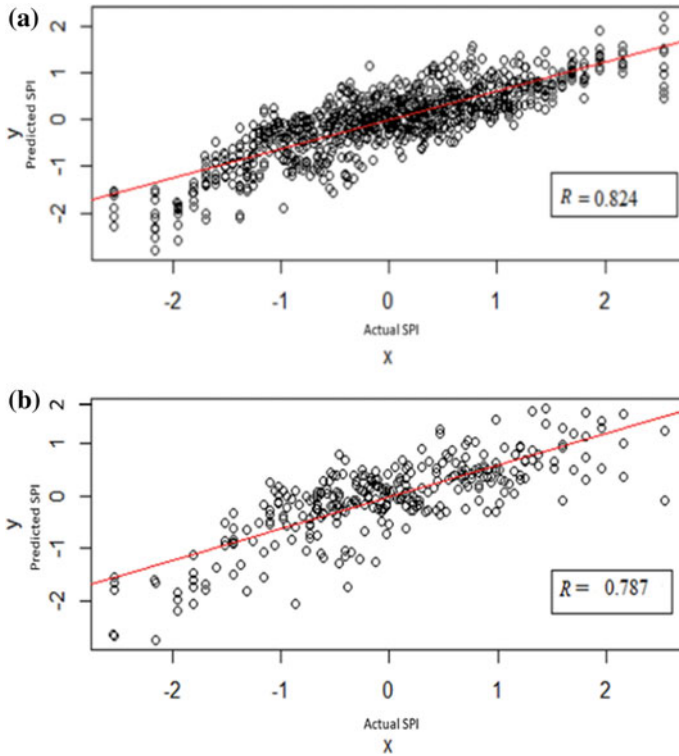


**Fig. 19.8** WSVM model performance for **a** training dataset and **b** testing dataset in Patna

for Aurangabad. The MAPE value is lower in traditional model as compared to wavelet-coupled model for Aurangabad SPI determination.

### 19.6 Conclusion

The Punpun river sub-basin is a drought-prone region of south Bihar, India. The Punpun riversub-basin is a dry sub-humid region as it faces drought problem frequently. This study has adopted the WMARS and WSVM algorithms, i.e., fast and efficient regression model to forecast drought. The WMARS and WSVM models should be adopted as drought forecasting models for large and complex input dataset. Application of wavelet on input variables has successfully improved the performance of traditional models (MARS and SVM) effectively, based on the result the WMARS and WSVM Model performed effectively. However, the WSVM model outperforms the WMARS model with a highest  $R^2 = 0.690, 0.650,$  and  $0.680$  in training and  $R^2 = 0.640, 0.610,$  and  $0.620$  in testing datasets of Aurangabad, Jehanabad, and Patna,

respectively, is far better than its counterpart for predicting data without wavelet transformation. Wavelet-coupled SVM (WSVM) model gives significantly best result for forecasting SPI.

Hence, we can conclude based on the study that application of wavelet on input variables has successfully improved the performance of traditional models (MARS and SVM) effectively; based on the result, the WMARS and WSVM model performed effectively; however, the WSVM model outperforms the WMARS model. Hence, we can use WSVM model in forecasting SPI in Punpun river sub-basin (Bihar).

## References

- Belayneh A, Adamowski J (2012) Standard precipitation index drought forecasting using neural networks, wavelet neural networks, and support vector regression. *Appl Comput Intell Soft Comput* 2012:6
- Cancelliere A, Di Mauro G, Bonaccorso B, Rossi G (2007) Drought forecasting using the standardized precipitation index. *Water Resour Manag* 21(5):801–819
- Cheng M-Y, Cao M-T (2014) Accurately predicting building energy performance using evolutionary multivariate adaptive regression splines. *Appl Soft Comput* 22:178–188
- Choubin B, Malekian A, Golshan M (2016) Application of several data-driven techniques to predict a standardized precipitation index. *Atmósfera* 29(2):121–128
- Daubechies I (1988) Orthonormal bases of compactly supported wavelets. *Commun Pure Appl Math* 41(7):909–996
- Deo RC, Kisi O, Singh VP (2017) Drought forecasting in eastern Australia using multivariate adaptive regression spline, least square support vector machine and M5Treemodel. *Atmos Res* 184:149–175
- Deo RC, Şahin M (2016) An extreme learning machine model for the simulation of monthly mean streamflow water level in eastern Queensland. *Environ Monit Assess* 188(2):90
- Deo RC, Samui P, Kim D (2015) Estimation of monthly evaporative loss using relevance vector machine, extreme learning machine and multivariate adaptive regression spline models. *Stoch Env Res Risk Assess* 30(6):1769–1784
- Friedman JH (1991) Multivariate adaptive regression splines. *Ann Stat* 1–67
- Guttman NB (1999) Accepting the standardized precipitation index: a calculation algorithm. *JAWRA J Am Water Resour Assoc* 35(2):311–322
- McKee TB, Doesken NJ, Kleist J (1993) The relationship of drought frequency and duration to time scales. *American Meteorological Society Boston, MA*, pp 179–183
- Mishra AK, Singh VP (2011) Drought modeling—a review. *J Hydrol* 403(1):157–175
- Naresh Kumar M, Murthy C, Sessa Sai M, Roy P (2009) On the use of Standardized Precipitation Index (SPI) for drought intensity assessment. *Meteorol Appl* 16(3):381–389
- Samui P, Kim D (2015) Determination of the angle of shearing resistance of soils using multivariate adaptive regression spline. *Mar Georesour Geotechnol* 33(6):542–545
- Santos CAG, Morais BS, Silva GB (2009) Drought forecast using an artificial neural network for three hydrological zones in San Francisco River basin, Brazil. *IAHS Publ* 333:302
- Şen Z (2015) *Applied drought modeling, prediction, and mitigation*. Elsevier
- Wilhite DA (2002) *Combating drought through preparedness*. Wiley Online Library, pp 275–285
- Wilhite DA, Hayes MJ (1998) *The arid frontier*, Springer, pp 33–54
- Wilhite DA, Hayes MJ, Knutson C, Smith KH (2000a) Planning for drought: moving from crisis to risk management. *JAWRA J Am Water Resour Assoc* 36(4):697–710

Wilhite DA, Sivakumar M, Wood DA (2000b) Early warning systems for drought preparedness and drought management.

Yang M, Sang Y-F, Liu C, Wang Z (2016) Discussion on the choice of decomposition level for wavelet based hydrological time series modeling. *Water* 8(5):197

# Chapter 20

## Error Due to DEM Sources in Catchment Area and River Network Using D8 Algorithm



Harikrishna Sukumaran and Sanat Nalini Sahoo

**Abstract** Digital elevation models (DEMs) are considered as an important spatial input parameter for hydrological models and have an inherent source of uncertainties which could be due to grid size or data sources. The acceptability of the DEM source for the research objective and appropriate resolution of the dataset has to be the prime question before considering DEMs. These areas potentially impact the results of the popularly used SWAT hydrological model, which predominantly relies on DEMs for the hydrological variables derived. Four popularly used DEMs, namely, AW3D30 DEM, CartoDEM, SRTM DEM, and ASTER GDEM have been considered for the present study in identifying the error in river network extraction using deterministic eight neighborhood (D8) method and error in automatic basin boundary delineation. It was found that the newly released AW3D30 global DEM had the best river network extraction capability compared with the digitized river network from google earth imagery. For stream network extraction, the delineation accuracy for AW3D30 was best compared to other DEMs whereas ASTER GDEM showed poor river network extraction capability. On the other hand, SRTM and CartoDEM showed good river network extraction ability. For basin boundary delineation, ASTER GDEM showed the maximum total error of 167.46 km<sup>2</sup> with AW3D30 basin boundary as reference boundary. The foremost question of applicability of dataset for the study area has been examined through this case study.

---

H. Sukumaran (✉) · S. N. Sahoo

Civil Engineering Department, National Institute of Technology, Rourkela, Rourkela 769008, India

S. N. Sahoo

e-mail: [sahoosanat@nitrkl.ac.in](mailto:sahoosanat@nitrkl.ac.in)

## 20.1 Introduction

For assigning beneficial management practices (BMP), hydrological models have been considered as a primary source of information. The ability of any hydrologic model to produce reliable hydrologic components depends on the spatial input parameters. There are four sources of uncertainty in a deterministic modeling. They are as follows:

- **Input uncertainty:** Uncertainties arising in input data, namely, precipitation, temperature, DEMs which represents the input conditions with respect to time and space in the catchment.
- **Output uncertainty:** Uncertainties in the recorded output data, namely, water level or discharge data which is used for comparing with the model simulation output.
- **Model structure uncertainty:** Uncertainties due to incomplete or biased model structure due to imperfect model physics and model approximations.
- **Parametric uncertainty:** Uncertainties resulting due to non-optimal parameter values due to the inability to identify exact values of model parameters.

One important source of uncertainty is associated due to DEM. In hydrologic modeling, Digital elevation models (DEMs) are used for the basin boundary extraction, river network delineation, and extraction of physical characteristics of a catchment including area, shape, slope of the catchment. Past studies have underlined the importance of DEM in hydrologic simulations in Soil and Water Assessment Tool (Lin et al. 2012; Reddy and Reddy 2015; Tan et al. 2018). This study utilizes physically distributed hydrological SWAT model. In SWAT, each watershed is lumped into hydrologic response units (HRUs) with homogenous combinations of soil, slope, and land cover. Different DEM source and resolutions results in different HRUs and thus eventually yields deviations in the resulting hydrologic components. DEM accuracy assessment is important for extraction of reliable watershed characteristics and thus ensuring further effective hydrologic applications.

Substantial amount of studies has been put in to assess DEM and its impact on watershed. Hammond (2006) explored two important issues in Bruce catchment, England, concluding that the basin area generated by the computer failed to delineate the boundary accurately mainly due to anthropogenic activities in addition to quality of data and algorithms. The study also explored the limit up to which coarser resolution delineates the boundary reliably than fine resolution data. Vladimir J. Alarcon and Chuck O' Hara (2006) studied the basin boundary delineation capability of DEMs, namely, Shuttle Radar Topographic Mission (SRTM), Interferometric Synthetic Aperture Radar (IFSAR), National Elevation Data (NED), and United States Geological Service Digital Elevation Model (USGS DEM) and concluded that SRTM DEM produced optimum basin boundary delineation results than NED. Paz et al. (2008) considered the application of automatic river network in Uruguay River basin comparing the results with digitized drainage lines from satellite images and concluded that relative error was higher than 30% in flat regions with coarse DEM resolution, though stream burning and distance transforms minimized the error range.



Rahman et al. (2010) carried out the study in 12 catchments of varying geomorphology from the five hydrological zones of Bangladesh with SRTM 90 m DEM and explored the limitation of SRTM 90 m in river network extraction with slope of 1:3600 and more. Also, he concluded that the catchment with slope 1:2850 and more steep catchments were delineated correctly. The study also showed how slope is significantly related to network delineation error. Kumar et al. (2017) considered three widely used DEMs, namely, ASTER DEM, SRTM (90 m), and SRTM (30 m) and found a significant error in SRTM 30 m and ASTER DEM while comparing with the reference boundary; also, the stream network delineation error was least for SRTM 90 m in a case study in Gandak basin.

The flow routing model in Digital elevation model (DEM) is based on popularly used D8 method which was introduced by O'Callaghan and Mark (1984). Initially, this method was problematic considering the lack of down slope called sink thus creating a discontinuous flow pattern.

This led Jenson et al. (1988) to develop a method so as to eliminate the sinks before computing flow direction. This later was followed in widely used ESRI products like ArcView, ArcGIS, Arc Info. Fairfield and Leymarie (1991) argued about the limitation of flow discretization into only one of the eight possible directions at  $45^\circ$  in D8 method. After this, many studies were carried out in developing flow direction algorithms, though it was not implemented due to practical reasons excluding D8 method. Therefore, the present study investigates the error in basin boundary delineation and river network delineation using the widely implemented D8 method and their relation to various popularly used different DEM sources.

## 20.2 Description of the Study Area

In the present study, Jeraikela catchment in India is selected as the case study to perform the analysis. Jeraikela catchment is the sub-basin of Brahmani River Basin. The geographical setting of the basin is shown in Fig. 20.1. The catchment covers areas in the states of Jharkhand and Odisha and drains an area of about 10,201 km<sup>2</sup>. While most of the Brahmani basin comprises of agricultural areas with reasonably high mountainous terrain, this region, Jeraikela sub-basin is the only part of the Brahmani basin that is characterized by a wide variation in topography with elevations ranging from 198 to 1089 m, thus making it an interesting case study for DEM related study.

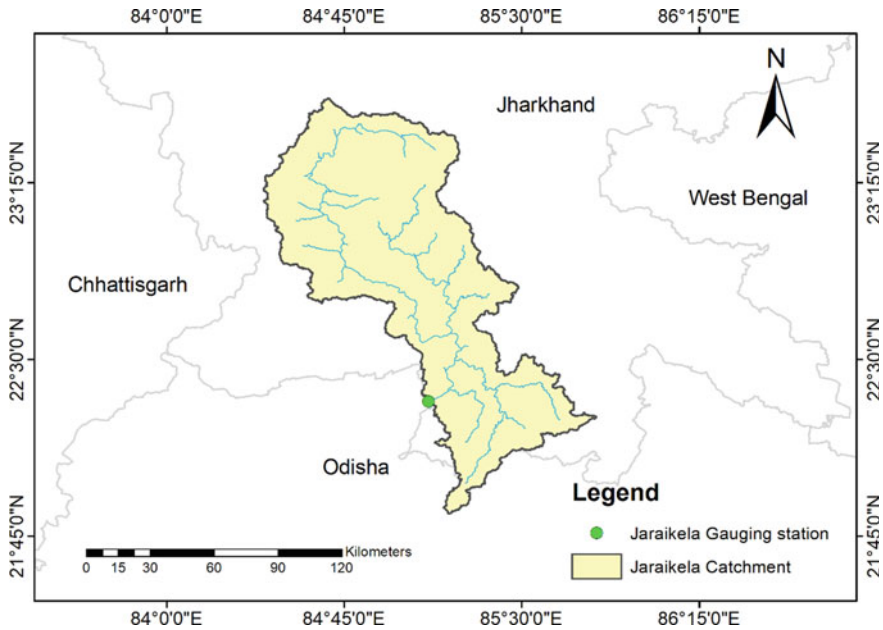


**Fig. 20.1** Location of Jeraikela basin, India

### 20.3 Description of Data Sets Used

Four popularly used DEM data products, namely, CartoDEM, AW3D30 global DEM, SRTM DEM, and ASTER GDEM were selected for this study. The details of the different DEM datasets are listed in Table 20.1. CartoDEM is a DEM dataset generated using cartosat-1 stereo data, developed by Indian Space Research Organisation (ISRO). CartoDEM was made available from 2005 onwards and can be accessed through Bhuvan geoportal, ISRO. AW3D30 global DEM was launched in 2016 by Japan Aerospace Agency (JAXA) and can be procured through the ALOS website free of cost. ASTER GDEM was released under the joint collaboration between

**Table 20.1** Details of different DEMs used in the study

S. No	DEM dataset	Resolution (m)	Source
1	CartoDEM	30	Indian Space Research Organisation (ISRO)
2	AW3D30 global DEM	30	Japan Aerospace Agency (JAXA)
3	SRTM DEM	30	National Geospatial-Intelligence Agency (NGA) and National Aeronautics and Space Administration (NASA)
4	ASTER GDEM	30	United States National Aeronautics and Space Administration (NASA) and Japan's Ministry of Economy, Trade, and Industry (METI)

National Aeronautics and Space Administration (NASA) and Japan's Ministry of Economy, Trade, and Industry (METI) and was made available to public from 2009 onwards and can be downloaded from USGS earth explorer website. SRTM was released by National Geospatial-Intelligence Agency (NGA) and National Aeronautics and Space Administration (NASA) and was initially available at 90 m. SRTM DEM data of 30 m resolution was made available to public in 2015 for Southeast Asian region and can be downloaded free of cost from USGS earth explorer website.

## 20.4 Methodology

In the present study, two types of errors are examined. They are as follows:

- Error due to different DEM sources in digital river network extraction using the traditional deterministic eight neighborhood (D8) method, and
- Error due to different DEM sources in catchment area using automatic basin boundary delineation.

The assessment of error in digital river network was delineated using ArcSWAT which is generated by the popular D8 algorithm through processing the depression, flow direction calculation, and the flow accumulation calculation. The delineated river network is then compared with the river network digitized from google earth which is considered as the reference river network for spatial agreement. The distance from the reference river network to the automatically delineated river network is measured at equal interval of 1 km in ArcGIS 10.1 in the catchment. The spatial disagreement between the reference river network and the automatically delineated river network is the alignment error. Error is considered as positive when automatically delineated river network is on the right side of the reference network and negative otherwise when measured from gauging station (outlet) to remote point.

For quantifying the error in the river network, two statistical parameters, namely, mean absolute error (MAE) and standard deviation (SD) were considered. MAE is reliable since measures of absolute error are less dominated by large numbers of small errors (Rahman et al. 2010).

MAE is calculated by using the formula,

$$MAE = \frac{1}{n} \sum_{i=1}^n |O(x_i y_i) - D(x_i y_i)| \quad (20.1)$$

where  $n$  is the number of intervals,  $O(x_i y_i)$  is the alignment of digitized river network at  $i$ th interval, and  $D(x_i y_i)$  is the location of the delineated river network at  $i$ th interval.

The error due to automatic basin boundary delineation is examined by assessing three error parameters, namely, overestimated area, underestimated area, and the total error which is the sum of the overestimated and underestimated area. The automatically delineated basin boundary by AW3D30 DEM was assumed to be the

reference basin boundary area since it had the best river network delineation capability compared with all the other DEMs. The overestimated area is the area which lies outside the reference basin boundary whereas the underestimated area is the area which shortfalls within the reference AW3D30 basin boundary. To clarify the statement, set notation can be used. If  $X$  is the catchment boundary that needs to be assessed (CartoDEM, ASTER GDEM, and SRTM automatically delineated catchment area) and  $Y$  is the catchment area that is considered as a reference (AW3D30 DEM), then in set notation, the overestimated and the underestimated areas can be expressed as,

$$\text{overestimated area} = X - X \cap Y \quad (20.2)$$

$$\text{underestimated area} = Y - X \cap Y \quad (20.3)$$

where  $X \cap Y$  is the intersection of areas which is under consideration (CartoDEM, ASTER GDEM, and SRTM) and reference area (AW3D30 DEM). The total error is analogous to the mean absolute error which is essentially the sum of overestimated area and underestimated area. This methodology gives the flexibility to compare between two catchment boundary areas that encloses different shapes and positions (Hammond 2006).

## 20.5 Results and Discussions

### 20.5.1 Error in Extraction of River Network Using D8 Method

The river network extraction is evaluated by considering total stream length and the tributaries. Spatial disagreement of the delineated river network by the DEMs considered and reference river network digitized from the google earth imagery is shown in Fig. 20.2.

Based on visual-based inspection, AW3D30 global DEM showed the best river network extraction capability compared with all the other DEMs considered. It was observed that total stream length was found to be greater in AW3D30 global DEM. In contrast, ASTER GDEM showed poor digital river network extraction ability in the Jeraikela catchment whereas Cartosat-1 showed better river network extraction ability over the considered SRTM DEM. Cartosat-1 has reliable flow-path prediction and proficient drainage demarcation capability (Muralikrishnan et al. 2013).

River characteristics, namely, total river length extracted, average slope, average width, and average depth extracted from various DEM sources considered are listed in Table 20.2. The highest range of the total river length 68.79 m for a particular constant area threshold value (1% of the total threshold area—10,000 Ha).

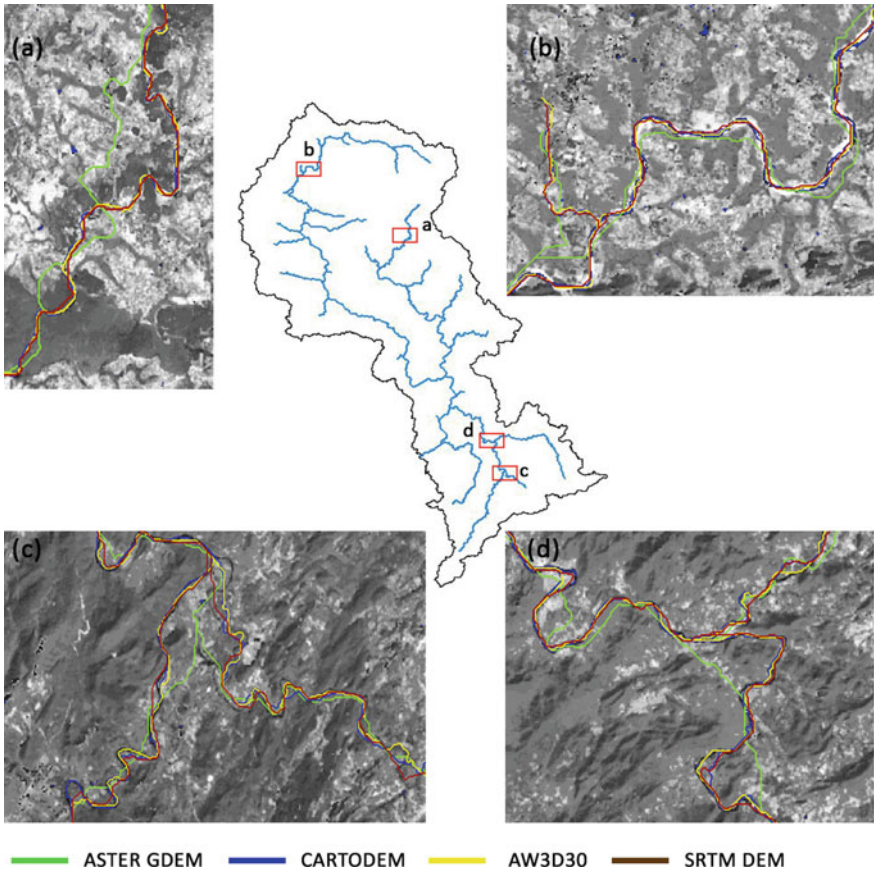


**Fig. 20.2** River network delineation by different DEM sources

**Table 20.2** River characteristics for DEM considered

S. No	DEM source	Total river length (km)	Average slope (%)	Average width (m)	Average depth (m)
1	AW3D30 global DEM	935.62	0.25	91.65	2.05
2	CartoDEM	922.97	0.22	96.92	2.14
3	SRTM DEM	895.07	0.23	96.94	2.14
4	ASTER GDEM	866.83	0.33	93.90	2.09

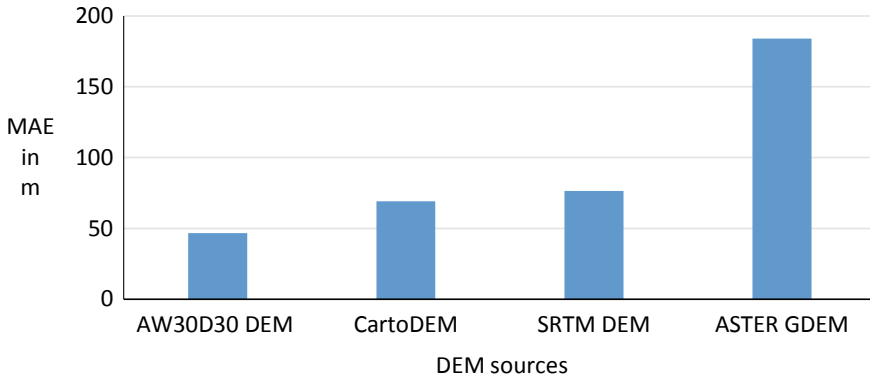


**Fig. 20.3** MAE error due to DEM sources in Jeraikela catchment

In general, ASTER GDEM was not able to generate reliable river network in the outlet and low-lying regions. A similar finding at the outlet was observed by Tan et al. (2018). The poor river network ability by ASTER GDEM may be due to local blunders and artifacts which are sometimes inherent in the ASTER GDEM data (Hirt et al. 2010). Figure 20.3 shows the behavior of MAE due to selected DEMs in Jeraikela catchment.

### 20.5.2 Error in Automatic Basin Boundary Delineation

The basin delineation which is typically executed as a single step algorithmic process was observed. All the DEMs except ASTER GDEM delineated a similar basin boundary. Figure 20.3 shows the sub-basins delineated by different DEM sources. The difference in the basin boundary in ASTER GDEM observed at the outlet region is shown in Fig. 20.4. The automatically delineated basin boundary by AW3D30 DEM was assumed to be the reference basin boundary area since it had the best river network delineation capability compared with all the other DEMs.

Table 20.3 lists the total error due to different DEMs in basin boundary delineation. The highest total error in basin boundary delineation was found to be 167.46 km<sup>2</sup> in ASTER DEM; therefore, the hydrologic analysis may respond differently in terms of quantification of discharge and other hydrological variables.

### 20.5.3 Topographic and Basin Characteristics

Figure 20.5 shows the sub-basin derived and the variation of shape in basin boundary due to different DEM sources. A difference in the number of HRU units were

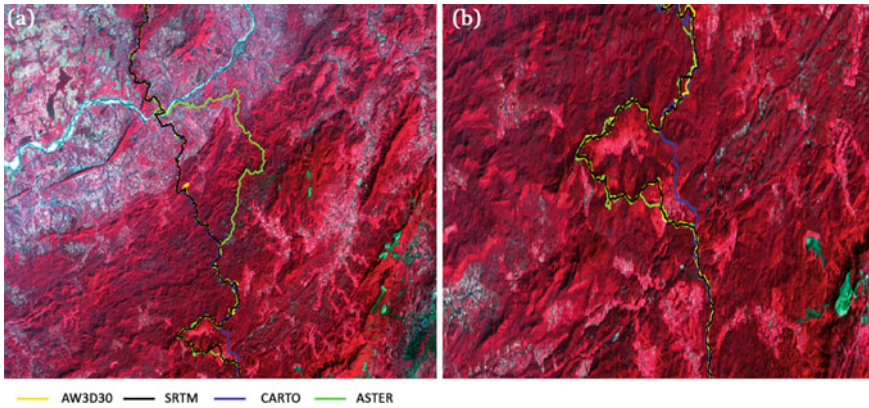


**Fig. 20.4** Differences in basin boundary delineation of DEMs considered in the study

**Table 20.3** Overestimated, underestimated, and total error due to DEM sources

DEM sources	Total area (km <sup>2</sup> )	Overestimated area (km <sup>2</sup> )	Underestimated area (km <sup>2</sup> )	Total error (km <sup>2</sup> )
AW3D30 DEM	10494.95	0.00	0.00	0.00
ASTER GDEM	10413.49	124.46	43.00	167.46
CartoDEM	10484.21	25.86	15.12	40.98
SRTM DEM	10492.98	17.84	15.88	33.72

found due to different DEM sources with highest being AW3D30 DEM (252 HRUs) followed by CartoDEM (237 HRUs), SRTM DEM (234 HRUs), ASTER GDEM (203 HRUs). Thus, AW3D30 could possibly provide more detailed basin characteristics in the form of topographic information and void conditioned treatment of DEM sources. For the catchment, maximum elevation and the minimum elevation was underestimated by CartoDEM. Similar results was reported by Goyal and Panchariya (2018) for upper Teesta and upper Narmada catchments.

The total basin area variation was found to be less between CartoDEM, AW3D30 DEM, and SRTM DEM with areas 10,484.21 km<sup>2</sup>, 10,494.95 km<sup>2</sup>, and 10,492.98 km<sup>2</sup>, respectively. The basin area delineated for ASTER GDEM was 10,413.49 km<sup>2</sup>. Table 20.4 lists the information about elevation and basin characteristics due to different DEM sources selected for the study. The obtained inferences are applicable in this catchment alone and should not be generalized. In a flat region or hilly mountainous regions, the results may be drastically different.



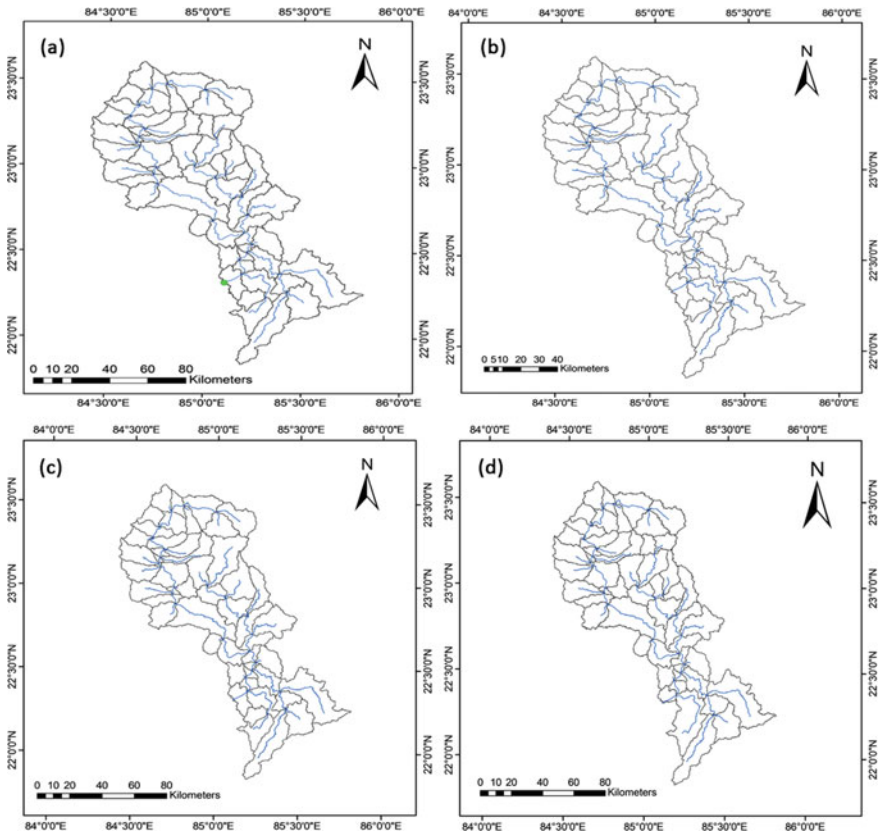


**Fig. 20.5** Sub-basins derived from **a** AW3D30 DEM, **b** CartoDEM, **c** SRTM, **d** ASTER DEM

**Table 20.4** Elevation information and basin characteristics

SI. No	DEM source	Elevation			Basin			
		Min elevation	Max. elevation	Mean elevation	Sub-basin	HRU	Area (km <sup>2</sup> )	Perimeter (km)
1	AW3D30 DEM	198	1088	541.82	55	252	10494.95	1173.77
2	CartoDEM	140	1032	486.94	51	237	10484.21	1171.01
3	SRTM DEM	200	1088	542.76	51	234	10492.98	1165.76
4	ASTER GDEM	171	1097	541.51	53	203	10413.49	1041.34



## 20.6 Conclusions

The study is conducted on Jeraikela catchment to evaluate the performance of the different DEM sources in deriving the physical characteristics of the watershed. The study found that out of the freely available DEMs, AW3D30 DEM provided better river network extraction capability and derived the longest stream for a particular threshold area. The HRU distribution also was found to be more thus representing detailed topographic information in hydrological analysis.

On the contrary, ASTER DEM had poor river network extraction capability and major mismatches were found whereas CartoDEM showed underestimation in both maximum and minimum elevation in the catchment. Thus in essence, care should be taken while considering different DEM sources before its applicability in the study area. This study shows that AW3D30 DEM was the best considering the basin boundary delineation and river network extraction criteria and thus it is recommended for future use of hydrological studies using SWAT in Jeraikela.

## References

- Alarcon VJ, O' Hara C (2006) Using IFSAR and SRTM elevation data for watershed delineation. In: MAPPS/ASPRS 2006 fall conference November 6-10, San Antonio, Texas, May 2014
- da Paz AR, Collischonn W, Risso A, Mendes CAB (2008) Errors in river lengths derived from raster digital elevation models. *Comput Geosci* 34(11):1584–1596
- Fairfield J, Leymarie P (1991) Drainage networks from grid digital elevation models. *Water Resour Res* 27(5):709–717
- Goyal MK, Panchariya VK (2018) Comparative assessment of SWAT model performance in two distinct catchments under various DEM scenarios of varying resolution, sources and resampling methods. *Water Resour Manag* 805–825
- Hammond M (2006) Issues of using digital maps for catchment delineation. (March):45–51
- Hirt C, Filmer MS, Featherstone WE (2010) Comparison and validation of the recent freely available ASTER-GDEM ver1, SRTM ver4.1 and GEODATA DEM-9s ver3 digital elevation models over Australia. *Aust J Earth Sci* 57(3):337–347
- Jenson SK, Domingue JO, Domingue JO (1988) Extracting topographic structure from digital elevation data for geographic information system analysis. *Engineering*
- Kumar B, Patra KC, Lakshmi V (2017) Error in digital network and basin area delineation using d8 method: a case study in a sub-basin of the Ganga. *J Geol Soc India*
- Lin S, Coles NA, Chaplot V, Moore NJ (2012) Impact of DEM mesh size and soil map scale on SWAT runoff, sediment, and NO<sub>3</sub>-N loads predictions. (January)
- Muralikrishnan S, Pillai A, Narender B, Reddy S, Venkataraman VR, Dadhwal VK (2013) Validation of Indian National DEM from Cartosat-1 Data. *J Indian Soc Remote Sens* 41(1):1–13
- O'Callaghan JF, Mark DM (1984) The extraction of drainage networks from digital elevation data. *Comput Vis Graph Image Process*
- Rahman MM, Arya DS, Goel NK (2010) Limitation of 90 m SRTM DEM in drainage network delineation using D8 method-a case study in flat terrain of Bangladesh. *Appl Geomat* 2(2):49–58
- Reddy AS, Reddy MJ (2015) Evaluating the influence of spatial resolutions of DEM on watershed runoff and sediment yield using SWAT. (7):1517–1529
- Tan ML, Ramli HP, Tam TH (2018) Effect of DEM resolution, source, resampling technique and area threshold on SWAT outputs. *Water Resour Manag* 4591–4606

# Chapter 21

## Dam Break Flow Simulation Model for Preparing Emergency Action Plans for Bargi Dam Failure



S. Verma, Sachin, and K. C. Patra

**Abstract** Study of dam breach analysis is necessary because of the tragic consequences that can result in dam failure. After dam had breached, it is difficult to prevent the flood. Therefore, engineers focused more over the flood management for the protection of the population at downstream of dam. This can be done by knowing different types of dam failure, by calculating the consequences of each type of failure, and by evaluating the risk associated with that failure type. In India, till now 37 dam's failure has been reported. Bargi dam or Rani Avanti Bai Lodhi Sagar Dam comes under the category of large dams constructed across Narmada river and breaching of this dam can cause disaster in Madhya Pradesh as well as Gujarat. This study is focused over the overtopping failure of the earthen part of the Bargi Dam. The present work comprises of three objectives: (1) case study of Bargi dam failure using hydrodynamic model mike11, (2) Bargi dam failure impact on Narmada river and Jabalpur city, (3) preparation of inundation map for Bargi dam failure. Further, the present research also presents the applicability and usability of mike11-DB developed by the Danish hydraulic institute.

### 21.1 Introduction

A structure used for impoundment of water is generally known as dam. It can also be defined as a barrier that is used to restrict or stop the water or stream flow beneath the ground. Dams create reservoirs that are used to fulfil the following basic needs of the society such as electricity, human consumption, irrigation, industrial use, navigability, and aquaculture and also it is the major factor in flood protection. The emerging knowledge of construction engineering and technology is helpful to engineers in constructing dams with more suitable design and safety factor, despite this nature is more powerful. Many dams that were previously considered to be safe are now facing maximum flow uncertainty which causes overtopping during high flood events that leads to safety concerns. Dam failure results in economic damage and

---

S. Verma (✉) · Sachin · K. C. Patra  
Civil Department, NIT Rourkela, Rourkela 769008, India

loss of life that totally depends on the magnitude of velocity of water, water depth, warning time, and population density at the time of the event. In flood-prone areas, early warning is essential for saving lives. People believe that due to construction of dams, floods are totally controlled due to which an increase in urbanization and development in industrialization in the floodplains are taking place. Hence, damage by flood caused due to structure failure might be much greater as compared to the damage that would occur in the absence of it.

Document no. 13 of U.S. Army Corps of Engineers' (USACE) Hydrologic Engineering Center (HEC) (U.S. Army Corps of Engineers, 1997) has listed the causes of dam failure such as landslide, piping, earthquake, extreme storm, structure damage, equipment malfunction, foundation failure, and others. Nevertheless, all these almost every dam failure starts with the formation of breach. Breach is basically a gap formed in the body of dam that causes failure of dam and this event leads to the flow of accumulated water at upstream to the downstream. Despite these entire factors, the main failure mode is overtopping or piping. Also, as we know that the continuous change in the climate has drawn an uncertainty in flow within the dam life span (FEMA 2001). Therefore, analysis of dam failure and preparation of inundation map is necessary.

Dam failure analysis purpose is to demonstrate the propagation and attenuation of flood wave beside the river. Dam break analysis consists of three distinct parts: (i) dam-break outflow hydrograph estimation, (ii) dam-break hydrograph routing of downstream valley, and (iii) damage and inundation level estimation at downstream structures. U.S. bureau of reclamation has categorized the method of analysis in four different types: (i) physically based methods; (ii) prediction models; (iii) parametric models; (iv) comparative analysis. Physically based dam break models work on the principle of hydraulics and sediment transport for the simulation of the breach developed. Prediction models use the data such as the breach outflow hydrographs from the past events and then put it in the routing models that are presently available to predict the data for the future events. Parametric models generally parameterize the breach (such as maximum breach size, shape of breach, and many more) so its advancement through time could be depicted in relative basic mathematical models to calculate the enlargement process of the breach (for example: linear increment of breach dimensions with time). Comparative analysis includes comparing the outcomes of historical failures of a dam to a similar study area. According to these types of analysis, many softwares have been developed such as NWS FLDWAV (Gee and Brunner, 2005), FLO-2D, HEC-River Analysis System (HECRAS) (U.S. Army Corps of Engineers (2002, 2006)), DAMBRK, MIKE-11 (DHI, 2009), SMPDBK, FLDWAV, BREAK, and many more for the analysis of dam break.

Reservoir outflow hydrograph prediction and hydrograph routing through the downstream valley are the two major tasks in the hydraulic study of a dam failure. Dam break simulation model in mike zero, i.e., MIKE-11 is used to simulate the flood wave propagation correlated with a potential failure of the dam. The objective of this paper is to use mike-11 for the analysis of dam failure based on given geometrical and hydrological data.

## 21.2 Study Area

Bargi dam also known Rani Avanti Bai Lodhi Sagar Dam is located at  $22^{\circ} 56' 30''$  N longitude and  $79^{\circ} 55' 30''$  E latitude. It was among the first completed dams out of the 30 major dam projects on river Narmada. Construction of this dam was started in the year 1974 and completed in the year 1990. Main dam is constructed near Bargi village, close to national highway-7 (connects **Jabalpur–Nagpur**), due to which it has been named Bargi dam.

In terms of river network, Narmada river rises in the Mikel range in Shahdol district near Amarkantak at an elevation of 1050 m (Fig. 21.1). Flowing generally in south western direction in a narrow valley, the river takes a northerly turn near Mandla after passing through Jabalpur, the river flows through a deep narrow channel through the famous “marble rocks” of Bhedaghat. The Narmada river after emerging from the gorge and continuing west enters the fertile Narmada valley which is a long and a narrow strip walled by Vindhya on the north and Satpuras on the south. Coming out of the gorge, the river enters the plains of Gujarat and finally discharges in the Gulf of Khambat. The Narmada river carries 0.67 mham (5.45 M.A.F) water at 75% dependability up to the Bargi dam. The Bargi dam visualizes a canal head use of 0.39 mham (3.20 M.A.F) and the storage capacity had been designed accordingly (Fig. 21.2).

The Rani Avanti Bai Lodhi Sagar Dam head works comprises of composite masonry and earth dam with central spillway. The masonry dam consists of 209.69 m left NOF and 231.74 m right NOF. The central spillway is 385.72 m long with maximum height of 69.8 m. The top width of service road and bridge over spillway is 7.2 m. The earth dam is 4.53 km long. The left earth dam is 2.77 km and right earth dam is 1.76 km long and maximum height is 29 m. The top width is 7.62 m.

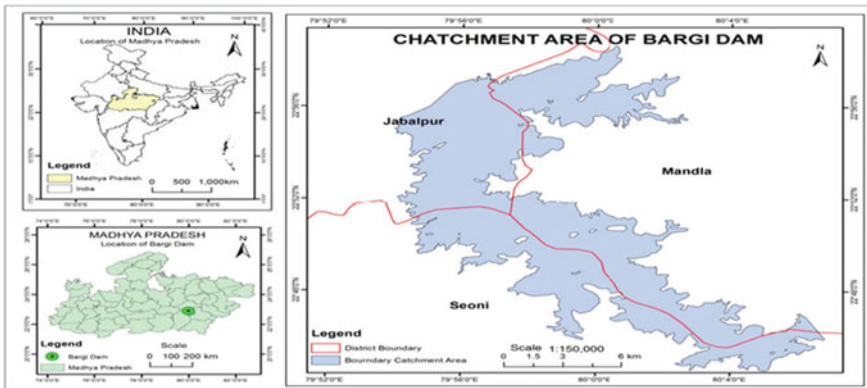


Fig. 21.1 Narmada basin

Bargi dam reservoir is almost 75 km long and 4.5 km wide, spread over an area of about 267.97 km<sup>2</sup> (Table 21.1; Fig. 21.2).

**Table 21.1** Salient features of Bargi dam

General				Reservoir data	
Lat. & long	22° 56' 30" N and 79° 55' 30" E			Minimum drawdown level (MDDL)	RL 403.55 m
Catchment	14,556 sq km			Full reservoir level (FRL)	RL 422.76 m
PMF	51,510 cumecs			Maximum reservoir level (MWL)	RL 425.70 m
Dam				Top of dam level (TBL)	RL 426.90 m
Type	Length (m)	Maximum height (m)	Top width (m)	Dead storage capacity at MDDL	740 M cum
Masonry	827.0	69.8	7.2	Gross storage capacity at MWL	4806 M cum
Earth	4540	29	7.62	Spillway crest level	407.5 m



**Fig. 21.2** Catchment area of Bargi dam

### 21.3 Methodology

This study comprises of dam break analysis of Bargi dam also known as Rani Avanti Bai Lodhi Sagar Dam by using Mike11. The mike software was developed by the Danish Hydraulic Institute (DHI). Mike-11 is a 1-D model that uses the dam break (DB) module to simulate a dam breach (DHI, 2009). From this dam breach, the outflow hydrograph can then be fed to any other flood routing software, and then the flood wave downstream routing can be done. Mike11 is a software package that consists of many different modules. These modules are stated under the following headings that are hydrodynamic module (HD), advection–dispersion (AD), and water quality (WQ). This study is basically focused on the use of hydrodynamic module (HD) (Fig. 21.3).

The hydrodynamic module uses an implicit, finite difference scheme, to calculate unsteady flows in rivers and estuaries. Depending on the local flow conditions, it can describe supercritical as well as subcritical flows within the river or estuary. Other computational models can be included within the HD-module to describe dam breaks or flow around structures.

For dam break analysis, the following data is needed in mike-11:

- Shape files of Narmada river and its tributaries.
- Various time series such as probable maximum flood values with respect to time, water level, and discharge values, and many more.
- A 90 m DEM file of Narmada catchment area which is generally processed in ArcGIS for extraction of data.
- Text files with cross-section data which is derived from the DEM file.
- Narmada catchment topographical image.

Before working with the dam failure analysis tool, it is essential to grasp the knowledge about the critical breach parameters. These parameters are of four types:

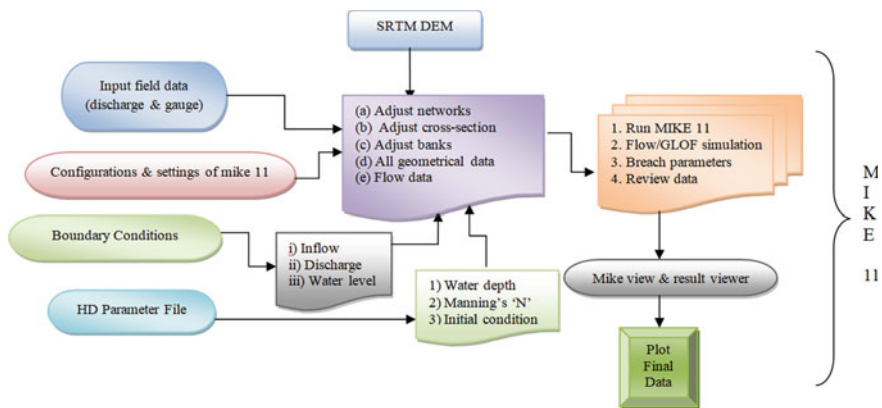


Fig. 21.3 Flow chart of methodology used in Bargi dam break simulation

1. Estimation of breach parameters such as breach size or shape and failure time.
2. Peak discharge during breach and estimation of breach hydrograph.
3. Routing of breach flood.
4. Hydraulic conditions estimation at critical location.

### 21.3.1 Empirical Method

For the prediction of time of failure, breach geometry and peak discharge during breach empirical methods are practiced. Empirical approach is based on statistical analysis of data which is attained from recorded failures. There are four mostly used empirical equations or empirically derived enveloping curves for the prediction of dam breach parameters (Fig. 21.4). They are listed below:

1. Macdonald and Langridge–Monopolis (1984)
2. U.S. Bureau of Reclamation (USBR 1988)
3. Von Thun and Gillette (1990)
4. Froehlich (1995a, b, 2008)

In this study, Froehlich (2008) is used for the estimation of dam breach parameters as it is considered as one of the most endorsed empirical tools under the guidelines for dam break analysis. Froehlich (2008) depends only on the reservoir volume, breach height, and the assumed side-slope of the breach. This method can also differentiate between overtopping and piping failure. Froehlich (2008) equation stands substantial because with his assumptions dams with more prominent stature tend to deliver shorter failure time for a given volume of reservoir.

$$B_{avg} = 0.27k_o V_w^{0.333} \text{ (overtopping, } k_o = 1.3 \text{ \& piping, } k_o = 1.0) \tag{21.1}$$

$$t_f = 0.0176 \sqrt{V_w / (gh_b^2)} \tag{21.2}$$

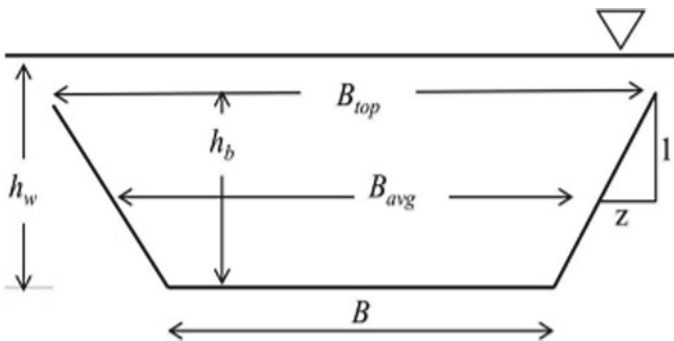


Fig. 21.4 Diagram showing breach parameters

where  $k_o$  = failure mode factor,  $h_b$  = height of breach (m),  $V_w$  = reservoir volume stored ( $m^3$ ),  $B_{avg}$  = average breach width (m),  $t_f$  = breach development time (h).

## 21.4 Result Analysis

It is fundamental to comprehend the aspects of probable dam-break floods in the absolute surroundings to lessen the danger of dam-prompted surges. For the estimation of storage level in dam under the condition of total gravity, dam failure according to the guidelines of the flood risk mapping, breach flow process calculation model along with the 90 m DEM data of the study area is needed. It is important to note that in this study, the dam failure occurring mode is assumed to be overtopping failure only on the earthen part (height of the earthen dam is 29.62 m) of the dam as the spillway (height of masonry dam is 69 m) has sufficient space to prevent overtopping failure of the dam.

### 21.4.1 Breach Parameter Results

Geometrical parameters of the dam used for the prediction of breach parameters are listed below: length of the dam = 4540 m (left flank + right flank), total height of the dam = 29.62 m, freeboard = 1.20 m, total volume of the reservoir (MWL) = 4806 M cum. By applying the Froehlich (2008) equations, the breach parameters calculated are:

Breach slope = 1:1 for overtopping, calculated time of failure ( $t_f$ ) = 47,226.9 s = 13 h, calculated breach width ( $b_w$ ) = 550 m, breach level = 396.7 m.

### 21.4.2 Analysis of Simulation Results

The water level in the dam before the failure was RL 425.7 m with a maximum storage of  $4.80 \times 10^9 m^3$ . A moderate flood of  $43,000 m^3/sec$  is seen over this area. After stimulation with the help of breach parameters, it is clearly shown that the maximum discharge during the dam break is  $114851.2 m^3/sec$  (Fig. 21.5) and it takes almost 18 h to get the water level down in the reservoir to its dead storage level (MDDL). Figure 21.6 demonstrates that with the increase of breach discharge, breach width also increases till the discharge reaches to its maximum value ( $114,851.2 m^3/sec$ ). After this event, breach width will become constant throughout and the discharge will start decreasing. This shows that breach discharge is dependent on the breach width. The level of breach during maximum discharge is RL 396.70 m (Fig. 21.7) and the velocity of the flow is 12.461 m/sec. During the maximum discharge through the breach, the water level in the reservoir is RL 424.84 m (Fig. 21.7) which is below the



**Fig. 21.5** Dambreach hydrograph

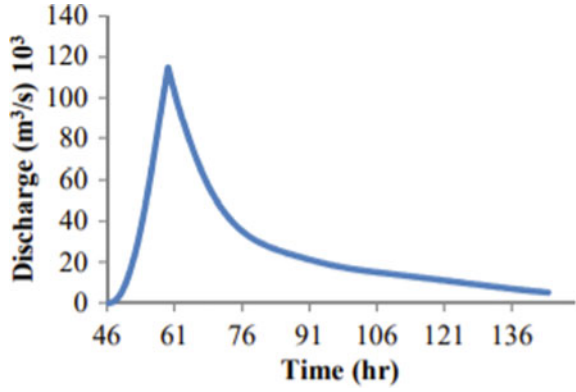


**Fig. 21.6** Breach width and discharge

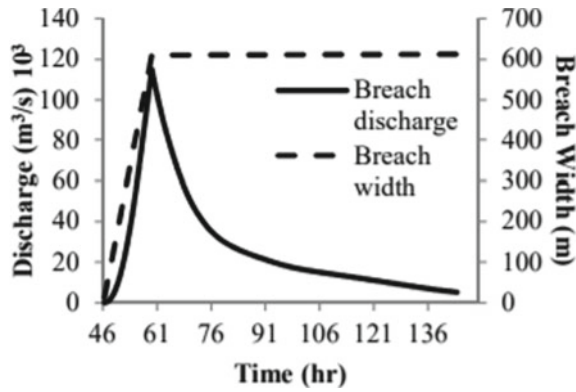
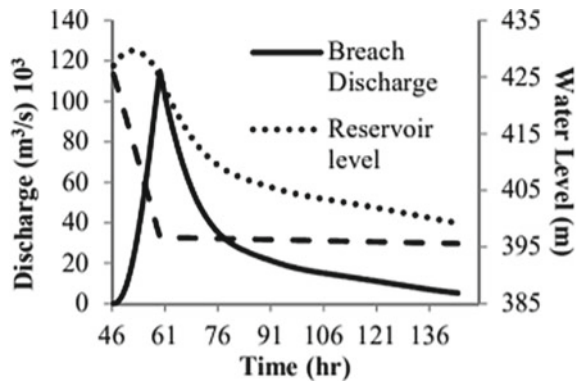


**Fig. 21.7** Relation between breach discharge, reservoir level, and breach level



MWL of the reservoir as it breaches into the dam structure; also, the breach width at the crest is RL 610.4 m (Fig. 21.6) which also affects the intensity of the flow during the process of breach. The peak flood discharge occurs after 13 h of the starting of the breach and it takes almost 4 days to put an end to the disastrous flood (Fig. 21.5). A sharp peak is seen (Fig. 21.5) at 59.56 h because as the maximum value of the flood is achieved, a sudden reduction in HFL is seen. Figure 21.7 illustrates that with the increase in breach discharge, reservoir level increases simultaneously but breach level gets reduced. It is due to the factor that as the water breaches into the dam, the coarse construction material of the dam gets washed and fissures get induced in the body of the dam due to which breach level get decreased. From Fig. 21.7, it can be drawn out that during the time of breach, reservoir was having water level of 427 m which has to be spilled out so as to prevent flooding as well as dam failure.

Table 21.2 illustrates 12-gauge stations during the dam failure. Generally, the tabular study is done to know the impact of flood over various chainages at Narmada river. Out of the 12-gauge stations, Ghansore (60,532.41 m) is the station that lies in the upstream of the dam. The main purpose of choosing one upstream station is to study the impact of probable maximum flood over the upstream of the Bargi dam. From the study, it is clear that the upstream station will be safe during flood event, as its danger level is far above the HFL received by the station. The remaining stations lie downstream of the river. From Fig. 21.8, a clear picture can be drawn for the time of arrival of the flood in various stations. As the flood moves towards the downstream regions from the dam, water level starts reducing for the other respective stations and after that becomes uniform. In Fig. 21.9, at upstream chainage (Ghansore), an irregular behavior of discharge is seen due to the presence of small reservoirs near to the gauge station. In the rest of the stations (downstream), discharge reduces while moving away from the dam in the direction of the flow of water.

It is predicted from Fig. 21.10 that almost 8 m of water level rises in Jabalpur district due to which all the low-lying regions of Jabalpur will get submerged into water as its mean sea level is 411 m and danger level of Jabalpur is 390 m. According to Fig. 21.11, a sudden increase of conveyance capacity of river Narmada near Jabalpur is seen till the high flood wave arrived, and after this point, increase in conveyance capacity becomes uniform. This shows that the velocity of the flow becomes uniform and the boundary shear stress decreases after the flood event. Figure 21.11 depicts the variation of water level increases uniformly after reaching high flood level (HFL) in Jabalpur, i.e., RL 399 m.

From the result, we can predict that the flood will hit the densely populated area Jabalpur (which exist at 25 km downstream of the dam site) in 10 h after the dam breach started (Fig. 21.12), while the maximum peak flood reached after 11 h from the initiation time of the flood in Jabalpur (Fig. 21.13). Research demonstrates that when alerts are issued 90 min or more prior to dam break, then there will be just 0.02% casualties to the population living in downstream area, but if the time of warning is less than 15 min then the casualties will increase by 50%. Therefore, Jabalpur has low risk levels under an appropriate disaster warning system regardless of the 109,704 m<sup>3</sup>/sec of the peak flood flow (Fig. 21.13).

**Table. 21.2** Analysis of mike 11 results with respect to 12-gauge station near Bargi dam

S. no.	Gauge station	Chainage (m)	Danger level (m)	Mike 11 results						Maximum discharge ( $q_{max}$ )		
				High flood			Arrival of 1st flood wave			Value in $m^3/sec$	Date*	Time*
				HFL in m	Date*	Time*	Date*	Time*				
1	Ghansore	60,532.41	558	429.69	24/09/2018	11:45:05	23/09/2018	07:08:24	73,196	24/09/2018	19:41:05	
2	Niwas	95,000	392	403.22	24/09/2018	20:13:05	24/09/2018	07:56:21	110,444	24/09/2018	19:58:00	
3	Jamtara	98,000	380	401.24	24/09/2018	20:18:00	24/09/2018	08:27:42	110,034	24/09/2018	20:03:05	
4	Jabalpur	102,000	388	398.43	24/09/2018	20:22:00	24/09/2018	08:42:17	109,704	24/09/2018	20:11:05	
5	Lakhnadoan	139,000	583	372.04	24/09/2018	22:28:00	24/09/2018	11:28:34	103,630	24/09/2018	21:20:00	
6	Gotagoan	158,000	344	367.88	24/09/2018	23:01:59	24/09/2018	12:47:20	99,982	24/09/2018	22:09:05	
7	Narshingpur	197,000	323	354.91	25/09/2018	00:35:59	24/09/2018	15:28:33	96,709	24/09/2018	23:35:05	
8	Tendukhera	234,000	346	343.65	25/09/2018	03:01:59	24/09/2018	18:05:36	91,099	25/09/2018	01:31:05	
9	Mohpani	240,000	649	341.91	25/09/2018	03:30:00	24/09/2018	18:44:52	90,194	25/09/2018	01:52:00	
10	Gadarwara	243,000	318	341.42	25/09/2018	03:35:59	24/09/2018	18:49:13	89,754	25/09/2018	02:00:00	
11	Udaipura	277,000	297	333.66	25/09/2018	06:18:00	24/09/2018	21:26:16	84,061	25/09/2018	03:48:00	
12	Bamhori	304,000	460	328.79	25/09/2018	08:54:00	24/09/2018	23:32:47	78,934	25/09/2018	05:30:00	

\* Note HFL stands for high flood level  
 Date is in the format of date/month/year  
 Time is in the format of hour:minute:second

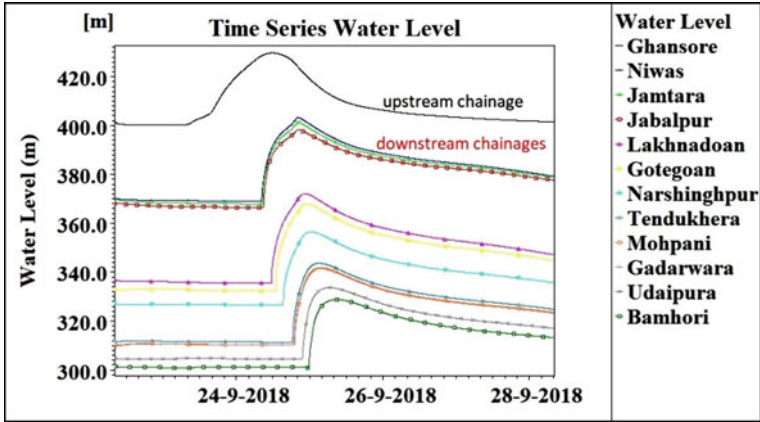


Fig. 21.8 Change of water level with time in different gauges during dam failure

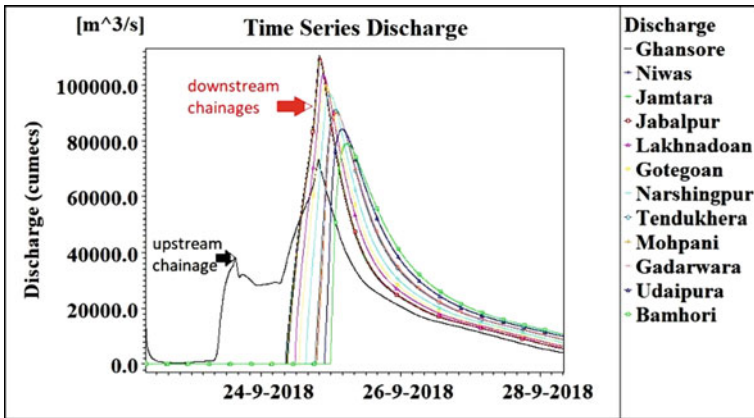
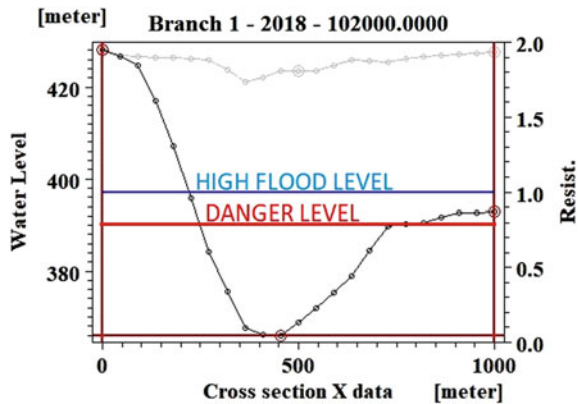


Fig. 21.9 Change of water level with time in different gauges during dam failure

Fig. 21.10 River Narmada cross-section profile near Jabalpur



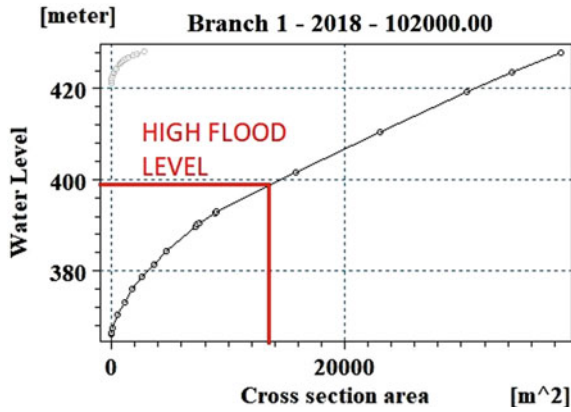


Fig. 21.11 Variation of water level w.r.t cross-section area of river Narmada near Jabalpur

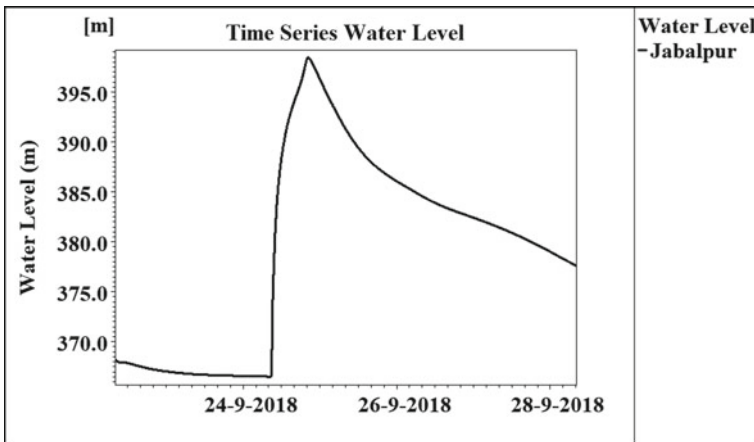
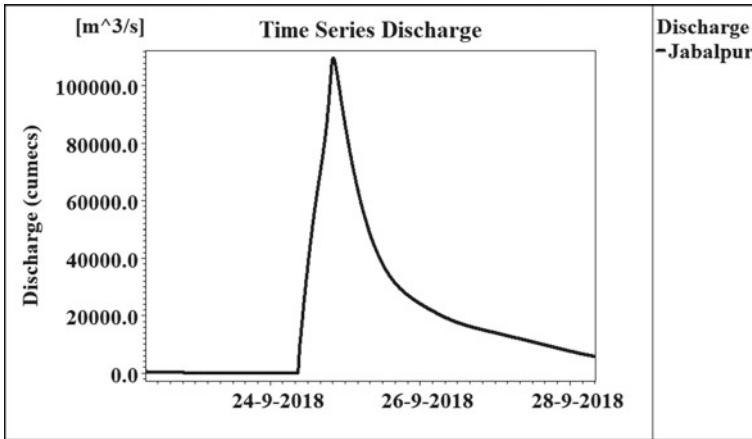


Fig. 21.12 Variation of water level in river Narmada near Jabalpur with respect to time during dam failure

### 21.4.3 Flood Inundation Map

Figures 21.14a and 21.15a represents Narmada river and Jabalpur city before dam failure. Figures 21.14b and 21.15b represents maximum water depth at various locations on Narmada river and in Jabalpur after the dam failure.



**Fig. 21.13** Variation of discharge in river Narmada with respect to time during dam failure near Jabalpur

### 21.5 Conclusion

For the analysis of dam, it is imperative to anticipate the breach parameters precisely as conditions like piping and overtopping causes failure of dam. For doing the same in this study, US National Weather Service (NWS) guidelines were chosen to figure out the dam breach parameters. This paper re-enacts the dam break flood evolution process with the help of geographical as well as hydrological data to analyze the failure condition which can further help in early warning for cataclysmic events. With the use of the hydrodynamic model for the simulation of dam break analysis, it is easier to visualize the drastic effects of flood on downstream area as well as to prepare an emergency action plan to prevent any causalities.

By analyzing the simulation results obtained from mike 11, it was found that a peak discharge flood of 114,851.2 m<sup>3</sup>/sec hits the dam at 59.56 h (from the starting of the flood) with a velocity of 12.46 m/sec. Dam breach hydrograph shows that the upcoming floods have the capability to engulf the downstream regions. It will take almost 18 h (after the arrival of the peak flood) to reduce the effects of flood. The breach level reduces from 425.5 to 396.7 m and breach width enlarges by 550 m, i.e., an opening of 1/8 times the length of dam is created in earthen part of Bargi dam. With the increase in breach width, the breach discharge increases; after achieving maximum breach discharge, the increase in breach width stopped and remained constant or slightly increased with the decrease in breached discharge. In this study, the dam break model for Bargi dam is set up in such a way that water level in the reservoir is at MWL at the time of arrival of peak of PMF.

Analysis also concludes that Ghansore (upstream gauge station) is totally saved during and after the flood event. Jabalpur (downstream gauge station) will receive the flood in 10 h after the dam failure and the maximum flood of 109,704 m<sup>3</sup>/sec will

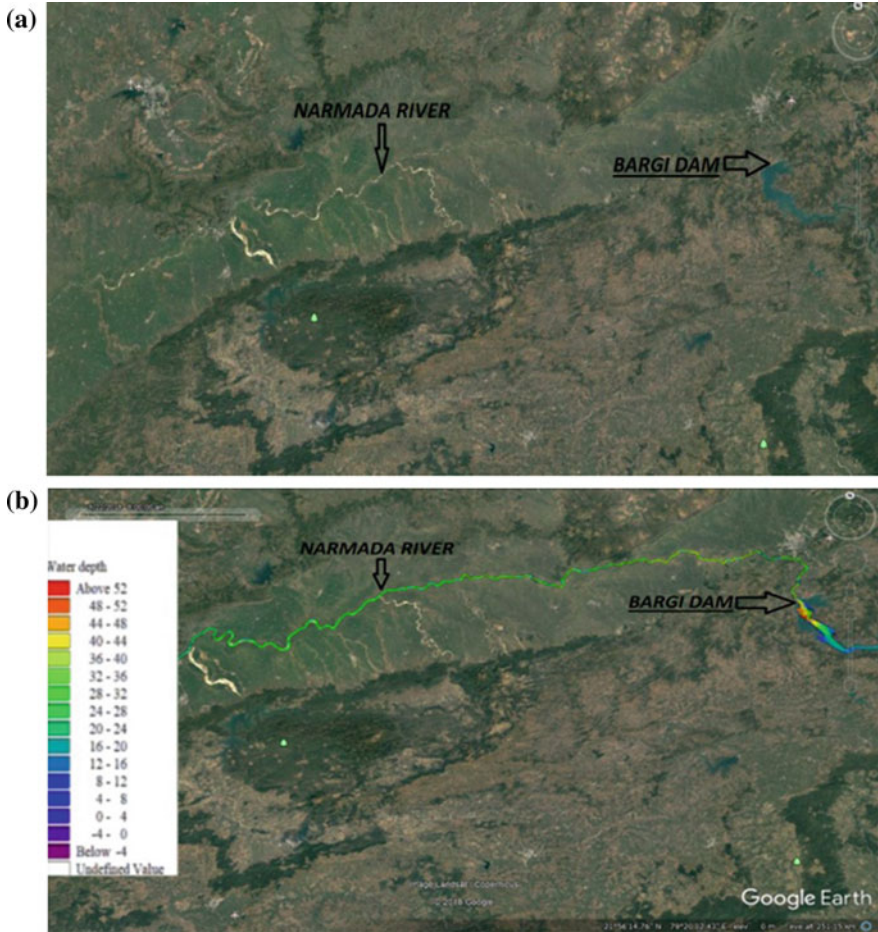


Fig. 21.14 Flood inundation map over Narmada river a before flood, b after flood

reach after 11 h of the initiation of the flood in Jabalpur. Hence, it can be concluded that with proper management of dam safety rules, proper risk management, and under proper warning system, dam breach as well as flood disaster at downstream can be prevented.



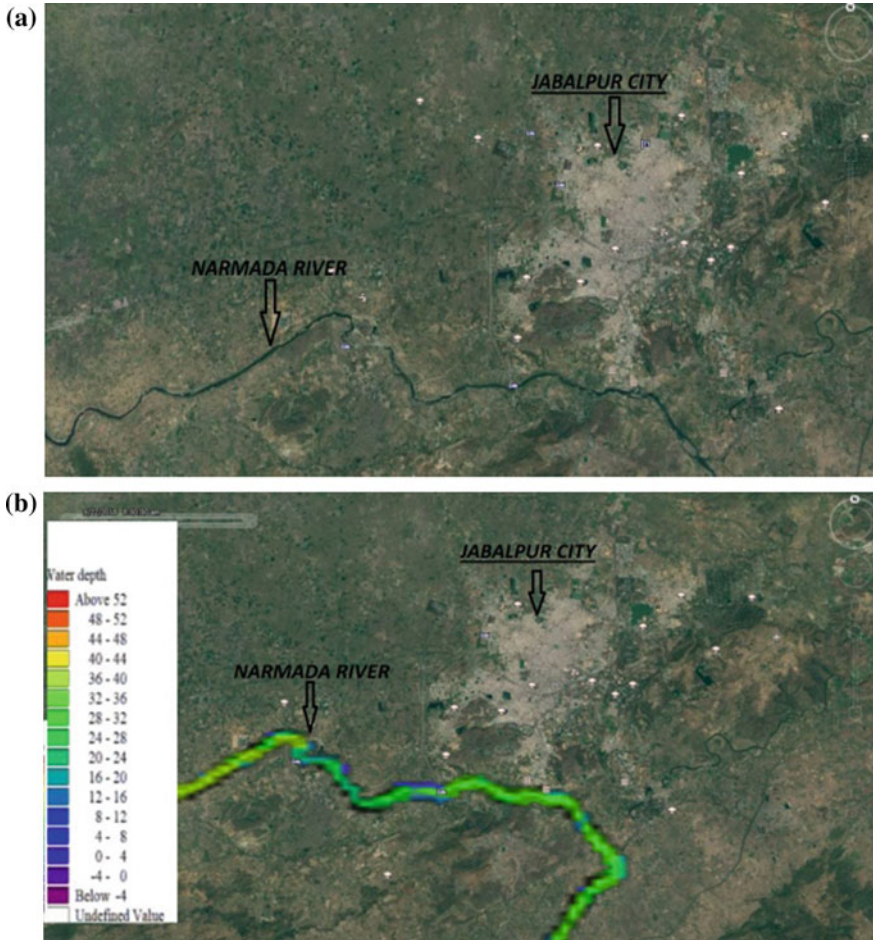


Fig. 21.15 Flood inundation map over Jabalpur a before flood, b after flood

**Acknowledgements** The author would like to acknowledge **Narmada Valley Development Authority (NVDA)** of M.P. government for providing necessary data to carry out this study on Bargi dam failure. The author also thanks National Institute of Technology, Rourkela for providing essential software “mike 11” for this study. Special thanks to Professor K. C. Patra and Asst. Professor Sachin for their guidance to carry out this study.



## References

- DHI (2009) MIKE FLOOD: 1d-2d modelling user manual. DHI Water and Environment, Hørsholm, Denmark
- Gee DM, Brunner GW (2005) Dam break flood routing using HEC-RAS and NWS-FLDWA. In: Proceeding of environmental engineering; Water Resources Management, World Water Congress
- FEMA (2001) The national dam safety program: embankment dam failure analysis
- Froehlich DC (1995a) Peak outflow from breached embankment dam. *J Water Resour Plan Manage* 121(1):90–97
- Froehlich DC (1995b) Embankment dam breach parameters revisited, water resources engineering. In: Proceedings of the 1995 conference on water resources engineering, San Antonio, Texas: S.N., pp 887–891
- Froehlich DC (2008) Embankment dam breach parameters and their uncertainties. *J Hydraul Eng* 134(12):1708–1721
- Macdonald TC, Langridge-Monopolis (1984) Breaching characteristics of dam failures. *J Hydraul Eng* 110(5):567–586
- U.S. Army Corps of Engineers (1997) Engineering and design—hydrologic engineering requirements for reservoirs. EM 1110-2-1420
- US Army Corps of Engineers (2002) HEC-RAS river analysis system, Applications Guide Version 3.1. Hydrologic Engineering Center
- US Army Corps of Engineers (2006) HEC-RAS river analysis system, User's Manual Version 4.0 Beta. Hydrologic Engineering Center
- U.S. Bureau of Reclamation (1988) Downstream hazard classification guidelines. In: Acer technical memorandum No. 11, Assistant Commissioner-Engineering and Research, Denver
- Von Thun JL, Gillette DR (1990) Guidance on breach parameters. US Department of the Interior, Bureau of Reclamation

# Chapter 22

## Discrepancy in Infiltration Equation Parameters While Using Pondered and Tension Boundary Pressure Head Conditions



Aparimita Priyadarshini Naik and Sreeja Pekkat

**Abstract** Soil hydraulic conductivity is one of the main properties considered to govern flow in porous media; however, its measuring methodologies are versatile in nature. In this study, an attempt is made to understand the discrepancy in hydraulic conductivity results obtained by using four different infiltration models, namely, Green Ampt, Horton, Haverkamp, and Zhang by making use of both positive and negative boundary head conditions during experiments. Field experiments at four locations in the study area having different soil types (sand, silt, loam, and loamy sand) are conducted at different +ve and -ve pressure head conditions ( $-0.5$  cm,  $-6$  cm, and  $\approx +6$  cm). The infiltration data is analyzed by using all the four methods to obtain hydraulic conductivity and compared with Guelph permeameter data. The results show considerable difference from Guelph permeameter values and also certain amount of variability within the model results is seen even for same location. The Zhang's method and Haverkamp methods are found to give least and most RMSE values. Sensitivity analysis is also carried out to check for measurement and parameter sensitivity.

### 22.1 Introduction

Infiltration is the movement of water into the soil from the surface governed by gravity and capillary forces. First, the water wets soil grains forming films around them and then the extra water moves down due to the gravitational force. Soil's hydraulic conductivity ( $K$ ) acts as an important parameter to quantify the flow of water and transport of chemicals in soils (Zhang 1997; Köhne et al. 2011). The in-situ measurement of hydraulic properties of soil surface horizons is a fundamental

---

A. P. Naik (✉) · S. Pekkat  
Department of Civil Engg., Indian Institute of Technology Guwahati, Guwahati, Assam 781039,  
India  
e-mail: [aparimita@iitg.ac.in](mailto:aparimita@iitg.ac.in)

S. Pekkat  
e-mail: [sreeja@iitg.ac.in](mailto:sreeja@iitg.ac.in)

requirement for physically based modeling of field infiltration and runoff processes (Smettem et al. 1994). The saturated hydraulic conductivity is the soil's K value when it is completely saturated. This can be obtained by using ponding or positive head condition while carrying infiltration experiments (e.g., using a Ring infiltrometer). Similarly, the near-saturated hydraulic conductivity is the K value obtained when the soil is very near to saturation condition, and this can be obtained by providing a very small negative potential to the flow (e.g., by using a disc infiltrometer). However, when compared to the very high negative potential or suction of dry soil, usually the small positive and negative heads used for infiltration experiments can be neglected and both the cases can be considered to give saturated K values at atmospheric pressure head condition.

The objective of this study is to understand the variation in infiltration equation parameter K for two different cases of boundary pressure head condition; one case with a small positive or ponding head condition obtained using Double Ring Infiltrometer (DR) and the other case with a small negative pressure head condition obtained using Mini Disc Infiltrometer (MDI) (formerly by Decagon Devices, Inc.; now METER Group, USA). During field experiments, when the soil is initially in a dry condition, the suction in soil is very high, or the existing soil potential is highly negative. In such a situation, a very small magnitude of positive or negative potential given on soil boundary may not influence the K value much. This study aims to get a clear inference for this hypothesis.

Therefore, for the current study, four different models are chosen; two of which use positive boundary head conditions and the other two use negative head conditions for analysis. These infiltration models, namely, Green and Ampt (1911), Horton (1940), Haverkamp (1994), and Zhang (1997) are used to obtain the soil hydraulic conductivity (K) by analyzing experimental infiltration data. The suitability of using Green Ampt (GA) and Horton (HT) models for obtaining saturated K values from ponding or positive boundary head conditions and that of Zhang (ZH) and Haverkamp (HV) models for obtaining near-saturated K values from negative boundary head conditions are widely witnessed (Van de Genachte et al. 1996; Dohnal et al. 2010; Gadi et al. 2017). However, not many literature exist which compare for the disparity or similarity of the infiltration parameters obtained using these models which is the main focus of this paper.

## 22.2 Study Area and Methodology

The study area is the campus of IIT Guwahati, located in the sub-basin of river Brahmaputra, Assam, North-east India, with its geographic location between  $26^{\circ} 11' 3.434''$  N and  $26^{\circ} 11' 55.122''$  N Latitude and  $91^{\circ} 41' 14.324''$  E and  $91^{\circ} 42' 10.578''$  E Longitude.

### 22.2.1 Field Experiments

To carry out the above objective, field infiltration tests have been carried out at four different sites (S1–S4) in the study area using two different instruments, namely, Double ring (DR) and Mini disc infiltrometer (MDI) (Fig. 22.1a, b). The experiments with DR are conducted at ponding head values lying within the range of +5.5 to +7.7 cm and for MDI at two different suction values of  $-0.5$  and  $-6$  cm. To ensure for the consistency of the results, several repetitions of the infiltration experiments are carried out at the same locations using same boundary head conditions. The surface soils on which the infiltration studies are conducted are identified to be of four different soil types, namely, sand, silt, loam, and loamy sand based on the United States Department of Agriculture (USDA) classification system. The details of the field experiments are given in Table 22.1. For each soil type, the MDI and DR experiments are conducted using the previously mentioned pressure head conditions and the cumulative infiltration values are calculated.

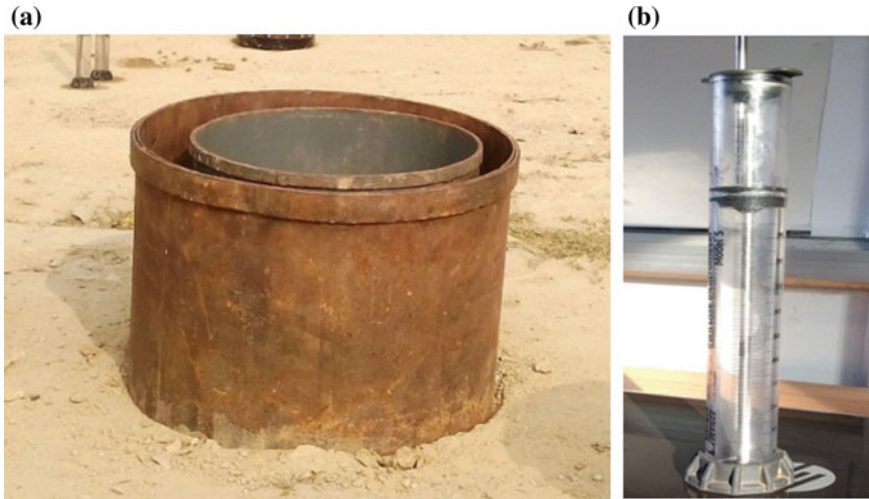


**Fig. 22.1** a Double ring infiltrometer and b mini disc infiltrometer used for field experiments

**Table 22.1** Details of the soil types and field experiments conducted

Station	Soil type	Pressure head used (cm)			$\theta_i$	$\rho_D$ (g/cc)
		DR	MDI (trial 1)	MDI (trial 2)		
1	Sand	6	0.5	6	0.017	2.02
2	Silt	5.5	0.5	6	0.024	1.42
3	Loam	7.7	0.5	6	0.006	1.58
4	Loamy sand	6.2	0.5	6	0.099	1.88

### 22.2.2 Models Used for Analysis

The GA model (Eq. 22.1) is used widely because of its simplicity and ease of obtaining the necessary input data from soil physical and hydraulic properties (Van de Genachte et al. 1996).

$$F(t) = Kt + |\Psi - h_0| \Delta\theta \ln \left| 1 + \frac{F(t)}{|\Psi - h_0| \Delta\theta} \right| \quad (22.1)$$

where  $F(t)$  is the cumulative infiltration (L);  $K$  is the hydraulic conductivity ( $LT^{-1}$ );  $\Psi$  is the wetting front soil suction head (L);  $\Delta\theta$  is the difference between porosity and initial soil water content;  $t$  is the time at which infiltration rate is calculated (T); and  $h_0$  is the ponded depth (L).

GA equation is a nonlinear ordinary differential equation that is derived from Darcy's law (Mailapalli et al., 2009). The basic assumptions of this model include a constant  $\Psi$  at the wetting front, a constant saturated  $K$  behind the wetting front, uniform antecedent moisture content throughout the soil profile, and an initially ponded soil of indefinite depth (Mailapalli et al. 2009). In this study, for calculating  $K$  using the GA model, first the parameters  $\Psi$  and  $\Delta\theta$  are determined using the soil moisture data recorded from the field during each experiment. Owing to a very small magnitude of  $h_0$  ( $-6$  cm to  $+7.7$  cm) compared to high negative  $\Psi$  value, it is neglected during calculation. Then, by using the experimental cumulative infiltration data, saturated  $K$  is calculated for individual experiments.

Horton has given an empirical approach (Eq. 22.2) which is the most widely used infiltration equation in hydrology. He observed that infiltration begins at some rate  $f_0$  and exponentially decreases until it reaches a constant rate  $f_c$ .

$$f(t) = f_c + (f_0 - f_c)e^{-kt} \quad (22.2)$$

where  $f(t)$  is the infiltration ( $LT^{-1}$ ) at time  $t$  (T);  $f_0$  is the initial infiltration rate ( $LT^{-1}$ ) at time  $t = 0$ ;  $k$  is the decay constant ( $T^{-1}$ ); and  $f_c$  is the constant or steady-state infiltration rate ( $LT^{-1}$ ). According to some literature, the  $f_c$  value can be considered as the saturated hydraulic conductivity for a soil. Thus, in this study, the  $f_c$  values obtained for each experiment is taken as the corresponding saturated  $K$  values.

The below given approximated form of Philips equation (Philips 1957) can also be used to analyze the infiltration data from the infiltrometers.

$$I = C_1\sqrt{t} + C_2t \quad (22.3)$$

where  $I$  is the cumulative infiltration rate (L),  $t$  is time (T), and  $C_1$  ( $LT^{-1/2}$ ) and  $C_2$  ( $LT^{-1}$ ) are coefficients that can be determined by fitting Eq. (22.3) to the measured cumulative infiltration vs. time data.

Haverkamp et al. have proposed the following expressions for  $C_1$  and  $C_2$  coefficients by using which near-saturated K can be obtained.

$$C_1 = S \quad (22.4)$$

$$C_2 = \left( \frac{2 - \beta}{3} \right) K + \left( \frac{\gamma}{r(\theta_0 - \theta_i)} \right) S^2 \quad (22.5)$$

where  $S$  ( $LT^{1/2}$ ) and  $K$  ( $LT^1$ ) are, respectively, the soil sorptivity and soil hydraulic conductivity corresponding to the imposed pressure head,  $h_0$  (L);  $\theta_0$  ( $L^3L^{-3}$ ) is the volumetric soil water content corresponding to  $h_0$  and  $\theta_i$  ( $L^3L^{-3}$ ) is the initial soil water content;  $\beta$  is a parameter in the interval (0, 1), generally taken as 0.6 and  $\gamma$  is a constant approximately equal to 0.75 (Haverkamp et al. 1994).

Zhang has given simple expressions for  $C_1$  and  $C_2$  coefficients from which K can be calculated.

$$C_1 = SA_1 \quad (22.6)$$

$$C_2 = KA_2 \quad (22.7)$$

where  $A_1$  and  $A_2$  are dimensionless coefficients determined by the following empirical equations obtained on the basis of numerous numerical experiments (Zhang 1997).

$$A_2 = \frac{11.65(n^{0.1} - 1) \exp[2.92(n - 1.9)\alpha h_0]}{(\alpha r_0)^{0.91}}; n \geq 1.9 \quad (22.8)$$

$$A_2 = \frac{11.65(n^{0.1} - 1) \exp[7.5(n - 1.9)\alpha h_0]}{(\alpha r_0)^{0.91}}; n < 1.9 \quad (22.9)$$

where  $n$  (dimensionless) and  $\alpha$  ( $cm^{-1}$ ) are the van Genuchten retention parameters and  $b$  is a constant equal to 0.55.

Both HV and ZH methods use the following assumptions: (i) the soil is homogeneous and isotropic in nature; (ii) the initial water content  $\theta_i$  or the initial pressure head  $\Psi$  is uniform throughout; (iii) the initial pressure head  $\Psi$  is sufficiently small (i.e., highly negative) so that the condition  $K(\Psi) \ll K(h_0)$  is fulfilled (Vandervaere et al. 2000a, 2000b).

Field experimental results of cumulative infiltration are fitted to Eq. 22.3 and the coefficients  $C_1$  and  $C_2$  are determined. This is followed by obtaining the K values separately by making use of individual expressions of HV and ZH model.

### 22.2.3 Comparison of the Model Results

The measured saturated  $K$  values from the four methods are compared for their accuracy and performance. For this purpose, at least three sets of Guelph permeameter (GP) tests are carried out in the field at each location (S1–S4) and the mean saturated  $K$  value obtained is taken as a reference or true value. To infer the best and least accurate models, the SSE (Sum of Square Error), the MSSE (Mean of Sum of Square Errors), and the RMSE (Root Mean Square Error) values are calculated given by the following expressions.

$$SSE = \sum_{i=1}^n (P_i - O_i)^2 \quad (22.10)$$

$$MSSE = \sum_{i=1}^m \frac{(SSE_i)}{m} \quad (22.11)$$

$$RMSE = \sqrt{\frac{1}{N} \sum_{i=1}^n (P_i - O_i)^2} \quad (22.12)$$

where  $P_i$  and  $O_i$  are the predicted (i.e., by using the four models) and observed (i.e., from the Guelph permeameter) saturated  $K$  values;  $n$  is the total number of parameter values at a particular station or soil type for each model;  $m$  represents the total number of parameter values, for a particular model; and  $N$  is the total number of parameter values used for RMSE calculation for each model.

### 22.2.4 Sensitivity Analysis

In this study, the measurement and parameter sensitivities are carried out to know the sensitivity of the same on hydraulic conductivity. For checking measurement sensitivity, the cumulative infiltration results for all the cases are varied by  $\pm 5\%$ , and  $\pm 10\%$  and their corresponding percentage change in  $K$  value is calculated. Similarly, the sensitivity of parameter  $K$  to another parameter  $\Delta\theta$ , i.e., soil moisture deficiency (i.e., the difference between final and initial moisture content) is checked for GA and HV models.

### 22.3 Results and Discussion

The plots for variation of cumulative infiltration (cm) with time (min) for all the four stations (S1–S4) and different heads are obtained and compared (Fig. 22.2). Out of several repeated experiments, one for each case (total 12) is selected and plotted as shown in Fig. 22.2. It clearly shows that the CI results (cm) obtained with DR for all the four soils are the lowest among all cases owing to its 1D flow condition unlike 3D flow in case of MDI.

The rate of infiltration is governed by several factors like type of soil, pore-size distribution, initial moisture content, density or compaction state of the soil, etc. Therefore, it is difficult to predict the infiltration behavior solely based on soil type only, if all other factors are not maintained constant.

Soil hydraulic conductivity (K) is also one such factor which influences the infiltration behavior of soil. It is claimed that the K values calculated using HV and ZH methods are not the saturated hydraulic conductivity values rather near-saturated hydraulic conductivity values owing to the small negative head provided in the infiltrometer to resist the water flow. However, a small suction (−0.5 to −6 cm) on the soil boundary is more or less close to the atmospheric boundary condition (0 cm). Thus, it is reasonable to say that the K obtained using HV and ZH methods represent saturated hydraulic conductivity values. Also, a small ponding head (+5.5 to +7.7 cm) stands negligible and represents atmospheric boundary condition only. Thus, these small positive heads obtained for DR experiments can be neglected while doing calculations using all the four models. Ultimately, it can be stated that all the hydraulic conductivity values calculated using the above four methods represent saturated hydraulic conductivities only (represented by K henceforth).

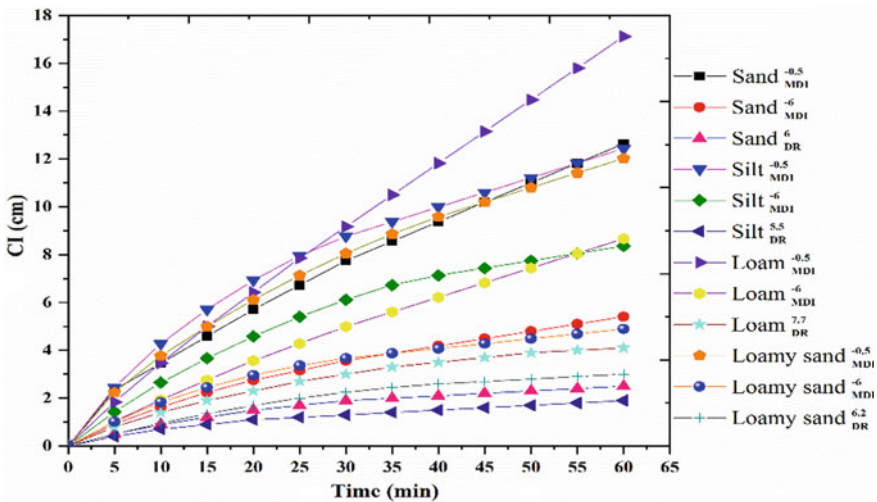


Fig. 22.2 Cumulative infiltration versus time for all the experiments



Here, in this study, the K values calculated for a particular location using four different methods are compared and given in Fig. 22.3a–d. As can be seen, Fig. 22.3a shows the comparison of K values for Station 1 with sandy soil. The MDI experiments conducted at suctions of 0.5 and 6 cm have generated greater K values when compared with the K obtained using certain positive head with DR. It may be due to the 3D flow of water in case of MDI compared to restricted 1D flow in case of DR. However, a wide variation in the K estimates is witnessed between the models as well as with the GP values when compared for individual experiments. Similar results are also sighted in case of three other stations with silt, loam, and loamy sand soil, respectively. This may be due to the different parameters in individual expressions. For example, the ZH method uses the van Genuchten  $\alpha$  and  $n$  parameters given by Carsel and Parrish (1988); HV method uses constant values of parameters  $\beta$  and  $\gamma$  irrespective of the soil type. Also, the use of  $f_c$  value as saturated K value for HT method is not able to give comparable results as can be seen from the difference when compared with the GP values.

To have a better insight of the model obtained K results, error calculation is done by using the expressions mentioned in Sect. 22.2.3, and the values are given in Table 22.2. It is observed from the table that the ZH method gives the least SSE values for all the four soil types with a mean value of 1.15E-03. Also, the RMSE value obtained for ZH method is the lowest with a magnitude of 1.96E-02 followed by

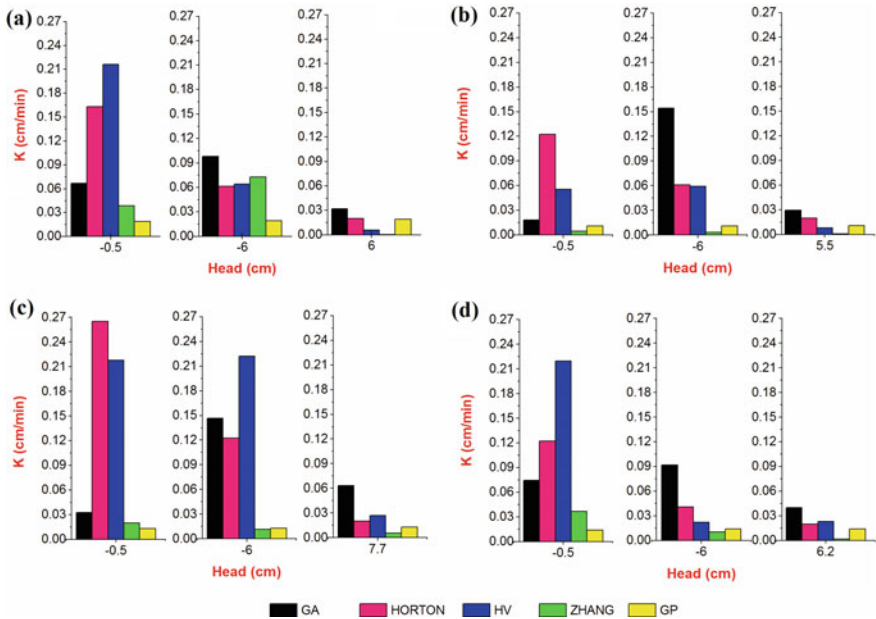


Fig. 22.3 Comparison of K (cm/min) values obtained by using Guelph permeameter and four infiltration models at three different pressure head conditions for a sand, b silt, c loam, and d loamy sand

**Table 22.2** The error values obtained for hydraulic conductivity values calculated using four different models

Model name	SSE				MSSE	RMSE
	Sand	Silt	Loam	Loamy sand		
GA	8.70E-03	2.09E-02	2.08E-02	1.04E-02	1.52E-02	7.12E-02
HT	2.25E-02	1.50E-02	7.55E-02	1.25E-02	3.14E-02	1.02E-01
HV	4.11E-02	4.29E-03	8.59E-02	4.25E-02	4.34E-02	1.20E-01
ZH	3.61E-03	2.03E-04	1.09E-04	6.79E-04	1.15E-03	1.96E-02

GA Green-Ampt; HT Horton; HV Haverkamp; ZH Zhang

GA, HT, and HV methods with magnitudes of 7.12E-02, 1.02E-01, and 1.20E-01, respectively.

All the four infiltration models make use of specific parameters for analyzing infiltration results to generate hydraulic conductivity. Therefore, sensitivity analysis is carried out to check for measurement and parameter sensitivity of K. It is observed that for the GA model, a 5 and 10% increase in CI values resulted in an average increase of 6 and 12% in the K results. Similarly, a decrease in the CI results by 5 and 10% resulted in an average decrease of 6 and 12% in the K values. In the case of the HT method, since the K value is taken directly as the steady state ( $f_c$ ) value from the measured infiltration results, therefore any change in the infiltration result will be linearly reflected in the calculated K value. For HV and ZH methods, the sensitivity results differed from soil to soil. Except for silt, all the other three soils, namely, sand, loam, and loamy sand showed similar trends with a mean variation of +2 to +3% for 5% increase and +6 to +7% for 10% increase in the CI values. The similar decreasing trend was also observed when checked for decreasing values of CI. However, K values for silt soil are found to be highly sensitive to measurement errors when obtained using HV and ZH methods.

Also, the sensitivity of parameter K to  $\Delta\theta$  is checked for GA and HV models. It was seen that both GA and HV models are very less sensitive to changes in  $\Delta\theta$  parameter. However, the relation between both the parameters is found to be non-co-directional, i.e., an increase of 5% and 10% in the parameter  $\Delta\theta$  results in a decrease of K value by 1% and 2%, respectively.

## 22.4 Conclusions

In this study, infiltration experiments of four soils at different locations in the study area were carried out using a MDI and DR with negative and positive boundary pressure head conditions, respectively. The measured infiltration responses were used to evaluate the soil hydraulic parameter hydraulic conductivity (K) by using four different models, namely, Green Ampt (GA), Horton (HT), Haverkamp (HV),

and Zhang (ZH), where the former two models use positive, and the latter two models use negative boundary head conditions for analysis.

Noting the fact that during an infiltration experiment, if the antecedent soil moisture is very less (i.e., dry state of soil), then the soil water potential is highly negative. In such situations, the suctions and the ponding heads provided by using the infiltrometers seem quite negligible thereby remaining ineffective in the parameter determination process. Thus, it is deemed justifiable to compare for K values obtained using the above four methods. A comparison between the RMSE and MSSE values for the four methods suggest that the Zhang method is the most accurate and the Haverkamp method is the least accurate.

Sensitivity analysis was also carried out to check for the sensitivity of parameter K. For all the four models, the measurement sensitivity was found to be co-directional, and parameter sensitivity concerning the parameter soil moisture deficiency was found to be non-co-directional. GA and HT methods were found to be moderately sensitive to the error in infiltration measurements, and HV and ZH methods were found to be comparatively less sensitive to the measurement errors. Parameter sensitivity of K with respect to the parameter  $\Delta\theta$  was very less for both GA and HV models.

**Acknowledgements** The authors would like to thankfully acknowledge Indian Institute of Technology, Guwahati, India for the financial support extended for performing this research work under Start up Research Grant program vide the project no. SG/CE/P/SP/2.

## References

- Carsel RF, Parrish RS (1988) Developing joint probability distributions of soil water retention characteristics. *Water Resour Res* 24(5):755–769
- Decagon Devices Inc. (2016) Mini disk infiltrometer user's manual version 10. Decagon Devices Inc., Pullman, WA
- Dohnal M, Dusek J, Vogel T (2010) Improving hydraulic conductivity estimates from mini-diskinfiltrometer measurements for soils with wide pore-size distributions. *Soil Sci Soc Am J* 74(3):804–811
- Gadi VK, Tang YR, Das A, Monga C, Garg A, Berretta C, Sahoo L (2017) Spatial and temporal variation of hydraulic conductivity and vegetation growth in green infrastructures using infiltrometer and visual technique. *CATENA* 155:20–29
- Green WH, Ampt GA (1911) Studies on soil physics. *J Agric Sci* 4(1):1–24
- Haverkamp R, Ross PJ, Smettem KRJ, Parlange JY (1994) Three-dimensional analysis of infiltration from the disc infiltrometer: 2. Physically based infiltration equation. *Water Resour Res* 30(11):2931–2935
- Horton RE (1940) An approach towards a physical meaning of infiltration capacity. *Soil Sci Soc Am Proc* 5:399–417
- Köhne JM, Schlüter S, Vogel HJ (2011) Predicting solute transport in structured soil using pore network models. *Vadose Zone J* 10(3):1082–1096
- Mailapalli DR, Wallender WW, Singh R, Raghuvanshi NS (2009) Application of a nonstandard explicit integration to solve Green and Ampt infiltration equation. *J Hydrol Eng* 14(2):203–206

- Philip JR (1957) The theory of infiltration: 1. The infiltration equation and its solution. *Soil Sci* 83(5):345–358
- Smettem KRJ, Parlange JY, Ross PJ, Haverkamp R (1994) Three-dimensional analysis of infiltration from the disc infiltrometer: I A Capillary-Based Theory. *Water Resour Res* 30(11):2925–2929
- Van de Genachte G, Mallants D, Ramos J, Deckers JA, Feyen J (1996) Estimating infiltration parameters from basic soil properties. *Hydrol Processes* 10(5):687–701
- Vandervaere JP, Vauclin M, Elrick DE (2000a) Transient flow from tension infiltrometers I. The two-parameter equation. *Soil Sci Soc Am J* 64(4):1263–1272
- Vandervaere JP, Vauclin M, Elrick DE (2000b) Transient flow from tension infiltrometers II. Four methods to determine sorptivity and conductivity. *Soil Sci Soc Am J* 64(4):1272–1284
- Zhang R (1997) Determination of soil sorptivity and hydraulic conductivity from the disc infiltrometer. *Soil Sci Soc Am J* 61:1024–1030

# Chapter 23

## Using CartoDEM Data for Dam Break Flood Hazard Mapping in a Hilly Terrain



Pankaj Mani, Rakesh Kumar, and J. P. Patra

**Abstract** With the development of computation capability and readily available computer programs, flow inundation modeling-based flood hazard mapping are widely practiced. For such analysis, Digital Elevation Models (DEMs) are necessary to define the river topography and terrain variability. Fine resolution DEMs are also used to extract the river cross sections that are subsequently utilized in flow model setup. But the availability of fine resolution DEM is the major constrain, especially in hilly and inaccessible terrains. The satellite-based DEMs like SRTM, ASTER, CartoDEM, etc. are the alternative sources in such cases and have been used in several flow modeling studies. In this paper, a dam break analysis of a small dam located in Uttarakhand in Kumaon Lesser Himalayas is reported. The various scenarios of flooding due to dam breach of the concrete face rockfill dam on Dhauliganga, a tributary of Kali river by routing flood waves in the downstream reach to compute flood inundation, time of occurrences, etc. are discussed. The hydraulic model for the river reach of about 30 km is developed in Mike 11 using surveyed river cross sections and a 10 m resolution digital elevation model of the study area generated using CartoDEM provided by NRSC, Hyderabad. Three cases of flooding are simulated; (i) flooding due to PMF in the river causing dam break condition; (ii) flooding due to PMF without dam break; and (iii) sunny day failure condition (dam failure with nominal inflow when the reservoir is full). It is observed that the time of travel of peak flood from the dam site to major settlement area at Dharchula, about 20 km downstream location, is 42 min for critical case of dam failure. The maximum flood level and time of travel of the peak flood at the important locations are estimated. However, no settlements/villages areas are under inundation for these conditions. The extent of flood hazards for various cases of flooding is estimated by superimposing the inundation map over Google Earth for a detailed description of inundated areas and affected infrastructures.

---

P. Mani (✉)

CFMS, National Institute of Hydrology Patna, Patna, India

R. Kumar · J. P. Patra

Department of Civil Engineering, Sharda University, Greater Noida 201310, India

## 23.1 Introduction

Dam break flood hazard assessment has become important as population and development are concentrated in areas downstream of the dams due to the availability of land and water. Hazard assessment helps in planning for flood mitigation plan and, thus, to reduce the loss of life and property. Dam break flood analysis can provide useful information about the flood inundation and warning time and help in reducing the tangible and intangible losses resulting from dam failures. The flow model provides the basic inputs for flood hazard assessment and the Digital Elevation Model (DEM) is the most influencing input for the model. Representation of river and floodplain geometry in the flood model is established through river cross section and DEM, respectively. DEM may be characterized by spatial resolution and vertical accuracy which affect the inundation accuracy. DEM being an areal representation of point elevation, its accuracy depends upon sampling and interpolation techniques in addition to its genetic source. For developing nations, the availability of accurate DEM data for the flood plain is a major hindrance to their limited resources. For many rivers and floodplains, these essential input data are either not sufficient or unavailable which is still a concern (Sanyal et al. 2014; Samantaray et al. 2014). On the other hand, the flood problem is more aggravated in this region only (WRI 2015). With the availability of inexpensive/public domain river flow models, the countries suffering from the frequent and devastating nature of flood hazards are also seeking advance tools to plan the flood mitigation. Next to the topographical survey, DEMs from LiDAR data are considered to be most accurate for flood study though very costly. Satellite-based global DEMs like ASTER and SRTM are freely available at a spatial resolution of 30 and 90 m and have been widely used in flood modeling (Yen et al. 2013). In this series, CartoDEM provides a more finer resolution DEM derived from the Cartosat-1 stereo payload launched in May 2005. The spatial resolution of CartoDEM is 2.5 m in the horizontal plane. As per the design of CartoDEM, the DEM accuracy is 8 m at LE 90 and 15 m at CE 90 for ortho data (NRSA 2015). CartoDEM is generated using Augmented Stereo Strip Triangulation (ASST), indigenously developed software by Space Application Centre, ISRO (India). The generated DEM and ortho images of each Cartosat-1 segment are cut into tiles of  $7.5' \times 7.5'$  extents and the entire Indian region is covered by approximately 500 Cartosat-1 segments with a total number of around 20,000 tile pairs while the DEMs are available at a spatial resolution of 2.5, 10, and 30 m. In this study, 10 m DEM has been used. In absence of surveyed river section, the cross sections are extracted from CartoDEMs. Generally, the accuracy of DEM is evaluated with observed elevation points, although in this study, the known elevation points are very selected and located mainly at the dam sections and the power house. The river cross sections are extracted from CartoDEM at 10 m resolution and used in MIKE 11 flow model setup to compute the flooding under different scenarios. This paper discusses the dam failure analysis of the Dhauliganga dam located on the Kali river in the Pithoragarh district of Uttarakhand. The study envisages identification of various scenarios of flooding, estimation of breach parameters, modeling of dam break flood, and its routing in the downstream reach to

compute the maximum flood inundation and its time of occurrences. The maximum flood levels and their time of occurrences have been estimated at the important locations in the downstream reach. The extent of maximum inundation for various cases of flooding has also been computed. The inundation maps are superimposed over Google Earth for a detailed description of inundated areas.

## 23.2 Study Area

The Dhauliganga dam, which is a part of hydropower project, is located on river Dhauliganga, a tributary of river Kali in the Pithoragarh district of Uttarakhand. Dhauliganga river originates in the high Himalayan mountain from the glaciers at an elevation of about 5160 m. The catchment area is 1372 Km<sup>2</sup>. The river flows in deep gorges with a very steep slope of about 48 m for every 1 Km length. The power house is located at about 9.4 km downstream of the dam site.

### 23.2.1 Description of Dhauliganga Dam

A concrete face rockfill embankment dam is of 56 m high above the river bed level while the length of the reservoir is about 1.4 km. The elevation of the dam crest is RL 1352.0 m and the length of the crest is 270 m. The Full Reservoir Level (FRL) of the reservoir formed by the construction of the dam is at RL 1345.0 m and Minimum Draw Down Level (MDDL) is at RL 1330.0 m. On the right flank of the dam, there are two gated spillways with an open chute and flip bucket (10 m × 6 m) with a discharge capacity of 3210 m<sup>3</sup>/s. The dam also consists of a Tunnel spillway with a radial size of 9 m × 16 m.

### 23.2.2 Downstream River Stretch

Dam break analysis for Dhauliganga dam is carried out and its impact in the downstream river stretch up to 30 km from dam site is reported. From the dam site, Dhauliganga flows in southeast direction up to 4.5 km and the confluence with Kali river from where it takes a turn toward southwest direction. The river is called now the Sharda river in its downstream stretch (from Tanakpur onward). It outfalls in Ghaghra river and finally joins the river Ganga. The power house is located at about 9.75 km while one major settlement, Dharchula, is located at about 21 km downstream of the dam site. Another settlement village Dhap is located 30 km downstream of the dam site. The location of the dam and the downstream river stretch is shown in Fig. 23.1.

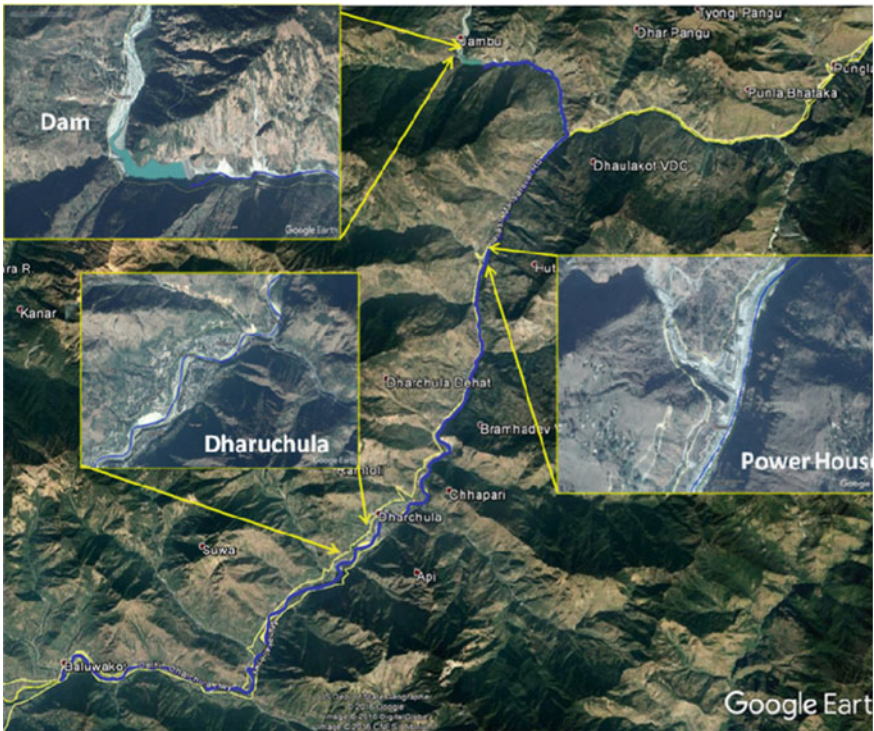


Fig. 23.1 Study area

### 23.3 Data Used

For dam break analysis, the reservoir is considered at Full Reservoir Level (FRL) when the design flood enters into the reservoir. Probable Maximum Flood (PMF) and 100 year return period flood, as shown in Fig. 23.2, are used as design flood in the analysis. The dam details like type of dam, construction materials and type, design details of dam and reservoir, bed level of the river at the dam site, the height of the top of the dam, area capacity details, etc. are obtained from the project authority.

The digital elevation model of the downstream area is generated using CartoDEM obtained from NRSC. The 10 m resolution CartoDEM for the study area is shown in Fig. 23.3. The cross section data for the river are extracted from this CartoDEM at every 500 m distance in ArcGIS. Altogether, 60 river cross sections have been used in the 30 km study stretch. The bed resistance for the river is assigned as 0.05 in accordance with Table 23.1 of AHEC guidelines (AHEC-IITR 2013) depending upon the river bed material as observed during a field visit.



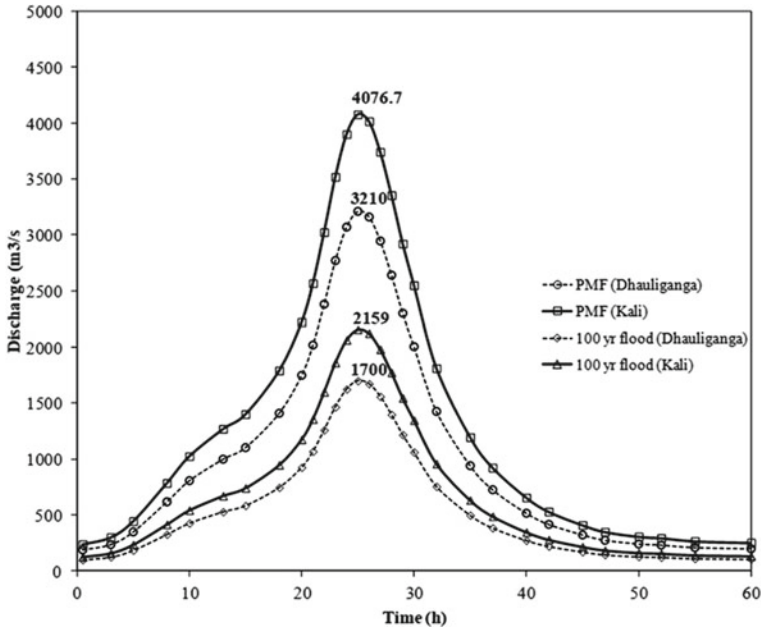


Fig. 23.2 Design flood hydrographs at Dhauliganga dam site

### 23.4 Methodology for Dam Break Analysis

The methodology of dam break analysis consists of two major components; estimation of breach outflow and movement of breached flow in downstream reach. The breach outflow depends upon the development of the breach section in the dam. The development of the breach can either be specified as a known function of time, or it can be simulated from the sediment transport capacity of the breach flow.

#### 23.4.1 Estimation of Breach Parameters

The estimation of the breach location, size, and development time is crucial in order to make an accurate estimate of the outflow hydrographs and downstream inundation. The breach parameters will directly affect the estimate of the peak flow coming out of the dam, as well as any possible warning time available to downstream locations. Unfortunately, the breach location, size, and formation time are often the most uncertain pieces of information in a dam failure analysis. A dam’s potential breach characteristics can be estimated in several ways, including the following: comparative analysis (comparing dam to historical failures of dams of similar size, materials, and water volume); regression equations (equations developed from historical dam

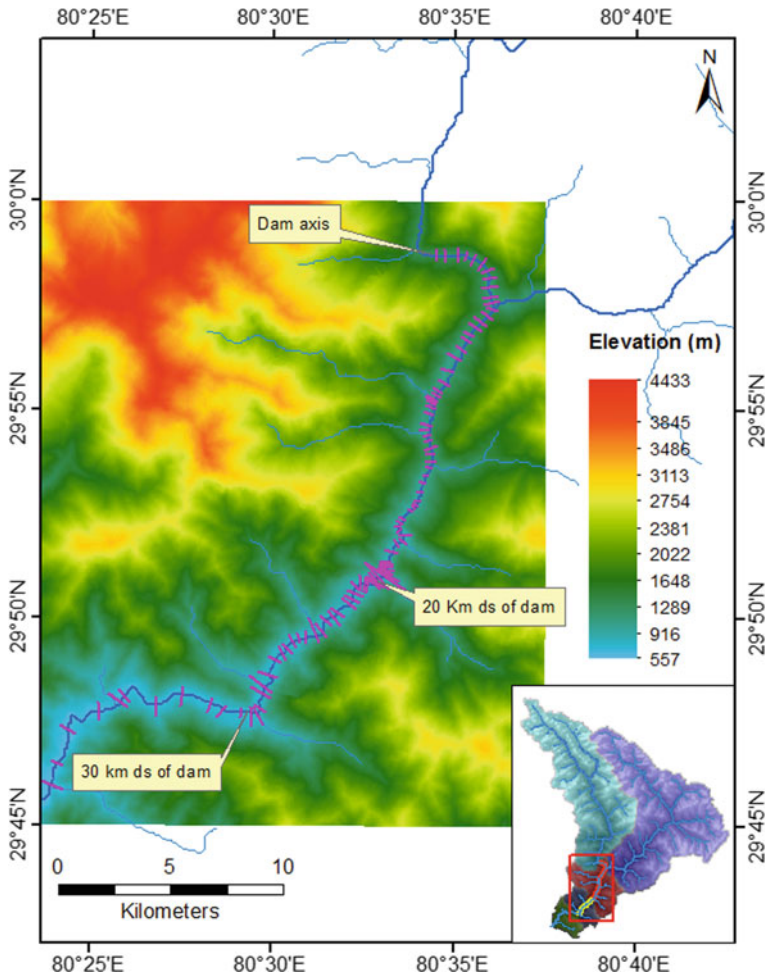


Fig. 23.3 CartoDEM for downstream reach

failures in order to estimate peak outflow or breach size and development time); utilization of velocity (or shear stress) versus erosion rates; and physically based computer models (software that attempts to model the physical breaching process by using sediment transport/erosion equations, soil mechanics, and principles of hydraulics). All of these methods are viable techniques for estimating breach characteristics. However, each of these methods has strengths and weaknesses and should be considered as a way of “estimating” the parameters and not utilized as absolute values. The breach dimensions, as well as the breach formation time, are the prerequisite of dam break modeling and should be estimated prior to model setup. Many case studies have been performed on data from historic dam failures in the US, leading to guidelines, regression equations, and computer modeling methodologies for the

**Table 23.1** Description of breach parameters

SN	Approach	Average Breach width (m)	Time of failure (hour)	Side slope of breach section
1	Froehlich (1995)	66	0.26	1.4:1
2	Froehlich (2008)	52	0.25	1.:1
3	MacDonald and Langridge-Monopolis (1984)	310	2.82	0.5:1
4	Von Thun and Gillette (1990)	128	1.13	1.:1
5	Xu and Zhang (2009)	27	1.9	0.5:1
6	Upper bound	28	4	1:1
7	Lower bound	225	0.1	1:1
8	<b>Estimated breach parameters</b>	<b>50</b>	<b>1</b>	<b>1:1</b>

prediction of the dam breach size and time. Wahl (1998) summarized comprehensive literature on historic dam failures data and recommends a range of breach parameter for dam break analysis. The regression equations are also suggested to make estimates of the breach dimensions and failure time namely by Froehlich (1995), Froehlich (2008), Von Thun and Gillette (1990), and Xu and Zhang (2009). These estimates should then be used to perform a sensitivity analysis. The Federal Agencies (FA) guidelines and regression equation-based approach are widely used. In fact, the guideline provides the upper and lower bound of parameters values while the range estimated from regression equations is used for parameter sensitivity analysis (TD-39 2014). In this study, the breach parameters have been estimated based on various regression analyses and average estimates for each parameter have been used for dam break analysis, as shown in Table 23.1. The progressive development of breach in the dam section is shown in Fig. 23.4.

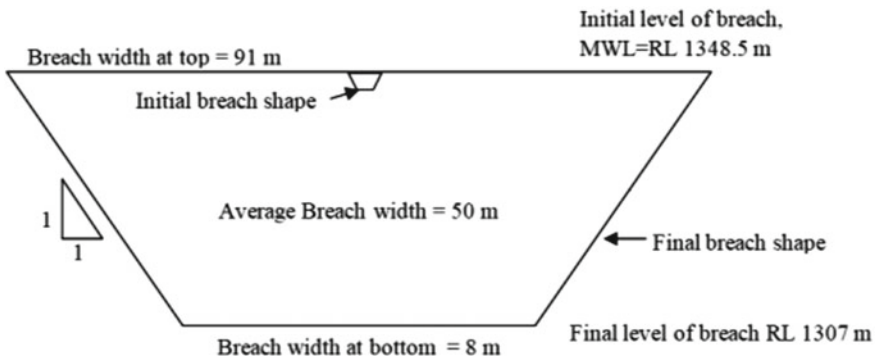


**Fig. 23.4** Estimated final breach shape for dam break analysis

### 23.4.2 Flood Routing

The movement of flood in the downstream reach is described through the solution of basic Saint Venant's partial differential equations of conservation of mass and momentum as shown below:

Conservation of mass (continuity) equation

$$(\partial Q/\partial X) + \partial(A + A_0)/\partial t - q = 0 \quad (23.1)$$

Conservation of momentum equation

$$(\partial Q/\partial t) + \{\partial(Q^2/A)/\partial X\} + g A ((\partial h/\partial X) + S_f + S_c) = 0 \quad (23.2)$$

where  $Q$  = discharge;  $A$  = active flow area;  $A_0$  = inactive storage area;  $h$  = water surface elevation;  $q$  = lateral outflow;  $x$  = distance along waterway;  $t$  = time;  $S_f$  = friction slope;  $S_c$  = expansion contraction slope; and  $g$  = gravitational acceleration.

The mathematical modeling of dam break flow is a cost- and time-effective approach to (approximately) solve the above governing equations. The present dam break study has been carried out using MIKE 11 HD model developed by the Danish Hydraulic Institute (DHI). The core of the MIKE 11 system consists of the HD (hydrodynamic) module, which is capable of simulating unsteady flows in a network of open channels. The results of a HD simulation consist of time series of water levels and discharges. MIKE 11 hydrodynamic module is an implicit, finite difference model for unsteady flow computation. The model can describe sub-critical as well as super-critical flow conditions through a numerical description which is altered according to the local flow conditions (in time and space). Advanced computational modules are included for the description of flow over hydraulic structures, including possibilities to describe structure operation. The formulations can be applied for looped networks and quasi-two-dimensional flow simulation on flood plains. The computational scheme is applicable for vertically homogeneous flow conditions extending from steep river flows to tidal influenced tributaries.

## 23.5 Results and Discussions

### 23.5.1 Dam Break Analysis

The design flood of PMF and 100 year return period flood is defined in the Dhauliganga reservoir in different cases of flood simulation. The dam fails when the reservoir is at MWL of RL 1348.5 m. The failure through overtopping of the dam is considered. Further, during the time of failure, all the spillway gates are considered to remain fully open. The downstream boundary condition is defined at Chainage

30 km of Kali river. The breach starts at RL 1348.5 m (MWL) and develops in a trapezoidal shape and the bottom of the section comes down to the lowest bed level of RL 1307 m (crest level of chute spillway) in a duration of 1 h. Three cases of flooding are considered in this study as follows:

1. Case-1, Breach occurs under PMF when the reservoir is at MWL.
2. Case-2, Routing of PMF is simulated without dam failure.
3. Case-3, Breach occurs when the reservoir is at MWL without any significant inflow (Sunny day failure).

Thus, Case-1 is the critical flooding condition for dam break analysis, and Case-3 is the sunny day failure. For Case-1 when inflow (PMF) is higher compared to breach outflow from a small reservoir storage (about 2.98 MCM), the peak of breach outflow is dominated by peak inflow and storage contribution remains comparatively less significant. Further, as the spillway gates are fully opened, a significant amount of flow passes through the spillway. The flood hydrograph at the dam section for Case-1 is shown in Fig. 23.5. The figure shows the outflow hydrographs at the breach section and through spillway gates. The food in the downstream reach of river is contributed from breach outflow and spillway outflow in addition to the contribution from the main Kali river. In the downstream river valley, the attenuation of flood hydrograph occurs as shown in Fig. 23.6. At Chainage 250 m, 5750 m, 11,750 m, 20,250 m, and 25,250 m, the peak flood is of 4421.47 m<sup>3</sup>/sec, 8466.55 m<sup>3</sup>/sec, 8466.17 m<sup>3</sup>/sec, 8466 m<sup>3</sup>/sec, and 8466.02 m<sup>3</sup>/sec, respectively. The increase in discharge beyond 2000 m is due to inflow from the Kali river wherein Dhaliganga river outfalls. Further small attenuation of flood hydrograph is due to gorge shape river valley with steep longitudinal slope. The time of occurrence of peak flood at 20 km d/s reach from dam site is about 42 min. The water surface profile for flooding conditions in Case-1

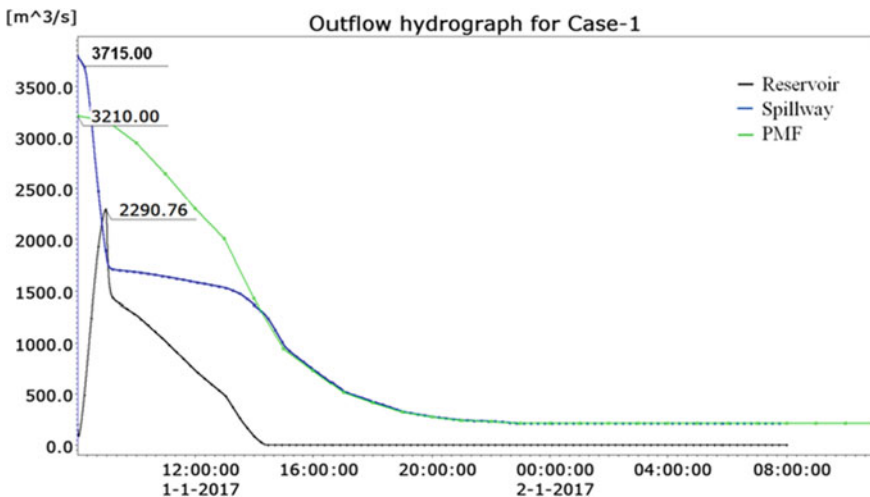


Fig. 23.5 Outflow hydrograph and design flood at dam section for Case-1

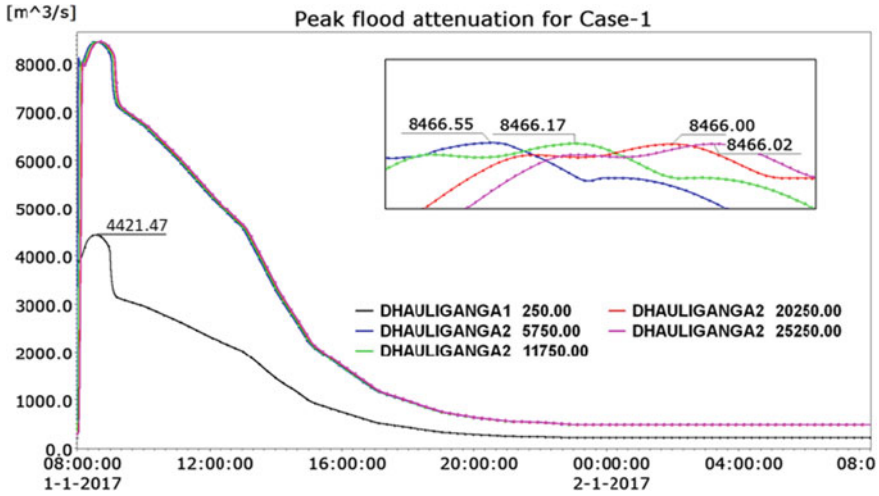


Fig. 23.6 Attenuation of flood hydrograph in downstream reach for Case-1

is shown in Fig. 23.7. The maximum flood elevation maps are superimposed over the high-resolution Google Earth image to prepare the inundation maps as shown in Fig. 23.8. As the river valley is very narrow, the spread area for dam breach flood is very limited. The detailed inundation may be visualized by zooming over a small river stretch. The study reach is divided into seven stretches and the inundation map for each reach is prepared. Figure 23.9 shows the inundation maps for reach-5

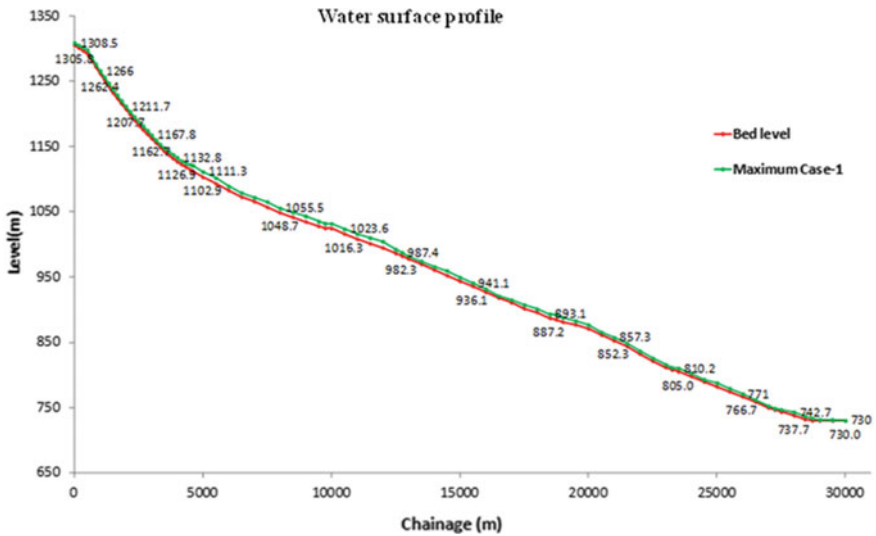


Fig. 23.7 Water surface profile for Case-1

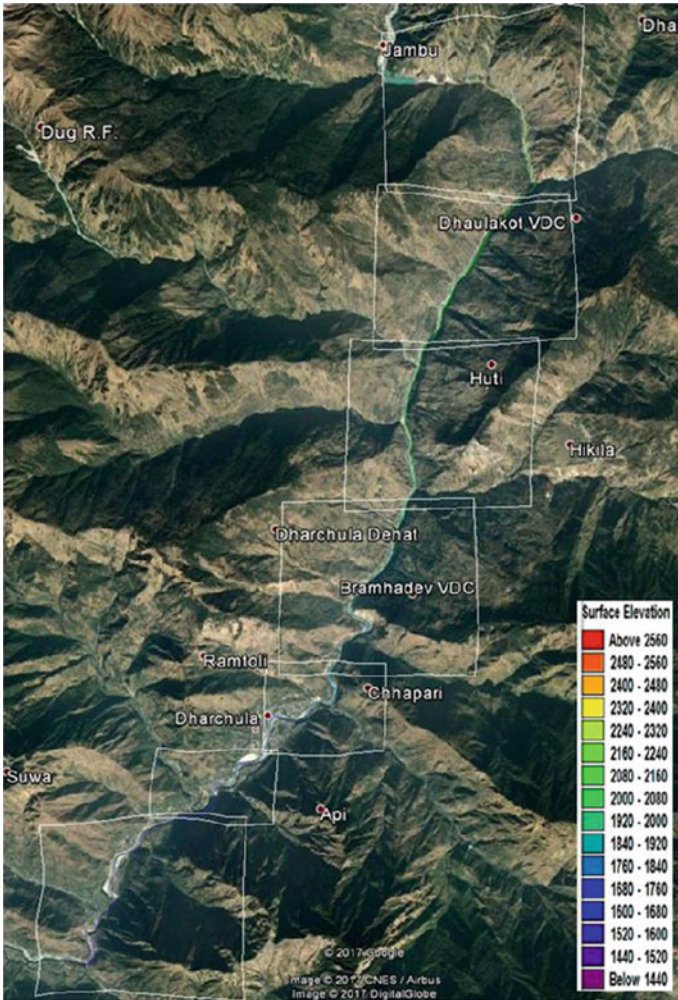
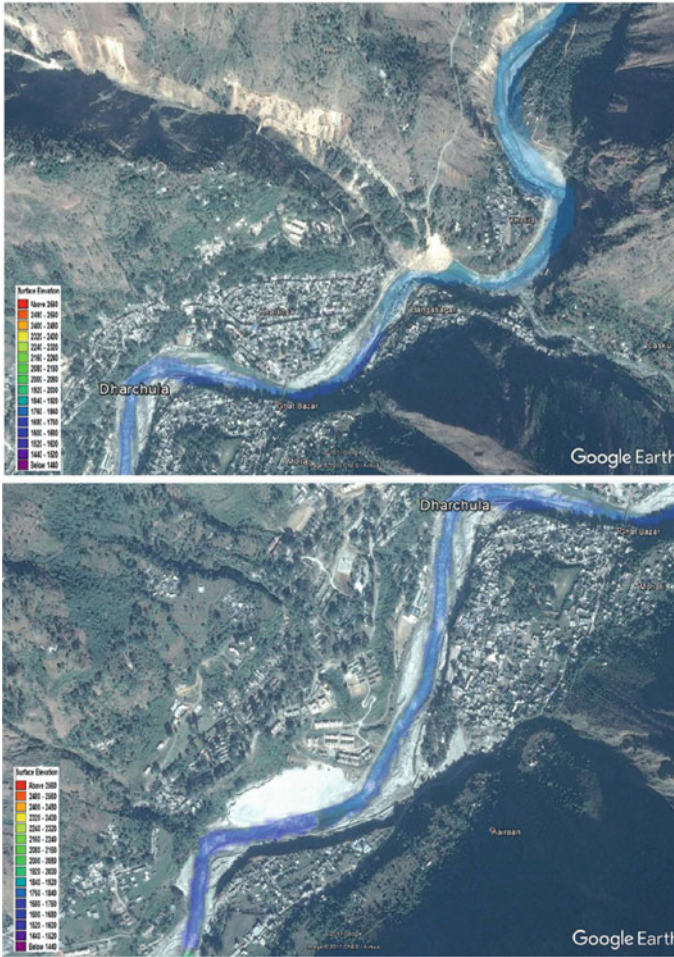


Fig. 23.8 Synoptic view of flood inundation over Google Earth for Case-1

and reach-6 where major settlements are located. Similar analysis is carried out for Case-2 and Case-3, attenuation of flood hydrographs are computed, and the extent of inundation is estimated.

The flood inundation attributes are computed using the results of the hydrodynamic model and CartoDEM. The maximum inundation (flood depth) depends upon the peak flood level and flood plain topography. For a flooding scenario, the flooding depths at a location depend upon the ground elevation at that location and, thus, are a localized phenomenon. The flood level (mean sea level) is influenced by the topography of the entire inundated area and, thus, is more global and representative in quantifying flood events along with the area of inundation. The important locations in the downstream reach of the Dhauliganga dam are Dhauliganga power house





**Fig. 23.9** Flood inundation map over Google Earth for Case-1 in Stretch 1

(Chainage-9.75 km) and Dharchula (Chainage 20 km) at which the maximum flood elevation (msl) has been computed for various cases of flooding. The peak flood level and its occurrence time estimated at these locations are shown in Table 23.2. The time of occurrence of maximum flood level is shown within the bracket. For Case-1 in which the dam break failure under PMF is simulated, the maximum flooding time is computed since the start of the breach. For Case-2 in which PMF is simulated without dam failure, the time of the peak is considered from the instance of peak inflow at the dam site. Further, the sunny day failure of Dhauligangadamis was also tabulated. This table also shows the maximum inundation area for various cases of flooding.



**Table 23.2** Maximum flood level at important locations for various cases of flooding

Particulars	Maximum inundation area (ha)	Important locations	
		Dhauliganga power house	Dharchula
MIKE 11 Chainage (km)		9.75	20
Case-1 (PMF flood and dam break)	163.27	1031.63 m (8:38:00 h)	857.06 m (8:42:00 h)
Case-2 (PMF flood only)	156.39	1031.36 m (21:04:00 h)	856.87 m (21:08:10 h)
Case-3 (only dam break)	94.53	1026.95 m (8:40:00 h)	853.84 m (8:43:00 min)

Time in bracket shows the time of travel of peak flood from the dam site to important locations

### 23.5.2 Disaster Management Plan

The maximum flood level, the extent of inundation, and time of flooding (flood above a threshold level at a particular location defined locally based on the site condition) are important inputs for preparing an emergency action plan during a disaster. Table 23.2 shows that the maximum flooding is due to Case-1. The two major components for a disaster management plan are flooding extent and its time of arrival, which are shown in this table. Such information along with the geographical extent of flooding are important inputs for the disaster management plan. In this study, no important areas/locations are inundated due to critical flooding scenarios as the river is flowing through very narrow and steep terrain while settlements are located at higher elevations.

### 23.5.3 Sensitivity of Breach Parameters

As discussed earlier, the estimation of breach parameters is based on regression equations developed from observed data from historical dam failure events and the technical guidelines based on scientific studies provided by various agencies of international repute. Still there is uncertainty in breach parameter estimates due to several reasons including different construction techniques and workmanship and other unforeseen conditions. The flood peak due to dam failure is highly affected by breach parameters and is influenced by the combination of various breach parameters. Hence, the sensitivity of the individual breach parameter is carried out. Sensitivity

analysis for three breach parameters namely breach width, time of the breach, and side slope of breach section has been done for the failure of the Dhauliganga dam. The range of estimates for various breach parameters is shown in Table 23.3.

The dam break model has been simulated with varying breach widths of 30, 50, 70, and 100 m, and the breach outflow is computed. The breach outflow hydrograph for various breach widths is shown in Fig. 23.10. With the increase in breach width, the peak flood increases. For breach width of 30 m, peak discharge is 2228.01 m<sup>3</sup>/s while for breach width of 100 m, peak discharge is 2309.46 m<sup>3</sup>/s. With an increase in breach width by 333%, the increase in peak discharge is computed to increase by 3.65% only. Similarly, the sensitivity analysis of the time of breach is carried out with varying times of failure to 0.25, 0.5, 1.0, 1.25, and 2.0 h, and its effect on breach outflow is analyzed. The breach outflow hydrograph for various failure times is shown in Fig. 23.11. With smaller breach time, the complete shape of the breach develops earlier; hence, higher peak discharge occurs quickly. The reverse happens with an increase in failure time; the peak reduces as by the time breach develops to its full size, and most of the upstream water outflows. The peak flow for 0.25 h is 4903.84 m<sup>3</sup>/s which reduces to 1476.58 m<sup>3</sup>/s for 2.0 h. Another effect of increased breach time is on the occurrence of peak discharge. For smaller failure times, the

**Table 23.3** Breach parameters estimates for sensitivity analysis

Breach parameters	Average estimates	Estimates for parameter sensitivity			
Breach width (m)	50	30	70	100	
Time of failure (hr)	1	0.25	0.5	1.25	2
Side slope (H:V)	1:1	0.5	0.75	1.25	1.5

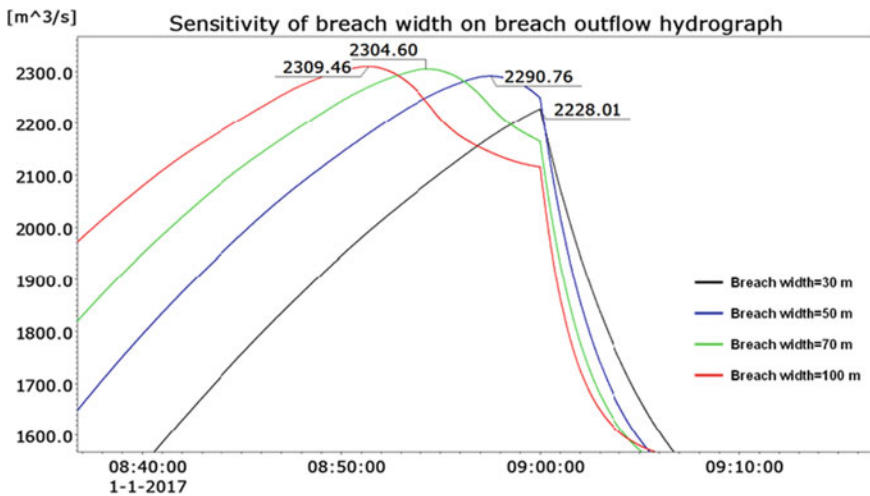


**Fig. 23.10** Sensitivity of breach width on peak discharge at breach section

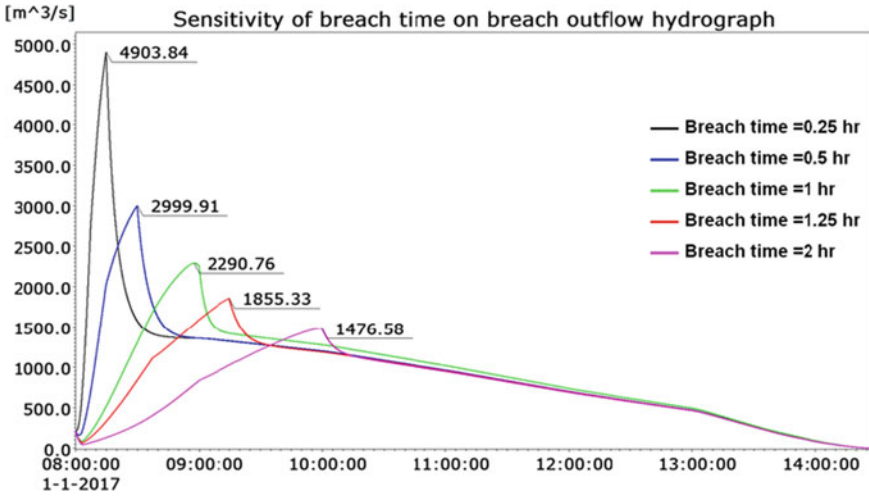


Fig. 23.11 Sensitivity of breach time on peak discharge at breach section

peak occurs earlier. The figure shows that this parameter is most sensitive in the computation of breach outflow. Another breach parameter is the shape of the breach section. The sensitivity of the breach section is shown in Fig. 23.12 which shows that this parameter is also not much sensitive.

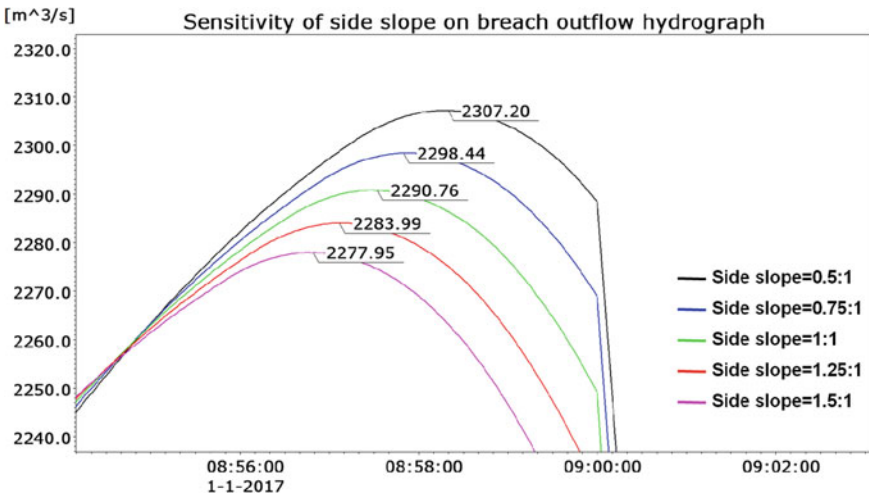


Fig. 23.12 Sensitivity of shape of breach section on peak discharge

## 23.6 Conclusions

Dam break study for the Dhauliganga dam has been carried out using the MIKE 11 model. Three cases of flooding are simulated in the study viz. Case-1: flooding due to PMF in the river causing dam break condition. The reservoir is considered at FRL during flooding. Case-2: flooding due to PMF without dam break. The entire flow passes through the spillway. Case-3: dam break failure with nominal inflow ( $100 \text{ m}^3/\text{s}$ ) in reservoir considering it at FRL. (sunny day failure condition). The breach parameters have been estimated using Federal Agency Guidelines and regression equation-based approach. The average estimate of parameters has been used. The breach parameters are breach width = 50 m and breach time = 1 h, and a trapezoidal breach section of 1:1 shape is considered for this earthen concrete faced dam. Further, sensitivity analysis has been carried out for the recommended range for different breach parameters. Flood attenuation hydrograph, water surface profile, stage hydrograph at important locations, and inundation maps superimposed over high-resolution satellite data and Google Earth have been prepared for each case. The flood inundation extent overlaid in Google Earth with detailed transport networks and other features are developed to visualize the inundation over populated/important locations. No important/populated locations are found affected by flood inundation for the severe most flooding condition. The time of travel of peak flood from the dam site to 20 km downstream end is 42 min for Case-1, 8 min for Case-2, and 43 min for Case-3. The maximum flood elevations for critical cases of flooding computed at Dhauliganga power house and Dharchula are RL 1031.63 m and 857.06 m, respectively. No populations/settlements are under inundation due to critical cases of dam failure. Though no settlements are found under inundation areas for critical flooding scenarios, and the downstream river reach is very steep and passing through densely populated Dharchula area, an effective public warning system is proposed to prevent any casualty as per the computed warning time at various locations downstream of the dam. The sensitivity of breach parameter in estimation of breach outflow has been assessed for different values of breach width and breach time. It is observed that breach time is the most sensitive parameter.

**Acknowledgement** This paper is the outcome of the study sponsored by the National Hydroelectric Power Corporation (NHPC), Faridabad. The authors hereby duly acknowledged the support provided by the project authority in carrying out the study. We also acknowledge the data support obtained from NRSC, Hyderabad.

## References

- AHEC-IITR (2013) Standard No. 2.2 & 2.3-Hydraulic and structural design, standard/manual/guideline with support from Ministry of New and Renewable Energy, Roorkee, July
- Dai J, Zhang S, Xue C (2010) Dam-break flood modeling for Tangjiashan Quake Lake. In: Second international conference on earth observation for global changes. Proceedings of SPIE, vol 7471, 74711D. <https://doi.org/10.1117/12.836313>
- NRSA (2015) Cartosat-1, 10 years and beyond. [https://nrsc.gov.in/sites/all/pdf/Chapter\\_5.pdf](https://nrsc.gov.in/sites/all/pdf/Chapter_5.pdf)
- Samantaray D, Chatterjee C, Singh R et al (2014) Flood risk modelling for optimal rice planning for delta region of Mahanadi river basin in India. *Nat Hazards* 76:347–372. <https://doi.org/10.1007/s11069-014-1493-9>
- Sanyal J, Carbonneau P, Densmore AL (2014) Low-cost inundation modelling at the reach scale with sparse data in the Lower Damodar River basin, India. *Hydrol Sci J* 59:2086–2102. <https://doi.org/10.1080/02626667.2014.884718>
- TD-39 (2014) Using HEC-RAS for Dam Break Studies, U.S. Army Corps of Engineers, Institute for Water Resources, Hydrologic Engineering Centre, 609 Second Street, Davis, CA 95616
- Wahl TL (1998) Prediction of Embankment Dam Breach parameters—a literature review and needs assessment. Dam Safety Research Report, DSO-98-004. Water Resources Research Laboratory, U.S. Dept. of the Interior, Bureau of Reclamation, Dam Safety Office (DSO), July
- WRI (2015), Annual expected populations affected by river floods compiled by World Resources Institute ([wri.org/floods](http://wri.org/floods)). [www.wri.org/sites/default/files/uploads/top\\_15\\_flooding\\_0.png](http://www.wri.org/sites/default/files/uploads/top_15_flooding_0.png)
- Yen K Di, Baldassarre G, Solomatine DP (2013) Exploring the potential of SRTM topographic data for flood inundation modelling under uncertainty. *J Hydroinf* 15(3):849–861

# Chapter 24

## Hydrologic and Hydraulic Modelling of a Bridge



Jagadish Prasad Patra, Rakesh Kumar, and Pankaj Mani

**Abstract** Bridges are an essential part of a nation's economy as they are crucial for transporting goods and people to and from major economic hubs. Failure of bridges leads to injuries, loss of life, and property damage and can drastically damage an area's local economy. High floods and bridge scour are major causes of bridge failure. In hilly terrain, highways and rail networks are generally designed along the banks of the river to optimize engineering investments and the availability of relatively flat terrain. However, bridges need to be built across tributaries and valleys. Estimation of design flood at bridge location with the water level, flow velocity, etc. are key factors to ensure the safety of the bridge. Scour in watercourses and drainage paths causes significant damage to the environment and engineering infrastructure. In order to address the issue of computing flood magnitude and corresponding water level in the river, design floods at a bridge site are estimated using various approaches, and the hydraulic modelling of the river reach with the bridge is carried out using HEC-RAS. The standard practice of estimating design flood using flood estimation report of Central Water Commission (CWC) is compared with regional flood frequency relationships developed for ungauged catchments for a bridge site with a catchment area of 251 km<sup>2</sup> for improving the accuracy of the hydrologic calculation. The peak flood for 50 and 100 year return periods areas is estimated as 3056.03 and 3450.8 m<sup>3</sup>/s following the approach given in Flood Estimation Report for Western Himalayan Zone 7. The proposed bridge is modelled using HEC-RAS by adding information of bridge deck, slopping abutments and five piers, etc. for simulating water surface profiles and velocities. The water surface profile with and without bridge is also compared in the 1 D model. The water surface elevation inside the bridge upstream for flood for 50 year and 100 year return periods are 405.84 m and 406.16 m while the total velocity is 5.73 m/s and 5.97 m/s, respectively. Further, the river flow is distributed into twenty sections in the river cross-section to analyse velocity distribution within

---

J. P. Patra (✉)

Surface Water Hydrology Division, National Institute of Hydrology, Roorkee 247667, India

R. Kumar

Department of Civil Engineering, Sharda University, Greater Noida 201310, India

P. Mani

Centre for Flood Management Studies, National Institute of Hydrology, Patna, India

the bridge section. The velocity varies from 1.8 m/s at banks to 9.3 m/s near the centre of the cross-section for 50 year return period. The maximum water depth is estimated to be 7.25 m. These various estimated hydraulic characteristics are prerequisite in designing the guide bund/river bank protection works, etc. for the design and construction of a bridge.

## 24.1 Introduction

Bridge failures can lead to injuries, loss of life, and property damage on a scale equal to plane crashes, terrorist attacks, and natural disasters. The principal causes of bridge failures were categorized as deficiencies in design, detailing, construction, maintenance, use of weak materials, and inadequate consideration of external events (Choudhury and Hasnat 2015). Failures of highway or railway bridges across the river due to high floods are one of the most common and important natural disasters (Flint et al. 2017). Every year, transport disruption caused by mountain bridge floods failures accounted for the vast majority of all natural disasters. In hilly terrain, highways and rail networks are generally designed along the banks of the river to optimize engineering investments and the availability of relatively flat terrain. However, bridges need to be built to across tributaries and valleys. Estimation of design flood at bridge location with the water level, flow velocity, etc. are key factors to ensure the safety of the bridge.

In India, flood estimation reports for various sub-zones have been prepared with joint efforts of the Central Water Commission (CWC), India Meteorological Department (IMD), and Research Design and Standards Organisation (RDSO) of the Ministry of Railways and Ministry of Surface Transport (MOST) for estimating design floods of 25, 50, and 100 year return periods for the design of waterways, bridge, culverts, etc. having small and medium catchments where hydrological data are inadequate or totally absent. Recently, PMP atlas for various basins of India has been developed by CWC and IMD for assessment of design storm as required in the assessment of design flood for any water resources development project. The point rainfall at various rain gauge stations is analysed and rainfall of various return periods has been estimated by fitting a two-parameter Gumbel frequency distribution. Various new techniques of flood frequency analysis by selecting candidate frequency distribution and parameter estimation techniques (L-Moments, PWM, etc.) are developed by various researchers (Hosking and Wallis 1997; Kumar et al. 2003; Cassalho et al. 2018). In this study, the design flood estimated by various techniques for a small ungauged Himalayan catchment is compared. Further, the hydraulic analysis of the bridge is also carried out using HEC-RAS.

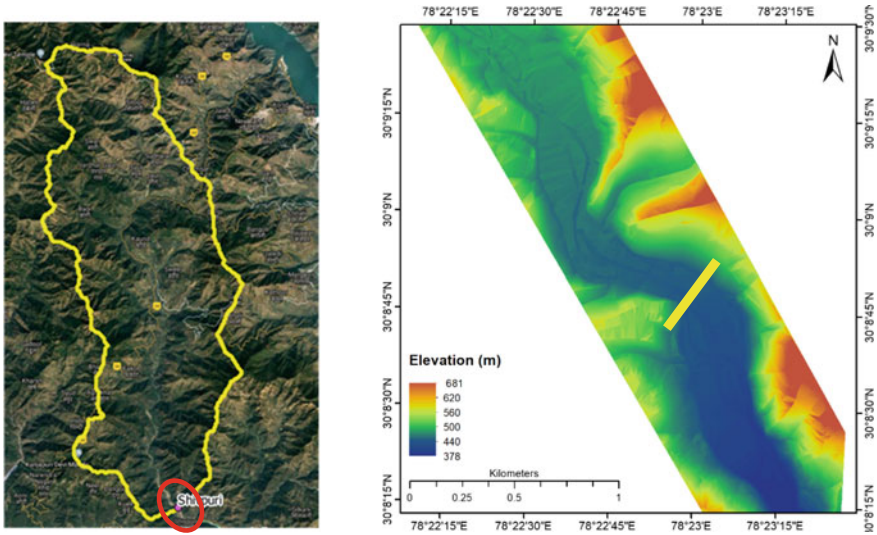


Fig. 24.1 Index map of the study area

## 24.2 Study Area and Data

The proposed bridge location is across at Shivpuri near Rishikesh. The river is a tributary of the Ganga river. The index map of the study area location of the bridge with catchment boundary is shown in Fig. 24.1. The river normally dries out after the monsoon. The DEM along the river reach which is prepared using the photogrammetric approach is also shown in Fig. 24.1.

## 24.3 Methodology

### 24.3.1 Derivation of Synthetic Unit Hydrograph

Initially, a wide extent of generated DEM has been used to delineate the catchment area of the proposed bridge site. The HEC-GeoHMS package in ArcGIS is used for delineation of catchments from DEM and extraction of various catchment characteristics. The delineated catchment area and various catchment characteristics are shown in Fig. 24.2. The Synthetic Unit Hydrograph is developed using these catchment characteristics and relationships provided in the flood estimation report for Western Himalayan Zone 7 (CWC-RDSO-IMD 1994).



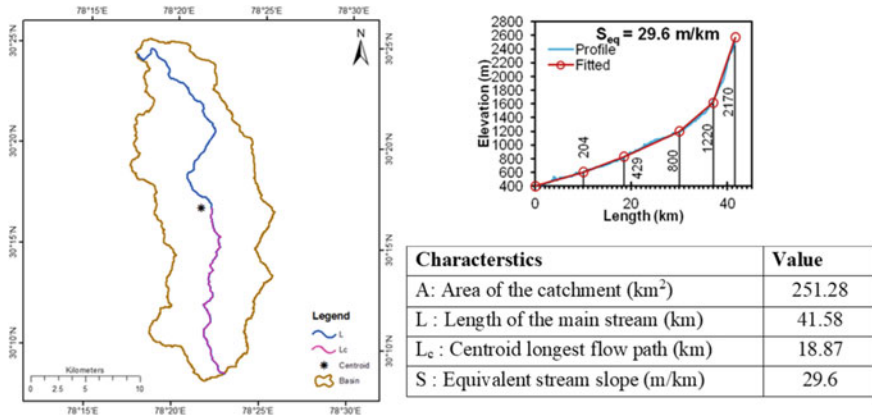


Fig. 24.2 Delineated catchments with catchment characteristics

### 24.3.2 Estimation of Design Flood Hydrographs

The design storm duration (TD) is adopted as  $1.1 \times t_p$  as recommended by CWC (1994). The rounding of the design storm duration to the nearest hour is 5 h. The ratio of 5–24 h rainfall is taken as 0.695. Areal reduction factor of 0.875 is adopted for converting areal rainfall to point rainfall. The estimated 5 h design storm after areal correction for 50 and 100 year return periods is 19.46 cm and 21.89 cm, respectively. The design storm is split into 1-h rainfall increments using the time distribution coefficient. A design loss rate of 0.20 cm/h as recommended (CWC 1994) is applied to get effective rainfall increments. The design loss rate is subtracted from the hourly rainfall to obtain an effective rainfall hyetograph and then direct runoff hydrograph is estimated by convoluting this effective rainfall with SUH. Finally, the base flow is added to obtain the design flood hydrograph.

### 24.3.3 Hydraulic Analysis in HEC-RAS

HEC-RAS is an integrated system of software, designed for interactive use in a multi-tasking environment. It has a separate steady flow water surface profile and unsteady flow simulation for one-dimensional hydraulic analysis of the river networks. The steady flow component is capable of modelling subcritical, supercritical, and mixed flow regime water surface profiles. The basic computational procedure is based on the solution of the one-dimensional energy equation. The hydraulic model setup is prepared to study river reach of about 2.5 km. The bridge geometry is created by adding information on the bridge deck, slopping abutments and piers, etc. in the 1D model. The developed bridge in HEC-RAS with various components is shown in

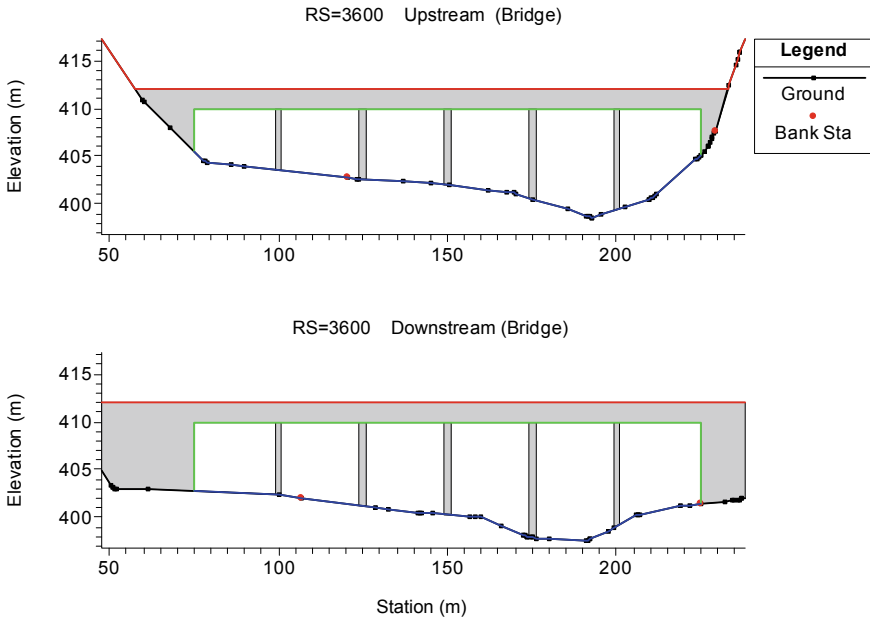


Fig. 24.3 Bridge setup in HEC-RAS

Fig. 24.3. The inflow boundary condition is basically the estimated floods of various return periods and the downstream boundary condition is considered as normal depth.

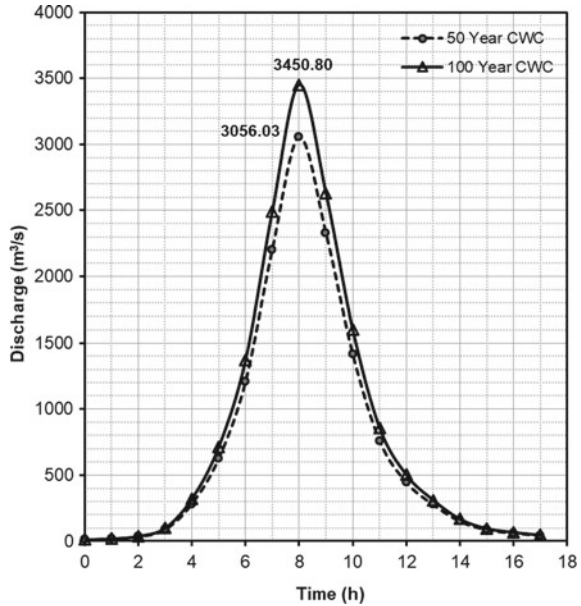
## 24.4 Result and Discussions

### 24.4.1 Estimation of Design Flood

For estimation of peak discharge, the effective rainfall increments are re-arranged against ordinates such that the maximum effective rainfall is placed against the maximum SUH ordinate, next lower value of effective rainfall against next lower value of SUH ordinate, and so on. The effective rainfall increments are then reversed to obtain a critical sequence (CWC 2001). These critical rainfall sequences are then convoluted with the SUH to estimate the direct surface runoff hydrograph. Finally, the base flow is added to estimate flood hydrograph. The estimated flood hydrographs of various return periods are shown in Fig. 24.4. The peak flood for 50 year and 100 year return periods is 3,056.03 m<sup>3</sup>/s and 3,450.80 m<sup>3</sup>/s, respectively.

For ungauged catchments, the at-site mean cannot be computed in absence of the observed flow data. Hence, a relationship between the mean annual peak flood of gauged catchments in the region and their pertinent physiographic and climatic

**Fig. 24.4** Design flood hydrographs for various return periods



characteristics is needed for the estimation of the mean annual peak flood (Kumar and Chatterjee 2005). The regional relationship in the form of a power law ( $Y = aX^b$ ) is developed for the region using the Levenberg–Marquardt (LM) iteration. For the development of a regional flood frequency relationship for ungauged catchments, the regional flood frequency relationship developed for gauged catchments is coupled with the regional relationship between mean annual peak flood and catchment area, and the regional frequency relationship is developed as  $Q_T = C_T \times A^b$ , where  $Q_T$  is the flood estimate in  $m^3/s$  for the  $T$  year return period, and  $A$  is the catchment area in  $km^2$ ,  $b$  and  $C_T$  are regional coefficients. Value of  $b$  is 0.046 and values of  $C_T$  are 61.334 and 71.788, respectively, for 50 year and 100 year return periods. Using the values of  $C_T$  and  $b$ , the peak discharge is found to be 578.32 and 676.89  $m^3/s$  for 50 and 100 year return periods.

### 24.4.2 Hydraulic Modelling of Bridge

The bridge geometry is created by adding information on the bridge deck, slopping abutments and piers, etc. The bridge is added to river section ID3600 in the HEC-RAS 1D model. The deck or roadway of the bridge is defined similar to a cross-section, with a station, high chord, and low chord. Here, the low chord is extended straight down to the ground surface where there is no opening of the bridge. Five piers are added based on the centreline of the pier at the upstream and downstream sections. Piers are drawn from the ground to the first point with the specified pier

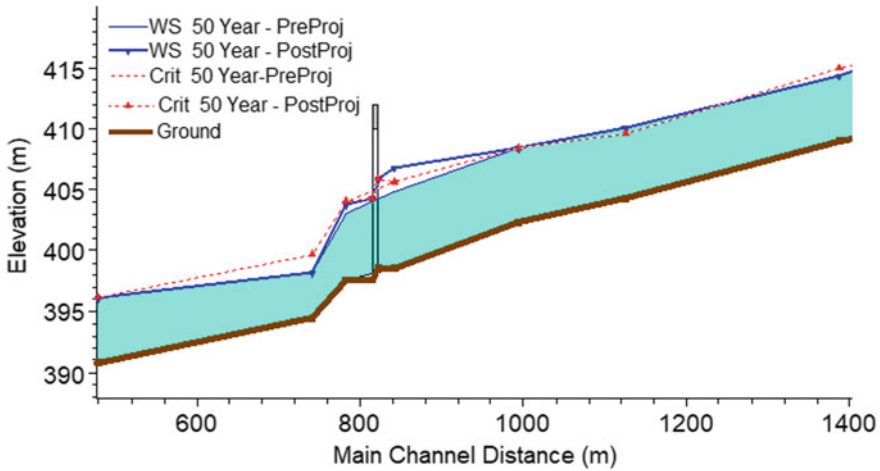


Fig. 24.5 Simulated water surface profile along the river reach

width at a certain elevation. The simulation of the river reach with the bridge is carried out with design floods of 3,056.03 m<sup>3</sup>/s and 3,450.80 m<sup>3</sup>/s for 50 year and 100 year return periods, respectively. The comparison of the longitudinal profile of river reach for pre-project (without bridge) and post-project (with bridge) is shown in Fig. 24.5. The water surface elevation inside the bridge upstream for flood for 50 and 100 year return periods is 405.84 and 406.16 m while the total velocity is 5.73 m/s and 5.97 m/s, respectively. The simulated detail output of various hydraulic properties due to 50 year return period flood at the bridge section is given in Table 24.1. Further, the river flow is distributed into twenty sections in the river cross-section to analyse velocity distribution within the bridge section. The velocity varies from 1.8 m/s at banks to 9.3 m/s near centre of the cross-section for 50 year return period. The plot of velocity distribution upstream of the bridge section due to 50 year return period

Table 24.1. Detail output at bridge section for the various 50 year return period flood

E.G. US. (m)	407.90	Element	Inside BR US	Inside BR DS
W.S. US. (m)	406.90	E.G. Elev (m)	407.71	406.13
Q Total (m <sup>3</sup> /s)	3056.00	W.S. Elev (m)	405.84	404.26
Q Bridge (m <sup>3</sup> /s)	3056.00	Crit W.S. (m)	405.84	404.26
Q Weir (m <sup>3</sup> /s)		Max Chl Dpth (m)	7.25	6.62
Weir Sta Lft (m)		Vel Total (m/s)	5.73	5.81
Weir Sta Rgt (m)		Flow Area (m <sup>2</sup> )	533.04	525.76
Weir Submerg		Froude # Chl	0.72	0.75
Weir Max Depth (m)		Specif Force (m <sup>3</sup> )	3076.39	3038.76
Min El Weir Flow (m)	412.00	Hydr Depth (m)	3.81	3.76
Min El Prs (m)	410.00	W.P. Total (m)	184.32	186.01
Delta EG (m)	2.24	Conv. Total (m <sup>3</sup> /s)	23670.6	23825.2
Delta WS (m)	3.13	Top Width (m)	140.00	140.00
BR Open Area (m <sup>2</sup> )	1114.96	Frctn Loss (m)		
BR Open Vel (m/s)	5.81	C & E Loss (m)		
BR Sluice Coef		Shear Total (N/m <sup>2</sup> )	472.70	456.03
BR Sel Method	Momentum	Power Total (N/m s)	2710.06	2650.66

flood is shown in Fig. 24.6. The maximum water depth is estimated to be 7.25 m. The simulated flood depth and velocity distribution along the reach for 50 year return period flood is shown in Fig. 24.7. It is observed that in downstream of the bridge, water depth decreases, whereas the velocity has increased. These various estimated hydraulic characteristics are pre-requisite in designing the guide bund/ river bank protection works, etc. for the design and construction of a bridge.

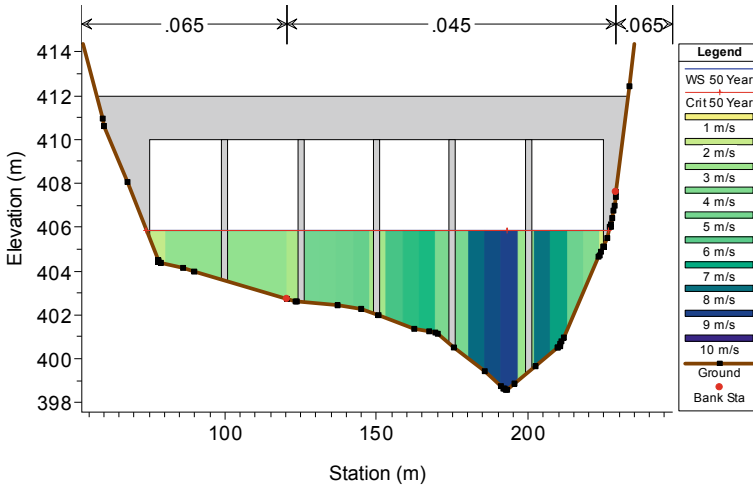


Fig. 24.6 Velocity distribution upstream of the bridge section

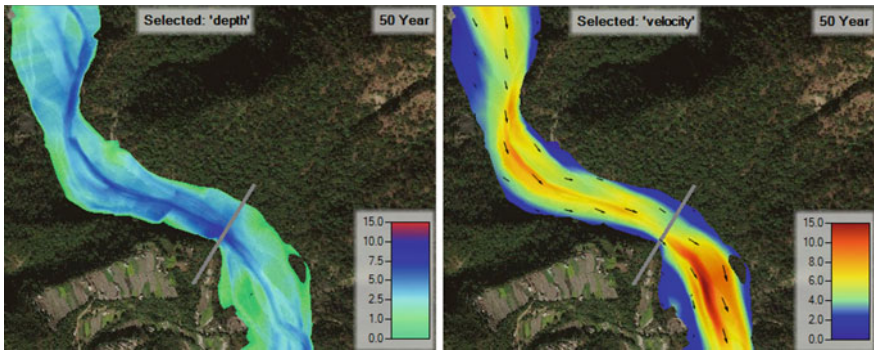


Fig. 24.7 Simulated water depth and velocity distribution along the reach

## 24.5 Conclusions

Failures of highway or railway bridge across the river due to high floods are one of the most common and important natural disasters. In hilly terrain, highways and rail networks are generally designed along the banks of rivers to optimize engineering investments and availability of relatively flat terrain. However, bridges need to be built across tributaries and valleys. Estimation of design flood at bridge locations with water levels, flow velocities, etc. are key factors to ensure the safety of the bridges. In this study, the design flood estimated by various techniques for a small ungauged Himalayan catchment is compared. The catchment area ( $251.28 \text{ km}^2$ ) of the proposed bridge location is delineated from 90 m SRTM DEM and various catchment characteristics are estimated. Synthetic Unit Hydrograph for the study area is developed using the procedure developed jointly by the CWC, RDSO, and IMD (1994) in the Flood Estimation Report for Western Himalayan Zone 7 and using the catchment characteristics of the study area. Flood hydrographs are derived using the design rainfall value given in Flood Estimation Report for Western Himalayan Zone 7. The critical rainfall sequences are convoluted with the SUH to estimate the direct surface runoff hydrograph and then the base flow is added to estimate the flood hydrograph. The estimated peak floods for 50 and 100 year return periods at the proposed bridge site are  $3056.03 \text{ m}^3/\text{s}$  and  $3450.8 \text{ m}^3/\text{s}$ , respectively. The peak floods are estimated to be  $578.32$  and  $676.89 \text{ m}^3/\text{s}$  for 50 year and 100 year return periods using regional flood frequency analysis. As a conservative approach, higher values are considered for the hydraulic analysis. The 1D hydraulic model setup of river reach of about 2.5 km is prepared in HEC-RAS from the high-resolution DEM (1 m). First, the simulation is carried out for the present condition without any bridge. Then, the bridge geometry is created by adding information on the bridge deck, abutments and piers, etc. in HEC-RAS for detail hydraulic analysis proposed. Comparison of water surface shows that the bridge will cause an increase in water level in the river reach of about 250 m length. The water surface elevation inside the bridge upstream for 50 year and 100 year return period floods are 405.84 m and 406.16 m while the total velocity is 5.73 m/s and 5.97 m/s, respectively. Further, the river flow is distributed into twenty sections in the river cross-section to analyse velocity distribution within the bridge section. It is observed that velocity varies from 1.8 m/s at banks to 9.3 m/s near the centre of the cross-section for 50 year return period. The maximum water depth is estimated to be 7.25 m. Water depth upstream of the bridge is higher than that downstream. However, the velocity is higher downstream of the bridge. These various estimated hydraulic characteristics are pre-requisite in designing the guide bund/ river bank protection works, etc. for the design and construction of a bridge.

## References

- Cassalho F, Beskow S, de Mello CR, Moura MM, Kerstner L, Ávila LF (2018) At-Site flood frequency analysis coupled with multiparameter probability distributions. *Water Resour Manag* 32(1):285–300. <https://doi.org/10.1007/s11269-017-1810-7>
- Choudhury JR, Hasnat A (2015) Bridge collapses around the world: causes and mechanisms. In: IABSE-JSCE joint conference on advances in bridge engineering-III, August 21–22, 2015, Dhaka, Bangladesh. ISBN: 978–984–33–9313–5
- CWC (2001) Manual on estimation of design flood. Hydrology studies organization. Central Water Commission, New Delhi, India
- CWC-RDSO-IMD (1994) Flood estimation report for western Himalyan zone 7. A joint work of Central Water Commission, Research Designs and Standards Organisation, India Meteorological Department and Min. of Surface Transport
- Flint MM, Fringer O, Billington SL, Freyberg D, Diffenbaugh NS (2017) Historical analysis of hydraulic bridge collapses in the continental united states. *J Inf Syst* 23(3). [https://doi.org/10.1061/\(ASCE\)IS.1943-555X.0000354](https://doi.org/10.1061/(ASCE)IS.1943-555X.0000354)
- Hosking JRM, Wallis JR (1997) Regional frequency analysis: an approach based on L-moments. Cambridge University Press, Cambridge, p 224
- Kumar R, Chatterjee C (2005) Regional flood frequency analysis using L-moments for North Brahmaputra region of India. *J Hydrol Eng Am Soc Civil Eng* 10(1):1–7
- Kumar R, Chatterjee C, Kumar S, Lohani AK, Singh RD (2003) Development of regional flood frequency relationships using L-moments for middle ganga plains subzone 1(f) of India. *Water Resour Manag* 17(4):243–257

# Chapter 25

## New Approach to Evolve Soil Water Retention Curve in Lower Kosi Basin, India



Ray Singh Meena Meena  and Ramakar Jha 

**Abstract** In recent years, several methods are developed empirically to estimate soil water content, develop soil water retention curves, and estimate hydraulic conductivity of the soil. Two new approaches based on non-linear function are evolved in the present work with exhaustive soil sampling from 29 locations of the lower Kosi basin. The lower Kosi basin is one of the important sub-basins of the Ganga River system, India, and is prone to flood inundation frequently. The physical and hydraulic properties of soil are important to predict flood inundation and are analysed in the laboratory using standard methods. The performances of existing and new approaches are evaluated using Standard Error (SE), Normalized Mean Error (NME), Mean Multiplicative Error (MME), and correlation coefficient ( $r^2$ ). The methods developed by (Genuchten, Soil Sci Soc Am J 44:892, 1980) showed good results. However, the new approaches evolved to estimate soil water retention characteristics provide better results and have been used successfully to estimate the hydraulic conductivity of the soil.

### 25.1 Introduction

To retain water content in the soil, adsorption and capillarity are prime factors. Adsorption is mainly responsible for moisture held on the surface of soil particles while capillarity holds water in the pores between the soil particles or between aggregates of the particles (Marshall et al. 1996). The relationship between the combined effect of these forces and soil water content forms a basic property of soil referred to as the Soil Water Retention Characteristics (SWRC) (Omuto and Gumbe 2009).

The indirect estimation of soil hydraulic properties using SWRC is in practice for long, and some of the commonly used analytical models of SWRC in the literature

---

R. S. M. Meena (✉)

Department of Civil Engineering, National Institute of Technology Hamirpur, Hamirpur, Himachal Pradesh 177005, India

R. Jha

Department of Civil Engineering, National Institute of Technology Patna, Bihar 800005, India



are shown in Appendix 1 (Saxton et al. 1986; Williams et al. 1992; Rawls et al. 1982; Leong and Raharjdo 1997; Rawls et al. 1998; Pachepsky and Rawls 1999; Mayr and Jarvis 1999; Nemes et al. 2001; Saxton and Willey 1999, 2004, 2006; Dexter et al. 2008; Omuto 2009, Patil et al. 2013).

In Gangetic plains having typical soil moisture characteristics and soil texture combinations, the estimation of soil water content from saturation to oven dryness is sparse, and very little work has been done in the past. No work is found in lower Gangetic plains to demonstrate soil water retention and hydraulic conductivity.

## 25.2 Review of Work

From the literature, it has been observed that (Brooks and Corey 1964) is a discrete model and does not represent continuous phenomena. Moreover, (van Genuchten 1980) model is a continuous and close form model. The model has been used extensively to estimate effective soil saturation and saturated hydraulic conductivity. In recent times, many studies have been conducted to improve the VG (1980) model. For example, (Genuchten and Nielsen 1985) derived the general VGM model; (Hutson and Cass 1987) added a parabolic approximation at the wet end to make the first derivative continuous; (Campbell and Shiozawa 1992) introduced a logarithmic section in the dry end to improve the fit in the dry range; (Rossi and Nimmo 1994) also preferred a logarithmic function over the Brooks-Corey power law; (Vogel et al. 2000) presented a modification to improve the description of the hydraulic conductivity near saturation without being aware of the physical explanation of the poor behaviour presented later by (Vogel and Cislserova 1988; Vogel et al. 2000; Ippisch et al. 2006) introduced a minimum capillary height in the (van Genuchten 1980) soil water retention equation; (Fayer and Simmons 1995) used the approach of (Campbell and Shiozawa 1992) to have separate terms for adsorbed and capillary bound water; (Kosugi 1996, 1999) presented a soil water retention curve for soils with a lognormal pore size distribution; (Schaap and Leij 2000) found that the parameter accounting for pore tortuosity and connectivity in the relative hydraulic conductivity function of the VGM model is predominantly negative; (Schaap and van Genuchten 2006) introduced a small air-entry value into the soil water retention curve; (Ippisch et al. 2006) suggested that an alternative model including an air-entry value should be used; (Khlosi et al. 2008) extended the approach of (Campbell and Shiozawa 1992) and (Fayer and Simmons 1995) to (Kosugi 1996, 1999); (Peters 2013) introduced four soil water retention models and used a logarithmic model for adsorbed water that differed from that of (Campbell and Shiozawa 1992) and the capillary model of either (van Genuchten 1980) or (Kosugi 1999); and (Iden and Durner 2014) proposed modifications of (Peters 2013) models that permitted an analytical expression for the conductivity function even if the water content was forced to be zero at dry head.

### 25.3 Study Area

River Kosi originates in Nepal and Tibet and carries a huge amount of sediment with it. Figure 25.1 indicates the location map and slope map of the Kosi basin. The topography of the basin is very steep in the upper reaches and mild in the lower reaches. Due to the very mild slope, it deposits fine sand, silt, and clay in the lower Kosi basin (Fig. 25.2). As a consequence, the soil water retention characteristics vary from upstream to downstream regions of the basin and need proper analysis.

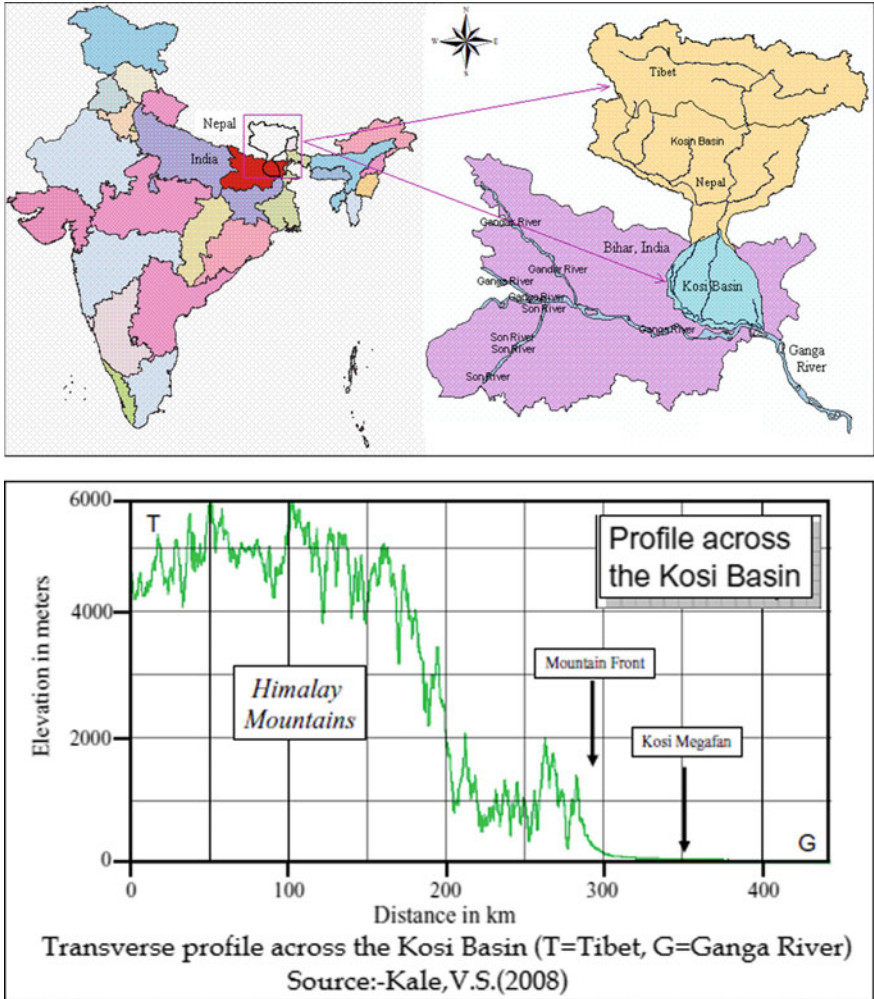


Fig. 25.1 Location and slope map of the Kosi basin of Ganga River system

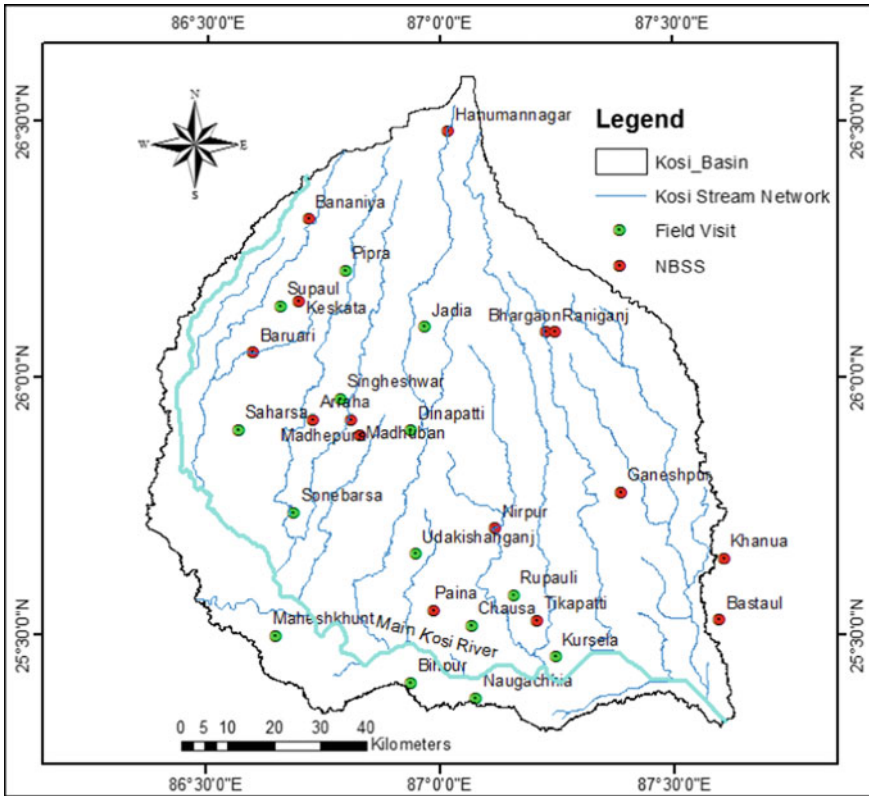


Fig. 25.2 Soil sampling locations in lower Kosi Basin, India

### 25.3.1 Soil Sample Collection and Laboratory Analysis

Undisturbed soil core samples have been collected from 29 different locations of the Kosi flood plain (at the depth of 100 cm) (Fig. 25.2) and analysis of the specific gravity, bulk density, porosity, organic carbon, particle size distribution, and water content at different pressures was done in the laboratory. For the determination of soil physical properties of disturbed and undisturbed soil samples, the following methods are applied and laboratory tests have been carried out:

### 25.3.2 Specific Gravity

It is used to determine the voids ratio, porosity, and degree of saturation if density and water content are known. The equation is as follows:

$$G = \frac{\text{Dry mass of soil}}{\text{Mass of water of equal volume}} = \frac{(M_2 - M_1)}{(M_4 - M_1) - (M_3 - M_2)} \quad (25.1)$$

where  $M_1$  is the mass of the empty pycnometer,  $M_2$  is the mass of pycnometer and oven-dried soil sample,  $M_3$  is the mass of pycnometer, soil and water taken up to the mark, and  $M_4$  is the mass of pycnometer and water filled up to the mark, and all the weights were measured in gm.

### 25.3.3 Bulk Density

The bulk density of the soil is the ratio of dry soil mass to bulk soil volume. It causes restrictions to root growth and poor movement of air and water through the soil in layers.

### 25.3.4 Porosity

Porosity or void fraction is a measure of the void (i.e. “empty”) spaces in a material and is a fraction of the volume of voids over the total volume, between 0 and 1, or as a percentage between 0 and 100%. It is defined by the ratio:

$$\phi = \frac{V_V}{V_T} \quad (25.2)$$

where  $V_V$  is the volume of void space (such as fluids) and  $V_T$  is the total or bulk volume of material, including the solid and void components.

### 25.3.5 Particle Size Distribution

The percentage of the various size of particles in the given soil samples is found based on particle size analysis using IS: 2720, Part-4, 1985 (Reaffirmed 2006). The wet sieve analysis method has been used to determine particle size less than 4.75 mm and greater than 75 microns. The percentage of soil retained on each sieve was calculated based on the total mass of the soil sample taken and the percent passing through each of the sieves.

To determine the distribution of particle size, a finer than 75-micron hydrometer analysis was conducted. Sodium Hexa-metaphosphate ( $\text{NaPO}_3$ ) was used as a dispersing agent. Hydrometer was calibrated and plotted a calibration curve between the effective depth ( $H_e$ ) and hydrometer readings ( $R_h$ ). This calibration curve was

used to find the  $H_e$  and  $R_h$  obtained during the test. Temperature correction ( $C_t$ ), meniscus correction ( $C_m$ ), and dispersing agent correction ( $C_d$ ) were considered for the hydrometer readings.

*Computation of D and N:* The particle size D is calculated from the following equation:

$$D = 10^{-5} F \sqrt{\frac{H_e}{t}} \quad (25.3)$$

where D is the diameter in mm,  $H_e$  is effective depth in cm, and t is the time in minutes. Percentage finer with respect to  $M_d$  is given by

$$N' = \frac{100G}{M_d(G-1)} R \quad (25.4)$$

where  $M_d$  is the mass of the sample, G is the specific gravity of the soil sample, and R is the corrected hydrometer reading. Overall percentage finer N is given by

$$N = N' \times \frac{M'}{M} \quad (25.5)$$

where  $M'$  is cumulative mass passing 2 mm sieve and M is the total dry mass of the soil sample.

### 25.3.6 Organic Carbon

Soil organic carbon content was determined by the chromic oxidation equivalent of soil organic matter proposed by (Walkley and Black 1934) (IS: 2720 (Part XXII)-1972). The percentage of organic matter in soil was estimated using the following equation:

$$\text{Organic carbon(\%)} = \frac{10(B-S)}{B} \times 0.3 \quad (25.6)$$

where B is ml of std. 0.5 N ferrous ammonium sulphate required for blank. S is ml of std. 0.5 N ferrous ammonium sulphate required for the soil sample. The percentage of organic carbon multiplied by 1.724 gives the percentage of organic matter,

$$\text{Organic matter(\%)} = \text{OC(\%)} \times 1.724 \quad (25.7)$$

### 25.3.7 Soil Water Content

Soil water content at -33, -100, -500, and -1500 k-Pa has been measured using the pressure plate apparatus (IS 14765: 2000) method. Soil samples passing through 2 mm sieve were taken for analysis. Soil samples were poured into the rubber ring and the samples were allowed to saturate for 20 h in the presence of free water. After this period, excess water was removed from the ceramic plate. Desired pressure was set slowly. At this point, water started flowing out of the outlet tube and continued to flow till equilibrium was reached inside the extractor. After the equilibrium was attained, the samples were removed and transferred immediately to the moisture boxes. The moisture boxes containing soil samples were weighed in the balance and fresh weight was recorded. The moisture boxes were put in the drying oven at 105 °C for 24 h to determine the gravimetric water content. To determine the volumetric water content for each case, gravimetric water content was multiplied by the corresponding bulk density. The procedure was repeated for determining water retention at other equilibrium pressures (-33, -100, -500, and -1500 k Pa) to construct the curve over the entire soil moisture range.

## 25.4 Evolving New Methods for Soil Water Retention Characteristics

In Appendix 1, the existing models used for the indirect measurement of soil moisture are shown. These models were found to underestimate the values of soil moisture at a different suction pressure in the lower Kosi basin and failed to represent the upper and the lower extremities. Moreover, they also failed to vary with variation in soil physical properties at various locations.

To overcome, two different approaches have been evolved (Eqs. 25.8 and 25.9). In new approaches, the following considerations are made:

1. Air-entry suction pressure ( $\varphi_a$ ) has been used as the denominator to saturated water pressure ( $\varphi$ ). The dimensionless value helps in relating hydraulic properties significantly at field capacity and wilting point of soil samples.
2. Variable “a” has been introduced in place of constant “1” in the denominator of the equation to make additional provisions to demonstrate a wide range of soil physical properties.
3. In approach two, the denominator value has been further reduced by reducing the dimensionless parameter by a constant “1” to fit in the upper and lower extremities of the soil water retention curve more effectively.

### 25.4.1 Governing Equations Evolved Using the Above Criteria

#### Approach I

$$\theta_r + \frac{(\theta_s - \theta_r)}{\left(a + \left(-\frac{\alpha\varphi}{\varphi_a}\right)^n\right)^m} \tag{25.8}$$

#### Approach II

$$\theta_r + \frac{(\theta_s - \theta_r)}{\left(a + \left(-\frac{\varphi}{\varphi_a} - 1\right)^n\right)^m} \tag{25.9}$$

## 25.5 Results and Discussions

In the analysis, soil physical properties are determined in the laboratory (Fig. 25.3) using standard methods. It has been observed that the lower Kosi basin is dominated by Sandy-loam soil. The porosity ranges between 30 to 50% and the bulk density is found to vary from 1.41 to 1.70 g/cc. A relationship between the porosity of various soil samples of the study area and their particle size has been developed (Fig. 25.4) for a better understanding of the soil water content in the study area. Porosity shows a very good positive correlation with silty soil in comparison to sandy soil. However, Porosity shows a good correlation with the clayey soil of the study area. It has been observed that the organic matter ranges between 0.23–0.81%, which is very less and does not have any significant effect on soil hydraulic property.

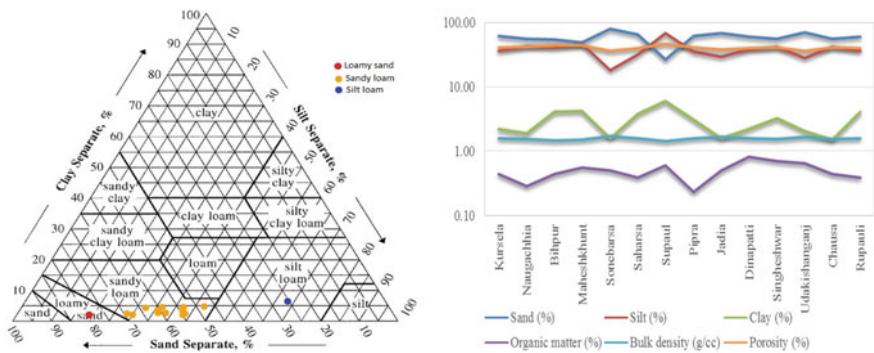


Fig. 25.3 Soil texture and physical properties of the study area

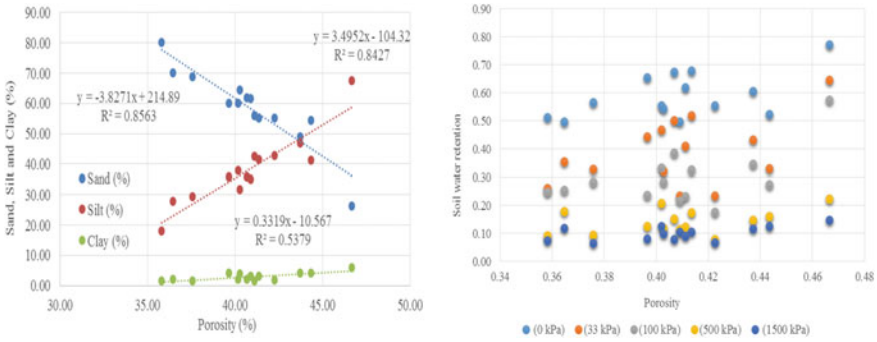


Fig. 25.4 Porosity in relation to particle size and water retention

Figure 25.5 illustrates the soil water content at the different pressure (suction) analysed and tested in the laboratory, which includes Field capacity (33 kPa) and Wilting point (1500 kPa) too. The minimum value of Wilting point (1500 k-Pa) is observed at Jadia (0.0667) and the maximum value at Supaul (0.1473). Similarly, the minimum value of Field capacity (-33 k-Pa) is observed at Pipra (0.2339) and maximum values are found at Supaul (0.6458). The saturated soil moisture is found minimum at Pipra (0.4964) and maximum at Supaul (0.7736). Finally, Supaul is found to have the highest moisture content.

The performance of all the equations shown in Appendix 1 is tested and results are not found suitable for the Lower Kosi basin. Interestingly, the results obtained using the Exponential, Power function, (Libardi and Reichardt 1979), and (Simmons, Nielsen, and Biggar 1979) show constant values and do not indicate any correlation

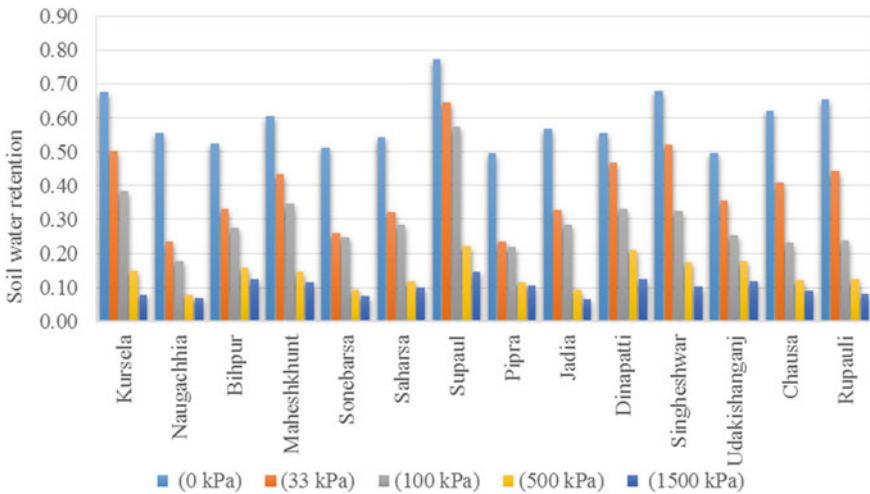
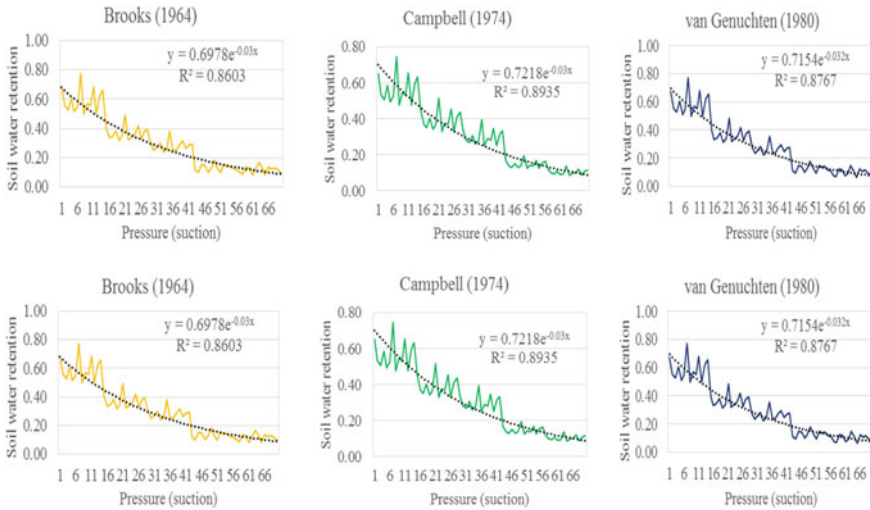


Fig. 25.5 Soil water content at different suction pressures





**Fig. 25.6** Results obtained at two soil sampling stations of the Lower Kosi basin using Brooks and Corey (1964), Campbell (1974), and Van Genuchten (1980) models

with the observed one. However, the results obtained using (Brooks and Corey 1964), (Campbell 1974), and (van Genuchten 1980) provided good results as shown in Fig. 25.6.

### 25.5.1 Approach 1 and Approach 2

The soil water retention curve results obtained using new Approach 1 and Approach 2 (as given in Eq. 25.8 and Eq. 25.9) for representative sampling stations are shown in Figs. 25.7 and 25.8, respectively. It has been observed that the soil water retention characteristics derived from both the approaches estimate wilting point and field capacity.

Essentially, the results for all the 29 sampling stations for different suctions pressures (0 kPa, 33 kPa, 100 kPa, 500 kPa, and 1500 kPa) were combined and computed as shown in Fig. 25.9. The results using Approach 1 ( $r^2 = 0.9447$ ) shows better agreement in comparison to Approach 2 ( $r^2 = 0.9132$ ).

The performance of each equation has been evaluated using statistics based on differential errors; Standard Error (SE), Normalized Mean Error (NME), and Mean Multiplicative Errors (MME), and a coefficient of determination ( $r^2$ ). The standard error and normalized mean errors have been determined using the following equations:

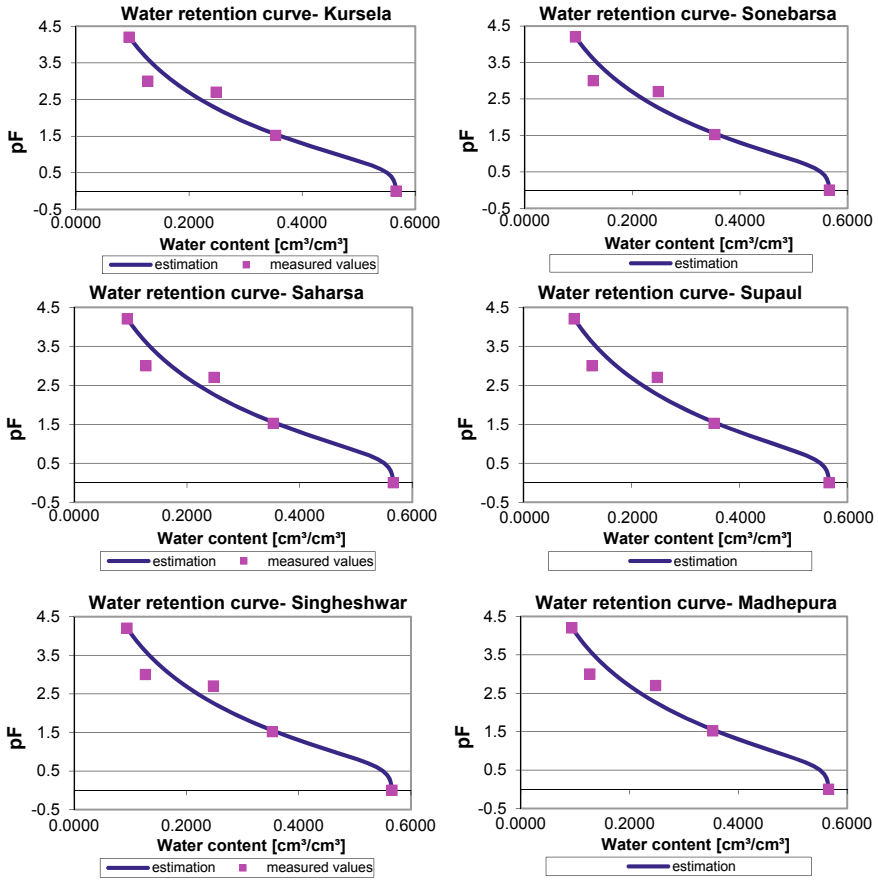


Fig. 25.7 Derived soil water retention curve using Approach 1

$$SE = \left[ \sum_{i=1}^N \frac{(E - M)_i^2}{N} \right]^{1/2} \tag{25.10}$$

$$NME = \frac{100\%}{N} \sum_{i=1}^N \left( \frac{E - M}{M} \right)_i \tag{25.11}$$

where N is the number of measurements and E and M are the estimated and measured values.

The Mean Multiplicative Error (MME) which is considered to provide a better basis for assessing the impact of inaccuracies in predicting (Moog and Jirka 1998; Jha et al. 2001, 2004) is defined as follows:

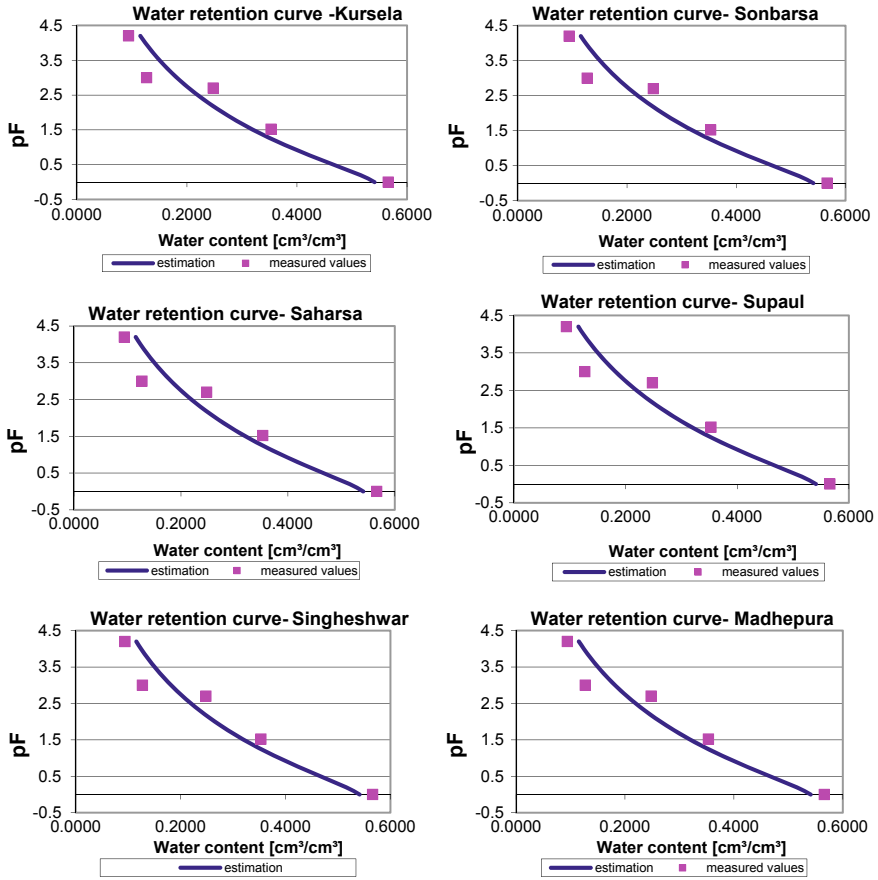


Fig. 25.8 Derived soil water retention curve using Approach 2

$$MME = \exp \left[ \frac{\sum_{i=1}^N |\ln(E/M)_i|}{N} \right] \tag{25.12}$$

If the model under use produces good results, the values of E and M will be close, and therefore, MME will be close to unity. Note that the statistical criteria described above are independent of each other. The SE uses the difference in magnitude of the observed and predicted values, while MME uses their ratios. The MME was also used herein to compare the performance of various approaches. Since it was used in a seminal paper by (Moog and Jirka 1998), the results can be readily compared. Various researchers have used these approaches (Jha et al. 2001, 2004, 2007; Jain and Jha, 2005; Kalburgi et al. 2015) and found MME to provide un-bias results for smaller as well as larger values.

Linear coefficient of determination ( $r^2$ )

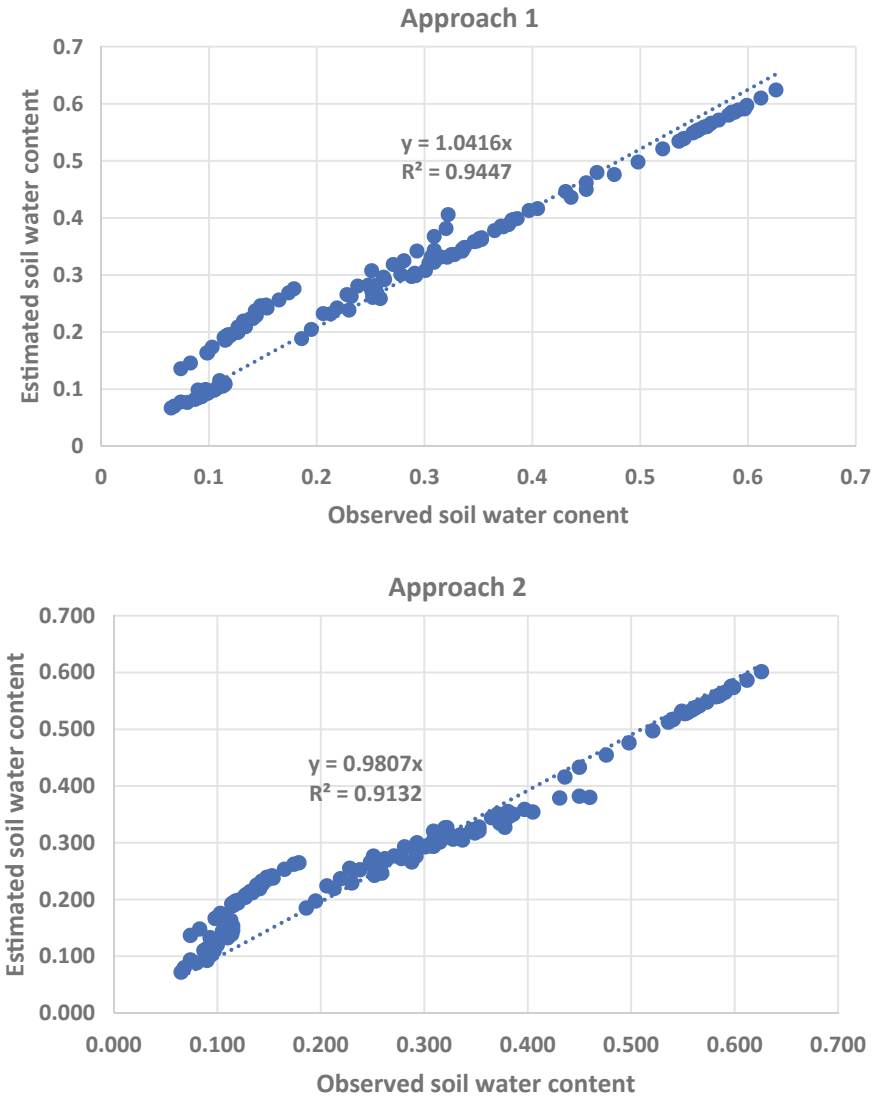


Fig. 25.9 Comparison of results of Approaches 1 and 2 with observed values

$$r^2 = \left( \frac{1}{n-1} \sum_{i=1}^n \frac{(M_i - \bar{M})(E_i - \bar{E})}{S_M S_E} \right)^2 \tag{25.13}$$

where  $E_i$  is estimated water content ( $\text{cm}^3/\text{cm}^3$ ) at pressure  $h$  for  $i$ th value,  $M_i$  is measured water content ( $\text{cm}^3/\text{cm}^3$ ) at  $i_{th}$  value,  $N$  is the total number of observations,

$\bar{M}$  is mean of measured water content,  $\bar{E}$  is mean of estimated water content,  $S_M$  is the sum of measured water content, and  $S_E$  is the sum of estimated water content.

The SE, NME, MME, and  $r^2$  estimated for Approaches 1 and 2 are shown in Fig. 25.10. Again, it has been observed that MME, which is one of the unbiased error estimates, provides better results for Approach 1 (values remain close to 1) in comparison to Approach 2. The values of SE and NME are very small and do show very small differences in both approaches.

In the next step, the estimated values of soil water content are compared with observed values at different suction pressures individually. Figure 25.11 illustrated that the estimated values of soil water content do not show excellent agreement with observed values at suction pressures of 1500 kPa (wilting point) and 100 kPa in both approaches. However, better results are observed for Approach 1.

## 25.6 Conclusions

In the Lower Kosi basin of Ganga River system, India, it is difficult to measure the soil water content of sandy loam soil due to inevitable expenses, manpower, and difficulty to approach the region. The use of indirect methods to estimate soil hydraulic properties as an alternative to direct estimation is found to be one of the most effective methods. Thirty most commonly used methods have been tested for their applicability in the lower Kosi basin, India. The function developed by (van Genuchten 1980) showed better results in comparison to other models. However, two new approaches based on non-linear functions are evolved and tested. The results obtained using both approaches provide very good results. However, when both the methods are compared, Approach 1 shows better agreement with observed values due to its better performance at different suction pressures individually. Both the models evolved in the present work could be successfully applied in other river basins too.



Fig. 25.10 Error statistics SE, NME, MME, and  $r^2$  for new approaches

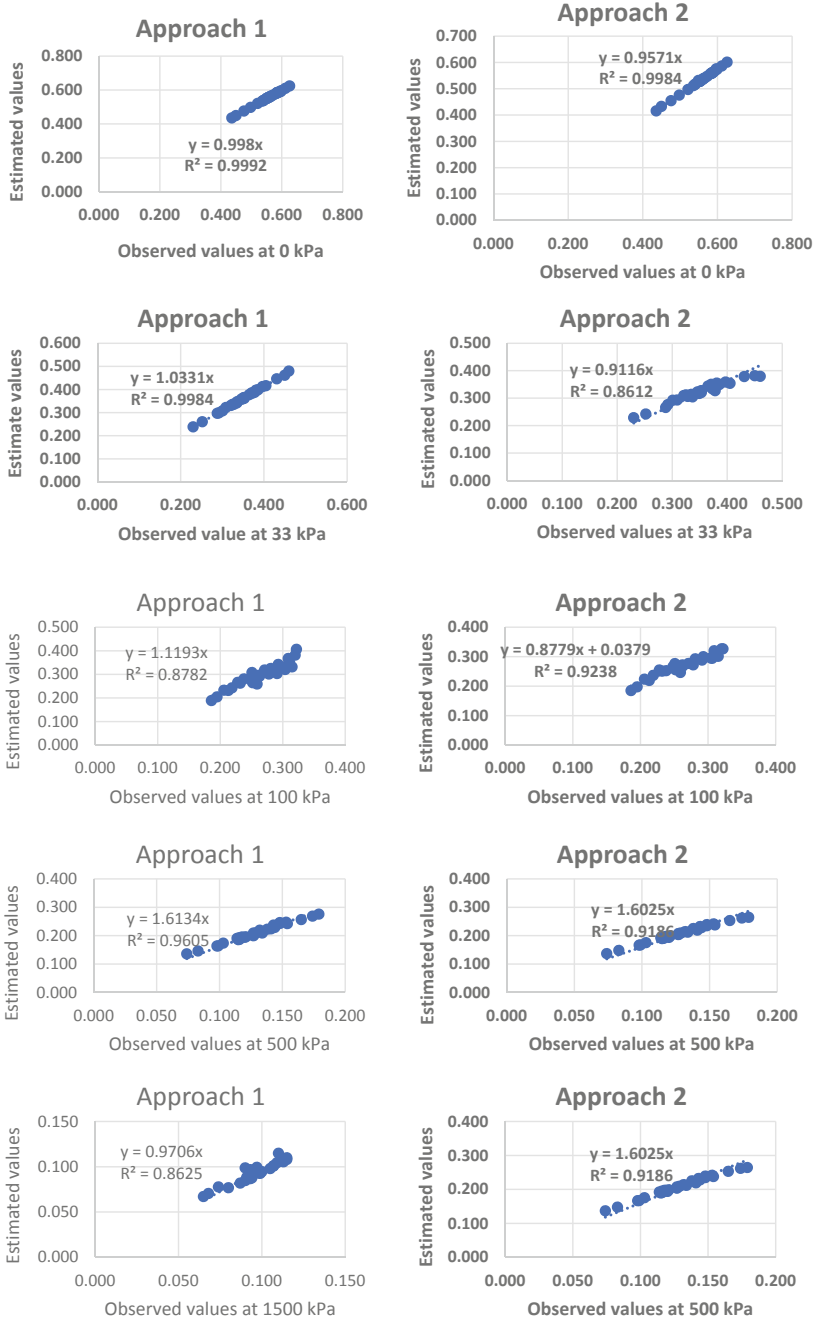


Fig. 25.11 Observed Vs Estimated soil water content at different suction pressures

**Acknowledgements** The authors would like to express their sincere thanks to the National Institute of Technology, Patna, and the National Institute of Technology, Rourkela, for providing all types of facilities and funding for conducting this study.

## **Appendix 1**

See Table [25.1](#).



**Table 25.1** Commonly used analytical models for SWRC

Sl. No	Reference	Function
1	Gardner (1958)	$\theta(h) = \theta_r + (\theta_s - \theta_r)[1 + (\alpha h)^n]^{-1}$
2	Brooks–Corey (1964)	$\theta(h) = \begin{cases} \theta_r + (\theta_s - \theta_r)\left(\frac{h}{h_{ae}}\right)^{-1}, & h \leq h_{ae} \\ \theta_s, & h > h_{ae} \end{cases}$
3	Farrel and Larson (1972)	$\theta = \theta_r + (\theta_s - \theta_r)[1 - 1/\alpha \ln(h/h_e)]$
4	Campbell (1974)	$\theta = \theta_s (h/h_b)^{-1/b}$
5	Libardi et al. (1979)	$\theta = \theta_s + (1/\beta) \ln(h/\alpha + 1)$
6	Simmons et al. (1979)	$\theta = \theta + (1/\beta) \ln(h/\alpha + 1)$
7	Van Genuchten (1980)	$\theta(h) = \theta_r + (\theta_s - \theta_r)(1 +  \alpha h ^n)^{-m}, h \leq 0$
8	Tani (1982)	$\theta = \theta_r + (\theta_s - \theta_r)[1 + (\alpha h)e^{-\alpha h}]$
9	Driessen (1986)	$\theta = \theta_s h^{-\gamma \ln(h)}$
10	Hutson–Cass (1987)	$\theta(h) = \begin{cases} \theta_s \left(\frac{h}{h_{ae}}\right)^{-\lambda}, & h \leq h_i \\ \theta_s \left[ 1 - \left(\frac{h}{h_{ae}}\right)^2 \frac{\left(1 - \frac{2}{\lambda+2}\right)}{\left(\frac{2}{\lambda+2}\right)^{\frac{2}{\lambda}}}\right], & 0 \geq h > h_i \end{cases}$
11	Ruso (1988)	$\theta(h) = \theta_r + (\theta_s - \theta_r)[(1 + 0.5\alpha h)e^{0.5\alpha h}]^2 h + 2$
12	Exponential	$\theta = -1/\beta \ln(h/\alpha)$
13	Power	$\theta = (h/\alpha)^{-1/\beta}$
14	Campbell and Shiozawa (1992)	$\theta(h) = \theta_a \left(1 - \frac{\ln h }{\ln h_d }\right) + A_2 \left(\frac{1}{1+ \alpha h ^4}\right)^m$
15	Rossi and Nimmo (1994)	$\theta(h) = \begin{cases} \theta_s \beta \ln\left(\frac{h_d}{h}\right), & h_d < h \leq h_j \\ \theta_s \left(\frac{h_{ae}}{h}\right)^\lambda, & h_j < h \leq h_{ae} \\ \theta_s, & h > h_{ae} \\ 0, & h \leq h_d \end{cases}$
16	Rossi and Nimmo (1994)	$\theta(h) = \begin{cases} 0, & h \leq h_d \\ \theta_s \left[ \left(\frac{h_c}{h}\right)^\lambda - \left(\frac{h_c}{h_d}\right)^\lambda + \xi_2 \ln\left(\frac{h_d}{h}\right) \right], & h_d \leq h \leq h_i \\ \theta_s \left[ 1 - c_2 \left(\frac{h}{h_c}\right)^2 \right], & h_i \leq h \leq 0 \end{cases}$

(continued)

**Table 25.1** (continued)

Sl. No	Reference	Function
17	Fredlund–Xing (1994)	$\theta = \theta_r + \frac{\theta_s - \theta_r}{\left\{ \ln \left[ e + \left( \frac{h}{\alpha} \right)^n \right]^m \right\}}$
18	Fayer and Simmons (1995)	$\theta(h) = \begin{cases} 0, & h \leq h_d \\ \theta_a \left( 1 - \frac{\ln h }{\ln h_d } \right) + \left[ \theta_s - \theta_a \left( 1 - \frac{\ln h }{\ln h_d } \right) \right] \left( \frac{h_{ae}}{h} \right)^\lambda, & h_d < h < h_{ae} \\ \theta_s, & h \geq h_{ae} \end{cases}$
19	Kosugi (1999)	$\theta(h) = \begin{cases} 0, & h \leq h_d \\ \theta_a \left( 1 - \frac{\ln h }{\ln h_d } \right) + \left[ \theta_s - \theta_a \left( 1 - \frac{\ln h }{\ln h_d } \right) \right] \frac{1}{2} \operatorname{erfc} \left[ \frac{\ln \left( \frac{h}{h_m} \right)}{\sigma \sqrt{2}} \right], & h_d < h < h_m \\ \theta_s, & h \geq h_m \end{cases}$
20	Vogel (2000)	$\theta(h) = \begin{cases} \theta_r + (\theta_m - \theta_r) (1 +  \alpha h ^n)^{-m}, & h < h_s \\ \theta_s, & h \geq h_s \end{cases}$
21	Groenevelt and Grant (2004)	$\theta(h) = \begin{cases} 0, & h \leq -10^{6.9} \text{ cm} \\ g_1 \left\{ \exp \left( \frac{-g_0}{6.9^n} \right) - \exp \left[ \frac{-g_0}{\log_{10} h ^n} \right] \right\}, & -10^{6.9} \leq h \leq -1 \text{ cm} \\ g_1 \exp \left( \frac{-g_0}{6.9^n} \right), & h \geq -1 \text{ cm} \end{cases}$
22	Ippisch et al. (2006)	$\theta(h) = \begin{cases} \theta_r + (\theta_s - \theta_r) \left( \frac{1 +  \alpha h ^n}{1 +  \alpha h_{ae} ^n} \right)^{-m}, & h < h_{ae} \\ \theta_s, & h \geq h_{ae} \end{cases}$
23	KCGS (2006)	$\theta = \theta_a \left( 1 - \frac{\ln(\Psi)}{\ln(\Psi_0)} \right) + \left( \theta_s - \theta_a \left( 1 - \frac{\ln(\Psi)}{\ln(\Psi_0)} \right) \right) \frac{1}{2} \operatorname{erfc} \left[ \frac{\ln \left( \frac{\Psi}{\Psi_m} \right)}{\sqrt{2}\sigma} \right]$
24	Omuto (2009)	$\theta(h) = \theta_r + \theta_1 e^{-\alpha_1 h} + \theta_2 e^{-\alpha_2 h}$
25	Peters (2013) van Genuchten-version with non-zero water content	$\theta(h) = \begin{cases} \theta_s w \left[ 1 + (-\alpha h)^n \right]^{\frac{1}{n}-1} + \theta_s (1-w) \frac{1 - \frac{\ln \left( 1 + \frac{h}{h_a} \right)}{\ln \left( 1 + \frac{h_d}{h_a} \right)}}{1 - \frac{\ln(2)}{\ln \left( 1 + \frac{h_d}{h_a} \right)}}, & h_d \leq h \leq h_a \\ \theta_s w \left[ 1 + (-\alpha h)^n \right]^{\frac{1}{n}-1} + \theta_s (1-w), & 0 \geq h \geq h_a \end{cases}$

(continued)

**Table 25.1** (continued)

Sl. No	Reference	Function
26	Peters (2013) Kosugi-version with non-zero water content	$\theta(h) = \begin{cases} \frac{\theta_s w}{2} \operatorname{erfc} \left[ \frac{\ln\left(\frac{h}{h_m}\right)}{\sigma\sqrt{2}} \right] + \theta_s(1-w) \frac{1 - \frac{\ln\left(1 + \frac{h}{h_a}\right)}{\ln\left(1 + \frac{h_d}{h_a}\right)}}{1 - \frac{\ln(2)}{\ln\left(1 + \frac{h_d}{h_a}\right)}}, & h_d \leq h \leq h_a \\ \frac{\theta_s w}{2} \operatorname{erfc} \left[ \frac{\ln\left(\frac{h}{h_m}\right)}{\sigma\sqrt{2}} \right] + \theta_s(1-w), & 0 \geq h \geq h_a \end{cases}$
27	Peters (2013) van Genuchten-version with zero water content	$\theta(h) = \begin{cases} 0, & 0 \geq h \geq h_a \\ \theta_s \left( w \left\{ \frac{1}{2} \operatorname{erfc} \left[ \frac{\ln\left(\frac{h}{h_m}\right)}{\sigma\sqrt{2}} \right] - 1 \right\} + 1 \right) \frac{1 - \frac{\ln\left(\frac{h}{h_m}\right)}{\ln\left(\frac{h}{h_m}\right)}}{1 - \frac{\ln\left(\frac{h}{h_m}\right)}{\ln(2)}}, & h_d \leq h \leq h_a \\ \frac{\theta_s w}{2} \operatorname{erfc} \left[ \frac{\ln\left(\frac{h}{h_m}\right)}{\sigma\sqrt{2}} \right] + \theta_s(1-w), & 0 \geq h \geq h_a \end{cases}$
28	Peters (2013) Kosugi-version with zero water content	$\theta(h) = \begin{cases} 0, & h \leq h_d \\ \theta_s \left( w \left\{ \frac{1}{2} \operatorname{erfc} \left[ \frac{\ln\left(\frac{h}{h_m}\right)}{\sigma\sqrt{2}} \right] - 1 \right\} + 1 \right) \frac{1 - \frac{\ln\left(1 + \frac{h}{h_a}\right)}{\ln\left(1 + \frac{h_d}{h_a}\right)}}{1 - \frac{\ln(2)}{\ln\left(1 + \frac{h_d}{h_a}\right)}}, & h_d \leq h \leq h_a \\ \frac{\theta_s w}{2} \operatorname{erfc} \left[ \frac{\ln\left(\frac{h}{h_m}\right)}{\sigma\sqrt{2}} \right] + \theta_s(1-w), & 0 \geq h \geq h_a \end{cases}$
29	Iden and Durner (2014)	$\theta_s  h ^{-k} \frac{dS^{ad}}{dh} = \frac{\theta_s  h ^{-k-1}}{\ln(10)(\log h_a  - \log h_d )} \left[ 1 - \frac{\exp\left(\frac{\log h_a  - \log h }{b}\right)}{1 + \exp\left(\frac{\log h_a  - \log h }{b}\right)} \right]$

## References

- Brooks R, Corey A (1964) Hydraulic properties of porous media and their relation to drainage design. *Trans ASAE*
- Campbell G (1974) A simple method for determining unsaturated conductivity from moisture retention data. *Soil Science*
- Campbell G, Shiozawa S (1992) Prediction of hydraulic properties of soils using particle-size distribution and bulk density data. *Estim Hydraul Prop Unsaturated Soils*
- Dexter AR, Czyż EA, Richard G, & Reszkowska A (2008) A user-friendly water retention function that takes account of the textural and structural pore spaces in soil. *Geoderma* 143(3-4):243–253
- Fayer M, Simmons C (1995) MCOdified soil water retention functions for all matric suctions. *Water Res Res*
- van Genuchten (1980) A closed-form equation for predicting the hydraulic conductivity of unsaturated soils1. *Soil Sci Soc Am J* 44(5):892. <https://doi.org/10.2136/sssaj1980.03615995004400050002x>
- Van Genuchten M, D Nielsen (1985) On describing and predicting the hydraulic properties. *Annal Geophys*
- Hutson J, Cass A (1987) A retentivity function for use in soil–water simulation models. *European J Soil Sci*
- Iden S, Durner W (2014) Comment on simple consistent models for water retention and hydraulic conductivity in the complete moisture range by A. Peters. *Water Res Res*
- Ippisch O, Vogel H, Bastian P (2006) Validity limits for the van Genuchten–Mualem model and implications for parameter estimation and numerical simulation. *Adv Water Res*
- Jain SK, Jha R (2005) Comparing the stream re-aeration coefficient estimated from ANN and empirical models. *Hydrol Sci J* 50(6):1037–1052. <https://doi.org/10.1623/hysj.2005.50.6.1037>
- Jha R, Ojha C, Bhatia K (2007) Development of refined BOD and DO models for highly polluted Kali River in India. *J Environ Eng*
- Jha R, Ojha CSP, Bhatia KKS (2001) Refinement a predictive reaeration equations for a typical Indian river. *Hydrol Process* 15(6):1047–1060. <https://doi.org/10.1002/hyp.177>
- Jha R, Ojha CSP, Bhatia KKS (2004) A supplementary approach for estimating reaeration rate coefficients. *Hydrol Process* 18:65–79
- Kalburgi P, Jha R, Ojha C (2015) Evaluation of re-aeration equations for river Ghataprabha, Karnataka, India and development of refined equation. *Environmental*
- Khlosi M, Cornelis WM, Douaik A, van Genuchten MT, Gabriels D (2008) Performance evaluation of models that describe the soil water retention curve between saturation and oven dryness. *Vadose Zone J* 7(1):87. <https://doi.org/10.2136/vzj2007.0099>
- Kosugi K (1996) Lognormal distribution model for unsaturated soil hydraulic properties. *Water Res Res*
- Kosugi K (1999) General model for unsaturated hydraulic conductivity for soils with lognormal pore-size distribution. *Soil Sci Soc Am J*
- Leong EC, Rahardjo H (1997) Review of soil-water characteristic curve equations. *J Geotech geoenvironmental Eng* 123(12):1106–1117
- Libardi P, Reichardt K (1979) Analise da redistribuicao de agua visando a condutividade hidraulica do solo. *Energ Nuclear*
- Mayr T, & Jarvis NJ (1999) Pedotransfer functions to estimate soil water retention parameters for a modified Brooks–Corey type model. *Geoderma* 91(1-2):1–9
- Moog D, Jirka G (1998) Analysis of reaeration equations using mean multiplicative error. *Environ Eng* 124(2):104–110
- Nemes AD, Schaap MG, Leij FJ, & Wösten JHM (2001) Description of the unsaturated soil hydraulic database UNSODA version 2.0. *J Hydrol* 251(3-4):151–162
- Omuto CT (2009) Biexponential model for water retention characteristics. *Geoderma* 149(3-4):235–242

- Pachepsky YA, & Rawls WJ (1999) Accuracy and reliability of pedotransfer functions as affected by grouping soils. *Soil Sci Soc Am J* 63(6):1748–1757
- Patil NG, Tiwary P, Pal DK, Bhattacharyya T, Sarkar D, Mandal C & Dongre V (2013) Soil water retention characteristics of black soils of India and pedotransfer functions using different approaches. *J Irrig Drainage Engineering* 139(4):313–324
- Peters A (2013) Simple consistent models for water retention and hydraulic conductivity in the complete moisture range. *Water Res Res*
- Rawls WJ, Brakensiek DL, Saxton KE (1982) Estimation of soil water properties. *Transactions of the ASAE* 25(5):1316–1320
- Rawls WJ, Gimenez D, Grossman R (1998) Use of soil texture, bulk density, and slope of the water retention curve to predict saturated hydraulic conductivity. *Transactions of the ASAE* 41(4):983
- Rossi C, Nimmo J (1994) Modeling of soil water retention from saturation to oven dryness. *Water Res Res*
- Saxton KE, Rawls W, Romberger JS & Papendick RI (1986) Estimating generalized soil-water characteristics from texture
- Saxton KE, & Rawls WJ (2006) Soil water characteristic estimates by texture and organic matter for hydrologic solutions. *Soil Sci Soc Am J* 70(5):1569–1578
- Saxton KE, & Willey PATRICK (1999, July). Agricultural wetland and pond hydrologic calculations using the SPAW-II model. In *Proceedings, Amer Soc Agric Eng Meeting, Toronto, ON*
- Saxton KE, & Willey MP (2004) Agricultural wetland and pond hydrologic analyses using the SPAW model. In *Self-Sustaining Solutions for Streams, Wetlands, and Watersheds*, 12-15, September 2004 (p. 9). American Society of Agricultural and Biological Engineers
- Saxton KE, & Willey PH (2006) The SPAW model for agricultural field and pond hydrologic simulation. *Watershed models*. CRC Press, Boca Raton, FL, 401–435
- Schaap M, van Genuchten M (2006) A modified Mualem–van Genuchten formulation for improved description of the hydraulic conductivity near saturation *Vadose Zone J* 5(1):27–34. <https://doi.org/10.2136/vzj2005.0005>
- Schaap M, Leij F (2000) Improved prediction of unsaturated hydraulic conductivity with the Mualem-van Genuchten model. *Soil Sci Soc Am*
- Simmons CS, Nielsen DR, Biggar JW (1979) Scaling of field-measured soil-water properties. I. Methodology. II. Hydraulic conductivity and flux. *Hilgardia* 47(4):75–174
- Vogel T, Cislérova M (1988) On the reliability of unsaturated hydraulic conductivity calculated from the moisture retention curve. *Transp Porous Media*
- Vogel T, Van Genuchten M, Cislérova M (2000) Effect of the shape of the soil hydraulic functions near saturation on variably-saturated flow predictions. *Adv Water Res*
- Walkley A, Black IA (1934) An examination of the Degtjareff method for determining soil organic matter, and a proposed modification of the chromic acid titration method. *Soil Sci* 37(1)
- Williams RD, Ahuja LR, Naney JW (1992) Comparison of methods to estimate soil water characteristics from soil texture, bulk density, and limited data. *Soil Science* 153(3):172–184

# Chapter 26

## Variability of Rainfall, Temperature, and Potential Evapotranspiration at Annual Time Scale Over Tapi to Tadri River Basin, India



Prem Mahyavanshi, V. D. Loliyana, and Priyank J. Sharma

**Abstract** The changes in the meteorological variables are one of the most important factors that affect crop water requirements and, subsequently, water allocation for food production in an agriculture-based country like India. The present study evaluates the application of statistical trend detection tests and examines the magnitude slope of trends in climatic variables viz., rainfall, Potential Evapotranspiration (PET), and temperature over the west-flowing rivers in the Tapi to Tadri basin, India. In the present study, high-resolution daily gridded rainfall dataset of India Meteorological Department (IMD) at  $0.25 \times 0.25^\circ$  resolution, while the PET and temperature data of Climate Research Unit (CRU) at  $0.5 \times 0.5^\circ$  resolution have been analyzed for a period of 116 years (1901–2016) at the annual scale. The trends in aforesaid climate variables have been detected using the non-parametric Mann–Kendall (MK) and the Modified Mann–Kendall (MMK) tests, and the slope of trend magnitude is computed from Sen’s Slope (SS) test. The results indicated an increasing trend in annual rainfall across 61% grids, while decreasing across 37% grids and no trends were observed at remaining grids out of 119 grids. Further, an increasing trend in potential evapotranspiration, maximum, mean, and minimum temperatures were observed at all the 40 grids. Thus, an increase in temperature was greatly responsible for increasing trends in potential evapotranspiration across the study region. The outcomes of the present study provide insight into the climate variability and interaction among the meteorological variables across the Tapi to Tadri basin for the study period.

---

P. Mahyavanshi

Department of Civil and Construction Engineering, University of Wolverhampton, Rustomjee Academy for Global Careers, Dahanu Road (East), Maharashtra 401602, India

V. D. Loliyana (✉)

Faculty, Department of Civil and Construction Engineering, University of Wolverhampton, Rustomjee Academy for Global Careers, Dahanu Road (East), Maharashtra 401602, India

P. J. Sharma

DST INSPIRE Fellow, Department of Civil Engineering, Sardar Vallabhbhai National Institute of Technology, Surat, Gujarat 395007, India

## 26.1 Introduction

The climate variability and its dynamics are the basis of several research on climate change and its impacts. The variability in precipitation and temperature results in climate changes that require consideration owing to their impact on the water-energy-nexus (Dore 2005). Numerous trends and indices of climatic variables obtained from the empirical data indicate an upward trend of average surface global temperature since the 1950s, and the highest rate of changes was detected since the middle of 1970s (Kundu et al. 2016; Quirk 2012; Alexander et al. 2006; Frich et al. 2002). Besides the basic meteorological variables viz., precipitation and temperature, Evapotranspiration (ET) is an important climate variable and essential element of the hydrological cycle that has substantial implications in the agricultural fields. The determination of evapotranspiration is necessary for effective water resources management in an agriculturally based country like India. The changing patterns of Potential Evapotranspiration (PET) have consequences on crop production and different hydrological processes (Hobbinset al. 2004). As per Doorenbos and Pruitt's (1977), 'the PET takes place when the ground is completely covered by actively growing uniform green grass of 8 to 15 cm tall in abundance of soil moisture'. PET could rise in most parts of the globe in near future as a result of water-retaining capacity of the atmosphere maximizes with higher temperature such as a 7% increase per 1 °C warming (Trenberth 2011). Subsequently, the evapotranspiration rate is expected to intensify due to the water vapor deficit. The factors affecting PET are the meteorological parameters, crop factor, and soil moisture content. The meteorological parameters are humidity, wind speed, rainfall, temperature, duration of sunshine hours, vapor pressure, station level pressure, etc. Therefore, long-term analysis of historical data of climatic variables is substantially required in understanding the basin behavior from a hydro-climatological perspective.

In the recent past, a number of researchers analyzed trends in mean and extreme precipitation as well as temperature (Zhai et al. 2005; Alexander et al. 2006; Martinez et al. 2012; Zhang et al. 2012; Bocolari and Malmusi 2013; Song et al. 2014; Sharma and Babel 2014; Soltani et al. 2016; Soro et al. 2016; Liu et al. 2016; Xiao et al. 2016; He et al. 2017; Caloiero 2017; Ye and Li 2017; Sharma et al. 2017) and largely reported their increasing trends across the globe. Few researchers reported trends in PET across various parts of the world (Goyal 2004; Helfer et al. 2012; Huo et al. 2013; Liu et al. 2013, 2014; Haijun et al. 2014; Sonali and Nagesh Kumar 2016). The Indian Summer Monsoon Rainfall (ISMR) exhibits wide spatial and temporal variability across India because of the influence of numerous local scale factors like variation in the growth rate of population, rapid urbanization, deforestation, etc. Their study analyzed data at finer scale, demonstrating high spatial variability in climate variables due to local level changes (in terms of population and urbanization), which contradicts results analyzed at larger scales (Ghosh et al. 2009; Sharma et al. 2017). Despite changing climate conditions, it is observed that very few studies are focusing on change detection in meteorological variables other than rainfall, viz., PET and temperature, at basin scale in India. The present study focuses on

the detection of long-term spatio-temporal changes in meteorological variables at finer spatial scales for west-flowing river basins from Tapi to Tadri. Further, a short length of meteorological data may exhibit specious inferences in trend analysis, and hence, dataset of 116 years (1901–2016) has been used in the present study. In this paper, the following objectives were studied out for Tapi to Tadri river basin, India, using high-resolution daily gridded rainfall data (119 grids) at  $0.25^\circ \times 0.25^\circ$  resolution, while the PET (40 grids) and temperature (40 grids) data at  $0.5^\circ \times 0.5^\circ$  resolution: (a) computation of the primary statistical parameters (mean, standard deviation, coefficient of variation, skewness, kurtosis) of the annual time series for 116 years (1901–2016), and (b) trend detection of annual series by application of non-parametric methods namely the Mann–Kendall, the Modified Mann–Kendall, and Sen’s slope tests.

### 26.2 Study Area

The Tapi to Tadri basin, see Fig. 26.1 (area  $\approx 55,940 \text{ km}^2$ ), exhibits an array of topographic elements ranging from laterite platforms, alluvial tracts along lagoons or estuary or rivers, coastal sand dunes or flats of mud, and sandy beaches to erosional

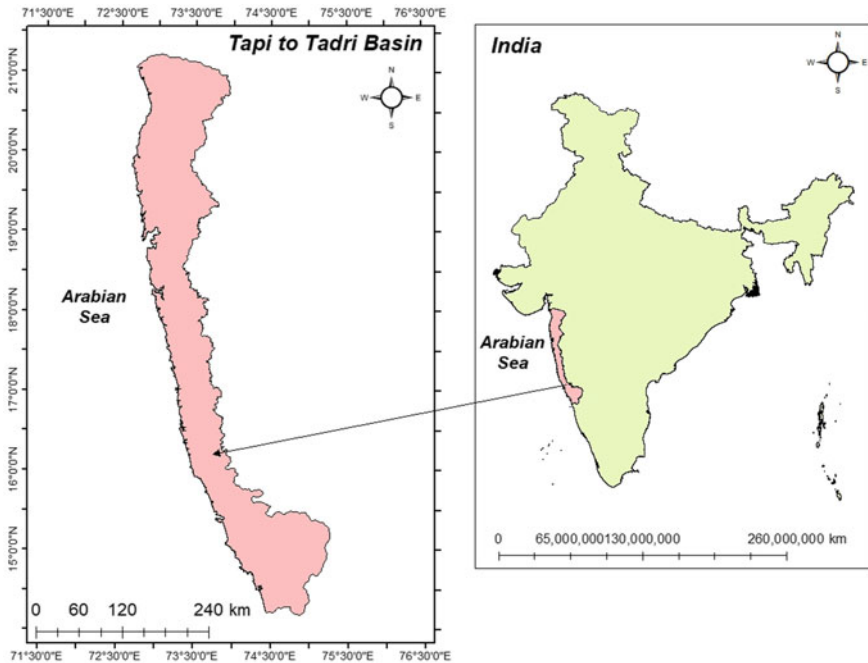


Fig. 26.1 Index map of the study area



surfaces in the residual hills or hard basement rock. With respect to physiographical nature, the entire basin is a distinct corridor of low land, having hills whose elevations rise up to 150 m at places to an excess of 300 m. The steep face of Sahyadris runs parallel to the basin and unveils an elevation between 760 and 1220 m. Along the western coast, plains of eroded marines and elevated beaches which were formed in earlier times are found at a height varying from 30 to 90 m, respectively. It can be observed that the highest recorded elevation of the basin is at 1402 m (Jain et al. 2007). The watershed area showcases a humid and moist atmosphere climate along the coastal belt which is relatively hot with a higher degree of humidity reaching an apex of 90%. The south-west and north-east monsoons control the summer and winter climate, with the winter beginning by December. The rainfall in the region is directly influenced by the south-west monsoon, which is usually heavy and assured between the June–August periods. Between the months of June and November, 90% of the rainfall is received. The peak rainfall received around Vasisthi was 2539.76 mm in 1975, whereas the minimum annual rainfall in the entire basin was 1601.7 mm in the year 2002. Out of all, Tillari dam, an inter-state project between Goa and Maharashtra; Damanganga dam, an inter-state project between Gujarat, Daman and Diu, and Dadra and Nagar Haveli; Surya Dam in Thane district of Maharashtra; and Anjunem Irrigation Project, located over Costi Nadi, Goa, are some of the important projects in the basin. Also, the Koyna and Kalinadi hydroelectric projects are two of the most important hydroelectric projects in the Tapi to Tadri basin. The agricultural land (44%) is a dominant land use in the basin followed by forest land (35%) (India-WRIS report 2014).

## 26.3 Materials and Methods

The daily rainfall data procured from India Meteorological Department (IMD), distributed in a gridded format ( $0.25^\circ \times 0.25^\circ$ ), over the basin was used as input data for the study. The daily temperature and potential evapotranspiration data downloaded from Climate Research Unit (CRU) website (<https://climatedataguide.ucar.edu/> accessed on June 13, 2018), distributed in a gridded format ( $0.5^\circ \times 0.5^\circ$ ), over the basin were also considered for the analysis; see Fig. 26.2.

### 26.3.1 Preliminary Statistical Analysis

The primary statistical parameters such as maximum, minimum, mean, standard deviation, coefficient of variation, skewness, and kurtosis were computed for annual rainfall, temperature, and PET time series at each grid for the period 1901–2016. It is observed that the overall mean and standard deviation of total annual rainfall in the Tapi to Tadri basin are 2396.8 mm and 654.3 mm, respectively, indicating it as a zone of high rainfall compared to other parts of the country.

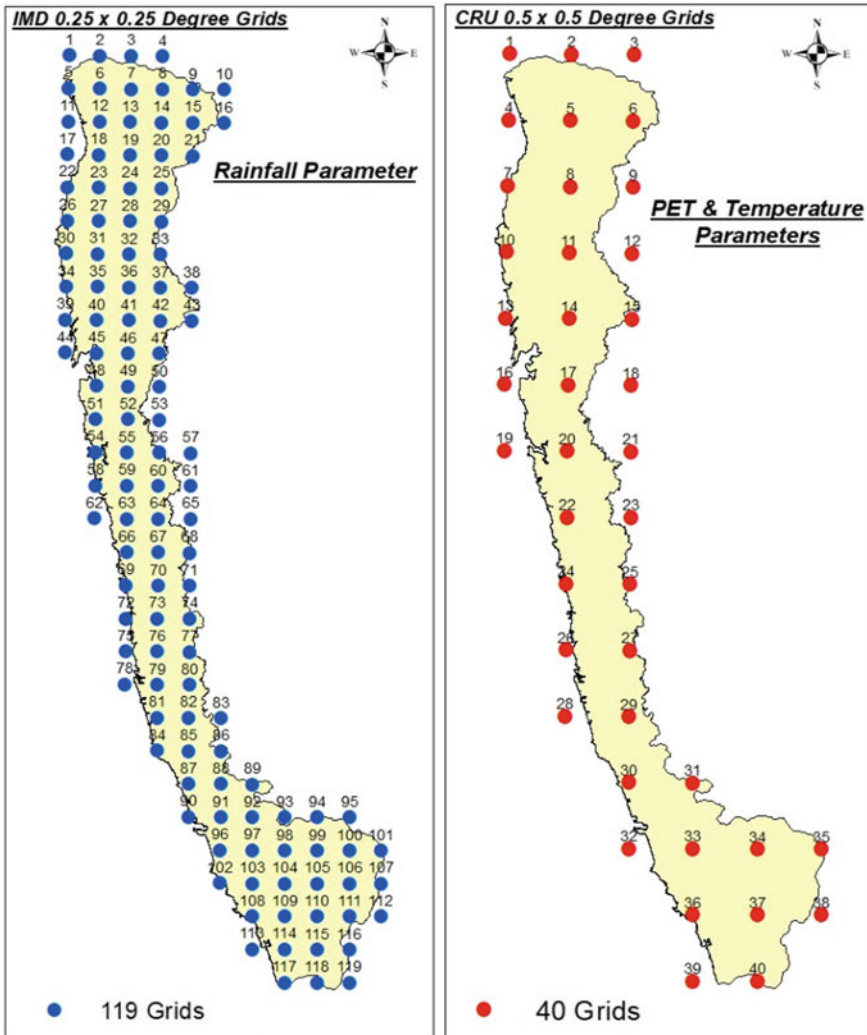


Fig. 26.2 IMD and CRU data grids for Tapi to Tadri river basin

The Tapi to Tadri basin receives heavy rainfall due to the orographic influence of the Western Ghats which bring heavy rainfall in the region. The average temperature in the basin varies from 21.9 to 32.5 °C during the entire year, while the highest and lowest temperatures recorded in the basin have been in May and January months, respectively. The mean PET is about 1568 mm within the Tapi to Tadri basin. As per the Koppen-Geiger climate classification (Peel et al. 2007), the Tapi to Tadri basin falls in Monsoon climate (Am). This region receives rainfall principally during the monsoon season and has a short dry winter season.

### 26.3.2 Methodology

The stepwise procedure adopted to ascertain the long-term temporal and spatial variability in rainfall, temperature, and PET data is included in Fig. 26.3. Before applying the trend test, the data were examined for the presence of serial correlation, which needs to be removed before applying the Mann–Kendall test (Mann 1945; Kendall 1975). Autocorrelation is a common problem in time series analysis and can cause the data to be biased to an extent. If there exists significant serial correlation, the pre-whitening process has to be performed on time series to remove autocorrelation. The Modified Mann–Kendall test (Hamed and Rao 1998) has a distinct advantage.

over the Mann–Kendall test that it can be applied to correlated data also. After detecting the nature of trends, Sen’s slope estimator method (Hirsch et al. 1982) is applied to estimate the slope of trend magnitude.

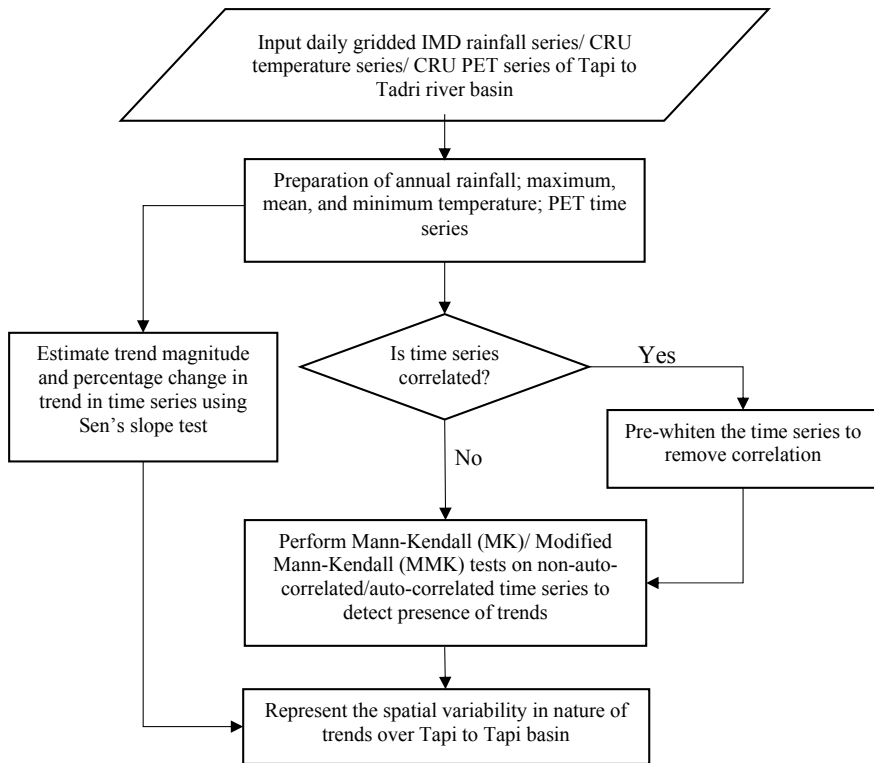


Fig. 26.3 The methodology adopted in the present study

## 26.4 Results and Discussions

### 26.4.1 Trends in Rainfall

The non-parametric tests such as MK, MMK, and Sen's slope estimator tests have been applied to the total annual rainfall series at each grid. The results indicated an increasing trend in annual rainfall across 61% grids (72 grids), while decreasing across 37% grids (44 grids) and no trends were observed at the remaining three grids out of 119 grids. Further, from MMK Z-statistic values, 49 grids exhibited significant increasing trends at 5% significance level, of which 43 grids exhibited a significant increasing trend at a 1% significance level also; see Table 26.1. On the other hand, 17 grids exhibited a significant decreasing trend at 5% significance level, of which 13 grids showed a significant decreasing trend at 1% significance level also; see Table 26.1. Moreover, the interior grids (i.e., away from the Arabian Sea and close to the Western Ghats) exhibited larger decreasing trends vis-à-vis the exterior grids (i.e., near to the Arabian Sea); see Fig. 26.4 (a). These might have resulted due to deforestation activities in the forest area along the Western Ghats and the rapid pace of urbanization in the basin. The Tapi to Tadri basin being an agriculture-dominated basin depends largely on monsoon rainfall for its water needs. The decrease in rainfall would affect the water requirements for the Kharif crops being cultivated in the basin. The maximum and minimum values of Sen's slope for total annual rainfall are found to be 35.36 mm/year and -20.50 mm/year at Grid-80 and Grid-50, respectively; see Table 26.1.

### 26.4.2 Trends in Temperature

The maximum mean and minimum average temperature series of each grid at annual time scales were investigated for the presence of trends. The trend detection carried out using MK, MMK, and Sen's slope estimator tests yielded results that agreed with each other. From the trend analyses of maximum, mean, minimum annual average temperature, increasing all 40 grids exhibited increasing trend across the basin (except at Grid-11 for mean temperature which exhibited no trend); see Table 26.2 and Fig. 26.4c–e. The increasing trend in maximum, mean, and minimum temperature at all the grids has been found to be significant at a 1% significance level. Thus, the temperature in the basin is found to severely rise over the past 116 years. In the Tapi to Tadri river basin, located nearer to the ocean in the west-south core of India, this increase in temperature would affect the water availability in the basin. The overall increase in temperature implies an increase in water vapor and its circulation pattern in the atmosphere, which could increase the frequency of occurrence of extreme events in the basin. However, the linkages of increase in temperature and their impact on the frequency of extreme events in the Tapi to Tadri basin is not

**Table 26.1** Results of trend analysis of total annual rainfall series

Grid	MK Z	MMK Z	Sen $\beta$ (mm/year)	Grid	MK Z	MMK Z	Sen $\beta$ (mm/year)	Grid	MK Z	MMK Z	Sen $\beta$ (mm/year)	Grid	MK Z	MMK Z	Sen $\beta$ (mm/year)
1	2.04	2.04	2.43	25	1.44	3.00	2.24	49	0.16	0.15	0.48	73	4.61	4.61	8.04
2	0.18	0.16	0.24	26	3.87	3.87	6.08	50	5.45	6.31	20.90	74	6.66	6.20	9.08
3	0.89	0.89	1.19	27	3.91	4.13	6.28	51	2.26	2.29	4.41	75	4.40	3.78	8.04
4	0.35	0.89	0.46	28	0.17	0.31	0.23	52	5.10	5.04	11.27	76	3.99	4.36	8.29
5	2.50	2.50	3.38	29	2.09	2.20	3.16	53	4.33	3.26	13.20	77	3.72	2.81	8.42
6	1.67	1.99	2.14	30	3.56	3.67	5.44	54	1.28	1.66	2.43	78	3.85	3.85	5.51
7	1.12	1.05	1.52	31	1.02	0.80	1.82	55	4.07	4.07	7.61	79	5.36	5.36	13.70
8	0.96	0.89	1.28	32	0.53	0.76	0.86	56	3.82	3.27	9.92	80	6.07	3.52	35.36
9	0.57	0.57	0.52	33	0.25	0.26	0.51	57	4.57	3.99	6.64	81	5.74	5.74	11.66
10	3.03	2.72	1.49	34	2.41	2.97	3.47	58	2.07	2.45	3.93	82	4.94	5.70	10.78
11	1.62	1.95	2.38	35	3.09	3.09	5.64	59	1.76	1.76	3.56	83	0.83	1.11	1.06
12	0.04	0.05	0.10	36	3.66	7.36	6.92	60	1.46	1.77	3.84	84	2.87	3.27	4.25
13	0.17	0.17	0.33	37	1.93	1.82	3.16	61	0.94	0.81	0.92	85	0.48	0.58	0.97
14	2.56	2.94	4.00	38	0.10	0.17	0.06	62	2.27	2.27	5.06	86	4.91	4.26	10.79
15	1.37	1.46	1.82	39	2.78	3.97	4.11	63	1.60	1.55	3.24	87	0.93	0.99	1.54
16	3.72	3.72	1.86	40	3.86	3.86	6.95	64	0.00	0.00	0.02	88	4.75	3.49	12.74
17	1.48	1.77	2.11	41	5.69	6.71	13.83	65	1.03	1.03	1.11	89	6.25	3.89	13.72
18	0.08	0.07	0.12	42	5.29	5.73	17.52	66	2.13	3.92	3.76	90	3.18	3.92	4.47
19	0.64	0.64	1.16	43	2.57	2.09	2.04	67	1.03	1.03	1.79	91	6.43	4.92	19.87
20	1.83	1.79	2.69	44	2.72	2.72	3.72	68	1.54	1.54	1.86	92	7.71	8.64	22.24
21	4.97	4.13	4.30	45	0.51	0.00	0.88	69	2.41	3.10	4.07	93	0.45	0.39	0.58

(continued)

**Table 26.1** (continued)

Grid	MK Z	MMK Z	Sen $\beta$ (mm/year)	Grid	MK Z	MMK Z	Sen $\beta$ (mm/year)	Grid	MK Z	MMK Z	Sen $\beta$ (mm/year)	Grid	MK Z	MMK Z	Sen $\beta$ (mm/year)				
22	3.66	3.66	5.14	<b>46</b>	4.10	4.10	10.33	<b>70</b>	3.33	8.51	5.14	<b>94</b>	1.30	1.30	0.76	<b>118</b>	4.80	4.80	8.76
23	2.94	2.94	5.02	<b>47</b>	5.35	8.97	19.22	<b>71</b>	1.40	1.40	1.39	<b>95</b>	1.55	1.67	1.03	<b>119</b>	-0.19	-0.15	-0.23
24	0.76	0.82	1.27	<b>48</b>	0.22	0.23	0.33	<b>72</b>	4.87	5.14	8.88	<b>96</b>	4.31	7.54	10.91	-	-	-	-

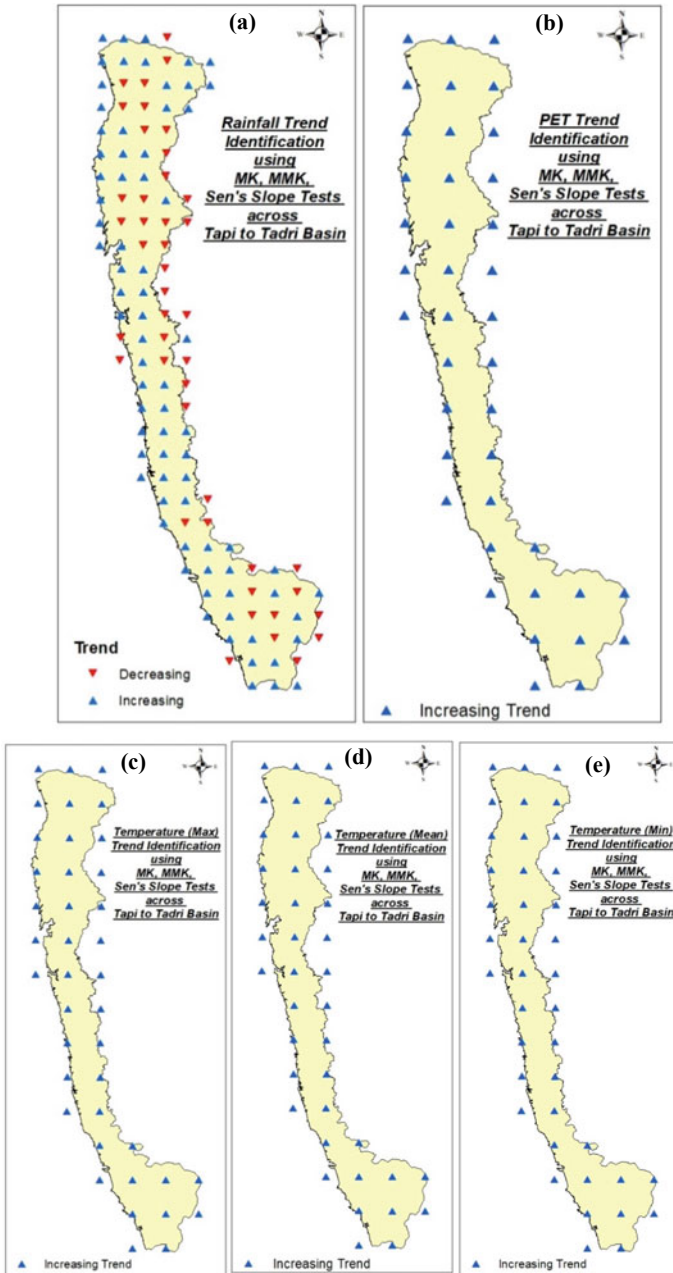


**Fig. 26.4** Trends in annual time series of (a) total rainfall, (b) PET, (c) maximum temperature, (d) mean temperature, and (e) minimum temperature over Tapi to Tadri river basin

**Table 26.2** Results of trend analysis of annual PET and temperature series

Potential evapotranspiration				Maximum temperature				Mean temperature				Minimum temperature			
Grid	MK Z	MMK Z	Sen $\beta$ (mm/year)	Grid	MK Z	MMK Z	Sen $\beta$ (°C/year)	Grid	MK Z	MMK Z	Sen $\beta$ (°C/year)	Grid	MK Z	MMK Z	Sen $\beta$ (°C/year)
1	2.58	3.51	0.141	1	6.36	5.86	0.0069	1	7.03	9.13	0.0070	1	6.77	6.77	0.0072
2	1.62	1.49	0.091	2	5.91	8.56	0.0063	2	6.68	7.38	0.0065	2	6.38	6.38	0.0068
3	1.44	1.70	0.065	3	5.83	5.45	0.0061	3	6.51	6.51	0.0063	3	6.27	10.79	0.0066
4	1.64	1.64	0.093	4	6.33	9.87	0.0066	4	7.07	6.87	0.0066	4	6.79	6.79	0.0070
5	1.24	1.12	0.067	5	6.08	11.69	0.0063	5	6.81	8.21	0.0063	5	6.45	6.45	0.0066
6	1.38	1.24	0.074	6	6.56	9.17	0.0069	6	7.24	12.04	0.0070	6	6.95	6.95	0.0073
7	0.99	0.84	0.052	7	6.45	7.54	0.0066	7	6.99	6.99	0.0065	7	6.70	5.95	0.0069
8	1.76	2.20	0.097	8	6.71	6.71	0.0069	8	7.28	0.00	0.0069	8	7.01	8.67	0.0071
9	1.47	1.47	0.079	9	6.38	6.38	0.0066	9	7.15	7.15	0.0067	9	6.74	10.93	0.0069
10	2.45	3.23	0.145	10	6.78	9.17	0.0069	10	7.33	8.97	0.0070	10	7.06	7.06	0.0072
11	1.29	1.24	0.073	11	6.46	6.97	0.0065	11	7.21	9.10	0.0067	11	6.74	8.13	0.0069
12	0.98	1.92	0.045	12	6.39	9.36	0.0064	12	6.98	10.23	0.0065	12	6.65	9.96	0.0067
13	2.04	2.37	0.117	13	6.58	6.58	0.0067	13	7.27	7.27	0.0068	13	6.89	6.73	0.0071
14	1.76	1.72	0.087	14	6.23	6.23	0.0062	14	6.94	6.94	0.0063	14	6.54	6.05	0.0066
15	1.49	1.54	0.074	15	5.92	7.33	0.0059	15	6.74	6.74	0.0061	15	6.19	8.27	0.0063
16	1.31	1.31	0.075	16	6.22	4.98	0.0061	16	6.86	5.90	0.0061	16	6.57	10.26	0.0064
17	1.00	1.64	0.055	17	5.92	5.61	0.0056	17	6.44	6.44	0.0057	17	6.28	7.41	0.0060
18	0.42	0.39	0.018	18	5.25	4.74	0.0050	18	5.79	8.07	0.0052	18	5.47	4.79	0.0054
19	1.53	1.33	0.082	19	6.19	8.73	0.0060	19	6.95	9.81	0.0062	19	6.47	7.28	0.0063

(continued)



**Table 26.2** (continued)

Potential evapotranspiration			Maximum temperature			Mean temperature			Minimum temperature					
20	1.68	2.10	0.079	6.06	5.21	0.0057	20	6.70	8.18	0.0059	20	6.23	8.53	0.0061
21	1.86	1.63	0.077	6.15	7.51	0.0057	21	6.71	8.30	0.0058	21	6.24	5.58	0.0061
22	1.99	1.99	0.102	6.43	6.85	0.0059	22	7.08	8.18	0.0061	22	6.53	6.71	0.0064
23	1.83	1.83	0.070	6.11	6.11	0.0057	23	6.89	8.45	0.0060	23	6.21	7.23	0.0062
24	2.60	2.40	0.136	6.45	6.45	0.0060	24	7.19	7.19	0.0062	24	6.50	13.66	0.0064
25	2.15	2.15	0.100	6.52	5.86	0.0060	25	7.17	7.17	0.0063	25	6.43	6.43	0.0064
26	3.45	3.82	0.174	6.74	7.78	0.0062	26	7.45	7.45	0.0065	26	6.65	6.65	0.0067
27	3.25	2.63	0.161	6.71	6.71	0.0061	27	7.41	7.41	0.0065	27	6.55	7.15	0.0066
28	4.66	3.91	0.261	6.85	6.85	0.0062	28	7.61	6.92	0.0066	28	6.64	9.19	0.0067
29	4.81	4.34	0.256	6.86	11.42	0.0062	29	7.44	7.97	0.0065	29	6.50	9.18	0.0067
30	4.62	4.98	0.254	7.21	11.59	0.0065	30	7.43	9.96	0.0066	30	6.42	7.48	0.0065
31	4.70	4.70	0.242	7.31	7.80	0.0065	31	7.46	6.92	0.0065	31	6.38	7.00	0.0065
32	4.93	4.33	0.258	7.52	9.29	0.0068	32	7.64	10.96	0.0068	32	6.31	6.31	0.0067
33	5.03	5.31	0.267	7.58	7.23	0.0068	33	7.51	9.35	0.0067	33	6.24	5.36	0.0065
34	5.52	7.13	0.268	7.67	7.67	0.0070	34	7.59	7.59	0.0068	34	6.31	7.13	0.0067
35	4.91	5.74	0.224	7.78	7.32	0.0071	35	7.59	8.58	0.0069	35	6.33	6.59	0.0066
36	5.25	6.45	0.279	7.76	7.76	0.0071	36	7.64	11.22	0.0070	36	6.31	5.46	0.0066
37	5.51	5.63	0.267	7.80	9.44	0.0072	37	7.73	9.50	0.0069	37	6.34	5.66	0.0065
38	5.43	6.02	0.257	7.84	7.33	0.0075	38	7.75	9.14	0.0071	38	6.42	6.42	0.0065
39	5.03	4.15	0.247	7.70	7.05	0.0074	39	7.75	9.30	0.0070	39	6.28	7.19	0.0066
40	5.46	5.96	0.279	7.87	24.21	0.0076	40	7.85	8.28	0.0071	40	6.45	8.67	0.0066

discussed in the present study and would form an interesting hypothesis for exploration by the research community. The maximum and minimum values of Sen's slope for maximum, mean, and minimum temperatures are found to be 0.0076 °C/year and 0.0050 °C/year at Grid-40 and Grid-18; 0.0071 °C/year and 0.0052 °C/year at Grids-38 and 40 and Grid-18; and 0.0073 °C/year and 0.0054 °C/year at Grid-6 and Grid-18, respectively; see Table 26.2.

### 26.4.3 Trends in PET

The MK, MMK, and Sen's slope estimator tests have been applied on the PET series of each grid at annual time scales. The trends in annual PET exhibited an increasing trend at all 40 grids across the basin; see Fig. 26.4b. Further, from MMK Z-statistic values, 23 out of 40 exhibited a significant increasing trend at 5% significance level, of which 17 grids showed a significant increasing trend at 1% significance level also. The increase in PET is directly influenced by a significant increase in temperature across the basin over the period of 116 years. The maximum and minimum values of Sen's slope for annual average PET are found to be 0.279 mm/year and 0.018 mm/year at Grids-36& 40 and Grid-18, respectively; see Table 26.2. The highest increase in PET is observed in the southern part of the basin, like maximum and mean temperature, with agricultural and forest land. The interrelationship of rainfall, PET, and temperature indicates that in areas of lower rainfall away from the ocean, higher PET and temperature are reported across the basin, which might require attention in terms of the supply and demand of available water resources (Boccolari and Malmusi (2013), Doorenbos and Pruitt (1977), Jain et al. (2007), Sharma and Babel (2014), Sonali and Kumar (2016)).

## 26.5 Conclusions

The trends and long-term variability in rainfall, PET, and temperature have been analyzed for Tapi to Tadri basin, India, for the period 1901–2016. The key conclusions resulting from the present study are outlined underneath:

- (1) The Tapi to Tadri basin experiences a Monsoon climate and the average annual rainfall over the basin for the period 1901–2016 is found to be 2400 mm. The maximum and minimum rainfall was found to be 5039.8 mm and 626.5 mm at Grid-60 and Grid-16, respectively. Thus, the basin experiences wide spatial and temporal rainfall variability.
- (2) The annual total rainfall has been found to increase and decrease at, respectively, 72 and 44 grids out of 119 grids across Tapi to Tadri basin. This non-uniformity could exhibit complications in the management of the water resources within the basin.

- (3) From the results, it is clear that the increase in PET in the study area is mainly due to a significant increase in the air temperature. A marginal increase in PET due to climate change would put enormous pressure on the existing water resources within the catchment. However, analyses at seasonal, monthly, and extreme indices may give a better understating of the interrelationship of climatic variables.
- (4) Planning and management of agriculture and water resources is important to understand the distribution and changing trend of rainfall, temperature, and potential evapotranspiration under climate variability. Therefore, the agro scientists, planners, and water resources managers shall formulate strategies to counter this effect and implement them to ensure better water management practices in the basin.

**Acknowledgements** The authors are also thankful to *India Meteorological Department (IMD)* for providing the necessary data to conduct the present study. The third author gratefully acknowledges the financial support received from the *Department of Science and Technology (DST), Ministry of Science and Technology, Government of India* vide their letter no. DST/INSPIRE Fellowship/2015/IF150634 dated January 11, 2016.

## References

- Alexander LV, Zhang X, Peterson TC, Caesar J, Gleason B, Klein Tank AMG, Haylock M, Collins D, Trewin B, Rahimzadeh F, Tagipour A, Rupa Kumar K, Revadekar J, Griffiths G, Vincent L, Stephenson DB, Burn J, Aguilar E, Brunet M, Taylor M, New M, Zhai P, Rusticucci M, Vazquez-Aguirre JL (2006) Global observed changes in daily climate extremes of temperature and precipitation. *J Geo Res* 111(5) D05109-1-22
- Boccolari M, Malmusi S (2013) Changes in temperature and precipitation extremes observed in Modena, Italy. *Atmos Res* 122:16–31
- Caloiero T (2017) Trend of monthly temperature and daily extreme temperature during 1951–2012 in New Zealand. *Theor Appl Climatol* 129(1–2):111–127
- Doorenbos J, Pruitt WO (1977) Guidelines for predicting crop water requirements. In: *Irrigation and Drainage Paper No 24, 2nd edn.*, Food and Agriculture Organization, Rome, p 156
- Dore MHI (2005) Climate change and changes in global precipitation patterns: what do we know? *Environ Int* 31:1167–1181
- Frich P, Alexander LV, Gleason B, Haylock M, Tank AMGK, Peterson T (2002) Observed coherent changes in climatic extremes during the second half of the twentieth century. *Clim Res* 19:193–212
- Ghosh S, Luniya V, Gupta A (2009) Trend analysis of Indian summer monsoon rainfall at different spatial scales. *Atmos Sci Let* 10(4):285–290
- Goyal RK (2004) Sensitivity of evapotranspiration to global warming: a case study of arid zone of Rajasthan (India). *Agric Water Manag* 69:1–11
- Haijun L, Yan L, Tanny J, Ruihao Z, Guanhua H (2014) Quantitative estimation of climate change effects on potential evapotranspiration in Beijing during 1951–2010. *J Geogr Sci* 24:93–112
- Hamed KH, Rao AR (1998) A modified Mann-Kendall trend test for autocorrelated data. *J Hydrol* 204:182–196
- He Y, Tian P, Mu X, Gao P, Zhao G, Wang F, Li P (2017) Changes in daily and monthly rainfall in the Middle Yellow River, China. *Theor Appl Climatol* 129(1–2):139–148

- Helfer F, Lemckert C, Zhang H (2012) Impacts of climate change on temperature and evaporation from a large reservoir in Australia. *J Hydrol* 475:365–378
- Hirsch RM, Slack JR, Smith RA (1982) Techniques of trend analysis for monthly water quality data. *Water Resour Res* 20(6):727–732
- Hobbins MT, Ramírez JA, Brown TC (2004) Trends in pan evaporation and actual evaporation across the conterminous U.S.: paradoxical or complementary? *Geophys Res Lett* 31:L13503
- Huo Z, Dai X, Feng S, Kang S, Huang G (2013) Effect of climate change on reference evapotranspiration and aridity index in arid region of China. *J Hydrol* 492:24–34
- India-WRIS report (2014) West flowing rivers from Tapi to Tadri basin. Central Water Commission, Govt. of India
- Jain SK, Agarwal PK, Singh VP (2007) Hydrology and water resources of India, vol 57. Springer Science & Business Media
- Liu B, Chen J, Lu W, Chen X, Lian Y (2016) Spatiotemporal characteristics of precipitation changes in the Pearl River Basin, China. *Theor Appl Climatol* 123(3–4):537–550
- Liu M, Tian H, Yang Q, Yang J, Song X, Lohrenz SE, Cai WJ (2013) Long-term trends in evapotranspiration and runoff over the drainage basins of the Gulf of Mexico during 1901–2008. *Water Resour Res* 49:1988–2012
- Liu Y, Zhuang Q, Pan Z, Miralles D, Tchekakova N, Kicklighter D, Chen J, Sirin A, He Y, Zhou G, Melillo J (2014) Response of evapotranspiration and water availability to the changing climate in Northern Eurasia. *Clim Change* 1–15
- Kendall MG (1975) Rank correlation methods. Charles Griffin London
- Kundu S, Khare D, Mondal A (2016) Interrelationship of rainfall, temperature and reference evapotranspiration trends and their net response to the climate change in Central India. *Theor Appl Climatol* 1–22
- Mann HB (1945) Nonparametric tests against trend. *Econometr J Econom Soc* 245–259
- Martinez CJ, Maleski JJ, Miller MF (2012) Trends in precipitation and temperature in Florida, USA. *J Hydrol* 452–453:259–281
- Peel MC, Finlayson BL, McMahon TA (2007) Updated world map of the Köppen–Geiger climate classification. *Hydrol Earth Syst Sci Discuss* 4(2):439–473
- Quirk T (2012) Did the global temperature trend change at the end of the 1990s? *Asia-Pac J Atmos Sci* 48:339–344
- Sharma D, Babel MS (2014) Trends in extreme rainfall and temperature indices in the western Thailand. *Int J Climatol* 34(7):2393–2407
- Sharma PJ, Loliyana VD, Resmi SR, Timbadiya PV, Patel PL (2017) Spatio-temporal trends in extreme rainfall and temperature indices over Upper Tapi Basin, India. *Theoret Appl Climatol* 1–26
- Soltani M, Laux P, Kunstmann H, Stan K, Sohrabi MM, Molanejad M, Zawar-Reza P (2016) Assessment of climate variations in temperature and precipitation extreme events over Iran. *Theor Appl Climatol* 126(3–4):775–795
- Sonali P, Kumar DN (2016) Spatio-temporal variability of temperature and potential evapotranspiration over India. *J Water Climate Change* 7(4):810–822
- Song X, Zhang J, AghaKouchak A, Roy SS, Xuan Y, Wang G, He R, Wang X, Liu C (2014) Rapid urbanization and changes in spatiotemporal characteristics of precipitation in Beijing metropolitan area. *J Geophys Res: Atmos* 119(19)
- Soro GE, Noufé D, Goula Bi TA, Shorohou B (2016) Trend analysis for extreme rainfall at sub-daily and daily timescales in Côte d’Ivoire. *Climate* 4(3):37
- Trenberth KE (2011) Changes in precipitation with climate change. *Climate Res* 47(1/2):123–138
- Xiao C, Wu P, Zhang L, Song L (2016) Robust increase in extreme summer rainfall intensity during the past four decades observed in China. *Sci Rep* 6
- Ye Z, Li Z (2017) Spatiotemporal variability and trends of extreme precipitation in the Huaihe River Basin, a climatic transitional zone in East China. *Adv Met* 3197435

- Zhai P, Zhang X, Wan H, Pan X (2005) Trends in total precipitation and frequency of daily precipitation extremes over China. *J Climate* 18(7):1096–1108
- Zhang Q, Singh VP, Peng J, Chen YD, Li J (2012) Spatial–temporal changes of precipitation structure across the Pearl River basin, China. *J Hydrol* 440:113–122

# Chapter 27

## Design of Water Distribution Network for Educational Institute for Revised Demand



Nishant Sourabh, Mustafa Batliwala, and P. V. Timbadiya

**Abstract** The present study is focussed on the design and analysis of the water distribution network of the Sardar Vallabhbhai National Institute of Technology-Surat (SVNIT-Surat). The forecasted population after the end of the year 2030 is about 12,000 including students, faculty, and other staff. The water distribution network is designed for existing as well as proposed facilities for which details were obtained from the Estate section of SVNIT-Surat. The proposed water distribution network is a single-source network with a total length of 7.85 km containing 159 pipes and 150 nodes with two loops. The peak factor is taken as 4 considering the total population and number of pumping hours. For the selection of pipe material, life cycle cost analysis including material and labour cost has been carried out for pipe materials such as HDPE, Cast Iron, Ductile Iron, and Mild Steel with respect to available diameters. Among these materials, Ductile Iron was selected as pipe material due to its low cost and high reliability. The design and analysis of the water distribution network were carried out using two software packages, viz., Loop v4.0 and Bentley WaterGEMS Connect Edition as per the CPHEEO Manual on Water Supply and Treatment (1999). These software use the Hazen-Williams formula for calculating the head loss through the pipe. The final design showed that pipes of 100 mm (5125 m), 150 mm (1437 m), 200 mm (1238 m), 250 mm (32 m), and 300 mm (16 m) diameters are required to safely distribute the proposed demand to the end user. The estimated cost of the network was derived from Civil SOR-2014/15 (Schedule of Rates) provided by Gujarat Water Supply and Sewerage Board (GWSSB). The isolation system can be created using isolation valves placed in the water distribution network. The optimal placement of the valve has been carried out for balancing the number of valves and corresponding undelivered demand at the least cost. The comprehensive study presented in this paper provides the way forward for the use of available software for the design/simulation of the water distribution network in the actual practices.

---

N. Sourabh · P. V. Timbadiya (✉)

Centre of Excellence on 'Water Resources and Flood Management', Department of Civil Engineering, Sardar Vallabhbhai National Institute of Technology, Surat 395007, India  
e-mail: [pvtimbadiya@ced.svnit.ac.in](mailto:pvtimbadiya@ced.svnit.ac.in)

M. Batliwala

Department of Civil Engineering, Sardar Vallabhbhai National Institute of Technology, Surat 395007, India

## 27.1 Introduction

The water distribution network is a complex infrastructure, and therefore, its construction and management require huge investments. It generates the huge possibilities of optimization of the network to minimize the cost and simultaneously maximize the network reliability and the benefits. So, the designing of the water distribution network can be multi-objective in nature. The water distribution network must also fulfil both the quality and quantity requirements of the end consumer. To achieve sustainability, several factors must be tackled at the same time such as climate change, rising energy costs, and increase in population. The network should supply water at all the intended places with sufficient pressure heads, fulfilling the firefighting demands, and must have minimum leakages to ensure the non-degradation of water quality. The design process involves simultaneous consideration of the energy and continuity equations and the head-loss function (Wood and Funk 1993). Most of the pipe network optimization methods have not considered the layout optimization along with the cost due to the extreme complexity involved and because layout is largely restricted by the location of roads (Prasad and Park, 2004).

The SVNIT is one of the institutes of national importance in our country and was established in the year 1961 as the Regional College of Engineering (REC). In the year 2002, it was converted from REC to the National Institute of Technology. The campus is located near the Tapi River in the city of Surat, Gujarat. The current population of the SVNIT campus (including the floating population) is about 7000 and is estimated to be increased to 12,000 by the year 2030. The existing water distribution network is supplying a total of 1.14 MLD (Million Litres per Day) and the future demand on the basis of the proposed population at the end of the year 2030 will be 1.74 MLD. Hence, it is required to design a new water distribution network that can serve the existing and forecasted population at the end of the year 2030 satisfactorily. The present study is focussed on the design of the water distribution network of the Sardar Vallabhbhai National Institute of Technology, Surat, for the revised demands up to the year 2030, and to check the functionality of the network in various conditions such as installation of various valves and pumps.

## 27.2 Study Area and Data Collection

The Sardar Vallabhbhai National Institute of Technology, Surat, was established in the year 1961 and is situated in Surat city of Gujarat state in India with a total area of 100 ha (1 km<sup>2</sup>). It has a total of 10 departments that focus on the fields of applied sciences, engineering, and technology. Also, it has nine hostels with three mega hostels and two buildings (G + 10) for the staff or faculty. The area is divided into two zones, i.e., Academic and Non-Academic Zone. Presently, the water supply for drinking purposes, SMC (Surat Municipal Corporation) is supplying 1.14 MLD of sweet water in the institute. The underground sumps are used to store the water

**Table 27.1** Demand computation for various zones in the institute for forecasted population

Sr No	Area	Water demand (litres per day)	Peak demand (litres per day)
1	Hostels	696060	2784240
2	Staff quarters	979750	3919000
3	Academic zone	72501.7	290006.8
	<b>Total</b>	<b>1748311.7</b>	<b>6993246.8</b>

supplied to the institute from SMC. There are two underground sumps having a capacity of 7.5 lakhs litres and 2.1 lakhs litres. The SMC water supply is transmitted through four pipes of diameter 4" (100 mm), 8" (200 mm), and 9" (225 mm). The computation of water consumption is categorized according to the nature of buildings, viz., academic buildings, staff quarters, and hostels. The demand computed according to the forecasted population is given in Table 27.1.

The Master plan of the institute prepared by the Estate Section of the institute was acquired to get information about the future developments. Also, the ground levels of the campus were extracted from the contour map. The campus is having ground levels in the range of +5.0 to +9.0 m above MSL (Mean Sea Level).

## 27.3 Model Development and Analysis

The water distribution network for the institute was modelled using two software packages, viz., LOOP v4.0 and Bentley WaterGEMS Connect Edition.

### 27.3.1 Loop v4.0

Loop v4.0 is freely available software designed by United Nations Organization (UNO) to design or to analyse the water distribution network for developing nations like India. This software models and designs the network with the least cost as its optimization function. The model uses the Newton–Raphson Method for the solution of simultaneous equations for the computation of discharge and head at all the nodes of the network. This software uses two different equations for the calculation of head loss in the pipe flow, viz., the Darcy-Weisbach Equation and the Hazen-Williams Equation. It can be used for the design and simulation of the gravity as well as pumped water distribution system. It has a limited configuration of 1000 pipes as well as 750 nodes.

$$h_f = \frac{10.68 * L * Q^{1.85}}{C_{HW}^{1.85} * D^{4.87}} \quad (27.1)$$



Equation 27.1 is a well-known empirical Hazen-Williams Equation, wherein  $L$  is the length of pipe in m,  $Q$  is the flow in the pipe in  $\text{m}^3/\text{s}$ ,  $C_{\text{HW}}$  is the Hazen-Williams coefficient which depends upon the roughness of the pipes, and  $D$  is the diameter of the pipe in m.

The existing and the proposed building according to the master plan are considered in the design. The ground elevations of the SVNIT campus were re-calculated from the temporary benchmark using the survey done by the Estate Section of the institute. The ground elevation of the nodes in the network is in the range of +5.90 m to +8.21 m above MSL. The analysis is carried out by using the Hazen-Williams formula (Eq. 27.1) with the Newton-Raphson stopping criterion of change in pipe discharge of 0.001 lps for minimum residual pressure of 5.0 m of water and maximum pressure of 20.0 m of water. The whole network is of the length of 7.85 km including all the laterals in the network. The network analysed is a single-source multi-looped network, having a total of 151 nodes (1 Source + 150 demand nodes), 159 pipes, and 2 loops. The network is analysed for the peak factor 4 as per the 6-h pumping schedule and future population of the campus. The best possible optimal solution was found out after five iterations. From the analysis, it was observed that the optimal diameters obtained for the pumping network are of four different sizes as 100, 150, 200, and 300 mm.

### 27.3.2 *Bentley WaterGEMS Connect Edition*

Bentley WaterGEMS is a hydraulic modelling application developed by Bentley Systems, for water distribution systems with advanced interoperability, geospatial model building, optimization, and asset management tools. Bentley Systems, Incorporated, is an American-based software development company that develops, manufactures, licenses, sells, and supports computer software and services for the design, construction, and operation of infrastructure. The Bentley WaterGEMS provides an easy-to-use environment for engineers/users to analyse, design, and optimize water distribution networks (Baek et al. 2008). It also has the fire flow, water quality, energy consumption, and cost management tool which makes it a better tool for the analysis of the water distribution networks.

The model was developed by laying out the network and its various components as per the master plan of the institute. The estimated demand according to the projected future population and daily requirement of various departments in the present scenario was given at demand nodes. Figure 27.1 shows the WaterGEMS software user interface window showing the water distribution network designed in the study.

The network was designed using the Darwin designer tool of WaterGEMS which optimizes the solution by incorporating a genetic algorithm. This tool simplifies the design process by allowing the user to run the manual or optimized designs of the system. The genetic algorithm-based approach includes grouping of the pipe design and rehabilitation needed for the complete design of the hydraulic model. This tool



**Fig. 27.1** Designed network map for the institute

retains the top feasible solutions according to the value of the objective functions like minimizing cost and maximizing benefits (User Manual, Bentley WaterGEMS Connect Edition 2016). The various parameters of the genetic algorithm used in this tool can be seen in Fig. 27.2.

The network was analysed and the best solution according to least cost was obtained for 20 m as head for pumping. The water supply through pumping is scheduled as shown below in Table 27.2. The hydraulic grade line profile of pipes from R-1(Source) to J-110 with the ground elevation profile has been shown in Fig. 27.3.

The Darwin designer has the ability to create as many design studies as needed including one or more design runs, manual or optimized. For the design of pumping machinery, the total supply head required for the network was computed to be 20 m (from design) + 3 m (suction head) + 3 m (factor of safety) = 26 m. The total amount of water to be supplied is 1.74 MLD. Using these conditions, the power required to supply the water demand is computed to be 40 hp and the total energy cost is found to be Rs. 5595 per day, as per the current tariff.

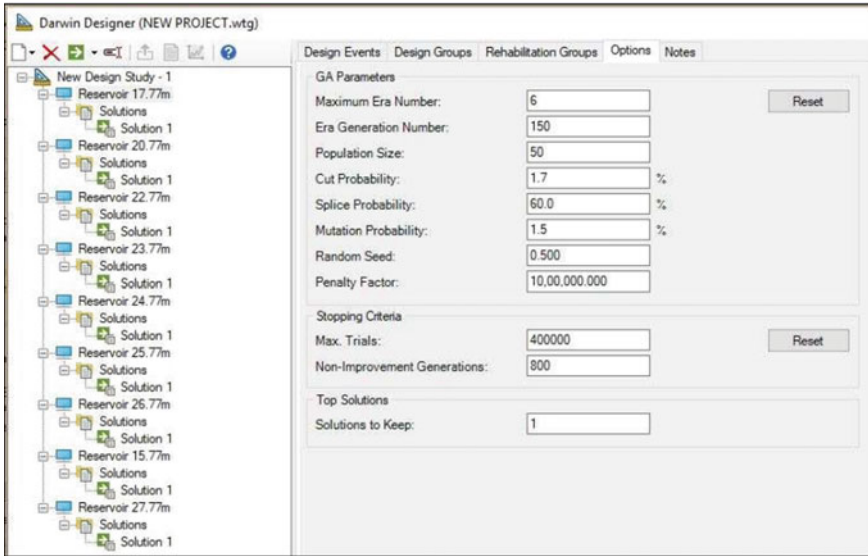


**Fig. 27.2** Genetic algorithm parameters of Darwin designer tool of WaterGEMS

**Table 27.2** Details of pumping schedule for the designed water distribution network

Pumping schedule  
Total of 6 h

Morning		Afternoon		Evening	
Start time	Stop time	Start time	Stop time	Start time	Stop time
5:30 a.m.	7:30 a.m.	1:30 p.m.	2:30 p.m.	7:30 p.m.	8:30 p.m.
9:30 a.m.	11:30 a.m.				
<b>2 + 2 = 4 h</b>		<b>1 h</b>		<b>1 h</b>	

### 27.4 Optimal Placement of Valves

The greater number of valves in the network will allow the users to control the flow but also increases the cost of the project. Also, the fact that the pipe is more fragile and deteriorates more quickly near valves suggests that the number of valves in the network should be optimized. The details of pipe length with valves and bends are given below in Tables 27.3 and 27.4, respectively. The cost of piping in the network is also given in Table 27.5.

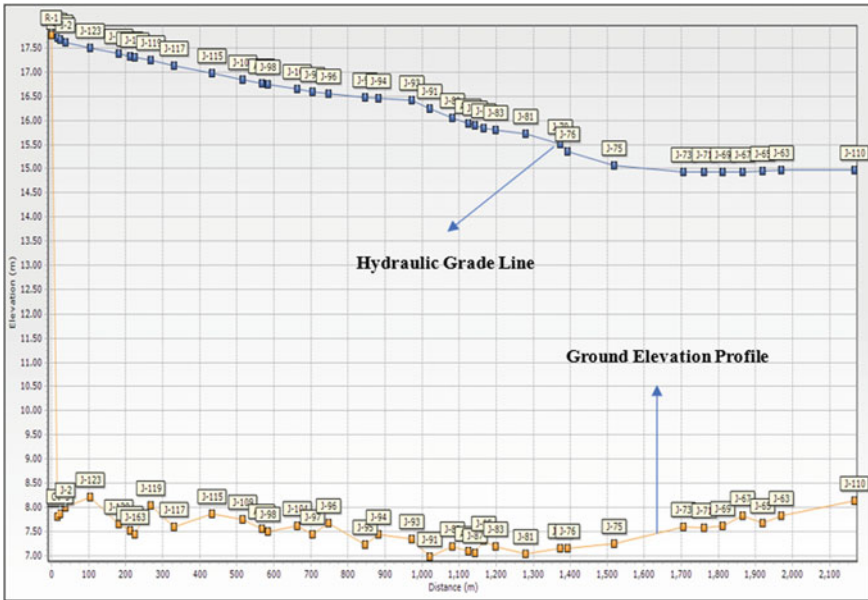


Fig. 27.3 Hydraulic grade line profile from R-1 to J-110 (with ground elevations)

Table 27.3 Pipe length, fixtures used, and valves details

Diameter (mm)	100	150	200	250	300
Length (m)	5125	1437	1238	32	16
No. of elbows	6	1	2	0	0
No. of tees	16	1	0	0	0
Isolation valve	9	3	3	0	0
Check valve	0	0	0	0	1
Air valve	0	0	0	0	0
45-bend	3	0	0	0	0

### 27.5 Results and Discussions

Based on the design and analysis of the water distribution network for the institute, the following results can be concluded:

- The total population for the year 2030 has been proposed to be 12,000 including the students and staff.
- According to the forecasted population, the water demands of various zones are computed as follows:
  - Hostel zone = 696,060 L per day.

**Table 27.4** Details of bends and sockets

Item	No	kg/No	Mass (kg)
Bend 100 mm	6	11	66
Bend 150 mm	1	20	20
Bend 200 mm	2	32	64
45D-Bend 100 mm	3	10	30
All socket tee (100 mm)	16	16	256
All socket tee (150 mm)	1	27	27
All socket tee (150 mm × 100 mm)	9	22	198
All socket tee (200 mm × 100 mm)	9	31	279
All socket cross tee (100 mm × 100 mm)	4	26	104
	<b>Total</b>		<b>1044</b>

Fittings as per ISO 2531:2009, BS EN 545:2010 and IS 9523:2000

**Table 27.5** Details of the cost of pipes in the network

S no	Diameter (mm)	Length (m)	Material cost per Rmt (Rs)	Labour cost per Rmt (Rs)	Total cost per Rmt (Rs)	Total cost (in Rs. *1000)	% of length in the network
1	100	5125	627	54	681	3490.2	65.4
2	150	1437	764	75	839	1205.7	18.4
3	200	1238	1433	98	1531	1895.4	15.4
4	250	32	1879	124	2003	64.1	0.5
5	300	16	2370	152	2522	40.4	0.3

Note Rmt is the abbreviation for Running meter

- Residential Zone = 975,750 L per day.
- Academic zone = 72,501.7 L per day.
- The total supply provided by the existing network is 1.14 MLD and the supply provided by the proposed network is computed to be 1.74 MLD (Average demand) taking peak factor as 4.
- The total length of the network required according to the proposed demand is found to be 7.85 km.
- The required head for the pumping of water is found to be 20 m (from design) + 3 m (suction head) + 3 m (factor of safety) = 26 m. The total amount of water to be supplied is 1.74 MLD. Using these conditions, the power required to supply the water demand is computed to be 40hp and the total energy cost is found to be Rs. 5595 per day, as per the current tariff.
- The maximum and minimum flow velocity in the network is 1.12 m/s and 0.02 m/s, respectively, while the minimum pressure in the whole network is maintained at

6.8 m fulfilling the criteria of keeping minimum pressure of 5 m required at the consumer end according to CPHEEO, 1999. The maximum pressure at the demand nodes in the network is 10.3 m.

- The total cost of piping in the network (including material, labour cost, laying cost, and operations maintenance) is computed as Rs. 81,76,000 whereas the overall cost of the project after installation of valves is computed as Rs. 91,11,000.

**Acknowledgements** The authors are thankful to the Centre of Excellence (CoE) on “Water Resources and Flood Management”, TEQIP-II, Ministry of EDUCATION (MoE), Government of India, for providing necessary infrastructural and financial support for conducting the study reported in the paper. The authors are also thankful to the Estate Section of the Sardar Vallabhbhai National Institute of Technology, Surat (SVNIT-Surat), for providing the necessary data to conduct the present study.

## References

- Baek CW, Jun HD, Kim JH, Yoo DG, Lee KC (2008) Evaluation of emergency water supply plan for block system of water network using WaterGEMS. *J Korean Soc Hazard Mitigat* 8(6):15–20
- Bentley Systems (2016) WaterGEMS Connect Edition, Bentley Systems Inc., Exton, Pa
- BS EN 545:2010. Standards for ductile iron pipes, fittings, accessories and their joints for water pipelines. Requirements and test methods
- Central Public Health and Environmental Engineering Organization (CPHEEO 1999) Manual on Water Supply and Treatment (2013) Third Ed.—Revised and updated. Ministry of Urban Development, New Delhi
- Civil SOR (2014–15) Gujarat Water Supply and Sewerage Board (GWSSB), Gandhinagar
- ISO 2531:2009 (en). Standards for Ductile iron pipes, fittings, accessories and their joints for water applications
- IS 9523:2000. Indian Standards for Ductile iron fittings for pressure pipes for water, gas and sewage
- Prasad TD, Park NS (2004) Multi-objective genetic algorithms for design of water distribution networks. *J Water Resour Plan Manag (ASCE)* 130(1):73–82
- WaterGEMS Connect Edition User guide (2016) Bentley Systems Inc., Exton, Pa
- Wood DJ, Funk JE (1993) Hydraulic analysis of water distribution systems. In: Cabrera E, Martinez F (eds) *Water Supply Systems, state of the art and future trends*. Computational Mechanics Publications, pp 41–85

# Chapter 28

## Application of Numerical Modelling for Geomorphological Evolution and River Bank Shifting Part of Damodar River



C. Prakasam and R. Aravinth

**Abstract** River bank erosion is a naturally occurring process along the lower parts of the River and Delta. Constant erosion and deposition due to natural and anthropogenic causes the River to migrate constantly and creating new geomorphological process. Numerical modelling helps in analyzing complex physical changes that occurred in a particular area. It can play a dominant role in studying the erosion and depositional rate along the River banks with higher accuracy. The current research is focussed on assessing the Geomorphological evolution and River bank shifting for the parts of the Bhagirathi River through numerical methods. A Survey of India's topographical maps is taken as a baseline for the study. The River bank was digitized from multi-temporal LANDSAT data from (1990–2018) at five years of temporal interval. The spatial variation in accretion and erosion rate was classified into five different types, namely: Extreme Erosion, High erosion, No change, High deposition, and Extreme deposition. The analysis revealed that both Extreme erosion and deposition were present during all of the study years. Both the east and west bank undergoes the River change at different rate for each period. The highest rate of erosion (–149 mts) and deposition (278 mts) for the west bank of the River was observed between the year (2005–2011) and (2015–2018). The highest rate of erosion (–168 mts) and deposition (375 mts) for the east bank of the River was observed between the year (2015–2018) and (1995–2000).

### 28.1 Introduction

Rivers play a pivotal role in the global sedimentary cycle. They are responsible for the transport of continental sedimentary particles to the oceans. According to a study annually, Rivers transport approximately  $34.7 * 10^{12} \text{ m}^3$  of water and  $13.5 * 10^{12} \text{ kg}$

---

C. Prakasam (✉)

Department of Geography, School of Earth Sciences, Assam University, Diphu Campus, Karbi Anglong 782462, Assam, India

R. Aravinth

Department of Geography, University of Madras, Chennai 600025, Tamil Nadu, India

(Al-Abadi et al. 2020; Chakrapani and Saini 2009). Rivers are highly sensitive to environmental and anthropogenic activities. They tend to migrate or readjust the course of the River drastically depending upon the type of causative factors such as tectonic activities, regional geomorphology, sediment inputs, and a number of human activities at temporal and spatial conditions (Dewan et al. 2017; Paul et al. 2019). Bhagirathi River is a part of the Bengal delta present in Eastern India. Bhagirathi River is one of the very few Rivers in West Bengal that undergoes severe bank erosion and accretion due to a variety of hydrological inputs (Islam and Guchhait 2018). In recent years, anthropogenic activities have enormously affected the course of the Bhagirathi River. Construction of Railroads, practicing of agriculture in tidal inlets had a great impact on the morphology of the River (Pal et al. 2016; Du et al. 2020; Schmidt and Barron 2020). Many researchers, both international and national, have studied the impact and morphology of changing Rivers to a certain extent. Islam and Guchhait (2018) have studied the societal and psychological victims due to River bank erosion. Yao et al. (2011) discussed the various causative factors and their impact on erosion and accretion rate along the yellow River of magnolia. Guchhait (2018), Thakur (2014), Das et al. (2014), Panda and Bandyopadhyay (2011), De Rose and Basher (2011) are some of the few other researchers to have extensively studied the Ganges and the Bhagirathi Rivers morphological changes to a greater extent.

The present study is focussed on assessing the erosion and accretion rate along the part of Bhagirathi River extending from Durgapur to Chalbapur. The study uses numerical-based modelling to analyze the rate of change for the years 1974–2018. The final output of the research is to delineate areas that had undergone enormous changes due to various fluvial process.

### **28.1.1 Objective**

- To digitize the River banks of the Bhagirathi River for the year 1974–2018 using various data sources.
- To spatially predict the rate of changes of erosion and accretion along the River course.
- To delineate the areas that have undergone extreme amount of erosion and deposition due to changes in River morphology.

## **28.2 Study Area**

The geographical extent of the study area is  $87^{\circ}16'24''$  to  $88^{\circ}1'59''$  East longitude to  $23^{\circ}5'14''$  to  $23^{\circ}30'43''$  North latitude. Damodar River flows from Jharkhand to West Bengal for 592 Kms. It has a number of tributaries and sub tributaries, such as Barakar, Konar, Bokaro, Haharo, Jamunia, Ghari, Guaia, Khadia, and Bhera. The



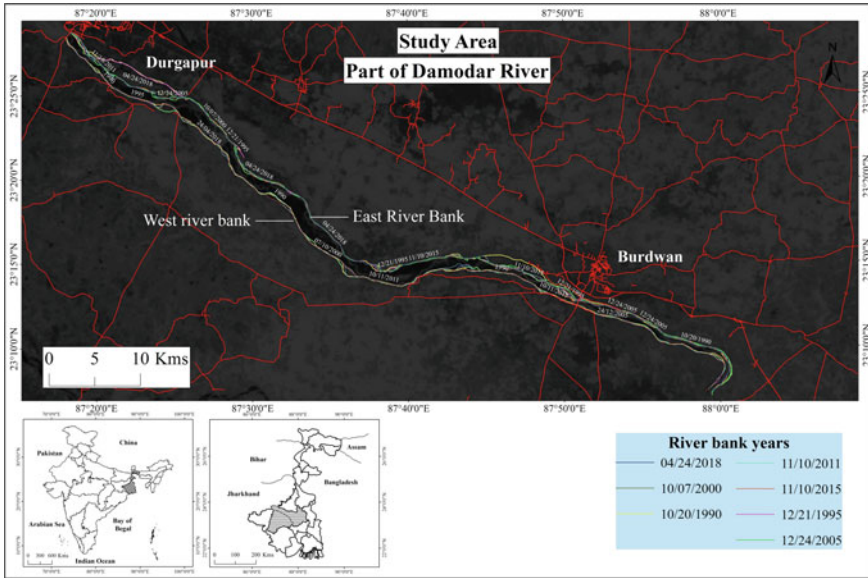


Fig. 28.1 Study area

total length of the River taken for the present study is 92 km. The River is located along Burdwan and Bankura district of West Bengal. The major Rivers of the study area are Hoogli, Damodar, Kangsbati, and the Dwarakeswar. The general geology of the state is occupied by the unconsolidated sedimentary deposits of the quaternary periods. About 75% of the land mass comprises of subrecent to recent alluvial deposits of the Quaternary period. The sedimentary formation includes essentially the Gondwana formations (Barakar formations, etc.) in the Eastern plateau (Outliers) that belong to the Permo Carboniferous to Triassic age, whereas the Siwalik formations belong to the Territories in Eastern Himalayas. The basic flows belonging to the upper Mesozoic age form a conspicuous horizon setting between the two broad sedimentary groups. The climate area consists of very mild winters and hot-wet summers. The mean annual rainfall of the West Bengal is 1,250 mm. The study area is given in Fig. 28.1.

### 28.3 Data Used and Method

The base map of the study area was digitized from Survey of India Toposheets. The River bank was digitized from multi-temporal LANDSAT data. Five decades of data were used to study the spatial variation of the River banks along the study area. The types of data used for the study are given in the table.

Sl. no.	Data	Source	Date	Resolution
1	Toposheets	SOI	1987	1:50,000
2	LANDSAT 8 OLI	USGS	24/04/2018	30 mts
3	LANDSAT 8 OLI	USGS	10/11/2015	30 mts
3	LANDSAT 8 OLI	USGS	10/11/2011	30 mts
4	LANDSAT 7ETM+	USGS	24/12/2005	30 mts
5	LANDSAT 7ETM	USGS	07/10/2000	30 mts
6	LANDSAT 7ETM	USGS	21/12/1995	30 mts
7	LANDSAT 7ETM	USGS	20/10/1990	30 mts

To analyze the long-term change in River bank, multi-temporal data from [Landsat 7, 8] for the years (1990, 1995, 2000, 2005, 2011, 2015, and 2018) were used at the five-year interval. Band 5 in Landsat 7, Pan-merged data from Band 6, and band 8 in Landsat 8 uses short wave infra-red that clearly distinguish between land and water. This band was used to clearly demarcate the River/land boundary in the satellite imageries. The digitized River banks were then assigned respective dates [mm/dd/year]. The digitized River was then processed in a GIS environment. Both the west and eastern River banks were processed individually. The entire length of the River bank was then divided into 100 mts of transects to individually analyze the erosion and accretion rate. The results were derived at five-year intervals for each year considered for the study. The results were then retrieved in excel sheets with erosion and accretion information for individual transects. These tables were then used to create maps to identify erosional and depositional areas throughout the study area. The research methodology is depicted in Fig. 28.2.

## 28.4 Result and Discussion

The long-term change in River bank from Durgapur to Chalbalpur was estimated using visual image interpretation for the year (1974–2018). The analysis was carried out in a GIS environment at the five-year interval for all the years, respectively (1990–1995, 1995–2000, 2000–2005, 2005–2011, 2011–2015, and 2015–2018). The analysis was also carried for the year 1974–2018 to study the decadal change in River banks for erosion and accretion along the study area. The spatial variation in accretion and erosion rate was classified into five different types, namely: Extreme Erosion, High erosion, No change, High deposition, and Extreme deposition. The final results were then plotted into maps and scatter plots through statistical means for final results.

The analysis revealed that both Extreme erosion and deposition were present during all of the study years. Both the east and west bank undergoes the River change at different rate for each period. The highest rate of erosion (–149 mts) and deposition (278 mts) for the west bank of the River was observed between the year

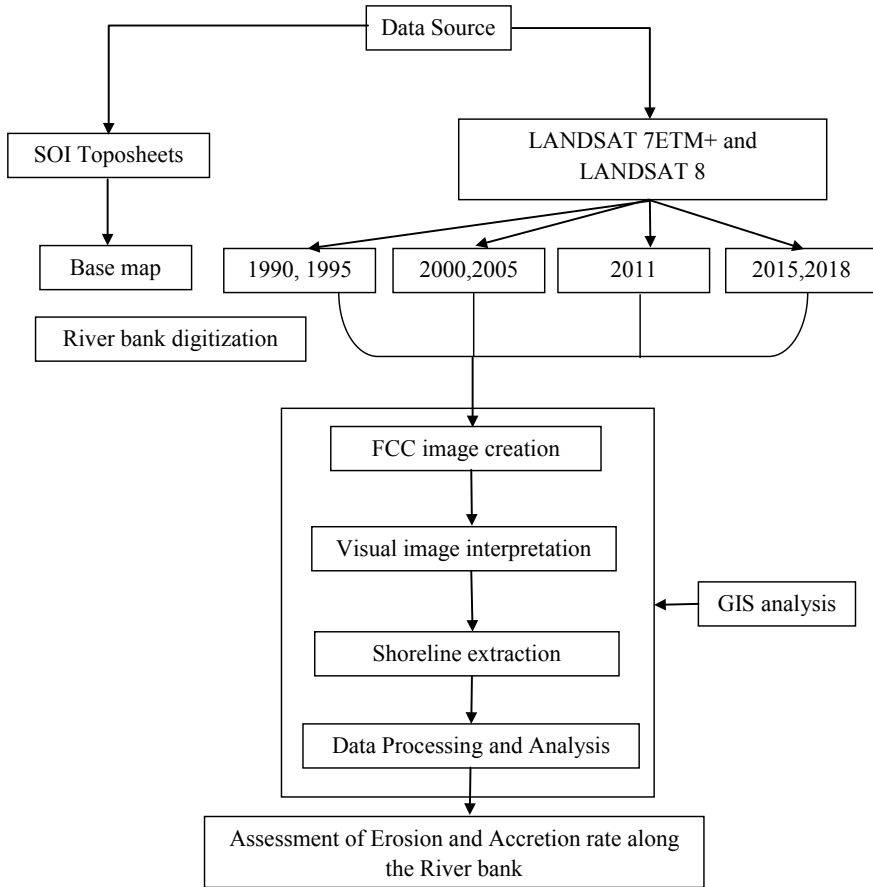


**Fig. 28.2** Research methodology

(2005–2011) Fig. 28.3c and (2015–2018) Fig. 28.3f. The highest rate of erosion (–168 mts) and deposition (375 mts) for the east bank of the River was observed between the year (2015–2018) and (1995–2000) Fig. 28.3a. These extreme level of change rates is attributed various anthropogenic and natural activities. These changes occur due to varying sediment transport and deposit in the area. In accordance with that various anthropogenic activities also pose stress along these River banks (Table 28.1).

The analysis was also separately calculated out between the years 1974 and 2018. Toposheets and LANDSAT 8 of the study area were used as reference data for the years. Two different types of analysis were carried for this study. One is to find out the total movement in River bank for the year considered and the second one is to estimate the average movement of the River bank for the period of the study. From the analysis, it can be interpreted that most of the Eastern bank of the River

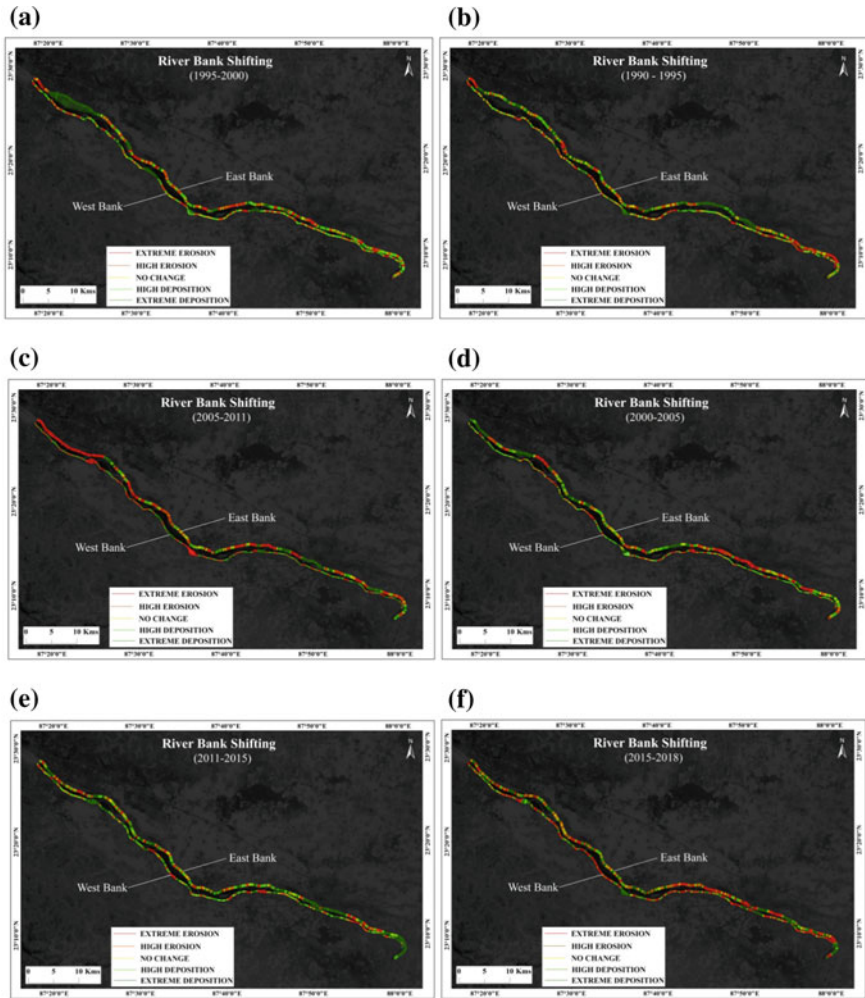


**Fig. 28.3** a Erosion and accretion rate between (1995–2000); b Erosion and accretion rate between (1990–1995); c Erosion and accretion rate between (2005–2011); d Erosion and accretion rate between (2000–2005); e Erosion and accretion rate between (2011–2015); f Erosion and accretion rate between (2015–2018)

(Fig. 28.6b) has undergone an extreme amount of erosion near the Babnabera area. The highest erosion and accretion rate along the eastern bank was (–1800 mts) and (586 mts). This is due to the encroachment of tidal inlet near that area. The inland was converted into an agricultural area for practices and joined with the adjoining land surfaces. Depositions were found along the area of Burdwan and Barsul. As for the western bank of the River (Fig. 28.6a), the highest amount of erosion (–746

**Table 28.1** Erosion and accretion rate for various years

Sl no	Year	West bank		East bank	
		Highest erosion (mts)	Highest deposition (mts)	Highest erosion (mts)	Highest deposition (mts)
1	1990–1995	−47	159	−123	52
2	1995–2000	−40	116	−49	375
3	2000–2005	−106	40	−102	131
4	2005–2011	−149	72	−76	86
5	2001–2015	−110	194	−58	182
6	2015–2018	−148	278	−168	111

mts) was observed near Beola and the highest amount of deposition (526mts) was observed along near Burdwan area (Figs. 28.4 and 28.5).

Figure 28.7 depicts some of the places that had undergone a massive amount of changes between the years 1974–2018. The image addresses the River bank change along the Eastern part, near Shrilampur, where a part of the land eroded over the course of the River. The rate of change of River bank near Shrilampur, Banpot, and Hotsimul area averages up to 900 mts. In another image, the inland has been converted for agricultural practices over the course of time. The average rate of the

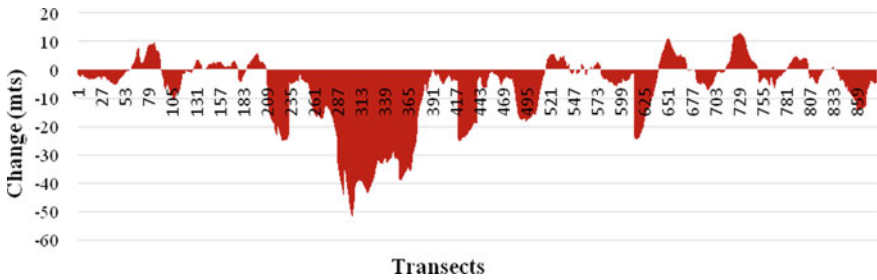


**Fig. 28.4** Average River shift of the Eastern bank (1974–2018)



**Fig. 28.5** Average River shift of the Western bank (1974–2018)

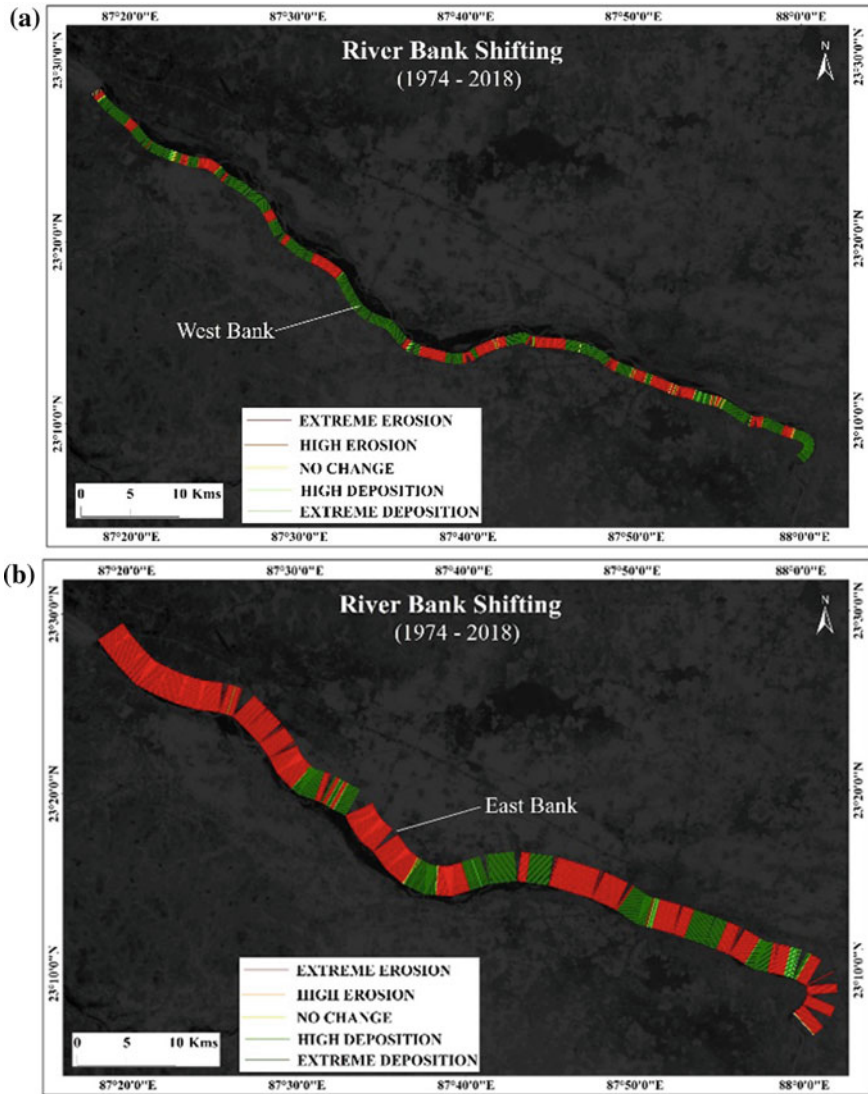


Fig. 28.6 River bank shifting (1974–2018)

River shift has been calculated for the year 1974–2018. This change in River shift was calculated by dividing the River bank through the number of years that had elapsed between them. The Eastern bank (Fig. 28.4) varies from  $-13.1$  (erosion) to  $13.2$  (deposition). Whereas the western bank (Fig. 28.5) ranges from  $-52$  mts (erosion) and  $12.3$  mts (deposition).



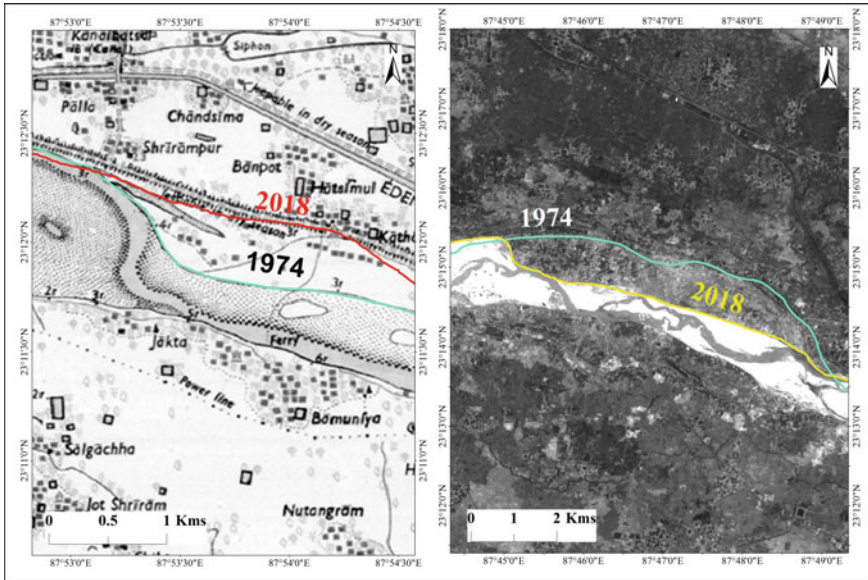


Fig. 28.7 Locations with part of River banks that had undergone massive erosion and deposition

### 28.5 Conclusion

The spatial and temporal variations of the River bank extending from Durgapur to Chalbalpur have been presented as a case study. The analysis revealed that both Extreme erosion and deposition were present during all of the study years. Both the east and west bank undergoes the River change at different rate for each period. The highest rate of erosion (−149 mts) and deposition (278 mts) for the west bank of the River was observed between the year (2005–2011) Fig. 28.3c and (2015–2018) Fig. 28.3f. The highest rate of erosion (−168 mts) and deposition (375 mts) for the east bank of the River was observed between the year (2015–2018) and (1995–2000) Fig. 28.3a. The overall results of the study area suggest that the eastern bank of the study area has undergone an enormous amount of change within these past five decades. Most of the area along the eastern bank had eroded. The western bank of the study area indicated that a major part of the study area had undergone a massive amount of deposition and erosions are found along the fewer parts such as Khandagosh, Somsar, Rupsa, and near Jamna areas. These results would indicate that the River is gradually shifting from western to side of the study area during the study period. The results presented here depict the application of satellite imageries for River bank modelling. However, remote sensing data coupled with field studies would provide much accurate information on River morphology and changing River dynamics overtime.

## References

- Al-Abadi AM, Ghalib HB, Al-Mohammdawi JA (2020) Delineation of groundwater recharge zones in Ali Al-Gharbi District, Southern Iraq using multi-criteria decision-making model and GIS. *J Geovis Spat Anal* 4:9. <https://doi.org/10.1007/s41651-020-00054-7>
- Chakrapani GJ, Saini RK (2009) Temporal and spatial variations in water discharge and sediment load in the Alaknanda and Bhagirathi Rivers in Himalaya, India. *J Asian Earth Sci* 35(6):545–553. <https://doi.org/10.1016/j.jseaes.2009.04.002>
- Das TK, Haldar SK, Das Gupta I, Sen S (2014) River bank erosion induced human displacement and its consequences. *Living Rev Landscape Res* 8(1):1–35. <https://doi.org/10.12942/lrlr-2014-3>
- Dewan A, Corner R, Saleem A, Rahman MdM, Haider MdR, Rahman MdM, Sarker MH (2017) Assessing channel changes of the Ganges-Padma River system in Bangladesh using Landsat and hydrological data. *Geomorphology* 276:257–279. <https://doi.org/10.1016/j.geomorph.2016.10.017>
- Du P, Bai X, Tan K (2020) Advances of four machine learning methods for spatial data handling: a review. *J Geovis Spat Anal* 4:13. <https://doi.org/10.1007/s41651-020-00048-5>
- Guchhait S (2018) Quantification of river bank erosion, accretion and its effect on land use: a case study of the Ganges (left bank) upstream of Farakka Barrage, Malda District, West Bengal 9(1):34–48
- Islam A, Guchhait SK (2018) Analysis of social and psychological terrain of bank erosion victims: a study along the Bhagirathi River, West Bengal, India. *Chin Geograph Sci* 28(1):1–18. <https://doi.org/10.1007/s11769-018-0937-7>
- Pal R, Biswas SS, Pramanik MK, Mondal B (2016) Bank vulnerability and avulsion modeling of the Bhagirathi-Hugli river between Ajay and Jalangi confluences in lower Ganga Plain, India. *Model Earth Syst Environ* 2(2):65. <https://doi.org/10.1007/s40808-016-0125-7>
- Panda S, Bandyopadhyay J (2011) Morphodynamic changes of Bhagirathi River at Murshidabad District using geoinformatics. *J Geogr Inf Syst* 3(1):85–97. <https://doi.org/10.4236/jgis.2011.31006>
- Paul GC, Saha S, Hembram TK (2019) Application of the GIS-based probabilistic models for mapping the flood susceptibility in Bansloi Sub-basin of Ganga-Bhagirathi River and their comparison. *Remote Sens Earth Syst Sci* 2:120–146. <https://doi.org/10.1007/s41976-019-00018-6>
- Rose RC De, Basher LR (2011) Measurement of river bank and cliff erosion from sequential LIDAR and historical aerial photography. *Geomorphology* 126(1–2):132–147. <https://doi.org/10.1016/j.geomorph.2010.10.037>
- Schmidt S, Barron C (2020) Mapping impervious surfaces precisely—a GIS-based methodology combining vector data and high-resolution airborne imagery. *J Geovis Spat Anal* 4:14. <https://doi.org/10.1007/s41651-020-00055->
- Thakur PK (2014) River bank erosion hazard study of river Ganga, upstream of Farakka barrage using remote sensing and GIS. *Our National River Ganga: Lifeline of Millions* 9783319005300(August 2015):261–283. [https://doi.org/10.1007/978-3-319-00530-0\\_11](https://doi.org/10.1007/978-3-319-00530-0_11)
- Yao Z, Ta W, Jia X, Xiao J (2011) Bank erosion and accretion along the Ningxia-Inner Mongolia reaches of the Yellow River from 1958 to 2008. *Geomorphology* 127(1–2):99–106. <https://doi.org/10.1016/j.geomorph.2010.12.010>



# Chapter 29

## Study on Impact of Urbanization by SWAT Model in Iril River, Northeast India



Pradyumna Kumar Behera and Thiyam Tampasana Devi

**Abstract** The study area chosen, Iril River in Manipur Valley Basin of Northeast India, is frequently inundated every year during monsoon season which leads to loss and damage of property. This region is mostly covered with hills with less than 10% of low-lying plain area comprising the valley region. Literature suggests that among various factors, one of the main reasons for the occurrence of flood is due to change in LULC (land use land cover) with time. An increase in urbanization, especially in the valley region and simultaneous decrease in vegetation cover has raised the susceptibility of flood in this study region. Change in LULC causes vulnerability in water-retaining capacity of the soil, leading to change in responsiveness of streamflow to rainfall. In this study, an effort is made to analyze the change in the LULC pattern of the study area for the past 16 years (2000–2016) and its response to discharge at a particular river section (Iril Bridge, Imphal) using the SWAT model. Results of the study are validated with ground observed data using root mean square error ( $R^2 = 0.96$ ) to know the accuracy of the SWAT model.

### 29.1 Introduction

Floods are one of the most common natural disasters worldwide, leading to economic losses and loss of human lives (Alexakis et al. 2014). Low-lying regions are particularly vulnerable to floods, making them naturally flood-prone zone. Estimation of extreme flood events is of great significance in minimizing damage by facilitating proper planning and design of several structures. A study conducted (Niemiczynowicz 2000; Solin et al. 2011; Adefioye 2013) in the past has shown that, in spite of various efforts to control floods, a new dimension of flood has arisen, particularly, more in the urbanized area due to changing LULC (land use land cover) characteristics in

---

P. K. Behera

Department of Civil and Environmental Engineering, Indian Institute of Technology, Patna  
801106, India

T. T. Devi (✉)

Department of Civil Engineering, National Institute of Technology, Manipur 795004, India

the region. The area is low-lying plain surrounded on all sides by hills affected by the frequent occurrence of floods. The increase in deforestation and urbanization in the valley region of Manipur has contributed significantly in making the area more vulnerable to flood events.

SWAT (Soil and Water Assessment Tool) model is a commonly used tool for prediction of runoff; and successful applications and simulation of SWAT model are reported by hydrologists for watershed hydrology related issues, e.g., Arnold and Stockle 1992; Srinivasan et al. 1993; Cao et al. 2006. Alansi et al. (2009) showed that SWAT was able to simulate and forecast flow in humid tropical conditions (Upper Bernam River Basin, Malaysia) successfully and can be used to study the effects of future land use changes on flow. Kangsabanik and Murmu (2017) reported that estimation of runoff (Ajay River Catchment in Bihar and West Bengal) by using SWAT can be enhanced furthermore by using more accurate input data, especially for the soil, land use, and DEM data.

Over the years, there is an increase in urbanization in Manipur causing degradation in cultivated land and vegetation. This is considered to be one of the important factors for increase in flood events along with other hydrological factors as the water-retaining capacity of soil decrease due to urbanization. Flood in the valley region of Manipur has become a serious concern as most of the population is concentrated in valley regions (Zutshi and Verma 2017). Thus, estimation and prediction of flood-related events has become of utmost importance in the present scenario for the region. The study is mainly concerned about the Iril river basin which is a sub-basin of Manipur river basin extending between latitude  $24^{\circ} 40' \text{ N}$ – $25^{\circ} 25' \text{ N}$  and longitude  $93^{\circ} 55' \text{ E}$ – $94^{\circ} 20' \text{ E}$  covering an area of  $1812.437 \text{ km}^2$ . The main objective is to predict runoff using SWAT and establish a relation between LULC (settlement), rainfall, and runoff depth for the catchment to find how LULC is influencing runoff for the considered catchment and subsequently to know the impact of urbanization on runoff.

## 29.2 SWAT Theory

Arnold et al. (1998) worked on hydrological modeling and assessment. The objective of the study is to briefly describe an overview of the model operation, model applications, and a description of model components of a river basin scale model called SWAT (Soil and Water Assessment Tool). The result of the study shows that the model works well for runoff–rainfall analysis with an RMS value of 0.86. Kangsabanik and Murmu (2017) conducted an analysis on the runoff–rainfall model of Ajay river catchment (located in Bihar and West Bengal) using SWAT. The main objective of their study is to estimate runoff using the SWAT model by utilizing applications of GIS (Geospatial Information System). The result reveals that the performances of SWAT in predicting runoff can be enhanced furthermore by using more accurate input data, especially for the soil, land use, and DEM (Digital Elevation Model) data. Priyalina and Singh (2016) conducted a study on the impact of Land use/Land cover

characteristics on the Flood Frequency of Nambul River Basin, Manipur. In their study, the flood frequency of Nambul river is analysed by using the Log Pearson Type III probability distribution method (statistical method). The result obtained provides the discharge values of 228, 234, 237, 238, 238, and 239 (in cumecs) for a recurrence interval of 5, 10, 25, 50, 100, and 200 years.

SWAT model is used to conduct the rainfall–runoff modeling for a catchment area. It is an interface of ArcGIS. It is a semi-distributed model in which the whole watershed area is sub-divided into various sub-basins and HRU (Hydrological Response Unit) analysis of runoff is done. The SWAT model uses water balance approach to compute runoff volume and peak flows express (Arnold et al. 1998):

$$SW_t = SW_o + \sum_{i=1}^t (R_{\text{day}} - Q_{\text{surf}} - E_a - W_{\text{seep}} - Q_{\text{gw}}) \quad (29.1)$$

where  $SW_t$  = the final soil water content (mm);  $SW_o$  = the initial soil water content (mm),  $t$  = time in days;  $R_{\text{day}}$  = amount of precipitation on day  $i$  (mm);  $Q_{\text{surf}}$  = the amount of surface runoff on day;  $E_a$  = the amount of evapotranspiration on day  $i$  (mm);  $W_{\text{seep}}$  = the amount of percolation and bypass exiting the soil profile both on day  $i$  (mm);  $Q_{\text{gw}}$  = the amount of return flow on day  $i$  (mm).

Runoff is calculated using USDA (United States Department of Agriculture) Soil Conservation Service runoff Curve Number ( $CN$ ) method (USDA 1972) as follows:

$$Q_{\text{surf}} = \frac{(R_{\text{day}} - I_a)^2}{(R_{\text{day}} - I_a + S)} \quad (29.2)$$

$$S = 25.4 \left[ \frac{1000}{CN} - 10 \right] \quad (29.3)$$

where,  $Q_{\text{surf}}$  = accumulated rainfall excess;  $R_{\text{day}}$  = rainfall depth for that day;  $I_a$  = initial abstraction;  $S$  = retention parameter;  $CN$  = Curve number become key factor for determining surface runoff.

Higher curve number correspond to high over land flow often associates with developed soils. The low curve value represents well-drained soils from hydrological group A or B and corresponds to the low rate of surface runoff.

### 29.3 Location of Study Area

The Iiril river catchment is located within the districts of Imphal East, Senapati, Ukhrul, and Imphal West. The Output point for the catchment is located at Iiril bridge having coordinates that extends between latitude  $24^{\circ} 45' N$  to  $13.267'' N$

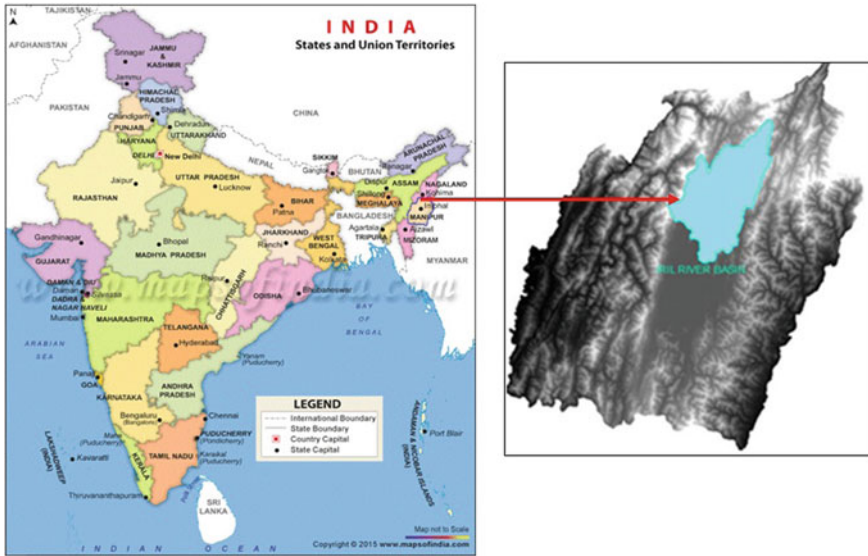


**Fig. 29.1** Location of study area

and longitude  $^{\circ}58' E$  to  $51.47'' E$ . The calculated area of the catchment is about  $1812.4 \text{ km}^2$ . Figure 29.1 shows the study area within the state of Manipur.

## 29.4 Data Materials and Methodology

The data required for this study are rainfall data, DEM data, LANDSAT data, and soil data obtained from various sources. These data are converted into layers to be put as input in swat models. The tools used for the analysis are ArcGIS and ArcSWAT.

DEM data, having a resolution of  $10 \text{ m} \times 10 \text{ m}$ , of the study area is collected from NRSC (National Remote Sensing Centre), Shillong. The data is provided as an input to the SWAT model so as to delineate the catchment area for a given outlet. Watershed Delineation provides sub-basin parameters such as elevation, stream networks, etc., for a specified catchment.

Satellite images of the study area are downloaded from USGS (United States Geological Survey) for the years 2003, 2007, 2010, 2016. This images are composite and Falsecolour composition images are obtained. Classification of the image is done using maximum likelihood classification.

Soil data obtained from NBSS (National bureau of soil survey, Nagpur) are georeferenced and digitized. The data obtained are related to the SWAT user database which contains US soil descriptions and MUIDs (Map Unit Identifiers). US soil series have similar properties and taxonomy as that of Indian soil series, and are linked by using MUIDs so that the SWAT model can use it. Weather data are obtained from

ICAR (Indian Council of Agricultural Research, Imphal, Manipur). The weather data generally consists of rainfall, relative humidity, temperature, wind speed, etc. DEM, LULC, soil, slope are overlaid in the SWAT model to obtain HRU, which divides the whole watershed into sub-basins to calculate runoff. The HRU obtained is simulated with weather data so as to estimate Runoff at an outlet point.

## 29.5 Prediction of LULC

The LULC for different classes is estimated in terms of percentage of the total area for the years 2003, 2007, 2010, and 2016. Supervised Classification has been done using the technique of maximum likelihood. Results of classification for years 2003, 2007, 2010, and 2016 are shown in Fig. 29.2 in a clockwise direction, respectively.

Eventhough study area is mostly covered by vegetation and by cultivated land as compared with settlement area, it is also equally important to understand the changes in the land use and land cover from the past years.

In Fig. 29.3, the percentage change in cultivated and barren land with respect to settlement in the study has been shown. It is evident that, significantly while the cultivated and barren land is decreasing from the year 2000 to 2016, settlement area increases. From Fig. 29.3, it can be observed that there is a considerable change of 16.9% total study area to 11.02% in the cultivated area (5.88% decrease) and 5.66% of the total study area to 0.13% in barren land (5.53% decrease) from 2000 to 2016. Thus, the cultivated land and barren land are converted into a settlement in the study area which plays a pivotal role in increasing urbanization. The change of LULC classes of vegetation and water bodies does not change significantly and its impact has not been reported in this study. As the data analyzed (satellite data) was varied temporally and seasonally and the land use land cover (vegetation and water bodies, in dry season, vegetation cover and water bodies found very less percentage) depend on these factors could not be compared for the subsequent years.

## 29.6 Runoff Depth and Maximum Discharge

The rainfall data from the year 2000 to 2016 are provided in the SWAT model as an input for estimation of runoff on daily basis for respective years. The surface runoff corresponding to maximum rainfall for each year from 2000–2016 is estimated. The maximum discharge is estimated by multiplying the total area of 1812.4 km<sup>2</sup> with corresponding runoff (Fig. 29.5). The analysis indicates the highest rainfall of 133.7 mm in the year 2000 resulting in runoff depth of 67.38 mm with the discharge of 1413.48 m<sup>3</sup>/sec at the outlet point (Iril Bridge). There is also a considerable amount of rainfall of 99.6, 125, and 103.1 mm in the years 2013, 2014, and 2016, respectively, resulting in runoff depth of 44.53, 45.78, and 41.46 mm, respectively. In addition, corresponding discharge at outlet point (Iril Bridge) for the years 2013, 2014, and

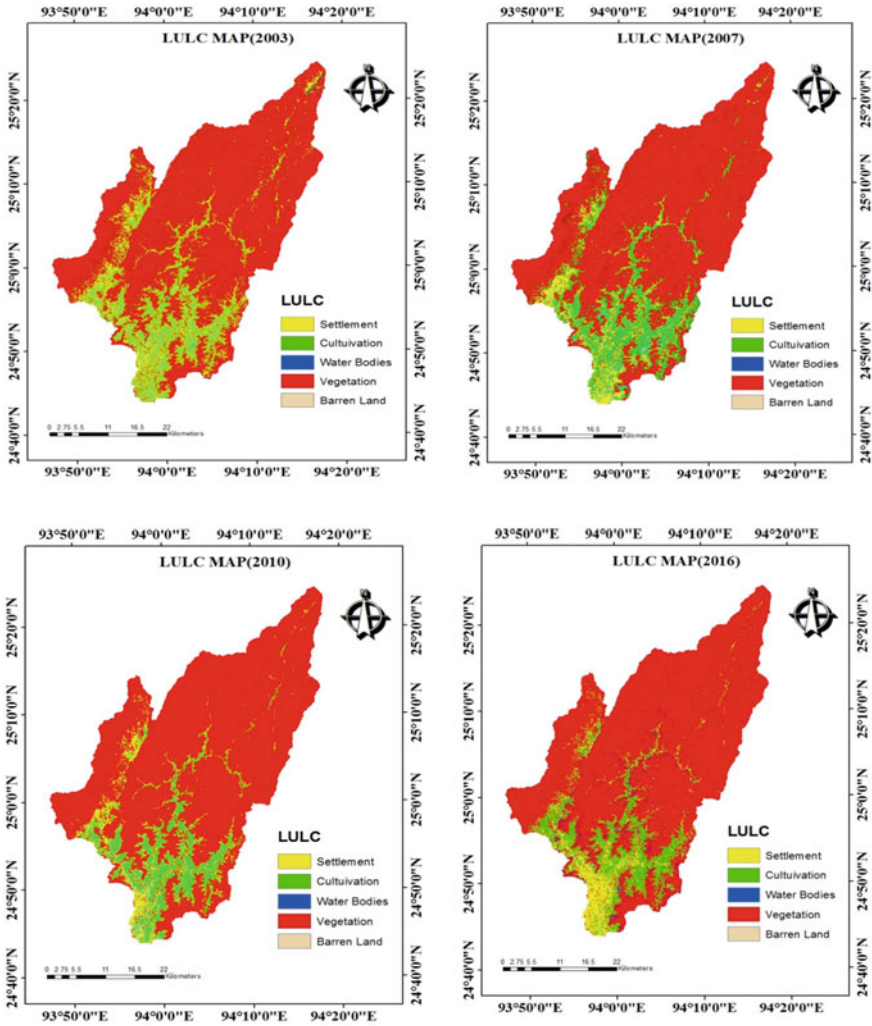


Fig. 29.2 LULC map for the years 2003, 2007, 2010, and 2016 (Clockwise)

2016 are 934.15, 960.36, and 869.7 m<sup>3</sup>/sec, respectively, as shown in Figs. 29.4 and 29.5.

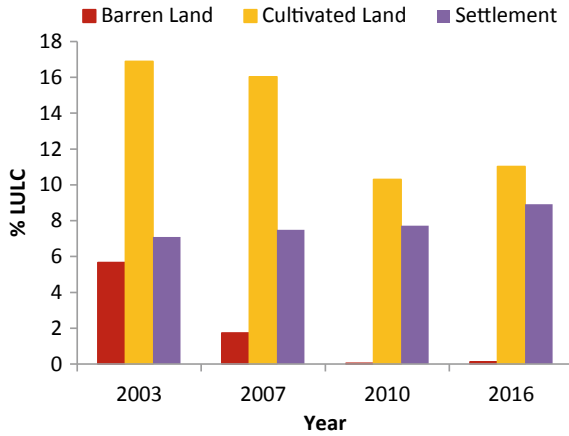


Fig. 29.3 LULC change pattern

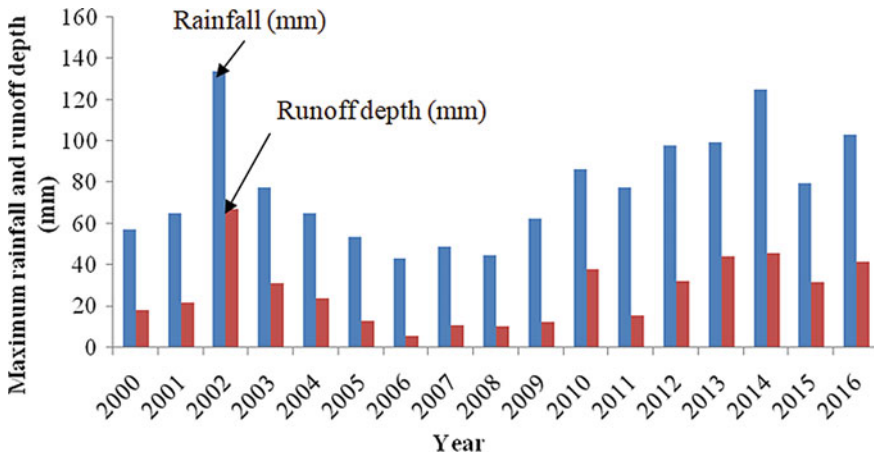


Fig. 29.4 Maximum rainfall and runoff depth (mm) (2000–2016)

### 29.7 Validation

Observed discharge data are collected from IFCD (Irrigation and Flood Control Department, Imphal, Manipur). The observed data and simulated discharge are validated using the root mean square method. The observed data and simulated discharge are plotted in the graph as shown in Fig. 29.6. The root mean square ( $R^2$ ) of the validation is found to be 0.96, which represents that, the observed data and the simulated data have a good correlation (Fig. 29.6).

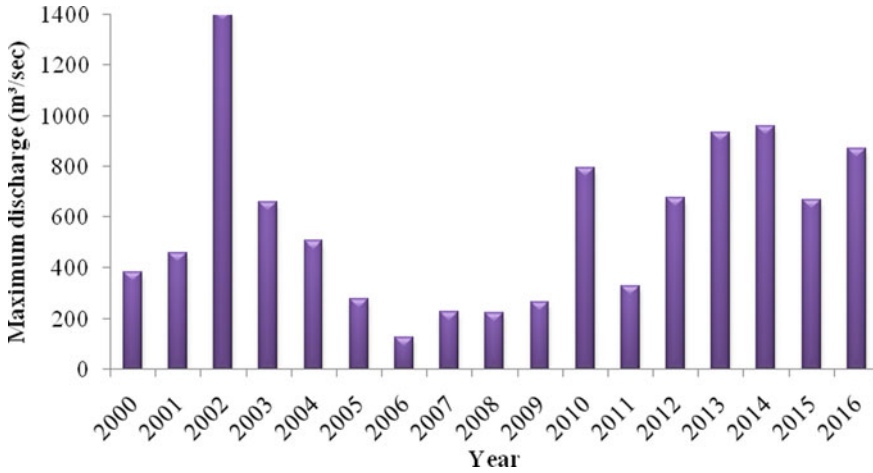
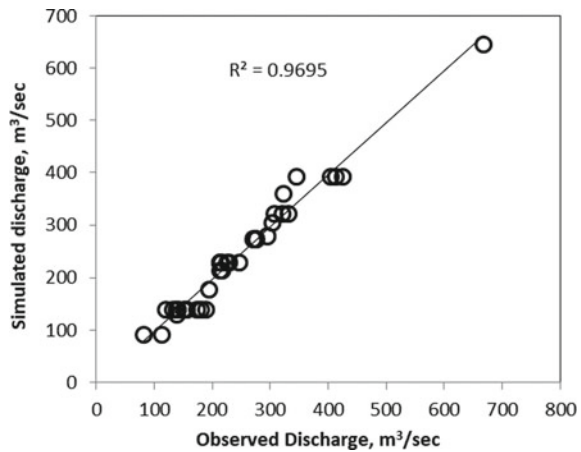


Fig. 29.5 Maximum discharge (2000–2016)

Fig. 29.6 Simulated discharge versus observed discharge



### 29.8 Conclusions

The cultivated land and barren land are converted into settlement in the study area which plays a pivotal role in increasing urbanization. The impact of change in LULC along with other hydrological factors (climate, soil type, antecedent moisture content) is the significant factor for increasing runoff. To determine the accuracy of results, simulated discharge and observed discharge is plotted on the arithmetic scale to determine their relationship. The correlation ( $R^2$ ) is found to be 0.96, which is determined by the root mean square method suggesting a good simulation of the SWAT Model.



## References

- Adefioye SA (2013) Analysis of land use/land cover pattern along River Benue channel in Adamawa State, Nigeria. *Acad J Interdiscip Stud* 2(5):95–107
- Alansi AW, Amin MSM, Abdul Halim G, Shafri HZM, Thamer AM, Waleed ARM, Aimrun W, Ezrin MH (2009) The effect of development and land use change on rainfall-10 runoff and runoff-sediment relationships under humid tropical condition. *Eur J Sci Res* 31(1):88–105
- Alexakis DD, Grillakis MG, Koutroulis AG, Agapiou A, Themistocleous K, Tsanis IK, Michaelides S, Pashiardis S, Demetriou C, Aristeidou K, Retalis A, Tymvios F, Hadjimitsis DG (2014) GIS and remote sensing techniques for the assessment of land use change impact on flood hydrology: the case study of Yialias basin in Cyprus. *Nat Hazards Earth Syst Sci* 14:413–426
- Arnold JG, Stockle CO (1992) Simulation of supplemental irrigation from On-Fann Ponds. *J Irrig Drain Div Am Soc Civil Eng* 117(3):408–424
- Arnold JG, Srinivasan R, Muttiah RS, Williams JR (1998) Large-area hydrologic modeling and assessment: part I, model development. *Water Resour Bull* 34(1):73–89
- Cao W, Bowden BW, Davie T (2006) Multi-variable and multi-site calibration and validation of SWAT in a large mountainous catchment with high spatial variability. *Hydrol Proc* 20:1057–1073
- Kangsabanik S, Murmu S (2017) Rainfall-runoff modeling of Ajay River catchment using SWAT Model. *Earth Environ Sci, IOP conference series*, 67, Kuala Lumpur
- Niemczynowicz J (2000) Urban hydrology and water management—present and future challenges. *Urban Water* 1(1):1–14
- Priyalina S, Singh KP (2016) Impact of land use/land cover characteristics on flood frequency of Nambul River Basin, Manipur. *Trans Inst Indian Geogr* 38:1
- Solin L, Feranec J, Novacek J (2011) Land cover changes in small catchments in Slovakia during 1990–2006 and their effects on frequency of flood events. *Nat Hazards* 56(1):195–214
- Srinivasan R, Arnold JG, Muttiah RS, Walker C, Dyke PT (1993) Hydrologic unit model of the United States (HUMUS). *Adv Hydro Sci Eng I(A)*:451–456
- USDA (1972) U.S Department of Agriculture, Soil Conservation Service, National Engineering Handbook. Hydrology Section 4. Chapters 4–10. Washington, D.C.: USDA
- Zutshi B, Verma RK (2017) Community response, preparedness and disaster risk-reduction a case study of Manipur floods 2015. *Eur Sci J* 322–346

# Chapter 30

## Comparison of Soil Infiltration Models Under Varying Land Cover Conditions in a Micro Watershed of Western Himalayan Region



Tabasum Rasool, Sajad Ahmad, Abdul Qayoom Dar, and Mushtaq A.Wani

**Abstract** The quantification of infiltration characteristics of soil is not a simple problem because of its variability and the selection of proper techniques used in the determination of parameters of various infiltration models which depend on various soil characteristics. This paper describes the infiltration characteristics under sandy clay soils on three different land-use practices, viz. agriculture, built-up and orchard in a micro watershed of the Western Himalayan region. The field infiltration rates were determined experimentally using double-ring infiltrometer along with the collection of soil samples to determine various soil properties which affect the infiltration characteristics of a given region. Numerical infiltration models were used for comparison of infiltration rates for particular land use with a graphical approach for determination of model coefficient. The accuracy of the simulation was performed using a statistical technique based on root mean square error (RMSE), Nash–Sutcliffe efficiency (NSE) and coefficient of determination ( $R^2$ ). It was observed that Horton's model had given the best prediction of infiltration rate in the study area followed by Philip and Kostiaikov models of infiltration.

### 30.1 Introduction

Infiltration is the process of the downward movement of water into the soil profile through the soil surface. The potential difference between energy states is the driving

---

T. Rasool · A. Q. Dar (✉)

Department of Civil Engineering, National Institute of Technology Srinagar, J&K, Srinagar 190006, India

S. Ahmad

Department of Civil Engineering, Model Institute of Engineering and Technology Jammu, J&K, Jammu 180006, India

M. A.Wani

Division of Soil Science, Sher-E-Kashmir University of Agricultural Sciences and Technology, Sopore J&K, Wadura 193201, India

force for water movement through the porous medium. The forces of gravity, capillarity and adsorption form the basis of soil infiltration and it is generally controlled by Darcy's law. The volume flux of water flowing into the ground surface into the profile per unit of soil surface area under any set of circumstances is defined as infiltration rate. It depends on some soil and water characteristics such as soil texture and structure, porosity, hydraulic conductivity, type of vegetative cover, antecedent moisture condition, water quality, etc. The quantification of infiltration is essential in the determination of soil moisture status, which is of great interest to irrigation and agricultural engineers, groundwater hydrologists and soil scientists. The evaluation of infiltration characteristics is of utmost importance in watersheds management.

The problem of categorizing infiltration is to describe the movement of water in unsaturated soil (Skaggs et al. 1968). A non-linear partial differential equation derived by Richards (Richard 1931) based on Darcy's law has been received by most researchers as the governing equation for unsaturated movement of moisture in the soil as well as in understanding many of the other equations to approximate infiltration. The Richards equation has been extended into many complex conditions (Ying et al. 2010), but the equation is non-linear, without closed-form analytical solutions, but it can be used for numerical modelling of infiltration by applying boundary conditions, initial conditions and then solving the equation for thin layers for small-time changes (Dingman 2002). Though the numerical solution of the Richards equation necessitates numerous measurements to be made to satisfactorily describe variations in soil properties that occur both vertically in the soil profile and from spot-to-spot in the field (Skaggs and Khaleel 1982), infiltration models with simplified data requisitions are advisable for practical utility.

For field applications, several physically-based models such as that of Philip (1957), and empirical models such as those of Kostiaikov (1932) and Horton (1940) has been developed that simplify the concepts involved in the infiltration process, yet not all models are applicable in all soils, but one infiltration characteristic that all the equations predict is an initial rapid decrease in rate with time for ponded surfaces (Skaggs and Khaleel 1982). The appropriate estimation of infiltration parameters for the infiltration models would help in more realistic infiltration simulation and aid in designing optimum irrigation facilities.

Land use (forest, grassland, cropland, urban area) has different impacts on the infiltration capacity and water storage of the soils. The assessment of the impacts of land-use change or land-management changes on a regional scale is difficult because detailed information on soil properties and land management is rarely available. Hence, estimation of infiltration in different land-use conditions will also help in the assessment of the impact of changing land-use pattern. Although to date, studies have been conducted to know the infiltration rate using several infiltration models at many locations worldwide by several researchers, but in the western Himalayan region, no such studies have been carried out. The western Himalayan region has heterogeneous topographical characteristics, varied landscape and diverse geomorphic units resulting in great spatial variability, it is thus of paramount importance to analyze variation in infiltration characteristics in this region. In the present study, a micro watershed of Dal lake catchment located in the western Himalayan region

has been taken up for infiltration studies with the objectives of. (i) evaluating and assessing the performance of three infiltration models (Horton, Philip and Kostikov) under three different land cover conditions; (ii) estimating the model parameters and (iii) comparison of infiltration rate estimated by models with their corresponding measured values.

## **30.2 Materials and Methods**

### ***30.2.1 Study Area***

The present study was carried out in a micro watershed of the western Himalayan region in the catchment of Dal Lake, Jammu & Kashmir. It is located between the geographical coordinates of 34°06′–34°10′N latitude and 74°49′–74°54′ E longitude and covers an area of 22.28 km<sup>2</sup>. The study area is characterized by complicated hydrology due to its undulating and diverse geomorphology. It consists of a dense population with a majority of land cover under built-up conditions, other land uses prevailing in the region can be characterized as grasslands, orchards, agriculture fields with thin vegetation, floating gardens, etc. The location map of the study area is shown in Fig. 30.1.

### ***30.2.2 Selection of Sampling Sites and Field Tests***

The selection of sites for performing infiltration experiments across the study area was done in Arc GIS 10.2 by overlaying land use and soil map. Information regarding land use land cover (LULC) and soil types were taken from available literature (Badar et al. 2013), however, a field survey was carried out to accurately describe the land cover classes and to determine soil texture. The LULC map was reclassified on the basis of ground-truthing into several land-use classes such as forest, agricultural land, built up, orchards and horticulture, recreational parks, scrubland and water bodies. Soil samples were collected randomly throughout the study area and soil texture was determined by the method of mechanical analysis. On the basis of the results obtained from the analysis, the soils were classified into different types using the United States Department of Agriculture (USDA) textural classification triangle. The LULC (Fig. 30.2) and soil map (Fig. 30.3) altogether generated in the GIS environment are shown below.

A total of six locations on sandy clay soil texture under three different land-use practices, viz. agriculture, built-up and orchard, with two from each land use, were selected. The selected sites under the land covers of agriculture, built-up and orchard were designated as A1, A2; BU1, BU2 and OR1, OR2, respectively. Each of the selected sites was plotted using Arc GIS and is depicted in Fig. 30.4. The samples

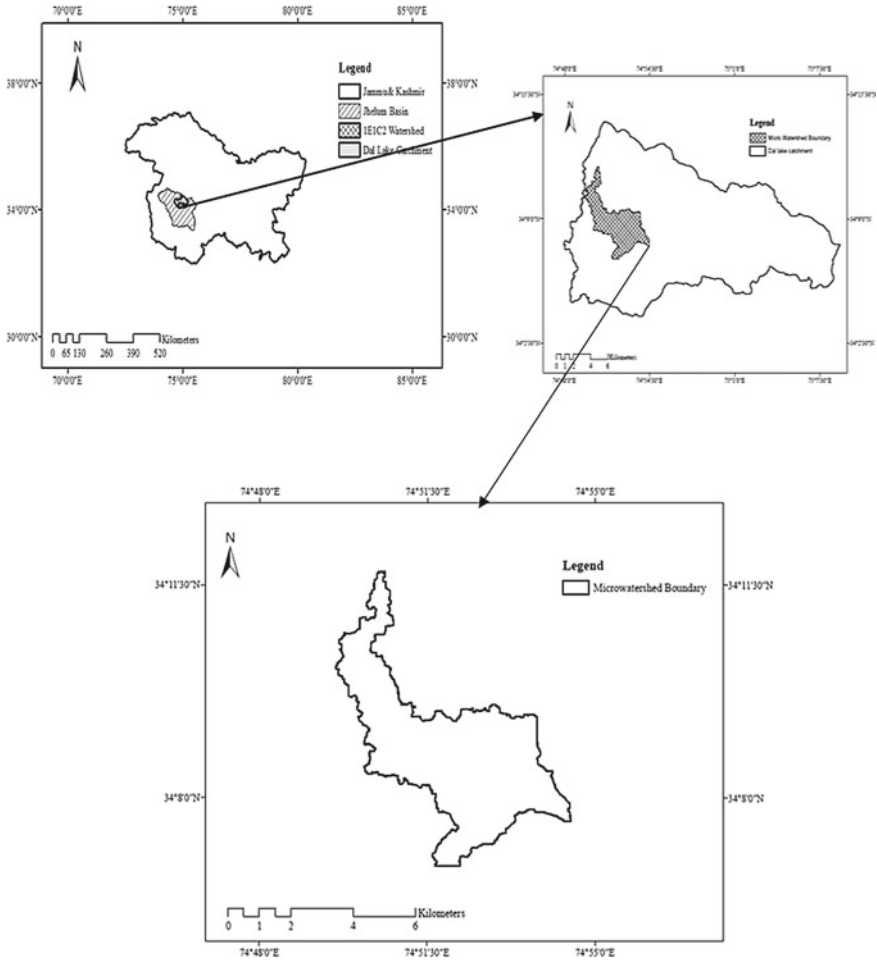


**Fig. 30.1** Location map of the study area

were collected from the study area using soil auger at 0–20 cm depths to determine various soil properties which affect the soil water infiltration. To obtain the infiltration data, a double-ring infiltrometer with 30 cm inner diameter and 60 cm outer diameter rings were used. For procuring the precise infiltration data, the experiments were replicated thrice at each of the selected sites and tests were run until the infiltration rate attains a constant value.

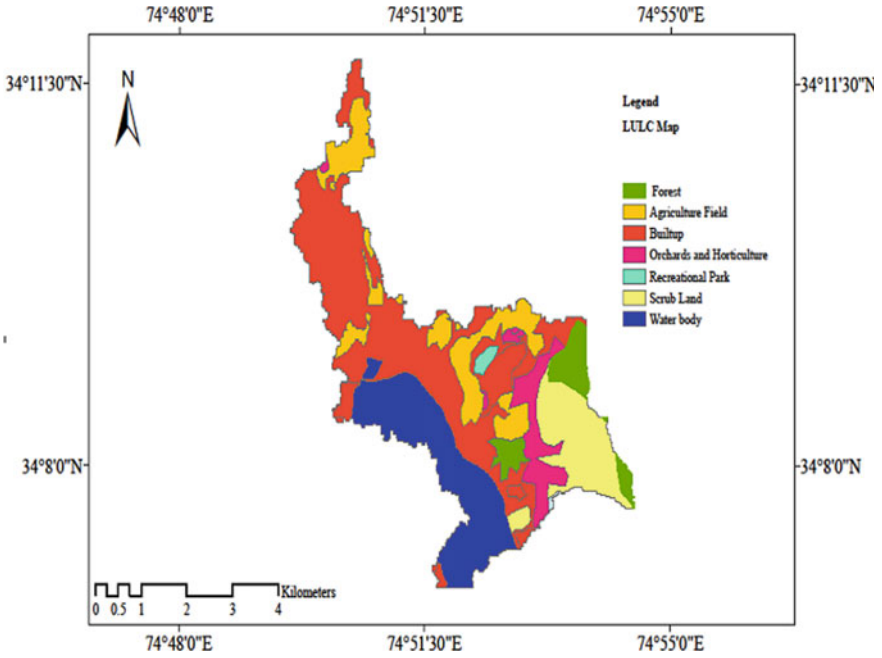


Fig. 30.2 Land-use/land cover map of the study area

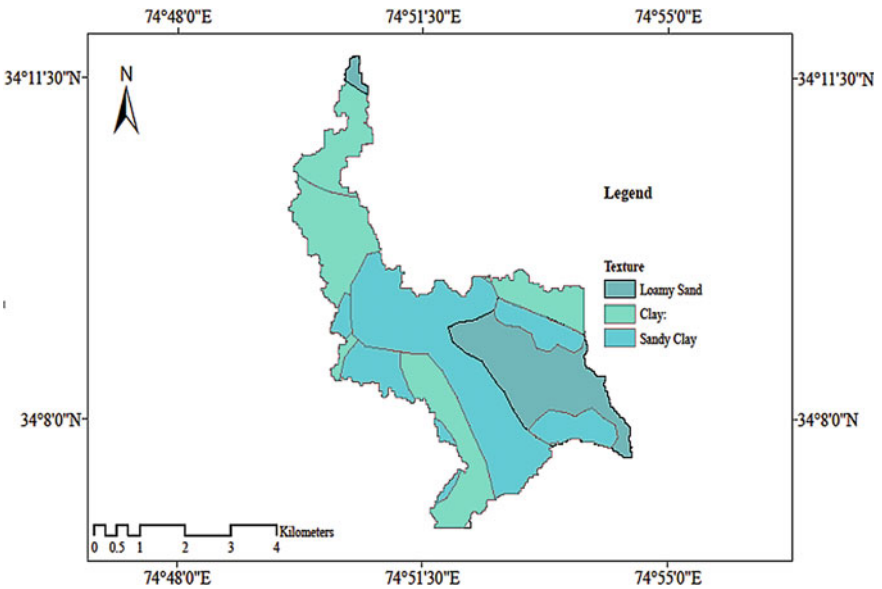


Fig. 30.3 Soil texture map of the study area

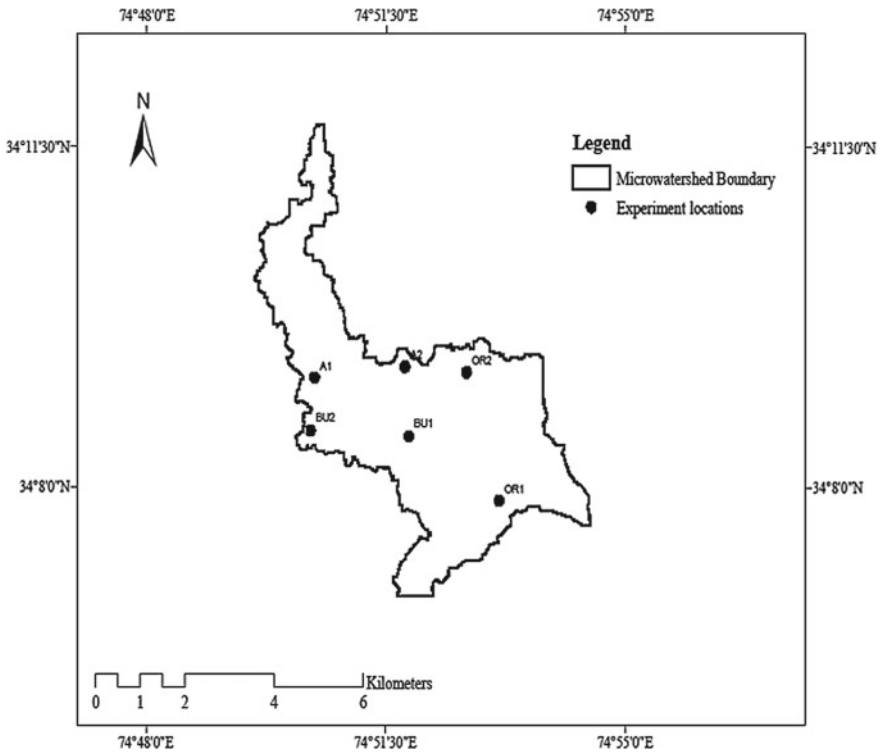


Fig. 30.4 Experimentation sites in the study area

### 30.2.3 Infiltration Models

#### 30.2.3.1 Infiltration Models Evaluated

The infiltration models assessed for obtaining the best fit model in the study area along with their respective model parameters are briefly described below (Table 30.1).

where  $F$  = cumulative infiltration (cm),  $f$  = infiltration rate (cm/hr.),  $t$  = time from the start of infiltration (hr.),  $a$  and  $b$  are Kostiakov empirical constants depending on the soil type, initial moisture content, rainfall rate and vegetative cover,  $k_h$  = Horton’s decay coefficient specific to the soil characteristics and vegetation cover [ $T^{-1}$ ],  $f_o$  = initial infiltration capacity,  $f_c$  = final steady-state infiltration capacity,  $S$  = Sorptivity (cm/hr<sup>1/2</sup>) and  $A$  = parameter related to saturated Hydraulic Conductivity.

**Table 30.1** Infiltration equations and fitting parameters of models evaluated

S. No	Model name	Infiltration-rate equation	Cumulative-infiltration equation	Fitting parameters
1	Kostiakov (1932)	$f = (ab)t^{b-1}$	$F = at^b$	$a$ and $b$
2	Horton (1940)	$f = f_c + (f_o - f_c)e^{-K_h t}$	$F = f_c t + \left(\frac{f_o - f_c}{k_h}\right)(1 - e^{-k_h t})$	$k_h, f_o$ and, $f_c$
3	Philip (1957)	$f = \frac{1}{2} S t^{-.5} + A$	$F = S t^{.5} + At$	$S$ and $A$

**30.2.3.2 Model Parameters Estimation and Model Validation**

The parameters of infiltration models were estimated using the least square method of curve fitting (Subramanya 2008). The Kostiakov model parameters were determined from the best fit straight line plot of  $\ln (F)$  versus  $\ln (t)$ , similarly, the Horton model parameters were determined by plotting a best fit straight line between  $\ln (f_o - f_c)$  and time. In order to obtain Philip’s model parameters, the infiltration rate is plotted against reciprocal square root time ( $t^{-0.5}$ ) on an arithmetic graph paper.

The values of the estimated parameters were then incorporated into the model equations to estimate the infiltration rate for all models. The field-measured infiltration rates for all the selected sites were then compared graphically with model-estimated data. The validation to check the closeness between the field-measured and model-simulated infiltration rates were analyzed using statistical parameters such as root mean squared error (RMSE), Coefficient of Determination ( $R^2$ ) and Nash–Sutcliffe Efficiency (NSE). The lower values of RMSE and higher values of the  $R^2$  and NSE were expected for better infiltration models selected for the sandy clay soils in this research.

**30.3 Results and Discussions**

The various soil properties analyzed prior to the commencement of infiltration experiments which affect the infiltration characteristics of the study area are presented in Table 30.2.

The average initial moisture content in the study area was found to be 22.92% with minimum and maximum values of 19.07 and 24.85% for orchard and agricultural land covers, respectively. This variation in moisture content reflected the predominant effect of different land covers. The average value of bulk density observed was 1.45 g/cm<sup>3</sup> with the minimum and maximum value of 1.35 g/cm<sup>3</sup> and 1.57 g/cm<sup>3</sup> for land under orchard and agricultural respectively. The higher value of bulk density for agricultural land is due to various tillage and other operations which results in increased compaction. The average porosity is 38.23% with the minimum and



**Table 30.2** Soil properties at selected sites

Study site	Moisture content (%)	Bulk density (g/cm <sup>3</sup> )	Particle density	Porosity (%)	Organic matter (%)
			(g/cm <sup>3</sup> )		
A1	23.07	1.45	2.36	38.56	5.506
A2	24.85	1.57	2.48	36.7	4.618
BU1	23.38	1.45	2.19	33.79	4.53
BU2	24.39	1.52	2.2	31.01	3.58
OR1	20.59	1.35	2.52	46.43	5.506
OR2	19.07	1.36	2.37	42.62	6.72

maximum value of 31.01 and 46.62% for built-up and orchard land covers, respectively. The higher value of porosity is due to low bulk density and high organic matter content in case of land under orchards.

Following the collection of soil samples, the infiltration rates measured in the field using double-ring infiltrometer on sandy clay soils under different land use/land cover conditions are shown in Table 30.3.

The effect exhibited by analyzed soil properties on the infiltration characteristics and estimated model parameters is reflected. It was observed that higher the initial moisture content as in case of site BU2 lower is the infiltration rate. Also, at places where bulk density was higher due to the compaction of soils, the porosity has been reduced resulting in lower initial infiltration rates. The parameters of the selected infiltration models were determined from field-measured infiltration data using the

**Table 30.3** Field measured infiltration rates (cm/hr.) of selected sites

Time (min)	A1	A2	BU1	BU2	OR1	OR2
2	31.11	30	28.5	24.6	45.51	43.8
4	28.71	27.21	26.01	22.3	41.1	40.2
7	25.3	24.7	23.8	18.9	34.1	32.9
10	22.4	21.6	20	15.6	30.2	28.7
15	20.004	20.004	17.4	12.408	26.4	24.9
20	16.2	17.4	13.8	10.896	23.004	20.208
30	13.398	14.808	11.808	9.204	19.2	17.802
40	11.802	11.4	9.702	7.1	17.1	14.808
55	9.648	10	7.308	5.8	15.4	12.7
70	7.2	7.6	6.408	4.2	13.7	10.9
85	7.2	6.8	5.604	3.7	12.5	8.3
100	7.2	6.8	5.2	3.7	12.2	8.3
115		6.8	5.2	3.7	12.2	8.3
130			5.2		12.2	
<b>Constant infiltration rate</b>	7.2	6.8	5.2	3.7	12.2	8.3

least square method of curve fitting. Table 30.4 displays the estimated values of different parameters under different land use/land cover conditions.

It was observed that Horton’s model parameter ‘ $K_h$ ’ ranges from 2.22 to 2.96  $h^{-1}$ ; the Kostiakov’s model parameter ‘ $a$ ’ varied from 9.68 to 21.19 cm/hr. and parameter ‘ $b$ ’ ranges from 0.66 to 0.73 and is in accordance with the theory of infiltration that puts the value to be positive and always less than unity (Ogbe et al 2011). Philip’s model parameter ‘ $S$ ’ ranges from 9.53  $cmhr^{-0.5}$  to 15.9  $cmhr^{-0.5}$  and parameter ‘ $K$ ’ ranges from 1.57 to 8.39 cm/hr. The value of the estimated parameters was then substituted in the selected infiltration equations to determine the infiltration rates. Tables 30.5, 30.6, 30.7, 30.8, 30.9 and 30.10 presents the model-predicted and field-measured infiltration rate for each of the selected sites, the same was compared and represented graphically as in Figs. 30.5, 30.6, 30.7, 30.8, 30.9 and 30.10.

For all the selected sites, it was found that model-predicted values are in close agreement with those measured in the field. However, Horton’s model was slightly

**Table 30.4** Values of the estimated model parameters

Study Site	Horton’s Model	Kostiakov Model		Philip’s Model	
	$K_h$	$a$	$b$	$S$	$K$
A1	2.55	14.83	0.73	10.83	5.48
A2	2.66	14.7	0.73	10.43	5.54
BU1	2.75	12.57	0.69	10.83	3.14
BU2	2.94	9.68	0.66	9.53	1.57
OR1	2.96	21.19	0.73	15.05	8.39
OR2	2.22	18.99	0.7	15.9	5.28

**Table 30.5** Simulated infiltration rate ( $f$ ) compared with field measured for site A1

Time (min)	Observed $f$ (cm/hr.)	$f$ by Horton’s model (cm/hr.)	$f$ by Kostiakov model (cm/hr.)	$f$ by Philip model (cm/hr.)
2	31.11	29.52	34.86	36.74
4	28.71	27.36	29.65	25.94
7	25.3	24.95	20.61	21.11
10	22.4	22.82	18.31	18.61
15	20.004	19.94	15.89	16.31
20	16.2	17.59	14.53	14.91
30	13.398	13.93	14.02	13.14
40	11.802	11.57	12.75	12.1
55	9.648	9.51	11.49	11.13
70	7.2	8.42	10.66	10.49
85	7.2	7.84	10.05	10.03
100	7.2	7.54	9.57	9.67

**Table 30.6** Simulated infiltration rate compared with field measured for site A2

Time (min)	Observed $f$ (cm/hr.)	$f$ by Horton's model (cm/hr.)	$f$ by Kostiakov model (cm/hr.)	$f$ by Philip model (cm/hr.)
2	30	30.53	34.03	35.65
4	27.21	28.13	29.14	25.25
7	24.7	25.48	20.31	20.59
10	21.6	23.15	18.07	18.19
15	20.004	20.02	15.7	15.97
20	17.4	17.48	14.37	14.62
30	14.808	13.59	13.88	12.92
40	11.4	11.12	12.64	11.91
55	10	9.02	11.41	10.98
70	7.6	7.94	10.59	10.36
85	6.8	7.39	9.99	9.92
100	6.8	7.1	9.53	9.58
115	6.8	6.96	9.15	9.3

**Table 30.7** Simulated infiltration rate compared with field measured for site BU1

Time (min)	Observed $f$ (cm/hr.)	$f$ by Horton's model (cm/hr.)	$f$ by Kostiakov model (cm/hr.)	$f$ by Philip model (cm/hr.)
2	28.5	28.22	33.06	34.4
4	26.01	25.82	26.42	23.61
7	23.8	23.17	17.96	18.77
10	20	20.86	15.73	16.27
15	17.4	17.77	13.48	13.97
20	13.8	15.29	12.19	12.57
30	11.808	11.52	11.63	10.79
40	9.702	9.16	10.45	9.75
55	7.308	7.19	9.33	8.78
70	6.408	6.2	8.57	8.15
85	5.604	5.7	8.02	7.68
100	5.2	5.45	7.59	7.33
115	5.2	5.33	7.25	7.05
130	5.2	5.26	6.97	6.82

under-predicted at the initial stage, but then very slightly over predicted at the end. Kostiakov and Philip's model was initially over-predicted, then under-predicted in the middle stage and then again over predicted towards the end.

**Table 30.8** Simulated infiltration rate compared with field measured for site BU2

Time (min)	Observed $f$ (cm/hr.)	$f$ by Horton's model (cm/hr.)	$f$ by Kostiakov model (cm/hr.)	$f$ by Philip model (cm/hr.)
2	24.6	23.38	28.7	29.08
4	22.3	21.2	21.51	19.58
7	18.9	18.81	14.29	15.33
10	15.6	16.74	12.35	13.13
15	12.408	14.01	10.45	11.1
20	10.896	11.85	9.36	9.86
30	9.204	8.64	8.82	8.31
40	7.1	6.69	7.83	7.39
55	5.8	5.14	6.92	6.54
70	4.2	4.39	6.3	5.98
85	3.7	4.03	5.86	5.57
100	3.7	3.86	5.51	5.26
115	3.7	3.77	5.24	5.01

**Table 30.9** Simulated infiltration rate compared with field measured for site OR1

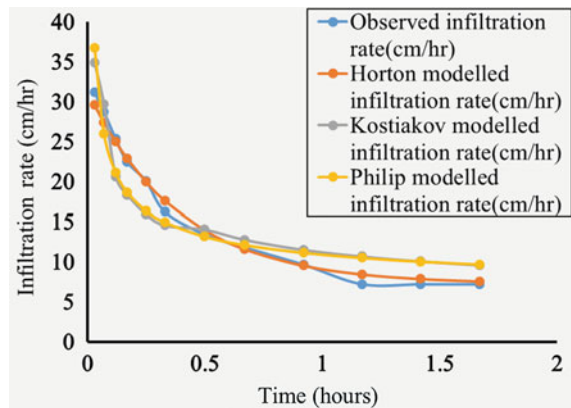
Time (min)	Observed $f$ (cm/hr.)	$f$ by Horton's model (cm/hr.)	$f$ by Kostiakov model (cm/hr.)	$f$ by Philip model (cm/hr.)
2	45.51	42.55	49.15	51.84
4	41.1	39.16	42.08	36.83
7	34.1	35.45	29.32	30.11
10	30.2	32.25	26.09	26.64
15	26.4	28.03	22.68	23.44
20	23	24.69	20.77	21.49
30	19.2	19.75	20.05	19.03
40	17.1	16.77	18.26	17.58
55	15.4	14.38	16.48	16.24
70	13.7	13.24	15.29	15.35
85	12.5	12.69	14.43	14.7
100	12.2	12.44	13.76	14.21
115	12.2	12.31	13.21	13.82
130	12.2	12.25	14.26	13.46

From the graphs of field-measured and predicted infiltration rate by selected infiltration models against time for each of the selected sites, it was observed that infiltration rates were high at the beginning but decreases steadily with time until a constant value is achieved. The high average infiltration rates were observed for land cover under orchards followed by agricultural and built-up land covers, respectively. This

**Table 30.10** Simulated infiltration rate compared with field measured for site OR2

Time (Min)	Observed $f$ (cm/hr.)	$f$ by Horton’s model (cm/hr.)	$f$ by Kostiakov model (cm/hr.)	$f$ by Philip model (cm/hr.)
2	43.8	37.75	48.94	51.18
4	40.2	35.25	39.62	35.33
7	32.9	32.42	27.06	28.23
10	28.7	29.88	23.77	24.56
15	24.9	26.37	20.43	21.18
20	20.208	23.43	18.52	19.12
30	17.802	18.67	17.7	16.52
40	14.808	15.41	15.95	14.99
55	12.7	12.38	14.26	13.57
70	10.9	10.64	13.13	12.63
85	8.3	9.65	12.31	11.95
100	8.3	9.07	11.67	11.43
115	8.3	8.74	11.16	11.02

**Fig. 30.5** Observed and simulated infiltration rate for site A1



sequence can be attributed to various soil properties such as high porosity and organic matter content, and low bulk density and initial moisture content. In order to select the best fit model for given regional characteristics, statistical analysis was carried out. The average value of the statistical parameters computed for each of the land cover is presented underneath in Table 30.11.

The result of the statistical analysis indicates that Horton’s model has the lowest value of RMSE and the highest value of NSE and  $R^2$  followed by Kostiakov and Philip’s model, respectively, for the built-up land cover. Thus, it can be concluded that of all the selected models Horton’s model performs satisfactorily on the land cover which is subjected to compaction and has decreased permeability resulting

**Fig. 30.6** Observed and simulated infiltration rate for site A2

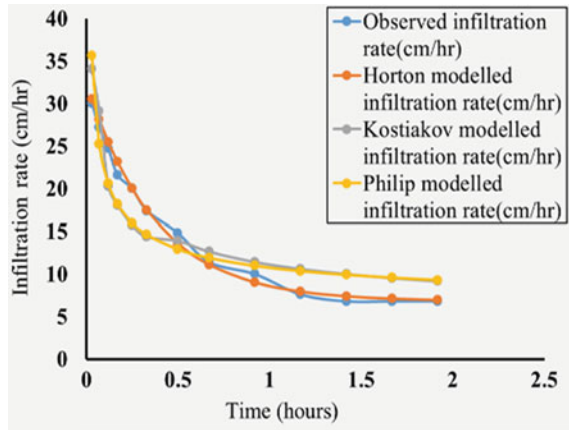


**Fig. 30.7** Observed and Simulated infiltration rate for site BU1

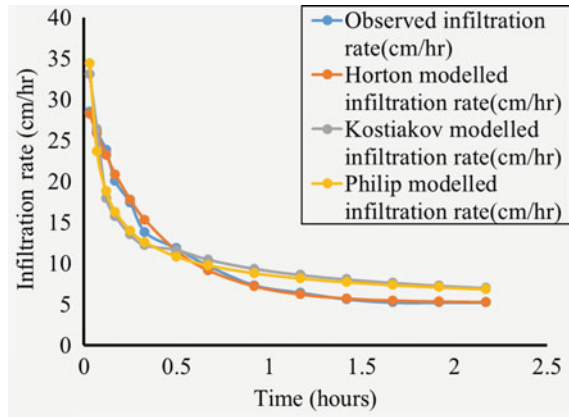


**Fig. 30.8** Observed and simulated infiltration rate for site BU2

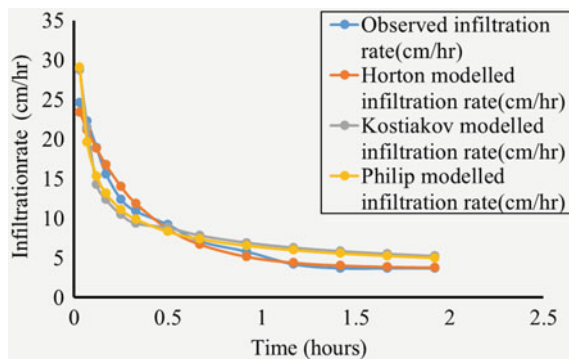


**Fig. 30.9** Observed and simulated infiltration rate for site OR1

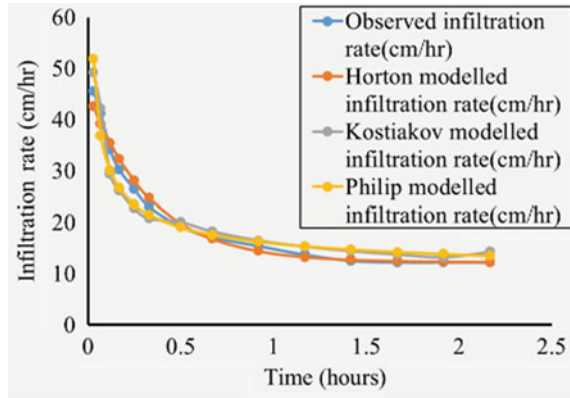


**Fig. 30.10** Observed and simulated infiltration rate for site OR2

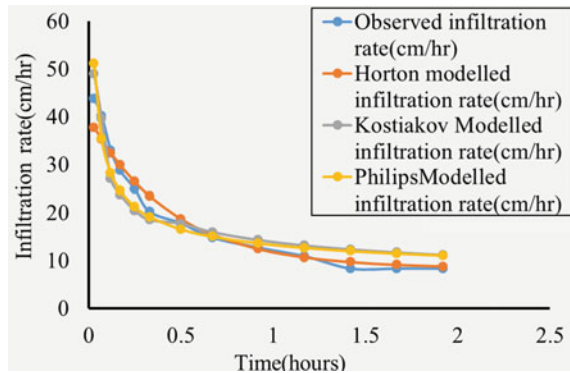


**Table 30.11** Average value of statistical parameters for selected land covers

Land cover	Horton model			Philip model			Kostiakov model		
	RMSE	NSE	R2	RMSE	NSE	R2	RMSE	NSE	R2
Agricultural land	0.81	0.99	0.99	2.97	0.87	0.87	3.09	0.68	0.86
Built-up	0.68	0.99	0.99	2.64	0.88	0.88	2.52	0.90	0.90
Orchard	1.91	0.96	0.98	2.98	0.94	0.93	3.23	0.92	0.92

in lower initial infiltration rates. Thus, for the land cover under built-up, Horton’s model can be selected as the best fit model.

Philip’s model has the highest value of NSE and  $R^2$  for the land cover under the orchard having the highest value of initial infiltration rate indicating that it is more satisfactory to use Philip’s model than the Horton and Kostiakov model when the initial infiltration rate is high.

The Kostiakov model, however, has the more satisfactory values of statistical parameters for the built-up land cover followed by land cover under orchard and

**Table 30.12** Average value of statistical parameters

Statistical parameters	Horton model	Philip model	Kostiakov model
RMSE	1.13	2.86	2.94
NSE	0.98	0.89	0.83
R2	0.98	0.9	0.89

agriculture respectively. However, on the basis of RMSE value, Horton's model has performed satisfactorily for all the land covers taken into consideration in the present research. The average value of statistical parameters for all the selected sites used in the present study for comparison of field-measured and model-predicted infiltration rates are presented below in Table 30.12.

By examining the statistical parameters, it was found that Horton's model has the lowest value of RMSE and Philips model ranked second with respect to RMSE and followed by Kostiakov model. The higher value of the coefficient of determination ( $R^2$ ) for Horton's, Philips and Kostiakov model indicates all the three models are capable of determining the infiltration rate under the given soil type and land-use conditions. However, by analyzing the value of all the statistical performance indices used for finding the best fit model for a given area, it was concluded that Horton's model is the most appropriate to predict the infiltration rate of sandy clay soils under the given land-use/land-cover conditions followed by Philips and Kostiakov models.

### 30.4 Conclusion

The average infiltration rate of sandy clay soil for selected sites under the agriculture field, built-up and the orchard was 16.23 cm/hr; 12.11 cm/hr and 21.7 cm/hr, respectively. The higher infiltration rate for the land cover under orchard is attributed to the fact that it is subjected to less compaction than the agricultural field and built-up land, thus having high porosity, low bulk density and a higher organic matter content which has increased the soil's water holding capacity. It was thus concluded that land cover and soil properties like moisture content, bulk density, porosity and organic matter affect the soil infiltrability in the micro watershed under investigation. The land cover under built-up have a lower initial infiltration rate because it is subjected to more compaction resulting in increased bulk density and low permeability, and thus have decreased capacity to absorb moisture. The land use under agriculture is also subjected to compaction but has higher infiltration rates than the built-up land cover because it has higher organic matter content. It can be thus concluded that organic matter has a significant influence on the infiltration rate in the given area under consideration. The computed average values of RMSE, NSE and  $R^2$  were (1.13, 0.98 and 0.98), (2.86, 0.89 and 0.9) and (2.94, 0.83 and 0.89) for Horton's, Philip's and Kostiakov's model, respectively. From the statistical analysis, it can be concluded that all the three selected models provide good overall agreement with the



field-measured infiltration rate and are, therefore, capable of simulating infiltration characteristics under the present land use/landcover and soil conditions. However, Horton's model with the lowest value of RMSE and the highest value of  $R^2$  and NSE provide the best fit to the measured infiltration rate and can be selected as the appropriate one to predict soil infiltration rate under the field conditions encountered in the present study.

## References

- Badar B, Romshoo SA, Khan MA (2013) Modelling catchment hydrological responses in a Himalayan Lake as a function of changing land use and land cover. *J Earth Syst Sci* 122(2):433–449
- Dingman SL (2002) *Physical hydrology*, 2nd edn. Prentice Hall, New Jersey, USA
- Horton RE (1940) An approach towards a physical interpretation of infiltration capacity. *Soil Sci Soc Am* 5:399–417
- Kostiakov AN (1932) On the dynamics of the coefficient of water-percolation in soils and on the necessity for studying it from a dynamic point of view for purposes of amelioration. *Trans Six Cong Int Soc Soil Sci Part A* 17–21
- Ogbe VB, Jayeoba OJ, Ode SO (2011) Comparison of four soil infiltration models on a sandy soil in Lafia, Southern Guinea Savanna zone of Nigeria. *Prod Agric Technol J* 7(2):116–126
- Philip JR (1957) The theory of infiltration: 1. "The infiltration equation and its solution." *J Soil Sci* 83:345–357
- Richard LA (1931) Capillary conduction through porous mediums. *Physics* 1:313–318
- Skaggs RW, Khaleel R (1982) Chapter 4: infiltration. In: *hydrology of small watersheds*. St Joseph, Michigan. Am Soc Agric Eng
- Skaggs RW, Huggins LE, Monke EJ Foster GR (1968) Experimental evaluation of infiltration equations. *Trans Am Soc Agric Eng* 3425:822–828
- Subramanya K (2008) *Engineering hydrology* 3rd (ed). Tata McGraw-Hill Publishing Company Limited, New Delhi
- Ying M, Shaoyuan F, Dongyuan S, Guangyao G, Zailin H (2010) Modeling water infiltration in a large layered soil column with a modified green-ampt model and Hydrus-1D. *Comput Electron Agric* 7(15):540–547

# Chapter 31

## Rainfall–Runoff Studies of Brahmani River Basin Using ANN



Swagatika Biswal, Bandita Naik, and K. K. Khatua

**Abstract** Rainfall–runoff is a very complicated process due to its nonlinear and multidimensional dynamics, hence it is difficult to model. There are various methods for time series based on the model of rainfall and runoff. In the present study, feed-forward back-propagation and auto-regressive integrated moving average models are applied to predict monthly runoff in the Brahmani river of the three stations: Jaraikela, Jenapur, and Tiliga. ANN with different transfer functions like TANSIG and PURELIN is used to find runoff prediction in these areas. Different statistical error analysis is done, to know better transfer function. From the observation, it was concluded that the transfer function gives better results than PURELIN. The predicted runoff found by TANSIG transfer function was again compared with ARIMA model. From the statistical error analysis, it was observed that ANN gave better results than the ARIMA method.

### 31.1 Introduction

Many natural resources are available on the earth. Water is one of the most important natural resources. Without water, life cannot be imagined on the earth's surface. 71% of the earth's surface is water-covered, and the oceans hold about 96.5% of all earth's water. Water also exists in the air as water vapors, in rivers and lakes, in icecaps and glaciers, in the ground as soil moisture, and in aquifers (Ref. water.usgs.gov). But the problem is that water is not available at the proper place at the proper time. Water is not constant. It always moves on from one place to another. Water in the different catchment areas always changes from one state to another under the effect of solar radiation. The water surface is converted to vapor by evaporation due to solar heat

---

S. Biswal (✉)

Department of Civil Engineering, CAPGS, BPUT, Rourkela, India

B. Naik

Faculty in Department of Civil Engineering, CAPGS, BPUT, Rourkela, India

K. K. Khatua

Department of Civil Engineering, NIT, Rourkela, Rourkela, India

radiation. The vapor goes continuously to the atmosphere, then due to sudden fall of temperature and pressure, by this process, clouds will be formed and precipitation occurs. Some vapors convert into ice at the peak of the mountain. This ice again melts in summer and flows as a river to meet the sea or ocean. These processes of evaporation, precipitation, and melting of ice go on continuously like an endless chain, and thus balance is maintained in the atmosphere. This phenomenon is known as the hydrology cycle. Rainfall is the major component of the hydrology cycle and runoff is the primary source of this cycle. Rainfall–runoff relationship is one of the most complicated hydrologic phenomena to comprehend due to the tremendous spatial and temporal variability of watershed characteristics and precipitation patterns, and the number of variables involved in the modeling of the physical processes. Since the 1930s, numerous rainfall–runoff models have been developed to forecast stream flow (Tokar and Johnson 1999). The ANN models are powerful prediction tools for the relationship between rainfall and runoff. The rainfall–runoff relationship is highly nonlinear, multidimensional, time dependence, and spatial varying parameter (Dibike and Solomatine 2001). Two types of ANN networks, MLP and RBF, were used to investigate downstream flow forecasting in the Apure river basin (Venezuela). Those networks were compared with the conceptual rainfall–runoff model and were found which one gives better for this river flow forecasting. Rajurkar et al. (2002) stated that a linear MISO model coupled with the ANN provided a better representation of the rainfall–runoff relationship in such a large size catchment compared with linear and nonlinear MISO models. The presented model provided systematic runoff estimation. Wilby et al. (2003) provided a neural network solution to develop for daily discharge series simulated by the conceptual rainfall–runoff model and observed daily precipitation total and evaporation rates of the test river basin in South England. Correlation analysis suggests that hidden nodes in the NN correspond to dominant processes within the conceptual model. Rajurkar et al. (2004) model daily flows during the flood event using ANN. The study uses data from two large-size catchments in India and five other catchments used earlier by the World Metrological Organization (WMO) for intercomparisons of the operational hydrological models. ANN proves to be very much useful in modeling the rainfall–runoff relationship in the nonupdating mode. Chiang et al. (2004) provided a systematic comparison of two basic types of neural networks, static and dynamic methods used in Lan-Yang-River of Taiwan. Somvanshi et al. (2006) predict rainfall based on past observation using ANN and ARIMA techniques. Aqil et al. (2007) suggested that recurrent and feed-forward network with Levenberg–Marquardt is able to forecast the catchment flow in advance with reasonable prediction accuracy (Nourani et al. 2009). Recently, ANN as a nonlinear extrapolator is extensively used by hydrologists for rainfall–runoff modeling as well as in other fields of hydrology. The model predicted both short- and long-term runoff discharges using multi-scale series of rainfall and runoff data as the ANN input layer. Ghumman et al. (2011) compared the ANN model with a mathematical conceptual model. An ANN model is an important alternative to a conceptual model and it was used when the range of collected data set is short and data is of low standard. Ghose et al. (2013) predict runoff using nonlinear multiple regression (NLMR) and adaptive neuro-fuzzy inference system (ANFIS).

Valipour et al. (2013) observed that the ARIMA model had less error compared with the ARMA model of Dez dam reservoir in the 12 past months. Elsafi (2014) used the ANN model to forecast flooding along the river Nile. This work provided baseline information toward the establishment of a flood warning system in certain sections of the river. Farajzadeh et al. (2014) was observed that estimated values of monthly rainfall through FFNN were close to the ARIMA model of the Urima lake basin. In this paper correlation of rainfall–runoff, prediction of runoff using precipitation, mean temperature, solar, wind, humidity, and discharge. ANN with different transfer functions is used to predict runoff and is analyzed with mean absolute deviation, mean square error, and root mean square error. To compare the validation phase of runoff predicted by ANN and ARIMA model use statistical error analysis.

### 31.2 Study Area

Brahmani river is the second largest river in Odisha after Mahanadi. The location of the Brahmani river basin and study area is shown in Figs. 31.1 and 31.2, respectively. It is a major seasonal river in the Odisha state of Eastern India. The Brahmani is formed by the confluence of the South Koel river and Sankh river near the Vedvyas, Panposh in Odisha. The latitude  $22^{\circ}14'45''N$  and longitude  $84^{\circ}47'02''E$  are the geo-coordinate of the river. At about 480 km long, its constituent rivers are included and its length extends to about 799 km, of which 541 km are in Odisha. It has a catchment area of about 39,033 km<sup>2</sup> in Odisha alone. Brahmani river basin has nine hydro-observation stations. In the present study three gauging stations, Jenapur, Jaraikela, and Tiliga, are discussed. These stations belong to the districts of Jajpur, Sundargarh, and Simdega (Jharkhand). Jaraikela and Tiliga are located on the tributary rivers Koel

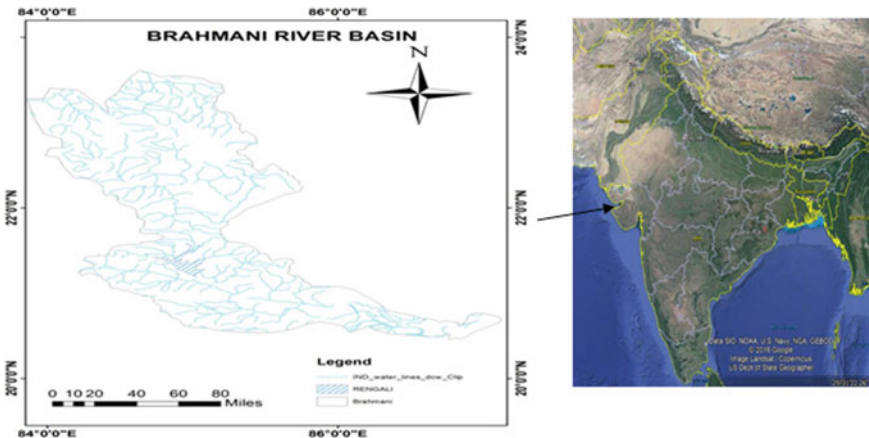


Fig. 31.1 Location of Brahmani river basin

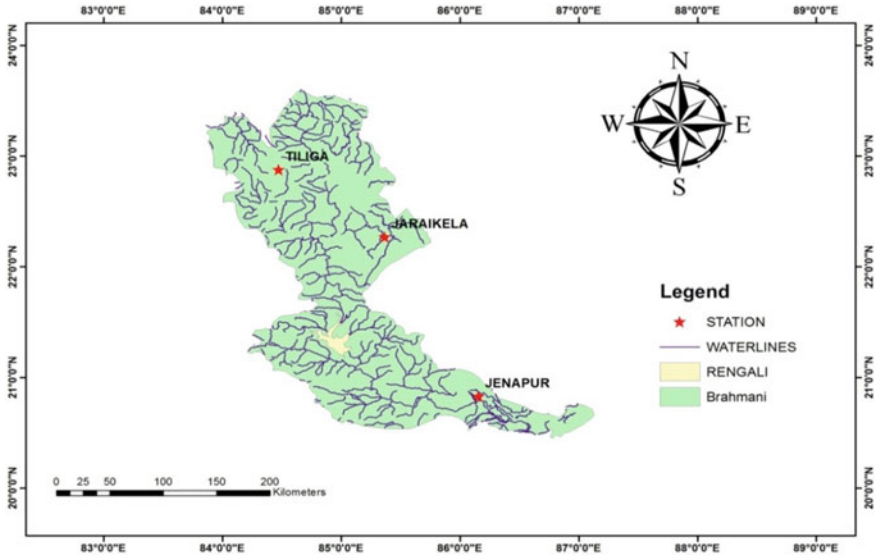


Fig. 31.2 Location of the study area

and Sankh. The Sankh river and the South Koel river are two major tributary rivers of Brahmani river basins. The Sankh river and the South Koel river originate from the Ranchi district of Jharkhand state. The latitude of the South Koel river is 23°20'N and longitude 85°12'E. The Sankh river latitude is 23°14'N and longitude 84°16'E geo-coordinate of the river. The total length of the Sankh river is 240 km. The gauging stations Jenapur, Jaraikela, and Tiliga drainage area are, respectively, 33,955, 9160, and 3160 km<sup>2</sup>.

### 31.3 Methodology

#### 31.3.1 Feed-Forward Back-Propagation Neural Network

In this study, the feed-forward back-propagation neural network is propagated in one direction from the input layer to the output layer. The MLP networks can be more than one hidden layer. The feed-forward network that has interconnected nodes is arranged in three layers: input layer, hidden layer, and output layer. In this study five input layers, one output layer, and 10 hidden layers are used in a multilayer feed-forward back-propagation algorithm to predict river basin runoff. The five input variables are temperature, solar, wind, humidity, and precipitation. The input nodes pass on the input signal values to the nodes depending on the connection weight between the input nodes and hidden nodes. The connection between weight and hidden nodes

is an interconnection link between the successive layers. Each neuron in a certain layer is connected to every single neuron to the next layer and adjustable connection weight. This network has been used for training purpose in Levenberg–Marquardt back-propagation (LMBP) algorithm because this technique is more effective than conventional gradient techniques.

$$X_{K+1} = [X_K - J^T J + \mu I]^{-1} J^T e \tag{31.1}$$

where  $X$  indicates the weight of the neural network and the scalar  $\mu$  control the learning process.  $J$  is the Jacobian matrix; ‘ $e$ ’ is the vector of the network.

In this present study, two types of transfer functions have been used: TANSIG and PURELIN. The TANSIG transfer function, hyperbolic tangent (tanh) is a symmetric s-shaped (sigmoid) function which lies in the range  $[-1, 1]$  with the identity function. The activation neuron is passed on directly as the output of the neuron and the output lies in the range  $[\infty, -\infty]$ . Purelin is a linear function values between  $[-1, 1]$ . The linear activation function is  $f(x) = x$ .

### 31.3.2 Autoregressive Integrated Moving Average (ARIMA)

Time-series models, such as autoregressive integrated moving average (ARIMA), are widely used for hydrological time series forecasting. They are basically a linear model assuming the data are stationary and have limited ability to capability nonstationarities and nonlinearities in hydrologic data. It has basically three parts in moving average and differencing process. In general, the autoregressive (AR) moving average (MA), autoregressive moving average (ARMA), and autoregressive integrated moving average (ARIMA) models are applied to time series. Therefore, the process is a nonstationary series before conducting a modeling process. In an ARIMA model, the further value of a variable is supposed to be a linear combination of past values and past errors which can be expressed as in Eq. (31.2):

$$Y_t = \theta_0 + \theta_1 y_{t-1} + \theta_2 y_{t-1} + \dots + \theta_p y_{t-p} + \dots + \epsilon_t - \theta_1 \epsilon_{t-1} - \theta_2 \epsilon_{t-2} - \dots - \theta_q \epsilon_{t-q} \tag{31.2}$$

where  $\theta_j, \theta_j$  are coefficients.  $Y_t$  is the actual value at time ‘ $t$ ’.  $P$  and  $q$  are the autoregressive and moving average coefficients.

### 31.3.3 Evaluation Criteria

The model is to obtain both statistical and graphical criteria. Statistical model criteria consist of mean absolute deviation, mean square error, and root mean square error.

$$\text{MAD} = \sum_{i=1}^n [Q_i - \hat{Q}_i] \quad (31.3)$$

$$\text{MSE} = \sum_{i=1}^n [Q_i - \hat{Q}_i]^2 \quad (31.4)$$

$$\text{RMSE} = \frac{\sqrt{\sum_{i=1}^n [Q_i - \hat{Q}_i]^2}}{n} \quad (31.5)$$

Here,  $Q_i$  is the observed value.  $\hat{Q}_i$  is the predicted value and 'n' is the total number of the observed sample.

### 31.3.4 ANN Model Development for Prediction Runoff

ANN model is used in three stations, Jaraikela, Jenapur, and Tiliga, for runoff modeling using MLP feed-forward back-propagation network. Solar, wind, temperature, humidity, and precipitation are taken as input parameters, and discharge is taken as the output parameter. Monthly weather data are collected from 1990 to 2014 available at <http://swat.tamu.edu> for each station. Out of 295 sample data, 70% is used for the training phase, 15% is used for the testing phase, and 15% is used for the validation phase. For the training phase minimize error, testing and validation phase properly training. The weather data set in the present study are input variables as well as target variables and are first normalized for the activation function using the following equation:

$$\bar{x} = \frac{x - x_{\min}}{x_{\max} - x_{\min}}$$

where  $\bar{x}$  is the standardized value of the input,  $x_{\min}$  and  $x_{\max}$  are, respectively, the minimum and maximum of the actual values in all observations, and  $x$  is the original data set. The main reason for standardizing the data matrix is input variables have been measured in different units, and then recasted in the dimensionless unit. The graphical performance indicator gives better results when the data pair are closing to 45° line and good superposition between the desired and calculated flow values in the training, testing, and validation. The activation function changed in the second layer because the hidden layer represents the output layer.

### 31.4 Results and Discussion

In the validation phase 15% of data should be used. The main aim of the validation phase is to use two types of transfer functions, TANSIG and PURELIN, properly. After training and validation phases, statistical error calculation is done to know which transfer function gives better performance. Tables 31.1, 31.2, and 31.3 show the statistical error analysis of three stations using different activation functions (Figs. 31.3, 31.4 and 31.5).

The performance measures of ANN models in terms of numerical computation are MAD, MSE, RMSE, and  $R^2$ , which are shown in Tables 31.1, 31.2, and 31.3. It is observed from the tables that the TANSIG function gives better results than the PURELIN.

#### 31.4.1 Comparison Graph of ANN Model and ARIMA Model

The predicted runoff is used by the ARIMA method and it is again compared with the best transfer function of ANN found by the observation, as shown in Figs. 31.6, 31.7, and 31.8. Performance evaluation statistics of ANN and time-series model at different stations.

**Table 31.1** Comparison of statistical analysis is done using two transfer functions of ANN at Jenapur during the validation phase

	Statistical analysis	TANSIG	PURELIN
Jenapur	MAD	0.033	0.032
	MSE	0.001	0.003
	RMSE	0.043	0.565
	$R^2$	0.917	0.866

**Table 31.2** Comparison of statistical analysis is done using two transfer functions of ANN at Jaraikela during the validation phase

	Statistical analysis	TANSIG	PURELIN
Jaraikela	MAD	0.056	0.045
	MSE	0.006	0.006
	RMSE	0.080	0.088
	$R^2$	0.734	0.681

**Table 31.3** Comparison of statistical analysis is done using two transfer functions of ANN at Tiliga during the validation phase

	Statistical analysis	TANSIG	PURELIN
Tiliga	MAD	0.034	0.034
	MSE	0.003	0.004
	RMSE	0.058	0.065
	$R^2$	0.920	0.915



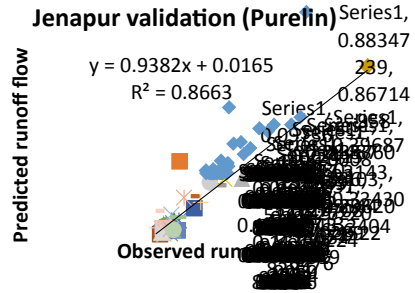
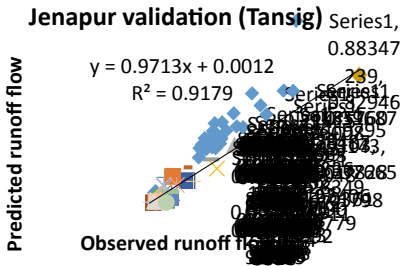


**Fig. 31.3** Coefficient of determination graph of using TANSIG and PURELIN transfer function at Jenapur

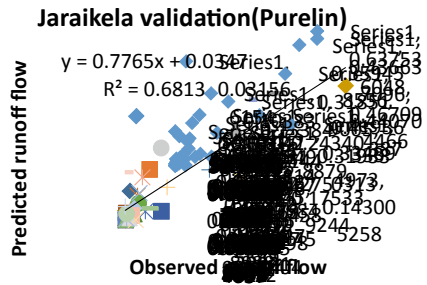
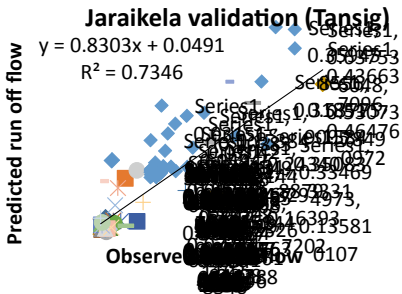


**Fig. 31.4** Coefficient of determination graph of using TANSIG and PURELIN transfer function at Jaraikela

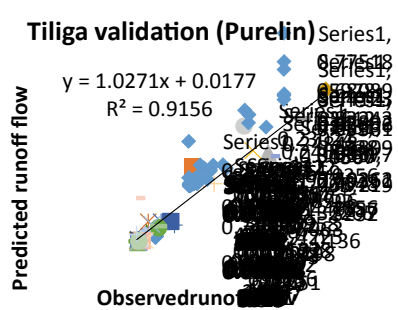
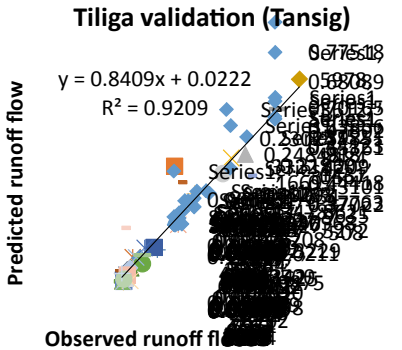


**Fig. 31.5** Coefficient of determination graph of using TANSIG and PURELIN transfer function at Tiliga

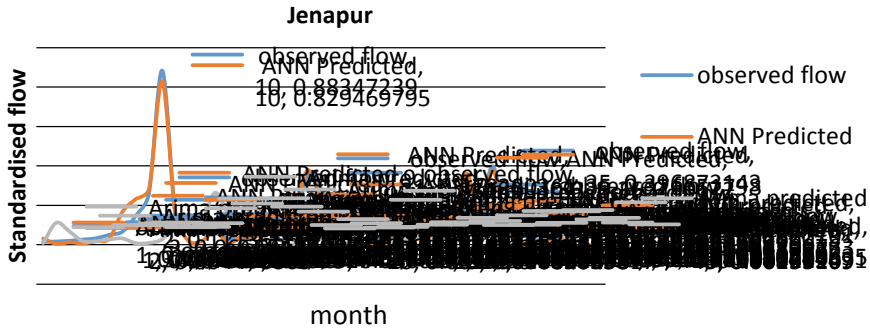


Fig. 31.6 Comparison graph of ANN and ARIMA predicted the flow of Jenapur

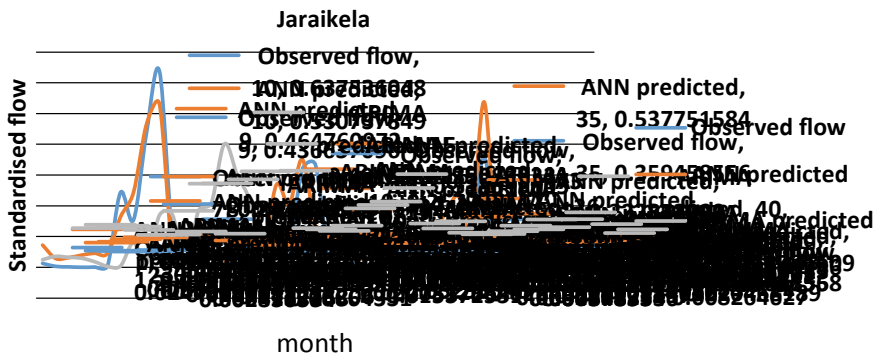


Fig. 31.7 Comparison graph of ANN and ARIMA predicted the flow of Jaraikela

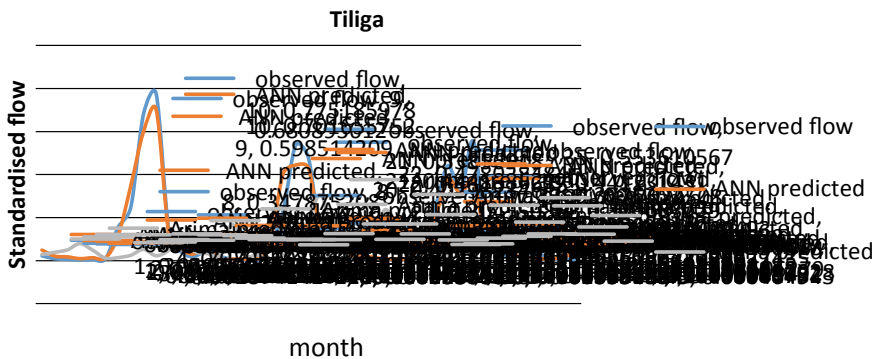


Fig. 31.8 Comparison graph of ANN and ARIMA predicted the flow of Tiliga

**Table 31.4** Comparison of statistical analysis of ANN and time-series model at different gauging stations

Stations	Techniques	MAD	MSE	RMSE
Jenapur	ARIMA	0.104	0.030	0.175
	ANN	0.033	0.001	0.043
Jaraikela	ARIMA	0.110	0.027	0.166
	ANN	0.053	0.005	0.005
Tiliga	ARIMA	0.142	0.050	0.224
	ANN	0.030	0.002	0.051

The performance measure of ANN and ARIMA models in terms of numerical computations are shown in Table 31.4. The table indicates that the ANN model outperforms the ARIMA model. The MAD error for the model data set of Jenapur, Jaraikela, and Tiliga for the ARIMA model is 0.104, 0.110, and 0.142, respectively, while the same error measure is considerably lower at 0.033, 0.053, and 0.030 in the ANN method. The other performance measures such as MSE at Jenapur, Jaraikela, and Tiliga for the ARIMA models are 0.030, 0.027, and 0.050, but in the same error, the measure is considerably lower at 0.001, 0.005, and 0.002 in ANN. The RMSE values of Jenapur, Jaraikela, and Tiliga in ANN models are 0.043, 0.005, and 0.051, which are lower than 0.175, 0.166, and 0.224. On the basis of error calculation of MAD, MSE, and RMSE, the ANN model is more appropriate than the ARIMA model. In our study, it is observed that the ANN model should be an appropriate prediction tool for the prediction of rainfall according to the ARIMA model.

## 31.5 Conclusions

Highly nonlinear multidimensional natural recorded parameter of rainfall–runoff studies using the ANN and ARIMA techniques 2010 December to 2014 July recorded data solar, wind humidity, temperature, precipitation, and runoff data was used for validation model or predict runoff. The ARIMA method uses runoff data of past observations as input to the neural network. For the present analysis five types of past observation data and one output data that is runoff are used, which was used to ANN. This study concluded that the ANN model is used as an appropriate model for prediction runoff than the performance of the ARIMA model.

## References

- Aqil M, Kita I, Yano A, Nishiyama S (2007) Neural networks for real time catchment flow modeling and prediction. *Water Resour Manage* 21(10):1781–1796
- Chiang YM, Chang LC, Chang FJ (2004) Comparison of static-feedforward and dynamic-feedback neural networks for rainfall–runoff modeling. *J Hydrol* 290(3–4):297–311
- Dibike YB, Solomatine DP (2001) River flow forecasting using artificial neural networks. *Phys Chem Earth Part B* 26(1):1–7
- Elsafi SH (2014) Artificial neural networks (ANNs) for flood forecasting at Dongola Station in the River Nile, Sudan. *Alexandria Eng J* 53(3):655–662
- Farajzadeh J, Fard AF, Lotfi S (2014) Modeling of monthly rainfall and runoff of Urmialake basin using “feed-forward neural network” and “time series analysis” model. *Water Resour Indus* 7:38–48
- Ghose DK, Panda SS, Swain PC (2013) Prediction and optimization of runoff via ANFIS and GA. *Alex Eng J* 52(2):209–220
- Ghumman AR, Ghazaw YM, Sohail AR, Watanabe K (2011) Runoff forecasting by artificial neural network and conventional model. *Alex Eng J* 50(4):345–350
- Nourani V, Komasi M, Mano A (2009) A multivariate ANN-wavelet approach for rainfall–runoff modeling. *Water Resour Manage* 23(14):2877
- Rajurkar MP, Kothiyari UC, Chaube UC (2002) Artificial neural networks for daily rainfall—runoff modelling. *Hydrol Sci J* 47(6):865–877
- Rajurkar MP, Kothiyari UC, Chaube UC (2004) Modeling of the daily rainfall-runoff relationship with artificial neural network. *J Hydrol* 285(1–4):96–113
- Somvanshi VK, Pandey OP, Agrawal PK, Kalanker NV, Prakash MR, Chand R (2006) Modeling and prediction of rainfall using artificial neural network and ARIMA techniques. *J Ind Geophys Union* 10(2):141–151
- Tokar AS, Johnson PA (1999) Rainfall-runoff modeling using artificial neural networks. *J Hydrol Eng* 4(3):232–239
- Valipour M, Banihabib ME, Behbahani SMR (2013) Comparison of the ARMA, ARIMA, and the autoregressive artificial neural network models in forecasting the monthly inflow of Dez dam reservoir. *J Hydrol* 476:433–441
- Wilby RL, Abraham RJ, Dawson CW (2003) Detection of conceptual model rainfall—runoff processes inside an artificial neural network. *Hydrol Sci J* 48(2):163–181

# Chapter 32

## Estimation and Management of Irrigation Water Using WEAP Model in Tandula Reservoir Command Area



Yashvant Kumar Tikariha and Ishtiyag Ahmad

**Abstract** Water availability for agriculture is decreasing day by day due to over-exploitation of groundwater and impacts of climate change in India. Agriculture being the backbone of the Indian economy is readily influenced by the scarcity of water. Chhattisgarh is one among various states which are facing scarcity problems. For the proper growth of every crop, a certain amount of water is required at different stages, thus making it necessary to estimate the actual amount of water required to prevent the crop from wilting. In this study, crop water requirement (CWR) and irrigation water requirement (IWR) have been computed by water evaluation and planning (WEAP) software using MABIA method for seven blocks of Chhattisgarh state, viz., Balod, Gurur, Durg, Gunderdehi, Patan, Dhamdha, and Berla. All major crops like rice, wheat, maize, pulses, oilseeds, sugarcane, vegetables, and fruits, which were grown traditionally, are considered for this study. The CWR and IWR have been computed as  $5814.19 \text{ Mm}^3$  and  $2445.24 \text{ Mm}^3$ , respectively. To fulfill this requirement water received from the sources like rainfall, groundwater, and canal were found to be  $3304 \text{ Mm}^3$ ,  $659.1 \text{ Mm}^3$ , and  $618.01 \text{ Mm}^3$ , respectively. Thus, the irrigation deficit was found to be  $1233.10 \text{ Mm}^3$ . In order to utilize the water resources reasonably for matching water supply and requirement and to reach the maximum economic benefit, an optimum crop pattern for each block was determined. A genetic algorithm was adopted in the present study to apply an optimization model for each branch canal separately and get an optimized cropping area, with the help of which farmers can produce extra income of Rs. 35,744,118. Finally, the cropping pattern and water allocation plans for various blocks have been prepared. This study will be helpful for policymaking, efficient irrigation scheduling, reservoir operation studies, optimization work, reservoir planning and restoration work, etc.

---

Y. K. Tikariha · I. Ahmad (✉)

Department of Civil Engineering, National Institute of Technology, Raipur 492010, Chhattisgarh, India

e-mail: [iahmad.ce@nitrr.ac.in](mailto:iahmad.ce@nitrr.ac.in)

## 32.1 Introduction

Agricultural production is essential in developing countries like India to fulfill food requirements for livelihood and maintain food security. Irrigation is one of the methods to increase agricultural production in the field. But irrigation water shortage is developing these days in India due to increasing agriculture, industry, and domestic uses of the growing population. The major population (80%) of the study area is dependent on agriculture farming, but the occurrence of drought in recent years was very painful. The farmers could not even grow food for their families to fulfill the requirement for one complete year. Many industries which are dependent on raw materials from the agricultural field also got affected. Per capita use of domestic water is also increasing due to the growth of population and various schemes of the government like ‘Har Ghar Shauchalaya Mission’, ‘Swachh Bharat Mission’, etc.

The major reasons behind water scarcity in the study area are the following:

- Rainfall in the months between June and September is very less which is not appropriate as farmers majorly grow rice in their field.
- Water draft for irrigation supply is increasing rapidly, and these huge drafts tend to fall in water level in the study area.

Keeping all these reasons in the background the study was carried out with the following objective to compute the agricultural water demand (crop water requirements) of seven major crops with the long-term climatic data (1985–2016) by using WEAP (2016). MABIA method is used in the present study for determining crop water requirement in WEAP; it is a dual Kc method for the calculation of evaporation and transpiration separately. MABIA method uses Penman–Monteith equation for determining reference crop evapotranspiration ( $ET_{ref}$ ). It is used worldwide by researchers because it provides very consistent values with respect to actual crop water use data of field (Allen et al. 1988a, b).

Finally, by using WEAP, reference evapotranspiration ( $ET_{ref}$ ), crop water requirement (CWR), and irrigation requirement (IWR) were computed.

In a particular area, where the availability of water is limited and every single farmer has not realized the potential benefits of irrigation, it is necessary to carry out research to maximize their benefit (Wang et al. 2004; Benli and Kodal 2003). In this study, optimization is performed to maximize economic benefit taking the cropping area as a decision variable. The objective function (to maximize benefit) and constraints (area and water supply) are prepared according to actual field conditions, and the genetic algorithm is adopted for performing optimization on each block separately. On the basis of the result obtained, the cropping pattern and water allocation plans for various blocks are prepared.

## 32.2 Materials and Methods

### 32.2.1 Study Area

Tandula reservoir command area is located at Lohara village of Balod block of Chhattisgarh. Geographical coordinate lies in between  $20^{\circ} 41' 13''$  N to  $21^{\circ} 37' 30''$  N and  $81^{\circ} 13' 59''$  E to  $81^{\circ} 40' 12''$  E. Average daily temperature is  $32.60^{\circ}\text{C}$ . Tandula project is a major irrigation project, whose culturable command area is 2,46,340 ha covering seven blocks, viz., Balod, Gurur, Durg, Patan, Gunderdehi, Dhamdha, and Berla of Chhattisgarh state. Dhamdha, Berla, and Gunderdehi are affected by drought in recent years. The total agricultural land of these seven blocks is 3,88,618 ha. This area contains soils like Entisol (Bhata-gravelly), Inceptisol (Matasi-Sandy loam), Alfisols (Dorsa-clay loam), Vertisols (Kanhra-clayey), Bharri, etc. In these seven blocks/tehsils majorly rice, wheat, maize, pulses, oilseeds, sugarcane, vegetable, and fruits are grown.

These blocks receive water for CWR in the form of rainfall mostly. During June–September the measured rainfall is 1086.4 mm with 65 rainy days. Water from ground is extracted through tube wells, bore wells, and also from canal supply. Totally, 13 distributaries of Tandula canal system supply water to the area whose main canal length is 110.47 km. Water is supplied in this area by distributaries and minor, mainly during the third week of January to the end of May in Rabi and Kharif seasons during the September and October months. In the Kharif season rainfall is sufficient to grow crops.

### 32.2.2 Crop Water Requirement

The amount of water required to compensate for the evapotranspiration loss from the agricultural field is termed crop water requirement. Although crop evapotranspiration ( $ET_c$ ) and crop water requirement are identical terms, the amount of water that needs to be supplied to the agricultural field is called crop water requirement, while the amount of water that is lost through evapotranspiration is called crop evapotranspiration.

Evapotranspiration ( $ET_c$ ) is computed by multiplying  $ET_{ref}$  by the crop coefficient ( $K_c$ )

$$ET_c = K_c * ET_{ref} \quad (32.1)$$

$$K_c = K_{cb} + K_e \quad (32.2)$$

where

$K_{cb}$  = basal crop coefficient representing transpiration from crop

$K_e$  = coefficient representing evaporation from the soil surface

$ET_{ref}$  = reference evapotranspiration.

Reference evapotranspiration  $ET_{ref}$  of individual crops in each block is computed by Penman–Monteith approach, and  $ET_c$  is computed through the above equation. MABIA method is described in FAO Irrigation and Drainage Paper 56 on WEAP software developed at the Institute National Agronomique de Tunisie by Dr. Ali Sahli and Mohamed Jabloun. The methodology here represents the procedure for the combined MABIA-WEAP calculations for reference crop evapotranspiration and crop water requirements and the simulation of water use under various climatic conditions, crop conditions, and soil conditions under daily time steps.

Meteorological parameters used for calculation of  $ET_{ref}$  are precipitation, maximum and minimum temperature ( $^{\circ}C$ ), maximum and minimum relative humidity (%), wind speed (km/day), and sunshine hours which were collected from the hydrometeorology department, Raipur and from the location (latitude, altitude) of each block. The above-mentioned data were fed in software and  $ET_{ref}$  is computed on daily basis.

Based on soil, field capacity (%), saturation point (%), wilting point (%), available water capacity (%), and depth of soil (m) are fed in software, and these data were collected from Indira Gandhi Krishi Vidyalaya, Raipur.

The crops which are majorly cultivated in the study area are rice, wheat, maize, pulses, oilseeds, sugarcane, vegetables, and fruits. Crop data like planting date, crop period (days), stage-wise crop coefficient ( $K_c$ ) values collected from IGKV, Raipur are fed in software.

These data are fed on WEAP after preparation and shapefile of command area and orientation of canals in that particular area are imported. Finally, on simulation of the model, reference evapotranspiration ( $ET_{ref}$ ) and crop water requirement (CWR) are obtained as results. Irrigation water requirement (IWR) is calculated by deducting CWR with effective rainfall.

### 32.2.3 Optimization Model for the Optimal Crop Pattern

#### (A) Selection of decision variables

There are seven major crops in the command area of the Tandula irrigation scheme, viz., rice, wheat, maize, pulses, oilseeds, sugarcane, vegetable, and fruits. In order to determine the optimum crop area irrigated on every block, the areas of different crops irrigated in each block were selected as decision variables (parameters). Therefore, the selected decision variables are as follows:

$$A_{i,j} = \text{optimum planting area of crop } j \text{ in the } i\text{th block (ha)}$$



where

$i = 1, 2, \dots, 7$  (1 stands for Balod, 2 for Gurur, 3 for Patan, 4 for Durg, 5 for Gunderdehi, 6 for Dhamdha, and 7 represents Berla)

$j = 1, 2, \dots, 7$  (1 stands for rice, 2 for wheat, 3 for maize, 4 for pulses, 5 for oilseeds, 6 for vegetable and fruits, and 7 represents sugarcane).

*(B) Objective function*

In this work, the objective function is to maximize the farmer's benefit, to get optimal cropping area. For maximization of farmer's benefit, we have to calculate first, how much the farmer invests to cultivate a particular crop and how much they earn after selling that crop.

- To calculate total earning, the cropping area is multiplied by minimum support price (MSP) of the crop and its increased production after irrigation. According to the physical condition of the area multiplying this term with benefit allocation coefficient (0.5).
- To calculate total investment cropping area is multiplied by farmer's investment per hectare.
- Finally, we deduct investment from earning to calculate the benefit, so we got the formula

$$\text{Max } Zi = \varepsilon \sum_{j=1}^N A_{i,j} P_j D_j - E \sum_{j=1}^N A_{i,j} \quad (32.3)$$

where

$i = 1 \dots 7$  (Blocks)

$j = 1 \dots 7$  (Crops)

$Z_i$  = Farmer's benefit

$\varepsilon$  = Benefit allocation coefficient (0.5)

$A$  = Cropping area

$P$  = Minimum support price of crops (MSP)

$D$  = Increase in production through irrigation

$E$  = Annual investment in different crop production

$Q_m$  = Average water supply during different schedules of crops.

The GA model with the above fitness function or objective function is subjected to the following constraints or boundary conditions for the calculation of the optimum

crop area, besides the maximum objective function. These consist of limitations of total area, maximum and minimum crop areas, and water supply. They are as follows:

*(C) Boundary constraints*

According to traditional practice and the food habitat of the population living over here, on every block there are maximum and minimum limitations on the planting area of different crops, which is prepared by the study of crop patterns. The maximum and minimum constraint conditions are as follows:

$$0.800A_i \geq A_{i, 1} \geq 0.550A_i \text{ (ha)} \quad (32.4)$$

$$0.060A_i \geq A_{i, 2} \geq 0.020A_i \text{ (ha)} \quad (32.5)$$

$$0.005A_i \geq A_{i, 3} \geq 0.001A_i \text{ (ha)} \quad (32.6)$$

$$0.32A_i \geq A_{i, 4} \geq 0.143A_i \text{ (ha)} \quad (32.7)$$

$$0.099A_i \geq A_{i, 5} \geq 0.009A_i \text{ (ha)} \quad (32.8)$$

$$0.097A_i \geq A_{i, 6} \geq 0.029A_i \text{ (ha)} \quad (32.9)$$

$$0.012A_i \geq A_{i, 9} \geq 0.001A_i \text{ (ha)} \quad (32.10)$$

$$\sum_{j=2}^7 A_{i, j} \leq A_i \quad (32.11)$$

*(D) Inequality constraints*

*(a) Total area constraint*

The combined crop area irrigated on every block should be equal to or smaller than the total irrigated area of that particular block. So constraint of the total area may be defined as

$$\sum A_{i, j} \leq A_i \text{ (ha)} \quad (32.12)$$

*(b) Constraints of water supply*

The irrigation area requires water at various months, with respect to various schedules annually. Every irrigation rotation should be finished within the required time; otherwise, the crop yields will be influenced. The volume of water use can be obtained through the calculation of crop area and the related irrigation delta. The volume of

**Table 32.1** Irrigation scheduling (observed water release data of Tandula major irrigation scheme)

j↓	First	Second	Third	Fourth	Fifth	Sixth	Seventh
Rice					1 May to 25 May	27 Sep to 12 Oct	15 Oct to 22 Oct
Wheat	21 Jan to 30 Jan	1 Feb to 28 Feb	1 Mar to 30 Mar	1 Apr to 30 Apr			
Maize	21 Jan to 30 Jan	1 Feb to 28 Feb					
Pulses	21 Jan to 30 Jan						
Oilseeds		1 Feb to 28 Feb					
Veg. and Fruit			1 Mar to 30 Mar	1 Apr to 30 Apr			
Sugarcane					1 May to 25 May	27 Sep to 12 Oct	
Q <sub>m</sub> (Cumec)	20	20	20	50	20	50	5
d(days)	10	28	30	30	25	15	7

water supply has been obtained from the maximum possible capacity of the Tandula irrigation project (Table 32.1). The constraints of water supply are as follows:

$$A_i, j M_i, j \leq n \frac{Q_m A_i}{F} * d_k * 24 * 3600 \tag{32.13}$$

Here,

$n$  = canal efficiency

$Q_m$  = maximum discharge through main canal

$d$  = number of days in schedule

$k$  = schedule number

$M$  = delta (m<sup>3</sup>/ha)

$$A_i, 2 M_2, 2 + A_i, 3 M_2, 3 + A_i, 5 M_2, 5 \leq n \frac{Q_2 A_i}{F} * d_2 * 24 * 3600 \tag{32.14}$$

$$A_i, 2 M_3, 2 + A_i, 6 M_3, 6 \leq n \frac{Q_3 A_i}{F} * d_3 * 24 * 3600 \tag{32.15}$$

$$A_i, 2 M_4, 2 + A_i, 6 M_4, 6 \leq n \frac{Q_4 A_i}{F} * d_4 * 24 * 3600 \tag{32.16}$$

$$A_{i, 1M5, 1} + A_{i, 7M5, 7} \leq n \frac{Q5A_i}{F} * d_5 * 24 * 360.0 \quad (32.17)$$

$$A_{i, 1M6, 1} + A_{i, 7M6, 7} \leq n \frac{Q6A_i}{F} * d_6 * 24 * 360.0 \quad (32.18)$$

$$A_{i, 1M7, 1} \leq n \frac{Q7A_i}{F} * d_7 * 24 * 3600 \quad (32.19)$$

## 32.3 Data Required

### 32.3.1 Meteorological Data

Meteorological parameters used for calculation of  $ET_{ref}$  are precipitation, maximum and minimum temperature ( $^{\circ}C$ ), maximum and minimum relative humidity (%), wind speed (km/day), and sunshine hours which were collected from the hydrometeorology department, Raipur, and the location (latitude, altitude) of each block is fed in software and  $ET_{ref}$  is calculated on a daily basis.

### 32.3.2 Soil Data

Based on all five kinds of soil, field capacity (%), saturation point (%), wilting point (%), available water capacity (%), depth of soil (m) are fed in software, these data are collected from IGKV, Raipur.

### 32.3.3 Crop Data

The crops which are majorly cultivated in the study area are rice, wheat, maize, pulses, oilseeds, sugarcane, vegetables, and fruits, etc. Crop data like planting date, crop period (days), stage-wise crop coefficient ( $K_c$ ) values are fed in software collected from IGKV, Raipur.

**Table 32.2** Parameters

Crop	MSP (Rs./qq)	E (Rs./qq)	D <sub>j</sub>
Rice	1550	1090	15
Wheat	1735	760	25
Maize	1425	999	10
Pulses	4400	2341	8
Oilseeds	3050	1952	15
Veg. and Fruit	3000	2100	5
Sugarcane	255	145	180

Source Department of Agriculture, Cooperation and Farmers Welfare

### 32.3.4 Minimum Support Price (MSP) and Annual Investment

A farmer needs some amount of money to be invested for cultivating crops from the land preparation stage to harvesting and that's what we call an annual investment. When farmers sell these crops in the open market or to the government they fetch some amount of money and that's what we call as minimum support price. The farmer should get a greater amount as support price in return for their investment. Data of minimum support price of the individual crop given by the government and the investment of farmer for cultivating that crop is very important to calculate actual farmer's benefit (Table 32.2). The online data source for these two data is the website of the Department of Agriculture and Farmer's Welfare, India.

## 32.4 Results and Discussion

### 32.4.1 Reference Evapotranspiration ( $ET_{ref}$ )

The  $ET_{ref}$  for the crops of different blocks ranged from 1534.46 to 1546.12 mm/year. It is observed that in the Berla block  $ET_{ref}$  is the lowest and in the Gurur block  $ET_{ref}$  is the highest.  $ET_{ref}$  significantly decreases in the rainy season and increases during the dry season. The reason behind all these differences is the change in meteorological parameters within the study area.

**Table 32.3** Total CWR and IWR

Block	CWR (MCM)	IR (MCM)
Balod	504.16	225.45
Gurur	644.22	226.94
Durg	759.93	482.18
Patan	1142.7	311.27
Genderdehi	947.68	369.06
Dhamdha	928.8	422.91
Berla	886.7	472.40

### 32.4.2 *Crop Water Requirement (CWR) or Crop Evapotranspiration (ET<sub>c</sub>)*

The crop water requirements for different crops of various blocks are shown in Table 32.3. It is highest in Patan block showing 1142.7 MCM and lowest in Balod block showing 504.16 MCM. From the results we can observe that crops like rice, sugarcane need more water than other crops due to longer growing period. So we should change the crop pattern and grow pulses, oilseeds, and vegetables more whose crop period is less.

### 32.4.3 *Net Irrigation Requirement (NIR)*

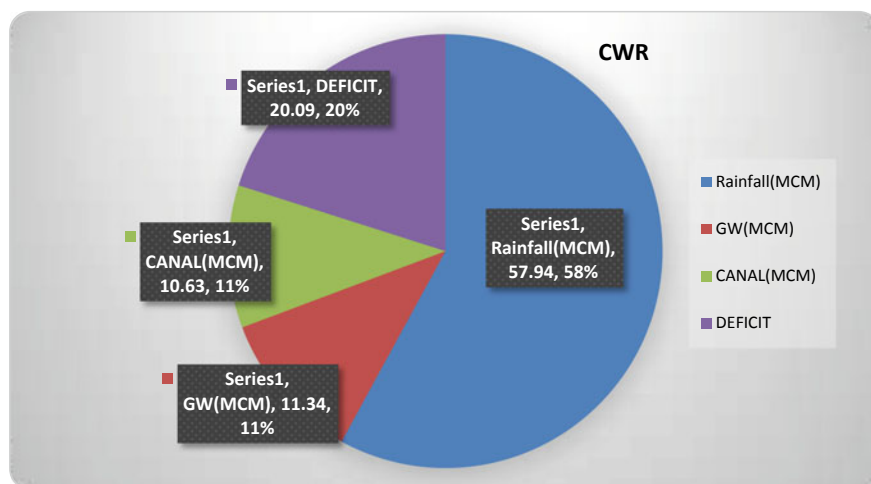
The NIR for different crops of various blocks is shown in Table 32.4. It is highest in Berla block showing 472.4 MCM and lowest in Balod block showing 225.45 MCM. This is mainly due to the geographical position of these blocks. Balod is at the starting point of the Tandula irrigation system and Berla is at the end of it (Fig. 32.1 and Tables 32.5, 32.6, 32.7).

## 32.5 Conclusions

An attempt has been made to reveal the monthly crop water requirement and irrigation requirement of major crops in seven different blocks of Tandula reservoir command area, using MABIA-2016 model, and finally, water balance has been worked out. Various parameters are taken for this study in this software, i.e., rainfall temperature, humidity, sunshine hours, field capacity, wilting point, total available water, and soil saturation capacity. On simulating the model, the results were obtained as water requirement of the crop which varies between 504.16 MCM and 1195.33 MCM, and irrigation requirement which varies between 225.45 MCM and 482.18 MCM. The

**Table 32.4** Contribution of various on CWR (unit: MCM)

Block	CWR (MCM)	Eff. rainfall	IR (MCM)	Supply through		Total Supply (MCM)	Deficit (MCM)
		R (MCM)		GW (MCM)	CANAL (MCM)		
[1]	[2]	[3]	[4] = [2] - [3]	[5]	[6]	[7] = [4] + [5]	[8] = [3] - [6]
Balod	504.16	278.71	225.45	45.09	101.45	146.54	78.91
Gurur	644.22	417.28	226.94	74.89	87.71	162.6	64.34
Genderdehi	759.93	277.75	482.18	103.34	36.9	140.24	341.94
Durg	1142.7	831.43	311.27	68.48	102.39	170.87	140.40
Patan	947.68	578.62	369.06	75.09	196.08	271.17	97.89
Dhamdha	928.8	505.89	422.91	126.87	55.68	182.55	240.36
Berla	886.7	414.30	472.40	165.34	37.8	203.14	269.26
Total	5814.19	3303.98	2510.213	659.1	618.01	1277.11	1233.10

**Fig. 32.1** Contribution of sources on CWR

contribution on crop water requirement of sources like groundwater is 659.1 MCM, canal water is 618.01 MCM, and rainfall is 3304 MCM. Thus irrigation deficit comes to be 1233.10 MCM. Estimation of water demand can be done for any of the crops or any of the blocks. By changing the crop pattern as specified, farmers can produce extra income of Rs. 35,744,118. The major cultivated crops are rice, wheat, maize, pulses, oilseeds, sugarcane, vegetables and fruits, etc. In general, the following points need to be considered as suggestions:

**Table 32.5** Proposed change of water allocation

Block	Allocation (%)	
	Before	Now
Balod	13	12
Gurur	1	2
Durg	8	10
Patan	28	23
Genderdehi	45	39
Dhamdha	2	6
Berla	3	8

**Table 32.6** Proposed change of crop pattern

Crop	Avg. change (%)
Rice	-8.04
Wheat	-0.61
Maize	-0.67
Pulses	10.90
Oilseeds	29.10
Veg. and fruit	19.66
Sugarcane	30.92

**Table 32.7** Change of farmer's benefit

Benefit before change (Rupees)	874,618,631
Benefit after change (Rupees)	910,362,749
Increase in benefit (Rupees)	35,744,118

- To enhance crop productivity and farmers' benefit, farmers need to be aware of changing crop pattern. Rice is the crop cultivated at almost 60% of total CCA requiring a maximum amount of water than any other crops; therefore, our main focus should be to reduce its cropping area.
- Irrigation efficiency should be improved by changing the traditional irrigation system to more efficient systems such as drip, sprinkler, and pipe irrigations.
- Preparing a compulsory policy for the farmers who have agricultural land greater than 2 ha and who are mainly using groundwater sources for cultivation to construct at least one recharge structure in their field.
- Constructing all types of recharging structures in blocks like Berla, Dhamdha which are mainly dependent on groundwater for artificial irrigation.
- Aware farmers to use minimum amount of water in their field according to growth stages. This will be beneficial for maintaining water balance.
- For proper functioning of MNREGA work, concentrate on an actual problem existing in a particular area and work accordingly.



## References

- Allen RG, Pereira LS, Raes D, Smith M (1998a) Crop evapotranspiration-guidelines for computing crop water requirements-FAO Irrigation and drainage paper 56. FAO, Rome 300(9):D05109
- Allen RG et al. (1998b) Crop evapotranspiration; Guideline for computing crop water requirement, pp 18–36
- Annual Progress Report (2000) Indian council of agricultural research, all India coordinated project for research on water management, Indira Gandhi Agricultural University, College of Agriculture and Research Station, Bilaspur, Chhattisgarh, India
- Benli B, Kodal S (2003) A non-linear model for farm optimization with adequate and limited water supplies: application to the southeast Anatolian Project (GAP) region. *Agric Water Manage'*. 62(3):187–203
- Wang Y, Li Q, Wu P, Li A (2016) Study on crop water requirement in the middle reaches of Heihe river basin based on model. In: Remote sensing symposium. IEEE, pp 6281–6283

# Chapter 33

## Integrated Hydrological and Hydraulic Model for Prediction of Inflows into Hathnur Reservoir



Vishal Kachhwaha and P. L. Patel

**Abstract** The real-time flood warning at the basin scale can be implemented by the integration of hydrological, hydraulic and reservoir simulation models and by creating a suitable user interface for disseminating the information to the society. In the present study, hydrologic–hydraulic modeling has been used for inflow prediction into the Hathnur reservoir of the upper Tapi basin, India. The semi-distributed hydrologic HEC-HMS model has been developed and its runoff component for each sub-basin (total 40) is utilized as inputs into the 1D hydraulic routing model, HEC-RAS. Finally, the calibrated HEC-HMS and HEC-RAS models are interfaced with the HEC-RTS for real-time flood prediction at the outlet of the basin. The integrated model has been developed using rainfall and stream gauging data, at a daily time scale, for the period 1998–2007 of the study area. The performance of the integrated model has been assessed using statistical performance indices for the prediction of floods along the main Tapi and Purna rivers as well as inflows into the Hathnur reservoir. The model performed reasonably well for the prediction of inflows into the Hathnur reservoir with NSE of 0.68–0.76, 0.71–0.81 and 0.74–0.83 for wet, normal and dry years, respectively. Also, it is reported that, invariably, the calibrated model performed better for the Burhanpur sub-catchment vis-à-vis Purna sub-catchment. The performance of the integrated hydrological and hydraulic models can be improved if more cross-sectional data are used for Purna river, including additional loss factors like a canopy in HEC-HMS in future studies.

---

V. Kachhwaha

Centre of Excellence On ‘Water Resources and Flood Management’, Department of Civil Engineering, Sardar Vallabhbhai National Institute of Technology, Surat 395007, India

P. L. Patel (✉)

Department of Civil Engineering, Sardar Vallabhbhai National Institute of Technology, Surat 395007, India

### 33.1 Introduction

Prediction of water availability in space and time has been a challenging task for the water resources fraternity. Also, the climatic extremes (floods and droughts) are aggravating due to changing climatic conditions across the globe. Flood disasters are responsible for huge tangible and intangible damages to society. The real-time flood monitoring and management are the keys to reducing the flood damages to the lives and properties located along the rivers. The real-time flood warning can be implemented by the integration of hydrological, hydraulic and reservoir simulation models and by creating a suitable user interface for disseminating the information to the society. The models which provide real-time information can be used for flood management and are useful in the early warning system.

Several attempts have been previously made to integrate models through the use of relevant techniques, especially gis-supported hydrologic and hydraulic modeling. Olivera and Maidment (1999) used HEC-HMS to develop a flood hydrograph and used the same as input for HEC-RAS to obtain corresponding flood maps, which were further used for designing highway drainage facilities. Knebl et al. (2005) integrated HEC-HMS and HEC-RAS by using nexrad level iii rainfall and GIS data at the regional level. The developed regional-scale model could be used as a prototype application in the field. Lastra et al. (2008) compared the geomorphological method and a hydrological model, which was followed by hydraulic modeling for flood hazard mapping in the northern Iberian Peninsula. Gül et al. (2010) combined hydrologic (HEC-HMS) and hydraulic (HEC-RAS) modeling approaches for testing the efficiency of structural flood control measures with GIS application, i.e., HEC-GEOHMS and HEC-GEORAS, for spatial operations. Şensoy et al. (2018) developed a decision support framework for real-time flood management using integrated models comprising hydrologic (HEC-HMS), reservoir simulation (HEC-RESSIM) and hydrodynamic (HEC-RAS) models.

The lower Tapi basin, particularly Surat city, was under severe floods in the recent past in the years 1994, 1998, 2006 and 2013. The prediction of inflows into the Ukai reservoir is the key in the management of floods in the lower Tapi river. Further, the Hathnur reservoir has been considered as a base station for the prediction of inflows into the Ukai reservoir. As the first step, for developing an early warning system of the lower Tapi river, in the present study, an effort has been made for developing real-time inflow prediction into the Hathnur reservoir. The objectives of the present study include calibration of HEC-HMS and HEC-RAS models for the upper Tapi basin and validation of calibrated model from the data of independent years.

### 33.2 Study Area

The Tapi river is the second-largest westward flowing river in India. The present study area, i.e., the upper Tapi basin covers two states, i.e., Maharashtra and Madhya Pradesh, of a total area 29,078 km<sup>2</sup> (see Fig. 33.1). The upper Tapi basin can be

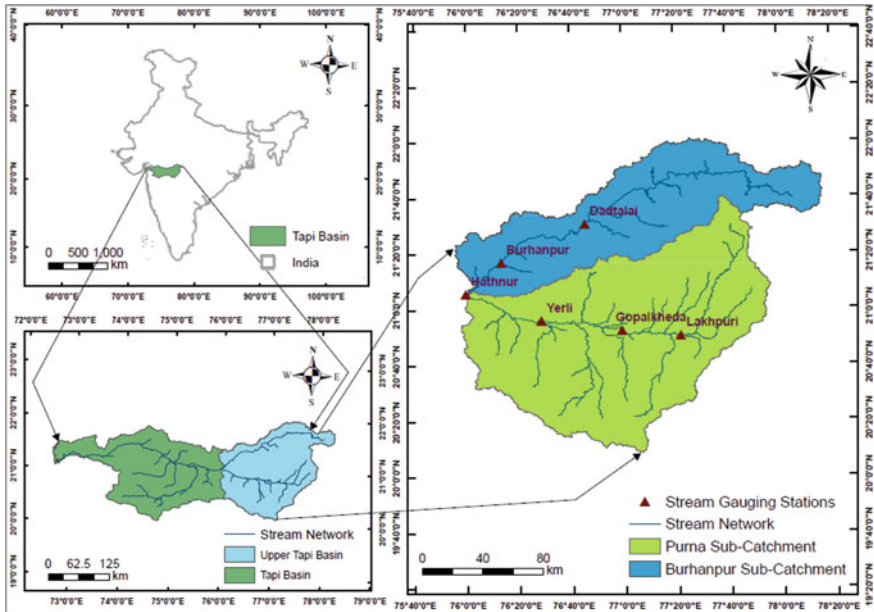


Fig. 33.1 Index map of the study area

divided into two sub-catchments, i.e., the Purna sub-catchment and the Burhanpur sub-catchment. The Burhanpur sub-catchment, which is covered by the main Tapi river from Betul (Madhya Pradesh) to the Hathnagar reservoir, is characterized by the hilly region with the deciduous forest as the dominant land-use land-cover with a total area of 10,577 km<sup>2</sup>. In the Purna sub-catchment, the Purna river (a major tributary of the Tapi river) drains with a total area of 18,501 km<sup>2</sup>. The Purna sub-catchment mainly consists of a flatter topography with most of the lands being used for agriculture purposes.

### 33.3 Methodology

The schematic flowchart of the methodology adopted for the present study is included in Fig. 33.2.

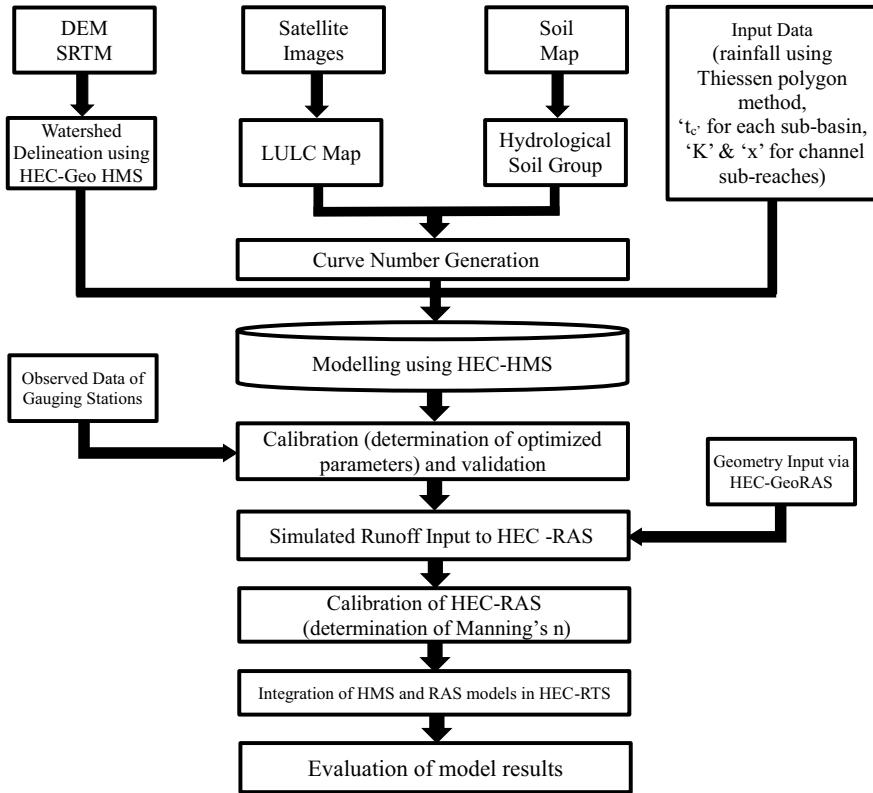
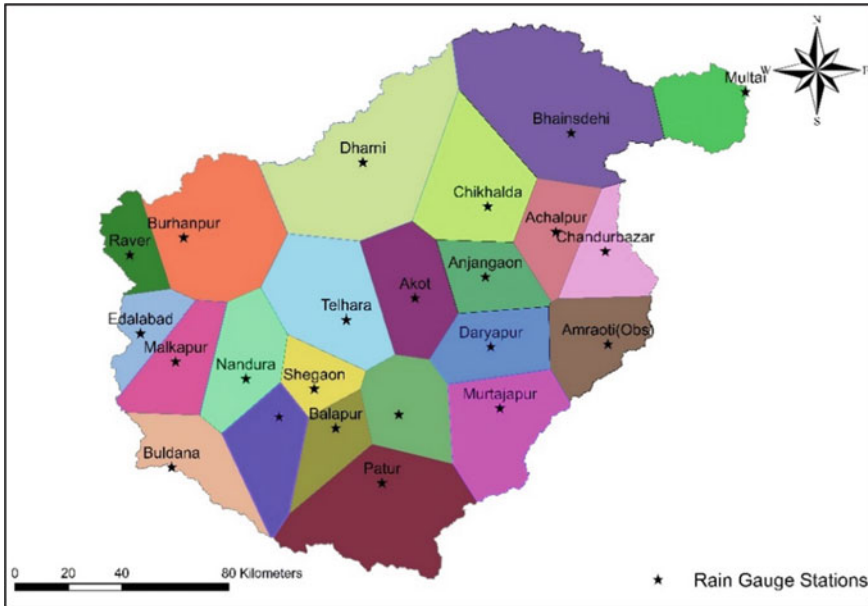


Fig. 33.2 Methodology used in the present study

### 33.3.1 Rainfall–Runoff Model HEC-HMS

The geospatial hydrologic modeling extension HEC-GEOHMS is used in ARCGIS to prepare a number of inputs for HEC-HMS (hydrologic engineering center–hydrologic modeling system). A total of 40 sub-basins were delineated for the selected study area. Basically, three methods are used for conversion of precipitation into a runoff in HEC-HMS, i.e., soil conservation service (SCS) curve number (CN) method (rainfall into excess precipitation), SCS unit hydrograph (UH) method (excess precipitation into UH) and Muskingum routing method (for routing through the reach). For the SCS-CN method, the curve number was determined using soil and land-use land-cover map prepared in ARCGIS; for the SCS-UH method, time of concentration was estimated using Kirpich (1940) equation, whereas for the Muskingum method, the initial values of  $k$  and  $x$  were determined from the criterion given in the literature (Chow 1959; Fread, 1993) and the methodology explained by Tewolde and Smithers (2006). The rainfall time series inputs were prepared using the Thiessen polygons approach in ARCGIS, using coordinates of 23 rain gauge stations (Fig. 33.3).



**Fig. 33.3** Thiessen polygon obtained from ARCGIS for the upper Tapi basin

Thiessen polygons and delineated sub-basins were merged together to calculate weighted rainfall for each rain gauge station in relevant sub-basins. The final sub-basins configuration of the upper Tapi basin for HEC-HMS is shown in Fig. 33.4.

In the present study, the daily rainfall data of all stations for the years 1998–2007 were used. The criteria given by Yoo (2006) have been used for the classification of years into wet, normal and dry years based on the climatic conditions. The years 1998, 2006 and 2007 were classified as wet years; years 1999, 2001 and 2002 as dry years and remaining years 2000, 2003, 2004 and 2005 as normal years. The model was calibrated for the years 1998, 1999 and 2000. Accordingly, three sets of parameters were determined for the identified three typical type years.

### 33.3.2 Hydrodynamic Model HEC-RAS

One-dimensional unsteady flow simulation is performed using HEC-RAS (hydrologic engineering center–river analysis system). The geometry of the model was prepared with the help of ARCGIS extension in HEC-GEORAS. The calibration of the HEC-HMS model has been undertaken for the entire upper Tapi river. Observed flood hydrograph at the Deditalai and water levels in the Hathnur reservoir were taken as upstream and downstream boundary conditions, respectively, for the simulation of the flows in the main Tapi river, while observed discharges at Lakhpuri and

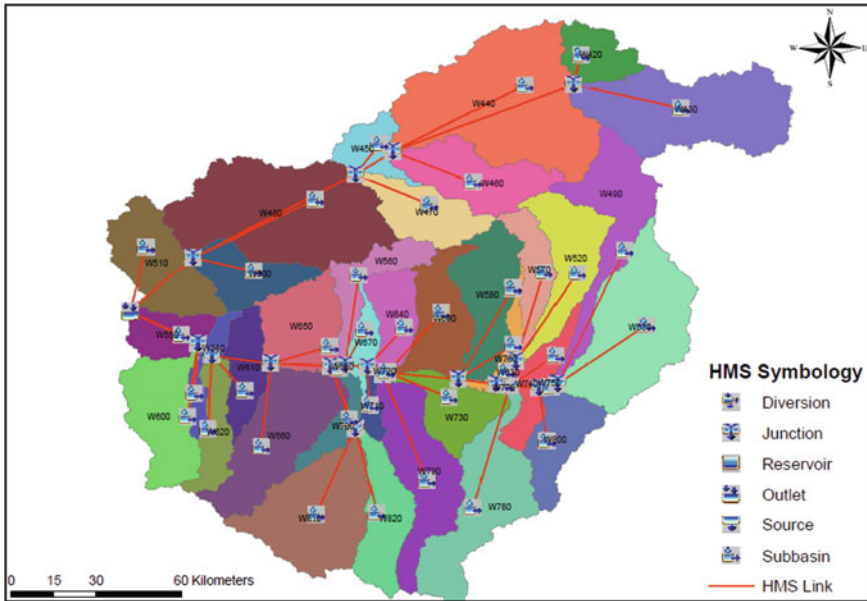


Fig. 33.4 Sub-basin configuration for HEC-HMS

water levels in Hathnur reservoir were taken as upstream and downstream boundary conditions, respectively, for simulating the floods in the Purna river. The intermediate stream gauging stations, viz., Burhanpur (for Tapi river) and Gopalkheda and Yerli (for Purna river) were used for calibration and assessing the performance of the model. The years 1998, 1999 and 2000 were selected as wet, normal and dry years for calibration of manning's  $n$  in the range of  $n = 0.015$ – $0.055$ . The most relevant values of manning's  $n$  which gave maximum NSE,  $r$  and  $r^2$  and minimum RMSE were selected as optimal values for wet, normal and dry years.

### 33.3.3 HEC-RTS Setup

In HEC-RTS it is mandatory to create a watershed initially for further analysis. The watershed was created by giving the inputs like watershed name, brief description, the coordinate system of map layers, time zone etc. After creating a watershed, the next step is to import developed HMS and HEC-RAS models into the HEC-RTS. The order of importing the models is HEC-HMS and then HEC-RAS. To link HEC-HMS output into HEC-RAS as input, the “.dss” file format is used. In HEC-HMS, junctions are the locations where sub-basins flow is accumulated. The junction locations are marked in HEC-RAS geometry and a particular cross-section is selected for each

junction such that all runoff components can be input as lateral inflow into the HEC-RAS. A total of 16 internal boundary conditions were introduced in the HEC-RAS unsteady flow editor. In the setup module, there is a model linking editor where the required data set from the HEC-HMS generated “.dss” file is assigned to HEC-RAS in the form of boundary conditions as stated above.

### 33.4 Results and Discussions

The performance of the integrated HEC-HMS and HEC-RAS model (HEC-RTS) in the prediction of inflow into the Hathnur reservoir and along with the main Tapi river and Purna river is included in Tables 33.1 and 33.2 and Figs. 33.5 and 33.6. The Coefficient of determination is the square of Pearson’s correlation coefficient ( $R$ ) varies from 0 to 1, values closer to one indicates less error variance, and ordinarily values greater than 0.5 seems acceptable (Santhi et al., 2001). Similarly, model output can be considered as satisfactory, if  $NSE > 0.50$  (Moriasi, 2007). It is recommended by ASCE (1993) and Sevat and Dezetter (1991) that NSE can be considered as best objective function for reflecting the overall fit of a hydrograph. The performance of the integrated HEC-RTS model indicated that calibrated model performs reasonably well for the prediction of inflows into the Hathnur reservoir with NSE of 0.68–0.76, 0.67–0.79 and 0.72–0.88 for wet, normal and dry years, respectively. The performance of the model is also satisfactory for the Burhanpur sub-catchment with NSE of 0.24–0.68, 0.58–0.73 and 0.50–0.84, respectively, for wet, normal and dry years. The corresponding values for wet, normal and dry years for the Purna sub-catchment (Yerli stream gauging station) are 0.30–0.50, 0.35–0.72 and 0.27–0.84, respectively. The inferior performance of the Purna sub-catchment in the prediction of flood from the integrated model could be due to the availability of only three

**Table 33.1** Output analysis of HEC-HMS and HEC-RTS for Hathnur

Year	Nature of year	NSE		$R^2$	
		HMS output	RTS output	HMS output	RTS output
1998	Wet	0.83	0.76	0.90	0.83
2006		0.77	0.71	0.83	0.78
2007		0.58	0.68	0.58	0.69
1999	Normal	0.79	0.79	0.80	0.79
2001		0.81	0.74	0.81	0.74
2002		0.71	0.67	0.87	0.86
2000	Dry	0.79	0.77	0.83	0.79
2003		0.74	0.73	0.85	0.81
2004		0.83	0.88	0.87	0.90
2005		0.74	0.72	0.75	0.74



**Table 33.2** Performance of HEC-HMS and HEC-RTS for Burhanpur and Yerli

Year	Nature of year	Nse			
		Burhanpur		Yerli	
		HMS	HEC-RTS	HMS	HEC-RTS
1998	Wet	0.55	0.60	0.50	0.82
2006		0.66	0.68	0.30	0.30
2007		0.25	0.24	0.34	0.68
1999	Normal	0.57	0.58	0.72	0.91
2001		0.67	0.66	0.60	0.75
2002		0.77	0.73	0.35	0.71
2000	Dry	0.75	0.84	0.63	0.66
2003		0.72	0.50	0.67	0.68
2004		0.50	0.51	0.84	0.86
2005		0.60	0.56	0.27	0.51

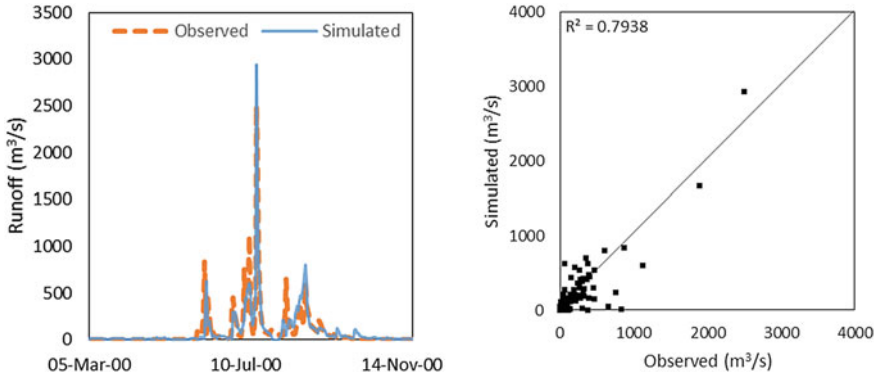


**Fig. 33.5** Observed and simulated runoff using HEC-RAS at hathnur for year 2000

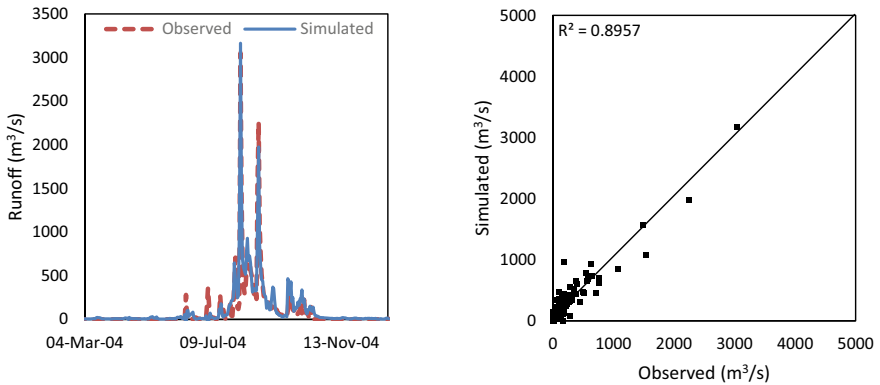


**Fig. 33.6** Observed and simulated runoff using HEC-RAS at hathnur for year 2004

measured cross-sections along the river. Overall, the performance of the model can be improved while considering the canopy losses and adding more cross-sections in the Purna river in near future.

### 33.5 Conclusions

A semi-distributed hydrological model (HEC-HMS) for the prediction of floods in the upper Tapi basin has been developed. The runoff component from HEC-HMS is integrated with 1D hydraulic routing model HEC-RAS. Finally, the integrated HEC-HMS and HEC-RAS model is interfaced with the HEC-RTS. The following are the key findings of the presented study:

- (a) The integrated HEC-HMS and HEC-RAS model performed satisfactorily for prediction of inflows into the Hathnur reservoir with NSE of 0.24–0.68, 0.58–0.73 and 0.50–0.84, respectively, for wet, normal and dry years.
- (b) The integrated model also performed reasonably well for the Burhanpur sub-catchment with NSE of 0.24–0.68, 0.58–0.73 and 0.50–0.84 for wet, normal and dry years, respectively.
- (c) The performance of the model is inferior for the Purna sub-catchment with NSE of 0.30–0.50, 0.35–0.72 and 0.27–0.84, respectively, for wet, normal and dry years.
- (d) The performance of the model can be improved further by considering the canopy losses and adding additional measured cross-sections in the Purna river in near future.

**Acknowledgements** The first author wishes to acknowledge Centre of Excellence (COE) on “water resources and flood management”, SVNIT Surat under teqip-ii funded by World Bank. The authors are also grateful to the Central Water Commission (CWC, Tapi division Surat, National Remote Sensing Centre (NRSC), Hyderabad and India Meteorological Department (IMD) for providing the relevant data in the present study.

### References

- ASCE Task committee on definition of criteria for evaluation of watershed models of the watershed management committee, irrigation and drainage division (1993) “criteria for evaluation of watershed models”. *J Irrigation Drainage Eng* 119(3):429–442
- Fread DL (1993) Flow routing in handbook of hydrology. In: Drmaidment (ed)
- Gül GO, Harmancioğlu N, Gül A (2010) A combined hydrologic and hydraulic modeling approach for testing efficiency of structural flood control measures. *Nat Hazards* 54(2):245–260
- Kirpich ZP (1940) Time of concentration of small agricultural watersheds. *Civil Eng* 10(6):362
- Knebl MR, Yang ZL, Hutchison K, Maidment DR (2005) Regional scale flood modeling using nexrad rainfall, gis, and HEC-HMS/ras: a case study for the san antonio river basin summer 2002 storm event. *J Environ Manage* 75(4):325–336

- Lastra J, Fernández E, Díez-herrero A, Marquínez J (2008) Flood hazard delineation combining geomorphological and hydrological methods: an example in the northern iberian peninsula. *Nat Hazards* 45(2):277–293
- Moriassi DN, Arnold JG, van Liew MW, Bingner RL, Harmel RD, Veith TL (2007) Model evaluation guidelines for systematic quantification of accuracy in watershed simulations. *Trans Asabe* 50(3):885–900
- Santhi C, Arnold JG, Williams JR, Dugas WA, Srinivasan R, Hauck LM (2001) Validation of the swat model on a large river basin with point and nonpoint sources. *J Am Water Resour Assoc* 37(5):1169–1188
- Servat E, Dezetter A (1991) Selection of calibration objective functions in the context of rainfall-runoff modelling in a sudanese savannah area. *Hydrol Sci J* 36(4):307–330
- Tewelde MH, Smithers JC (2006) Flood routing in ungauged catchments using muskingum methods. *Water Sa* 32(3):379–388

# Chapter 34

## Hydrologic Modeling with SWAT in an Eastern Indian River Basin Using Different Gridded Data Sets



Soorya Sudesan, Renji Remesan, and Dhrubajyoti Sen

**Abstract** Integrated assessment and management of water resources in a basin can be achieved through the application of distributed hydrological models and subsequent spatial analysis of water balance component characteristics. This study aims to assess the performance of the model SWAT in an Eastern Indian River basin (viz., Upper Kangsabati River basin) using gridded input precipitation data from IMD, WFDEI, and NCEP-CFSR sources. The model performances were observed in the river basin in terms of parameter and predictive uncertainty considering IMD-based SWAT model as the benchmark. All the three SWAT model constructions with different precipitation inputs have given reasonably good performances, but some disparities were found in certain seasons in the river basin during simulation time. The study results also indicate that the spatial variability of different water balance components change with the selection of different precipitation gridded data in SWAT input space.

### 34.1 Introduction

Water management is a purposeful activity with multiple and partly conflicting goals to maintain and improve the state of water resources (Pahl-Wostl 2007). Water management planners are facing considerable uncertainties on future demand and availability of water; which is further aggravated by climate change and its potential hydrological effects (Middelkoop et al. 2001). Management of water is of great importance for an agricultural country like India; since the water demand for the production of their staple food, rice itself takes almost a major part of the country's

---

S. Sudesan (✉) · R. Remesan  
School of Water Resources, Indian Institute of Technology Kharagpur, Kharagpur, West Bengal  
721 302, India  
e-mail: [ss@ce.iitr.ac.in](mailto:ss@ce.iitr.ac.in)

D. Sen  
Dept. of Civil Engineering, Indian Institute of Technology Kharagpur, Kharagpur, West Bengal  
721 302, India

water resources. Precipitation is one of the most important components of the hydrological cycle affecting water resources; and its variability is important from both scientific as well as practical points of view (Pahl-Wostl 2007; Dlamini et al. 2017). Precipitation changes can alter the water availability and balance in a basin and can also affect the discharge regime of rivers.

The most important aspect in water resources development and management programs is to understand the water balance of a basin. Most of the watershed models basically simulate the transformation of precipitation into runoff, sediment outflow, and nutrient losses. Soil and Water Assessment Tool (SWAT) (Arnold et al. 1998) is a widely used, semi-distributed river basin scale water quality and quantity model. Precipitation is the most sensitive driving factor for hydrological models. Selection of the best precipitation input data for the SWAT models is basin-specific. Precipitation estimates based on a combination of multi-source data (historical observed, radar, and satellite) have been widely used for model applications. Uncertainties in meteorological forcing data (especially precipitation) have a predominant effect and impact on runoff estimates from models. In recent years, apart from gauge-based data sources, a large numbers of globally remote satellite-based precipitation products have become popular among researchers. In India, the commonly used precipitation data products used are Indian Meteorological Department (IMD) data, Tropical Rainfall Measurement Mission (TRMM) data, Coordinated Regional Climate Downscaling Experiment (CORDEX) data, Climate Hazards Group Infrared Precipitation with Station data (CHIRPS), WATCH Forcing Data methodology applied to ERA-Interim reanalysis (WFDEI), National Centers for Environmental Prediction—Climate Forecast System Reanalysis (NCEP-CFSR), Asian Precipitation—Highly-Resolved Observational Data Integration Towards Evaluation (APHRODITE), etc. (Mondal et al. 2016; Tuo et al. 2016; Strauch et al. 2017; Yang et al. 2014). Several studies have revealed that there are some uncertainties between different available precipitation datasets (Camargos et al. 2018) and better input dataset have to be chosen for developing an accurate model (Tuo et al. 2016; Yang et al. 2014). There is a high possibility that errors and uncertainties in these precipitation data products can impart uncertainties in hydrologic simulations (Yang et al. 2014). Quantification of the contributions of uncertainties from precipitation products to hydrological model is a very important aspect to modellers expecting high quality reliable representation of temporal and spatial variability of precipitation as a prerequisite for developing accurate hydrological models; which can be used to predict trustworthy forecasts for the future.

Taking these facts into consideration, the overall purpose of this study is to investigate the effect of employing three different precipitation datasets (viz., NCEP–CFSR, IMD, and WFDEI) on the performance of physically based semi-distributed hydrological model SWAT in the Kangsabati River basin, located in Eastern India. This study also investigates how the input precipitation datasets affect SWAT parameter uncertainty during streamflow quantification and compares the predictions obtained with the NCEP–CFSR and WFDEI data sets taking the IMD-based SWAT model output as the benchmark. The paper is organized as follows: study area, data sets, model settings, result discussion, and conclusions.

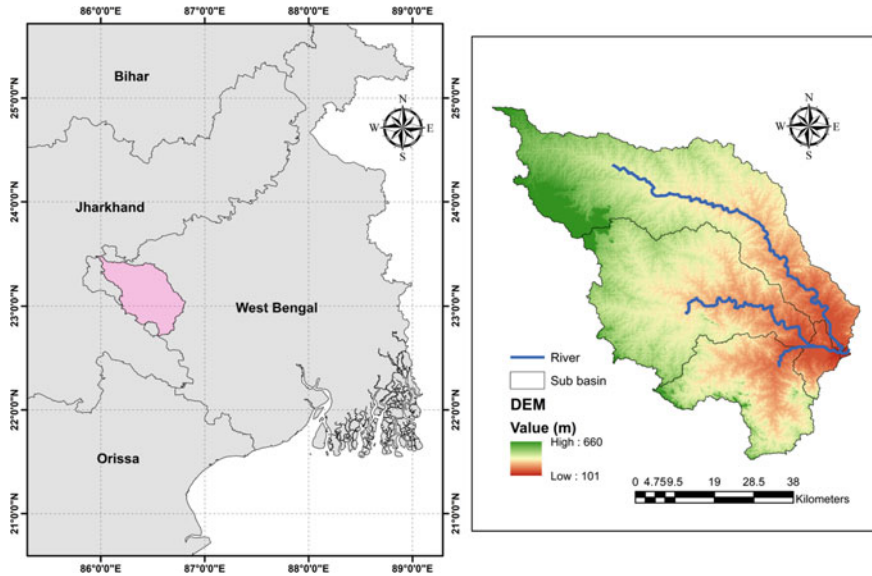


Fig. 34.1 Study region: location of catchment and catchment area

## 34.2 Materials and Methods

### 34.2.1 Study Area

The upper portion of the Kangsabati River basin (3630 km<sup>2</sup>) extending over the state of West Bengal, India is considered as the study region (Fig. 34.1). It receives an annual average precipitation of around 1400 mm and has an annual mean temperature of about 25.9 °C (Bhave et al. 2014). It is a drought prone region during summers, but still receives a heavy concentration of rainfall during the monsoon months. The Kangsabati River originates from the Chota Nagpur plateau and flows south eastwards toward the Bay of Bengal; also is the last contributing river to the Hooghly, a distributary of Ganges. The Kangsabati reservoir located at the confluence of the Kangsabati River and its major tributary, Kumari marks the outlet of upper Kangsabati River basin.

### 34.2.2 Data Used

#### Digital Elevation Map (DEM)

The Digital Elevation Map used in this study was a Shuttle Radar Topography Mission (SRTM) product of USGS, having a resolution of 90 m × 90 m. The

latest version was downloaded from (<http://srtm.csi.cgiar.org/SELECTION/listIm ages.asp>) and projected to WGS 1984 UTM Zone 45 N.

### ***Land Use and Soil***

The land-use map for the study area has been obtained from National Remote Sensing Centre (NRSC), Government of India (GOI). The NRSC land-use data contains crop specific digital layers, suitable for use in Geographic Information System (GIS). Soil map obtained from FAO soil database was used in the SWAT model. Based on the texture the soil was classified as loam, sandy loam, sandy clay loam, and clay loam which come under the soil hydraulic group A, B, C, and D respectively.

### ***Weather Inputs***

Precipitation (mm/day), maximum and minimum temperature at 2 m above the surface of earth(°C), relative humidity at 2 m (%), wind speed at 10 m above the surface of the Earth (m/s), daily insolation incident on a horizontal surface (MJ/m<sup>2</sup>/day) are the weather inputs given to SWAT model. All these data except the precipitation spanning from 1997 to 2008 (resolution of 1° × 1°) were downloaded from the NASA Langley Research Center Atmospheric Science Data Center Surface meteorological and Solar Energy (SSE) web portal supported by the NASA LaRC POWER Project. The parameters contained in the agroclimatology archive are based primarily upon solar radiation derived from satellite observations and meteorological data from NASA's assimilation models.

Three different precipitation data were used for creating three individual models for the same catchment. These are (a) NCEP-CFSR: The National Centers for Environmental Prediction (NCEP) Climate Forecast System Reanalysis (CFSR) which is a third generation reanalysis product was completed over the 36-year period of 1979 through 2014. The CFSR was designed and executed as a global, high resolution, coupled atmosphere–ocean–land surface–sea ice system to provide the best estimate of the state of these coupled domains over this period. (b) IMD: This data of 0.25° × 0.25° resolution was developed by applying standard interpolation to the data available from Automatic Weather Station. Observed precipitation from more than 4000 gauge stations across India was used in the preparation of data; although they are not uniformly distributed in both space and time over India. (c) WFDEI: WATCH project has produced a large number of data sets which should be of considerable use in regional and global studies of climate and water. WFDEI was produced post-WATCH using WATCH Forcing Data (WFD) methodology applied to ERA-Interim data. It is a meteorological forcing dataset extending into early twenty-first Century (1979–2012).

### ***34.2.3 Model Setup***

The hydrological model, SWAT developed by United States Department of Agriculture (USDA) Agricultural Research Service (ARS), is based on the water balance

equation as given below

$$SW_t = SW_0 + \sum_{i=1}^t (R_{day} - Q_{surf} + E_a - w_{seep} + Q_{gw})$$

where  $SW_t$  is the final soil water content (mm),  $SW_0$  is the initial soil water content (mm),  $t$  is the time (days),  $R_{day}$  is the amount of precipitation on day  $i$  (mm),  $Q_{surf}$  is the amount of surface runoff on day  $i$  (mm),  $E_a$  is the amount of evapotranspiration on day  $i$  (mm),  $w_{seep}$  is the amount of water entering the vadose zone from the soil profile on day  $i$  (mm), and  $Q_{gw}$  is the amount of return flow on day  $i$  (mm) (Thom et al. 2017). SCS curve number procedure was used by the model to estimate surface runoff and modified rational method calculates the peak runoff. The evapotranspiration was estimated using Penman–Monteith method and the channel routing simulation is calculated based on the Muskingum Method.

Three SWAT models were developed for the study area using the three precipitation data, and a warm up period of 3 years was given for each of the model run. The SUFI 2 algorithm in SWAT-CUP was used for the calibration / validation and for the sensitivity analysis; which categorizes the main parameters that affects the stream flow more. Calibrations for these models were based on the inflow discharge data at Kangsabati reservoir during a period of 2000–2005 and were validated for 2006–2008. The inflow discharges are recorded by the Irrigation and Waterways Directorate of the Government of West Bengal, which manages the reservoir and the dam.

The efficiency of the model in simulating the outflow was judged by observing the Nash–Sutcliffe Efficiency (NSE),  $R^2$  (coefficient of determination) values, RSR (ratio of root mean square to standard deviation of measured data), etc. Relative sensitivity between each parameter was found out using  $t$ -test and  $p$ -value. The measure of sensitivity of a parameter is given by  $t$ -test, whereas the importance of sensitivity of that parameter is given by  $p$ -value (Thavhana et al. 2017). The parameter is more sensitive if it has a low  $p$ -value and vice-versa. A satisfactory model is expected to give  $NSE > 0.5$  and  $RSR \leq 0.7$ .

## 34.3 Results and Discussions

### 34.3.1 Uncertainty in Precipitation Products

The study on three different precipitation data (viz., CFSR, IMD, and WFDEI) considered for the study area shows variations with respect to each other, both during the rainy season as well as at other times in terms of mean precipitation, standard deviation, etc. The annual average of monthly precipitation for the catchment was computed to be 162, 124, and 119 mm/month according to the three data sets, CFSR, IMD, and WFDEI, respectively (Table 34.1).



**Table 34.1** Descriptive statistics of different monthly precipitation data (mm) during monsoon period and pre-monsoon period during 2000–2008

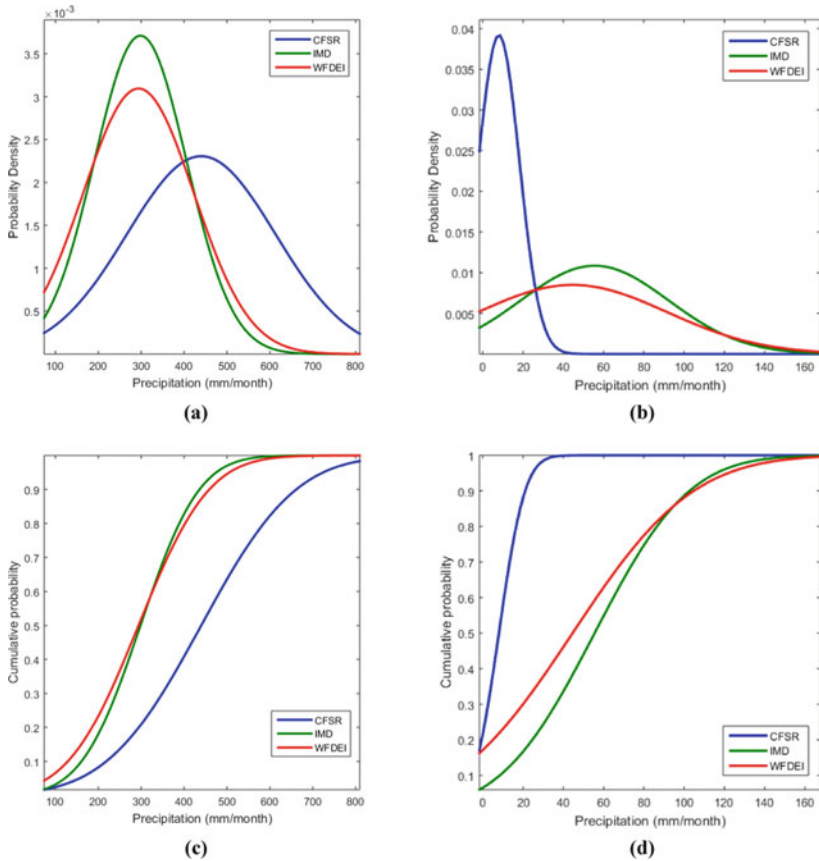
Data/index	Monsoon period (June–September)			Pre-monsoon period (March–May)		
	CFSR	IMD	WFDEI	CFSR	IMD	WFDEI
Mean	439.91	298.26	293.73	8.02	55.56	44.60
Standard Deviation	173.03	107.50	128.87	10.18	36.77	46.98
Skewness	0.16	1.89	1.06	2.03	0.41	1.43
Kurtosis	−0.16	6.70	1.25	4.72	−0.93	1.37

The variations in the PDF and CDF of three precipitation data used are shown in Fig. 34.2. It is observed that the maximum difference in mean precipitation is around 145 mm/month (between WFDEI and CFSR) during the monsoon period and around 48 mm/month (between IMD and CFSR) during the pre-monsoon period. It indicates that monthly average values of CFSR precipitation during monsoon period is 47.4% higher than that of IMD-based data product, whereas WFDEI precipitation data product show 1.5% lower values than IMD precipitation product during the monsoon period. When checked for pre-monsoon period, CFSR and WFDEI products have shown −85.5% and −19.7% differences in comparison to respective values obtained from IMD product. Here, one can clearly see the uncertainty associated with different gridded precipitation estimates especially during monsoon and pre-monsoon periods, though their annual average monthly values are reasonably closer.

### 34.3.2 Hydrological Model Evaluation

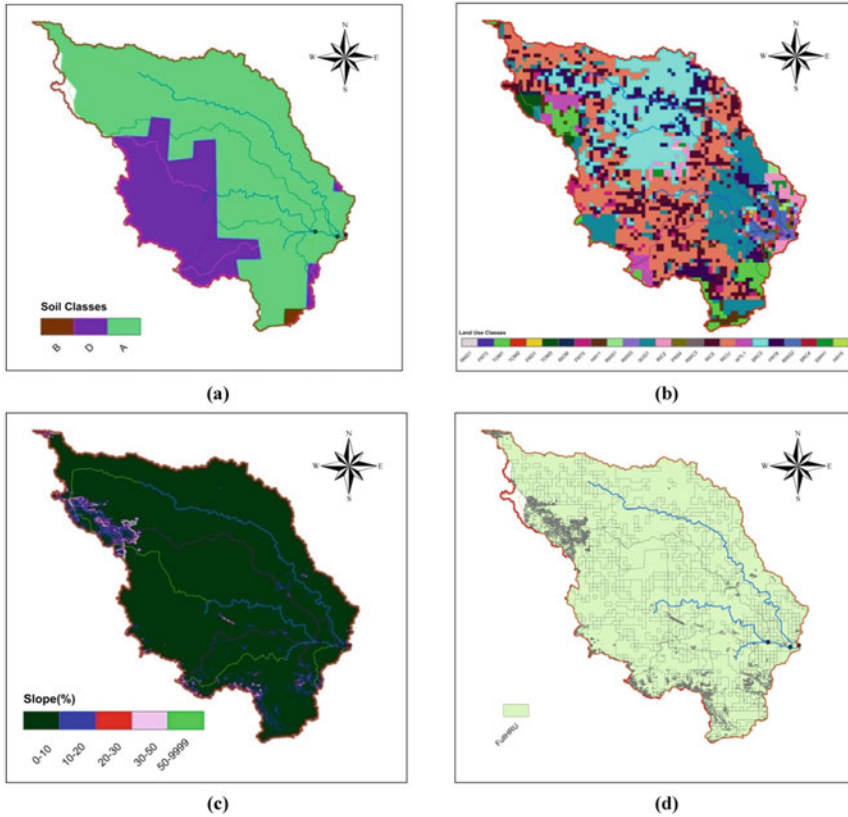
Three SWAT model settings with three different precipitation data products were calibrated against observed discharges, calibrating 14 parameters which significantly influence the hydrological response of a catchment.

Figure 34.3 shows the soil classes, land-use pattern, slope variations, and the HRU layer formed in the study area and used to build the SWAT model. Two points may be noted for the region: (a) a major part of the area has a slope between 0 and 10% and (b) rice and sugarcane, which require large quantity of water for their growth, are the major cultivations in the region. The study area is subdivided into five sub-catchments in SWAT. The graphs plotted between the observed discharge and simulated runoff for the three models are shown in Fig. 34.4. All the three models gave almost the same range of NSE,  $R^2$ , and RSR values during the calibration and validation phases. The model with CFSR rainfall data gives an NSE of 0.76,  $R^2$  of 0.76, and RSR of 0.49 during calibration; during the validation, it shows NSE of 0.76,  $R^2$  of 0.85, and RSR of 0.48. The model using IMD data gives NSE of 0.69,  $R^2$  of 0.71, and 0.56 for RSR during calibration while it gives NSE of 0.72,  $R^2$  of 0.73, and 0.52 for RSR during validation.



**Fig. 34.2** Probability distribution of precipitation during monsoon period (a) and pre-monsoon period (b); Cumulative probability distribution during monsoon period (c) and pre-monsoon period (d)

The model developed using the WFDEI gave  $NSE = 0.70$ ,  $R^2 = 0.75$  and  $RSR = 0.55$  during calibration and  $NSE = 0.86$ ,  $R^2 = 0.88$  and  $RSR = 0.37$  during validation. From the results, it may be interpreted that disparities in precipitation products are influencing the variations in the simulated outflow. However, the models have been calibrated in such a way that all models get closer calibration performance ( $NSE$  value between 0.69 and 0.76) to see how these models adjust to give a better result by altering the parameters within it (Table 34.2). The most sensitive parameters and their range of values and the best parameter value found for each of the models are mentioned in Table 34.3. Best parameters indicate that the huge uncertainty associated with the precipitation products are getting compensated by the best parameter values and best parameter ranges while running the SUFI2 algorithm in SWAT. During calibration process, it is observed that SOL\_BD(1).sol, GW\_REVAP.gw,



**Fig. 34.3** SWAT Layers showing (a) Soil classes, (b) Land-use classes, (c) Slope in %, and (d) HRUs

ALPHA\_BNK.rte are the most sensitive parameters for the model running with the CFSR data.

It is observed that ALPHA\_BNK.rte, ESCO.hru, CN2.mgt are the most sensitive parameters for the model with IMD data, whereas ALPHA\_BNK.rte, GW\_DELAY.gw, OV\_N.hru remain the most sensitive parameters for the model with WFDEI precipitation data. From Table 34.3, one can note that different best parameter values as obtained with the CFSR model is greatly different from those obtained from the IMD and WFDEI-based models. This indicates that the parameters are effectively adjusting to the undesired effect of uncertainties in inputs and trying to fit closer to the observed streamflow.

The CFSR model with highest annual average monthly precipitation simulates almost the same runoff as that of the model with lowest annual average monthly precipitation (WFDEI) by self-adjusting the most sensitive parameters (by increasing the value of ALPHA\_BNK, GW\_DELAY, SOL\_BD, and GW\_REVAP; decreasing the value of OV\_N). The probability of exceedance curve of streamflow at inflow

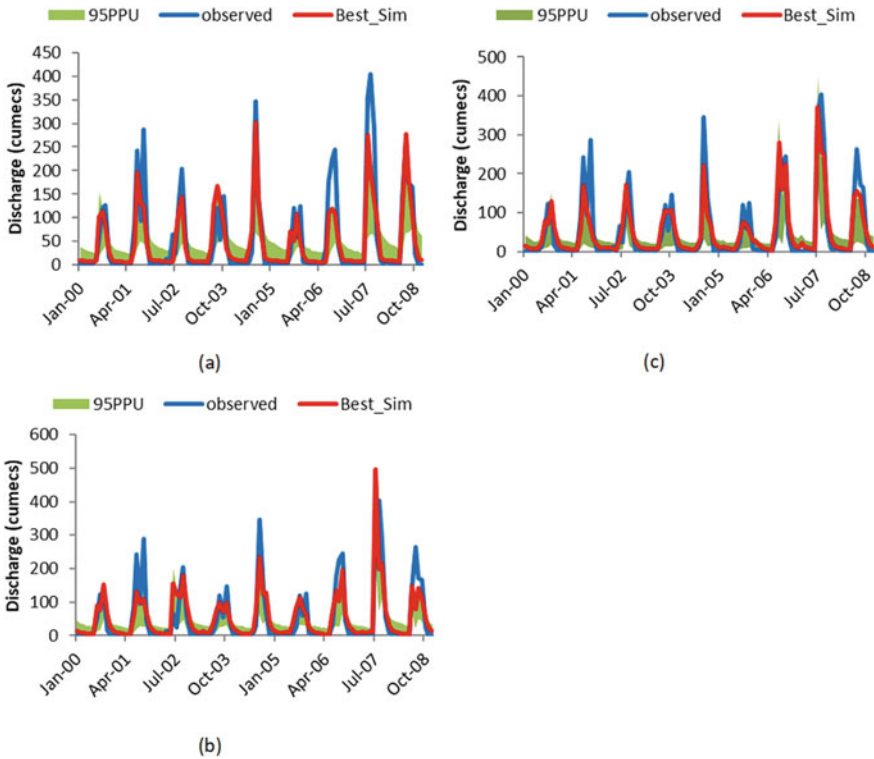


**Fig. 34.4** Calibration–validation plots of SWAT models with CFSR (a), IMD (b), and WFDEI (c) precipitation

**Table 34.2** Summary statistics of SWAT simulation

		<i>p</i> factor	<i>r</i> factor	$R^2$	NSE	PBIAS	RSR	RMSE
CFSR	Calibration	0.29	0.46	0.76	0.76	-2.76	0.49	34.73
	Validation	0.03	0	0.85	0.76	22.93	0.48	55.48
IMD	Calibration	0.33	0.46	0.71	0.69	-11.75	0.56	39.33
	Validation	0.31	0.45	0.73	0.72	11.93	0.52	60.27
WFDEI	Calibration	0.33	0.43	0.75	0.7	7.02	0.55	38.95
	Validation	0.28	0.41	0.88	0.86	0.99	0.37	42.09

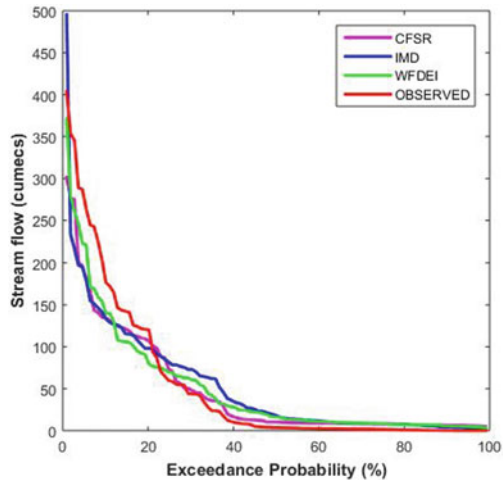
to the Kangsabati dam from multiple SWAT simulations with different precipitation data product is given in Fig. 34.5 along with observed streamflow values. The figure indicates that all three models (based on three different precipitation products) capture behavior of streamflow, but further improvement of parameters are needed to capture higher flows with better accuracy. However, further comparison of SWAT simulations

**Table 34.3** Parameter values used in each of the SWAT models

Parameter	Description	Initial parameter range given	Best parameter values used in different SWAT models		
			CFSR	IMD	WFDEI
r_CN2.mgt	SCS runoff curve number $f$	-0.2, 0.2	0.03	0.14	0.25
v_ALPHA_BF.gw	Baseflow alpha factor (days)	0.0, 1.0	-0.09	-0.27	-0.35
v_GW_DELAY.gw	Groundwater delay (days)	30.0, 450.0	248.03	15.21	93.44
v_GWQMN.gw	Threshold depth of water in the shallow aquifer required for return flow to occur (mm)	0.0, 2.0	1.69	0.02	0.23
v_CH_N2.rte	Manning's " $n$ " value for the main channel	0.0, 0.3	0.28	-0.13	-0.03
v_CH_K2.rte	Effective hydraulic conductivity in main channel alluvium	5.0, 130.0	105.37	72.65	79.44
v_ALPHA_BNK.rte	Baseflow alpha factor for bank storage	0.0, 1.0	0.12	0.03	0.04
r_SOL_AWC(1).sol	Available water capacity of the soil layer	-0.2, 0.1	0.32	0.14	-0.07
r_SOL_K(1).sol	Saturated hydraulic conductivity	-0.8, 0.8	0.13	-0.01	0.21
v_GW_REVAP.gw	Groundwater "revap" coefficient	0.0, 0.2	0.18	0.01	0.06
r_SOL_BD(1).sol	Moist bulk density	-0.5, 0.6	0.35	-0.17	0.18
r_OV_N.hru	Manning's " $n$ " value for overland flow	-0.2, 0.0	-0.04	-0.03	0.001
v_REVAPMN.gw	Threshold depth of water in the shallow aquifer for "revap" to occur (mm)	0.0, 10.0	-0.41	-2.30	6.29
v_ESCO.hru	Soil evaporation compensation factor	0.8, 1.0	0.41	0.22	0.64

v\_ means the existing parameter value is to be replaced by a given value, a\_ means a given value is added to the existing parameter value, and r\_ means an existing parameter value is multiplied by (1 + a given value)

**Fig. 34.5** Probability exceedance curves of stream flow from all three models and observed data



with ground-based gauge precipitation is needed to be performed to authenticate inter-comparison results.

### 34.4 Conclusion

This study attempts to evaluate the performances of the physically based SWAT hydrological model driven with different precipitation datasets (from IMD, WFDEI, and NCEP-CFSR sources) and study the impact of the precipitation data sets on hydrological simulations. In the reasonably calibrated models obtained with closer performance, one may observe variation of model parameters due to input data errors and how the SWAT parameters self-adjust to simulate outflow discharge closer to the observed values. The results show that the sensitive SWAT parameters get self-adjusted according to the disparities of precipitation dataset to simulate almost same range of outflow. The preliminary results reported herein indicate that CFSR and WFDEI data-based SWAT model gives an overall good agreement between observed and computed streamflow during calibration and validation. Slightly lower performance of IMD data-based model could be connected with larger underestimation of precipitation values during monsoon period. However, the findings in this study cannot be generalized because of the following reasons: (i) there is further scope of calibration of these models and (ii) a longer period of data need to be checked and comparison with ground-based rainfall data must be carried out to ascertain underestimation of IMD data product, etc. Nevertheless, this study indicates that accuracy of precipitation data play a vital role in hydrological research and it is the modeller's responsibility to ensure that the rainfall data product employed has an acceptable accuracy to avoid undesirable water resource management decisions based upon the modelled results.

**Acknowledgements** This research was funded by Department of Science and Technology, Government of India.

## References

- Arnold JG, Srinivasan R, Muttiah RS, Williams JR (1998) Large area hydrologic modeling and assesment Part I: model development. *JAWRA J Am Water Resour Assoc* 34(1):73–89
- Bhave G, Mishra A, Raghuvanshi NS (2014) A combined bottom-up and top-down approach for assessment of climate change adaptation options. *J Hydrol* 518:150–161
- Camargos C, Julich S, Houska T, Bach M, Breuer L (2018) Effects of input data content on the uncertainty of simulating water resources. *Water (switzerland)* 10(5):1–18
- Dlamini NS, Kamal MR, Soom MABM, Bin Mohd MSF, Bin Abdullah AF, Hin LS (2017) Modeling potential impacts of climate change on streamflow using projections of the 5th assessment report for the Bernam river basin, Malaysia. *Water (Switzerland)* 9(3):1–23
- Middelkoop H, Daamen K, Gellens D, et al (2001) Impact of climate change on hydrological regimes and water resources management in the Rhine Basin. *Clim Change* 49:105–128
- Mondal B, Sekhar NM, Mujumdar PP (2016) Hydrologic modelling. *Proc Ind Natl Sci Acad* 82(3):817–832
- Pahl-Wostl C (2007) Transitions towards adaptive management of water facing climate and global change. *Water Resour Manag* 21(1):49–62
- Strauch M, Kumar R, Eisner S, et al (2017) Adjustment of global precipitation data for enhanced hydrologic modeling of tropical Andean watersheds. *Clim Change* 141:547–560
- Thavhana MP, Savage MJ, Moeletsi ME (2018) SWAT model uncertainty analysis, calibration and validation for runoff simulation in the Luvuvhu River catchment, South Africa. *Phys Chem Earth Parts A/B/C* 105:115–124
- Thom VT, Khoi DN, Linh DQ (2017) Using gridded rainfall products in simulating streamflow in a tropical catchment—a case study of the Srepok River Catchment, Vietnam. *J Hydrol Hydromech* 65(1):18–25
- Tuo Y, Duan Z, Disse M, Chiogna G (2016) Evaluation of precipitation input for SWAT modeling in Alpine catchment: a case study in the Adige river basin (Italy). *Sci Total Environ* 573:66–82
- Yang Y, Wang G, Wang L, Yu J, Xu Z (2014) Evaluation of gridded precipitation data for driving SWAT model in area upstream of three gorges reservoir. *PLoS One* 9(11)

# Chapter 35

## Analysis of Seepage from Parallel Triangular Furrows by Inverse Hodograph and Conformal Mapping Technique



Kshyana Prava Samal and G. C. Mishra

**Abstract** Furrow irrigation is a conventional method of irrigation practiced in tropical region to grow vegetable crops. In furrow irrigation, water is conveyed in small channels or furrows. In this case the suitability of furrow irrigation has been clearly checked for shallow rooted, moderately deep rooted crops and deep rooted crops by analyzing the seepage flow from the furrow. The analysis has been done from a triangular furrow using inverse hodograph and conformal mapping technique. The loci of the phreatic lines in the furrow ridge have been found for various side slopes. For a given furrow spacing, variation of the depth of saturation front at the middle of the furrow ridge for different side slopes (i.e. for  $m = 0.5, 1, 1.5,$  and  $2$ ) of the furrows has been found out. Here in the analysis the spacing has been properly mentioned for Moderately deep rooted and deep rooted crops. (i) The spacing of the furrows should be such that, at the middle of the ridge, the sum of depth of saturation and free board less than about  $1/4$ th of the root zone depth ( $R_d$ ); hence, the plant can get proper amount of water which has been properly verified in the present analysis. (ii) The suitability of furrow spacing for different crops has been checked by published secondary data.

### 35.1 Introduction

Furrow irrigation is suitable for mostly for all crops. In furrow irrigation, water is conveyed in small channels or furrows. From field study, it is reported that about half of the water delivered in the channel or a furrow gets lost as seepage and other losses (Carter 1985). Many researchers have reported that the furrow irrigation has lower application efficiency in comparison to drip irrigation (Tiwari et al. 1998). The obvious reasons for lower efficiency are (i) excess seepage losses as irrigation water

---

K. P. Samal (✉)

School of Civil Engineering, KIIT Deemed to be University, Bhubaneswar 751024, India  
e-mail: [kshyanaprava.samal@kiit.ac.in](mailto:kshyanaprava.samal@kiit.ac.in)

G. C. Mishra

Water Resources Development and Management, IITR, Roorkee, India



is conveyed in the furrows for a duration more than required and (ii) inappropriate furrow spacing. Close spacing of the furrows leads to unwise use of land resources whereas wide spacing leads to non-availability of irrigation water to crops grown in the central part of the furrow ridge. There is a need to find the appropriate spacing of the furrows. The spacing of furrows is influenced by the soil type and the cultivation practice. In general, furrows should be spaced quite close so that water can spread laterally to sides into the land between the two successive furrows to replenish the soil moisture in the root zone of crops. As a rule, for sandy soils the spacing should be between 30 and 60 cm. On clayey soils, the spacing between two adjacent furrows should be 75–150 cm (Michael 1999; Brouwer et al. 1990). On clayey soils, double-ridged furrows, sometimes called beds, can also be used. Their advantage is that more plant rows are possible on each ridge, facilitating manual weeding. Depth of irrigation needed is related to the water holding capacity of the soil and depth of rooting of the crop. In clays the depth of irrigation ranges from 7.5 to 15 cm, in loams the depth varies from 5 to 10 cm and in sands the depth is 5, 7.5, and 10 cm (Michael 1999).

Solutions for seepage from parallel triangular and rectangular canals in a soil layer of finite as well as of infinite thickness have been presented by Bruch and Street (1967) and Choudhary and Chahar (2007). The Dirichlet boundary condition has been assumed to prevail at the interface of the finite soil layer and an underlying highly pervious draining layer. In this paper, an analysis is presented for seepage from parallel triangular furrows assuming the porous medium to be of infinite depth and Neumann boundary condition prevailing at infinity. In case of interfering furrows, the Neumann type of boundary condition implies that the seepage from a single furrow in parallel furrows system is hydraulic conductivity times the furrow spacing irrespective of shape of the furrow section by Samal and Mishra (2016), Samal et al. (2019). Only locus of the phreatic line is unknown a priori. Inverse hodograph method suitable for solving unconfined flow problems has been used to find the locus of the phreatic line. Vedernikov (vide. Polubarinova-Kochina 1962) has solved seepage from a single triangular canal in a porous medium of infinite depth for Neumann boundary condition prevailing at infinity.

## 35.2 Statement of the Problem

An array of parallel triangular furrows at distance  $L_f$  apart is shown in Fig. 35.1a. The porous medium is of infinite depth having hydraulic conductivity  $k$ . The depth of water in a furrow is  $H$ ; top width of a furrow is  $2H \cot(\alpha\pi)$ , and the sides of the furrows make an angle  $\alpha\pi$  with the horizontal.  $D$  is the point of inflection on the phreatic line. It is aimed to find the locus of the phreatic line.

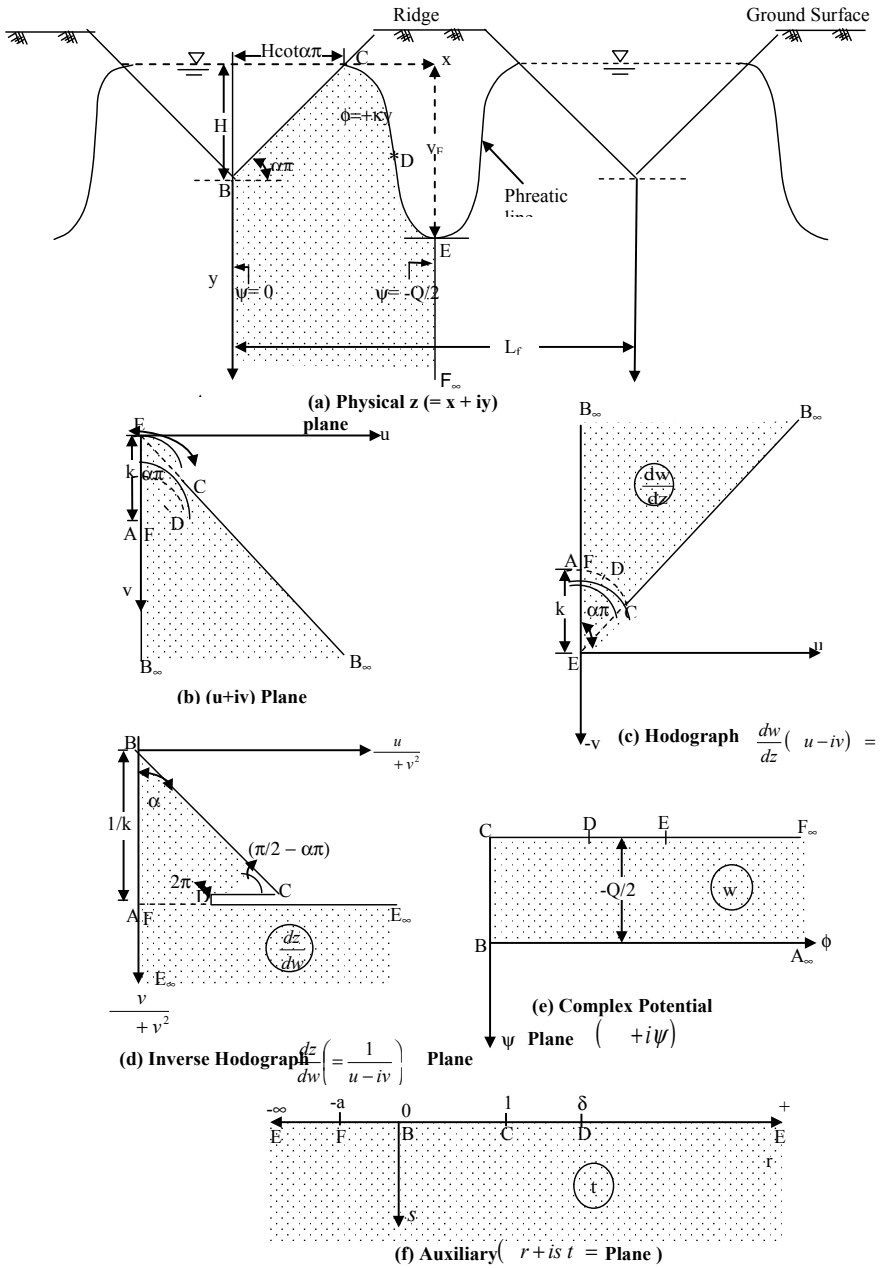


**Fig. 35.1** Steps of conformal mapping for seepage analysis for an array of triangular furrows in soils without capillarity

### 35.3 Mapping of the One Half of the Inverse Hodograph (dz/dw) Plane onto Auxiliary t-Plane

The hodograph and the inverse hodograph planes pertaining to one half of the symmetrical flow domain of one of the furrows are shown in Fig. 35.1b through Fig. 35.1d. The conformal mapping of the inverse hodograph plane to the lower half of the auxiliary  $t$ -plane shown in Fig. 35.1f is given by

$$\frac{dz}{dw} = M_1 \int_0^t \frac{(\delta - \tau)d\tau}{\tau^{1-\alpha}(1 - \tau)^{1-(\frac{1}{2} - \alpha)}} + N_1 \tag{35.1}$$

The vertices  $B$ ,  $C$ , and  $D$  being mapped onto 0, 1, and  $\delta$  respectively on the real axis of the  $t$ -plane.

For the vertex ‘ $B$ ’,  $t = 0$ , and  $\frac{dz}{dw} = 0$ ; hence, the constant  $N_1 = 0$ . The constant  $N_1$  is governed by the lower limit of integration.

For  $0 \leq t \leq 1$ ,

$$\frac{dz}{dw} = M_1 \int_0^t \frac{(\delta - \tau)d\tau}{\tau^{1-\alpha}(1 - \tau)^{1-(\frac{1}{2} - \alpha)}} = M_1 \left\{ \delta B_t \left( \alpha, \frac{1}{2} - \alpha \right) - B_t \left( 1 + \alpha, \frac{1}{2} - \alpha \right) \right\} \tag{35.2}$$

where  $B_t(\alpha, \frac{1}{2} - \alpha)$ ,  $B_t(1 + \alpha, \frac{1}{2} - \alpha)$  are incomplete beta functions.

For vertex ‘ $C$ ’,  $t = 1$  and  $\frac{dz}{dw} = \frac{1}{k} \sec(\alpha\pi) e^{i\pi(\frac{1}{2} - \alpha)}$

Incorporating this condition in (35.2)

$$\frac{1}{k} \sec(\alpha\pi) e^{i\pi(\frac{1}{2} - \alpha)} = M_1 \left\{ \delta B \left( \alpha, \frac{1}{2} - \alpha \right) - B \left( 1 + \alpha, \frac{1}{2} - \alpha \right) \right\} \tag{35.3}$$

Solving for  $M_1$ ,

$$M_1 = \frac{\frac{1}{k} \sec(\alpha\pi) \cdot e^{i\pi(\frac{1}{2} - \alpha)}}{\delta B(\alpha, \frac{1}{2} - \alpha) - B(1 + \alpha, \frac{1}{2} - \alpha)} \tag{35.4}$$

where  $B(\alpha, \frac{1}{2} - \alpha)$ ,  $B(1 + \alpha, \frac{1}{2} - \alpha)$  are complete beta functions.

### 35.4 Mapping of the $dz/dw$ Plane onto the Auxiliary $t$ -Plane; $-\infty \leq t \leq 0$

$$\frac{dz}{dw} = M_1 \int_0^t \frac{(-1)^{1-\alpha}(\delta - \tau)}{(-\tau)^{1-\alpha}(1 - \tau)^{1-(\frac{1}{2} - \alpha)}} d\tau \tag{35.5}$$

For points  $A_\infty$  and  $F_\infty t = -a$  and  $\frac{dz}{dw} = \frac{i}{k}$ . Incorporating this condition in (35.5)

$$\frac{i}{k} = M_1 (-1)^{1-\alpha} \int_0^{-a} \frac{(\delta - \tau)}{(-\tau)^{1-\alpha}(1 - \tau)^{1-(\frac{1}{2} - \alpha)}} d\tau \tag{35.6a}$$

Substituting  $\tau = -\xi$ ,  $d\tau = -d\xi$  in (35.6a)

$$\frac{i}{k} = -M_1 (-1)^{1-\alpha} \int_0^a \frac{(\delta + \xi)}{(\xi)^{1-\alpha}(1 + \xi)^{1-(\frac{1}{2} - \alpha)}} d\xi = -M_1 (-1)^{1-\alpha} I_1 \text{ (} I_1 \text{ is evaluated in Appendix 1)} \tag{35.6b}$$

Incorporating  $M_1$  in (35.6b).

$$\frac{i}{k} = \frac{(-1)^{\frac{1}{k}} \sec(\alpha\pi)}{\delta B(\alpha, \frac{1}{2} - \alpha) - B(1 + \alpha, \frac{1}{2} - \alpha)} e^{i\pi(\frac{1}{2} - \alpha)} e^{-i\pi(1-\alpha)} I_1 \tag{35.6c}$$

Simplification leads to

$$\frac{\sec(\alpha\pi)}{\delta B(\alpha, \frac{1}{2} - \alpha) - B(1 + \alpha, \frac{1}{2} - \alpha)} I_1 = 1 I_1 \text{ is a function of unknown } a \text{ and } \delta \tag{35.7}$$

### 35.5 Mapping of the Complex Potential $w$ -Plane onto the Auxiliary $t$ -Plane

The mapping of the  $w$ -plane shown in Fig. 35.1e onto the lower half of the  $t$  plane is given by

$$\frac{dw}{dt} = \frac{M_2}{t^{1/2}(1 - t)^{1/2}(t + a)} \tag{35.8}$$

Integrating,

$$w = M_2 \int_0^{t'} \frac{dt}{t^{1/2}(1-t)^{1/2}(t+a)} + N_2 \tag{35.9}$$

Corresponding to vertex 'B',  $w = 0$  and  $t = 0$ . Hence, constant  $N_2 = 0$ .  
 For vertex 'C',  $t = 1$  and  $w = -\frac{iQ}{2}$ . Incorporating this condition in (35.9)

$$\frac{-iQ}{2} = M_2 \int_0^1 \frac{dt}{t^{1/2}(1-t)^{1/2}(t+a)} = M_2 I_2 \tag{35.10}$$

where  $I_2 = \int_0^1 \frac{dt}{t^{1/2}(1-t)^{1/2}(t+a)} = \frac{\pi}{\sqrt{a(1+a)}}$ .  $I_2$  is evaluated in Appendix 2.  
 From (35.10), constant  $M_2$  is given by

$$M_2 = \frac{-iQ}{2I_2} = \frac{-iQ}{2} \frac{\sqrt{a(1+a)}}{\pi} \tag{35.11}$$

### 35.6 Relation Between the Physical Flow Domain $z$ -Plane and the Auxiliary $t$ -Plane for $0 \leq t \leq 1$

$$\frac{dz}{dt} = \frac{dz}{dw} \cdot \frac{dw}{dt} = M_1 \left\{ \delta B_t \left( \alpha, \frac{1}{2} - \alpha \right) - B_t \left( 1 + \alpha, \frac{1}{2} - \alpha \right) \right\} \frac{M_2}{t^{1/2}(1-t)^{1/2}(t+a)} \tag{35.12}$$

Integrating,

$$z = M_1 M_2 \int_0^{t'} \left\{ \delta B_t \left( \alpha, \frac{1}{2} - \alpha \right) - B_t \left( 1 + \alpha, \frac{1}{2} - \alpha \right) \right\} \frac{dt}{t^{1/2}(1-t)^{1/2}(t+a)} + z_B \tag{35.13}$$

For vertex 'C',  $t' = 1$  and  $z = z_C$ . Incorporating this condition in (35.13),

$$z_C = M_1 M_2 \int_0^1 \left\{ \delta B_t \left( \alpha, \frac{1}{2} - \alpha \right) - B_t \left( 1 + \alpha, \frac{1}{2} - \alpha \right) \right\} \frac{dt}{t^{1/2}(1-t)^{1/2}(t+a)} + z_B \tag{35.14}$$

or

$$z_C = M_1 M_2 I_3 + z_B \tag{35.15}$$

where  $I_3 = \int_0^1 \left\{ \delta B_t \left( \alpha, \frac{1}{2} - \alpha \right) - B_t \left( 1 + \alpha, \frac{1}{2} - \alpha \right) \right\} \frac{dt}{t^{1/2}(1-t)^{1/2}(t+a)}$   $I_3$  has been evaluated in Appendix 3.

Substituting  $M_1$  and  $M_2$  in (35.15),

$$\begin{aligned}
 z_C &= \frac{1}{k} \frac{\sec(\alpha\pi)}{\delta B\left(\alpha, \frac{1}{2} - \alpha\right) - B\left(1 + \alpha, \frac{1}{2} - \alpha\right)} e^{i\pi\left(\frac{1}{2} - \alpha\right)} \left(-\frac{iQ}{2I_2}\right) I_3 + z_B \\
 &= \frac{Q}{k} \left\{ \frac{\sec(\alpha\pi)}{\delta B\left(\alpha, \frac{1}{2} - \alpha\right) - B\left(1 + \alpha, \frac{1}{2} - \alpha\right)} \right\} \{\sin(\alpha\pi) + i \cos(\alpha\pi)\} (-i) \frac{I_3}{2I_2} + z_B \tag{35.16a}
 \end{aligned}$$

Incorporating  $z_C = H \cot(\alpha\pi)$ , and  $z_B = iH$

$$H \cot(\alpha\pi) = \frac{Q}{k} \left\{ \frac{\sec(\alpha\pi)}{\delta B\left(\alpha, \frac{1}{2} - \alpha\right) - B\left(1 + \alpha, \frac{1}{2} - \alpha\right)} \right\} \frac{I_3}{2I_2} \{\cos(\alpha\pi) - i \sin(\alpha\pi)\} + iH \tag{35.16b}$$

Equating the real parts in either side of (35.16b)

$$\frac{Q}{kH} \left\{ \frac{\sec(\alpha\pi)}{\delta B\left(\alpha, \frac{1}{2} - \alpha\right) - B\left(1 + \alpha, \frac{1}{2} - \alpha\right)} \right\} \left(\frac{I_3}{2I_2}\right) \sin(\alpha\pi) = 1 \tag{35.17}$$

The same equation is obtained equating the imaginary parts on either sides of (35.16b). Equating (35.7) and (35.17),

$$\frac{\sec(\alpha\pi)}{\delta B\left(\alpha, \frac{1}{2} - \alpha\right) - B\left(1 + \alpha, \frac{1}{2} - \alpha\right)} I_1 = \frac{Q}{kH} \left\{ \frac{\sec(\alpha\pi)}{\delta B\left(\alpha, \frac{1}{2} - \alpha\right) - B\left(1 + \alpha, \frac{1}{2} - \alpha\right)} \right\} \left(\frac{I_3}{2I_2}\right) \sin(\alpha\pi) \tag{35.18}$$

Incorporating  $Q = kL_f$  in (35.18) and simplifying

$$\frac{L_f}{H} \left(\frac{I_3}{2I_1I_2}\right) \sin(\alpha\pi) = 1 \tag{35.19}$$

For an assumed value of  $\delta$ , the corresponding parameter  $a$  is evaluated from (35.19) for a given  $L_f/H$  using an iteration procedure.

### 35.7 Location of the Phreatic Line

For  $1 \leq t \leq \infty$ ,

$$\begin{aligned}
 \frac{dz}{dw} &= M_1(-1) \left(\frac{1}{2} - \alpha\right)^{-1} \left\{ \delta \int_1^t \tau^{\alpha-1} (\tau - 1) \left(\frac{1}{2} - \alpha\right)^{-1} d\tau - \int_1^t \tau^{(1+\alpha)-1} (\tau - 1) \left(\frac{1}{2} - \alpha\right)^{-1} d\tau \right\} \\
 &\quad + \frac{1}{k} \sec(\alpha\pi) e^{i\pi\left(\frac{1}{2} - \alpha\right)}, \\
 \frac{dw}{dr} &= \frac{M_2(-1)^{1/2}}{t^{1/2}(t-1)^{1/2}(t+a)} \text{ and}
 \end{aligned}$$

$$\frac{dz}{dt} = M_1 M_2 (-1)^{1/2} (-1)^{\left(\frac{1}{2} - \alpha\right) - 1} \left\{ \delta \int_1^t \tau^{\alpha-1} (\tau - 1)^{\left(\frac{1}{2} - \alpha\right) - 1} d\tau - \int_1^t \tau^{(1+\alpha)-1} (\tau - 1)^{\left(\frac{1}{2} - \alpha\right) - 1} d\tau \right\} \\ \times \frac{1}{(t)^{1/2} (t - 1)^{1/2} (t + a)} + \frac{M_2 (-1)^{1/2} \sec \alpha \pi}{k} e^{i\pi \left(\frac{1}{2} - \alpha\right)} \frac{1}{i^{1/2} (t - 1)^{1/2} (t + a)} \tag{35.20}$$

Integrating

$$z(t') = M_1 M_2 (-1)^{1/2} (-1)^{\left(\frac{1}{2} - \alpha\right) - 1} I_4(t') + M_2 (-1)^{1/2} e^{i\pi \left(\frac{1}{2} - \alpha\right)} \frac{\sec(\alpha\pi)}{k} I_5(t') + z_C \tag{35.21}$$

where

$$I_4(t') = \int_1^{t'} \left\{ \delta \int_1^t \tau^{\alpha-1} (\tau - 1)^{\left(\frac{1}{2} - \alpha\right) - 1} d\tau - \int_1^t \tau^{(1+\alpha)-1} (\tau - 1)^{\left(\frac{1}{2} - \alpha\right) - 1} d\tau \right\} \frac{dt}{(t)^{1/2} (t - 1)^{1/2} (t + a)}$$

and

$$I_5(t') = \int_1^{t'} \frac{dt}{(t)^{1/2} (t - 1)^{1/2} (t + a)}$$

Incorporating  $M_1$  and  $M_2$

$$z(t') = \left[ \left\{ \frac{\frac{1}{k} \sec(\alpha\pi) e^{i\pi \left(\frac{1}{2} - \alpha\right)}}{\delta B\left(\alpha, \frac{1}{2} - \alpha\right) - B\left(1 + \alpha, \frac{1}{2} - \alpha\right)} \right\} \left\{ \frac{(-iQ)}{2I_2} \right\} (-1)^{1/2} e^{-i\pi \left(-\frac{1}{2} - \alpha\right)} I_4(t') \right] \\ + \left[ \left\{ \frac{(-iQ)}{2I_2} \right\} (-1)^{1/2} \frac{\sec(\alpha\pi)}{k} \{\sin(\alpha\pi) + i \cos(\alpha\pi)\} I_5(t') \right] + z_C \\ = \left\{ \frac{(-iQ)}{2kI_2} (-1)^{1/2} \right\} \left[ \left\{ \frac{\sec(\alpha\pi)}{\delta B\left(\alpha, \frac{1}{2} - \alpha\right) - B\left(1 + \alpha, \frac{1}{2} - \alpha\right)} \right\} \left\{ e^{i\pi} \right\} I_4(t') + \{\tan(\alpha\pi) + i\} I_5(t') \right] + z_C \tag{35.22}$$

Incorporating  $z_C = H \cot(\alpha\pi)$  in (35.22)

$$z(t') = \left\{ \frac{Q}{k2I_2} \right\} \left[ \frac{-\sec(\alpha\pi)}{\delta B\left(\alpha, \frac{1}{2} - \alpha\right) - B\left(1 + \alpha, \frac{1}{2} - \alpha\right)} I_4(t') + \tan(\alpha\pi) I_5(t') + i I_5(t') \right] + H \cot(\alpha\pi) \tag{35.23}$$

The real part is given by

$$\frac{x(t')}{H} = \cot(\alpha\pi) + \left\{ \frac{Q}{kH2I_2} \right\} \left[ \frac{-\sec(\alpha\pi)}{\delta B\left(\alpha, \frac{1}{2} - \alpha\right) - B\left(1 + \alpha, \frac{1}{2} - \alpha\right)} I_4(t') + \tan(\alpha\pi) I_5(t') \right] \tag{35.24}$$

and the imaginary part is given by

$$\frac{y(t')}{H} = \left\{ \frac{Q}{kH2I_2} \right\} I_5(t') \tag{35.25}$$

Evaluations of  $I_4(t')$  and  $I_5(t')$  are given in Appendices 4 and 5.

The point of inflection is given computing  $\frac{x(t')}{H}$  and  $\frac{y(t')}{H}$  for  $t' = \delta$

### 35.8 Results and Discussion

#### 35.8.1 Variation of $y_E/H$ with Spacing ( $L_f/H$ )

For a given furrow spacing,  $L_f/H$ , assigning a value to the parameter  $\delta$ , the corresponding value of parameter  $a$  is obtained using Eq. (35.19).  $y_E/H$  is then computed from (35.25) after evaluating  $I_5(t')$ ;  $t' \rightarrow \infty$ . The variation of  $y_E/H$  versus spacing  $L_f/H$  for different side slopes (i.e. for  $m = 0.5, 1, 1.5,$  and  $2$ ) of the furrows are shown in Fig. 35.2.  $y_E/H$  increases with increase in spacing of the furrows. For the spacing for which the furrows do not interfere,  $y_E/H \rightarrow \infty$ .  $y_E/H$  also increases with increase in  $m$ , i.e.  $y_E/H$  is less for steep slope and more for flatter slope. At the minimum furrow spacing i.e. for  $L_f/H = 2m$ ,  $y_E/H \rightarrow 0$ .

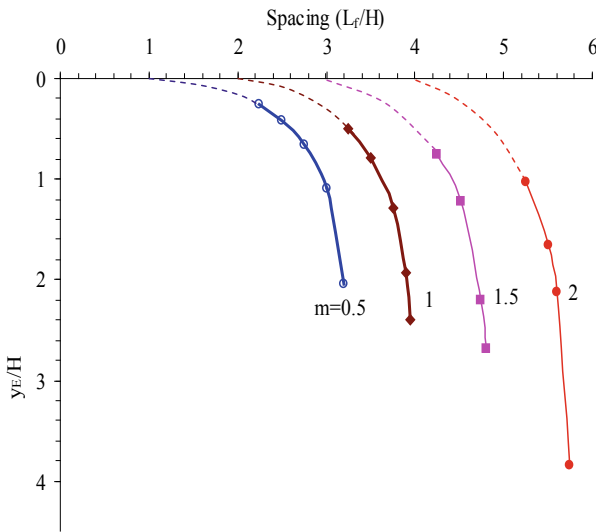


Fig. 35.2 Variation of  $y_E/H$  with spacing,  $L_f/H$  for different  $m$



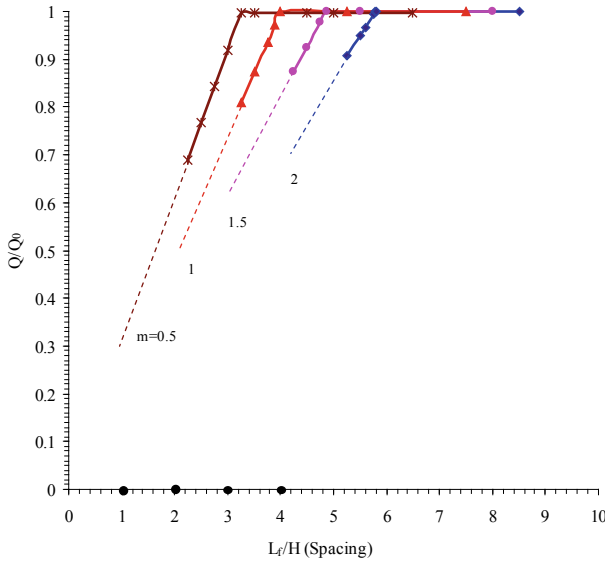


Fig. 35.3 Variation of  $Q/Q_0$ , with, spacing,  $L_f/H$ , for an array of triangular furrows

### 35.8.2 Variation of $Q/Q_0(m)$ with Spacing ( $L_f/H$ )

The variations of  $Q/Q_0(m)$  with furrow spacing  $L_f/H$  is shown in Fig. 35.3 for various values of  $m$ .  $Q_0(m)$  is the seepage from a single furrow without interference, and it is a function of  $m$ .  $Q_0(m)/(kH)$  has been computed using an approximate relation  $Q_0(m)/(kH) = \left\{ (4\pi - \pi^2)^{1.3} + (2m)^{1.3} \right\}^{0.77}$  derived by Chahar (2000).  $Q/Q_0(m)$  increases with increase in spacing till the furrows interfere, beyond which  $Q/Q_0(m) = 1$ .  $Q$  being equal to  $kL_f$  as per Neumann boundary condition prevailing at large depth, for a given  $m$ ,  $Q/Q_0(m)$  varies linearly with  $L_f/H$ . At the minimum spacing (starting of the dotted part of the straight line in the figure),  $(L_f/H)_{\min} = 2m$ , and  $Q/Q_0(m) = \frac{2m}{\left\{ (4\pi - \pi^2)^{1.3} + (2m)^{1.3} \right\}^{0.77}}$ .

### 35.8.3 Loci of Phreatic Lines for Different Side Slopes

The loci of the phreatic lines are plotted in Fig. 35.4 through Fig. 35.7 for different side slopes and spacing of the furrows. The point of inflection has been shown on the phreatic surface. With increasing spacing the point of inflection shifts toward point  $E$  (Figs. 35.5 and 35.6).

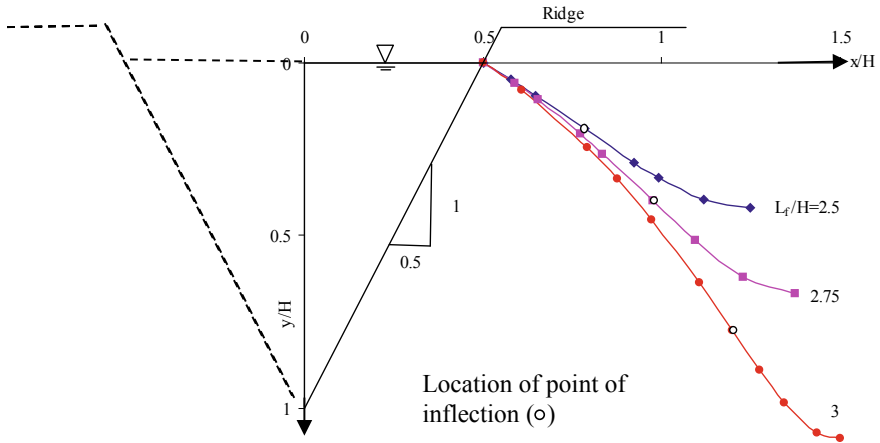


**Fig. 35.4** Loci of phreatic lines for different spacing of an array of triangular furrows for  $m = 0.5$  ( $\alpha = 0.3524$ )

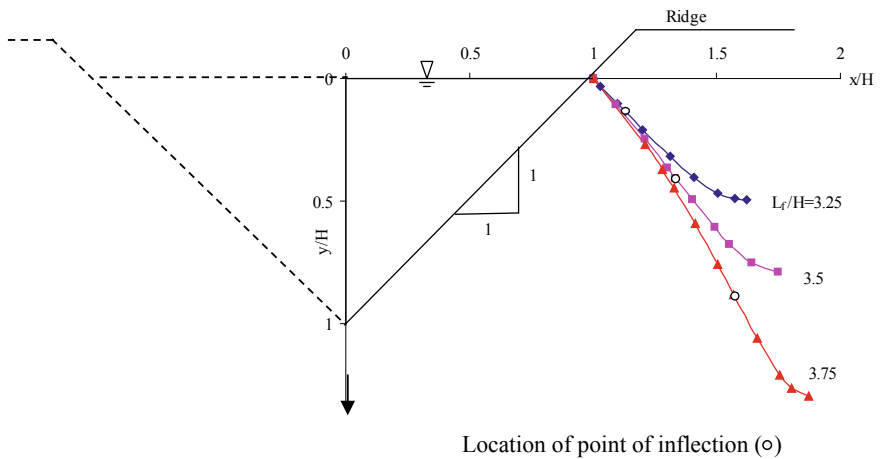


**Fig. 35.5** Loci of phreatic lines for different spacing of an array of triangular furrows for  $m = 1$  ( $\alpha = 0.25$ )

### 35.8.4 Variation of Slope of the Tangent to the Phreatic Line

Slope of the tangent to the phreatic line at a point  $(x, y)$  on the phreatic line is given by  $\frac{dy}{dx} \left\{ = \frac{y(t' + \Delta t') - y(t')}{x(t' + \Delta t') - x(t')} ; 1 \leq t' < \infty \right\}$ . The variation of  $\frac{dy}{dx}$  with  $x$  for  $m = 1$ , and  $\frac{L_f}{H} = 3.5$  is shown in Fig. 35.8. 'D' is the point of inflection. At this point the slope of the tangent,  $\frac{dy}{dx}$ , is the maximum.

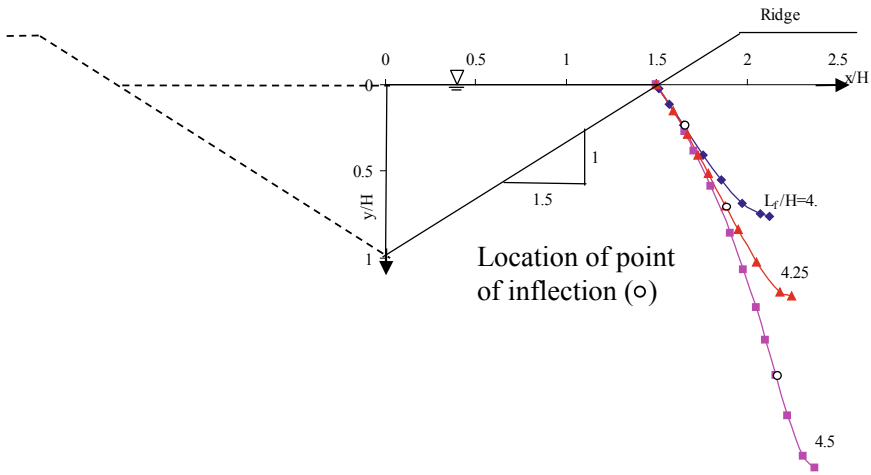


**Fig. 35.6** Loci of phreatic lines for different spacing of an array of triangular furrows for  $m = 1.5(\alpha = 0.1872)$

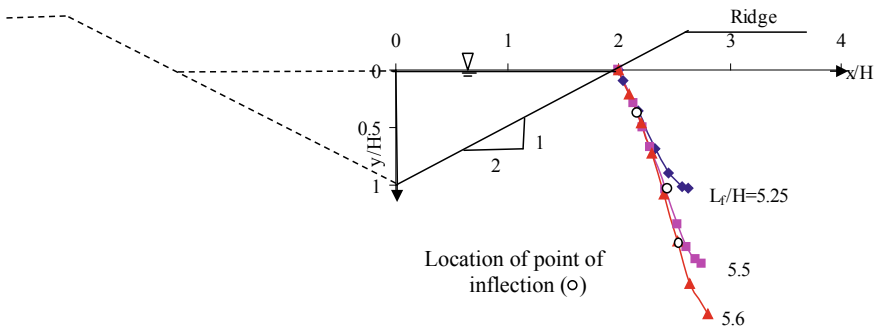


**Fig. 35.7** Loci of phreatic lines for different spacing of an array of triangular furrows for  $m = 2(\alpha = 0.1476)$

### 35.8.5 Adequacy in Furrow Spacing

An example is presented here to check the adequacy of furrow spacing. The moisture extraction pattern by plant and extent of saturation of the soil by furrow irrigation are shown in Fig. 35.9. The root zone depth, ( $R_d$ ), measured from the ridge of the furrow, is assumed to be 30 cm (Kemble and Sanders 2000). The free board is assumed to be 5 cm (Unger 1992). The depth of water in the furrow  $H = 10$  cm. If a spacing  $L_f/H = 3.25$  is adopted i.e. if  $L_f = 32.5$  cm, then the upper 9.9 cm of the root zone at the middle of the ridge does not get water. Corresponding to spacing  $L_f = 35, 36,$  and  $37.5$  cm, the upper 12.8, 14.5, and 17.9 cm of the root zone do not get water respectively. For such spacings,  $(y_E + f_b) > 0.25 R_d$ . As the upper 1/4th of the root

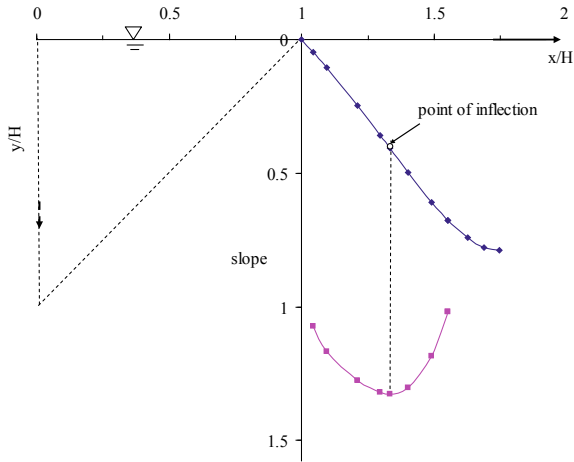


Fig. 35.8 Slope along the phreatic line

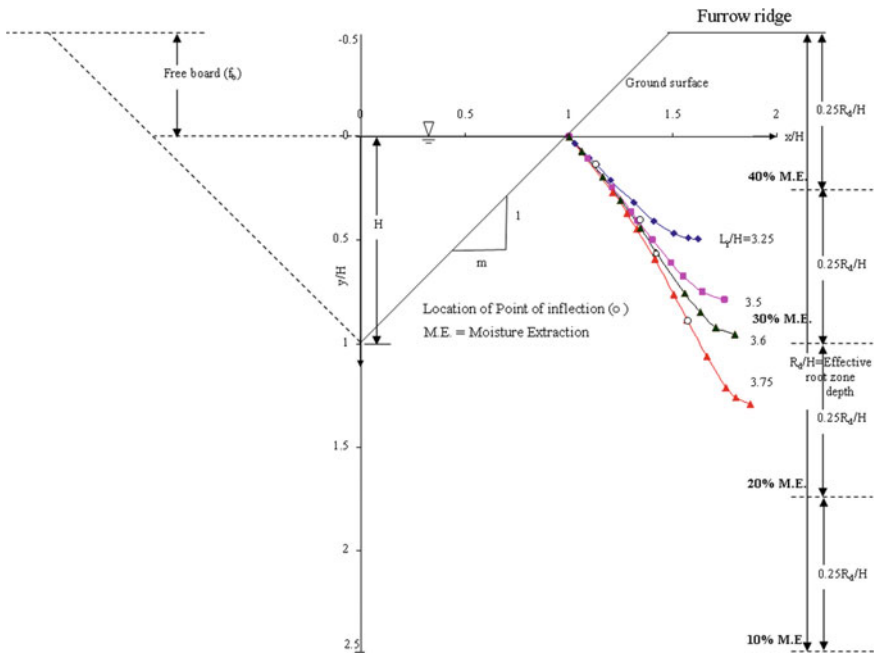


Fig. 35.9 Furrow profile showing the loci of phreatic lines, root zone depth ( $R_d/H$ ) and the moisture extraction percentage by plants at different root zone depth for  $m = 1$ ,  $H = 10$  cm and  $f_b = 5$  cm

zone remains in an unsaturated state, such furrow spacings are not recommended for shallow rooted crops.

### 35.8.6 *Checking the Water Availability in Root Zone at Various Furrow Spacing*

The spacing of the furrows should be such that, at the middle of the ridge, the sum ( $y_E + f_b$ ) < about 1/4th of the root zone depth. In Table 35.1, the suitability of furrow spacing is examined corresponding to a free board,  $f_b = 5$  cm and depth of water in the furrow,  $H = 10$  cm. From Table 35.1, it is inferred that the spacings are only suitable for moderately deep and deep rooted crops.

**Table 35.1** The maximum depth to phreatic surface below the middle of ridge, ( $y_E + f_b$ ), for different spacings and side slope of the triangular furrows;  $f_b = 5$  cm, depth of water in the furrow,  $H = 10$  cm and suitability of furrow spacings

	cot = $m$	Spacing ( $L_F/H$ )	Spacing $L_F$ (cm)	$y_E/H$	$y_E$ (cm)	$y_E + f_b$ (cm)	The spacing suitable for
0.3524	0.5	3.26	32.6	$\infty$	$\infty$	$\infty$	Not suitable
		3.0	30	1.09	10.9	15.9	D
		2.75	27.5	0.67	6.7	11.7	D
		2.5	25	0.42	4.2	9.2	M
0.25	1	4.02	40.2	$\infty$	$\infty$	$\infty$	Not suitable
		3.75	37.5	1.29	12.9	17.9	D
		3.5	35	0.79	7.9	12.9	D
		3.6	36	0.953	9.53	14.53	D
		3.25	32.5	0.49	4.9	9.9	M
0.1872	1.5	4.86	48.6	$\infty$	$\infty$	$\infty$	Not suitable
		4.75	47.5	2.2	22	27	D
		4.5	45	1.2	12	17	D
		4.25	42.5	0.76	7.6	12.6	D
0.1476	2	5.79 <sup>a</sup>	57.9	$\infty$	$\infty$	$\infty$	Not suitable
		5.75	57.5	3.85	38.5	43.5	D
		5.5	55	1.69	16.9	21.9	D
		5.25	52.5	1.03	10.3	15.3	D

<sup>a</sup> Obtained from Vedernikov’s analysis (Vedernikov 1934)

D: Deep rooted crops

M: Moderately deep rooted crops

### 35.9 Conclusions

- An analytical solution for unconfined seepage from parallel triangular furrows in an isotropic porous medium of infinite depth has been derived using the inverse hodograph pertaining to half of the flow domain of one of the furrows and Schwarz–Christoffel transformation. The boundary condition assumed is Neumann-type i.e. at infinity the hydraulic gradient is 1. This boundary condition implies that the seepage from one of the furrows is hydraulic conductivity times spacing of the furrows irrespective of the shape of the furrows. The locus of the phreatic line is governed by the furrow spacing and furrow geometry.
- Saturation of soil under the furrow ridge increases with steeper slope of the furrow banks.
- The slope of the tangent to the phreatic line at point of inflection on the phreatic line attains the maximum.
- With increase in furrow spacing the point of inflection moves downwards
- For side slopes (i.e. for  $m = 0.5$  and  $1$ ) of the furrows, the sum of depth of saturation and free board is at less depth and hence suitable for deep and moderately deep rooted crops, whereas for ( $m = 1.5$  and  $2$ ) it is at higher depth and is suitable for only deep rooted crops.

### 35.10 Appendix(es)

### 35.11 Appendix 1

#### Evaluation of Integral $I_1$

$$I_1 = \int_0^a \frac{(\delta + \xi)}{(\xi)^{1-\alpha}(1+\xi)^{1-(\frac{1}{2}-\alpha)}} d\xi \quad \xi = 0 \text{ is a singular point.}$$

Incorporating  $\xi = X^{1/\alpha}$ ,  $d\xi = \frac{1}{\alpha} X^{\frac{1}{\alpha}-1} dX$  for removing the singularity.

$$I_1 = \frac{1}{\alpha} \int_0^{a^\alpha} \frac{(\delta + X^{1/\alpha}) X^{\frac{1}{\alpha}-1}}{(X)^{\frac{1-\alpha}{\alpha}} (1 + X^{1/\alpha})^{(\frac{1}{2}+\alpha)}} dX = \frac{1}{\alpha} \int_0^{a^\alpha} \frac{(\delta + X^{1/\alpha})}{(1 + X^{1/\alpha})^{(\frac{1}{2}+\alpha)}} dX$$

Further substituting  $X = \frac{a^\alpha}{2} (1 + \eta)$ ,  $dX = \frac{a^\alpha}{2} d\eta$

$$\begin{aligned} I_1 &= \frac{a^\alpha}{2\alpha} \int_{-1}^1 \frac{(\delta + X^{1/\alpha})}{(1 + X^{1/\alpha})^{(\frac{1}{2}+\alpha)}} d\eta; \quad X = \frac{a^\alpha}{2} (1 + \eta) \\ &= \frac{a^\alpha}{2\alpha} \sum_{i=1}^N F(\eta_i) w(i) \end{aligned}$$

$I_1$  is evaluated using Gaussian weights.

### 35.12 Appendix 2

#### Evaluation of Integral $I_2$

$$I_2 = \int_0^1 \frac{dt}{t^{1/2}(1-t)^{1/2}(t+a)}$$

In  $I_2$ ,  $t = 0$  and  $t = 1$  are singular points. Substituting  $t = \sin^2 \theta$ ,  $dt = 2 \sin \theta \cos \theta d\theta$  for removing the singularities,  $I_2$  reduces to

$$I_2 = 2 \int_0^{\pi/2} \frac{d\theta}{(a + \sin^2 \theta)}$$

Further substituting  $\theta = \frac{\pi}{4}(1 + \Phi)$ ,  $d\theta = \frac{\pi}{4} d\Phi$

$$I_2 = \frac{\pi}{2} \int_{-1}^1 \frac{d\Phi}{a + \sin^2 \left\{ \frac{\pi}{4}(1 + \Phi) \right\}}$$

$I_2$  is evaluated using Gaussian weights.

The constant  $M_2$  can also be obtained using the condition at points  $A$  and  $F$ . Going around a small circle of radius  $r$ ,  $r \rightarrow 0$  around  $t = -a$ , results in a jump equal to  $\frac{-iQ}{2}$  in  $w$  plane. Substituting  $(t + a) = re^{i\theta}$ ,  $dt = re^{i\theta} i d\theta$  in (4.8).

$$\frac{-iQ}{2} = \lim_{r \rightarrow 0} M_2 \int_0^\pi \frac{re^{i\theta} i d\theta}{(re^{i\theta} - a)^{1/2}(1 + a - re^{i\theta})^{1/2} re^{i\theta}} = \frac{\pi}{\sqrt{(1+a)a}} M_2$$

$$M_2 = \frac{-iQ\sqrt{a(1+a)}}{2\pi} I_2 = \frac{\pi}{2} \int_{-1}^1 \frac{d\Phi}{a + \sin^2 \left\{ \frac{\pi}{4}(1 + \Phi) \right\}} = \frac{\pi}{\sqrt{a(1+a)}}$$

### 35.13 Appendix 3

#### Evaluation of Integration $I_3$

$$I_3 = \int_0^1 \left\{ \delta B_t \left( \alpha, \frac{1}{2} - \alpha \right) - B_t \left( 1 + \alpha, \frac{1}{2} - \alpha \right) \right\} \frac{dt}{t^{1/2}(1-t)^{1/2}(t+a)}$$

Substituting  $t = \sin^2 \theta$ ,  $dt = 2 \sin \theta \cos \theta d\theta$

$$I_3 = \int_0^{\pi/2} \left\{ \delta B_{\sin^2 \theta} \left( \alpha, \frac{1}{2} - \alpha \right) - B_{\sin^2 \theta} \left( 1 + \alpha, \frac{1}{2} - \alpha \right) \right\} \frac{2 \sin \theta \cos \theta d\theta}{\sin \theta \cos \theta (a + \sin^2 \theta)}$$

Further substituting  $\theta = \frac{\pi}{4}(1 + \Phi)$ ,  $d\theta = \frac{\pi}{4}d\Phi$ ,

$$\begin{aligned} I_3 &= \int_{-1}^1 \left\{ \delta B_{\sin^2 \left\{ \frac{\pi}{4}(1+\Phi) \right\}} \left( \alpha, \frac{1}{2} - \alpha \right) - B_{\sin^2 \left\{ \frac{\pi}{4}(1+\Phi) \right\}} \left( 1 + \alpha, \frac{1}{2} - \alpha \right) \right\} \frac{2 \frac{\pi}{4} d\Phi}{a + \sin^2 \left\{ \frac{\pi}{4}(1 + \Phi) \right\}} \\ &= \frac{\pi}{2} \int_{-1}^1 \left\{ \delta B_{\sin^2 \left\{ \frac{\pi}{4}(1+\Phi) \right\}} \left( \alpha, \frac{1}{2} - \alpha \right) - B_{\sin^2 \left\{ \frac{\pi}{4}(1+\Phi) \right\}} \left( 1 + \alpha, \frac{1}{2} - \alpha \right) \right\} \frac{d\Phi}{a + \sin^2 \left\{ \frac{\pi}{4}(1 + \Phi) \right\}} \end{aligned}$$

### 35.14 Appendix 4

#### Evaluation of $I_4(t')$

$$I_4(t') = \int_1^{t'} \left\{ \delta \int_1^t \tau^{\alpha-1} (\tau-1)^{\left(\frac{1}{2}-\alpha\right)-1} d\tau - \int_1^t \tau^{(1+\alpha)-1} (\tau-1)^{\left(\frac{1}{2}-\alpha\right)-1} d\tau \right\} \frac{dt}{(t)^{1/2}(t-1)^{1/2}(t+a)}; 1 \leq t \leq \infty$$

Substituting  $t = \frac{1}{\xi}$ ,  $dt = -\frac{1}{\xi^2}d\xi$ ,

$$I_4(t') = \int_{1/t'}^1 \left\{ \delta \int_1^{1/\xi} \tau^{\alpha-1} (\tau-1)^{\left(\frac{1}{2}-\alpha\right)-1} d\tau - \int_1^{1/\xi} \tau^{(1+\alpha)-1} (\tau-1)^{\left(\frac{1}{2}-\alpha\right)-1} d\tau \right\} \frac{d\xi}{(1-\xi)^{1/2}(1+a\xi)}$$

$\tau = 1$  is a singular point. The singularity is removed substituting  $\tau - 1 = \eta^m$ ,  $d\eta\tau = m^{m-1}d\eta$  and selecting  $m = \frac{1}{0.5-\alpha}$ . Incorporating the substitution

$$I_4(t') = \int_{1/t'}^1 \left\{ \delta m \int_0^{\left(\frac{1}{\xi}-1\right)^{1/m}} (1+\eta^m)^{\alpha-1} d\eta - m \int_0^{\left(\frac{1}{\xi}-1\right)^{1/m}} (1+\eta^m)^{(1+\alpha)-1} d\eta \right\} \frac{d\xi}{(1-\xi)^{1/2}(1+a\xi)}$$

Further substituting  $1 - \xi = V^2$ ,  $d\xi = -2VdV$ ,

$$I_4(t') = \int_0^{\sqrt{\left(\frac{t'-1}{t'}\right)}} \left\{ \delta m \int_0^{\left(\frac{V^2}{1-V^2}\right)^{1/m}} (1+\eta^m)^{\alpha-1} d\eta - m \int_0^{\left(\frac{V^2}{1-V^2}\right)^{1/m}} (1+\eta^m)^{(1+\alpha)-1} d\eta \right\} \frac{2dV}{\{1+a(1-V^2)\}}$$



Let  $\frac{1}{2}\sqrt{\frac{t'-1}{t'}}(1+X) = V, dV = \frac{1}{2}\sqrt{\frac{t'-1}{t'}}dX$

$$I_4(t') = \int_{-1}^1 \left\{ \delta_m \int_0^{\left(\frac{V^2}{1-V^2}\right)^{1/m}} (1+\eta^m)^{\alpha-1} d\eta - m \int_0^{\left(\frac{V^2}{1-V^2}\right)^{1/m}} (1+\eta^m)^{(1+\alpha)-1} d\eta \right\} \frac{\sqrt{\frac{t'-1}{t'}} dX}{\{1+a(1-V^2)\}}$$

Further let  $\frac{1}{2}\left(\frac{V^2}{1-V^2}\right)^{1/m} [1+Y] = \eta, d\eta = \frac{1}{2}\left(\frac{V^2}{1-V^2}\right)^{1/m} dY$

$$I_4(t') = \int_{-1}^1 \left\{ \delta_m \int_{-1}^1 (1+\eta^m)^{\alpha-1} \frac{1}{2}\left(\frac{V^2}{1-V^2}\right)^{1/m} dY - m \int_{-1}^1 (1+\eta^m)^{(1+\alpha)-1} \frac{1}{2}\left(\frac{V^2}{1-V^2}\right)^{1/m} dY \right\} \frac{\sqrt{\frac{t'-1}{t'}} dX}{\{1+a(1-V^2)\}}$$

$$V = \frac{1}{2}\sqrt{\frac{t'-1}{t'}}(1+X) \quad \eta = \frac{1}{2}\left(\frac{V^2}{1-V^2}\right)^{1/m} [1+Y]$$

$I_4(t')$  is evaluated numerically using Gaussian weights.

### 35.15 Appendix 5

#### Evaluation of $I_5(t')$

$I_5(t') = \int_1^{t'} \frac{dt}{t^{1/2}(t-1)^{1/2}(t+a)}$ . Substituting  $t = \frac{1}{\xi}, dt = -\frac{d\xi}{\xi^2}$

$$I_5(t') = \int_{1/t'}^1 \frac{d\xi}{(1-\xi)^{1/2}(1+a\xi)}$$

Further substituting  $1-\xi = V^2, d\xi = -2VdV$   $I_5(t') = \int_0^{\sqrt{\frac{t'-1}{t'}}} \frac{2dV}{\{1+a(1-V^2)\}}$

Let

$$\frac{1}{2}\sqrt{\frac{t'-1}{t'}}(1+X) = V, dV = \frac{1}{2}\sqrt{\frac{t'-1}{t'}}dX \quad I_5(t') = \int_{-1}^1 \frac{\sqrt{\frac{t'-1}{t'}} dX}{\{1+a(1-V^2)\}}$$

$I_5(t')$  is evaluated using Gaussian weights.

## Notations

The following symbols are used in this paper:

$B$ (...)	complete beta function	
$f_b$	free board	(L)
$k$	hydraulic conductivity	(L/T)
$L_f$	furrow spacing	(L)
$m$	side slope of the furrow	
$Q$	seepage loss per unit length	(L <sup>2</sup> /T)
$Q_0$	seepage per unit length loss from a non interfering furrow	(L <sup>2</sup> /T)
$R_d$	root zone depth	(L)
$t$	parametric plane	
$w$	+ $i\psi$ complex potential	
$z$	$x + iy$ , complex variable	
	velocity potential function	(L <sup>2</sup> /T)
$\psi$	stream function	(L <sup>2</sup> /T)
$\delta, a$	mapping parameters	
$\tau, \xi, \eta, \theta, \varphi$	dummy variables	

**Acknowledgements** I am immensely grateful to Prof. Nayan Sharma (Retired Prof.), Dept. of WRD&M, IIT Roorkee, for his unwavering support and encouragement to make this manuscript in this present form.

## References

- Bruch JC, Street RL (1967) Seepage from an array of triangular channels. J Eng Mech Div Proc ASCE 93(EM3):63–82
- Brouwer C, Prins K, Kay M, Heibloem M (1990) Irrigation water management: irrigation methods. Training Manual No-5, FAO, Land and Water Development Division
- Carter DL (1985) Controlling erosion and sediment loss on furrow-irrigated land. Reprinted From Soil Erosion and Conservation, Soil Conservation Soc. of America
- Chahar BR (2000) Optimal design of channel sections considering seepage and evaporation losses. Ph.D. thesis, Dept. of Civil Engineering, Univ. of Roorkee, Roorkee, India
- Choudhary M, Chahar BR (2007) Recharge/seepage from an array of rectangular channels. J Hydrol 343:71–79
- Kemble JK, Sanders DC (2000) Basics of vegetable crop irrigation. ACES Publication, ANR-1169
- Michael AM (1999) Irrigation theory and practice. Vikas Publishing House Pvt. Ltd., New Delhi
- Polubarinova-Kochina PYa (1962) Theory of groundwater movement. Princeton University Press, New Jersey

- Samal KP, Mishra GC (2016) Analysis of seepage from a triangular furrow considering soil capillarity using inverse hodograph and conformal mapping technique. *ISH J Hydra Eng.* <https://doi.org/10.1080/09715010.2016.1213144>
- Samal KP, Mishra GC, Sharma N (2019) Analysis of seepage from a triangular furrow with negligible free-board considering soil capillarity using inverse hodograph and conformal mapping technique. In: International conference on recent developments in sustainable infrastructure. KIIT DU, BBSR
- Tiwari KN, Mal PK, Singh RM, Chattopadhyay A (1998) Response of Okra (*Abelmoschus Esculentus* (L.) Moench.) to drip irrigation under mulch and non-mulch condition. *Agric Water Manage* 38:91–102
- Unger WP (1992) Ridge height and furrow blocking effects on water use and grain yield. *Soil Sci Soc Am J* 56(5):1609–1614
- Vedernikov VV (1934) Seepage from Channels (in Russian). Gosstroydat, Moscow, also in German: *Wasserkrafts-Wasserwirtsch*, pp 11–13

# Chapter 36

## Sustainable Rainwater Harvesting System and Storm Water Management: A Case Study in Raipur Airport



Digeshwar Prasad Sahu and Mani Kant Verma

**Abstract** The immense and growing scarcity of freshwater across the globe arises as a troubling issue for both developed and developing countries. Groundwater is the only source of water of the Swami Vivekananda Airport Raipur, and it faces a water crisis when the groundwater level decreases. In this scenario, Rainwater Harvesting (RWH) can contribute considerably to tackle these problems. Rainwater treatment systems can be installed at different potential locations in the study area based on their physical site conditions such as slope and elevation. The airport has a total area of 2.108 km<sup>2</sup> (Kms<sup>2</sup>); through the properly designed drainage system, storm water is collected and separated into three potential zones. Zones I, II and III having areas 0.2393, 0.4307 and 1.4382 sq. Kms, respectively, which produce different runoff amounts based on maximum daily rainfall. The airport has a 38,955.62 m<sup>2</sup> rooftop area, and water collected from the rooftop will fulfil approximately 30% of the total daily demand of the airport. Storm water is treated by Slow Sand Filter (SSF) at the rate of 200 L per hour per square metre and stored under design capacity, and size and number of treatment units depend on the maximum discharge at their respective zones. Excess water of storage tank is used for groundwater recharge, and a recharge well is provided at different depths according to fracture available below the ground.

### 36.1 Introduction

Water is crucial and it has always been considered throughout history as a natural resource for the survival of humanity. Worldwide, the important issue is the shortage of water either by quantity or quality (Gogate and Rawal 2012). In highly populated areas like urban area, the availability of freshwater even for daily use is not within reach and need external processes to get the water to the inhabitants of the area.

---

D. P. Sahu (✉) · M. K. Verma  
NIT Raipur, Raipur, India

M. K. Verma  
e-mail: [manikverma.ce@nitrr.ac.in](mailto:manikverma.ce@nitrr.ac.in)

Assessing and managing the justified use of water resources can help for preservation, and sustainable use becomes a vital issue in people's life, mainly in an area where the groundwater level is very low and there is very low rainfall. In this sequence to complete the freshwater demand of inhabitants, the use of rainwater is becoming an extensively influential instrument. For harvested water to remove microbial contamination and other chemical substances, rainwater needs some treatment system prior to utilising that water. The type of treatment to be provided depends on the purpose of intended use and characteristics of collected water from the ground surfaces or roofs (Helmreich and Horn 2009). A low-cost traditional treatment method like slow sand filter and disinfection by chlorination can be used for the region like an airport where treatment should be done only for rainy days and SSF is a highly efficient filter that removes 98–99% of bacterial contamination from water.

India has approximately 17% of the world's population and has only 4% of water resources in the world. India gets freshwater from precipitation about 4000 trillion litres in the form of snowfall and rain, and the maximum of this water reaches to the ocean and seas through the so many rivers which are flowing across the country. The United Nations (UN) apprise that the shortage of freshwater is the most serious problem to produce enough amount of food for a growing population of the world. The declination in per capita availability of water from 1947 to 2017 is 5200 m<sup>3</sup> to 1500 m<sup>3</sup> per year, respectively (Report of Indian Institute of Remote Sensing, Dehradun). In different parts of India, water is being used at a much faster rate than can be only refilled by rainwater. Therefore, we can say that India is not far away from water crises so we need to adopt some other water resource.

The location such as the airport required water at a significant amount to manage their operational routine and infrastructural demand (Gurung and Sharma 2014). The main purpose of this study is to reduce flash floods and use rainwater for the non-potable demand of airports. A proper drainage system is also required for the collection of storm water at different potential zones where water gets treated. Problem related to this must be taken for granted in India because, in scarcity, this will become a most treasured resource (Helmreich and Horn 2009). After knowing all the significance of freshwater to our growing inhabitants and thriving industries, to compensate for these, highly increasing demands RWH techniques can be adopted.

## 36.2 Methodology

### Study Area

In Raipur, the capital city of Chhattisgarh, Swami Vivekananda Airport is near to the city and its boundaries spread in the range between 21°10'15" to 21°12'00" North latitudes and 81°43'27" to 81°46'20" East longitudes (Fig. 36.1). Airport bounds are limited to toposheet no. 64G/12 and 64G/11 which is provided by the Survey of India (SOI). The total plot area of the airport is approximately 520.89 acre (2.108 Kms<sup>2</sup>). Semi-arid tropical climatic conditions prevail in Raipur urban area (Fernandes et al.

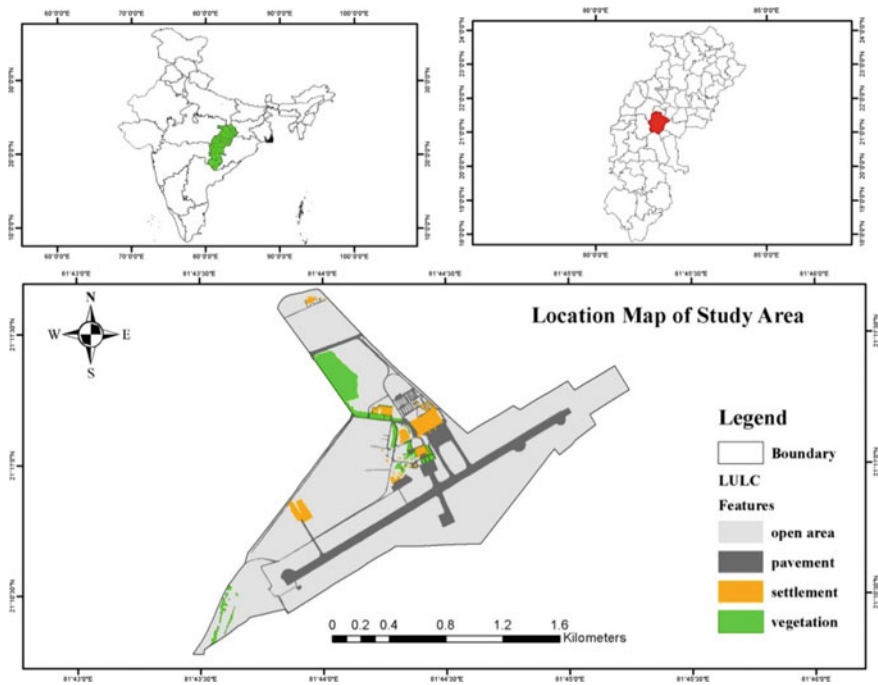


Fig. 36.1 Location map of the study area

2012). The area experiences a very warm summer of longer duration of March to the middle of June, and after this, the monsoon season will be started, which lasts for almost four months from the middle of June to September (Campisano et al. 2017). December to the end of February study area faces the winter season. Temperature varies from 10–46 °C, and humidity ranges from 30–85% and it receives 1185 mm average rainfall.

Physiographically study area is situated in the South-Central part of the Chhattisgarh basin having gentle undulating topography. Raipur is situated on the Proterozoic Chandi Formation of the Raipur group (Chhattisgarh Super Group), comprising of limestone, shale and sandstone. In the airport area, there is the occurrence of limestone and shale.

### Rainfall-Runoff Modelling

The model was created using ArcGIS extension known as HEC-GeoHMS, which includes various steps in a series collectively term called as terrain preprocessing (Kumar and Jhariya 2017). The data needed for modelling such as DEM, LULC and soil maps are imported and merged with the proper projection system. Hydrologic Engineering Center’s Hydrologic Modelling System (HEC-HMS) of version 4.1 is used for rainfall-runoff modelling. The HMS model allowed parameterisation of various infiltration losses could choose by the modeler (Fig. 36.2). For spatially

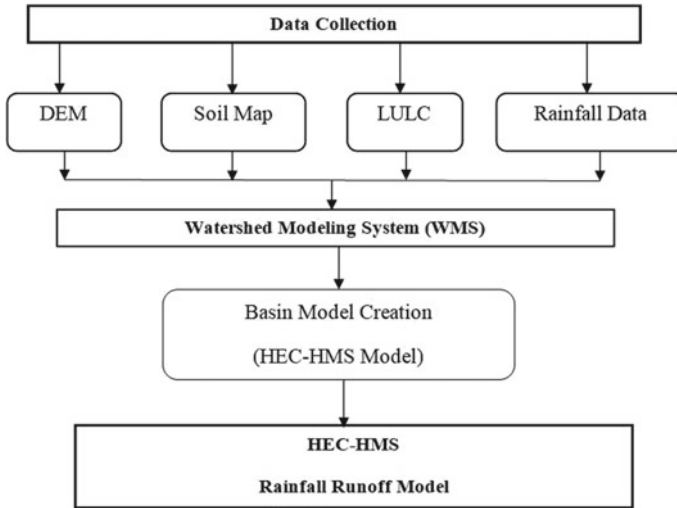


**Fig. 36.2** Flow chart of rainfall-runoff model

dispensed calculation of infiltration enables by the Soil Conservation Service (SCS) curve number (CN) method (Kadam et al. 2012). The SCS-CN method is used for quantifying storm runoff of a particular area on the basis of their soil, land use land cover type and hydrological soil group (Domènech and Saurí 2011). The ability of infiltration of any soil helps to decide that soil fall under which hydrological soil group (Kumar et al. 2006). To differentiate the infiltration and runoff from the rainfall, some important equations are used which are empirical and derived by the infiltration loss method.

$$Q = \frac{(P - I_a)^2}{(P - I_a + S)}$$

where P is effective rainfall depth, Q is event discharge or Surface runoff (mm), S is the potential maximum soil retention and  $I_a$  is Initial abstraction.

$$I_a = \lambda S$$

$$S = \frac{25400}{CN} - 254$$

where the value of  $\lambda$  varies according to soil type and Antecedent Moisture Content (AMC) and CN also varies in the range of 0 (no runoff produce) to 100 (produce all rain as runoff) which depend on LULC and soil condition (Kumar and Jhariya 2017).

$$Q = \frac{(P - I_a)^2}{(P - I_a + S)} \text{ if } P > I_a; \text{ Produce runoff}$$

$$Q = 0 \text{ if } P < I_a; \text{ No runoff}$$

### Drainage Design

The Storm Water Management Model (SWMM) is developed by EPA, which is extensively used for urban runoff simulation (Xing et al. 2016). The SWMM is widely operating for analysis, design and planning related to the urban drainage system. SWMM of version 5.1 is used for designing the drainage network, input data editing and simulation run and showing the results in the suitable form of tables, thematic maps, graphs and reports in a statistical format. IDF curve has been generated to determine the intensity of the rainfall event at various time durations for different return periods. These curves have been generated for the return periods of 2, 5, 10, 20, 25, 30, 50 and 100 years. The design of the drainage system was done for the 20 year return period. The cross-section of the barrel is taken as a rectangle and the size (depth & width) of the barrel is depending on the water accumulated at a particular point (Bitterman et al. 2016). The study area has 14 sub-catchments and 27 junctions which collect and divert storm water towards the outfall. The outfall is located at the lowest elevated point of respective zones, and water is forwarded to the treatment unit where it gets treated and stored.

### Rainwater Treatment and Storage

Storm water contains sediment particle, and to remove the sediment, a settling tank can be constructed so that the filter will not be choked during filtration (Bitterman et al. 2016). The size of the settling tank and SSF is based on the maximum discharge at the outlet point (Burman 1978). The Rate of Filtration (ROF) must be high so that the filter system can complete the demands and to meet this filtration, the rate thickness of the layers in the filter will be specified (Fig. 36.3).

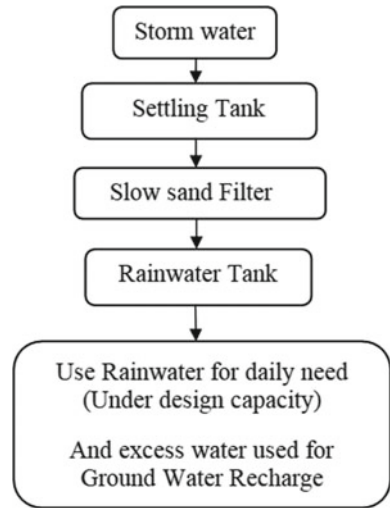
After filtration, clear water is forwarded to the rainwater tank, water can be stored in the tank under its design capacity and excess water is used for groundwater recharge when it reaches to recharge structure (Moreira et al. 2012). In the recharge pit, two perforated borewells are installed to recharge groundwater because of the geological formation in the form of limestone and shale available in the study area (Burman 1978). Therefore, some fractures are present in the ground, which can be utilised for water recharge, and the depth of the borewells depends on the availability of fracture below the recharge structure.

## 36.3 Result and Discussion

Estimating the maximum daily water demand of the airport is essential to know the consumption profile of the premises and terminal building because to find the



**Fig. 36.3** Flow chart of rainwater treatment



duration of service provided with the utilisation of harvested water. The data were collected from the airport authority of Raipur, which shows the consumption profile of the area. The rooftop water has enough to serve approximately 30 % of the total daily demand of the airport (Fig. 36.4).

**Models Calibration**

Rainfall-runoff relation monthlywise is calibrated through the HEC-HMS modelling. This relation is essential for managing the drainage design, and dimensions of barrel and junctions are provided for 20 year return period (Fig. 36.5).

In the HMS, the monthly variation of rainfall-runoff is calculated for 34 years (1980 to 2013) which shows the scenario of runoff (Table 36.1).

The drainage system is designed using SWMM, and a detailed network system is shown in (Fig. 36.6); through the barrels, storm water passes and goes to the treatment

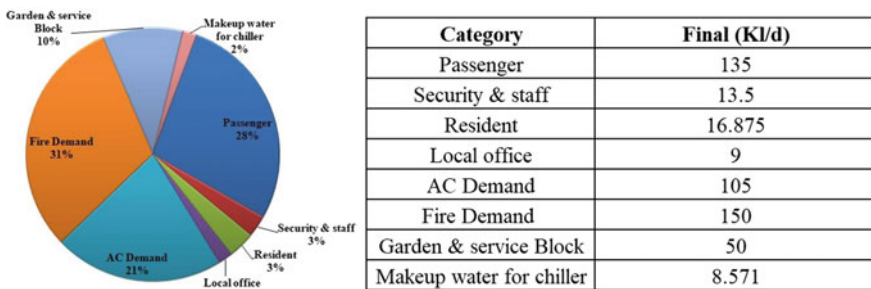


**Fig. 36.4** Water consumption profile of study area

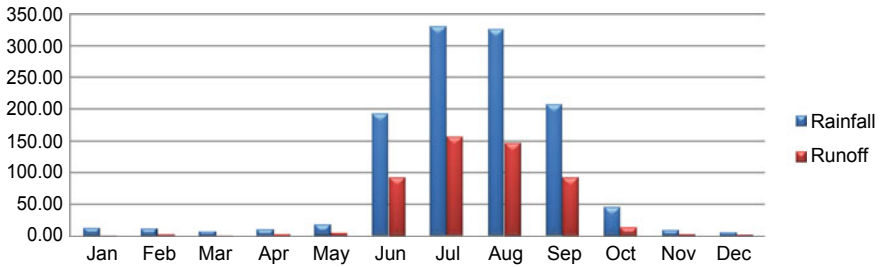


**Fig. 36.5** Monthly rainfall—runoff relation

**Table 36.1** Runoff volume of the study area

Region	Basin No	Area (km <sup>2</sup> )	Runoff volume (1000 Cubic metre)	Total volume of runoff water (1000 cubic metre/year)
A	1	0.062	73.90	283.31
	2	0.113	133.64	
	4	0.064	75.76	
B	3	0.303	358.64	510.13
	5	0.128	151.49	
C	6	0.149	176.72	1703.47
	7	0.512	605.88	
	8	0.060	70.83	
	9	0.170	200.87	
	10	0.068	80.43	
	11	0.257	304.29	
	12	0.084	99.14	
	13	0.078	92.37	
	14	0.062	72.93	

unit. Some essential flow checks can be provided inside the storm water drains to retain the debris.

**Sedimentation Tank**

The design of the sedimentation tank is based on the maximum daily runoff in the study area (Gurung and Sharma 2014). Some important flow checks should be installed within the drains which contain storm water so that settling of the silt is restricted. A mesh can be provided near the inlet of the tank to remove the debris entering inside the settling tank. The size of the sedimentation tank is varied according to the water availability at outlet points (Fig. 36.7).



Fig. 36.6 Drainage map of the study area

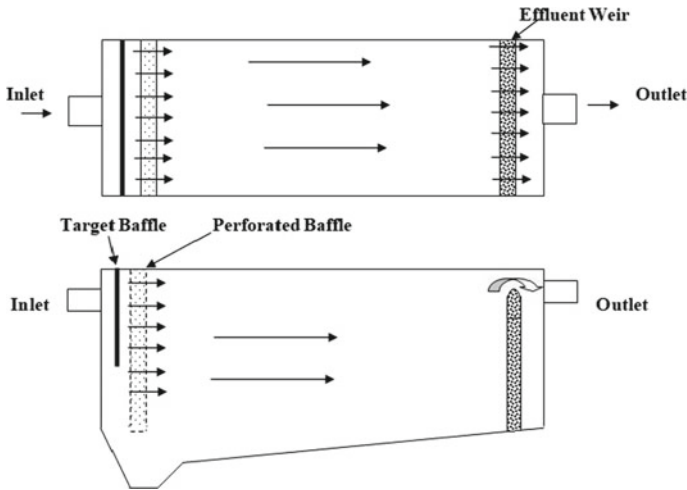


Fig. 36.7 Sedimentation tank

### Slow Sand Filter

Clean river sand is of effective size 0.2–0.35 mm and thickness of the sand bed is 0.9 m. Gravel effective size is 3–60 mm and thickness of gravel bed is 0.4 m (Fig. 36.8). The rate of filtration is 200 L per hour per square metre and the width of the wall is taken as 0.23 m of the filter (Burman 1978). SSF should be installed parallel near the settling tank and a minimum of 2 filters must be provided as per guidelines (Table 36.2).

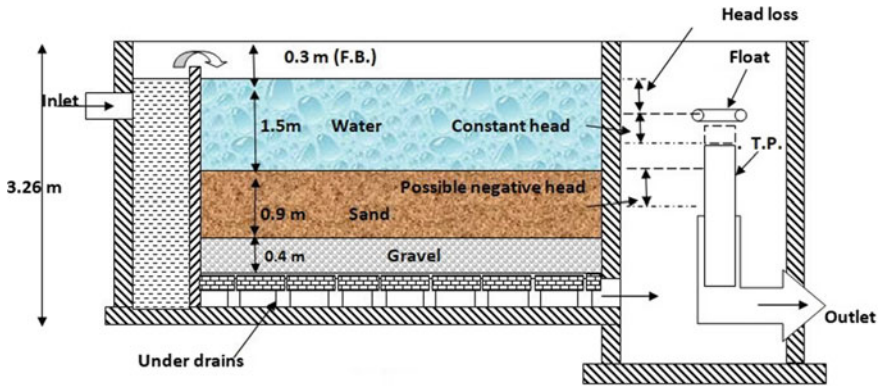


Fig. 36.8 Section view of SSF

Table 36.2 Depth of layers in SSF

Freeboard	0.3 m
Supernatant water	1.5 m
Filter medium (sand)	0.9 m
Gravel bed	0.4 m
Brick filter bottom	0.16 m
Total depth	3.26 m

**Rainwater Tank**

A rainwater tank is designed for 80% capacity of total runoff accumulated in 48 hours because of the limited area and 10% extra volume is provided for airspace in the tank (Fig. 36.9). Excess water goes to the recharge trench to raise the groundwater level

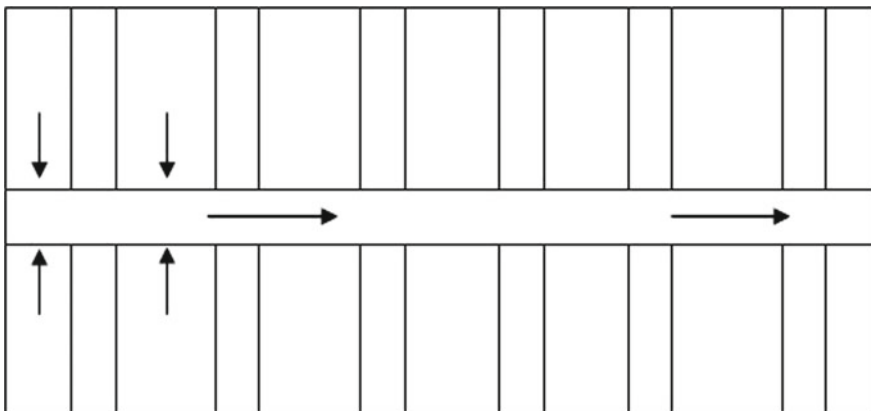
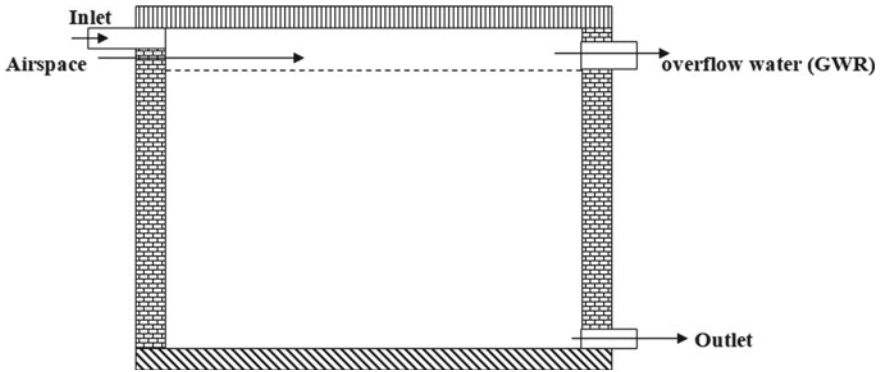


Fig. 36.9 Plan view of SSF



**Fig. 36.10** Section view of Rainwater tank

(Gurung and Sharma 2014). A separate rainwater tank is also constructed for rooftop water which is collected near the existing treatment unit of the airport (Moreira et al. 2012). The rainwater tank should be clean before the rainy season so that the tank is free from any contamination (Fig. 36.10).

### Recharge Structure

The artificial recharge systems are engineering techniques, where available surface water is injected in or on the ground for the process like infiltration and some other subsequent movements to aquifers to increase groundwater level (Yadav and Setia 2016). Some other purposes of artificial recharge are to improve the quality of the water through soil-aquifer treatment or geo-purification, to make groundwater out of the surface water where groundwater is traditionally preferred over surface water for drinking purpose, to store surface water and to use the aquifers as a water conveyance system. The geological formation of the airport is situated on the Proterozoic Chandi Formation, which is having a low infiltration capacity. Therefore, a recharge well can be constructed at significant depth based on the geological survey by instruments such as resistivity metre which can show the availability of fracture below the ground.

## 36.4 Conclusion

In Swami Vivekananda Airport, the application of rainwater harvesting is needed to meet the increasing water consumption demands such as cooling system and domestic use. The water supply at the airport depends on groundwater which is taken from five borewells located within the study area. The wastewater from the terminal building is treated at the sewage treatment plant and the treated wastewater is used for irrigation of gardens. The model performance criteria with different parameters showed that the model's results were excellent in runoff estimation, drainage design, rainwater treatment and recharge of groundwater in the study area.

The airport has a large open area that collects a huge amount of storm water at different zones of the study area that will help to save about  $126.34 \times 10^3 \text{ m}^3$  of water per year and excess water is used for groundwater recharge. Filter systems such as slow sand filter can provide economical and sustainable water reuse facilities for large areas like the airport, and it is used where the rate of filtration demand is less.

Construction of the recharge wells can be done at pre-determined locations. The depth of the recharge wells may vary as per specific site conditions and depth is to be restricted up to the depth where the well starts giving discharge. This will ensure the intake of runoff water so that water gets recharged at a rapid rate.

## References

- Bitterman P, Tate E, Van Meter KJ, Basu NB (2016) Water security and rainwater harvesting: a conceptual framework and candidate indicators. *Appl Geogr* 76:75–84. <https://doi.org/10.1016/j.apgeog.2016.09.013>
- Burman NP (1978) Slow sand filtration. *H2O* 11(16):348. <https://doi.org/10.1201/9781439895092-22>
- Campisano A, Butler D, Ward S, Burns MJ, Friedler E, DeBusk K, Jeffes LNF, Ghisi E, Rahman A, Furumai H, Han M (2017) Urban rainwater harvesting systems: research, implementation and future perspectives. *Water Res* 115:195–209. <https://doi.org/10.1016/j.watres.2017.02.056>
- Domènech L, Saurí D (2011) A comparative appraisal of the use of rainwater harvesting in single and multi-family buildings of the Metropolitan Area of Barcelona (Spain): Social experience, drinking water savings and economic costs. *J Clean Prod* 19(6–7):598–608. <https://doi.org/10.1016/j.jclepro.2010.11.010>
- Fernandes R, Neto M, Carvalho IDC, Calijuri ML (2012) Resources, conservation and recycling rainwater use in airports : a case study in brazil. *Resour Conser Recycl* 68:36–43. <https://doi.org/10.1016/j.resconrec.2012.08.005>
- Gogate NG, Rawal PM (2012) Sustainable stormwater management in developing and developed countries: a review. *Proceedings of the International Conference on Advances in Design and Construction of Structures 2012*:1–6
- Gurung TR, Sharma A (2014) Communal rainwater tank systems design and economies of scale. *J Clean Prod* 67:26–36. <https://doi.org/10.1016/j.jclepro.2013.12.020>
- Helmreich B, Horn H (2009) Opportunities in rainwater harvesting. *Desalination* 248(1–3):118–124. <https://doi.org/10.1016/j.desal.2008.05.046>
- Kadam AK, Kale SS, Pande NN, Pawar NJ, Sankhua RN (2012) Identifying potential rainwater harvesting sites of a semi-arid, basaltic region of western India using SCS-CN method. *Water Resour Manag* 26(9):2537–2554. <https://doi.org/10.1007/s11269-012-0031-3>
- Kumar MD, Ghosh S, Patel A, Singh OP, Ravindranath R (2006) Rainwater harvesting in India : Some critical issues for basin planning and research. *Land Use Water Res* 6:1–17
- Kumar T, Jhariya DC (2017) Identification of rainwater harvesting sites using SCS-CN methodology, remote sensing and geographical information system techniques. *Geocarto Int* 32(12):1367–1388. <https://doi.org/10.1080/10106049.2016.1213772>
- Moreira RFN, Calijuri ML, Carvalho IDC, Santiago ADF (2012) Rainwater treatment in airports using slow sand filtration followed by chlorination: efficiency and costs. *Resour Conserv Recycl* 65:124–129. <https://doi.org/10.1016/j.resconrec.2012.06.001>
- Xing W, Li P, Cao SB, Gan LL, Liu FL, Zuo JE (2016) Layout effects and optimization of runoff storage and filtration facilities based on SWMM simulation in a demonstration area. *Water Sci Eng* 9(2):115–124. <https://doi.org/10.1016/j.wse.2016.06.007>

Yadav M, Setia B (2016) Conceptualization and design of an efficient groundwater recharge system for NIT Kurukshetra. *Procedia Technol* 25(Raerest):138–145. <https://doi.org/10.1016/j.protcy.2016.08.090>

# Chapter 37

## Hydrological Modeling of Dam Inflow Data Under Restricted Upstream Abstraction Data



### Impact of Restricted Upstream Data in Calibration and Validation of HYSIM Model for the Kangsabati River Basin of India

Mridusmita Debnath and Ashok Mishra

**Abstract** This paper reports on the application of a daily rainfall-runoff model HYSIM upstream of Kangsabati reservoir, covering three drought-prone districts of West Bengal. The upstream part comprises mainly of two rivers upper Kangsabati river and Kumari river and they have their outlets at the Kangsabati reservoir. A lumped conceptual hydrological model linked to a Geographical Information System was developed on the basis of simplified physical process representations (infiltration, evapotranspiration, base flow, interflow, overland flow, channel routing), using conventional hydro-meteorological data and readily accessible geographical maps. The model parameters were estimated from a Digital Elevation Model, soil and landuse maps, and only four parameters were calibrated for the sub basins. The results of both calibration and validation were compared on the basis of their performance with regards to objective criteria representing the Index of agreement, the Nash and Sutcliffe efficiency and the correlation coefficient. Analysis showed that monthly objective criteria values for both the sub basin were mostly more than daily as rainfall compiled for a longer period is more precise than for a shorter period of time. For the Kangsabati sub basin, the flow was well simulated by the model, following the trend of observed flows. However, the peaks of simulated flows were more than the observed flow due to the effect of storage structures in the upstream of gauging stations. However, simulated peaks well matched the peak in rainfall. Furthermore, for the Kumari sub basin, the Nash–Sutcliffe Efficiency was very less, i.e. 0.05 in the validation period and 0.32 during the calibration period as the observed mean flow was very less during the validation period due to the more amounts of abstractions. The findings imply that nonavailability of abstractions data as well as the storage

---

M. Debnath (✉) · A. Mishra  
Agricultural and Food Engineering Department, Indian Institute of Technology Kharagpur,  
Kharagpur 721302, West Bengal, India

M. Debnath  
Land and Water Management Division, ICAR-Research Complex for Eastern Region, Patna  
800014, India



capacity of structures built by local people, in the upstream part of gauging stations, poses great challenges to modeling of discharge in a river.

### 37.1 Introduction

The rising level of water abstraction from rivers has resulted in erroneous estimation of future water amount available at the downstream discharge point by models. According to the US data, more than 50% of irrigated water consists of surface water and 79% comprises for aquaculture. Water extraction due to increasing population and agricultural activities has alleviated the chances of increasing the number of rivers running dry (Postel et al. 2006). Water being a vital natural resource of a country, its accountability or auditing is as much necessary for proper allocation of water resources. This allows for the allocation on demand of water based on availability (Graff et al. 2014). Furthermore, the rate of the amount of water extracted for living purposes is heading the population growth and socio-economic development rate. This accounts for the fact that water resources especially surface water of a region are affected both by climate change as well as abstraction (Felfelani et al. 2017).

A basin hydrological model provides a tool for estimating the future discharge of a river and it includes relevant descriptions of dominant processes in particular geographical and climatological conditions. A number of such water resources models have been applied at basin scale by various institutions, e.g. PITMAN (Hughes et al. 2006), HYRRROM (Blackie et al. 1991) and CATCHMOD (Wilby et al. 1994). For these models, it is very much important for the models to replicate the basins' behavior accurately. Low model output reliability will prohibit the use of models linked to scenarios as it will not be the feasible way to predict changes in stream flow. If we fail to model the present, we fail to model the future. Ensuring that simulated stream flow accounts for anthropogenic changes besides spatial differences in physical and climatic characteristics in a basin poses a great challenge and a prerequisite for future model-based hydrological scenario assessments (Hughes et al. 2006).

India, being one of the developing countries of the world, comes across various socio-economic changes like development in irrigated agriculture and industries (Biemans et al. 2013). For the various developmental activities, a large amount of water is required which may have a profound impact on the water resources of India (Gupta and Deshpande 2004). India is life lined by three major rivers Indus, Ganga, Brahmaputra and its tributaries. Hence, understanding basin natural and anthropogenic characteristics and its replication for estimating future water demand is urgent. Parameterization, calibration and validation are the basic phenomena in comprehending the complex rainfall-runoff relationships owing to the tremendous spatial and temporal variability of watershed characteristics and precipitation patterns and to the number of variables involved in the modeling of the physical process (Kumar et al. 2005). Numerous studies have been conducted involving calibration and validation of models for simulation of various parameters including India (Brown

et al. 2013; Hancock et al. 2017; Roy et al. 2013; Loliyana and Patel 2015). However, few studies have been conducted with respect to water abstractions. Therefore, the objectives of the study were as follows: (i) to develop a conceptual lumped model HYSIM; (ii) to establish parameterisation, calibration and validation procedures that highlight the model performances at different spatial scales and (iii) to identify the domain and limitations for the model performance given only traditional data.

## 37.2 Materials and Methods

### 37.2.1 Model Description

The first version of the Hydrological Simulation Model (HYSIM) was developed by Ronald E. Manley in the year 1974. The model HYSIM has been built around two sub-routines; the first of these was HYDLGY, which performed the hydrological calculations, and the second, HYDLCS, which performed the hydraulic routing calculations (Manley 1973) (Fig. 37.1). In the hydrologic routine, the precipitation in the form of rainfall or snowfall was routed through the seven reservoirs (Manley 1973). In the hydraulic routine, the channel was divided into a number of lengths. In each of these, it was assumed that discharge is proportional to storage raised to the power of 1.5. The calculation of the constant of proportionality was based on channel dimensions and roughness. Simply routing the flow through such a series of reservoirs does not, however, account for the delay due to translation effects. This is handled by a consideration of the flow time of a kinematic wave, which was assumed to be a function of channel storage.

### 37.2.2 The Study Site

The river Kangsabati is a right bank tributary of the Bhagirathi (Hugli) river systems. It emanates from Jabarban peak on the Ghoramara hill. The hill is located on the east of the Chotanagpur Plateau at a latitude–longitude of 23° 32' 30" North and 85° 56' 30" East (Gope 2012). The Kangsabati basin is located in the eastern part of India and passes through the three drought-prone districts of West Bengal. Also, this river basin homes about 6 million inhabitants of these districts, most of whose livelihoods were directly dependent on the availability of water from the river for the production of food and various other activities like livestock production, industrial, domestic, etc.

The study area is located in the upper reaches of the river. It drains a total basin area of 3578.74 km<sup>2</sup>. Kumari River, a major tributary of Kangsabati River, joins at the upstream part of Kangsabati River. The Kangsabati reservoir is present at the confluence of these rivers. It is marked as the outlet of upstream reaches of the river

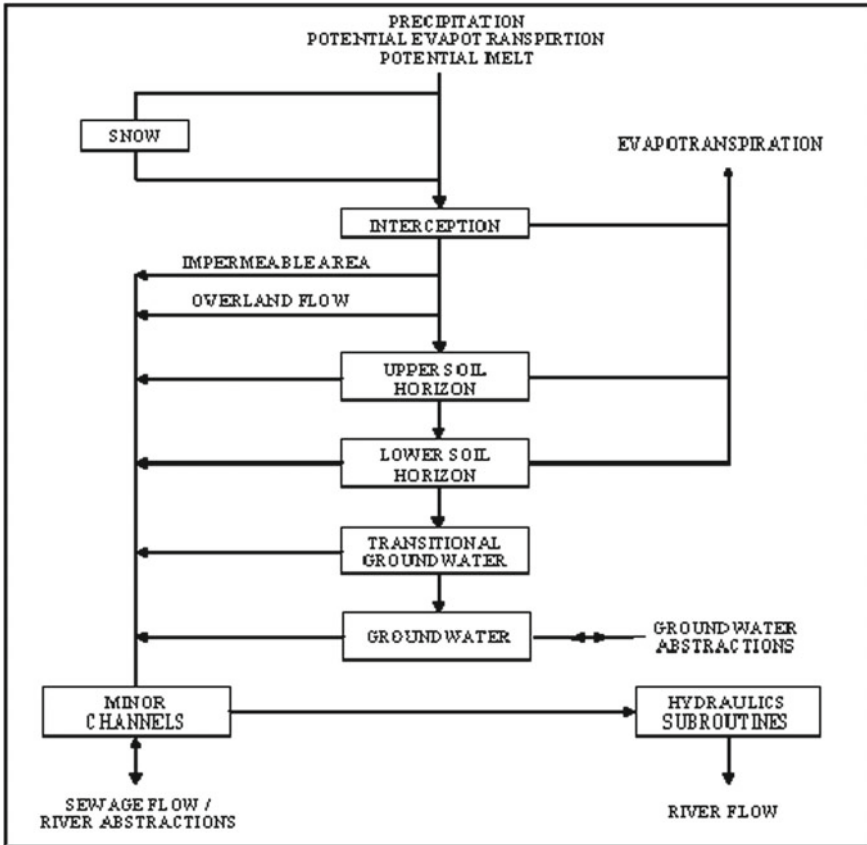


Fig. 37.1 Flow chart of HYSIM model (Murphy et al. 2006)

basin. The main river reach extends up to the Kangsabati reservoir having a length of 46.65 km. The Kumari River has a total length of 9.393 km. The whole river basin area is traditionally a drought-prone region with frequent floods due to heavy monsoon rainfall. The major part of the basin has laterite soils (Bhave et al. 2013). Agriculture is the main source of livelihood for the people residing in the basin. Major crops grown are rice, wheat, potato, oilseeds and sugarcane. Thus, the water required for irrigation is diverted from the rivers using several check dams including the Murguma dam in the upstream part of Kangsabati River. The upstream part of the Kangsabati reservoir had been divided into two sub basins; the Kangsabati sub basin has the main reach of Kangsabati River and has a total area of 1587.23 km<sup>2</sup>. The gauging stations present in the river are Simulia and Tusuma. Kumari sub basin has the Kumari river and comprises an area of 1991.52 km<sup>2</sup>. Rangagora and Khariduar were the rain gauge stations present in this basin (Fig. 37.2).

The daily precipitation data for the basin had been collected from the India Meteorological Department (IMD) for the seven stations (Table 37.1).

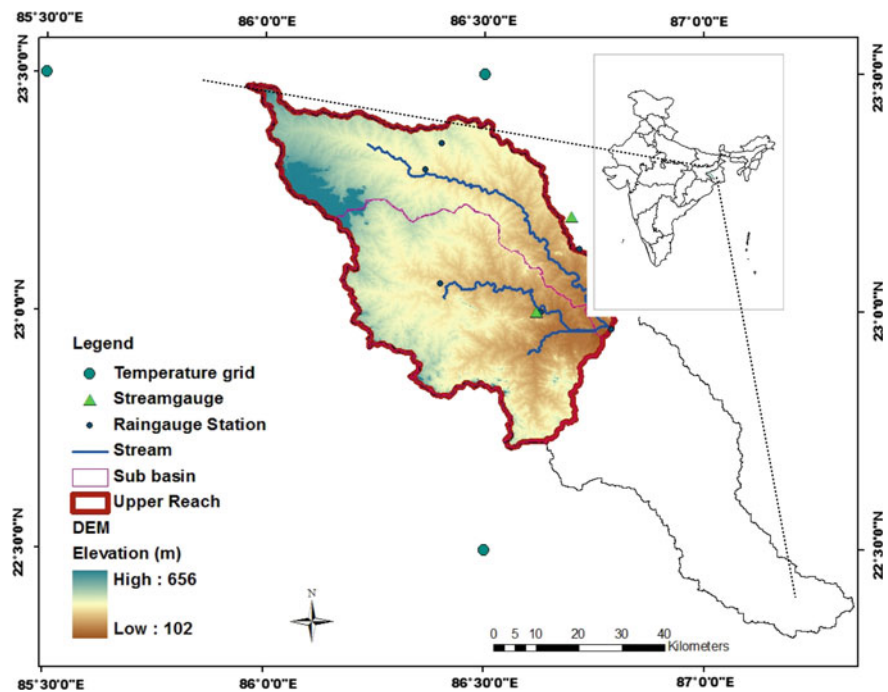


Fig. 37.2 Map of the study area: Upper reaches of Kangsabati River

Table 37.1 Data for rain gauge stations

Sub basin	Station name	Altitude (m)	Latitude	Longitude	Period of data	Time step
Kangsabati	Simulia	220.9	23° 18' 0''	86° 21' 36''	1/1/1986–31/12/2011	Daily
	Hatwara	255.4	23° 21' 0''	86° 24' 0''	1/1/1990–31/10/2007	
	Tusuma	163.3	23° 74' 8''	86° 42' 36''	1/1/1986–31/12/2011	
Kumari	Rangagora	197.8	23° 3' 36''	86° 24' 0''	1/1/1986–31/12/2011	
	Khariduar	152.4	23° 0' 0''	86° 37' 48''	1/1/1986–31/12/2010	
	Kangsabati dam	135	22° 57' 36''	86° 46' 48''	1/1/1986–31/12/2010	

The Thiessen weights for each station were input into the model to give the weighted mean rainfall of the basin. The Kangsabati river basin receives heavy monsoon rainfall from July to September along with dry summer months from March to May. The average annual rainfall in the Kangsabati basin is about 1400 mm (Bhave

et al. 2013). Daily maximum and minimum temperatures were available from the IMD for the three grids that were covering the basin. Potential evapotranspiration was calculated using the Hargreaves equation in the DSS\_ET model (Bandyopadhyay et al. 2012). Weighted PET for the basin was calculated for the period 1996–2005. The stream gauge data has been collected from Central Water Commission (CWC) and Irrigation Waterways Department for the two stream gauge stations that were Tusuma for the Kangsabati sub basin and Khariduar for the Kumari sub basin. The data was available for the period 1991–2010.

### 37.2.3 Model Parameterisation, Calibration and Validation Procedures

#### 37.2.3.1 The Field Assessed Parameters

Geographical Information Systems (GIS) had been used for model parameterization. This can be classified into three types of parameters. They were (1) the parameters calculated from DEM. In addition to the delineation of sub basin of the channel network reaches, this step insured the determination of the geometric characteristics of sub basin and reaches. Hydraulic parameters were derived from DEM; (2) the parameters calculated from processed soil map (Fig. 37.3). Each classes of soil within the basin were examined and the proportions of each soil type within the basin were considered. Calculating the area under each soil class, the weighted soil parameter (pore size distribution index, porosity, bubbling pressure) was calculated; (3) parameters related to vegetation and landuse (interception storage, interception factor, impermeable portion, rooting depth) were derived from the landuse/land cover map (Fig. 37.4). Again the areas under each class were calculated and weighted parameters were input into the model.

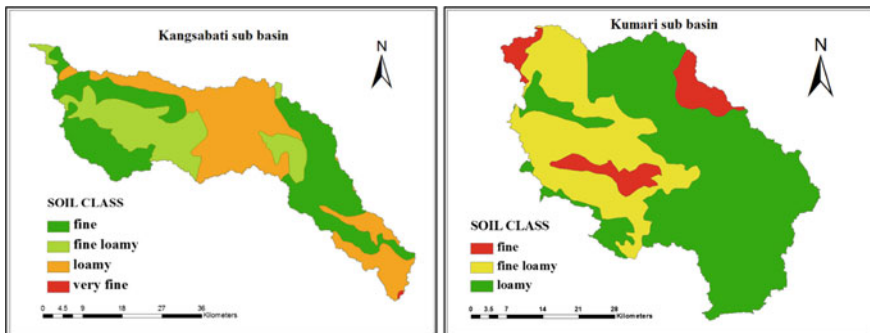


Fig. 37.3 Soil map of sub basins of upper reaches of Kangsabati River

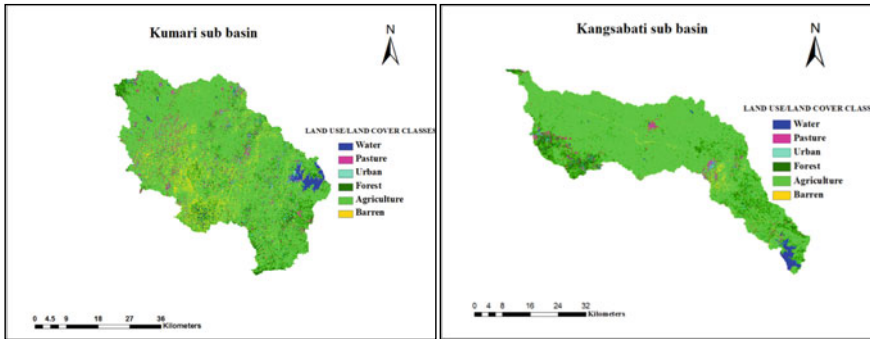


Fig. 37.4 Landuse/land cover map of sub basins of upper reaches of Kangsabati River

### 37.2.3.2 The Calibrated Parameters

The parameters that were to be calibrated concern the main hydrological processes. It included the saturated permeability at the horizon ( $SP_h$ ) and at the base of the lower horizon boundary ( $SP_l$ ) having a range from 5 to 200 and 1 to 100, respectively; interflow runoff at upper ( $I_u$ ) and lower horizon ( $I_l$ ) whose range were not available.

### 37.2.3.3 Calibration and Validation Procedures

The procedure of calibration was performed to estimate values for the process parameters. The model was calibrated for 5 years that was from January 1996 to December 2000. Within HYSIM calibration was catered for by a multi-parameter optimization procedure, in which several parameters were changed, using an optimization algorithm, in order to find the best value of an objective function. HYSIM employed the Rosenbrock method, a local search algorithm (Murphy et al. 2004).

After calibration, the optimized parameter sets needed to be validated using another independent set of observed data. Proper validation of the calibrated model was essential to understand its performance without any change in the parameter file. The model was validated for again 5 years period that is from January 2001 to December 2005 for the two sub basins.

### 37.2.4 Model Performance Criteria

Performance criteria of the model were determined by pairwise comparison of model simulated or predicted values with the observed values. Both graphical and statistical methods were used to compare the simulated and observed runoff values. The statistical indicators described below were used in this study for model calibration and validation.

i. Correlation coefficient

$$r = \frac{\sum_{i=1}^N [(P_i - P_{avg})(O_i - O_{avg})]}{\sqrt{[\sum_{i=1}^N (P_i - P_{avg})^2] [\sum_{i=1}^N (O_i - O_{avg})^2]}}$$

The correlation coefficient represents the degree of linear association between observed and predicted values. Its value lies between  $-1$  and  $1$ , with  $r = 1$  indicating perfect linear correlation.

ii. The Nash–Sutcliffe model efficiency coefficient:

$$E = 1 - \frac{\sum_{i=1}^N (O_i - P_i)^2}{\sum_{i=1}^N (O_i - O_{avg})^2}$$

The Nash–Sutcliffe model efficiency coefficient value may vary from  $-∞$  to  $1$ , with  $1$  indicating a perfect fit. It represents an improvement over  $r^2$  for model evaluation as it is sensitive to the differences in the observed and model simulated means and variances.

iii. Index of Agreement:

$$d = 1 - \frac{\sum_{i=1}^N (O_i - P_i)^2}{\sum_{i=1}^N [ |P_i - O_{avg}| + |O_i - O_{avg}| ]^2}$$

The index of agreement varies between  $0.0$  and  $1.0$  with higher values indicating better agreement between the model and observations. The index of agreement is also sensitive to extreme values.

### 37.3 Results and Discussion

The model was calibrated and validated to simulate the daily flow from the Kangsabati and Kumari sub basin for five years period that was from 1996 to 2000 and from 2001 to 2005, respectively (Table 37.2). Table 37.3 provides the HYSIM model performance criteria for the Kangsabati river.

**Table 37.2** Calibrated parameters of each sub basin

Sub basin	Saturated permeability at horizon boundary (mm/hr)	Saturated permeability at the base of the lower horizon (mm/hr)	Interflow runoff from the upper horizon at saturation (mm)	Interflow runoff from the lower horizon at saturation (mm)
Kangsabati	141.612	27.176	20.671	3.197
Kumari	59.149	39.826	7.941	7.577

**Table 37.3** Performance results for the calibration and validation steps for the sub basins

Step	Period	Criteria		Station	
				Kangsabati	Kumari
Calibration	1996–2000	IOA	Daily	0.85	0.79
			Monthly	0.91	0.70
		NS	Daily	0.46	0.35
			Monthly	0.60	0.34
		R	Daily	0.75	0.65
			Monthly	0.90	0.59
Validation	2001–2005	IOA	Daily	0.82	0.71
			Monthly	0.95	0.63
		NS	Daily	0.44	0.05
			Monthly	0.80	0.42
		R	Daily	0.70	0.56
			Monthly	0.91	0.81

The daily flows for the Kangsabati sub basin were well simulated by the model following the trend of observed flows but only at some points, the peaks of simulated flows are more than the observed flow (Fig. 37.5). This can be due to the presence of the Murguma dam, a small dam in the upstream part of the gauging station of the Kangsabati reservoir, and dams reduce the peak discharges of observed flow (Graf 2006). The dam inflow-outflow data have not been input into the model due to which the simulated flow is somewhat more than the observed flow. However, the peak of simulated flow matched almost all the time with rainfall peak thereby suggesting a good rainfall-runoff relationship in the Kangsabati sub basin by the model except in some cases. In the Kumari river, the simulated flow varies most of the time with the observed flow; this is due to the downstream effect of various small storage structures that were present in the Kumari river. It is also found that the observed flow trend varies from the rainfall trend whereas the simulated flow follows the rainfall trend almost all the time. Thus, the presence of these structures in the Kumari river upstream to the gauging station alters the timing of high and low flows in the basin. Storage structures in the river, for water abstraction, are responsible for substantially decreasing the wet season flows and increasing the dry season flows (Andersson et al. 2006). This is the reason for which the simulated is more than the observed flow during the monsoon months. The dam restricts the natural flow of water to its outlet. The amount of water that is stored in the upstream part resulted in less observed flow at its outlet. Again during the non-monsoon months, the observed flow is more than the simulated flow. A prominent sudden rise in the observed flow at the end of the year 1999 suggests that there is a release of water from the dam as there was no comparatively prominent effective rainfall during that part of the year.

The validation result of the sub basin with the calibrated parameters showed that during the validation period, the Kangsabati sub basin simulated better than the



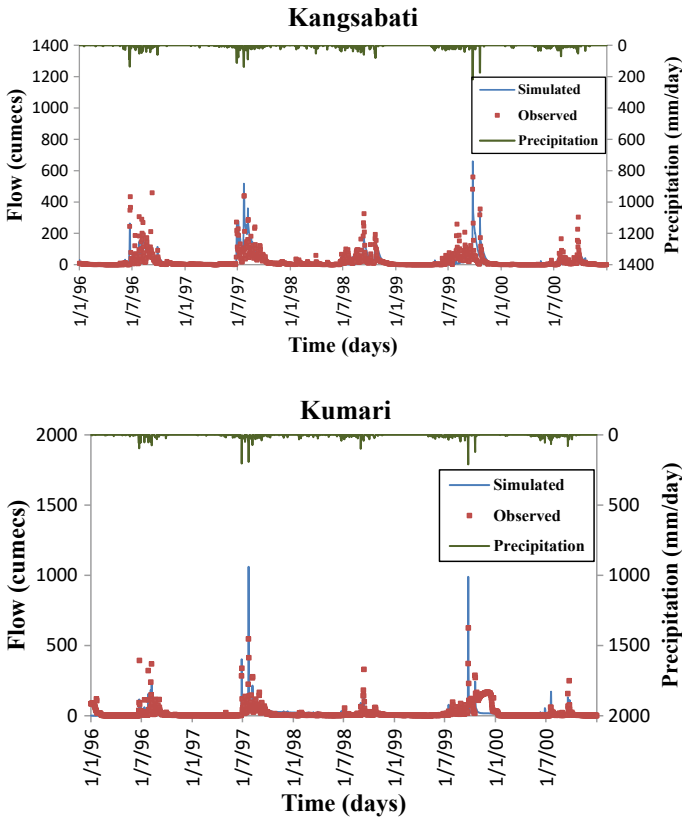


Fig. 37.5 Observed versus simulated flow for the sub basins during the calibration period

Kumari sub basin (Fig. 37.6). It is seen that inspite of heavy rainfall, the observed flow shows a lesser peak than the peak during the light rainfall. From this, it can be inferred that due to the presence of storage structures, the observed and simulated peak discharges vary though the trend is the same. For the Kumari basin around the year 2002, many small check dams were made which were as well not modeled in HYSIM which resulted in much flow lag in the validation period which was from 2001 to 2005. The flow lag is very much visible at the end of 2003 and the beginning of 2004. Therefore, with the same calibrating parameters, the mean of simulated flow calculated by the model was much less during the validation period as compared to the calibration period.

The overall results showed that monthly Nash–Sutcliffe Efficiencies gave a better value than daily as runoff compiled for a longer period was more precise than for a shorter period of time. For the Kangsabati sub basin, the efficiency for the calibration period for monthly, i.e. 0.60 is lower than the validation period 0.79 which may be due to lag in observed flows during the calibration period. The Index of agreement values for daily as well as monthly flows were greater than 0.80 in both calibration

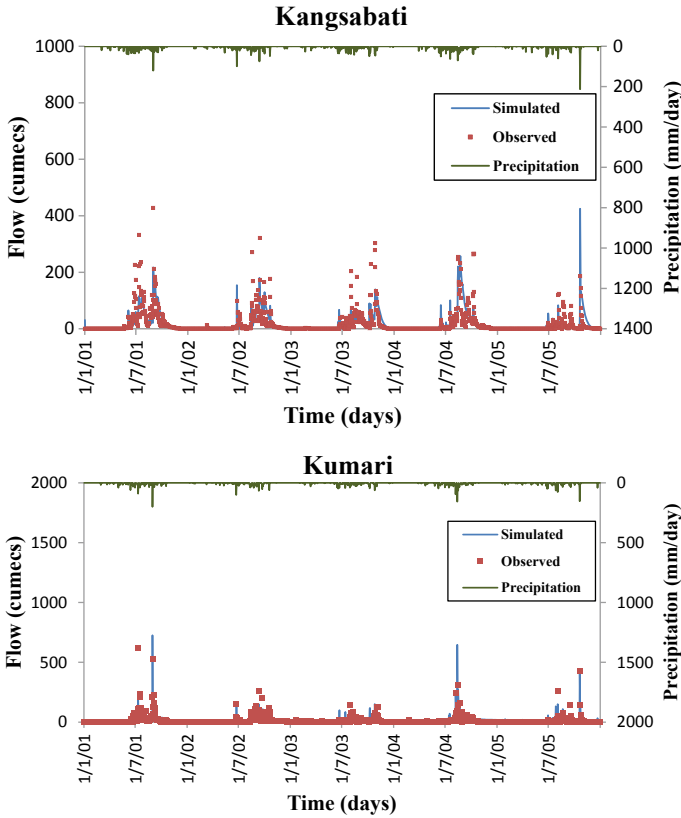


Fig. 37.6 Observed versus simulated flow for the sub basins during the validation period

and validation periods which suggests that there was a good agreement between the observed as well as simulated flows thereby suggesting that the flow prediction performance of the model was satisfactory. For the Kumari sub basin, the Nash–Sutcliffe Efficiency was very less, i.e. 0.05 in the validation period than the 0.32 during the calibration period as the observed mean flow was very less during the validation period due to the more amounts of abstractions. The index of agreement for daily flows was found to be 0.82 during the calibration period and 0.71 in the validation period whereas in monthly flows, it was 0.95 and 0.63, respectively.

### 37.4 Conclusions

HYSIM is a conceptual lumped hydrological water resources model that has been developed and applied to the upper reaches of Kangsabati reservoir by three procedures; parameterization, calibration and validation procedures. The calibration of the

HYSIM model for the upper reaches of the Kangsabati river basin showed that the model simulated the monthly flow more satisfactorily than the daily flows for both the sub basins except during the validation period of the Kumari sub basin showing that runoff calculated for longer time period was more accurate than calculated for a shorter time period. The study also found that the stream flow calculated by the model was more compared to the observed value most of the time. Regulated flow from the various storage structures resulted in such variance in river flows, as the stored water data for extraction purposes by the localities were not available. Thus, the presence of local reservoirs or storage structures in a river poses a great challenge in calibration and validation procedures if restricted information of upstream structures is available.

**Acknowledgements** The authors would like to thank Dr. Ajay Bhawe, Post Doc Research Fellow, University of Leeds, UK, for assisting in manuscript review.

## References

- Andersson L, Wilk J, Todd MC, Hughes DA, Earle A, Kniveton D, Layberry R, Savenije HHG (2006) Impact of climate change and development scenarios on flow patterns in the Okavango River. *J Hydrol* 331:43–45
- Bandyopadhyay A, Bhadra A, Swarnakar RK, Raghuvanshi NS, Singh R (2012) Estimation of reference evapotranspiration using a user-friendly decision support system: DSS\_ET. *Agric for Meteorol* 154–155:19–29
- Bhawe AG, Mishra A, Raghuvanshi NS (2013) A combined bottom-up and top-down approach for assessment of climate change adaptation options. *J Hydrol* 1–12
- Biemans H, Spleeman LH, Ludwig F, Wiltshire AJ, Kumar P (2013) Future water resources for food production in five South Asian river basins and potential for adaptation—a modeling study. *Sci Total Environ* 1–15
- Blackie JR, Hughes C, Simpson TKM (1991) Derivation of theoretical flows for the Colliford Reservoir Model. Institute of Hydrology
- Brown RA, Skaggs RW, Hunt III WF (2013) Calibration and validation of DRAINMOD to model bioretention hydrology. *J Hydrol* 486:430–442
- De Graaf IEM, Van Beek LPH, Wada Y, Bierkens MFP (2014) Dynamic attribution of global water demand to surface water and groundwater resources: Effects of abstractions and return flows on river discharges. *Adv in Water Resour* 64:21–33
- Felfelani F, Wada Y, Longuevergne L, Pokhrel YN (2017) Natural and human-induced terrestrial water storage change: a global analysis using hydrological models and GRACE. *J Hydrol* 553:105–118
- Gope A (2012) The dreams and realities of Kangsabati command area, West Bengal. *Geo-Analyst* 2(2):107–117
- Graf WL (2006) Downstream hydrologic and geomorphic effects of large dams on American rivers. *Geomorphology* 79:336–360
- Gupta SK, Deshpande RD (2004) Water for India in 2050: first order assessment of available options. *Curr Sci* 86(9):1216–1224
- Hancock GR, Webb AA, Turner L (2017) Sediment transport in forested head water catchments—calibration and validation of a soil erosion and landscape evolution model. *J Hydrol* 554:12–23
- Hughes DA, Andersson L, Wilk J, Savenije HHG (2006) Regional calibration of the Pitman model for the Okavango River. *J Hydrol*

- Kumar R, Singh RD, Sarmah KD (2005) Water resources of India. *Curr Sci* 89:794–811
- Loliyana VD, Patel PL (2015) Lumped conceptual hydrological model for Purna river basin, India. *Sadhana* 40(8):2411–2428
- Manley R (1973) A hydrological model with physically realistic parameters. 154–161
- Murphy C, Charlton R, Sweeney J, Fealy R (2004) Catering for uncertainty in a conceptual rainfall runoff model: model preparation for climate change impact assessment and the application of glue using latin hypercube sampling. *Natl Hydrol Semin* 64–74
- Murphy C, Fealy R, Charlton R, Sweeney J (2006) The reliability of an ‘off-the-shelf’ conceptual rainfall runoff model for use in climate impact assessment: uncertainty quantification using Latin hypercube sampling. *Area* 38(1):65–78
- Postel SL (2006) For our thirsty world, efficiency or else. *Sci* 313(5790):1046–1047
- Roy D, Begam S, Ghosh S, Jana S (2013) Calibration and validation of HEC-HMS model for a river basin in Eastern India. *ARPN J Eng Appl Sci* 8(1):33–49
- Wilby RL, Greenfield B, Glenny C (1994) A coupled synoptic-hydrological model for climate change impact assessment. *J Hydrol* 153:265–329

# Chapter 38

## Assessment of Agricultural Drought Vulnerability Using Remote Sensing and GIS: A Case Study of Lower Cauvery Basin, Tamil Nadu, India



**Ramanarayan Sankriti, Saravanan Subbarayan, Manjunath Aluru, Leelambar Singh, Jacinth Jennifer J, and Devanantham Abijith**

**Abstract** MODIS satellite provides many data products, including MOD11A2 and MOD13Q1, for the assessment of agricultural drought in a region. This study area of the lower Cauvery basin of Tamil Nadu was affected by agricultural drought as a result of scanty rainfall in the period 2010–2015. To assess the drought condition in the study area over nearly six years (2010–2015), certain drought indices are used. These include the Normalised Difference Vegetation Index (NDVI) from MOD13Q1 data product and seasonal Land Surface Temperature (LST) from MOD11A2 data product. After calculation of NDVI and LST, three other indices were derived: Vegetation Condition Index (VCI), Temperature Condition Index (TCI), and Vegetation Health Index (VHI). The spatial variation in VHI was also analysed. From the study, a significant relationship was observed between NDVI and LST—decreasing NDVI and increasing surface temperature. Results show that nearly one-third of the lower Cauvery basin was affected by mid to severe drought. During the dry season (February to May), the severity of drought has increased both in terms of intensity and extent towards the north.

### 38.1 Introduction

Drought is a natural hazard that affects a significant proportion of population in the world. Considering the aftermath of drought and its widespread nature, it is important to make an assessment of the severity of drought. Drought is defined as an extreme

---

R. Sankriti (✉) · S. Subbarayan  
Department of Civil Engineering, National Institute of Technology, Tiruchirappalli, Tamil Nadu  
620015, India

S. Subbarayan  
e-mail: [ssaravanan@nitt.edu](mailto:ssaravanan@nitt.edu)

M. Aluru · L. Singh · J. J. J. D. Abijith  
Department of Civil Engineering, MVSR Engineering College, Nadargul, Hyderabad, Andhra  
Pradesh 501510, India

weather event characterised by an extended period of dry weather in a region where scarcity of water exists. Drought occurs in four temporal stages, viz., meteorological/climatological, agricultural, hydrological and socio-economic in the same order (Wilhite and Glantz 1985). Meteorological/climatological drought is characterised by precipitation deficiency which in turn causes soil moisture deficiency (agricultural drought). As a result of reduced stream flow and inflow into the reservoir, hydrological drought occurs. Due to excessive demand than supply of products that require water for production and thereby resulting in loss of income in food industry, socio-economic drought arises. Based on the type of drought, certain drought indices are employed for the assessment of drought in a region. Patel et al. (2009) and Chen et al. (2011) suggested the use of Temperature Vegetation Dryness Index (TVDI) derived from MODIS data to give information on soil moisture status in the study areas of Western UP, India and Huang-huai-hai plain, China, respectively. Tran et al. studied the monitoring of drought using various multispectral indices, including the Vegetation Health Index, in a study area of south coastal Vietnam by using the MODIS and Landsat data. Dalezios et al. (2012) used NOAA-AVHRR data to find the Reconnaissance Drought Index (RDI) to quantify drought in the Thessaly region of Greece. Palchaudhuri et al. (2016) showed how an analytic hierarchy process (AHP) can be combined with GIS to provide an assessment of risk for drought condition in Puruliya district, India. Parinaz et al. (2012) applied the concept of improved TVDI (iTVDI), Temperature Vegetation Dryness Index (TVDI) and Vegetation Dryness Index (VDI) to monitor vegetation and soil water stress by using AVHRR data in semi-arid regions of Iran. Ghulam et al. (2007) proposed how Modified Perpendicular Drought Index (MPDI) can be used as a method of drought monitoring in real-time for the study area of Shunyi district in China using MODIS data and data of Landsat ETM+. Tadesse et al. (2017) developed Veg-DRI (Drought Response Index) models for the Canada Prairie region using MODIS data and AVHRR data. Moon et al. 2004 used Leaf Area Index (LAI) in place of NDVI to calculate the TVDI in the study of evaluation of soil moisture status of the Western basin of South Korea, using MODIS data. Soil moisture status for entire China was also evaluated using the TVDI by Wang et al. Finally, Zargar et al. (2011) performed the review of different drought indices to be evaluated at different stages of drought, viz., meteorological drought, agricultural drought and hydrological drought. Thus, this study focuses on the usage of MODIS data for this study area of the lower Cauvery basin to assess the drought condition with the concept of VCI, TCI and VHI.

## 38.2 Study Area

Lower Cauvery river basin is located in the central portion of Tamil Nadu state in Southern India with spatial extent between longitudes  $76^{\circ}18'48''$  and  $79^{\circ}51'16''$  E and latitudes  $10^{\circ}8'10''$  and  $12^{\circ}42'35''$  N, covering approximately 47,483 sq km (Fig. 38.1). This region is characterised by a typical tropical hot and humid climate with a distinctive monsoon summer wet season (May–September) and a dry season

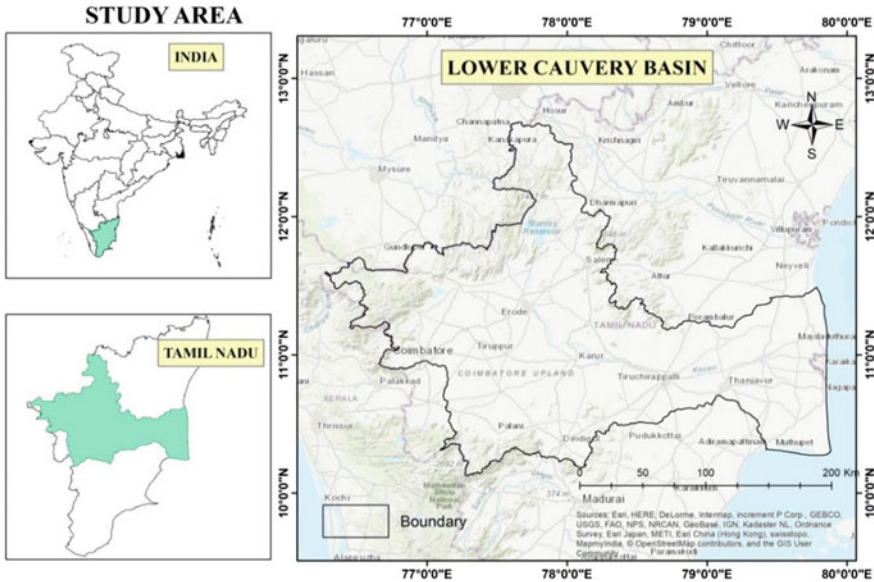


Fig. 38.1 Map showing lower Cauvery basin in Tamil Nadu

(February–April). During summer months, the Southwest Monsoon brings moisture to India from the southwest, traversing the Deccan plateau through the Utkal coast, and then moves north-west. The lithology of the basin is made up of metamorphic and igneous rocks although sedimentary rocks are exposed on the eastern side. The delta is the most fertile area in the basin and comprises alluvial soil. The major soil types existing in the basin are red soils, black soils, laterite soil, alluvium, forest soils and mixed soils. Red soils cover most of the areas in the basin. Also, in the basin exists a particular special kind of forest with well-defined species of flora and fauna and comprises many national parks and sanctuaries. Average population density in the basin is nearly 350 people per sq. km higher than the global average. Important urban centres of the past were Thanjavur and Madurai and the important urban centre of today is Tiruchirappalli. Rice is the principal crop cultivated in this basin. Major commercial crops are groundnut, sugarcane and cotton. Some other important food grain crops are bajra, jowar and pulses. The cultivable area in the basin is nearly 3.2 million hectares, which is 2% of the total cultivable area of the country.

### 38.3 Methodology

Vulnerability is the diminished ability of an entity to cope up with the hazard. Drought assessment is needed in order to take necessary steps to mitigate the hazard before it actually becomes a disaster. In this study, an effort is made to assess the drought

condition affecting crops in the lower Cauvery river basin of Tamil Nadu, India. An attempt is made to address the agricultural drought with the help of agricultural drought indices. The four parameters to determine vulnerability index signifying crop health and cover are the vegetation indices like NDVI (Rouse et al. 1974), Vegetation Condition Index (VCI), Temperature Condition Index (TCI) and Vegetation Health Index (VHI). MODIS data product MOD11A2 is used for deriving land surface temperature (LST) maps. NDVI maps are derived from MODIS data product MOD13Q1. Time-series analysis of NDVI and LST would reveal VCI and TCI, respectively. The VHI was estimated with the help of the two indices Vegetation condition Index(VCI) and Temperature condition Index (TCI). Vegetation Health Index (VHI) is given by the Equation 38.1:

$$VHI = a(VCI) + (1 - a)TCI \quad (38.1)$$

where 'a' is a value between 0–1. In this study, the value of 'a' is taken to be 0.5, indicating that thermal condition and moisture condition have equal weightage in the assessment of agricultural drought in this region. The index related to moisture condition is Vegetation condition Index (VCI) is given by Equation 38.2 and the index related to thermal condition is Temperature condition Index (TCI) and is given by the Equation 38.3, depicts the methodology in assessment of agricultural in the study area.

The equations of VCI and TCI are shown as follows (Table 38.1).

$$VCI = 100X \frac{NDVI_{max} - NDVI}{NDVI_{max} - NDVI_{min}} \quad (38.2)$$

$$TCI = 100X \frac{LST_{max} - LST}{LST_{max} - LST_{min}} \quad (38.3)$$

## 38.4 Results and Discussion

Spatial distribution of drought severity was constructed. The spatial relationships between LST and NDVI are depicted in Figs. 38.3 and 38.4. The spatial distribution of the Vegetation Condition Index, Temperature Condition Index and Vegetation Health Index is depicted in Figs. 38.5, 38.6 and 38.7 respectively. Overall, it was observed that LST and NDVI possessed a significant negative relationship with each other (see Figs. 38.8 and 38.9). This result is likely because the lower Cauvery basin is located at lower latitude (10° N) where the climate is hot and humid. Also, the monthly variation of mean NDVI, mean LST, mean VCI, mean TCI and mean VHI are plotted with time factor for the years 2010–2015. At the time of the dry season, the density of vegetation reduced, and the value of temperatures was very high, and at the time of the mid-dry season, the high proportion of the area had surface temperatures



**Fig. 38.2** Flowchart illustrating the methodology

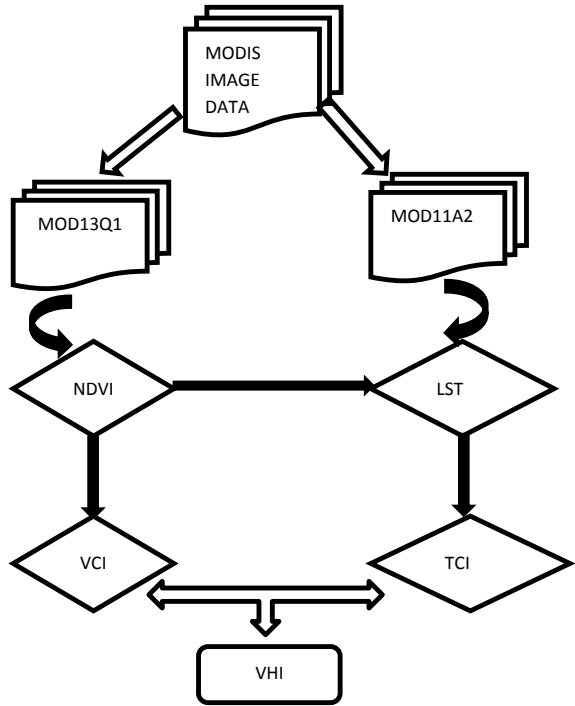


**Table 38.1** Categorisation of drought severity based upon values of VHI (Kogan 1995; Le Hung and Hoai 2015)

S. No	Value of VHI	Drought severity
1	0–10	Extreme
2	10–20	Severe
3	20–30	Moderate
4	30–40	Mid
5	>40	Nil

greater than 32 °C (red color). During the wet season, the density of vegetation was high, the surface temperature was low, but varied. Figure 38.9 describes the plot between monthly mean NDVI, LST, VCI, TCI and VHI and time factor, respectively. Figure 38.8 shows the spatial distribution of VHI for the dry year 2013.

### 38.5 Conclusion

From the spatial distribution maps, it can be inferred that the western and central regions of the study area in the rainfall deficient year 2011 are under stress, whereas the deltaic region in the east is not under the influence of drought conditions. The

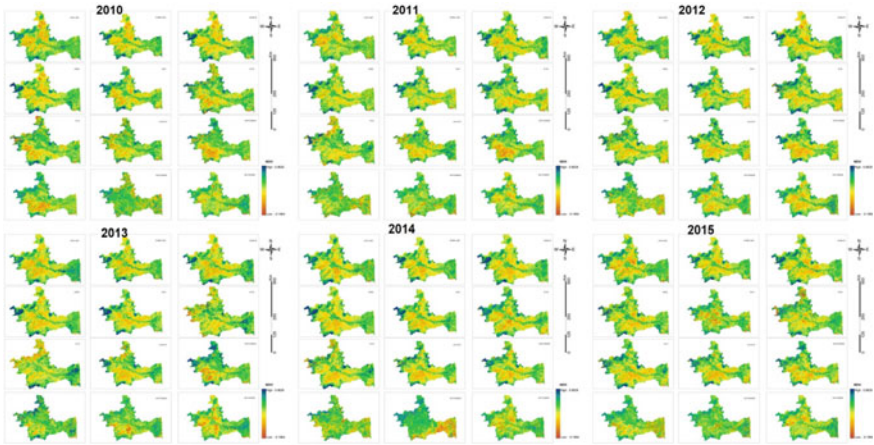


Fig. 38.3 NDVI images of study area of each month from 2010 to 2015

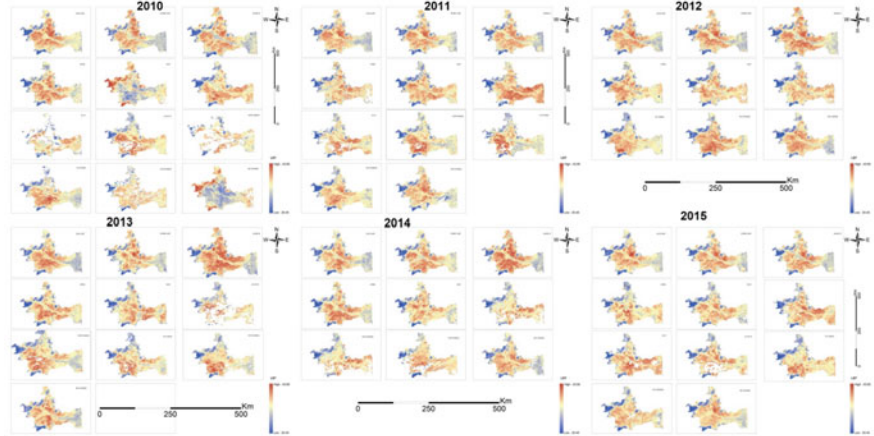


Fig. 38.4 LST images of study area of each month from 2010 to 2015

graphs show an inverse relationship between LST and NDVI for the different years. Relatively less NDVI is characterised by relatively high LST and vice versa. The year 2010 was a relatively wet year when compared to subsequent years of 2011, 2012 and 2013 with less rainfall, and which show stress in vegetation as seen in spatially distributed maps. The study also concludes that MODIS data offers freely available data at suitable resolution of 250 m which enable to conduct effective drought survey over large areas using drought indicators such as the VHI, TCI and VCI.

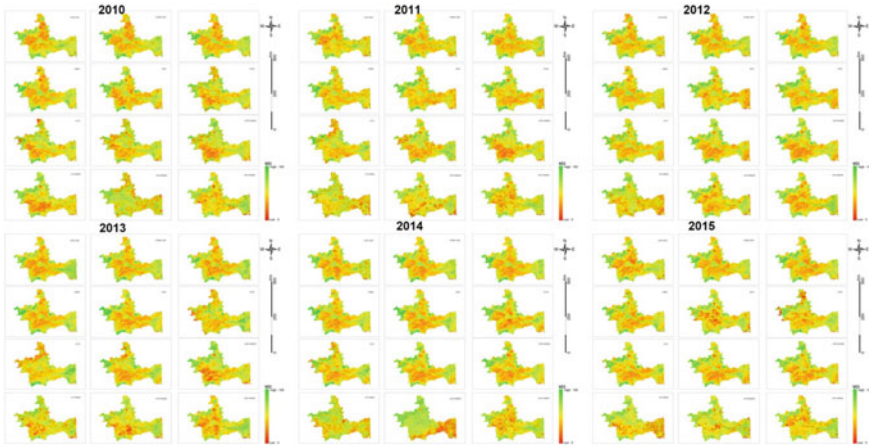


Fig. 38.5 VCI images of study area of each month from 2010 to 2015

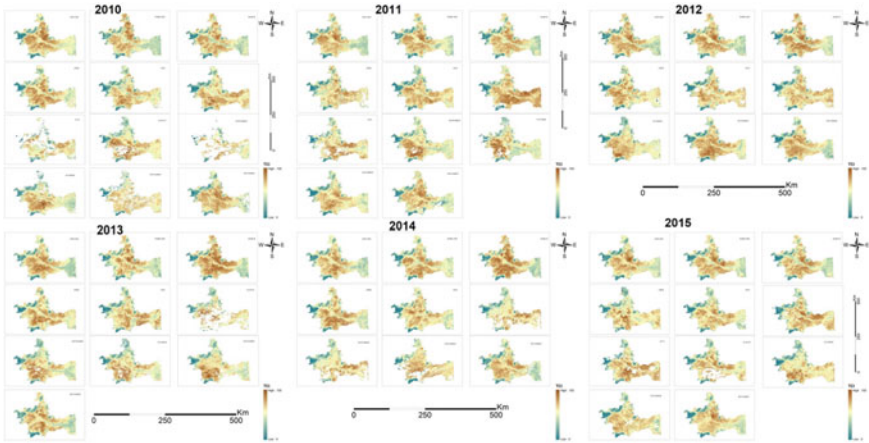


Fig. 38.6 TCI images of study area of each month from 2010 to 2015

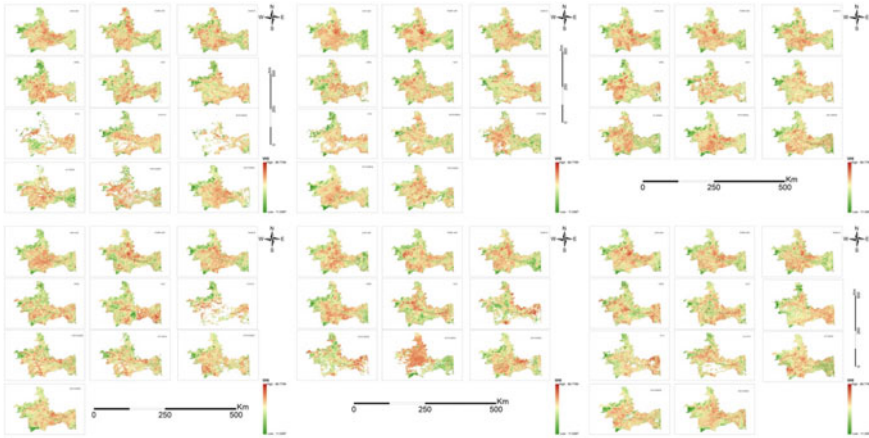


Fig. 38.7 VHI images of study area of each month from 2010 to 2015

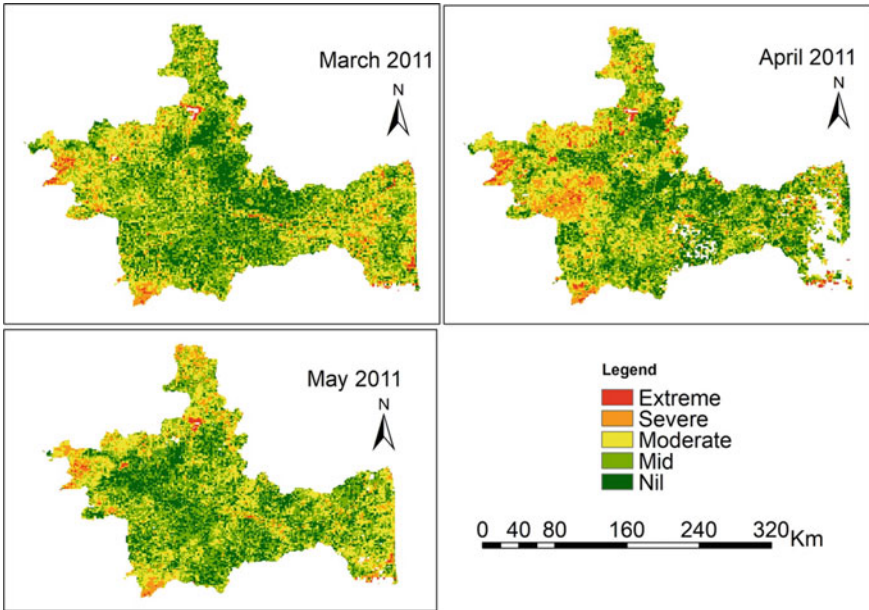


Fig. 38.8 Maps showing VHI for March, April and May for the year 2011

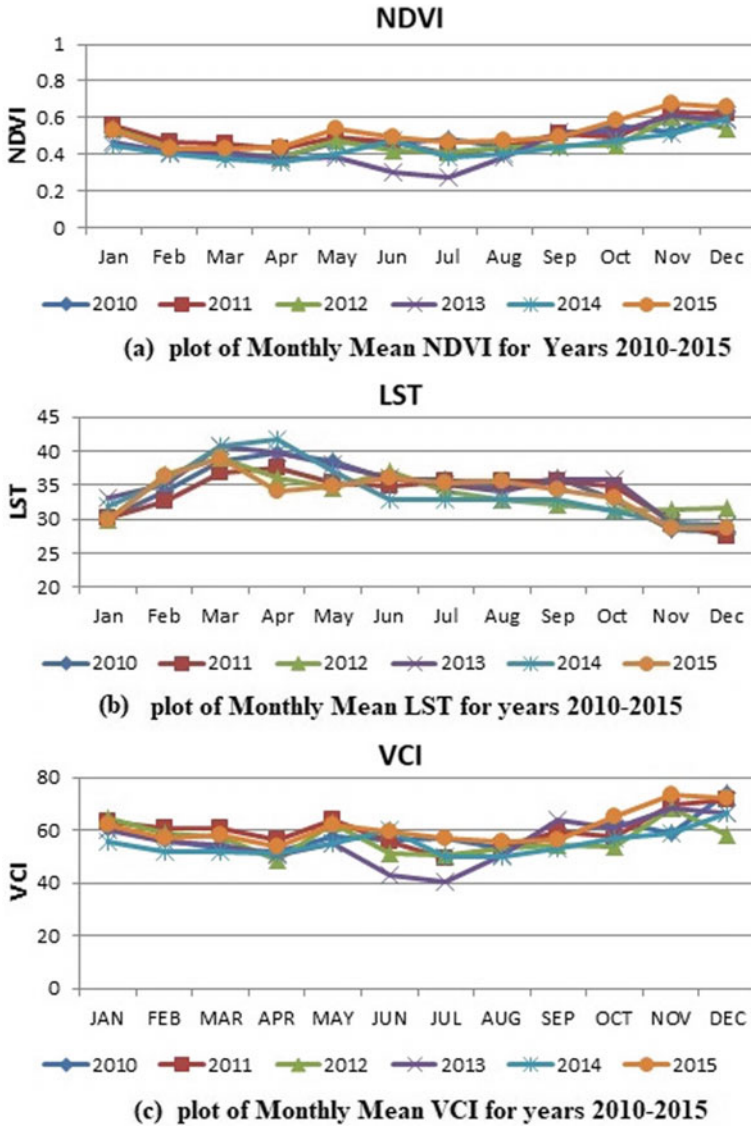
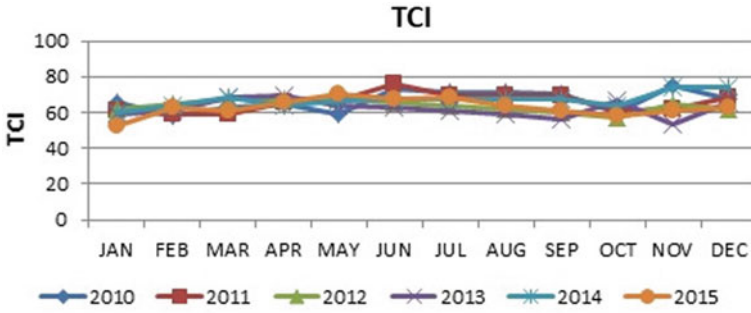
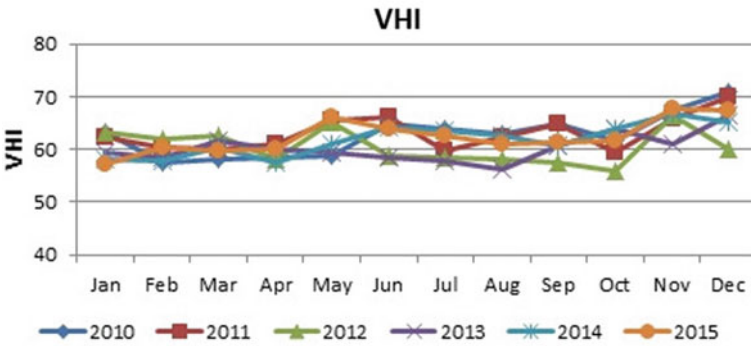


Fig. 38.9 Plot showing the monthly mean drought indices and time factor



(d) plot of Monthly Mean TCI for years



(e) plot of Monthly Mean VHI for years 2010-2015

Fig. 38.9 (continued)

## References

- Chen J, Wang C, Jiang H, Mao L, Yu Z (2011) Estimating soil moisture using temperature-vegetation dryness index (TVDI) in the Huang-huai-hai (HHH) plain. *Int J Remote Sens* 32(4):1165–1177
- Dalezios NR, Blanta A, Spyropoulos NV (2012) Assessment of remotely sensed drought features in vulnerable agriculture. *Nat Hazard Earth Syst Sci* 12(10):3139–3150
- Ghulam A, Qin Q, Teyip T, Li ZL (2007) Modified perpendicular drought index (MPDI): a real-time drought monitoring method. *ISPRS J Photogramm Remote Sens* 62(2):150–164
- Hung LT, Hoai DK (2015) drought risk evaluation using remote sensing: a case study in BacBinh District, BinhThuan Province. *Sci J Ho Chi Minh Educ Univ* 5
- Kogan FN (1995) Droughts of the late 1980s in the United States as derived from NOAA polar-orbiting satellite data. *Bull Am Meteor Soc* 76(5):655–668
- Palchaudhuri M, Biswas S (2016) Application of AHP with GIS in drought risk assessment for Puruliya district. *Ind Nat Hazards* 84(3):1905–1920
- Patel NR, Anapashsha R, Kumar S, Saha SK, Dadhwal VK (2009) Assessing potential of MODIS derived temperature/vegetation condition index (TVDI) to infer soil moisture status. *Int J Remote Sens* 30(1):23–39
- Rouse JW, Haas RH, Schell JA, & Deering DW (1974) Monitoring vegetation systems in the Great Plains with ERTS. *NASA special publication*, 351(1974):309
- Tadesse T, Champagne C, Wardlow BD, Hadwen TA, Brown JF, Demisse GB, ... Davidson AM (2017). Building the vegetation drought response index for Canada (VegDRI-Canada) to monitor agricultural drought: first results. *GISci Remote Sens* 54(2):230–257
- Wilhite DA, Glantz MH (1985) Understanding: the drought phenomenon: the role of definitions. *Water Int* 10(3):111–120
- Zargar A, Sadiq R, Naser B, Khan FI (2011) A review of drought indices. *Environ Rev* 19(NA):333–349



## Chapter 39

# Assessment of Impact of Spatial Distribution of Rainfall on Streamflow Modelling Using Arcswat in the Noyyal River Catchment Tamil Nadu, India



Leelambar Singh, Saravanan Subbarayan, J. Jacinth Jennifer, D. Abhijith, and Ramanarayan Sankriti

**Abstract** The potential impact studies of climate change on resources of water is a major concern for water experts, water managers and policymakers. Hydrological models play an important role in understanding and managing surface water resources. In this study, an urbanised watershed Noyyal is taken for streamflow simulation for the uncertainties in the input rainfall. Accurate streamflow model simulation is very useful for forecasting, planning and managing water resources. Currently, satellite-based precipitation product is more popular instead of ground-based data. Rainfall is more important, and principal inputs for precise runoff simulation and the spatial distribution of rainfall strongly affect the runoff hydrograph time and its peak amount. To assess the streamflow prediction tropical rainfall measuring mission (TRMM) 3B42 product was used. In this present study, the Soil and Water Assessment Tool (SWAT) semi-distributed model was applied and tested to evaluate its ability to reproduce these processes in a small watershed on water, sediment and agricultural produce. The coefficient of determination ( $R^2$ ) and Nash Sutcliffe efficiency (NSE) for calibration and validation are 0.53, 0.51 and 0.54, 0.50, respectively.

## 39.1 Introduction

Water is a divine source in the form of precipitation on the earth and plays a vital role in the hydrological process, which transports water from the ocean to land and back again. Water in the form of rainfall is significant to maintain the hydrological cycle components, which affect ecological, agricultural and economic development. Both spatial and temporal resolution of precipitation data is mutually related and significantly impact surface hydrology (Michaelides et al. 2009). Water quantity and quality are an index of amount and intensity produced by watershed. Mostly, the main aim of watershed resources is for irrigation and drinking purposes throughout

---

L. Singh (✉) · S. Subbarayan · J. Jacinth Jennifer · D. Abhijith · R. Sankriti  
Department of Civil Engineering, National Institute of Technology, Tiruchirappalli, Tamil Nadu, India



the year. Another objective is to reduce the peak runoff rate to reduce soil erosion and flood. Hydrological models are playing a significant and vital role in watershed to understand some aspects of behaviour (Weizenbaum (1976). Precipitation gauge data are the primary source for determining the regional weather response by interpolation methods. It is a more reliable precipitation estimate near a high rain gauge density area. However, in many regions ground observation rain gauge is not installed due to economic and limitations. In developing countries like Africa most of the areas have not installed ground observation stations and are not available in real time (Hughes 2006). It has been found that satellite, radar and topography are other options for improved spatial rainfall distribution. Many studies have used these data for hydrological applications (Li et al. 2018; Masih et al. 2009; Zhang et al. 2009). First, the tropical rainfall measuring mission (TRMM) radar-based precipitation started in 1997 (Kummerow 1998). Recently, studies evaluated the performance of satellite rainfall data in a different region (Hu et al. 2013; Dinku et al. 2008). Especially, the TRMM 3B42 product performs well than other products with a low bias percentage. A number of studies that compare the gauge vs TRMM rainfall show the analysis results for the hydrological application (Li et al. 2018; Kneis et al. 2014).

The present study works with consideration of the above studies for the application of TRMM 3B42 product in the study area. The aim of the present work is to assess the streamflow prediction with radar weather data instead of rain gauge for simulation by the SWAT model.

## 39.2 Description of the Study Area

### 39.2.1 Study Area

The Noyyal river catchment is situated in the western part of Tamil Nadu in India at an average latitude of 43 °N and an average longitude of 77.50 °E (Fig. 39.1). It covers an area of 3541.41 km<sup>2</sup>. It originates from the Wingli hills in the Western Ghats of Tamil Nadu, flowing west to east direction and draining into the Cauvery river at Noyyal. One Central Water Commission (CWC) stream gauging station at E-Managalam was selected as an outlet point. The average annual rainfall varies from 700–770 mm; the mean annual temperature is 28 °C and the mean annual discharge flow is 5.75 cumecs.

The elevation of the river catchment ranges from 134 m at the outlet point of the catchment to 1957 m at a high peak. Most slope is less than 5%. The primary types of soil are Lc76-2b-3782(Clay Loam) and Nd49-2bc-3818(Loam). The land use of catchment is mainly agricultural and pastureland.

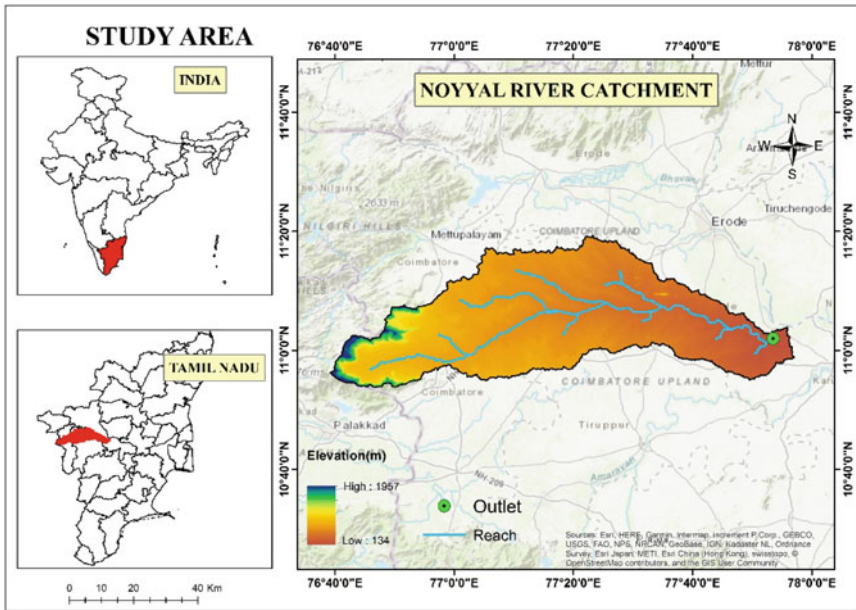


Fig. 39.1 Study area location

### 39.2.2 Data Collection

The tropical rainfall measuring mission (TRMM) radar weather data are more popular, monitored by The National Aeronautics and Space Administration NASA and Japan Aerospace Exploration Agency (JAXA) under a joint mission to study tropical rainfall. TRMM mission was launched on 27 November 1997 at Tanegashima Space Center with specific objectives, i.e., advance understanding of global energy and water cycle by providing rainfall, to understand the mechanics of tropical rainfall that affect the global circulation. TRMM generated global rainfall on a variety of weather satellites application (Huffman et al. 2010), i.e., precipitation radar (PR) and TRMM Microwave Imager (TMI), Microwave (MW) radiometer to calibrate the rainfall estimate (Ochoa et al 2014). TRMM 3B42 is the gauge-adjusted data ultra-modern version and better than all old versions (Yong et al. 2014). The daily rainfall data of the TRMM 3B42 product is used for analysis. Land-use land-cover (LULC) map is generated from LANDSAT 30 m and classified in ArcGIS environment. Soil data are collected from NBSS and LUP, Indian Council of Agricultural Research, Nagpur, India (1:50,000 scale) and Shuttle Radar Topography Mission (SRTM) 30 m downloaded from the United States Geological Survey. Monthly streamflow was collected from Central Water Commission (CWC) Department of India.

### 39.3 Methodology

#### 39.3.1 Hydrological Model

Semi-distributed process-based river-based Soil and Water Assessment Tool (SWAT) is a well-established operated model at yearly, monthly and daily scale (Arnold et al. 1998). SWAT has been developed for a long-term impact study of land management practice on water resources, stream sediment and the agricultural-chemical yield on the large watershed with various soil, land use and management practices (Neitsch et al. 2009). For modelling, SWAT divides watershed into a number of sub-watersheds or sub-basins and each sub-basin is divided into numbers of hydrological response units (HRUs), groundwater, ponds, and main channel. Each HRU acted as a lumped model comprising land, soil and management data. SWAT simulates the hydrological process in pursuance of the water balance equation Eq. (39.1):

$$SW_t = SW_0 + \sum_{i=1}^t (R_{day} - Q_{surf} - E_a - W_{seep} - Q_{gw})_i \quad (39.1)$$

where  $SW_t$  is soil water content on day  $t$  (mm),  $SW_0$  is the initial soil water content (mm),  $t$  is the time (days),  $R_{day}$  is precipitation on day  $i$  (mm),  $Q_{surf}$  is surface runoff on day  $i$  (mm),  $E_a$  is evapotranspiration  $i$  (mm),  $W_{seep}$  is water entering the vadose zone from the soil profile  $i$  (mm) and  $Q_{gw}$  is return flow  $i$  (mm). For calibration of measured discharge, the sequential uncertainty fitting (SUFI-2) algorithm using SWAT-CUP software is used. (Abbaspour et al. 2007). SUFI-2 is easy to implement. Since the sampling method in Sufi-2 is a Latin hypercube sample method, it can reduce the sample size compared to the Monte Carlo random sampling method (Wu and Chen 2015).

#### 39.3.2 SWAT Parameters

SWAT model calibration and validation is done through SWAT-CUP. During the calibration number of parameters were selected based on the literature reviews and sensitivity analysis (Woznicki and Nejadhashemi 2012). Concerning streamflow, 17 as shown in Table 39.1.

#### 39.3.3 Model Efficiency Index

The accuracy of the model is carried out in calibration and validation by the coefficient of determinate and two efficiency expressions (Moriassi et al 2007). The index are

**Table 39.1** List of SWAT model parameter and optimal value

Parameter	Lower limit	Upper limit	Optimal value
r_CN2	-0.2	0.2	-0.42
v_ALPHA_BF	0	1	0
v_GW_DELAY	0	450	322.94
v_GWQMN	0	1500	-57.39
v_ESCO	0	1	1.03
v_EPCO	0	1	0.46
v_GW_REVAP	0.02	0.2	0.17
v_REVAPMN	0	1000	327.68
a_RCHRG_DP	-0.05	0.05	0.12
r_SOL_AWC()	-0.25	0.25	0.11
r_SOL_BD()	-0.25	0.25	0.18
r_SOL_K()	-0.25	0.25	0.44
r_SOL_Z()	-0.25	0.25	-0.06
r_SURLAG	-5	5	0.85
v_CANMX	0	10	4.16
v_CH_K2	0	200	43.42
v_CH_N2	0	0.4	0.02

*Note* r multiply the existing value with (1+ given value), v for replacing the given value and adding the given value to the existing value

Nash–Sutcliffe efficiency index (NSE) and the percentage of bias (PBIAS) (Figs. 39.2 and 39.3).

## 39.4 Results and Discussion

### Hydrologic simulation

To investigate the runoff prediction obtained from the TRMM dataset, the SWAT model parameter is required to be approximated through classification. The prior model calibration parameters were identified as the most sensitive parameters in the catchment. SUFI-2 is a widely used tool for auto-calibration (Wu and Chen 2015; Zhou et al. 2014). The monthly streamflow from Jan 2000 to December 2008 was used for model calibration. Yang et al. (2008) explain the expansion steps of the optimisation algorithm of SUFI-2. The simulation was analysed by comparing the monthly observed streamflow with simulated at the station. On average, the modelled monthly streamflow matched the observed data both in the calibration period and in the verification period. The selected parameters of the SWAT model for streamflow simulation are shown in Table 39.1, which represent the lower, upper limit and

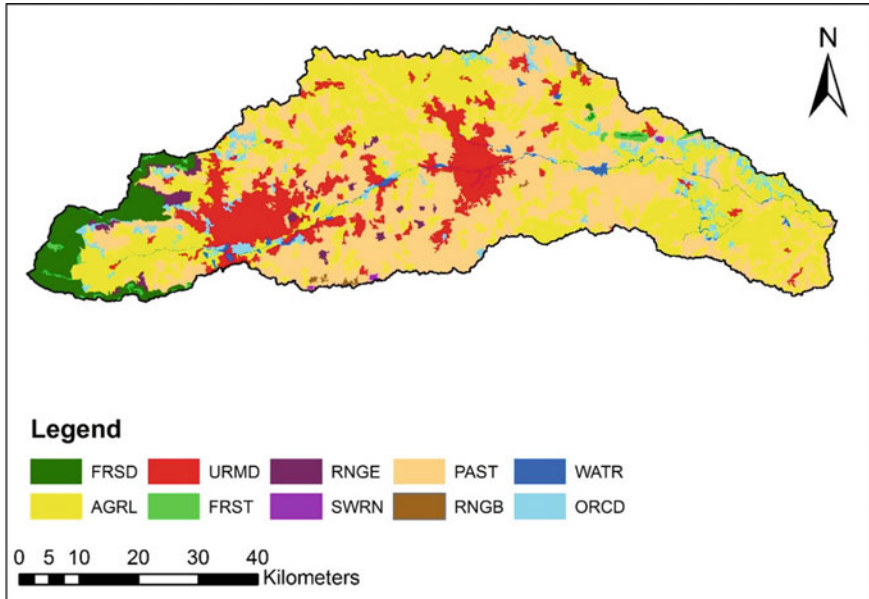


**Fig. 39.2** The land-use map of the study area. The land-use map was generated by GIS environment and classified into ten classes as follows: 1. Deciduous broadleaf forest (FRSD), 2. Agricultural land (AGRL), 3. Built-up land (URMD), 4. Mixed forest (FRST), 5. Shrubland (RNGE), 6. Barren land (SWRN), 7. Fallow land (PAST), 8. Wasteland (RNGB), 9. Water bodies (WATR), 10. Plantations (ORCD)

optimal values of soil, management, HRU, groundwater, routing and basin after the SUFI-2 algorithm calibration. After receiving proper streamflow data, the calibrated hydrological parameter was used for the validation period. The model was calibrated by considering the main objective function NSE (Table 39.2).

The sensitivity analysis was done through SWAT-CUP global sensitivity tool that uses the Latin Hypercube One-factor-At-a-Time (LH-OAT) (Griensven 2005). Sensitivity rank is based on the p-value and negative t-test value. The lowest p-value and negative t-test were assigned a high rank, while high p-value and positive t-test were assigned a low rank of the SWAT model parameter.

The goodness of fit of the model results is shown in Figs. 39.4 and 39.5. The modelled values of  $R^2$  for calibration (2000–2006) and validation (2007–2008) are 0.53 and 0.54. The results indicate that the model results produced for the streamflow are satisfactory. After successful simulation of the model NSE results for calibration and validation are 0.51 and 0.50, respectively, as shown in Table 39.3.

Results of the stream flow model showed that PBIAS is 7.5 for calibration and 1.5 for validation. Therefore, in pursuance of Moriasi et al. (2007), the SWAT model was well calibrated. Sensitivity analysis shows that the top five most sensitivity parameter is ALPHA\_BF, CH\_K2, SOL\_BD, REVAPMN, and CN2 respectively and lowest rank in simulation Groundwater “revap” coefficient (GW\_REVAP). Peak flow was

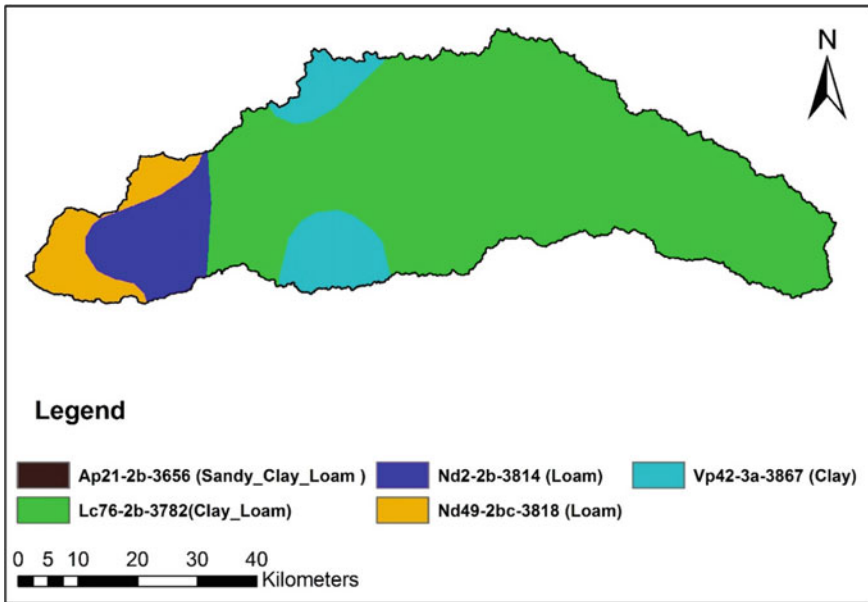


Fig. 39.3 The soil type map of the Noyyal river catchment

observed in 2004 and the lowest flow was observed in 2000. Simulation result of the model shows a good match depending upon the TRMM data. The hydrological SWAT model in many research articles, Jaikrishnan et al. (2005) and Fadil et al. (2011), has described the lack of stream flow during the peak flow events.

### 39.5 Conclusions

This study tried to identify the streamflow prediction and SWAT model parameters feasibility with radar rainfall data. Noyyal river catchment of South India, the SWAT model was calibrated using 2000–2006 discharge data at the outlet. The average Nash-Sutcliffe model efficiency of discharge were 0.51 and the average coefficient of determination ( $R^2$ ) 0.50. The result of sensitivity analysis indicates that the most sensitivity parameters are the ALPHA\_BF, CH\_K2, SOL\_BD, REVAPMN and (CN2). The present study represents that TRMM data could also be another solution for hydrological modeling globally. The performance of the SWAT model can be further enhanced by the integration of climate data such as moisture, wind speed and solar radiation. This calibrated model results can be used for understanding of watershed behaviour and determine the various hydrological processes, which dam reservoirs help to optimum use of water. Using a calibrated model is recommended to assess and manage for different similar watershed important components like water

**Table 39.2** Sensitivity analysis and rank

Parameter name	Description	t-Stat	P-Value	Sensitivity rank
GW_REVAP	Groundwater “revap” coefficient	0.028	0.978	17
SOL_K(..)	Saturated hydraulic conductivity	-0.040	0.968	16
SURLAG	Surface runoff lag time	-0.108	0.914	15
RCHRG_DP	Deep aquifer percolation fraction	-0.340	0.734	14
GW_DELAY	Groundwater delay time (days)	-0.649	0.517	13
CANMX	Maximum canopy storage	-0.934	0.351	12
CH_N2	Manning’s “n” value for the main channel	0.979	0.328	11
SOL_Z(..)	Depth from the soil surface to bottom of the layer	-1.150	0.251	8
GWQM	Threshold depth of water in the shallow aquifer required for return flow to occur (mm)	1.254	0.211	10
EPCO	Plant uptake compensation factor	1.316	0.189	9
SOL_AWC(..)	Available water capacity of soil layer (mm H <sub>2</sub> O/mm soil)	-1.668	0.096	7
ESCO	Soil evaporation compensation factor	1.777	0.076	6
CN2	Initial SCS runoff curve number for moisture condition II	-2.174	0.030	5
REVAPMN	Threshold depth of water in shallow aquifer for “revap” to occur (mm)	-2.232	0.026	4
SOL_BD(..)	Moist bulk density (g/cm <sup>3</sup> )	-6.194	0.000	3
CH_K2	Effective hydraulic conductivity in main channel alluvium (mm/h)	-12.196	0.000	2
ALPHA_BF	Baseflow alpha factor and baseflow recession constant	-13.941	0.000	1

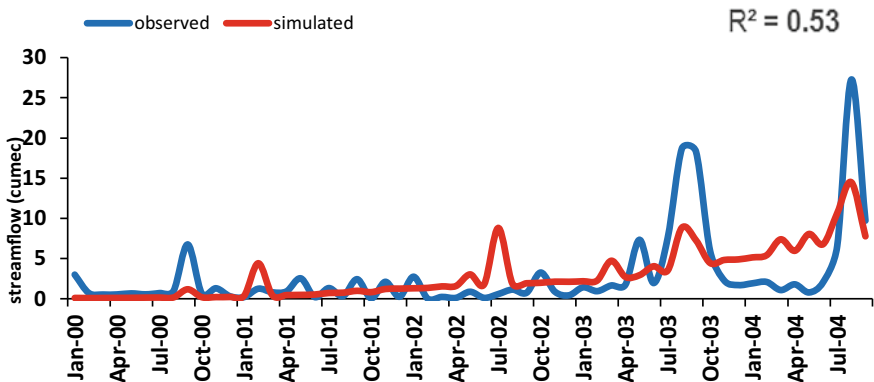


**Fig. 39.4** Monthly observed and simulated stream flow for the Calibration period (2000–2006)

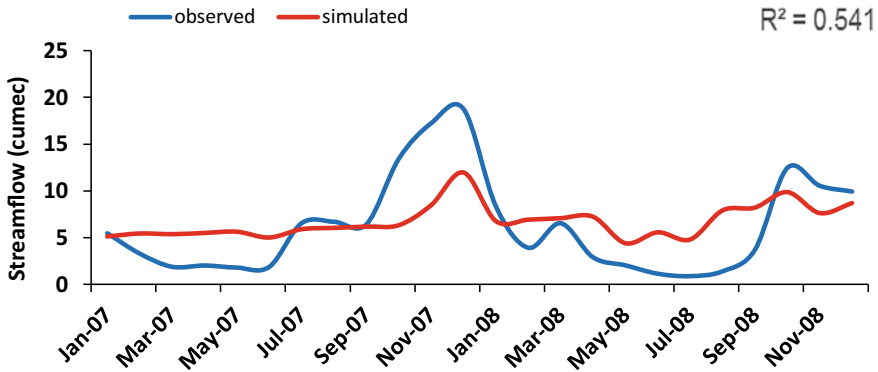


Fig. 39.5 Monthly observed and simulated stream flow for the Validation period (2007–2008)

Table 39.3 Simulation results

Coefficient	Calibration	Validation
–	2000–2006	2007–2008
R <sup>2</sup>	0.53	0.54
NSE (objective function)	0.51	0.50
PBAIS	7.5	1.5

quality, sediment and analysis of climate change and climate change analysis, along with water resources.

## References

Abbaspour KC, Yang J, Maximov I, Siber R, Bogner K, Mieleitner J, Zobrist J, Srinivasan R (2007) Modelling hydrology and water quality in the pre-alpine/alpine Thur watershed using SWATJ. Hydrol 333(2007):413–430

Arnold JG, Srinivasan R, Muttiah SR, Williams JR (1998) Large area hydrologic modelling and assessment part I. Model development 1. J Am Water Resour Assoc 34(1):73–89

Dinku T, Chidzambwa S, Ceccato P, Connor SJ, Ropelewski CF (2008) Validation of high-resolution satellite rainfall products over complex terrain. Int J Remote Sens 29:4097–4110

Fadil A, Hassan Rhinane K, Abdelhadi KY, Bachir OA (2011) Hydrologic modeling of the bouregreg watershed (morocco) using GIS and SWAT model. J Geogr Inform Syst 3(2011):279–289

Griensven AV (2005) Sensitivity, auto-calibration, uncertainty and model evaluation in SWAT, UNESCO-IHE, p 48

Habib E, Larson BF, Grascel J (2009) Validation of NEXRAD multisensor precipitation estimates using an experimental dense rain gauge network in south Louisiana. J Hydrol 373(2009):463–478. <https://doi.org/10.1016/j.jhydrol.2009.05.010>

Hu Q, Yang D, Wang Y, Yang H (2013) Accuracy and spatio-temporal variation of high resolution satellite rainfall estimate over the Ganjiang River Basin. Sci China Technol Sci 56:853–865



- Huffman G, Adler R, Bolvin D, Nelkin E (2010) The TRMM multi-satellite precipitation analysis (TMPA). In: Gebremichael M, Hossain F (eds) *Satellite rainfall applications for surface hydrology*. Springer, pp 3–22
- Hughes DA (2006) Comparison of satellite rainfall data with observations from gauging station networks. *J Hydrol* 327:399–410
- Jayakrishnan R, Srinivasan R, Santhi C, Arnold JG (2005) Advances in the application of the SWAT model for water resources management. *Hydrol Process* 19(3):749–762
- Kneis D, Chatterjee C, Singh R (2014) Evaluation of TRMM rainfall estimates over a large Indian River basin (Mahanadi). *Hydrol Earth Syst Sci* 18:2493–2502
- Kummerow C (1998) Beamfilling errors in passive microwave rainfall retrievals. *J Appl Meteorol* 37:356–370
- Li D, Christakos G, Ding X, Wu J (2018) Adequacy of TRMM satellite rainfall data in driving the SWAT modeling of Tiaoxi catchment (Taihu lake basin, China). *J Hydrol* 556:1139–1152
- Michaelides S, Levizzani V, Anagnostou E, Bauer P, Kasparis T, Lane JE (2009) Precipitation: measurement, remote sensing, climatology and modelling. *Atmos Res* 94:512–533. <https://doi.org/10.1016/j.atmosres.2009.08.017>
- Moriassi D, Arnold JD, Liew MWV, Bingner RL, Harmel RD, Veith TL (2007) Model evaluation guidelines for systematic quantification of accuracy in watershed simulations. *Trans ASABE* 50(3):885–900
- Neitsch SL, Arnold JG, Kiniry JR, Srinivasan R, Williams JR (2009) Soil and water assessment tool theoretical documentation version 2009, Temple, Texa, Grassland. Soil Water Res Lab
- Ochoa A, Pineda L, Crespo P, Willems P (2014) Evaluation of TRMM 3B42 precipitation estimates and WRF retrospective precipitation simulation over the Pacific-Andean region of Ecuador and Peru. *Hydrol Earth Syst Sci* 18:3179–3193
- Weizenbaum J (1976) *Computer power and human reason: from judgment to calculation*. W.H. Freeman, New York
- Woznicki SA, Nejadhashemi AP (2012) Sensitivity analysis of best management practices under climate change scenarios. *J Am Water Resour As* 48:90–112
- Wu H, Chen B (2015) Evaluating uncertainty estimates in distributed hydrological modeling for the Wenjing River watershed in China by GLUE, SUFI-2, and ParaSol methods. *Ecol Eng* 76:110–121
- Yang J, Reichert P, Abbaspour KC, Xia J, Yang H (2008) Comparing uncertainty analysis techniques for a SWAT application to the Chaohe Basin in China. *J Hydrol* 358(1–2):1–23
- Yong B, Chen B, Gourley JJ, Ren L, Hong Y, Chen X, Wang W, Chen S, Gong L (2014) Inter-comparison of the Version-6 and Version-7 TMPA precipitation products over high and low latitudes basins with independent gauge networks: is the newer version better in both real-time and post-real-time analysis for water resources and hydrologic ext. *J Hydrol* 508:77–87
- Zhou J, Liu Y, Guo H, He D (2014) Combining the SWAT model with sequential uncertainty fitting algorithm for streamflow prediction and uncertainty analysis for the Lake Dianchi Basin. *China Hydrol Process* 28(2014):521–533. <https://doi.org/10.1002/hyp.9605>